WOODHEAD PUBLISHING SERIES IN ELECTRONIC AND OPTICAL MATERIALS

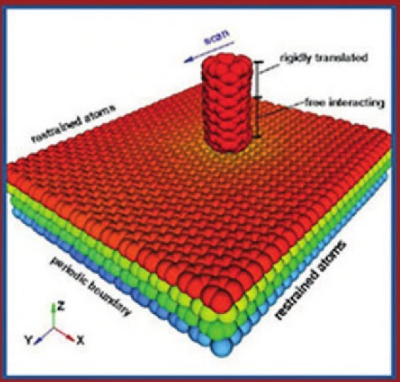

Modeling, Characterization and Production of Nanomaterials

Electronics, Photonics and Energy Applications

Edited by Vinod K. Tewary and Yong Zhang

WP
WOODHEAD PUBLISHING

List of contributors

D. Balzar University of Denver, Denver, CO, USA

D.M. Bortz University of Colorado, Boulder, CO, USA

B. Cao University of New Orleans, New Orleans, LA, USA

D. Casimir Howard University, Washington, DC, USA

J. Chen University of New Orleans, New Orleans, LA, USA

C.V. Ciobanu Colorado School of Mines, Golden, CO, USA

H. Cronk State University of New York at Binghamton, Binghamton, NY, USA

M.M. De Souza University of Sheffield, Sheffield, UK

J. DeJoannis Accelrys, Inc., Burlington, MA, USA

J. Eymery Univ. Grenoble Alpes, Grenoble, France; CEA, INAC-SP2M, Grenoble, France; CEA-CNRS-UJF group "Nanophysics and Semiconductors", Grenoble, France

G. Fitzgerald Accelrys, Inc., San Diego, CA, USA

R. Garcia-Sanchez Howard University, Washington, DC, USA

B. Gittleman Applied Science and Technology Consulting LLC, Centennial, CO, USA

M.K. Harbola Indian Institute of Technology Kanpur (IITK), Kanpur, India

L. Hu Jiangnan University, Wuxi, PR China

M. Hu RWTH Aachen University, Aachen, Germany

P. Joseph State University of New York at Binghamton, Binghamton, NY, USA

N. Kang State University of New York at Binghamton, Binghamton, NY, USA

D. Le Si Dang Univ. Grenoble Alpes, Grenoble, France; CNRS, Institut Néel, Grenoble, France; CEA-CNRS-UJF group "Nanophysics and Semiconductors", Grenoble, France

G. Li Northeastern University, Shenyang, China

J. Li State University of New York at Binghamton, Binghamton, NY, USA

J. Luo State University of New York at Binghamton, Binghamton, NY, USA

E. Mansfield National Institute of Standards and Technology, Boulder, CO, USA

M. Meunier Accelrys Limited, Cambridge, UK

P. Misra Howard University, Washington, DC, USA

A. Mookerjee S N Bose National Centre for Basic Sciences, Kolkata, India

P. Pillai University of Sheffield, Sheffield, UK

L. Rast National Institute of Standards and Technology, Boulder, CO, USA

S. Shan State University of New York at Binghamton, Binghamton, NY, USA

P. Singh Ames Laboratory, Ames, IA, USA

Z. Skeete State University of New York at Binghamton, Binghamton, NY, USA

A. Smolyanitsky National Institute of Standards and Technology, Boulder, CO, USA; NIST Center for Nanoscale Science, and Technology (CNST), Gaithersburg, MD, USA

M. Stowell Advanced Technologies Group, Applied Materials, Santa Clara, CA, USA

V.K. Tewary National Institute of Standards and Technology, Boulder, CO, USA

K. Wang Northeastern University, Shenyang, China

K. Wang University of New Orleans, New Orleans, LA, USA

Q. Wang Northeastern University, Shenyang, China

H. Wu Zhejiang University, Hangzhou, PR China

J. Wu State University of New York at Binghamton, Binghamton, NY, USA

S. Yan State University of New York at Binghamton, Binghamton, NY, USA

N. Yue The University of North Carolina at Charlotte, Charlotte, NC, USA

Y. Zhang The University of North Carolina at Charlotte, Charlotte, NC, USA

W. Zhao State University of New York at Binghamton, Binghamton, NY, USA

Y. Zhao State University of New York at Binghamton, Binghamton, NY, USA

C.-J. Zhong State University of New York at Binghamton, Binghamton, NY, USA

W. Zhou University of New Orleans, New Orleans, LA, USA

S. Zhuiykov CSIRO, Materials Science and Engineering Division, Highett, VIC, Australia

Modeling, Characterization and Production of Nanomaterials

Related titles

Semiconductor nanowires: Materials, synthesis, characterization and applications
(ISBN 978-1-78242-253-2)

Nanosensors for chemical and biological applications: Sensing with nanotubes, nanowires and nanoparticles
(ISBN 978-0-85709-660-9)

Handbook of magnetic nano- and microwires
(ISBN 978-0-08100-164-6)

Woodhead Publishing Series in Electronic and Optical Materials: Number 73

Modeling, Characterization and Production of Nanomaterials

Electronics, Photonics and Energy Applications

Edited by

Vinod K. Tewary and Yong Zhang

AMSTERDAM • BOSTON • CAMBRIDGE • HEIDELBERG
LONDON • NEW YORK • OXFORD • PARIS • SAN DIEGO
SAN FRANCISCO • SINGAPORE • SYDNEY • TOKYO
Woodhead Publishing is an imprint of Elsevier

Woodhead Publishing Series in Electronic and Optical Materials

1 **Circuit analysis**
J. E. Whitehouse
2 **Signal processing in electronic communications: For engineers and mathematicians**
M. J. Chapman, D. P. Goodall and N. C. Steele
3 **Pattern recognition and image processing**
D. Luo
4 **Digital filters and signal processing in electronic engineering: Theory, applications, architecture, code**
S. M. Bozic and R. J. Chance
5 **Cable engineering for local area networks**
B. J. Elliott
6 **Designing a structured cabling system to ISO 11801: Cross-referenced to European CENELEC and American Standards**
Second edition
B. J. Elliott
7 **Microscopy techniques for materials science**
A. Clarke and C. Eberhardt
8 **Materials for energy conversion devices**
Edited by C. C. Sorrell, J. Nowotny and S. Sugihara
9 **Digital image processing: Mathematical and computational methods**
Second edition
J. M. Blackledge
10 **Nanolithography and patterning techniques in microelectronics**
Edited by D. Bucknall
11 **Digital signal processing: Mathematical and computational methods, software development and applications**
Second edition
J. M. Blackledge
12 **Handbook of advanced dielectric, piezoelectric and ferroelectric materials: Synthesis, properties and applications**
Edited by Z.-G. Ye
13 **Materials for fuel cells**
Edited by M. Gasik
14 **Solid-state hydrogen storage: Materials and chemistry**
Edited by G. Walker
15 **Laser cooling of solids**
S. V. Petrushkin and V. V. Samartsev
16 **Polymer electrolytes: Fundamentals and applications**
Edited by C. A. C. Sequeira and D. A. F. Santos
17 **Advanced piezoelectric materials: Science and technology**
Edited by K. Uchino

18 **Optical switches: Materials and design**
Edited by S. J. Chua and B. Li
19 **Advanced adhesives in electronics: Materials, properties and applications**
Edited by M. O. Alam and C. Bailey
20 **Thin film growth: Physics, materials science and applications**
Edited by Z. Cao
21 **Electromigration in thin films and electronic devices: Materials and reliability**
Edited by C.-U. Kim
22 ***In situ* characterization of thin film growth**
Edited by G. Koster and G. Rijnders
23 **Silicon-germanium (SiGe) nanostructures: Production, properties and applications in electronics**
Edited by Y. Shiraki and N. Usami
24 **High-temperature superconductors**
Edited by X. G. Qiu
25 **Introduction to the physics of nanoelectronics**
S. G. Tan and M. B. A. Jalil
26 **Printed films: Materials science and applications in sensors, electronics and photonics**
Edited by M. Prudenziati and J. Hormadaly
27 **Laser growth and processing of photonic devices**
Edited by N. A. Vainos
28 **Quantum optics with semiconductor nanostructures**
Edited by F. Jahnke
29 **Ultrasonic transducers: Materials and design for sensors, actuators and medical applications**
Edited by K. Nakamura
30 **Waste electrical and electronic equipment (WEEE) handbook**
Edited by V. Goodship and A. Stevels
31 **Applications of ATILA FEM software to smart materials: Case studies in designing devices**
Edited by K. Uchino and J.-C. Debus
32 **MEMS for automotive and aerospace applications**
Edited by M. Kraft and N. M. White
33 **Semiconductor lasers: Fundamentals and applications**
Edited by A. Baranov and E. Tournie
34 **Handbook of terahertz technology for imaging, sensing and communications**
Edited by D. Saeedkia
35 **Handbook of solid-state lasers: Materials, systems and applications**
Edited by B. Denker and E. Shklovsky
36 **Organic light-emitting diodes (OLEDs): Materials, devices and applications**
Edited by A. Buckley
37 **Lasers for medical applications: Diagnostics, therapy and surgery**
Edited by H. Jelínková
38 **Semiconductor gas sensors**
Edited by R. Jaaniso and O. K. Tan
39 **Handbook of organic materials for optical and (opto)electronic devices: Properties and applications**
Edited by O. Ostroverkhova
40 **Metallic films for electronic, optical and magnetic applications: Structure, processing and properties**
Edited by K. Barmak and K. Coffey
41 **Handbook of laser welding technologies**
Edited by S. Katayama
42 **Nanolithography: The art of fabricating nanoelectronic and nanophotonic devices and systems**
Edited by M. Feldman
43 **Laser spectroscopy for sensing: Fundamentals, techniques and applications**
Edited by M. Baudelet

44 **Chalcogenide glasses: Preparation, properties and applications**
Edited by J.-L. Adam and X. Zhang
45 **Handbook of MEMS for wireless and mobile applications**
Edited by D. Uttamchandani
46 **Subsea optics and imaging**
Edited by J. Watson and O. Zielinski
47 **Carbon nanotubes and graphene for photonic applications**
Edited by S. Yamashita, Y. Saito and J. H. Choi
48 **Optical biomimetics: Materials and applications**
Edited by M. Large
49 **Optical thin films and coatings**
Edited by A. Piegari and F. Flory
50 **Computer design of diffractive optics**
Edited by V. A. Soifer
51 **Smart sensors and MEMS: Intelligent devices and microsystems for industrial applications**
Edited by S. Nihtianov and A. Luque
52 **Fundamentals of femtosecond optics**
S. A. Kozlov and V. V. Samartsev
53 **Nanostructured semiconductor oxides for the next generation of electronics and functional devices: Properties and applications**
S. Zhuiykov
54 **Nitride semiconductor light-emitting diodes (LEDs): Materials, technologies and applications**
Edited by J. J. Huang, H. C. Kuo and S. C. Shen
55 **Sensor technologies for civil infrastructures**
Volume 1: Sensing hardware and data collection methods for performance assessment
Edited by M. Wang, J. Lynch and H. Sohn
56 **Sensor technologies for civil infrastructures**
Volume 2: Applications in structural health monitoring
Edited by M. Wang, J. Lynch and H. Sohn
57 **Graphene: Properties, preparation, characterisation and devices**
Edited by V. Skákalová and A. B. Kaiser
58 **Silicon-on-insulator (SOI) technology**
Edited by O. Kononchuk and B.-Y. Nguyen
59 **Biological identification: DNA amplification and sequencing, optical sensing, lab-on-chip and portable systems**
Edited by R. P. Schaudies
60 **High performance silicon imaging: Fundamentals and applications of CMOS and CCD sensors**
Edited by D. Durini
61 **Nanosensors for chemical and biological applications: Sensing with nanotubes, nanowires and nanoparticles**
Edited by K. C. Honeychurch
62 **Composite magnetoelectrics: Materials, structures, and applications**
G. Srinivasan, S. Priya and N. Sun
63 **Quantum information processing with diamond: Principles and applications**
Edited by S. Prawer and I. Aharonovich
64 **Advances in non-volatile memory and storage technology**
Edited by Y. Nishi
65 **Laser surface engineering: Processes and applications**
Edited by J. Lawrence, C. Dowding, D. Waugh and J. Griffiths
66 **Power ultrasonics: Applications of high-intensity ultrasound**
Edited by J. A. Gallego-Juárez and K. F. Graff
67 **Advances in delay-tolerant networks (DTNs): Architectures, routing and challenges**
Edited by J. J. P. C. Rodrigues

68 **Handbook of flexible organic electronics: Materials, manufacturing and applications**
Edited by S. Logothetidis
69 **Machine-to-machine (M2M) communications: Architecture, performance and applications**
Edited by C. Anton-Haro and M. Dohler
70 **Ecological design of smart home networks: Technologies, social impact and sustainability**
Edited by N. Saito and D. Menga
71 **Industrial tomography: Systems and applications**
Edited by M. Wang
72 **Vehicular communications and networks: Architectures, protocols, operation and deployment**
Edited by W. Chen
73 **Modeling, characterization and production of nanomaterials: Electronics, photonics and energy applications**
Edited by V. K. Tewary and Y. Zhang
74 **Reliability characterisation of electrical and electronic systems**
Edited by J. Swingler
75 **Handbook of industrial wireless sensor networks: Monitoring, control and automation**
Edited by R. Budampati S. Kolavennu
76 **Epitaxial growth of complex metal oxides: Techniques, properties and applications**
Edited by G. Koster, G. Rijnders and M. Huijben
77 **Semiconductor nanowires: Materials, synthesis, characterization and applications**
Edited by J. Arbiol and Q. Xiong
78 **Superconductors in the Power Grid**
Edited by C. Rey
79 **Optofluidics, sensors and actuators in microstructured optical fibres**
Edited by S. Pissadakis
80 **Handbook of Magnetic Nano- and Microwires**
Edited by M. Vázquez
81 **Robust design of microelectronic assemblies against mechanical shock, temperature and moisture**
E-H. Wong and Y-W. Mai
82 **Biomimetic technologies: Principles and applications**
Edited by T. D. Ngo
83 **Directed self-assembly of block co-polymers for nano-manufacturing**
Edited by R. Gronheid and P. Nealey

Index

Note: Page numbers followed by *f* indicate figures and *t* indicate tables.

A

Abinit, 356
Accurate viscosity model, 428
Adaptive intermolecular reactive empirical bond order (AIREBO), 184
AGNR. *See* Armchair-edge graphene nanoribbon (AGNR)
Akaike Information Criterion (AIC), 429–430
Alcohol fuel cells. *See* Direct ethanol fuel cells (DEFCs)Direct methanol fuel cells (DMFCs)
Alloy nanoparticles
  behavior (*see* Atomic behavior)
  elements selection, 235–236
  interaction potential, 234–235
  molecular dynamics procedure, 234
  properties, 233
  segregation (*see* Atomic segregation)
AMBER forcefield, 32
Ambipolar transport, 489
Anharmonic lattice dynamics (ALD) method, 452–453
Anisotropic continuum theory, 56
Annular bright-field (ABF) imaging technique, 115–116
Armchair-edge graphene nanoribbon (AGNR), 209–210
Atomic behavior
  bond order parameter W_6, 241, 242–243, 243*f*
  cluster morphology, 245–246, 246*f*
  coalesced cooling process, 245, 245*f*
  cooling clusters, 247–248, 248*f*
  cooling rate, 244
  cuboctahedral nanoparticles, 241
  Cu-Co alloy nanoparticle structures, 244, 245
  Cu content and atomic distribution, 248
  different atomic diffusion, 241–242, 242*f*
  frozen structures, 241–242, 242*f*, 243–244, 243*f*
  mode of controlling, 248
  PDF, 246, 247*f*
  spherical cutoff radii, 244
  structural transformation, 244
  surface energy, 244
Atomic force microscopy (AFM), 98–99, 99*f*, 102
Atomic layer deposition (ALD), 481–482
  cycle of, 514–515
  MoS_2 nanosheet-based transistor, 481–482, 483*f*
  self-limiting film growth mechanism, 514
  temperature range, 515
  2D Al_2O_3 layer, 515
  2D sandwich nanostructures, 513–514
Atomic segregation
  Ag-core nanoparticle, 236
  Ag-surface nanoparticle, 236
  bond order parameter, 240–241, 240*f*
  energy and atomic numbers, 237–238, 238*f*
  icosahedral-decahedral structural, 241
  simulated and fitted energy, 238, 239*f*
  temperature dependence, 239–240, 239*f*
  temperature-energy curves, 236–237, 237*f*
  variation, 240–241
Atomistic modeling
  BTE, 446
  classical MD simulations, 445–446
  Green's function, 445
  interfacial thermal resistance (*see* Interfacial thermal resistance)
  lattice dynamics, 445, 447*t*
  material research, 443–444
  multiscale simulation, 446–447
  thermal conductivity (*see* Thermal conductivity)
  thermoelectric materials, 444
  transistor power density, 444
Au-core/Pt-shell model, 268*f*

B

Band-gap calculations
  density-functional theory and derivative discontinuity, 408–409
  graphene and hexagonal boron nitride, 414–415
  HS potential, 411–412
  Kohn-Sham potential, 408–411
  vLB potential, 412–414
Band-to-band tunneling (BTBT) current, 216, 217, 217*f*
Bayesian model selection, 430
Begrenzung effect, 360–362
Black phosphorus FETs
  anisotropic structure, 504
  band structure, 504, 505*f*
  configuration, 504–505, 506*f*, 507
  graphene and MoS_2, 507
  structural anisotropy, 504
Boltzmann inversion, 19
Boltzmann/random distribution, 8
Boltzmann transport equation (BTE), 445, 446
Bond order-length-strength (BOLS) mechanism, 185, 192–193
Born-Oppenheimer approximation, 5
Born's method, 71, 78–79
Born von Karman (BvK) model, 64–65
Bose-Einstein statistics, 102
Bravais lattice, 65
Bright field (BF) imaging, 115–116
Brillouin zone, 67
Brownian motion, 421
Bulk nanostructured materials, 449–450

C

Carbon-based nanostructures, 12
Carbon nanotube (CNT), 12, 38–41, 41*f*, 171–172, 175–176, 455–456
  arc discharge, 180
  armchair tubes, 208, 209*f*
  atomic force microscopy, 183
  CVD, 179
  vs. graphene nanoribbon, 224–225, 225*f*
  hexagonal arrays, 182
  laser ablation, 180
  mechanical properties, 182
  metallic and semiconducting nanotubes, 209, 210*f*
  MWCNT, 182
  structural properties, 181–182
  SWCNT, 182–183
  tensile stiffness value, 182
  tunnel FET (*see* Carbon nanotubes tunnel FETs (CNT-TFET))
  Young's moduli, 182–183
  zigzag, 209
Carbon nanotubes tunnel FETs (CNT-TFET)
  aggressive scaling, 218
  BTBT, 216, 217*f*
  carbon-based materials, 220–221
  CMOS-compatible method, 221
  diameter-dependent bandgap, 221–222
  vs. MOSFET, 223, 224*f*
  NANOTCAD ViDES, 222
  n-type and p-type, 218–220
  ON and OFF-state performance, 216, 217*f*, 220–221, 220*f*
  on-state current and inverse subthreshold slope, 218–220
  parameters, 218, 218*t*
  purification methods, 221
  Schottky barrier, 220–221
  simulated transfer characteristics, 222, 223*f*
  spectroscopic measurements, 221–222, 222*f*
  strategies/device architectures, 218, 219*t*
  tunneling mechanism, 216
Carbon-vapor-deposition (CVD), 94–95, 179
Cartesian frame of reference, 65
Catalysts, 30–31
Catalytic CO oxidation
  dealloying, 272
  downstream process, 272
  factors, 275–276
  probe molecule, 272
  Pt-based nanoalloy properties, 274*f*, 275
  PtNiCo/C and PtIrCo/C catalysts, 274*f*, 275
  reaction rates, 273, 274*f*
  self-tunable oxophilicity and structural integrity, 275
  in situ HE-XRD/PDF, 275

type-I sites, 272–273, 273*f*
type-II sites, 272–273, 273*f*
water gas shift reaction, 272
CdSe/ZnTe core-shell nanowires, 133–134, 133*f*
CGMD. *See* Coarse-grained molecular dynamics (CGMD)
CHARMM forcefield, 32
Chemical vapor deposition (CVD), 491–493
Christoffel matrix, 72
Coarse-grained molecular dynamics (CGMD)
forcefields, 14–15
lipid component, 33
mesoscale modeling, 12–14
Newtonian dynamics, 17–18
parameters, 18
potential energy, 16–17
Coaxial core-shell nanowires
CdSe/ZnTe nanowires, 133–134, 133*f*
ZnO/ZnSe and ZnO/ZnS, 130–132, 131*f*, 132*f*
CoCo model, 265–266, 265*t*
Cohesive energy density (CED), 11
COMPASS forcefield, 26, 27
Computational modeling
asymmetric capped decahedron, 271–272
complex phase properties, 270
DFT-calculated lattice constants, 270, 271*f*
lattice expansion and shrinking, 275–276
Mackay icosahedron, 271–272
molecular dynamics simulations, 271–272
nanoscale phase evolution, 270
Pt-core/Au-shell structure, 271–272
spin-polarized DFT method, 270, 271*f*
Vienna *Ab initio* Simulation Package, 270
Configuration interaction (CI) method, 5–6
Consistent valence forcefield (CVFF), 10*f*
Continuum GF (CGF), 71
Continuum theory, 56–57
Convergent beam electron diffraction (CBED), 117–118, 119–120
Core-shell InGaN/GaN multi-quantum-well heterostructures
ammonia flux, 325
Ga-polar orientation, 324–325
"green-gap,", 330
homogeneous c-axis GaN wires and heterostructures, 324
light extraction, 330
multi-color devices, 330
nano-characterization
APT reconstruction, 328–329
EBIC, 329
EDS, 327–328
EELS, 327–328
emission properties, 328–329
IDB, 328–329
quantum confinement, 330
quantum well geometry and strains, 327–328
Raman spectroscopy, 327
X-ray diffraction measurement, 327
optical and structural properties, 324
quantum-confined Stark effect, 324
sidewall emission, 325–326
top-down and bottom-up-approaches, 324
Core-shell type nanostructure, 256
Coupled-cluster calculations with single and double excitations (CCSD), 6
Coupled-cluster methods, 6
3C-SiC thin film
laser-induced conversion, 340–344
Si (111), MBE, 337–339

D

Dark-field (DF) imaging, 115–116
Datta's approach, 205–206
Debye-Hückel interaction, 14
Debye-Hückel screening approximation, 33
DEFC. *See* Direct ethanol fuel cells (DEFCs)
Density functional theory (DFT), 6–7, 255–256, 407
Abinit, 356
DFT computation (*see* Computational modeling)
electron energy loss function calculations, 355
exchange-correlation functional, 354–355
GPAW, 356
local density approximation, 353–354
optical limit, 355
Quantum ESPRESSO, 356
SIESTA, 355
VASP, 356

Density of states (DOS), 35
  circular coordinates, 212
  definition, 210–211
  delta function, 211, 212–213
  Fermi functions, 210–211, 213
  Van-Hove singularities, 213
  zigzag nanotube *vs*. 2D graphene sheet, 211, 211*f*
Differential scanning calorimetry (DSC), 169–170
  chemical composition, 172
  indomethacin, 170–171
  nanocomposites, 173
  oxidation temperature, 171–172
  size and morphology, 170–171
Dirac delta function, 61, 67
Dirac points, 450–451
Direct ethanol fuel cells (DEFCs), 254–255
  applications, 276
  catalytic selectivity data, 278–279
  C-C bond cleavage, 278
  CO_2 product release, 279, 279*f*
  design and control, 276
  electrocatalytic activity, 279
  high efficiency, 276, 278
  high power density, 276
  light weight, 276
  low cost, 276
  low pollution, 276
  PdCu alloy catalysts, 278–279
Direct methanol fuel cells (DMFCs), 254–255
  applications, 276
  electrocatalytic activity, 279
  enhance fuel sustainability, 276
  EOR, 276
  fuel utilization and cell performance, 276
  HE-XRD/PDF techniques, 276
  high conversion efficiency, 276
  high power density, 276
  light weight, 276
  low cost, 276
  low pollution, 276
  mass activity, 276, 277*f*
  open-circuit conditions, 276
  relative Pt-specific mass activity, 276–278
  safety improvement, 276
  surface adsorption and hydrogenation, 276, 277*f*
  synergistic effect, 276–278, 277*f*
Discrete lattice theory, 57
Dissipative particle dynamics (DPD) method
  atomistic forcefield calculations, 40, 41*f*
  Brownian forces, 18
  Flory-Huggins theory, 14
  "hard and sticky" particle model, 13
  inter-particle force, 16
  Newtonian dynamics, 17
  nonionic surfactants, 32
  parameterization, 19
Divide and conquer (DC), 7
DMFC. *See* Direct methanol fuel cells (DMFCs)
Donnan approximations, 33
Double tip nanoneedles, 118, 119*f*
DPD method. *See* Dissipative particle dynamics (DPD) method
Dreiding forcefield, 10–11
Duffin's lemma, 71
Dynamic density functional theory (DDFT)
  dynamics, 18
  parameterization, 18, 19
  PS-b-PB polymer, 34*f*
  use of, 33
Dynamic light scattering (DLS), 420
Dynamic ram (DRAM) cells, 399–401
Dyson equation, 70

E

EAM. *See* Embedded atom method (EAM)
Electric polarization effects, 56
Electron beam induced current (EBIC) measurements, 329
Electron-correlated methods, 5–6
Electron energy loss spectroscopy (EELS), 115–116
Embedded atom method (EAM), 31, 234–235
Energy conversion efficiency, 444
Energy dispersive X-ray spectroscopy (EDS), 115–116
EOR. *See* Ethanol oxidation reaction (EOR)
Equilibrium molecular dynamics (EMD) simulation, 445–446
Ethanol oxidation reaction (EOR), 276
Exchange-correlation energy, 6

F

Fabrication methods
  ALD (*see* Atomic layer deposition (ALD))
  2D nanocrystals, 508–513
Fast Fourier transformations (FFT), 126–127
Faujasite (FAU), 28, 29*f*
Field-effect transistor (FET), 481
Finite element methods (FEM), 21, 424–426
Fischer-Tropsch catalysts, 29
Flocculation model, 421–423
Flory-Huggins theory, 14
Flux method, 426–427
Fock matrix, 5
Fock operator, 6
Force-constant matrix, 65–66, 69–70
Forcefields
  AMBER forcefield, 32
  classical mechanics, 10–11, 10*f*
  consistent valence forcefield, 10*f*
  dreiding forcefield, 32
  GROMOS/Berger, 32
  MARTINI forcefield, 14, 17
  mesoscale modeling, 14–15
  Monte Carlo simulation, 9
  PCFF, 39*f*
  Shinoda forcefield, 14–15
Force-matching method, 19
Fourier transforms, 61, 62, 67
Fragment molecular orbital (FMO) method, 7
Friction force, 99, 100*f*
Friedel's law, 117–118
Full width at half maximum (FWHM), 394–395

G

Galderma modeled nonionic surfactants, 33
Gelation, 423
GF method. *See* Green's function (GF) method
Graphene, 12, 25, 25*f*, 180–181, 180*f*. *See also* Graphite
  AFM topography, 343*f*
  dynamic ripples, 102–106, 103*f*
  EELF, 361*f*, 362*f*
  few-layer-graphene, 341–343
  graphene nanostructures, 337
  HOPG, 341–343
  LLG techniques, 337
  Raman spectrum, 340–341
  SEM surface morphology, 339*f*
  TEM micrograph, 343*f*
Graphene nanoribbons (GNRs), 94–95, 95*f*, 96–98, 97*f*, 461–462
Graphite
  Brillouin zone, 207, 208*f*
  Datta's approach, 205–206
  Dirac points, 207
  energy dispersion curve, 207
  graphene unit cell, 204–205
  hexagonal structure, 204, 204*f*
  nanoribbons, 209–210
  Schrodinger equation, 204–205
  valence and conduction bands, 206
  vector distances, 204*f*, 205–206
  wave function, 204–205
Graphitic nanomaterials
  graphene, 180–181, 180*f*
  Raman spectroscopy, 184–186
  simulation techniques (*see* Molecular dynamics (MD))
  thermal expansion (*see* Carbon nanotube (CNT))
Green's function (GF) method
  atomistic potential models, 445
  bridging length scales, 55–56
  characteristics of, 63
  Dirac delta function, 61
  discrete lattice model, 63–68
  Fourier transforms, 61, 62
  GFMD, 73–75
  LSGF, 68–71
  MSGF method, 58, 59, 71–73
  response function, 59
  spring constant φ, 59–60, 60*f*
  time scales, 57–58
  2D graphene application, 76–81, 77*f*, 80*f*

H

Hagen-Poiseuille flow, 422
Hamiltonian matrix sparse, 6–7
Harbola-Sahni (HS) potential, 411–412
Hartree-Fock-Roothan (HFR) method, 5
Hartree-Fock theory, 5, 6
Hexagonal boron nitride, 360–362
Hierarchical methods, 20–21

High angle annular dark-field (HAADF) images, 115–116
Highest occupied molecular orbital (HOMO), 408
High-resolution transmission microscopy (HRTEM) imaging, 115–116, 120, 121*f*
Homotopy analysis methods (HAMs), 430
Hybrid methods, 21–22, 21*f*
Hybrid QM/MM methods, 29

I

InGaN/GaN core-shell, 325–326
Inorganic nanostructures
  catalysts, 30–31
  MOFs, 29–30, 30*f*
  zeolites, 28–29
Interfacial thermal resistance
  CNT, 455–456
  research motivation, 454–455
  solid-liquid interfaces, 456–457
Isothermal titration calorimetry (ITC), 170

K

Kanzaki force, 71, 73
Kinetic friction, 98–102
Kinetic Monte Carlo (KMC), 30
Koch-Friedlander predictions, 424
Kohn-Sham (KS) potential, 408–411
Kullback-Leibler (KL) divergence, 429–430

L

LAMMPS, 91
Landauer formalism, 92–94
Langevin dynamics, 14
Langevin thermostat, 98–99
Lattice-Boltzmann (LB), 13
Lattice defects, 56
Lattice dynamics, 445, 447*t*
Lattice models, 14
Lattice statics Green's function (LSGF), 68–71
Lipids, 31–33
Liposomes, 31
Lithium-ion battery, 36–38, 37*f*
Low-density linear polyethylene (LLDPE), 35–36
Lowe-Andersen thermostat, 18

M

Magneto-hydrodynamic (MHD) nanofluid, 430
Many-body perturbation theory (MBPT), 6
MARTINI forcefield, 14–15, 15*f*, 16*f*, 17, 18–19, 32
Mathematical Principles of Natural Philosophy, 7
MD simulation. *See* Molecular dynamics (MD)
Mean time to failure (MTTF), 395, 396
Mermin-Wagner theorem, 102
Mesoscale models, 12–20, 13*f*
Metal-ligand binding, 21–22
Metal-organic frameworks (MOFs), 29–30, 30*f*
Metal-organic vapor phase epitaxy (MOVPE)
  core-shell InGaN/GaN MQWs heterostructures (*see* Core-shell InGaN/GaN multi-quantum-well heterostructures)
  electron microscopy techniques, 327–328
  GaN micropillars, 328–329
  reactor geometries, 325
  on sapphire substrates, 329
  sidewall emission, 325–326
Method of moments (MOM), 427
Model selection criteria (MSC), 429
Modified embedded atom method (MEAM), 90–91
Molecular dynamics (MD), 8–9, 12, 88–91, 445–446, 447*t*
  algorithm, 187–188
  atomic-level stress tensor, 195
  atomistic modeling, 58
  dynamic ripples in graphene, 102–106, 103*f*
  equations of motion, 189–190
  force computation, 189
  initial conditions and parameters, 188–189
  interatomic potential, 190
  kinetic friction, 101
  MEAM/Tersoff-Brenner potentials, 90–91
  Newton's second law of motion, 88–89
  nonbonded Lennard-Jones cutoff, 196, 196*t*
  potential energy, 88–89
  sampling geometry, 196, 197*f*

sampling phase, 195
simple velocity rescaling, 196
thermodynamic quantities, 190
X-ray diffraction, 195–196
Molecular mechanics, 8
Molecular orbitals (MOs), 5
Molecular statics (MS)
GNRs, 94–95, 95*f*, 96–98
MEAM or Tersoff-Brenner potentials, 90–91
potential energy, 88–89
SWCNTs, 92, 93*f*, 94*f*
Moller-Plesset (MP) perturbation, 6
Molybdenum disulfide (MoS_2) nanocrystals
crystal phase and electronic band structures, 484, 486*f*
fabrication of, 481–482, 483*f*
FET, 481
fluorine-doped tin oxide (FTO) substrates, 486–487
optical and PL properties, 486, 487*f*
photoluminescence (PL) effect, 481
structure and AFM imaging, 481, 482*f*
thickness-modulated phototransistor, 483*f*, 484
transfer characteristic, 484, 485*f*
UV-vis-NIR absorption spectra, 484–486
XPS measurements, 487–489, 488*f*
MOM with interpretive closure (MoMIC), 427
Monte Carlo (MC) method, 9, 446
Multiparticle collision dynamics (MPC), 13
Multiple quantum wells (MQWs), 323. *See also* Core-shell InGaN/GaN multi-quantum-well heterostructures
Multiple quantum wells (MQWs), 323
Multiscale Green's function (MSGF) method, 58, 59, 71–73

N

Nanoalloy (NA) catalysts
alcohol fuel cells, 254–255
binary and ternary systems, 253–254, 254*f*
CO and alcohol oxidation reactions, 254
DFT, 255–256
encapsulated nanoparticles, 258–259
Griffith and Pauling configurations, 255–256
HE-XRD/PDF study, 260–261
HRTEM and EDS composition mapping, 259, 260*f*
metal nanocrystal cores, 258–259
PDF analysis, 261–262, 261*f*
reactor-type cell, 261–262
strong metal-support interaction, 254
synthesis, 256–258
ternary PtVFe particles, 255–256
thermal treatment, 258–259
thermochemical process, 258–259, 258*f*
XAFS spectra, 262
XANES spectra, 260–261
Nanoparticle self-assembly
DLS, 420
finite element method, 424–426
flocculation phenomena, 421–423
flux method, 426–427
maximum likelihood estimator (MLE), 428
method of moments (MOM), 427
model selection criteria (MSC), 429
nanofluid model, 428–430
nanofluids, 430–431
PBEs, 423, 424
PSDs, 423
sectional methods (SM), 428
Nanopatterned devices
α-Ta concentration, 376*f*
Cu electroplating, 372
Cu recrystallization, 376
deposition technology, 371–372
electromigration reliability, 372
iPVD technology and Cu interconnects, 398–399
metrology techniques, 394–397
microwave PECVD technology, 390–394
MW-PECVD SiO_2, 381*f*, 391*f*
MW-PECVD technology, 399
oxide films, 379
SiO_2 deposition, 379–380, 399
stress migration, 372–375, 373*f*
Ta depositions, 372
transmission electron micrographs, 372–375
trench orientation, 374*f*
upper insulating layer, 377–378
upper SiO_2 layer, 379
XRD tool, 376

Nanophotonics
applications, 352–353
Bloch hydrodynamic model, 357–358
continuum models, collective modes, 356–357
DFT, 352, 353–356
electromagnetic continuum models, 364–367
graphene/noble metal multilayer composites, 359–360
Lambin's model, 357–358
plasmonics, 360–362
plasmon oscillations, 352
plasmon resonances, 351–352
silicene and germanene systems, 362–364
Navier-Stokes fluid mechanics, 13
Newtonian dynamics, 17–18
Newtonian mechanics, 7
Newton's second law of motion, 88–89
Ni-C interaction, 95–96
Nonbond interactions, 10–11
Nonequilibrium Green's function (NEGF), 447*t*
Nonequilibrium molecular dynamics (NEMD) simulation
interface thermal conductance, 456–457
nanowire-based heterostructures, 454
Si nanowires, 453–454
solid-liquid interfaces, 455–456
thermal conductivity of silicene, 452–453
Nonionic surfactants, 33
Nosé -Hoover thermostat algorithm, 89–90, 101

O

One-dimensional (1D) nanoheterostructure
axially heterostructured nanowires, 126–128, 126*f*, 127*f*, 128*f*, 129*f*
coaxial core-shell nanowires (*see* Coaxial core-shell nanowires)
Pd decoration, 134–137, 135*f*
QDSSC, 137–139, 138*f*, 139*f*
One-dimensional (1D) nanostructures
1D nanoheterostructure, 125–139
superlattice nanowires, 122–125, 123*f*, 124*f*
TEM, 115–117
2D confinement endows, 115
ZnO nanostructures (*see* ZnO nanostructures)
ONIOM approach, 23–24
Optimized effective potential (OEP) method, 409–410

P

Pair distribution function (PDFs) analysis, 246, 247*f*, 261–262, 261*f*
Parrinello-Rahman fluctuation method, 27
Particle-based simulation
MD (*see* Molecular dynamics (MD))
MS (*see* Molecular statics (MS))
Particle size distributions (PSDs), 423
Peptide self-assembly, 34
Peptosomes, 34
Phenyl rings, 15
Phonon glass-electron crystal, 448, 449*f*
Photooxidation effect
BEE blue shifts, 298–299
CdSe QDs-PMMA composites, 299–300
fluorescent colors, 299
PMMA-QDs/toluene solution, 296–297
QYs *vs*. UV irradiation times, 299
UV light irradiation, 296–297
Piezoelectric effects, 56
Plasmonic coupling effect
Ag nanostructures, 304–310
layer thickness, 303–304
size effects, 301–302
Plasmons
Ag nanostructures, 304–310
CQDs size effect, 301–302
microscale fluorescent color patterns, 312–314
PMMA-graphene composite model, 26, 27*f*
Polycrystalline SnO2-coated ZnO nanowires, 134–135
Polyethylene, 25*f*, 26
Polyethylene/graphene nanocomposites, 25, 25*f*
Polymer nanocomposites (PNCs), 24–27, 25*f*, 26*f*, 28*f*
Polymer nanodielectrics, 34–36
Polystyrene-block-polybutadiene, 33
Population balance equation (PBE), 423, 424
Potential defects, 56
Potential energy, 16–17, 16*f*

Potential of mean force (PMF), 18–19
Pulsed laser deposition (PLD), 130–131

Q

QM/MM methods, 21–24, 22*f*, 23*f*
QM-Pot approach, 22
Quadrature method of moments (QMOM), 427
Quantum capacitance
  C_q, 213
  gate terminal, 214
  inverse subthreshold slope, 215
  I-V device, 215
  MOSFET device, 213, 214–215, 214*f*
  ON and OFF current, 215, 215*f*
  one-dimensional FETs, 215*f*, 216
Quantum dots (QDs), 56, 115
Quantum-dot-sensitized solar cells (QDSSC), 137–139, 138*f*, 139*f*
Quantum ESPRESSO, 356
Quantum mechanics (QM) methods, 4–7

R

Raman spectroscopy, 327
  AIREBO, 184
  BOLS mechanism, 185, 192–193
  bulk *vs.* individual SWCNT, 191–192
  instrument setup, 185, 186*f*
  laser power setting, 185
  linear frequency downshift, 185, 186*f*, 187*f*, 188*f*, 194
  SEM, 185
  SWCNTs, 185
  temperature slopes, 185, 189*t*
Resolution of the identity (RI) approach, 6
Root mean-square displacement (RMSD), 104

S

Scanning electron microscopy (SEM) analysis, 185
Scanning transmission electron microscope (STEM) mode, 115–116
Scatchard-Hildebrand theory, 19
Schödinger's wave equation, 4
Schrodinger equation, 445
Seebeck coefficient, 444
Select-area electron diffraction (SAED) patterns, 115–116
Self-assembly. *See* Nanoparticle self-assembly
Semiconductor colloidal quantum dots (CQDs)
  band-to-band and SSs, 292
  BEE and SSE, 291–292
  BEE intensity, 294–295
  chemical and physical properties, 289–290
  chemical synthesis and physical treatment, 293
  hot-injection route, 290–291
  light emission efficiencies and stability, 289–290
  light-emitting diodes, 290–291
  optoelectronic technologies, 290–291
  photoluminescence (PL) spectra, 291–292
  photooxidation effect, 296–300
  plasmonic coupling effect, 300–311
  PL spectrum, 294, 294*f*, 295*f*
  Raman scattering, 290–291
  surface states emission, 291
  white LEDs, 314–315
  WLE, single-size, 296
  ZnS shell, 290
Shinoda forcefield, 15, 15*f*, 19
Shirley method, 501
SIESTA, 355
Silicene, 451–453
Single and double electron configurations (CISD), 5–6
Single, double, and a limited class of triple excitations (CCSD(T)), 6
Single, double, triple,and quadruple excitations (CISDTQ), 5–6
Single-wall carbon nanotubes (SWCNT), 92–94, 93*f*
  CNT (*see* Carbon nanotube (CNT))
  Raman spectroscopy (*see* Raman spectroscopy)
SODF. *See* Strain and stress ori-entation distribution functions (SODF)
Solid electrolyte interphase (SEI), 37, 38*f*
Spherical harmonics
  Clebsch-Gordon coefficients, 148–149
  cubic crystal symmetry, 148–149
  Euler matrix elements, 154
  ground state, 149

Spherical harmonics *(Continued)*
Legendre function, 150–152
orthorhombic sample symmetry, 148–149
Rietveld program, 154–155
selection rule, 152, 152*t*, 153*t*
strain tensor, 153–154
stress tensor, 154
WSODF, 148–149
Stacking-fault-induced growth, ZnO nanobelts, 120–122
Static calculations, 91–98
Steele potential, 26
STEM-HAADF mode, 124, 124*f*
Stillinger-Weber (SW) parameters, 452–453
Strain and stress ori-entation distribution functions (SODF)
averaged macro strain, 147
averaged strains/stresses, 147–148
coefficients of expansion (*see* Spherical harmonics)
diffraction stress factors, 148
direction cosines, 147
Hooke equations, 145–146
intergranular tensor, 147
Laue equation, 146–147
plastic interactions, 148
reduced pole distribution, 147
sample reference system, 146
strain pole distribution, 147, 148
Structural defects, 56
Studio Studio package, 26
Superlattice nanowires, 122–125, 123*f*
Surface plasmon resonances (SPRs), 351–352
Surfactants, 33
SWCNT. *See* Single-wall carbon nanotubes (SWCNT)
Synchrotron X-ray-based techniques
Au-Au partial PDF, 267, 268*f*
Au_mPt_{100-m} particles anneal, 267, 268*f*
fcc-lattice parameters, 266–267, 266*f*
fct-type model, 262, 263–265
HE-XRD diffraction patterns, 263–265, 264*f*
hypothetical fcc model, 263–265
OR-RR treatment atmosphere, 262, 263*f*
PtCo model and Co K edge data, 265–266, 265*t*
PtNiCo nanoalloy, 266–267, 266*f*
in situ real-time, 267, 269*f*
structural characterizations, 260–261, 261*f*
thermochemical evolution processes, 267

T

Taylor series, 65–66
Tersoff-Brenner potential, 90–91
Tersoff potential, 64, 76–77
TGA. *See* Thermogravimetric analysis (TGA)
Thermal analysis methods
calorimetry, 174
CNT, 171–172
cure kinetics, 174
DSC, 169–170
experimental enthalpy, 174
ITC, 170
nanomedical-based products, 175
thermogravimetric analysis, 168–169
Thermal conductivity
bulk nanostructured materials, 449–450
energy conversion efficiency, 448
graphene and graphene-based heterostructures, 450–451
nanowire-based heterostructures, 454
phonon glass-electron crystal, 448, 449*f*
silicene, 451–453
single-component nanowires, 453–454
Thermogravimetric analysis (TGA), 168–169
adsorbed protein mass, 173
chemical composition, 172
mass loss measurements, 172
microscale, 175–176
nanocomposites, 173
oxidation temperature, 171–172
solution-based process, 170–171
Thermostatic control, 89–90
Thin-film deposition, 479, 480*t*
Thin-film ferroelectric (FE) material
capacitance and dielectric loss, 158
coupled scans, 159, 160*f*
Curie-Weiss temperature, 163–164, 163*f*
dielectric measurement, 158
dielectric permittivity and loss, 159, 159*f*
dislocation density, 162–163, 162*f*
elastic strains, 157, 161, 161*f*
energy density, 157–158

inhomogeneous strain, 157
lattice parameters, 155
optical properties, 158
polarization, 156–157
potential applications, 155–156
properties, 156
relaxation process, 161–162
Scintag four-circle diffractometers, 158
tetragonal distortion, 159–161
two-circle double-axis diffractometers, 158
Through silicon vias (TSVs), 399–401
Transmembrane proteins, 32
Transmission electron microscope (TEM), 327–328. *See also* One-dimensional (1D) nanostructures
Triethylenetetramine (TETA), 27
Tungsten oxide (WO_3) nanocrystals
AFM images, 494, 495*f*
bearing analysis, 494, 496*t*
black phosphorus FETs, 504–507
charge carrier mobility, 500
Coulomb charges, 500
experimental characteristics on, 495–498, 497*f*
FET device, 498–500, 499*f*
H^+ intercalation process, 495–498, 500–501
nonstoichiometric properties, 493
photocatalysis and sensing, 493–494
WO_{3-x}, 503
XPS measurements and analysis, 501, 502–503, 502*f*
2D hybrid-domain superlattices
armchair and zigzag cases, 465, 466–468
bandgap, 461–462
boundary energy and stress, 464–465, 466, 467*f*, 467*t*
C–BN superlattice models, 465–466
deformation behaviors, 464, 469*f*
DFT computations, 461–462
elastic properties, 464
electronic properties, 471–472, 471*f*
GNRs and BNNRs, 468
graphene–BN ribbons, 464
Monkhorst-Pack scheme, 465–466
N- and B-terminated edges, 468–469
oscillating behavior, 470–471, 470*f*
plane-wave basis, 468
SIESTA program, 465
synthesis, 462–463, 463*f*
Tersoff potential, 469
Two-dimensional (2D) nanocrystals
features of, 513
graphene, 508
molecular-level thickness, 511–513
nanosheet-based 2D composite materials, 509*f*, 510–511
properties and applications, 510, 510*f*
Two-dimensional semiconductors
fabrication methods (*see* Fabrication methods)
MoS_2 nanocrystals (*see* Molybdenum disulfide (MoS_2) nanocrystals)
semiconductor nanocrystals, 477–481, 478*f*
WO_3 nanocrystals, 493–503
WSe_2 nanocrystals, 489–493

U

Ultraviolet (UV) laser, 293

V

van der Waals interactions, 16, 90
Vapor-liquid-solid (VLS), 117
Vienna Ab-initio Simulation Package (VASP), 356
VLS-grown ternary nanowires, 126–127

W

WSe_2 *p-n* diode
ambipolar transport, 489
current-voltage characteristics, 489–490
CVD, 491–493
electroluminescence efficiency, 489–490
electroluminescence spectrum, 491, 492*f*
fabrication methods, 493
lateral diode, 489, 490*f*
photovoltaic power generation, 491, 492*f*
Wurtzite (WZ) structure, 117–118

X

XAFS. *See* X-ray absorption fine structure (XAFS)
X-ray absorption fine structure (XAFS), 256

X-ray diffraction
  residual strains/stresses (*see* Strain and stress ori-entation distribution functions (SODF))
  strain broadening, crystalline defects (*see* Thin-film ferroelectric (FE) material)
  three-dimensional crystalline, 145
X-ray photoelectron spectroscopy (XPS) measurements, 487–489, 488*f*

Y

Young's modulus, 27

Z

Z-contrast imaging, 119–120
Zeolites, 22, 28–29, 29*f*
Zigzag-edge ribbons graphene nanoribbon (ZGNR), 209–210
Zinc blende (ZB) structure, 117–118
ZnO nanostructures
  polarity determination, 117–120
  stacking-fault-induced growth, 120–122, 121*f*
ZnO/ZnS core-shell nanowire, 130–131, 131*f*, 132*f*

Woodhead Publishing is an imprint of Elsevier
80 High Street, Sawston, Cambridge, CB22 3HJ, UK
225 Wyman Street, Waltham, MA 02451, USA
Langford Lane, Kidlington, OX5 1GB, UK

Copyright © 2015 Elsevier Ltd. All rights reserved.
Exceptions to the above:
Chapters 2, 3, 6 and 14 were prepared by US Government employees; they are therefore in the public domain and cannot be copyrighted. Published by Elsevier Ltd.

No part of this publication may be reproduced, stored in a retrieval system or transmitted in any form or by any means electronic, mechanical, photocopying, recording or otherwise without the prior written permission of the publisher.

Permissions may be sought directly from Elsevier's Science & Technology Rights Department in Oxford, UK: phone (+44) (0) 1865 843830; fax (+44) (0) 1865 853333; email: permissions@elsevier.com. Alternatively you can submit your request online by visiting the Elsevier website at http://elsevier.com/locate/permissions, and selecting Obtaining permission to use Elsevier material.

Notice
No responsibility is assumed by the publisher for any injury and/or damage to persons or property as a matter of products liability, negligence or otherwise, or from any use or operation of any methods, products, instructions or ideas contained in the material herein. Because of rapid advances in the medical sciences, in particular, independent verification of diagnoses and drug dosages should be made.

British Library Cataloguing-in-Publication Data
A catalogue record for this book is available from the British Library

Library of Congress Control Number: 2014954544

ISBN 978-1-78242-228-0 (print)
ISBN 978-1-78242-235-8 (online)

For information on all Woodhead Publishing publications visit our website at http://store.elsevier.com/

Typeset by SPi Global
www.spi-global.com
Printed and bound in the United Kingdom

Multiscale modeling of nanomaterials: recent developments and future prospects

1

G. Fitzgerald[1], *J. DeJoannis*[2], *M. Meunier*[3]
[1]Accelrys, Inc., San Diego, CA, USA; [2]Accelrys, Inc., Burlington, MA, USA; [3]Accelrys Limited, Cambridge, UK

1.1 Introduction

Molecular modeling has long been used to predict the properties of molecules and crystals at the atomic scale, where the size is less than 10 nm. A number of techniques are required in order to provide a complete picture via molecular modeling. As a rule, more accurate techniques require substantially more computer time and are hence limited to smaller size systems. As one tries to model larger systems, more approximations are required in order to maintain reasonable computational resources.

In the past, a single method appropriate to one's research topic could be selected. However, the emergence of nanomaterials in the last few decades has posed a particular challenge because modeling on multiple length and time scales involves a hierarchy of methods as shown in Figure 1.1. Nanomaterials may consist of several thousand atoms and are still governed by quantum mechanical (QM) effects, but even the best QM modeling methods are limited to around 10^3 atoms. How then, can we create models that incorporate the requisite accuracy but are fast enough to be applicable to large length scales? This is the question that we will explore in the present chapter.

Section 1.2 will provide an overview of the major modeling methods currently in use. QM, forcefield-based, and coarse-grained approaches are introduced; then it will be shown how these methods can be combined into multiscale models. However, a discussion of continuum models is not included. Section 1.3 contains examples of how these methods have been applied to different classes of materials, including inorganic nanomaterials, nanocomposites, and bio-like materials. Section 1.4 provides some case studies that delve into greater detail: lithium ion batteries, nanodielectrics, and resins for aerospace applications.

Modeling, Characterization and Production of Nanomaterials. http://dx.doi.org/10.1016/B978-1-78242-228-0.00001-6
Copyright © 2015 Elsevier Ltd. All rights reserved.

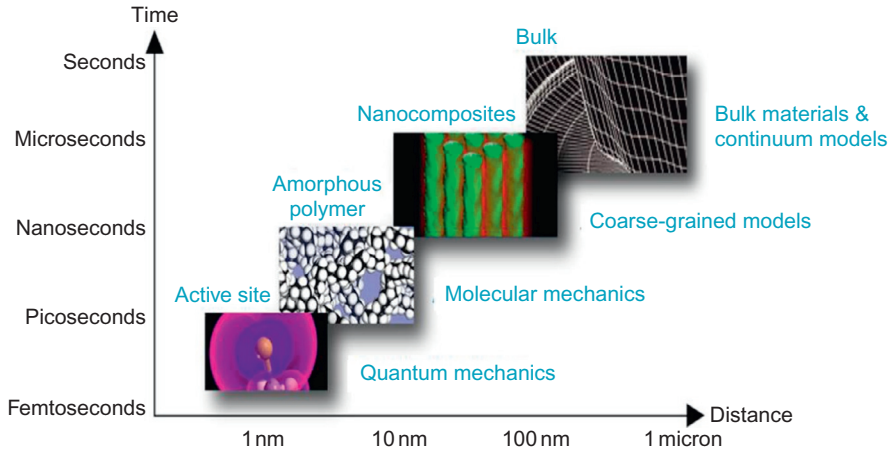

Figure 1.1 Length and time scales of different modeling methods. Each scale is labeled by a method and example application.

1.2 Methods

1.2.1 Quantum mechanics

1.2.1.1 Introduction

Calculations based on *ab initio* QM methods are the most accurate of all molecular modeling approaches. These calculations, based on the solution of Schrödinger's wave equation, require no empirical parameters or previous experimental knowledge. They are essential for modeling chemical reactions and for studying electronically excited states. However, such methods are limited to systems containing on the order of $\sim 10^3$ atoms and to dynamic simulations of a few picoseconds. The length and timescales of relevance to laboratory research problems are considerably larger: systems containing Avogadro's number of atoms ($\sim 10^{23}$) evolving for minutes or hours. *Ab initio* methods are nevertheless essential for obtaining chemical accuracy. By themselves, they can be applied to model systems that provide insight into real-world chemical behavior. In addition, when used in multiscale modeling, they provide an accurate foundation that can be extended to much larger, practical systems.

All the methods described in this section will be based on the time-independent Schrödinger equation and the Born-Oppenheimer approximation (Born and Oppenheimer, 1927). This assumes that the motion of atomic nuclei is slow compared to electronic motion and allows us to define a potential energy surface. We can specify a particular molecular geometry and assume the nuclei are stationary while we solve for the wave function. Given the wave function, we can obtain the energy and forces on the atoms and search for minimum energy structures, or we can obtain properties such as ionization potentials, dipole moments, and IR and Raman spectra.

1.2.1.2 Hartree-Fock theory

The Hartree-Fock method (Fock, 1930) as implemented by Roothan (1951) formed the first practical approach to obtaining energies and wave functions for polyatomic molecules. In this approach, the wave function Ψ consists of an anti-symmetrized determinant of molecular orbitals (MOs) φ_i. Each orbital is further broken down into a set of atomic orbitals, χ_μ.

$$\phi_i = \sum c_{i\mu}\chi_\mu \tag{1.1}$$

The $c_{i\mu}$ are MO coefficients that express the MOs in terms of atomic orbitals. A detailed exposition of the Roothan equations is beyond the scope of the present chapter. In simplified form, however, the equations can be reduced to the matrix expression:

$$FC = \epsilon SC \tag{1.2}$$

which must be solved for C. Here F is the so-called Fock matrix, C is the matrix of MO coefficients, S is the overlap between two atomic orbitals, and ε are the eigenvalues of F corresponding to the energies of each MO. Equation (1.2) appears deceptively simple. In fact, the Fock matrix F depends on C, the coefficients we are trying to solve for. Hence an iterative approach is needed: An initial guess for C_0 is used to construct F, and then solve the Roothan equations to yield a new result, C_1. The process continues until C_i does not change from one iteration to the next.

The Hartree-Fock-Roothan (HFR) method has been used extensively since its inception. As a practical method for large-scale calculations, however, HFR is too slow. Formally, the computational cost increases as N^4 increases, where N is the number of electrons. Although broadly successful, it is not accurate enough for many cases, such as metal-metal bonds, heats of formation, and chemical bond breaking (Szabo and Ostlund, 1982).

1.2.1.3 Electron-correlated methods

HFR is based on a mean-field that ignores instantaneous correlations among the electrons. A number of approaches have been developed to compute this missing contribution, referred to as the *correlation energy*. All of these methods increase the accuracy of the results, but they also increase the computational cost significantly. As a consequence, these methods are not used extensively in multiscale approaches, and so will be touched upon only briefly.

The configuration interaction (CI) method (Shavitt, 1977) uses the HFR wave function as the starting point. It then constructs additional electron configurations by exciting electrons from the occupied MOs to the unoccupied (virtual) MOs, each of which is described by its own Slater determinant. The CI wave function is taken as a linear combination of these determinants. A *full-CI* would include all possible excitations of electrons. This would provide the total correlation energy, but the calculation would be prohibitively expensive because the number of configurations scales factorially (as $N!$). The choice of determinants is typically limited to chemically significant electron configurations. Selecting the configurations from all single and

double electron configurations (CISD) can yield 80-90% of the correlation energy (Harrison and Handy, 1983) for a fraction of the cost. Including single, double, triple, and quadruple excitations (CISDTQ) can achieve over 99% of the correlation energy.

An alternative approach is that based on many-body perturbation theory (MBPT), some forms of which are commonly called Møller-Plesset (MP) perturbation theory (Møller and Plesset, 1934). The Fock operator is taken as the zeroth-order Hamiltonian, and the perturbation is the difference between the Fock operator and the exact Hamiltonian. MP2 is the simplest approximation and can recover ~80% of the correlation energy, but scales only as N^5.

Coupled-cluster methods apply more sophisticated perturbations. Coupled-cluster calculations with single and double excitations (CCSD) (Bartlett and Purvis, 1980), for example, obtain more than 90% of the correlation energy, and scale as N^6. Currently, coupled-cluster methods including single, double, and a limited class of triple excitations (CCSD(T)) (Purvis and Bartlett, 1982) represent some of the most accurate calculations possible. Because these scale as N^7, however, they are not widely used in commercial applications.

1.2.1.4 Density functional theory

Density functional theory (DFT) represents an alternative approach based on Hartree-Fock theory. DFT begins with a theorem by Hohenberg and Kohn (1964), later generalized by Levy (1979), which states that all ground-state properties are functionals of the charge density field ρ. The total energy, E_t, may be written as:

$$E_t[\rho] = T[\rho] + U[\rho] + E_{xc}[\rho] \tag{1.3}$$

where $T[\rho]$ is the kinetic energy, $U[\rho]$ is the classical electrostatic energy due to Coulombic interactions, and E_{xc} $[\rho]$ includes the exchange and correlation contributions. Hartree-Fock includes the complete exchange energy but none of the correlation. DFT, by contrast, includes a portion of both exchange and correlation. The expression for E_{xc} requires an approximation to become computationally practical. The simplest approximation is the local density approximation, which is based on the known exchange-correlation energy of the uniform electron gas (Hedin and Lundqvist, 1971; Ceperley and Alder, 1980; Lundqvist and March, 1983). Analytical representations have been made by several researchers (Hedin and Lundqvist, 1971; Ceperley and Alder, 1980; von Barth and Hedin, 1972; Vosko et al., 1980; Perdew and Wang, 1992). Improved expressions for E_{xc} can be obtained by expanding it as a function of $\nabla\rho$ or $\nabla^2\rho$ (Ziegler, 1991; Perdew and Wang, 1992; Lee et al., 1988). Perdew (2013) recently outlined a scheme for systematically generating even more accurate functionals.

By using the so-called resolution of the identity (RI) approach (Feyereisen et al., 1993), DFT methods can be made to scale as N^3, which is considerably less expensive than any electron-correlated method. Despite its simplicity, DFT can predict bond lengths to picometer (10^{-12} m) accuracy and enthalpies of reaction to within approximately 5 kcal/mol (Labanowski and Andzelm, 1991).

This performance is adequate for calculations on nanoclusters containing 1000-2000 atoms, but is still too slow for QM calculations on models greater than

10 nm. Other methods are required to push DFT to that scale. Linear scaling DFT (Skylaris et al., 2005) has significantly extended the capability of DFT. Linear scaling is achieved by performing a transformation on the MOs to localize them. This makes the Hamiltonian matrix sparse, significantly reducing computational effort.

Linear scaling DFT has been applied to systems with more than 1000 atoms, including proteins, semiconductors, and microelectronics (Skylaris et al., 2005). Linear scaling methods require considerably less CPU time than conventional DFT methods, but even so, calculations are still expensive. This is because computational overhead is required to localize the MOs. This overhead is recovered when doing larger calculations, but not in the case of smaller calculations. The break-even point is around 300-400 atoms. Below that, conventional DFT methods appear to be more efficient; above that linear scaling methods win out.

1.2.1.5 Other methods

A number of other methods have been developed with the goal of delivering higher accuracy for lower computational cost. The most relevant for this chapter are the fragmentation methods recently reviewed by Gordon et al. (2012). As the name suggests, such methods make calculations more tractable by breaking molecules into fragments and combining results into a total. These approaches include the divide and conquer (DC) (Yang, 1991) and fragment molecular orbital (FMO) (Kitaura et al., 1999) methods, to name just two. In DC, an *ad hoc* total density is constructed from fragment calculations, followed by a single energy evaluation. In the FMO method, one performs fragment calculations in the electrostatic field of other fragments, until the results are internally self-consistent. Such methods have been applied to polypeptides (Li et al., 2002; Jensen et al., 2005) and even protein-ligand interactions (Fukuzawa et al., 2005; Sawada et al., 2006) that contain thousands of atoms.

Despite the promise of such methods, they remain underutilized. Reasons for this include the lack of commercially available (i.e., easy-to-use) packages and uncertainly about their accuracy (Gordon et al., 2012). They remain promising, however, and can be expected to play a significant role as modelers demand calculations on larger molecular and solid-state systems in the near future.

1.2.2 Classical mechanics

The next class of molecular modeling tools is based on classical or Newtonian mechanics. In fact, most foundations of classical mechanics can be found in Newton's *Mathematical Principles of Natural Philosophy* first published in 1687. The main differences with *ab initio* methods is that here (i) electrons are not explicitly included (atoms are the smallest fragments) and (ii) intrinsic (empirical) parameters are employed to describe the behavior and relations of *atom types*. An atom type includes the atomic number of the atom as well as information such as the hybridization state and the local environment (e.g., neighbor atoms it is bonded to). A forcefield or an atomistic potential is employed to describe the interactions between all the atoms of the model; there are many types of such forcefields or potential functions and they too will be reviewed in the present section.

1.2.2.1 Molecular mechanics

In molecular mechanics, the energy of the model is computed by adding up the strain energy in all the chemical bonds (valence terms) plus all the nonbonded interactions. A single-point energy can be used to estimate the stability of a particular model. More commonly, a geometry optimization (also called energy minimization) is performed to find the conformation of lowest energy.

Conformational searches can be performed when the model is flexible (e.g., a polymer chain) to explore energy changes with conformational changes. When the model size becomes too large, it becomes difficult or impossible to find the global energy minimum. Typically, nanomaterials such as nanoparticle-reinforced polymers are too complex to be fully "energy minimized." In any case, their dynamical properties at a given temperature and/or pressure are often of greater interest. To that end, modelers will use molecular dynamics (MD) simulations.

1.2.2.2 Molecular dynamics

MD can be defined as the simulation of the motion of a system of particles (atoms and/or molecules) with respect to the forces that are present. Only the most fundamental aspects and equations used in MD simulations are mentioned in this section. For a more extensive review of the theory of MD simulation, please see Leach (2001) or Allen and Tildesley (1987).

MD starts by assigning kinetic energies to every atom from a Boltzmann or random distribution at the temperature of study. Newton's second law of motion ($F = ma$) is then used so that the trajectory of each atom can be obtained:

$$F_i = m_i a_i = m_i \frac{\mathrm{d}v_i}{\mathrm{d}t} = m_i \frac{\mathrm{d}^2 x_i}{\mathrm{d}t^2} \tag{1.4}$$

The classical equations of motion are deterministic, meaning that the initial coordinates and velocities completely determine the coordinates and velocities at later times. The set of coordinates and velocities for a complete dynamics run is called a trajectory.

In the simple case of a particle in one dimension, a is the acceleration:

$$a = \frac{\mathrm{d}v}{\mathrm{d}t} \tag{1.5}$$

If a is constant we have:

$$v(t) = at + v_0 \tag{1.6}$$

where $v(t)$ is the velocity and is given by:

$$v(t) = \frac{\mathrm{d}x(t)}{\mathrm{d}t} \tag{1.7}$$

The particle position is:

$$x(t) = v.t + x_0 = a.\frac{t^2}{2} + v_0 t + x_0 \tag{1.8}$$

The position at time t is obtained by integration considering the initial position (x_0) and the initial velocity (v_0). For the following step, at $t+\Delta t$, where Δt is the "time step," a truncated Taylor series for displacement is used for computing the positions x_i of each atom:

$$x_i(t+\Delta t) = x_i(t) + (\delta x_i/\delta t)\Delta t + \left(\delta^2 x_i/\delta^2 t\right)\Delta t^2/2 + \cdots \tag{1.9}$$

The time step Δt can be chosen according to the system of study and the integration method, one of the most popular being that of Verlet (1967). The time step should be large enough to minimize computational cost, but it must be smaller than the highest vibrational frequency of the system (to avoid atomic overlap or excessive stretching of bonds). A time step of one femtosecond ($\text{fs} = 10^{-15}$ s) is the most common value employed in MD simulations of organic materials because it is 10 times smaller than typical C—H vibrational frequency in hydrocarbons (10^{14} Hz) (Lide, 1997).

Most simulations aim to reproduce conditions where the system is exposed to external pressure and/or exchanges heat with the environment. Multiple methods exist to control the temperature and pressure of the system of study. Different simulation ensembles can be used to that end, for instance, the microcanonical ensemble where both energy and volume are kept constant (NVE). The NVT ensemble (canonical) where both volume and temperature are kept constant is probably the most popular one. A variety of structural, energetic, and dynamic properties can then be calculated from the averages or the fluctuations of these quantities over the ensemble generated (Salomon-Ferrer et al., 2013).

1.2.2.3 Monte Carlo

It is reported that the first computer simulation of a molecular system was performed using the Monte Carlo technique. During a Monte Carlo simulation, an ensemble of configurations is generated by randomly moving (translation, rotation, etc.) one or more atoms present in the model (*random sampling*). In some schemes, atoms, fragments, or molecules can also be created or removed from the model. Just as in MD, a forcefield is used to update the configuration; however, the updated configuration depends on the potential energy of the system rather than the forces on the atoms.

Monte Carlo methods are particularly well suited for the simulation of disordered materials like liquids and polymeric materials. More recently, kinetic Monte Carlo methods have also emerged. In particular, such techniques provide a computationally efficient way to study systems where the structural evolution is defined by a finite number of thermally activated elementary processes.

1.2.2.4 Forcefields

A forcefield consists of a set of interatomic potentials (see Figure 1.2) and empirical parameters. It allows one to calculate the total potential energy of a system (and from this the forces). The parameters used in a forcefield are empirically derived from experimental or computational data or both. Some forcefields aim for high accuracy for a limited set of elements and molecules, thus enabling good predictions of many molecular properties. Others aim for the broadest possible coverage of the periodic table, with necessarily lower accuracy (Mayo et al., 1990).

Typically, the total energy of a system is comprised of the valence and non-bonded interactions. Some forcefields also have cross terms:

$$E_{\text{total}} = E_{\text{valence}} + E_{\text{cross term}} + E_{\text{nonbond}} \tag{1.10}$$

The valence terms correspond to chemical bonding and molecular geometry (bond stretching, angle bending, torsional, etc.). Nonbond interactions are made up of the van der Waals and electrostatics terms, with some forcefields including an explicit term for hydrogen bonding (often used in simulations of biological entities). For example, the Dreiding forcefield uses:

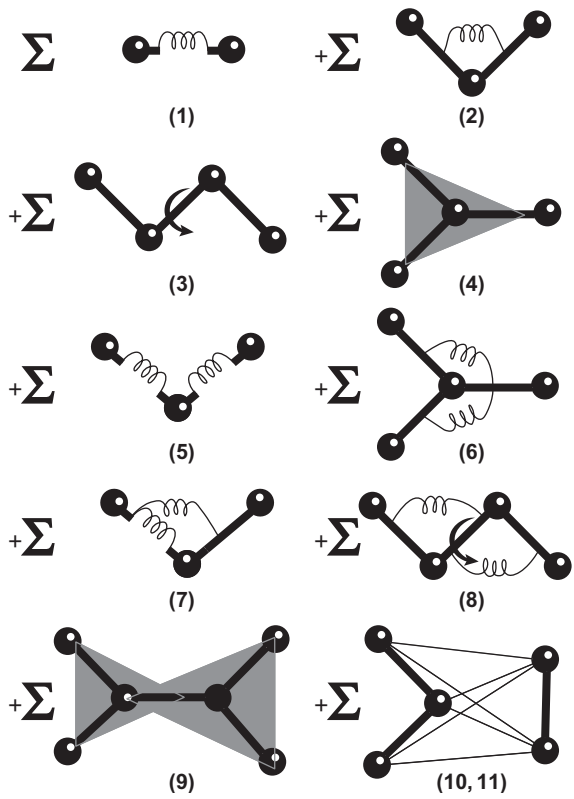

Figure 1.2 Graphical illustration from Dauber-Osguthorpe et al. (1988) of the potentials making up the consistent valence forcefield (CVFF). Terms 1 to 4 are the diagonal terms of the forcefield and describe successively bond stretching, angle bending, torsion, and out-of-plane interactions. Terms 5 to 9 are the cross terms and represent the coupling between terms 1 to 4. Terms 10 and 11 represent the nonbonded interactions.

$$E_{\mathrm{H-bonded}} = \sum\nolimits_{ij \in \mathrm{H-bond}} \left[\frac{C_{ij}}{R_{ij}^{12}} - \frac{D_{ij}}{R_{ij}^{10}} \right] \tag{1.11}$$

1.2.2.5 Applications of classical tools to nanomaterials

Atomistic modeling has been at the forefront of computational investigation of nanomaterials (Zhigilei et al., 2012), where it is often the interfacial regions that play a critical role (see, for example, the discussion of nanodielectrics in Section 1.4.1). Building complex (interface) models using molecular modeling tools has been very effective in predicting the relationship between observed macroscopic properties and the underlying atomistic structure.

At the end of a MD or a Monte Carlo simulation, the modeler performs some analysis of the structure and trajectory obtained. Often, $g(r)$, a pair correlation function (also known as a radial distribution function) is computed. The function $g(r)$ gives a measure of the probability that a pair of atoms are separated by a distance r. It can be compared to experimental data in order to validate the methodology employed (and the quality of the forcefield). It can also be used to validate the model itself and its final state, ensuring that the material simulated corresponds to that of the experimental setup. Similarly, it is possible to analyze the atomic scattering and compare these with, for example, X-ray diffraction patterns, again giving some validity to the model employed. The distribution (or concentration profile) of a set of atoms or molecules (or e.g., nanoinclusions) can also be estimated from the simulation run giving a good idea of the organization or morphology of the system studied. Computation of the cohesive energy (a term closely related to the enthalpy of vaporization) is calculated with:

$$E_{\mathrm{coh}} = \Delta H_{\mathrm{vap}} - \Delta(pV) = \Delta H_{\mathrm{vap}} - RT \tag{1.12}$$

Subsequently the cohesive energy density (CED, expressed in cal/cm^3 or MPa or J/cm^3) as defined by:

$$\mathrm{CED} = E_{\mathrm{coh}}/V \tag{1.13}$$

allows for the prediction of the Hildebrand solubility parameter δ (Hildebrand, 1916), using:

$$\delta = \sqrt{\mathrm{CED}} \tag{1.14}$$

Such parameters can then be used to estimate the miscibility or compatibility of the various components of a system and to some extent allow for the prediction of their solubility. Such parameters can also subsequently be used to create coarse-grained parameters for mesoscale simulations (Akkermans, 2008), as reviewed in the next section.

Inspection of the MD trajectory also allows for the computation of the mean square displacement that is used to estimate the diffusion coefficients of, for example, small gas molecules (Meunier, 2005; Gestoso and Meunier, 2008). Applying stress on the structure can be used to estimate the mechanical properties (and in particular the elastic constants) of the model (Bauer et al., 2010). Recently, Bauer et al. (2010) used both quantum and classical methods to estimate the elastic stiffness coefficients of aspirin crystals. Their results compared well with experimental data using ultrasonic techniques. Carbon-based nanostructures such as graphene sheets or carbon nanotubes (CNTs) have been the subject of many atomistic modeling studies. Often, such materials are used to reinforce polymers, such as polyethylene in particular for automotive or aerospace applications (Doyle, 2009). Atomistic simulations of such polymer nanocomposites will be described in more detail in Section 1.3.1.

When using molecular mechanics to model nanomaterials, a few issues often arise. The most common problem is in selecting a forcefield that can model all of the interactions, because nanomaterials are often inhomogeneous, that is, containing both organic and inorganic components (e.g., a polymer matrix with dispersed silicon based nanoparticles). Not uncommonly, the modelers will use separate potential functions to model the various components and create a special function to handle the mixed interactions. Usually, the atomistic description of such mixed phases requires a large number of particles in the model and so will be computationally expensive. Most, if not all, simulation tools from commercial vendors or from academia and government bodies will offer parallel versions of the software for speed as well as simulation tricks (efficient ways to treat nonbonded interactions, most often the most expensive part of the simulation). Last, the simulation times might also have to be increased in order to obtain the properties of study. Most simulations in the area of materials research do not exceed tens of nanoseconds.

1.2.3 Mesoscale

The prefix meso- is Greek for middle, and hence mesoscale usually denotes a model that bridges the gap between the atomic scale ($<$10 nm) and finite element modeling ($>$1000 nm). Molecules and surfaces are coarse-grained to retain the distinguishing molecular architecture but the atomistic details are averaged out.

Perhaps the first coarse-grained model to be introduced was the united-atom model, which lumps hydrogen atoms together with the heavy atoms to which they are bound. For example, a CH3 group is replaced by a single bead, reducing the degrees of freedom by a factor of four. Mesoscale models go even further down the reductionist path, as illustrated in Figure 1.3, reducing the computational complexity by two to three orders of magnitude.

1.2.3.1 Models

Coarse-grained molecular dynamics (CGMD) is the most popular technique in mesoscale modeling. Typically each bead represents three to five heavy atoms and their pendant hydrogen atoms (Marrink et al., 2007; Shinoda et al., 2007). This kind of

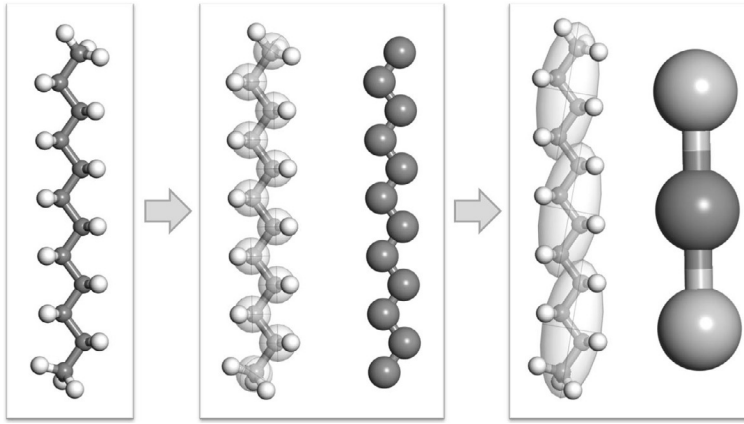

Figure 1.3 Coarse-graining a polyethylene chain (left) into a united atom model (middle) and mesoscale model (right).

mapping aims to replace functional groups by corresponding beads that represent their level of polarity and affinities to other chemical groups. Specific interactions like hydrogen bonds are not explicitly modeled. The advantage of this approach is that it is a straightforward extension of the tools used in atomistic MD reviewed in the previous section. Bead interactions may be modeled using potentials of the same functional form. Bead motion is simulated with the same Newtonian dynamics, but with a larger time step (10-50 fs vs. 1-2 fs), resulting in at least an order of magnitude increase in speed from the time step alone.

Naturally, the reliability of CGMD tends to break down as the atom-to-bead mapping scale increases. The interactions and dynamics of a bead that represents dozens of heavy atoms becomes a difference in kind. New models must be introduced to capture this larger-scale collective behavior in which large aggregations of atoms are represented as the unit of simulation. For instance, a bead can no longer be considered as having a hard surface because its underlying collection of particles is more pliable. Such is the case especially when a bead represents a group of small solvent molecules.

For these reasons, the dissipative particle dynamics (DPD) technique replaced the conventional "hard and sticky" particle model with a softer and purely repulsive bead. Similarly, the dynamic of the beads was retooled to better account for the hydrodynamic and thermodynamic behavior of the system. The DPD model has been applied to an amazing range of materials from polymers (Groot and Warren, 1997; Maiti et al., 2005) and self-assemblies (Groot and Warren, 1997; Groot and Rabone, 2001) to DNA (Symeonidis et al., 2005) and concrete (Roussel et al., 2007). Lattice-Boltzmann (LB) is a related approach in that it aims to construct a particle-based version of Navier-Stokes fluid mechanics, but it is more narrowly applied to the study of fluid flows (Aidun and Clausen, 2010). Another interesting method in this genre is multiparticle collision dynamics (MPC), which has been applied to colloids and polymers (Kapral, 2008; Noguchi et al., 2007).

The DPD method has gained considerable popularity since its introduction in 1992 (Hoogerbrugge and Koelman, 1992), especially as a tool for non-experts to investigate qualitative or semiquantitative phenomena at larger length and time scales than CGMD. Although it was initially focused on hydrodynamics, it was soon adapted for the study of thermodynamics of liquids in the canonical ensemble (Espanol and Warren, 1995). The core DPD method was elucidated by Groot and Warren with a connection to the Flory-Huggins theory of polymers (Groot and Warren, 1997).

A further abstraction is to adopt an implicit particle model using dynamic density functional theory (DDFT) (Fraaije et al., 1997). Rooted in polymer physics, beads are represented through the interactions and motion of bead density fields—effectively recycling ideas from *ab initio* modeling of electron density fields (Section 1.2.1). Although the modeler must choose bead interaction parameters, there are no actual beads or particles in the simulation. Instead, the equations of motion determine the flow of bead density fields of each bead type.

Some of the oldest mesoscale modeling approaches are purely qualitative in nature, addressing the underlying physics. For instance, Langevin dynamics uses an implicit solvent that subjects the beads to random Brownian forces. Similarly, Monte Carlo simulations are greatly simplified by ignoring the solvent and identify the effect of salt concentration with a screened Debye-Hückel interaction. Lattice models, too, have been applied to vastly reduce the computational complexity of a simulation.

1.2.3.2 Forcefields

The downside of mesoscale modeling is that while it speeds up the simulation itself, it requires more effort to set up the model. There are fewer forcefields available, and the selection of parameters is difficult to automate. There are some forcefields available for CGMD but for DPD and DDFT there are not.

The most widely used mesoscale forcefield is probably MARTINI. In its original form, 18 bead types were defined (Marrink et al., 2007), ranging in polarity, charge, and hydrogen bonding ability. The parameters were validated against experimental values of free energies of vaporization, hydration, and phase partitioning. The forcefield was initially designed for hydrated lipid bilayers and has since been extended to proteins (Monticelli et al., 2008; de Jong et al., 2013) and carbohydrates (López et al., 2009).

Application of the MARTINI forcefield is straightforward for new materials, because it contains a look-up table that allows the user to identify a chemical group (or a similar one) with a particular bead type. One simplifying assumption is that all bead sizes are the same, with a diameter of 4.7 Å. An exception is the parameterization of rings, where smaller beads are used with a heavy atom to bead mapping of 2:1 or 3:1 as shown in Figure 1.4.

Another popular forcefield for CGMD was developed by Shinoda et al. (2007) for aqueous non-ionic surfactants. The parameters can be directly applied to alkanes, ethers, and alcohols. Each bead represents two to three heavy atoms and their pendant hydrogen atoms; a total of seven bead types are defined, as shown in Figure 1.5. The parameters were fitted to match experimental values for pure component liquid density, surface tension, and compressibility. The Shinoda forcefield

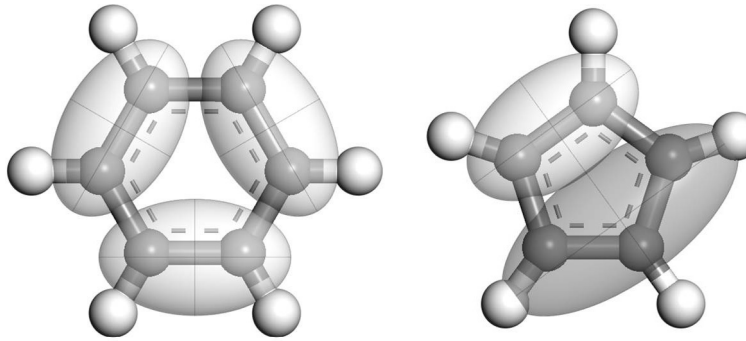

Figure 1.4 Examples of 2:1 and 3:1 ring particle mapping in the MARTINI coarse-grained forcefield. To account for the smaller units, the bead diameter is reduced from 4.7 to 4.2A.

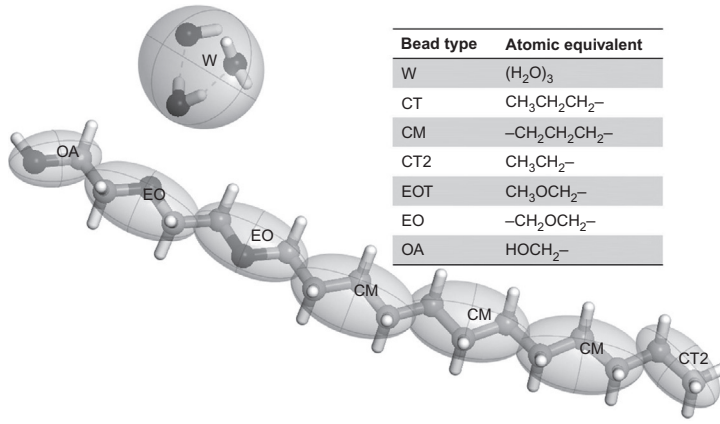

Bead type	Atomic equivalent
W	$(H_2O)_3$
CT	$CH_3CH_2CH_2$–
CM	–$CH_2CH_2CH_2$–
CT2	CH_3CH_2–
EOT	CH_3OCH_2–
EO	–CH_2OCH_2–
OA	$HOCH_2$–

Figure 1.5 Illustration of a nonionic surfactant modeled with the Shinoda coarse-grained forcefield (Shinoda et al., 2007).

has reproduced micelle, bilayer, hexagonal (cylindrical micelle), and lamellar transitions. In contrast to MARTINI, the size of the bead types varies from 3.7 to 4.6 Å in diameter.

The Shinoda forcefield has since been extended to cover peptides (DeVane et al., 2009), ionic surfactants (He et al., 2010; Shinoda et al., 2011), and zwitterionic lipid assemblies (Shinoda et al., 2010), giving it a similar coverage to MARTINI. Sodium cations are modeled using a bead with a full +1 charge that represents a cluster of three waters and one sodium ion. Phenyl rings have been alternatively represented with two (He et al., 2010) or four beads (DeVane et al., 2010). The latter was recently used to study buckyballs and CNTs (Chiu et al., 2010).

Many other efforts have been made to coarse grain different materials, but most lack the generality of the two examples above (Voth, 2008).

1.2.3.3 Potentials

In CGMD, the terms used to compute the potential energy are given in the following equation:

$$E_{CG} = E_{bond} + E_{angle} + E_{vdW} + E_{Coulomb} \tag{1.15}$$

This makes for a much simpler expression than that given for atomistic simulations (Figure 1.2). Torsional potentials are usually not necessary. Exceptions include carbohydrates (López et al., 2009) and peptides (Monticelli et al., 2008; DeVane et al., 2009) where torsional terms are used to enforce the right spatial arrangement of side chains or the desired secondary structure of the backbone (e.g., alpha helix). The electrostatic interactions are also greatly reduced, because only a fraction of beads are charged, whereas atoms almost always carry a partial charge.

The van der Waals interactions are typically modeled using Lennard-Jones potentials, just as in atomistic simulations. The Martini forcefield uses a 12-6 form and Shinoda uses a combination of 9-6 and 12-4 terms. These two-parameter potentials provide the particle with a hard core and a short-range attraction ("stickiness"). This is in marked contrast to the inter-particle force used in DPD as shown in Eq. (1.16) and Figure 1.6, which, in combination with specialized dynamics (see below), produces a soft, viscous bead.

$$F_{DPD}(r) = a_{ij}\left(1 - \frac{r}{R_c}\right) \tag{1.16}$$

Here a_{ij} is the interaction parameter between species i and j, r is the separation distance, and R_c is the cutoff beyond which the force is zero. Because the cutoff is fixed, all DPD beads have the same size. One shortcoming of the soft DPD potential is that

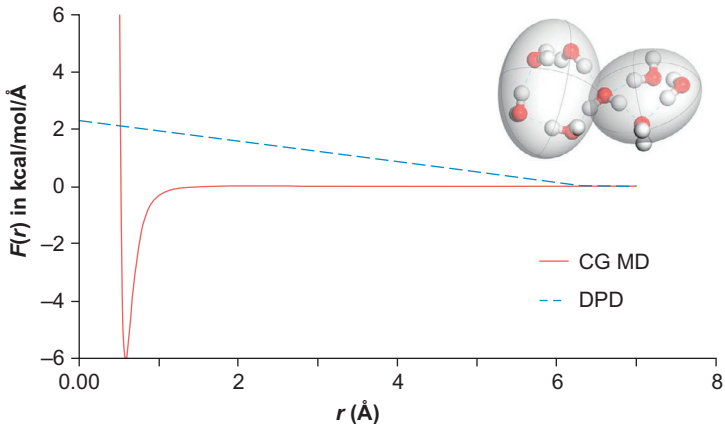

Figure 1.6 Comparison of the force between two beads as a function of separation distance for water-water interactions in MARTINI (Marrink et al., 2007) and DPD (Groot and Warren, 1997). The MARTINI interaction has a hard core and an attractive part while the DPD interaction is soft and purely repulsive.

beads can completely overlap, which means that charges interactions cannot included because they would induce opposite pairs to superpose.

The DPD interaction is too simple to produce vapor-liquid coexistence, because its equation of state is essentially quadratic. Thus, many-body DPD (MDPD) is an extension that can be applied to vapor interfaces or wetting that introduces a dependence of a_{ij} on the local density (Pagonabarraga and Frenkel, 2001; Warren, 2003).

The interactions in DDFT are more complex in that they are treated within the framework of non-equilibrium statistical thermodynamics. Intra-molecular interactions are governed by a Gaussian (or ideal) chain model, akin to a chain of non-interacting beads connected by Gaussian springs. Nonbond interactions are introduced via Flory-Huggins theory, making the parameters similar to those in DPD.

1.2.3.4 Dynamics

The Newtonian dynamics of atoms covered earlier applies equally well to beads in CGMD. The main difference is that the time step can be increased. This can be understood by way of analogy again to the united-atom model, which allows the modeler to increase the time step from 1 to 2 fs, essentially averaging out the rapid vibrations of the hydrogen atoms. Coarse graining takes this concept further, averaging out the motion of the atoms represented by each bead and allowing a time step of at least 10 fs.

The MARTINI forcefield was originally introduced with a time step of 40 fs, or 30 fs if rings were present (Marrink et al., 2007). Some argue for a smaller time step of 10 fs (Winger et al., 2009; Marrink et al., 2010). Shinoda et al. (2007) used a split time step scheme with 10 and 2 fs for nonbond and bonded terms respectively; but they have since used a single time step of 10 fs (Shinoda et al., 2010).

The interpretation of the time step in CGMD needs further consideration. Coarse-graining effectively smooths the molecules, reducing the friction between them. Hopefully, this impacts everything in a similar way and a single scaling constant can be applied to time. Marrink et al. (2007) settled on fourfold scaling after comparing diffusion constants, permeation rates, and aggregation time scales, but it can vary with different molecules (Marrink and Tieleman, 2013).

In DPD, Newtonian dynamics is extended to include two additional contributions to the nonbonded forces between each pair of beads. The first is the dissipative term:

$$F_{ij}^{\mathrm{D}} = -\gamma_{ij}\left(1-\frac{r_{ij}}{R_C}\right)^2 \mathbf{v}_{ij}\cdot\mathbf{e}_{ij} \tag{1.17}$$

and amounts to a frictional or drag term. Here $\gamma_{ij}=\gamma_{ji}>0$ are frictional coefficients (usually all the same) and $\mathbf{v}_{ij}=\mathbf{v}_i-\mathbf{v}_j$ is the velocity of bead i relative to the velocity of bead j, and $\mathbf{e}_{ij}$ is the unit vector along $\mathbf{r}_{ij}$. Thus each bead j imposes a drag force F_{ij}^{D} on each bead i that is proportional to their relative velocity and decays quadratically with increasing separation. The dot product also indicates the role of the relative orientation of the displacement and velocity vectors: The full drag force is experienced when beads are moving straight at or away from one another and the drag force decays to zero as their velocity vectors become orthogonal.

The second additional force in DPD represents the Brownian forces that act randomly on each bead:

$$F_{ij}^{\mathrm{R}} = -\sqrt{\gamma_{ij} 2k_{\mathrm{B}}T}\left(1 - \frac{r_{ij}}{R_C}\right)\xi_{ij}\frac{1}{\sqrt{\Delta t}} \tag{1.18}$$

where ξ_{ij} is a random number with zero mean and unit variance and Δt is the time step. This expression is somewhat peculiar in that each pair of beads receives equal and opposite random forces, obeying Newton's third law. This combination of dissipative and random forces imposes the canonical (NVT) ensemble via the fluctuation dissipation theorem and also produces hydrodynamic behavior through its momentum conservation (Flekkøy et al., 2000).

This novel method of controlling the temperature is called the DPD thermostat, and it has even been applied in non-DPD contexts. An alternative is the Lowe-Andersen thermostat, which allows use of a traditional Verlet integration scheme and a larger time step (Koopman and Lowe, 2006).

DDFT uses a completely different approach to dynamics based on the time evolution of a free energy functional of the density fields representing the distribution of each bead type. The driving force for motion (i.e., redistribution of the fields) is the chemical potential gradient vis-à-vis Fick's law of diffusion. A Langevin equation governs the dynamics and produces the canonical ensemble. The dynamics of the system follow a local minimum path in the free energy space. Like DPD, DDFT dynamics are capable of representing a significantly longer time scale than CGMD.

1.2.3.5 Parameterization

Often the difficult part in a mesoscale study is the development of interaction parameters for the model. Validation of parameters can be time-consuming and it may be difficult to obtain relevant data. It often amounts to a "research project within a research project." Hence generalized CGMD forcefields such as MARTINI and Shinoda are in great demand.

Usually, the best data for the development and validation of a set of CGMD, DPD, or DDFT parameters are condensed phase thermodynamic data that will be predictive of segregation effects. The intra- and intermolecular parameters can be pursued along parallel tracks, much in the way that has been done traditionally for atomistic forcefield development. Bond and angle parameters are chosen to reproduce the minima, and distributions are obtained from *ab initio*, atomistic, or experimental knowledge. The nonbond parameters should be chosen with reference to such data as liquid density, interfacial tension, partition coefficients, phase boundaries, radial distribution functions, and concentration profiles. These will be crucial in predicting the correct aggregation behavior.

The parameters in the MARTINI forcefield were derived from experimental values for free energies of vaporization, hydration, and partitioning between water and organic phases. Further validation was done by comparing the potential of mean force (PMF) for extracting a lipid molecule from and moving it through a bilayer (Marrink

et al., 2007). They extended it to study polyethylene oxide using experimental densities and atomistic distributions of the chain size in solution (Lee et al., 2009).

The original Shinoda forcefield was parameterized from experimental densities and interfacial tensions and complemented by atomistic simulations of radial distribution functions and the concentration profile across a bilayer. For a family of ionic surfactants it was parameterized from the radial concentration profiles of micelles (He et al., 2010). Fullerenes such as C60 and CNTs were parameterized from free energies of transfer from heptane to benzene and of dimerization in water (Chiu et al., 2010).

One advantage of deriving parameters from atomistic simulations is that one has greater control, ensuring a closer correspondence between the data from each scale. In fact, three systematic methods exist for deriving coarse-grained parameters from atomistic simulations. In Boltzmann inversion (Reith et al., 2003), a large representative set of frames from the atomistic trajectory are collected. The trajectory is coarse-grained and used to measure the distributions of bonds, angles, and pair distances. If uncorrelated, each energy term can be decoupled in the expression for the Boltzmann distribution $\rho \propto \exp(-\beta E)$. The potentials can then be fitted to the distribution for each type of interaction. This does not work as well for nonbond interactions so these usually need further refinement against condensed phase data as mentioned above.

The force-matching method fits the coarse-grained forces against the net forces between the centers of mass of the corresponding groups in atomistic simulations (Izvekov and Voth, 2005). Another approach called reverse Monte Carlo derives an effective interaction potential from knowledge of the radial distribution function by iterating Monte Carlo simulations until the results converge (Lyubartsev and Laaksonen, 1995). A good review of these methods can be found in Voth (2008).

DPD and DDFT follow a more top-down approach to parameterization with the Flory-Huggins interaction parameter χ_{ij} as the basis. DDFT uses χ directly whereas, for DPD, a linear correlation between a_{ij} and χ_{ij} was derived based on the empirical DPD equation of state (Groot and Warren, 1997). Experimental data for χ_{ij} exists for standard polymers in common solvents, but is usually insufficient to provide a complete parameterization. The most common method to derive interaction parameters is from the Scatchard-Hildebrand theory of solutions:

$$\chi_{ij} = \frac{V_{\text{ref}}}{k_{\text{B}}T}\left(\delta_i - \delta_j\right)^2 \tag{1.19}$$

where δ is the Hildebrand solubility parameter of each component and V_{ref} is the reference volume of a bead. This approximation works best for nonpolar solutions of like-sized molecules. The solubility parameters can be obtained from handbooks, QSPR models, or atomistic simulations of the CED (Eq. (1.13)).

The interaction parameter is more closely associated with the enthalpy of mixing:

$$\chi_{ij} = \frac{\Delta E}{\varphi_i \varphi_j k_{\text{B}}T} \tag{1.20}$$

where φ is the volume fraction of each component in the mixture. However, this approach is more unwieldy because an energy of mixing simulation must be conducted for every binary pair of components.

1.2.4 Multiscale modeling

Up to this point, only methods appropriate for a particular length and time scale have been described. These methods offer a tradeoff between scale and accuracy. How, then, can one apply methods with the accuracy of quantum mechanics to problems on the scale of meters? The answer lies in multiscale approaches. Multiscale modeling received significant recognition this year when the Nobel Prize in chemistry was awarded to Martin Karplus, Michael Levitt, and Arieh Warshel for "the development of multiscale models for complex chemical systems." Their work formed the basis for the methods that will be discussed in this section.

There are two primary approaches to multiscale simulation (Karakasidis and Charitidis, 2007): hierarchical and hybrid methods. Hierarchical modeling builds up a model starting at the highest resolution (e.g., quantum mechanics) and uses the results to create a model at the next level (e.g., molecular mechanics). A single method is used at a time, and the final, high-level model is developed with minimal reference to experimental data. Hybrid methods, by contrast, employ multiple levels within a single computation, each describing a particular region to the necessary level of resolution.

1.2.4.1 Hierarchical methods

As mentioned above, hierarchical methods operate by modeling a small portion of the system at high resolution and using the results to drive a lower resolution model. This generally takes the form of fitting parameters at the higher resolution for use in the lower level of resolution. An example of this is the use of *ab initio* calculations to develop forcefield parameters. If forcefields are fitted to experimental data, their validity is limited to a narrow region around the experimental geometry. In addition, the limited amount of experimental data restricts the number of terms that can be used in the forcefield. By contrast, *ab initio* results can be generated for molecular geometries at points other than the global energy minimum. By generating a greater number of points one obtains sufficient data to fit the forcefield to more complex functional forms. This results in forcefields with higher accuracy and greater transferability (generality). The so-called class II forcefields were developed in this manner (Maple et al., 1994). The fitting procedure used not only geometries and energies but also the first and second derivatives of the energy. The initial work on hydrocarbons reproduced the *ab initio* potential energy surface to within 7%. The procedure is applicable to a broad range of functional groups including amides, peptides (Maple et al., 1998), and carbohydrates (Hwang et al., 1998).

The process is repeated when going from atomistic to mesoscale. One must first define how atoms will be grouped into beads and then determine the parameters for bead-bead interactions. This is similar to the approaches used in fitting forcefields

to *ab initio,* but because mesoscale methods are commonly employed in condensed phases, additional effort is invested in fitting the nonbond terms (Coulomb and van der Waals). A more recent approach developed coarse-grained polymer parameters by fitting nonbond terms to the density and radius of gyration of the monomer units (Rossi et al., 2011). Experimental data were used where available but were supplemented with molecular mechanics results. The approach has also been used to derive mesoscale parameters for polymer cross-linking on metal oxide surfaces (Iwamoto, 2012).

Methods such as finite element methods (FEM) are used to model materials at the macroscale. FEM models require as input fundamental materials properties, such as Young's modulus. Molecular modeling can provide these even when they are not known from experiment. These properties can be computed by DFT when the structure has a small unit cell or by forcefield methods if the structure is amorphous. For example, elastic constants of Ti-X (with X = V, Nb, Ta, Mo, W) computed with DFT were used in the development of novel, multifunctional titanium alloy with a low Young's modulus and high strength (Ikehata et al., 2006).

1.2.4.2 Hybrid methods

Hybrid methods incorporate multiple resolutions side by side in a single simulation as illustrated in Figure 1.7. The 2013 Nobel Prize in chemistry was awarded for developing the "secret handshake" that merges the results of the different scales seamlessly. QM methods are needed to model a catalyzed reaction in a zeolite pore and to describe the chemical bond formation. A forcefield can describe any distortions in the zeolite lattice. Effects such as stress-induced fracture of the zeolite crystal or fluid flow of reactants can be described with FEM. There is no need to limit calculations to methods illustrated in Figure 1.7. In principle it is possible to combine any of the methods into a hybrid multiscale model, but the most common is called QM/MM: a model combining QM and molecular mechanics (MM), It will be the focus of the remainder of this section.

QM/MM approaches offer several advantages over pure QM or pure MM calculations. The QM method is accurate but more expensive than MM. By limiting its application to a small region of interest, high precision can be maintained for much lower

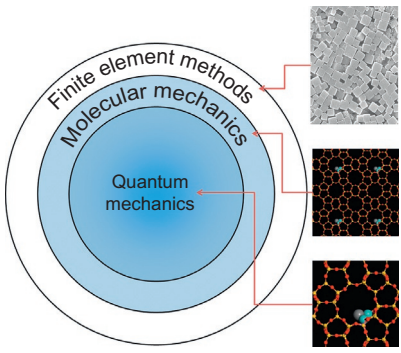

Figure 1.7 Schematic view of hybrid model for zeolite-support catalysts. See text for details.

cost. QM can also be used in situations where forcefield parameters are unavailable or inaccurate, such as metal-ligand binding. These advantages make it possible to apply the accuracy and capabilities of QM to systems that would normally need to be treated by MM.

1.2.4.3 QM/MM

Consider a system like the zeolite fragment in Figure 1.8. A QM-based method is applied to a small inner region (***I***). The outer region (***O***) is treated with MM. The total system ***S***, is the combination of the two. A distinct boundary demarcates the two regions.

QM/MM methods can be categorized based on:

1. The interaction between ***O*** and ***I***, "mechanical" versus "electronic" embedding.
2. The schemes to handle bonds that cross between regions.
3. The way the total energy of ***S*** is computed.

In electronic embedding, the atomic MM charges are allowed to polarize the charge density in the ***I*** region. The MM atoms are likewise subject to electrostatic forces from their interaction with the QM electron density. Electronic embedding is generally used when polarization of the QM will be significant. Examples of this situation include bulk or surface systems with ionic character. This embedding type is also dominant in biological applications. In mechanical embedding schemes, the quantum calculation on ***I*** is carried out ignoring any forcefield charges on the atoms in the ***O*** region. The MM region physically constrains the QM region. Further details on embedding may be found in Antes and Thiel (1998) and Bakowies and Thiel (1996).

The occurrence of covalent bonds between the QM and MM regions in the structure makes modifications of the QM and MM calculations necessary. Simply truncating the QM region would leave dangling bonds that are unphysical. The most common approach is to cap these bonds with a so-called *link atom*, usually hydrogen, as illustrated in Figure 1.9. The QM-Pot approach (Eichler et al., 1997) positions the link atom on a line connecting the QM and MM atom and freezes its bond distance at a standard value. This approach has been widely used in zeolites (Rodriguez-Santiago et al., 1998) and has been employed using two QM regions of different accuracy (DFT/MBPT2) (De Moor et al., 2008).

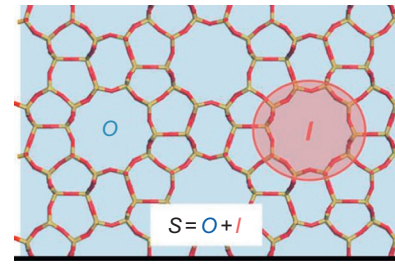

Figure 1.8 Partitioning of a system (S) into an inner region (I) treated with quantum mechanics and an outer region (O) treated with molecular mechanics.

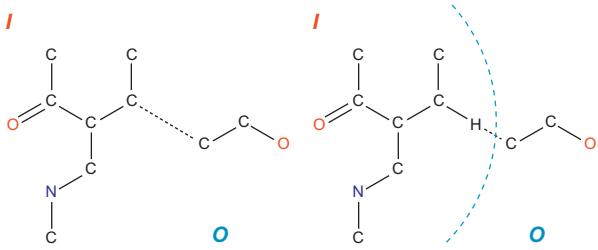

Figure 1.9 Bonds that connect the quantum region (I) with the molecular mechanics region (O) are capped with hydrogen atoms.

Another approach is to cap the broken bonds with frozen MOs (Phillipp and Friesner, 1999). This approach has been widely used in models of ligand-protein docking (Murphy et al., 2000).

The general expression for the total energy E_{tot} in QM/MM can be written as:

$$E_{\text{tot}} = E_{\text{QM}} + E_{\text{MM}} + E_{\text{QMMM}} \tag{1.21}$$

where E_{QM} is the energy from the quantum region, E_{MM} that from the molecular mechanics region, and E_{QMMM} is an interaction term.

In subtractive QM/MM, three calculations are performed:

- An MM calculation on the entire system ***S***
- A QM calculation on the inner region ***I***
- An MM calculation on the inner region ***I***

and the total energy E_{tot} is taken as the subtractive energy:

$$E_{\text{tot}}^{\text{sub}} = E_{\text{QM}}(I) + E_{\text{MM}}(S) - E_{\text{MM}}(I) \tag{1.22}$$

Alternatively, additive QM/MM requires

- An MM calculation on the outer region ***O.***
- A QM calculation on the inner region ***I.***
- An QM/MM energy term based on total region ***S.***

The total energy E_tot is taken as the additive energy

$$E_{\text{tot}}^{\text{add}} = E_{\text{QM}}(I) + E_{\text{MM}}(O) \mp E_{\text{QMMM}}(S) \tag{1.23}$$

The expression for E_{QMMM} depends on the type of embedding. For additive electronic embedding, the QM region is polarized by the point charges in the MM region, so $E_{\text{QM}}(I)$ includes contributions from this polarization. In additive mechanical embedding, E_{QMMM} is calculated at the classical level by using QM-derived point charges on the atoms in region *I*.

Although simple to compute, the subtractive scheme requires MM parameters in the ***I*** region, while the additive scheme does not. Therefore, even if the forcefield

parameters are not available for atoms in the ***I*** region, it is still possible to use the additive scheme. Mechanical subtractive embedding is similar to the ONIOM approach (Maseras and Morokuma, 1995), which was recently reviewed by Chung et al. (2012).

1.3 Nanomaterials

1.3.1 Polymer nanocomposites

Composites are defined as a "combination of two or more materials (reinforcing elements, fillers, and composite matrix binder), differing in form or composition on a macroscale. The constituents retain their identities, that is, they do not dissolve or merge completely into one another although they act in concert. Normally, the components can be physically identified and exhibit an interface between one another" (Davis, 1992). Examples are cements and metal-matrix composites. Polymer nanocomposites (PNCs) are a relatively new class of materials in which nanofillers that have at least one dimension in the range of 1-100 nm are dispersed in a polymer matrix (Michler, 2008).

Bakelite, a thermosetting resin used in household products for its insulating properties, is often cited as one of the first mass-produced PNCs (Balazs et al., 2006). However, tire manufacturers were already developing PNCs using carbon black filled rubber for improved mechanical properties. PNC materials are of high interest in the aerospace, automotive, and nuclear power industries because they are light and strong (Voronina, 2011); research in this area has been reviewed by Doyle (2009). To a large degree, it is the high specific surface area of the fillers that confers specific properties to a PNC. Hence, the interfacial regions between matrix and filler are critical. One of the key challenges to the commercialization of polymer nanocomposites lies in the difficulty of controlling the dispersion of nanoparticles in the polymer host (Michler, 2008). Another issue is to establish valid structure-property relationships. Simulation techniques have been frequently and successfully employed over the years to tackle such problems.

Simulating composite materials offers new challenges. An atomistic description is often needed to be able to accurately describe the bulk polymer matrix or the filler interface, but the mechanics of the entire filler particle within the matrix is on a much larger scale. Moreover, it is usually macroscopic properties such as viscosity and tensile strength that are of interest. Linking the molecular and nanostructure to the macroscopic property of interest (structure-property relationship) is the real challenge here.

To that end, multiscale simulation techniques described in Section 1.2.4 have increasingly been applied over the years. Recent reviews have focused on polymer-nanotube (Zeng et al., 2008) and polymer-clay nanocomposites (Scocchi et al., 2007a,b, 2009). Other studies have investigated polymer-talcum systems (Na et al., 2012) and epoxy resins (Yu et al., 2009), including their application in microelectronics (Iwamoto et al., 2011) and delamination in electronic packages (Fan and Yuen, 2010).

Molecular modeling is well suited to study materials and estimate their properties at the nanoscale for multiple reasons. First, it is relatively easy to build complex nanoscopic models with current commercial modeling packages. Using relevant building tools, such as those implementing Monte Carlo techniques, the modeler can "disperse" the nanofillers within a model polymer matrix. A wide variety of surface modifications can easily be applied to, for instance, a CNT filler (Maiti et al., 2005), enabling screening of potential dispersion solutions for testing in the laboratory. Similarly in clays, Monte Carlo tools can be used to intercalate polymer chains between nano-sized layers (Na et al., 2012). Second, molecular properties (electronic, miscibility, mechanical, etc.) can be estimated using the simulation techniques described in Section 1.2, which helps to establish the property-structure relationship.

In a recent study, Sheng et al. (2013) estimated the glass transition temperature of polyethylene/graphene nanocomposites using MD simulations (Figure 1.10). The authors tested the effect of the number graphene sheets inserted on the glass transition temperature. Graphene is a new material with promising applications due to its exceptional intrinsic properties (Geim and Novoselov, 2007).

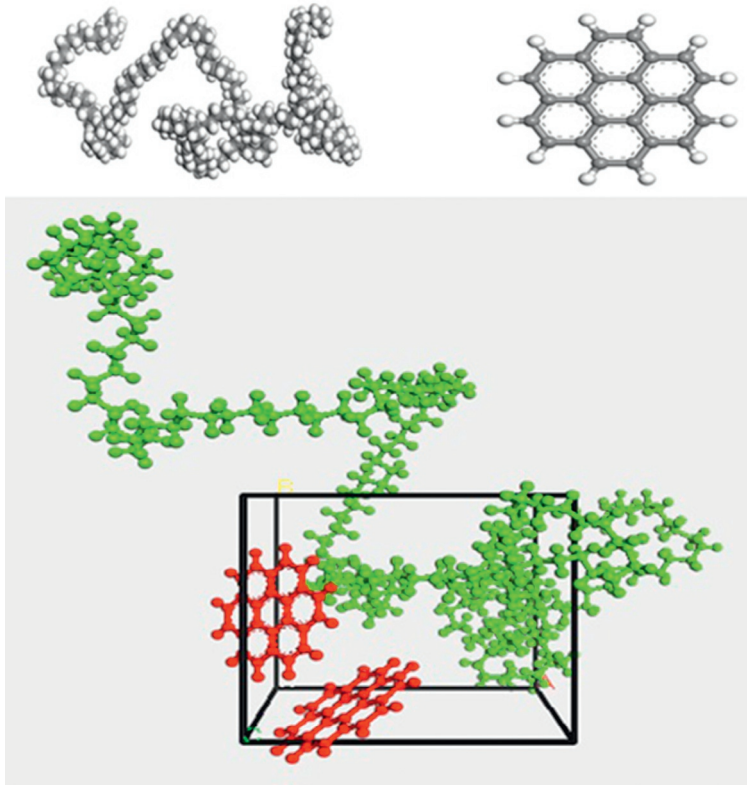

Figure 1.10 Molecular model of amorphous phase of mixture of polyethylene and graphene particles.

Compared to pure polyethylene, such composites have demonstrated an improvement in thermal/flame resistance (Xiong et al., 2004, 2007), mechanical properties (Doyle, 2009), and electrical properties (Tuncer and Sauers, 2010). Polyethylene has been the subject of many MD simulations (Pant et al., 1993; Paul, 1999). In such simulations, the glass transition of polymer was estimated (Soldera and Metatla, 2006; Barrat et al., 2010). Graphene and other nanostructured carbon-based materials have also been extensively simulated over the years (Thostenson et al., 2001). Recently, functionalized graphene sheets for polymer nanocomposites were studied (Ramanathan et al., 2008; Awasthi et al., 2009).

In their study, Sheng et al. (2013) performed successive NPT MD simulations of polyethylene models made up of a single 100-monomer chain with zero to two graphene sheets (see Figure 1.11) using the COMPASS forcefield (Sun, 1998) from the Materials Studio package (Accelrys, 2013). By varying the temperature and plotting it against the simulated specific volume, the glass transition of the various models was estimated.

The composite showed a lower glass transition temperature than pure polyethylene; increasing the graphene content decreased Tg further. In other words, the inserted graphene sheets behave like a plasticizer. Various energy components such as van der Waals and torsional were studied in order to explain this phenomenon.

Rissanou and Harmandaris (2013) recently studied poly(methyl methacrylate)-graphene composites using MD simulations. Their goal was to study the effect of graphene on the structural and dynamical properties of PMMA. Their models consisted of a number of PMMA chains inserted between two sheets of graphene of various widths (Figure 1.12). They used atomistic NPT and NVT MD simulations using the all-atom OPLS forcefield (Jorgensen et al., 1996). The Steele potential (Steele, 1973) was used to describe the graphene layers because this is a well validated forcefield for purely carbon-based structures. A series of high temperature MD runs were performed to equilibrate the models. The density of the simulated bulk material was in agreement with that of experimental data, although slightly underestimated.

The simulations clearly demonstrated the attraction between the polymer chains and the graphene sheets. The polymer concentration profiles plots showed high-

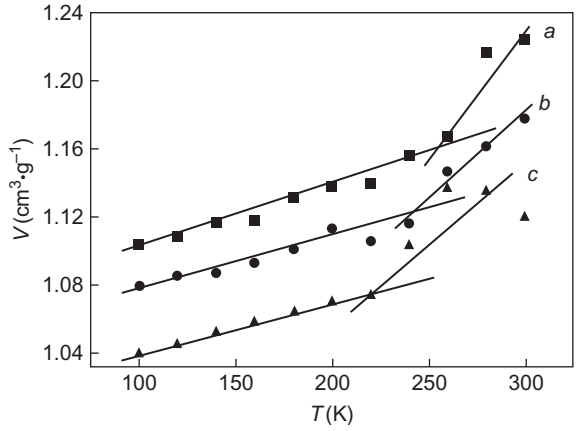

Figure 1.11 Specific volume versus temperature for (a) pure PE, (b) PE with one graphene sheet, and (c) PE with two graphene sheets (Sheng et al., 2013).

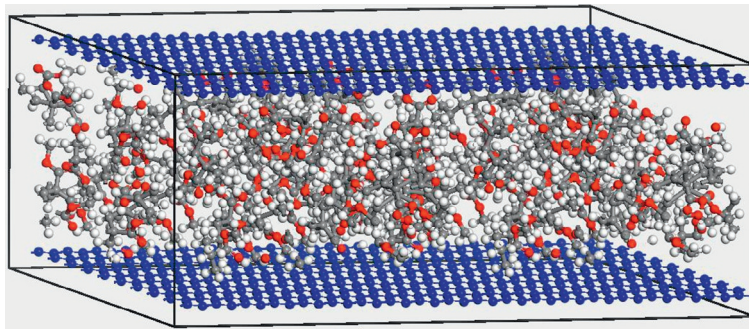

Figure 1.12 PMMA-graphene composite model.

intensity peaks in the vicinity of the carbon surfaces, similar to those in polyethylene-graphene systems (Daoulas et al., 2005). Moreover, it was found that the polymer chain ends had the greatest affinity for the graphene. The simulations also revealed that "segmental dynamics close to the surface is much slower (from two up to four orders of magnitude) than the bulk one." Future work will explore different polymers and the coarse graining of the models.

A multiscale modeling approach has also been applied to the polymer nanocomposite problem by Yu et al. (2009). Combining MD simulations and a sequential scale bridging method, they studied epoxies containing alumina (Al_2O_3) nanoparticles of variable size. The mechanical properties of the various models were investigated using the Parrinello-Rahman fluctuation method (Parrinello and Rahman, 1982). Using the COMPASS forcefield (Sun, 1998), models of EPON862® (DGEBF) cured with triethylenetetramine (TETA) were built. These building blocks are depicted in Figure 1.13.

A box with a mixture of both components was simulated, and when the relevant atoms of curing pairs came within a minimum distance (5 Å), a bond was created representing a crosslink. The final crosslinking level was around 50%. A good agreement with previous simulations and experimental data was obtained for the prediction of the glass transition temperature and Young's modulus. Equipped with a good representative model of epoxy resins, nanoparticles of alumina of sizes ranging from 6 to 10 Å were then inserted in the simulation boxes. The elastic moduli of the unit cells were estimated. Results showed that the Young's and shear moduli are enhanced as the particle size decreases, in agreement with previous experimental studies (Cho et al., 2006). The authors then applied a sequential scale bridging method (Yang and Cho, 2008), which description is beyond the scope of the present chapter.

1.3.2 Inorganic nanostructures

Inorganic materials constitute an enormous breadth of substances. In this section we will describe how multiscale modeling has been applied to some commercially significant materials: metal-organic frameworks (MOFs), zeolites, and heterogeneous catalysts. Modern DFT methods have little problem performing accurate calculations on any of these materials. Forcefields are available for many metal-organic and

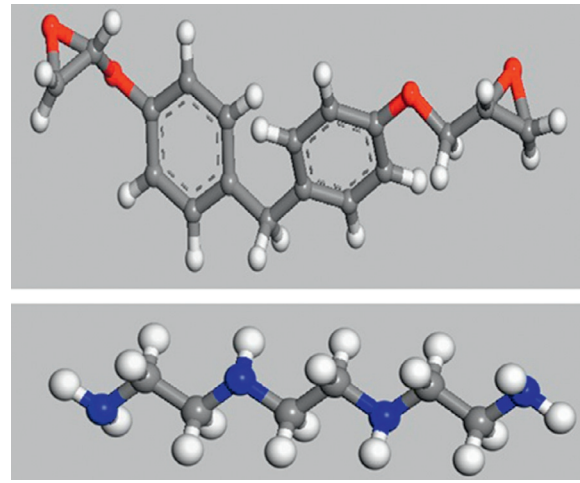

Figure 1.13 Molecular models of crosslinking precursors: DGEBF (top) and TETA (bottom).

metal-oxide interactions. By fitting results to analytical expressions, it is possible to model many of these materials at the macroscale such as in a chemical reactor. This section will explore how these methods can be combined to deliver multiscale models of these materials.

1.3.2.1 Zeolites

Zeolites are microporous aluminosilicates widely used in commercial applications for separations and catalysis. Zeolites can serve as catalysts for propane aromatization (Biscardi et al., 1998) or dehydrogenation (Ono, 1992), among many other reactions. Zeolites are challenging to model primarily because of the number of atoms in the unit cell. Faujasite (FAU), pictured in Figure 1.14, has 576 atoms in the unit cell, which stretches the capabilities of QM modeling—at least on a time frame acceptable to industrial research. Use of forcefields and hybrid methods is necessary to make modeling of such systems tractable. Detailed aspects of modeling of zeolites and other microporous materials have been reviewed by Catlow et al. (2004).

Generally speaking, adsorption and diffusion processes that are driven by van der Waals and Coulomb interactions have been studied with forcefields, while chemical reactions have been modeled using DFT or hybrid methods. For instance, the selectivity of zeolites toward hydrocracking versus isomerization can be understood in terms of the adsorption of reactants in the zeolite cavity (Benazzi et al., 2003). In their case, it was not necessary to model the entire reaction pathway quantum mechanically, but only to compute the binding energy at the forcefield level. The effects of zeolite pore size can also be understood this way (Toulhoat et al., 2004).

Fully QM approaches have been used in the study of methanol activation to form gasoline. Some of these calculations have been quite successful using molecular

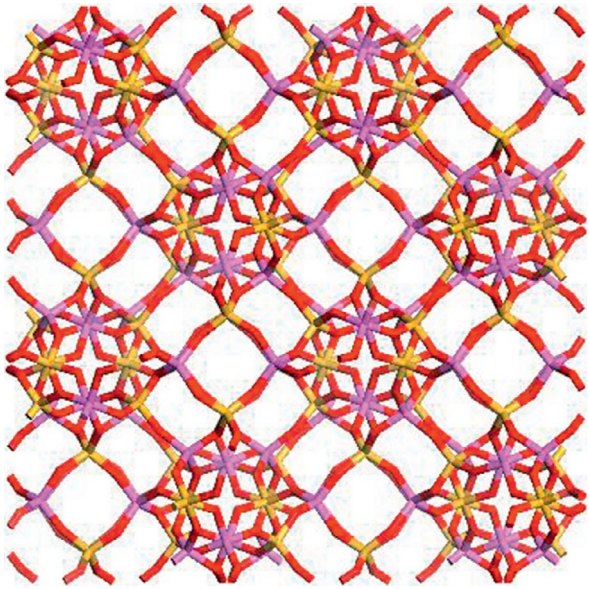

Figure 1.14 Unit cell of zeolite faujasite (red = O; yellow = Si; magenta = Al).

clusters to model the zeolite framework (Blaszkowski and van Santen, 1997), while others model the entire zeolite with periodic boundary conditions (Andzelm et al., 2003).

Hybrid QM/MM methods make it possible to include the effects of framework atoms without the concomitant computational cost. Applications to zeolites were pioneered by Sauer and Sierka (2000), who was able to predict proton mobility (Sierka and Sauer, 2001) and energy barriers (Clark et al., 2004) using forcefields and DFT. More recently, QM/MM has been used to predict the UV spectrum of $Ti(OH)_4$ clusters embedded in MFI (Halasz et al., 2011). Recent work on Fischer-Tropsch catalysts used QM/MM to predict the structure of Mo_2 and Mo_4 carbide clusters in zeolite ZSM-5 and to understand how the Mo-C bond activates methane (Gao et al., 2013).

1.3.2.2 Metal-organic frameworks (MOFs)

MOFs are framework materials consisting of metal ions or clusters connected by organic ligands. A typical example is shown in Figure 1.15. MOFs have received much attention because of their abilities to absorb small molecules and to act as catalysts. The ability to absorb molecular hydrogen (Murray et al., 2009; Getman et al., 2012) makes them attractive for energy storage. The U.S. Department of Energy has mandated hydrogen storage capacities of 40 g H_2/liter by 2015 (Yang, 2010). Some materials already achieve capacities in excess of that (Furukama et al., 2007), although unfortunately only at 77 K. Their ability to absorb CO_2 also makes them promising candidates for use in capture and sequestration of this greenhouse gas (Liu et al., 2012a,b).

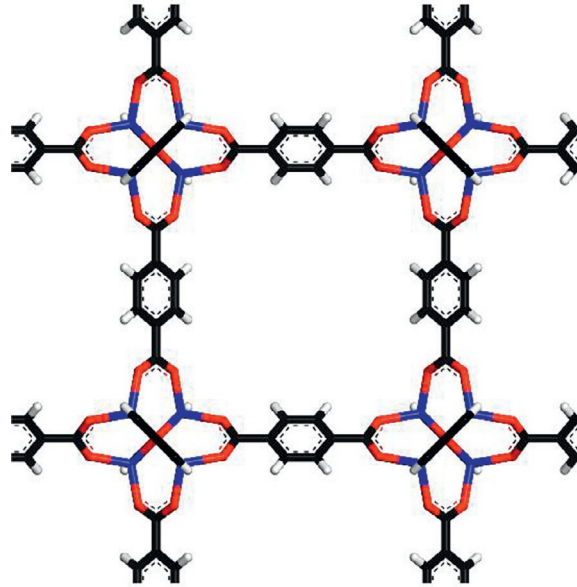

Figure 1.15 Unit cell of MOF-5 based on coordinates from Eddaoudi et al. (2001) (black = C; red = O; blue = Zn; white = H).

MOFs have been studied by both hierarchical and hybrid multiscale methods. Amirjalayer et al. (2011), for example, derived a forcefield from *ab initio* calculations for use with a $Cu_2(O_2C)_4$ paddle wheel compound. Other research groups have used the DFT-validated charge equilibration method to produce a forcefield with variable atomic charges (Wilmer and Snurr, 2011). The hierarchical approach was extended to the coarse-grained level to create a semiquantitative approach for very rapid screening of MOFs as adsorbents (Yu et al., 2012). A hybrid QM/MM approach was employed by Oxford et al. (2010) to study the effect of substituents on catalytic selectivity.

1.3.2.3 Catalysts

Catalysts are computationally challenging because a full description encompasses several orders of magnitude. Elementary reactions at the catalytically active centers require QM models. Diffusion processes are treated using molecular mechanics. Long-term kinetics can be treated with kinetic Monte Carlo (KMC). Ultimately, engineers will model the flow of reactants and product with computational fluid dynamics. Raimondeau and Vlachos (2002) produced a comprehensive review of multiscale modeling of chemical reactors.

For elementary reactions, DFT still remains the method of choice for computing heats of reaction, energy barriers, and transition states. As already mentioned, DFT is reliable to ~5 kcal/mole. This is adequate for many applications, but accurate kinetic models require greater accuracy because the reaction rate decays exponentially

with the energy barrier $E^{\ddagger}$: rate $\propto \exp(-E^{\ddagger}/kT)$. An error of 5 kcal/mol can lead to errors of several orders of magnitude in the predicted rate. Electron-correlated methods such as CCSD and MCSCF can deliver the requisite accuracy but are limited to small elementary reactions. In most cases, DFT is the only practical option. Researchers can in some cases calibrate the computed results against experiment to obtain a "fudge factor." Another approach is to employ sensitivity analysis (Gupta and Khammash, 2013; Vlachos et al., 2006). A full description of a chemical reactor may require hundreds of coupled chemical reactions (Vlachos et al., 2006). A sensitivity analysis can be used to determine which reaction parameters (heats of reaction, energy barriers) are key to predicting reactor performance. High-level electron-correlated methods can be applied to the most important reactions, DFT to others, and the least important can be estimated by empirical means.

DFT has other limitations when studying such materials. Generally, calculations are performed on ideal crystal surfaces, but defects like steps and kinks are often the active sites. A large number of surface structures must be explored in order to ascertain the "real" surface. DFT can be used to derive parameters for forcefields such as the embedded atom method (EAM), an approach that has been successful in the description of metallic systems (Sutton and Chen, 1990), or COMPASS (Sun, 1998), which has been successful with metal oxides.

Optimization of the entire chemical reactor requires models of even greater length and time scales. The chemistry of the reactants can be computed as described above and input to a microkinetic model. The goal is subsequently to optimize conditions such as temperature and flow rates to maximize yield. A detailed description is beyond the scope of this paper, but a number of recent reviews are available (Vlachos et al., 2006; Keil, 2012, 2013).

1.3.3 Soft matter

Many nanomaterials exploit the special properties of "soft matter" such as surfactants, polymers, and biomaterials. Liposomes composed of phospholipids are designed as nanocapsules for the delivery of drugs, genes, and nutrients in the body, helping to solubilize the cargo, protect it from harm, and home in on the target. Liposomes are also used in textile dyeing and cosmetics.

Industrial surfactants are capable of self-assembling into an amazing variety of structures and morphologies including micelles, hexatic arrays of cylindrical micelles, inverse micelles, and lamellar phases. They too have been used in drug delivery, but also in nano-templating applications or as nanoparticle coatings.

1.3.3.1 Lipids

Typical simulations of phospholipid bilayers consider 10-50 ns of dynamics of a 128-lipid, 6-nm square patch of bilayer surrounded on either side by a layer of water molecules. These systems have been as large as 1024 DPPC lipids (20 nm) (Lindahl and Edholm, 2000), 1600 DPPC (Scott, 2002), and 1800 GMO lipids (Marrink and Mark, 2001). The longest atomistic simulations have gone up to 800 ns and 1 μs (Lyubartsev,

2005). Depending on the temperature and composition, the bilayer can exhibit two lateral ordering regimes described as liquid crystal and gel phases. Reproducing these may require a careful treatment of electrostatic interactions of the zwitterionic head groups and water. Modelers often apply a special constant surface tension ensemble in which P_1 and P_2 are separately coupled pressures in the lateral and normal directions (Scott, 2002). The typical diffusion time of a phospholipid is slow, requiring about 50 ns to diffuse to site of its nearest neighbor (Stevens and Ha, 2004). The "flip" time for diffusing from one side of the bilayer to the other is much longer and can only be accessed by mesoscale modeling.

Forcefields are expected to reproduce lipid packing and ordering properties. The most commonly used forcefields for phospholipids are GROMOS/Berger and CHARMM (Lyubartsev and Rabinovich, 2011). Recently, the AMBER forcefield has been extended (Cordomí et al., 2012; Dickson et al., 2012; Skjevik et al., 2012). These have the advantage that they can be used to study peptide interactions with the bilayer. The Dreiding forcefield has also been used as part of a three-tiered multiscale model of human skin (Akkermans and Wescott, 2011).

At the mesoscale, lipid forcefields have come a long way. The MARTINI and Shinoda forcefields, as mentioned in the methodology section, are attractive for their explicit coverage and transferability to other materials. These and others have permitted the simulation of a wide range of phenomena including spontaneous aggregation, domain formation, pores, budding, inclusions, and vesicles (Lyubartsev, 2005; Marrink and Tieleman, 2013).

Nanoparticle applications include fullerenes, graphene, and gold nanoparticles embedded in lipid bilayers (Marrink and Tieleman, 2013). CNT interactions have also been considered with interest toward solubilization (Wallace and Sansom, 2009; Qiao and Ke, 2006) and nanoinjectors (Wallace and Sansom, 2008). A recent review is available of lipid interactions with carbon nanoparticles (Monticelli et al., 2009).

Another review focuses on liposomal drug transport (Xiang and Anderson, 2006). Liposomes, because of their small radius, are subject to curvature strain and flip-flop equilibration of lipid mixtures must be considered (Risselada and Marrink, 2009). Similarly, disk-shaped nanoparticles called bicelles require redistribution of lipids for edge stabilization (de Joannis et al., 2006). Another application is as a nanocapsule for gene delivery (Marrink and Tieleman, 2013). DPD simulations have been used to study the cause of cell death under exposure to nonionic surfactants (Groot and Rabone, 2001). Another group studied the penetrating ability of nanoparticles as a function of shape (Yang and Ma, 2010). Transmembrane proteins have been modeled as a cylindrical assembly of DPD beads held together rigidly and with hydrophobic mid-section and hydrophilic ends (Venturoli et al., 2005). The tilt angle as a function of mismatch was analyzed.

A multiscale model for human skin—the stratum corneum—has been developed with emphasis on topical drug delivery (Akkermans and Wescott, 2011). At the macroscale, researchers modeled permeation through the interstices of a matrix of impermeable corneocyte cells. At the mesoscale, they studied how the composition of extracellular material impacts morphology. At the microscale, they considered the effect of a TeCd quantum dot on a lipid multilayer.

Another interesting example of a hybrid multiscale model was reported for the self-assembly of lipid bilayers (Huang et al., 2012). A simple CGMD model was used for the lipid component while MPC was used for the water. The interactions between the two species were treated with CGMD. Self-assembly is a very slow process, and elimination of some of the solvent degrees of freedom is helpful. They were able to generate liquid and gel phases and to reproduce elastic properties of the bilayer as well.

1.3.3.2 Surfactants and polymers

Polymers and surfactants are characterized by long chains that introduce new entropic driving forces into the material. Surfactants and block copolymers are both amphiphilic and consequently exhibit a diverse array of nanoscale morphologies. Nanoscale design using these materials is possible with knowledge of the phase diagram and precise control over synthesis of the components.

Nonionic surfactants are more easily modeled than ionic surfactants such as CTAB or SDS because of the long-range interactions that complicate charged materials. The presence of ions means that charge groups cannot be used and more expensive Ewald methods must be used—limiting the simulation size and length. Electrostatic interactions also present a problem for mesoscale methods. The soft beads of DPD with point charges at their center would result in unphysical superposition of oppositely charged beads. A work-around has been devised that replaces the point charges by a distribution of charge. In the density function approach, Donnan and Debye-Huckel screening approximations have been adopted for cases where the charges are low and salt concentration is significant.

Galderma modeled nonionic surfactants as carriers for a dermatological drug that cannot otherwise be delivered because it is lipophilic (Rigby and Pitré, 2013). DPD parameters for the surfactant and other formulation components were derived from atomistic simulations of the cohesive energy using the COMPASS forcefield. The mesoscale simulations were then used to predict under what conditions micellar encapsulation of the drug is obtained.

Another hierarchical multiscale study (Velinova et al., 2011) of surfactant morphologies discovered a sphere to rod transition. For validation of the coarse-grained model, it would be difficult or even impossible to run atomistic simulations that could capture significant aggregation events of the polyethylene glycol in water. Instead, dimerization simulations were performed and distributions for the end-to-end distance, cluster type, and dihedral angle were compared.

Block copolymer melts are well-known for their morphological complexity, and this can be amplified by confinement at the nanoscale. One study considered a polystyrene-block-polybutadiene melt known to adopt a toroidal morphology when confined in an alumina nanopore (Sevink and Zvelindovsky, 2008). They revealed a whole host of interesting structures as shown in Figure 1.16, which could have applications for templating. The use of DDFT greatly simplified the model because the pore can be considered as a boundary condition rather than being treated as a collection of restrained particles.

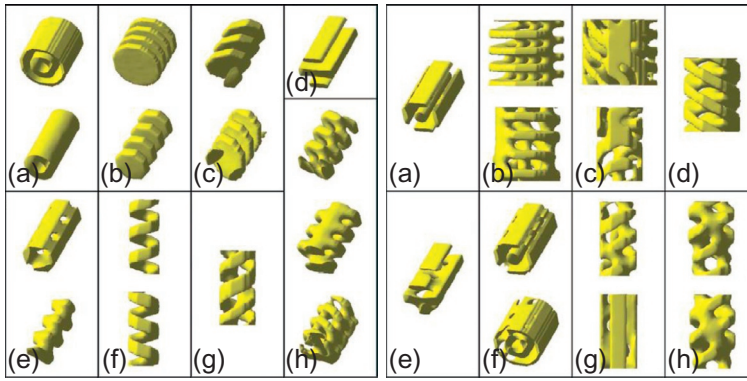

Figure 1.16 Morphologies of PS-b-PB polymer confined in a nanopore as modeled with DDFT and rendered as isosurfaces of the S component (Sevink and Zvelindovsky, 2008). Two degrees of freedom are varied to generate these shapes: the reduced pore radius and the surface adsorption/repulsion energy. When the pore is large and surface energy small, the bulk lamellar behavior takes over as in (left side: b). When the pore is smaller and surface energy significant, concentric cylinders form as in (left side: a).

1.3.3.3 Peptide assemblies

Peptide self-assembly has attracted interest for applications in nanomedicine and electronics, and modeling work in this area has recently been reviewed by Marrink and Tieleman (2013). The simplest building blocks are dipeptides, of which there are $20 \times 20 = 400$ essential combinations. Thus computational screening has been applied to identify viable candidates for assembly. Peptides aggregate into nanotubes, fibers, micelles, and even "peptosomes."

Peptides and lipids often combine to form complex assemblies and nanoparticles; for example, the lipoproteins HDL and LDL, which are responsible for cholesterol transport. Both have been simulated using the MARTINI forcefield and allow the modeler to understand the detailed distribution of components within the particle. Some proteins are capable of regulating lipid assemblies, for instance, in protein-mediated fusion of vesicles. In the body, nanoparticles quickly develop a corona of adsorbed proteins.

1.4 Application examples

1.4.1 Polymer nanodielectrics

Nanometric dielectrics or nanodielectrics were first mentioned in the literature in 1994 by Lewis (1994, 2004), who discussed the likely role of nanoscale interfacial processes in the initiation of electrical breakdown in insulating materials. In the last few years, it has been recognized that incorporating fillers such as silica nanoparticles into dielectric polymers such as polyethylene can greatly enhance stability (Roy et al., 2005; Nelson, 2010; Tuncer and Sauers, 2010; Li et al., 2010) and that the same effect is not observed when using micron scale fillers (Roy et al., 2007). The main difference in the observed electrical

properties originates from the difference in interfacial areas. In addition, surface modified nanofillers have an even larger impact (Huang et al., 2009; Olmos et al., 2012).

Recently Shi and Ramprasad (2008) and Wang and Ramprasad (2011) used DFT calculations to study the interfacial properties of nanodielectrics. For SiO_2-polymer composites, the dielectric constant near the interface was enhanced relative to the bulk (Figure 1.17).

In addition, analysis of the density of states (DOS) reveals the presence of defect states in the band gap of the materials at the interfacial region (Ramprasad et al., 2010). Such localized states act as potential traps for itinerant conduction electrons and valence holes, thus reducing their energy and explaining the higher breakdown strength of the composite material (Figure 1.18).

Meunier and Quirke (2013) estimated the DOS for various models of polymer nanocomposites, namely, low-density linear polyethylene (LLDPE) containing silica nanoparticles. DFT was used as implemented in the code DMol^3 of Materials Studio® (Accelrys, 2013). Initially, the band structures of the bulk materials (LLDPE and silica) were estimated. Computational results showed good agreement with experimental values and other computational studies, although the band gaps were somewhat underestimated—a well-known deficiency of the DFT approach. The DOS for various interfaces were subsequently computed, including the chemical modification of silica nanoparticles by trimethoxysilane and dimethyldichlorosilane. Defect states appeared

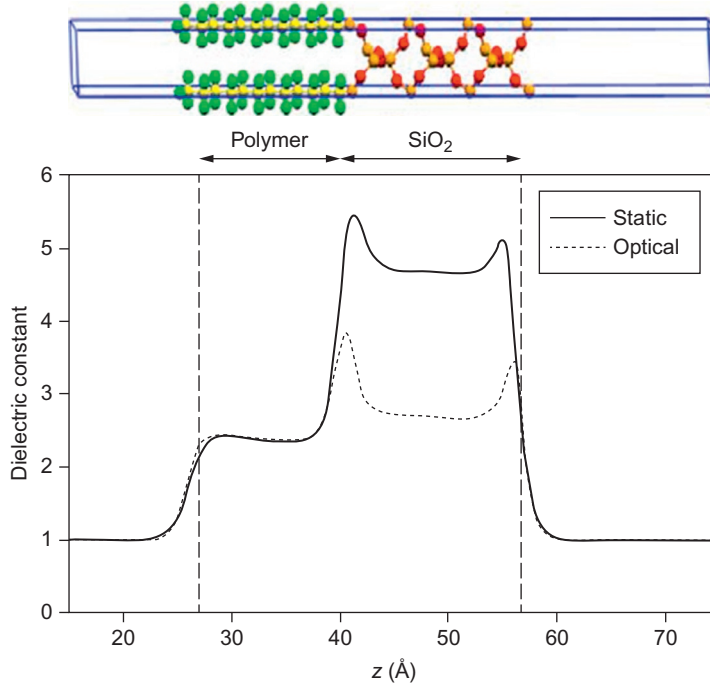

Figure 1.17 Schematic of $C_{12}H_{26}$-SiO_2 interface (top) and plot of dielectric constant along a direction normal to the interface (bottom). Dashed vertical lines indicate the experimental values of the bulk dielectric constants for each material (Shi and Ramprasad, 2006).

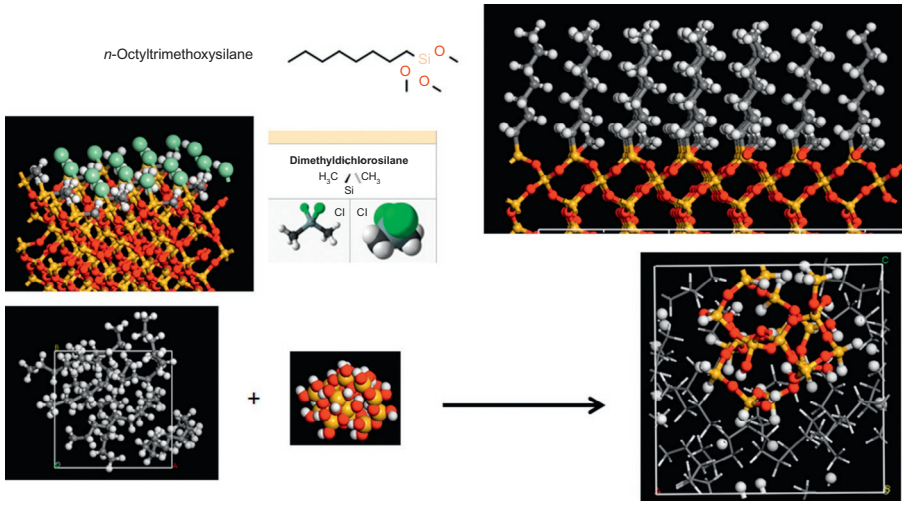

Figure 1.18 Surface modified models of nanofillers.

below the minimum of the conduction band (at ~0.2 eV) in the vicinity of the interfaces. Such states are thought to be responsible for the trapping of electrons and are involved in the conduction mechanism of such space charges.

1.4.2 Lithium-ion batteries

Rechargeable lithium-ion batteries are widely used in electronic devices and in both hybrid and electric vehicles. They provide high energy density and operate within a high voltage window (van Schalkwijk and Scrosati, 2002). The challenge is to simultaneously improve performance, lifetime, and cost. Modeling has already improved our understanding and accelerated the discovery of active electrode materials (Ceder, 2010). However, battery design is a challenging balancing act because the anode and cathode materials need to have their electrochemical potentials well matched to the oxidation and reduction potentials of the electrolytes (Goodenough and Kim, 2010).

A schematic of a lithium-ion battery appears in Figure 1.19. In its charged state, lithium ions are intercalated within a cathode material such as a spinel. During discharge, the ions migrate through an electrolyte to the anode, which is typically carbon. The electrolyte consists of a number of lithium salts such as $LiBF_4$ and $LiPF_6$ in an organic solvent such as ethylene carbonate or dimethyl carbonate. The scale of a completed battery is on the order of centimeters, but there is no shortage of research topics that can be addressed at the nanometer scale, as we will explore in this section.

The cathode must store lithium ions and release them when power is required. The capacity of the battery is limited by the number of ions that can be stored within the cathode material, power depends upon the rate at which ions can be extracted, and lifetime is limited by the number of charge/discharge cycles that the material can sustain. Cathode materials are typically oxides of transition metals that can accommodate

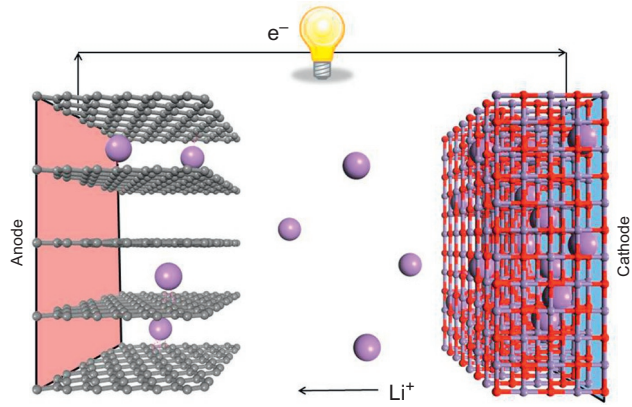

Figure 1.19 Schematic of a lithium-ion battery. Initially the lithium ions (gray spheres) are incorporated within the metal oxide cathode. During discharge, lithium diffuses through an electrolyte to the carbon anode, creating an electric current. During the charging cycle, the process is reversed.

lithium by changing their oxidation states (Guyomard, 2000; Whittingham, 2004). The most common material is $LiCoO_2$ (Antolini, 2004), but a number of other spinel structures such as $MgAl_2O_4$ and $LiTi_2O_4$ have been used (Ariyoshi et al., 2009). Layered, olivine, and silicate materials have also been used (Xu et al., 2012). Modeling has been used to predict the thermochemical stability of these materials and the total amount of lithium that can be loaded. Several studies have been performed using DFT (Armstrong et al., 2011; Cai et al., 2011).

Another key challenge is the formation of the solid electrolyte interphase (SEI) at the boundary between the anode and electrolyte. Whenever the voltage of an electrode exceeds the reduction and oxidation range of the electrolyte, it is necessary for the electrode surface to develop a passivating film. During initial charging, organic solvents and salt components are readily decomposed. These decomposition products form a passivating film that electronically isolates the negative electrode from the electrolyte but does not preclude Li^+ transport. One of the most common failure modes for these batteries involves excess SEI formation or loss of electron insulating and lithium ion transporting properties. As seen in Figure 1.20, the SEI thickness is on the order of 10s of nanometers, which requires a model in excess of 10^4 atoms. The need to account for chemical reactions, the lack of well-parameterized forcefields, and the sheer size of these systems requires the use of multiscale models.

Few computational studies have attempted to model the electrode and electrolyte simultaneously. The stability of the electrolytes themselves can be studied by *ab initio* methods. Halls and Tasaki (2011) used high-throughput computation to rank the stability of potential electrolytes. Zhang et al. (2001) calculated solvent oxidation potentials using DFT, assuming a one-electron transfer mechanism. Other work examined the effect of anions on decomposition using DFT (Xing et al., 2011) or using reactive forcefields (Bedrov et al., 2012).

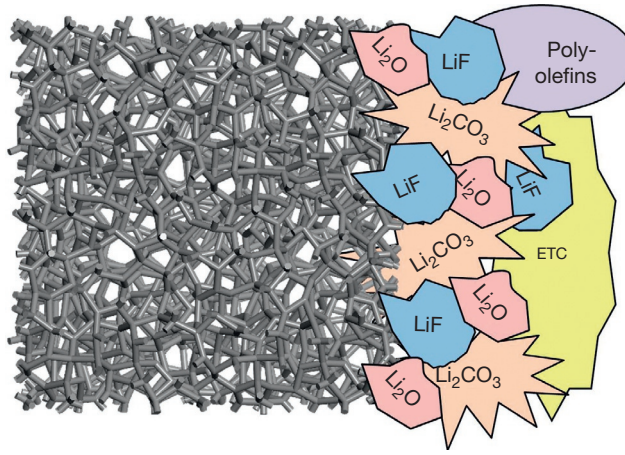

Figure 1.20 Illustration of solid electrolyte interphase (SEI). SEI forms on the carbon anode due to electrolyte decomposition. The illustration shows typical decomposition products and highlights the amorphous nature of the layer.

Leung et al. (2011) used DFT-based MD to track the electrolyte decomposition on bare and coated surfaces. Both one- and two-electron decomposition pathways of ethylene carbonate electrolyte have been studied (Leung, 2013). The models account, for example, for the significant quantities of CO and C_2H_4 gases observed during charging. In cases where it is necessary to model ion migration without decomposition, it is feasible to use molecular mechanics rather than DFT. Vatamanu et al. (2012) studied ethylene carbonate, dimethyl carbonate, and $LiPF_6$ at the surface of a graphite anode and demonstrated how the concentrations of Li^+ and PF_6^- varied as a function of electrode potential.

Unhindered diffusion of the lithium ions through the SEI is essential for battery performance. Useful results have been obtained using DFT (Iddir and Curtiss, 2010; Shi et al., 2013) and classical mechanics (Kerisit et al., 2009).

1.4.3 Reinforced resins for aerospace

Will CNTs take us to Mars? Already they have crossed the finish line first at the Tour de France! Aerospace materials scientists follow the imperative "lighter, thinner, stronger." Another important consideration is high-temperature resistance. Polymer resins and metals are used as structural materials reinforced with fillers such as carbon fiber, glass, or Kevlar; research is ongoing in the substitution of CNTs and graphene. CNTs can increase the tensile strength of these materials significantly (Thostenson and Chou, 2004). Commercial production of CNTs is currently in the thousands of tons per year, and leading structural commercial products include bicycle frames, turbine blades, and tennis rackets (De Volder et al., 2013). Traditional carbon fibers consist of stacked layers or cones of graphene sheets. CNTs are stiffer and stronger under tension but can also be bent without the brittleness of carbon fibers (Ajayan and Tour,

2007). The main issues are dispersion, alignment, scale-up, and cost (Moniruzzaman and Winey, 2006; Thostenson et al., 2005). Aerospace materials can bear the higher cost; consequently, such materials are emerging in this market (Ajayan and Tour, 2007; De Volder et al., 2013).

Just as multiscale modeling contributed substantially the development of CNTs themselves, it is helping to realize the use of CNTs in epoxy composites. These modeling efforts span the range from quantum to atomistic to mesoscale to engineering scale, although most are at the atomistic scale. Here we will focus on structural CNT-polymer composites.

Lordi and Yao (2000) conducted the first major molecular modeling study of these composites, anticipating major advances in mechanical properties. They focused on the adhesion between the two materials as key to transferring the nanotube strength to the polymer matrix. Adhesive wrapping of the nanotube was observed with polymers that have a helical bias in their backbone of commensurate diameter as shown in Figure 1.21. Helical wrapping has been seen in other studies, and atomistic forcefields were validated using *ab initio* methods (Haghighatpanah and Bolton, 2013). In order to make these latter calculations tractable, smaller sections of polymer and nanotube were necessary, but these indicated a bias for adsorption at a non-zero angle relative to the nanotube axis.

Molecular simulations have elucidated the factors that promote adhesion. Hydroxyl and phenyl side chains on the polymer promote adhesion (Lordi and Yao, 2000). Larger simulations in which a nanotube was pulled out of an amorphous polymer matrix revealed stronger frictional stresses than those in traditional carbon fibers (Liao and Li, 2001). Adhesion is also promoted by a larger nanotube radius and depends strongly on nanotube chirality (armchair is best) (Zheng et al., 2007). Adhesion can further be enhanced by functionalizing the nanotube surface with, for example, methyl or phenyl groups (Chen et al., 2008).

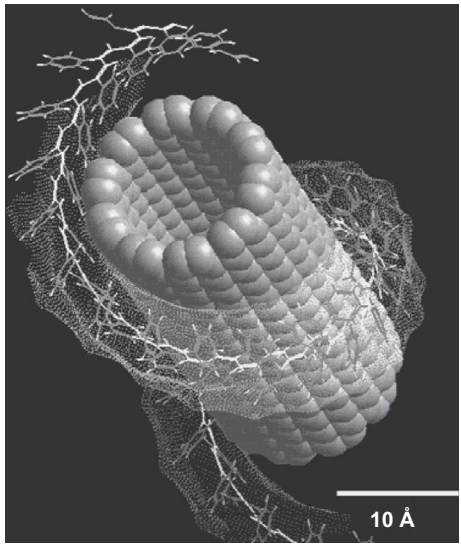

Figure 1.21 Poly(phenyl-acetylene) helically wrapped around a (10,10) SWNT and energy minimized with the PCFF forcefield. Sliding friction was inferred from the curve of binding energy versus axial polymer displacement relative to the nanotube. Taken from Lordi and Yao (2000).

Adhesion was also studied at the mesoscale level (Gurevitch and Srebnik, 2008). Monte Carlo was used to generate conformations of a generic bead-spring polymer around a smooth, attractive rod. Random to helical conformational transformations were seen as the adsorption energy and chain flexibility were varied. They also considered surface coverage and block copolymers. A recent mesoscale study explored the novelty of branched CNTs (Liu et al., 2012a,b). The presence of orthogonal nanotube branches increases the pullout shear stress by an order of magnitude, and the optimal configuration seems to be shorter more frequent branches.

Instead of adhesion, chemisorption can be used to hold the composite together, although high crosslink densities between CNT and polymer may damage the CNT's integrity. Frankland et al. (2002) matched an atomistic and macroscale model to show that less than 1% of the CNT atoms should be crosslinked to achieve load transfer in either crystalline or amorphous matrices.

As mentioned above, one of the major problems in making composites is obtaining a good dispersion of the nanotubes within the polymer matrix, that is, preventing the aggregation of CNTs into bundles. Another major issue is controlling their alignment. But larger scale simulations are needed in order to gain any insight. A first step in this direction is a DPD model, which was able to simulate a large number of CNTs interacting within a polymer matrix (Maiti et al., 2005). The nanotubes were simply modeled as bead-spring chains connected by stiff angle restraints. Shearing the polymer melt produced significant alignment as shown in Figure 1.22b. This study is an example of hierarchical modeling, as the DPD model was parameterized on the basis of atomistic forcefield calculations. The cohesive energies were calculated between bundles of nanotubes and between amorphous polymer chains in order to obtain interaction parameters. These values, as well as mixture simulations, have been used to estimate the energy of mixing (Nyden and Stoliarov, 2008). The miscibility was independent of CNT length and chirality, and increased with diameter—perhaps explaining why it is more difficult to disperse SWNTs than MWNTs.

Ultimately the objective of an aerospace materials scientist is to produce well-integrated composites with exceptional mechanical strength. A number of simulations have investigated the mechanical properties; this is an inherently multiscale problem because the coupling between a single nanotube and the polymer matrix is just a piece of the larger microscale picture. Typically, an embedded CNT is subjected to small deformations, and the stress response is measured in order to obtain the elastic constants. These deformations can involve elongation and compression, transverse stretching, and compression and shearing.

One of the earliest studies looked at the effect of short nonperiodic CNTs as compared to periodic models with effectively infinite length (Frankland et al., 2003). This study found that the stiffness of the material was only increased for the long nanotubes and only in the direction of the nanotubes. A similar study employed the reactive Brenner forcefield, but no significant bonding between the matrix and nanotube occurred (Griebel and Hamaekers, 2004). Researchers reported Young's modulus enhancements of a factor of 2 to 30 for the short (60 Å), capped nanotube (Figure 1.23) and infinite nanotube respectively. A recent study reported more modest (10-30%) enhancements for a shorter 20 Å nanotube. While most studies have

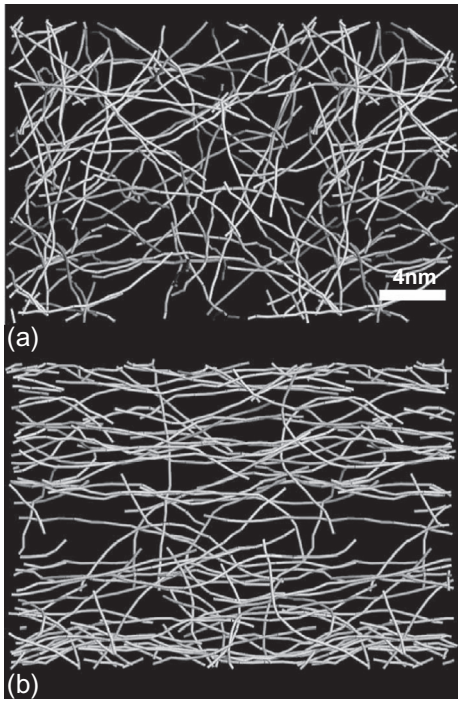

Figure 1.22 DPD simulation of (10,10) CNT dispersion (white) in amorphous PMMA polymer matrix (hidden) (a) no shear, (b) with shear (Maiti et al., 2005).

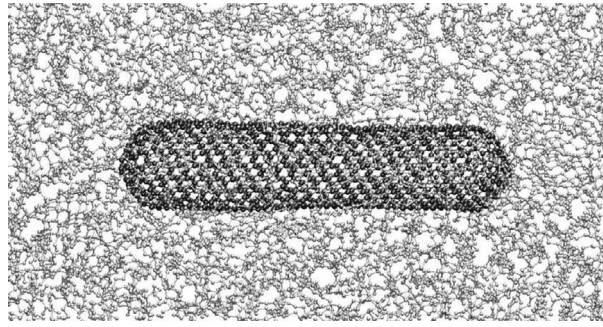

Figure 1.23 Capped (10,10) CNT of length 60A embedded in a polyethylene matrix (Griebel and Hamaekers, 2004).

investigated elasticity, one study looked at stress-strain curves until material failure as a function of volume fraction (Zeng et al., 2008).

There is more work for multiscale modeling to do on this emerging material. In particular, more information is required about how the distribution of nanotube orientations and lengths impacts the mechanical properties. Most of the above work has been done on perfectly aligned systems (because of periodic boundary conditions). Finite element modeling will be necessary to make further progress in this direction (Lusti and Gusev, 2004).

1.5 Conclusion

This chapter reviewed the application of molecular modeling techniques, in particular multiscale methods, to nanomaterials. It was shown that there exist many different such tools and that their combination offers a powerful new microscope at the nanoscale. At first *ab initio* or electronic structure methods were introduced and in particular the popular DFT method was presented. Many studies of nanomaterials have been performed using such QM methods. Classical simulation was then introduced. Its simpler theoretical foundation allows for the study of larger models at greatly reduced computational cost. Another level of reduction leads to the mesoscale; various methods such as CGMD and DPD were detailed. Multiscale modeling can be performed as a single simulation combining multiple methods (hybrid) or a series of simulations performed in sequence (hierarchical). The variety of nanomaterials is quite large and only a few examples could be reviewed here, although we hope to have covered new promising ones. For example, polymer nanocomposites represent one of the most popular nanomaterials for automotive or aerospace applications. Catalysts, also presented here, have long been the subject of computational studies. More recently, metal-organic framework appeared as a very promising type of materials that can be functionalized in so many different ways. Finally, three case studies on dielectrics, batteries, and resins were presented to illustrate in greater detail how multiscale modeling can be used to advance the development of nanomaterials. No doubt continuing advances in computer hardware and the lowering of its cost will promote further use of multiscale modeling and yield ever more accurate and relevant predictions for the properties of novel nanomaterials.

References

Accelrys, 2013. Help Documentation for Materials Studio 7.0.

Aidun, C.K., Clausen, J.R., 2010. Lattice-Boltzmann method for complex flows. Annu. Rev. Fluid Mech. 42, 439–472.

Ajayan, P.M., Tour, J.M., 2007. Materials science: nanotube composites. Nature 447 (7148), 1066–1068.

Akkermans, R., 2008. Mesoscale model parameters from molecular cluster calculations. J. Chem. Phys. 128, 244904–244913.

Akkermans, R., Wescott, J., 2011. Multiscale modeling of human skin. Curr. Nanosci. 7, 736–742.

Allen, M.P., Tildesley, D.J., 1987. Computer Simulation of Liquids. Clarendon Press, New York.

Amirjalayer, S., Tafipolsky, M., Schmid, R., 2011. Exploring network topologies of copper paddle wheel based metal-organic frameworks with a first-principles derived force field. J. Phys. Chem. C 115, 15133–15139.

Andzelm, J., Govind, N., Fitzgerald, G., Maiti, A., 2003. DFT study of methanol conversion to hydrocarbons in a zeolite catalyst. Int. J. Quantum Chem. 91, 467–473.

Antes, I., Thiel, W., 1998. On the treatment of link atoms in hybrid methods. In: Gao, J.L., Thompson, M.A. (Eds.), Combined Quantum Mechanical and Molecular Mechanical Methods. ACS, New York, pp. 50–65.

Antolini, E., 2004. $LiCoO_2$: Formation, structure, lithium and oxygen nonstoichiometry, electrochemical behavior and transport properties. Solid State Ionics 170, 159–171.

Ariyoshi, K., Makimura, Y., Ohzuku, T., 2009. Lithium insertion materials having spinel-framework structure for advanced batteries. In: Ozawa, K. (Ed.), Lithium Ion Rechargeable Batteries. Wiley-VCH, Weinheim, pp. 11–38.

Armstrong, A.R., Lyness, C., Panchmatia, P.M., Islam, M.S., Bruce, P.G., 2011. The lithium intercalation process in the low-voltage lithium battery anode $Li_{1+x}V_{1-x}O_2$. Nat. Mat. 10, 223–229.

Awasthi, A.P., Lagoudas, D.C., Hammerand, D.C., 2009. Modeling of graphene-polymer interfacial mechanical behavior using molecular dynamics. Mod. Sim. Mat. Sci. Eng. 17, 015002.

Bakowies, D., Thiel, W., 1996. Hybrid models for combined quantum mechanical and molecular mechanical approaches. J. Phys. Chem. 100, 10580–10594.

Balazs, A.C., Emrick, T., Russell, T.P., 2006. Nanoparticle polymer composites: where two small worlds meet. Science 314, 1107–1110.

Barrat, J.L., Baschnagel, J., Lyulin, A., 2010. Molecular dynamics simulations of glassy polymers. Soft Matter 6, 3430–3446.

Bartlett, R.J., Purvis III, G.D., 1980. Molecular applications of coupled cluster and many-body perturbation methods. Phys. Scr. 21, 255–265.

Bauer, J.D., Haussuhl, E., Winkler, B., Arbeck, D., Milman, V., Robertson, S., 2010. Elastic properties, thermal expansion, and polymorphism of acetylsalicylic acid. Crystal Growth Des. 10, 3132–3140.

Bedrov, D., Smith, G.D., van Duin, A.C.T., 2012. Reactions of singly-reduced ethylene carbonate in lithium battery electrolytes: a molecular dynamics simulation study using the ReaxFF. J. Phys. Chem. A 116, 2978–2985.

Benazzi, E., Leite, L., Marchal-George, N., Toulhoat, H., Raybaud, P., 2003. New insights into parameters controlling the selectivity in hydrocracking reactions. J. Catal. 217, 376–387.

Biscardi, J.A., Meitzner, G.D., Iglesia, E., 1998. Structure and density of active Zn species in Zn/H-ZSM5 propane aromatization catalysts. J. Catal. 179, 192–202.

Blaszkowski, S.R., van Santen, R.A., 1997. Theoretical study of C-C bond formation in the methanol to gasoline process. J. Am. Chem. Soc. 119, 5020–5027.

Born, M., Oppenheimer, J.R., 1927. Zur Quantentheorie der Molekeln. Ann. Phys. 84, 457–484.

Cai, Y., Chen, G., Xu, X., Du, F., Li, Z., Meng, X., Wang, C., Wei, Y., 2011. First-principles calculations on the $LiMSO_4F/MSO_4F$ (M = Fe, Co, and Ni) systems. J. Phys. Chem. C 115, 7032–7037.

Catlow, C.R.A., van Santen, R.A., Smit, B., 2004. Computer Modelling of Microporous Materials. Elsevier, New York.

Ceder, G., 2010. Opportunities and challenges for first-principles materials design and applications to Li battery materials. MRS Bull. 35, 693–701.

Ceperley, D.M., Alder, B.J., 1980. Ground state of the electron gas by a stochastic method. Phys. Rev. Lett. 45, 566–569.

Chen, H., Xue, Q., Zheng, Q., Xie, J., Yan, K., 2008. Influence of nanotube chirality, temperature, and chemical modification on the interfacial bonding between carbon nanotubes and polyphenylacetylene. J. Phys. Chem. C 112, 16514–16520.

Chiu, C.C., DeVane, R., Klein, M.L., Shinoda, W., Moore, P.B., Nielsen, S.O., 2010. Coarse-grained potential models for phenyl-based molecules: II. Application to fullerenes. J. Phys. Chem. B 114, 6394–6400.

Cho, J., Joshi, M.S., Sun, C.T., 2006. Effect of inclusion size on mechanical properties of polymeric composites with micro and nano particles. Compos. Sci. Tech. 66, 1941–1952.

Chung, L.W., Hirao, H., Li, X., Morokuma, K., 2012. The ONIOM method: its foundation and applications to metalloenzymes and photobiology. Comp. Mol. Sci. 2, 327–350.

Clark, L.A., Sierka, M., Sauer, J., 2004. Computational elucidation of the transition state shape selectivity phenomenon. J. Am. Chem. Soc. 126, 936–947.

Cordomí, A., Caltabiano, G., Pardo, L., 2012. Membrane protein simulations using AMBER force field and Berger lipid parameters. J. Chem. Theory Comp. 8, 948–958.

Daoulas, K.C., Harmandaris, V.A., Mavrantzas, V.G., 2005. Detailed atomistic simulation of a polymer melt/solid interface: structure, density, and conformation of a thin film of polyethylene melt adsorbed on graphite. Macromolecules 38, 5780–5795.

Dauber-Osguthorpe, P., Roberts, V.A., Osguthorpe, D.J., Wolff, J., Genest, M., Hagler, A.T., 1988. Structure and energetics of ligand binding to proteins: Escherichia coli dihydrofolate reductase-trimethoprim, a drug-receptor system. Proteins: Struct. Func. Bioinf. 4, 31–47.

Davis, J.R., 1992. ASM materials engineering dictionary. ASM Int.

de Joannis, J., Jiang, F.Y., Kindt, J.T., 2006. Coarse-grained model simulations of mixed-lipid systems: composition and line tension of a stabilized bilayer edge. Langmuir 22, 998–1005.

de Jong, D.H., Singh, G., Bennett, W.D., Arnarez, C., Wassenaar, T.A., Schafer, L.V., Periole, X., Tieleman, P., Marrink, S.J., 2013. Improved parameters for the martini coarse-grained protein force field. J. Chem. Theory Comp. 9, 687–697.

De Moor, B.A., Reyniers, M.-F., Sierka, M., Sauer, J., Marin, G.B., 2008. Physisorption and chemisorption of hydrocarbons in H-FAU using QM-Pot(MP2//B3LYP) calculations. J. Phys. Chem. C 112, 11796–11812.

De Volder, M.F., Tawfick, S.H., Baughman, R.H., Hart, A.J., 2013. Carbon nanotubes: present and future commercial applications. Science 339, 535–539.

DeVane, R., Shinoda, W., Moore, P.B., Klein, M.L., 2009. Transferable coarse grain nonbonded interaction model for amino acids. J. Chem. Theory Comp. 5, 2115–2124.

DeVane, R., Klein, M.L., Chiu, C.C., Nielsen, S.O., Shinoda, W., Moore, P.B., 2010. Coarse-grained potential models for phenyl-based molecules: I. Parametrization using experimental data. J. Phys. Chem. B 114, 6386–6393.

Dickson, C.J., Rosso, L., Betz, R.M., Walker, R.C., Gould, I.R., 2012. GAFFlipid: a general Amber force field for the accurate molecular dynamics simulation of phospholipid. Soft Matter 8, 9617–9627.

Doyle, M., 2009. Predictive modeling. In: Farahmand, B. (Ed.), Virtual testing and predictive modelling. Springer, New York, pp. 247–289.

Eddaoudi, M., Moler, D.B., Li, H., Chen, B., Reineke, T.M., O'keeffe, M., Yaghi, O.M., 2001. Modular chemistry: secondary building units as a basis for the design of highly porous and robust metal-organic carboxylate frameworks. Acc. Chem. Res. 34, 319–330.

Eichler, U., Kölmel, C.M., Sauer, J., 1997. Combining ab initio techniques with analytical potential functions for structure predictions of large systems: method and application to crystalline silica polymorphs. J. Comp. Chem. 18, 463–477.

Espanol, P., Warren, P., 1995. Statistical mechanics of dissipative particle dynamics. Europhys. Lett. 30, 191.

Fan, H.B., Yuen, M.M., 2010. A multiscale approach for investigation of interfacial delamination in electronic packages. Microelectron. Reliab. 50, 893–899.

Feyereisen, M., Fitzgerald, G., Komornicki, A., 1993. Use of approximate integrals in ab initio theory—an application in MP2 energy calculations. Chem. Phys. Lett. 208, 359.

Flekkøy, E.G., Coveney, P.V., De Fabritiis, G., 2000. Foundations of dissipative particle dynamics. Phys. Rev. E. 62, 2140.

Fock, V., 1930. Näherungsmethode zur Losung des quanten-mechanischen Mehrkörperprobleme. Z. Phys. 61, 126–148.

Fraaije, J.G.E.M., Van Vlimmeren, B.A.C., Maurits, N.M., Postma, M., Evers, O.A., Hoffmann, C., Altevogt, P., Goldbeck-Wood, G., 1997. The dynamic mean-field density functional method and its application to the mesoscopic dynamics of quenched block copolymer melts. J. Chem. Phys. 106, 4260.

Frankland, S.J.V., Caglar, A., Brenner, D.W., Griebel, M., 2002. Molecular simulation of the influence of chemical cross-links on the shear strength of carbon nanotube-polymer interfaces. J. Phys. Chem. B 106, 3046–3048.

Frankland, S.J.V., Harik, V.M., Odegard, G.M., Brenner, D.W., Gates, T.S., 2003. The stress-strain behavior of polymer-nanotube composites from molecular dynamics simulation. Comp. Sci. Tech. 63, 1655–1661.

Fukuzawa, K., Kitaura, K., Uebayasi, M., Nakata, K., Kaminuma, T., Nakano, T., 2005. Ab initio quantum mechanical study of the binding energies of human estrogen receptor α with its ligands: an application of fragment molecular orbital method. J. Comp. Chem. 26, 1–10.

Furukama, H., Miller, A., Yaghi, O.M., 2007. Independent verification of the saturation hydrogen uptake in MOF-177 and establishment of a benchmark for hydrogen adsorption in metal-organic frameworks. J. Mater. Chem. 17, 3197–3204.

Gao, J., Zheng, Y., Fitzgerald, G.B., de Joannis, J., Tang, Y., Wachs, I.E., Podkolzin, S.G., 2013. Structure of Mo_2 and Mo_4 carbide nanoparticles and their anchoring sites on ZSM-5 zeolites. J. Phys. Chem.

Geim, A.K., Novoselov, K.S., 2007. The rise of graphene. Nat. Mater. 6, 183–191.

Gestoso, P., Meunier, M., 2008. Barrier properties of small gas molecules in amorphous cis-1,4 polybutadiene estimated by simulation. Mol. Sim. 34, 1135–1141.

Getman, R.B., Bae, Y.-S., Wilmer, C.E., Snurr, R.Q., 2012. Review and analysis of molecular simulations of methane, hydrogen, and acetylene storage in metal-organic frameworks. Chem. Rev. 112, 703–723.

Goodenough, J.B., Kim, Y., 2010. Challenges for rechargeable Li batteries. Chem. Mater. 22, 587–603.

Gordon, M.S., Fedorov, D.G., Pruitt, S.R., Slipchenko, L.V., 2012. Fragmentation methods: a route to accurate calculations on large systems. Chem. Rev. 112, 632–672.

Griebel, M., Hamaekers, J., 2004. Molecular dynamics simulations of the elastic moduli of polymer-carbon nanotube composites. Comp. Meth. Appl. Mech. Eng. 193, 1773–1788.

Groot, R.D., Rabone, K.L., 2001. Mesoscopic simulation of cell membrane damage, morphology change and rupture by nonionic surfactants. Biophys. J. 81, 725–736.

Groot, R.D., Warren, P.B., 1997. Dissipative particle dynamics: bridging the gap between atomistic and mesoscopic simulation. J. Chem. Phys. 107, 4423.

Gupta, A., Khammash, M., 2013. Unbiased estimation of parameter sensitivities for stochastic chemical reaction networks. SIAM: J. Sci. Comp. 35, A2958–A2620.

Gurevitch, I., Srebnik, S., 2008. Conformational behavior of polymers adsorbed on nanotubes. J. Chem. Phys. 128, 144901.

Guyomard, D., 2000. Advanced cathode materials for lithium batteries. In: Osaka, T., Datta, M. (Eds.), Energy Storage Systems for Electronics (New Trends in Electrochemical Technology). Gordon and Breach, Amsterdam, pp. 253–350.

Haghighatpanah, S., Bolton, K., 2013. Molecular-level computational studies of single wall carbon nanotube-polyethylene composites. Comp. Math. Sci. 69, 443–454.

Halasz, I., Liang, J.-J., Fitzgerald, G., 2011. Zeolite confined $Ti(OH)_4$ nanoparticles in highly active and aelective oxidation catalyst. Catal. Lett. 141, 948–953.

Halls, M.D., Tasaki, K., 2011. High-throughput quantum chemistry and virtual screening for lithium ion battery electrolyte additives. J. Power Sources 195, 1472–1478.
Harrison, R.J., Handy, N.C., 1983. Full CI calculations on BH, H_2O, NH_3, and HF. Chem. Phys. Lett. 95, 386–391.
He, X., Shinoda, W., DeVane, R., Anderson, K.L., Klein, M.L., 2010. Paramaterization of a coarse-grained model for linear alkylbenzene sulfonate surfactants and molecular dynamics studies of their self-assembly in aqueous solution. Chem. Phys. Lett. 487, 71–76.
Hedin, L., Lundqvist, B.I., 1971. Explicit local exchange correlation potentials. J. Phys. C 4, 2064–2083.
Hildebrand, J.H., 1916. Solubility. J. Am. Chem. Soc. 38, 1452–1473.
Hohenberg, P., Kohn, W., 1964. Inhomogeneous electron gas. Phys. Rev. B 136, 864–871.
Hoogerbrugge, P.J., Koelman, J.M.V.A., 1992. Simulating microscopic hydrodynamic phenomena with dissipative particle dynamics. Europhys. Lett. 19, 155.
Huang, X., Jiang, P., Yin, Y., 2009. Nanoparticle surface modification induced space charge suppression in linear low density polyethylene. Appl. Phys. Lett. 95, 242905.
Huang, M.J., Kapral, R., Mikhailov, A.S., Chen, H.Y., 2012. Coarse-grain model for lipid bilayer self-assembly and dynamics: multiparticle collision description of the solvent. J. Chem. Phys. 137, 055101.
Hwang, M.J., Ni, X., Waldman, M., Ewig, C.S., Hagler, A.T., 1998. Derivation of class II force fields. VI. Carbohydrate compounds and anomeric effects. Biopolymers 45, 435–468.
Iddir, H., Curtiss, L.A., 2010. Li ion diffusion mechanisms in bulk monoclinic Li_2CO_3 crystals from density functional studies. J. Phys. Chem. C 114, 20903–20906.
Ikehata, H., Nagasako, N., Kuramoto, S., Saito, T., 2006. Designing new structural materials using density functional theory: the example of gum metal. MRS Bull. 31, 688–692.
Iwamoto, N., 2012. Developing the stress-strain curve to failure using mesoscale models parameterized from molecular models. Microelectron. Reliab. 52, 1291–1299.
Iwamoto, N., Hölck, O., Noijen, S., 2011. Multiscale perspectives of interface delamination in microelectronic packaging applications. Mol. Sim. 37, 710–717.
Izvekov, S., Voth, G.A., 2005. A multiscale coarse-graining method for biomolecular systems. J. Phys. Chem. B 109, 2469–2473.
Jensen, J.H., Li, H., Robertson, A.D., Molina, P.A., 2005. Prediction and rationalization of protein pK_a values using QM and QM/MM methods. J. Phys. Chem. A 109, 6634–6643.
Jorgensen, W.L., Maxwell, D.S., Tirado-Rives, J., 1996. Development and testing of the OPLS all-atom force field on conformational energetics and properties of organic liquids. J. Am. Chem. Soc. 118, 11225–11236.
Kapral, R., 2008. Multiparticle collision dynamics: simulation of complex systems on mesoscales. Adv. Chem. Phys. 140, 89.
Karakasidis, T.E., Charitidis, C.A., 2007. Multiscale modeling in nanomaterials science. Mat. Sci. Eng. C 27, 1082–1089.
Keil, F., 2012. Multiscale modelling in computational heterogeneous catalysis. Top. Curr. Chem. 307, 69–108.
Keil, F., 2013. Complexities in modeling of heterogeneous catalytic reactions. Comput. Math. Appl. 65, 1674–1697.
Kerisit, S., Rosso, K., Yang, Z., Liu, J., 2009. Dynamics of coupled lithium/electron diffusion in TiO_2 polymorphs. J. Phys. Chem. C 113, 20998–21007.
Kitaura, K., Ikeo, E., Asada, T., Nakano, T., Uebayasi, M., 1999. Fragment molecular orbital method: an approximate computational method for large molecules. Chem. Phys. Lett. 313, 701–706.

Koopman, E.A., Lowe, C.P., 2006. Advantages of a Lowe-Andersen thermostat in molecular dynamics simulations. J. Chem. Phys. 124, 204103.
Labanowski, K., Andzelm, J., 1991. Density Functional Methods in Chemistry. Springer-Verlag, New York.
Leach, A.R., 2001. Molecular Modelling: Principles and Applications. Prentice Hall.
Lee, C.T., Yang, W.T., Parr, R.G., 1988. Development of the Colle-Salvetti correlation-energy formula into a functional of the electron density. Phys. Rev. B 37, 785–789.
Lee, H., de Vries, A.H., Marrink, S.J., Pastor, R.W., 2009. A coarse-grained model for polyethylene oxide and polyethylene glycol: conformation and hydrodynamics. J. Phys. Chem. B 113, 13186–13194.
Leung, K., 2013. Electronic structure modeling of electrochemical reactions at electrode/electrolyte interfaces in lithium ion batteries. J. Phys. Chem. C 117, 1539–1547.
Leung, K., Qi, Y., Zavadil, K.R., Jung, Y.S., Dillon, A.C., Cavanagh, A.S., Lee, S.H., George, S.M., 2011. Using atomic layer deposition to hinder solvent decomposition in lithium ion batteries: first-principles modeling and experimental studies. J. Am. Chem. Soc. 133, 14741–14754.
Levy, M., 1979. Universal variational functionals of electron densities, first-order density matrices, and natural spin-orbitals and solution of the v-representability problem. Proc. Natl. Acad. Sci. U. S. A. 76, 6062–6065.
Lewis, T.J., 1994. Nanometric dielectrics. IEEE Trans. Dielect. Electric. Insulation 1, 812–825.
Lewis, T.J., 2004. Interfaces are the dominant feature of dielectrics at the nanometric level. IEEE Trans. Dielect. Electric. Insulation 11 (5), 739–753.
Li, H., Hains, A.W., Everts, J.E., Robertson, A.D., Jensen, J.H., 2002. The prediction of protein pKa's using QM/MM: the pKa of lysine 55 in turkey ovomucoid third domain. J. Phys. Chem. B 106, 3486–3494.
Li, S., Yin, G., Chen, G., Li, J., Bai, S., Zhong, L., Zhang, Y., Lei, Q., 2010. Short-term breakdown and long-term failure in nanodielectrics: a review. IEEE Trans. Dielect. Electric. Insulation 17, 1523–1535.
Liao, K., Li, S., 2001. Interfacial characteristics of a carbon nanotube-polystyrene composite system. Appl. Phys. Lett. 79, 4225–4227.
Lide, D.R., 1997. Handbook of Chemistry and Physics. CRC, New York.
Lindahl, E., Edholm, O., 2000. Mesoscopic undulations and thickness fluctuations in lipid bilayers from molecular dynamics simulations. Biophys. J. 79, 426–433.
Liu, L., Zhang, L., Lua, J., 2012a. Branched carbon nanotube reinforcements for improved strength of polyethylene nanocomposites. Appl. Phys. Lett. 101, 161907.
Liu, Y., Liu, J., Chang, M., Zheng, C., 2012b. Theoretical studies of CO_2 adsorption mechanism on linkers of metal-organic frameworks. Fuel 95, 521–527.
López, C.A., Rzepiela, A.J., de Vries, A.H., Dijkhuizen, L., Hunenberger, P.H., Marrink, S.J., 2009. Martini coarse-grained force field: extension to carbohydrates. J. Chem. Theory Comp. 5, 3195–3210.
Lordi, V., Yao, N., 2000. Molecular mechanics of binding in carbon-nanotube-polymer composites. J. Mat. Res. 15, 2770–2779.
Lundqvist, S., March, N.H., 1983. Theory of the Inhomogeneous Electron Gas. Springer, New York.
Lusti, H.R., Gusev, A.A., 2004. Finite element predictions for the thermoelastic properties of nanotube reinforced polymers. Mod. Sim. Mat. Sci. Eng. 12, S107.
Lyubartsev, A.P., 2005. Multiscale modeling of lipids and lipid bilayers. Eur. Biophys. J. 35, 53–61.

Lyubartsev, A.P., Laaksonen, A., 1995. Calculation of effective interaction potentials from radial distribution functions: a reverse Monte Carlo approach. Phys. Rev. E. 52, 3730.

Lyubartsev, A.P., Rabinovich, A.L., 2011. Recent development in computer simulations of lipid bilayers. Soft Matter 7, 25–39.

Maiti, A., Wescott, J., Kung, P., 2005. Nanotube-polymer composites: insights from Flory-Huggins theory and mesoscale simulations. Mol. Sim. 31, 143–149.

Maple, J.R., Hwang, M.-J., Stockfisch, T.P., Dinur, U., Waldman, M., Ewig, C.S., Hagler, A.T., 1994. Derivation of class II force fields. I. Methodology and quantum force field for the alkyl functional group and alkane molecules. J. Comp. Chem. 15, 162–182.

Maple, J.R., Hwang, M.-J., Jalkanen, K.J., Stockfisch, T.P., Hagler, A.T., 1998. Derivation of class II force fields: V. Quantum force field for amides, peptides, and related compounds. J. Comp. Chem. 19, 430–458.

Marrink, S.J., Mark, A.E., 2001. Effect of undulations on surface tension in simulated bilayers. J. Phys. Chem. B 105, 6122–6127.

Marrink, S.J., Tieleman, D.P., 2013. Perspective on the Martini model. Chem. Soc. Rev. 42, 6801–6822.

Marrink, S.J., Risselada, H.J., Yefimov, S., Tieleman, D.P., de Vries, A.H., 2007. The MARTINI force field: coarse grained model for biomolecular simulations. J. Phys. Chem. B 111, 7812–7824.

Marrink, S.J., Periole, X., Tieleman, D.P., de Vries, A.H., 2010. Comment on "On using a too large integration time step in molecular dynamics simulations of coarse-grained molecular models". Phys. Chem. Chem. Phys. 12, 2254–2256.

Maseras, F., Morokuma, K., 1995. IMOMM: a new integrated ab initio+molecular mechanics geometry optimization scheme of equilibrium structures and transition states. J. Comp. Chem. 16, 1170–1179.

Mayo, S.L., Olafson, B.D., Goddard, W.A., 1990. DREIDING: a generic force field for molecular simulations. J. Phys. Chem. 94, 8897–8909.

Meunier, M., 2005. Diffusion coefficients of small gas molecules in amorphous cis-1,4 Polybutadiene estimated by molecular dynamics simulations. J. Chem. Phys. 123, 134906–134913.

Meunier, M., Quirke, Q., 2013. D.O.S. studies of polymer nanocomposites interfaces. In: Third Zing Bionanomaterials Conference, 16-19 February, Lanzarote, Spain.

Michler, G.H., 2008. Electron Microscopy of Polymers. Springer, Berlin, pp. 419-428.

Møller, C., Plesset, M.S., 1934. Note on an approximation treatment for many-electron systems. Phys. Rev. 46, 618–622.

Moniruzzaman, M., Winey, K.I., 2006. Polymer nanocomposites containing carbon nanotubes. Macromolecules 39, 5194–5205.

Monticelli, L., Kandasamy, S.K., Periole, X., Larson, R.G., Tieleman, D.P., Marrink, S.J., 2008. The MARTINI coarse-grained force field: extension to proteins. J. Chem. Theory Comp. 4, 819–834.

Monticelli, L., Salonen, E., Ke, P.C., Vattulainen, I., 2009. Effects of carbon nanoparticles on lipid membranes: a molecular simulation perspective. Soft Matter 5, 4433–4445.

Murphy, R.B., Phillipp, D.M., Friesner, R.A., 2000. A mixed quantum mechanics/molecular mechanics (QM/MM) method for large-scale modeling of chemistry in protein environments. J. Comp. Chem. 21, 1442–1457.

Murray, L.J., Dinca, M., Long, J.R., 2009. Hydrogen storage in metal-organic frameworks. Chem. Soc. Rev. 38, 1294–1314.

Na, S., Wang, Q., Zhang, X.J., Ding, P., 2012. Molecular dynamics simulations of polypropylene and talcum nanocomposites. In: Jinhui, W., Zhao, M., Wu, B. (Eds.), Advanced Materials Research, vols. 466–467, pp. 161–164.

Nelson, J.K., 2010. Background, principles and promise of nanodielectrics. In: Nelson, J.K. (Ed.), Dielectric Polymer Nanocomposites. Springer, New York, pp. 1–30.

Noguchi, H., Kikuchi, N., Gompper, G., 2007. Particle-based mesoscale hydrodynamic techniques. Europhys. Lett. 78, 10005.

Nyden, M.R., Stoliarov, S.I., 2008. Calculations of the energy of mixing carbon nanotubes with polymers. Polymer 49, 635–641.

Olmos, D., Rodriguez-Gutierrez, E., Gonzales-Benito, J., 2012. Polymer structure and morphology of low density polyethylene filled with silica nanoparticles. Polym. Compos. 33, 2009–2021.

Ono, Y., 1992. Transformation of lower alkanes into aromatic hydrocarbons over ZSM-5 zeolites. Catal. Rev. 34, 179–226.

Oxford, G.A.E., Snurr, R.Q., Broadbelt, L.J., 2010. Hybrid quantum mechanics/molecular mechanics investigation of (salen) Mn for use in metal-organic frameworks. Ind. Eng. Chem. Res. 49, 10965–10973.

Pagonabarraga, I., Frenkel, D., 2001. Dissipative particle dynamics for interacting systems. J. Chem. Phys. 115, 5015.

Pant, P.K., Han, J., Smith, G.D., Boyd, R.H., 1993. A molecular dynamics simulation of polyethylene. J. Chem. Phys. 99, 597.

Parrinello, M., Rahman, A., 1982. Strain fluctuations and elastic constants. J. Chem. Phys. 76, 2662.

Paul, W., 1999. Atomistic molecular dynamics simulations of the static and dynamic properties of a polyethylene melt. In: Landau, D.P., Schuttler, H.B. (Eds.), Computer Simulation Studies in Condensed-Matter Physics XI. Springer, Berlin, Heidelberg, pp. 197–211.

Perdew, J.P., 2013. Climbing the ladder of density functional approximations. MRS Bull. 38, 743–750.

Perdew, J.P., Wang, Y., 1992. Accurate and simple analytic representation of the electron-gas correlation energy. Phys. Rev. B 45, 13244–13249.

Phillipp, D.M., Friesner, R.A., 1999. Mixed ab initio QM/MM modeling using frozen orbitals and tests with alanine dipeptide and tetrapeptide. J. Comp. Chem. 20, 1468–1494.

Purvis III, G.D., Bartlett, R.J., 1982. A full coupled-cluster singles and doubles model: the inclusion of disconnected triples. J. Chem. Phys. 76, 1910–1918.

Qiao, R., Ke, P.C., 2006. Lipid-carbon nanotube self-assembly in aqueous solution. J. Am. Chem. Soc. 128, 13656–13657.

Raimondeau, S., Vlachos, D.G., 2002. Recent developments on multiscale, hierarchical modeling of chemical reactors. Chem. Eng. J. 90, 3–23.

Ramanathan, T., Abdala, A.A., Stankovich, S., Dikin, D.A., Herrera-Alonso, M., Piner, R.D., Brinson, L.C., 2008. Functionalized graphene sheets for polymer nanocomposites. Nat. Nanotech. 3, 327–331.

Ramprasad, R., Tang, C., Shi, N., 2010. Modeling the physics and chemistry of interfaces in nanodielectrics. In: Nelson, J.K. (Ed.), Dielectric Polymer Nanocomposites. Springer, New York, pp. 133–161.

Reith, D., Pütz, M., Müller-Plathe, F., 2003. Deriving effective mesoscale potentials from atomistic simulations. J. Comp. Chem. 24, 1624–1636.

Rigby, D., Pitré, F., 2013. Simulation of non-ionic surfactant micelles for controlled drug release, Accelrys chemical case study, Available from: http://accelrys.com/resource-center/case-studies/pdf/galderma-case-study-1208.pdf [Accessed 19 December 2013].

Rissanou, A.N., Harmandaris, V., 2013. Structure and dynamics of poly (methyl methacrylate)/graphene systems through atomistic molecular dynamics simulations. J. Nanoparticle Res. 15, 1–14.

Risselada, H.J., Marrink, S.J., 2009. Curvature effects on lipid packing and dynamics in liposomes revealed by coarse grained molecular dynamics simulations. Phys. Chem. Chem. Phys. 11, 2056–2067.

Rodriguez-Santiago, L., Sierka, M., Branchadell, V., Sodupe, M., Sauer, J., 1998. Coordination of Cu + ions to zeolite frameworks strongly enhances their ability to bind NO_2. An ab initio density functional study. J. Am. Chem. Soc. 120, 1545–1551.

Roothan, C.C.J., 1951. New developments in molecular orbital theory. Rev. Mod. Phys. 23, 69–89.

Rossi, G., Monticelli, L., Puisto, S.R., Vattulainenaef, I., Ala-Nissilaag, T., 2011. Coarse-graining polymers with the MARTINI force-field: polystyrene as a benchmark case. Soft Matter 7, 698–708.

Roussel, N., Geiker, M.R., Dufour, F., Thrane, L.N., Szabo, P., 2007. Computational modeling of concrete flow: general overview. Cement Concrete Res. 37, 1298–1307.

Roy, M., Nelson, J.K., MacCrone, R.K., Schadler, L.S., Reed, C.W., Keefe, R., Zenger, W., 2005. Polymer nanocomposites dielectrics—the role of the interface. IEEE Trans. Dielect. Electric. Insulation 12, 629–643.

Roy, M., Nelson, J.K., MacCrone, R.K., Schadler, L.S., 2007. Candidate mechanisms controlling the electrical characteristics of silica/XLPE nanodielectrics. J. Mat. Sci. 42, 3789–3799.

Salomon-Ferrer, R., Case, D.A., Walker, R.C., 2013. An overview of the Amber biomolecular simulation package. Comp. Mol. Sci. 3, 198–210.

Sauer, J., Sierka, M., 2000. Combining quantum mechanics and interatomic potential functions in ab initio studies of extended systems. J. Comp. Chem. 21, 1470–1493.

Sawada, T., Hashimoto, T., Nakano, H., Suzuki, T., Ishida, H., Kiso, M., 2006. Why does avian influenza A virus hemagglutinin bind to avian receptor stronger than to human receptor? Ab initio fragment molecular orbital studies. Biochem. Biophys. Res. Comm. 351, 40–43.

Scocchi, G., Posocco, P., Danani, A., Pricl, S., Fermeglia, M., 2007a. To the nanoscale, and beyond!: multiscale molecular modeling of polymer-clay nanocomposites. Fluid Phase Equilib. 261, 366–374.

Scocchi, G., Posocco, P., Fermeglia, M., Pricl, S., 2007b. Polymer-clay nanocomposites: a multiscale molecular modeling approach. J. Phys. Chem. B 111, 2143–2151.

Scocchi, G., Posocco, P., Handgraaf, J.W., Fraaije, J.G., Fermeglia, M., Pricl, S., 2009. A complete multiscale modelling approach for polymer-clay nanocomposites. Chem. A Eur. J. 15, 7586–7592.

Scott, H.L., 2002. Modeling the lipid component of membranes. Curr. Opin. Struct. Biol. 12, 495–502.

Sevink, G.J.A., Zvelindovsky, A.V., 2008. Block copolymers confined in a nanopore: pathfinding in a curving and frustrating flatland. J. Chem. Phys. 128, 084901.

Shavitt, I., 1977. The method of configuration interaction. In: Schaefer, H.F. (Ed.), Methods of Electronic Structure Theory. Plenum Press, New York, pp. 189–275.

Sheng, Y.Z., Yang, H., Li, J.Y., Sun, M., 2013. Predicting glass transition temperature of polyethylene/graphene nanocomposites by molecular dynamic simulation. Chem. Res. Chin. Univ. 29, 788–792.

Shi, N., Ramprasad, R., 2006. Dielectric properties of nanoscale multi-component systems: a first principles computational study. J. Comput. Aided Mater. Des. 14, 133–139.

Shi, N., Ramprasad, R., 2008. Local properties at interfaces in nanodielectrics: an ab initio computational study. IEEE Trans. Dielectr. Electr. Insul. 15, 170–177.
Shi, S., Qi, Y., Li, H., Hector, L.G., 2013. Defect thermodynamics and diffusion mechanisms in Li2CO3 and implications for the solid electrolyte interphase in Li-ion batteries. J. Phys. Chem. C 117, 8579–8593.
Shinoda, W., Devane, R., Klein, M.L., 2007. Multi-property fitting and parameterization of a coarse grained model for aqueous surfactants. Mol. Sim. 33, 27–36.
Shinoda, W., DeVane, R., Klein, M.L., 2010. Zwitterionic lipid assemblies: molecular dynamics studies of monolayers, bilayers, and vesicles using a new coarse grain force field. J. Phys. Chem. B 114, 6836–6849.
Shinoda, W., DeVane, R., Klein, M.L., 2011. Coarse-grained force field for ionic surfactants. Soft Matter 7, 6178–6186.
Sierka, M., Sauer, J., 2001. Proton mobility in chabazite, faujasite, and ZSM-5 zeolite catalysts. Comparison based on ab initio calculations. J. Phys. Chem. B 105, 1603–1613.
Skjevik, Å.A., Madej, B.D., Walker, R.C., Teigen, K., 2012. LIPID11: a modular framework for lipid simulations using Amber. J. Phys. Chem. B 116, 11124–11136.
Skylaris, C.-K., Haynes, P.D., Mostofi, A.A., Payne, M.C., 2005. Introducing ONETEP: linear-scaling density functional simulations on parallel computers. J. Chem. Phys. 122, 084119.
Soldera, A., Metatla, N., 2006. Glass transition of polymers: atomistic simulation versus experiments. Phys. Rev. E. 74, 061803.
Steele, W.A., 1973. The physical interaction of gases with crystalline solids. Surf. Sci. 36, 317–352.
Stevens, B.C., Ha, T., 2004. Discrete and heterogeneous rotational dynamics of single membrane probe dyes in gel phase supported lipid bilayer. J. Chem. Phys. 120, 3030.
Sun, H., 1998. COMPASS: an ab initio force-field optimized for condensed phase applications—overview with details on alkanes and benzene compounds. J. Phys. Chem. B 102, 7338–7364.
Sutton, A.P., Chen, J., 1990. Long-range Finnis-Sinclair potentials. Phil. Mag. Lett. 61, 139–146.
Symeonidis, V., Karniadakis, G.E., Caswell, B., 2005. Dissipative particle dynamics simulations of polymer chains: scaling laws and shearing response compared to DNA experiments. Phys. Rev. Lett. 95, 076001.
Szabo, A., Ostlund, N.S., 1982. Modern Quantum Chemistry. MacMillan, New York.
Thostenson, E.T., Ren, Z., Chou, T.W., 2001. Advances in the science and technology of carbon nanotubes and their composites: a review. Comp. Sci. Tech. 61, 1899–1912.
Thostenson, E.T., Chou, T.-W., 2004. Nanotube buckling in aligned multi-wall carbon nanotube composites. Carbon 42, 3015–3018.
Thostenson, E.T., Li, C., Chou, T.W., 2005. Nanocomposites in context. Comp. Sci. Tech. 65, 491–516.
Toulhoat, H., Raybaud, P., Benazzi, E., 2004. Effect of confinement on the selectivity of hydrocracking. J. Catal. 221, 500–509.
Tuncer, E., Sauers, I., 2010. Industrial applications perspective of nanodielectrics. In: Nelson, J. K. (Ed.), Dielectric Polymer Nanocomposites. Springer, New York, pp. 321–338.
van Schalkwijk, W.A., Scrosati, B., 2002. Advances in Lithium-Ion Batteries. Kluwer, New York.
Vatamanu, J., Borodin, O., Smith, D., 2012. Molecular dynamics simulation studies of the structure of a mixed carbonate/$LiPF_6$ electrolyte near graphite surface as a function of electrode potential. J. Phys. Chem. C 116, 1114–1121.

Velinova, M., Sengupta, D., Tadjer, A.V., Marrink, S.J., 2011. Sphere-to-rod transitions of non-ionic surfactant micelles in aqueous solution modeled by molecular dynamics simulations. Langmuir 27, 14071–14077.

Venturoli, M., Smit, B., Sperotto, M.M., 2005. Simulation studies of protein-induced bilayer deformations, and lipid-induced protein tilting, on a mesoscopic model for lipid bilayers with embedded proteins. Biophys. J. 88, 1778–1798.

Verlet, L., 1967. Computer experiments on classical fluids. I. Thermodynamical properties of Lennard-Jones molecules. Phys. Rev. 159, 98–103.

Vlachos, D.G., Mhadeshwar, A.B., Kaisare, N.S., 2006. Hierarchical multiscale model-based design of experiments, catalysts, and reactors for fuel processing. Comp. Chem. Eng. 30, 1712–1724.

von Barth, U., Hedin, L., 1972. A local exchange-correlation potential for the spin polarized case. J. Phys. C 5, 1629–1642.

Voronina, E.N., 2011. Multiscale simulation of polymer nanocomposites. Phys. Atomic Nuclei 74, 1623–1643.

Vosko, S.H., Wilk, L., Nusair, M., 1980. Accurate spin-dependent electron liquid correlation energies for local spin density calculations: a critical analysis. Can. J. Phys. 58, 1200–1211.

Voth, G.A. (Ed.), 2008. Coarse-Graining of Condensed Phase and Biomolecular Systems, CRC Press, Boca Raton.

Wallace, E.J., Sansom, M.S., 2008. Blocking of carbon nanotube based nanoinjectors by lipids: a simulation study. Nano Lett. 8, 2751–2756.

Wallace, E.J., Sansom, M.S., 2009. Carbon nanotube self-assembly with lipids and detergent: a molecular dynamics study. Nanotechnology 20, 045101.

Wang, C.C., Ramprasad, R., 2011. Dielectric properties of organosilicons from first principles. J. Mater. Sci. 46, 90–93.

Warren, P.B., 2003. Vapor-liquid coexistence in many-body dissipative particle dynamics. Phys. Rev. E. 68, 066702.

Whittingham, M.S., 2004. Lithium batteries and cathode materials. Chem. Rev. 104, 4271–4301.

Wilmer, C.E., Snurr, R.Q., 2011. Towards rapid computational screening of metal-organic frameworks for carbon dioxide capture: calculation of framework charges via charge equilibration. Chem. Eng. J. 171, 775–781.

Winger, M., Trzesniak, D., Baron, R., van Gunsteren, W.F., 2009. On using a too large integration time step in molecular dynamics simulations of coarse-grained molecular models. Phys. Chem. Chem. Phys. 11, 1934–1941.

Xiang, T.X., Anderson, B.D., 2006. Liposomal drug transport: a molecular perspective from molecular dynamics simulations in lipid bilayers. Adv. Drug Delivery Rev. 58, 1357–1378.

Xing, L., Borodin, O., Smith, G.D., Li, W., 2011. Density functional theory study of the role of anions on the oxidative decomposition reaction of propylene carbonate. J. Phys. Chem. A 115, 13896–13905.

Xiong, J., Liu, Y., Yang, X., Wang, X., 2004. Thermal and mechanical properties of polyurethane/montmorillonite nanocomposites based on a novel reactive modifier. Polym. Degrad. Stab. 86, 549–555.

Xiong, J., Zheng, Z., Jiang, H., Ye, S., Wang, X., 2007. Reinforcement of polyurethane composites with an organically modified montmorillonite. Compos. A: Appl. Sci. Manuf. 38, 132–137.

Xu, B., Qian, D., Wang, Z., Meng, Y.S., 2012. Recent progress in cathode materials research for advanced lithium ion batteries. Mat. Sci. Eng. R 73, 51–65.

Yang, W., 1991. Direct calculation of electron density in density-functional theory. Phys. Rev. Lett. 66, 1438–1441.
Yang, J., 2010. High capacity hydrogen storage materials: attributes for automotive applications and techniques for materials discovery. Chem. Soc. Rev. 39, 656–675.
Yang, S., Cho, M., 2008. Scale bridging method to characterize mechanical properties of nanoparticle/polymer nanocomposites. Appl. Phys. Lett. 93, 043111.
Yang, K., Ma, Y.Q., 2010. Computer simulation of the translocation of nanoparticles with different shapes across a lipid bilayer. Nat. Nanotech. 5, 579–583.
Yu, S., Yang, S., Cho, M., 2009. Multi-scale modeling of cross-linked epoxy nanocomposites. Polymer 50, 945–952.
Yu, K., McDaniel, J.G., Schmidt, J.R., 2012. An efficient multiscale lattice model approach to screening nano-porous adsorbents. J. Chem. Phys. 137, 244102.
Zeng, Q.H., Yu, A.B., Lu, G.Q., 2008. Multiscale modeling and simulation of polymer nanocomposites. Prog. Polymer Sci. 33, 191–269.
Zhang, X., Pugh, J.K., Ross, P.N., 2001. Computation of thermodynamic oxidation potentials of organic solvents using density functional theory. J. Electrochem. Soc. 148, E183–E188.
Zheng, Q., Xue, Q., Yan, K., Hao, L., Li, Q., Gao, X., 2007. Investigation of molecular interactions between SWNT and polyethylene/polypropylene/polystyrene/polyaniline molecules. J. Phys. Chem. C 111, 4628–4635.
Zhigilei, L.V., Volkov, A.N., Dongare, A.M., 2012. Computational study of nanomaterials: from large-scale atomistic simulations to mesoscopic modeling. In: Bhushan, B. (Ed.), Encyclopedia of Nanotechnology. Springer, Netherlands, pp. 470–480.
Ziegler, T., 1991. Approximate density functional theory as a practical tool in molecular energetics and dynamics. Chem. Rev. 91, 651.

Multiscale Green's functions for modeling of nanomaterials*

2

V.K. Tewary
National Institute of Standards and Technology, Boulder, CO, USA

2.1 Introduction

Fabrication and analysis of nanostructures and new nanomaterials have been growing exponentially over the last few years (see, for example, the papers quoted in this volume). However, to advance the nanotechnology in a systematic way, it is absolutely vital that robust and reliable mathematical models are available. In fact, materials modeling has now emerged as a new branch of knowledge that has tremendous scientific and industrial applications. These models help in the visualization of materials and understanding of the physical processes at length and time scales that are difficult and indeed expensive to explore by direct experimental methods. The models are therefore useful for scientific research as well as pedagogical purposes. Moreover, they are indispensable tools for industry for designing and testing new materials because they can provide quick and inexpensive answers to "what if"-type questions and can give an estimate of the lifetime and reliability of the materials for different applications and under different operating conditions. Modeling supported by data is the basis of the materials genome initiative, a major new research initiative being pursued in the United States.

In this chapter we describe a Green's function (GF) method for multiscale modeling of nanomaterials and nanostructures. Green's function is a well-established technique for solving a variety of problems in science and engineering (Morse and Feshbach, 1953; Barton, 1989). The application of the GFs to phonons in a lattice is given in the excellent treatise by Maradudin et al. (1971). The static GF, which is the zero frequency limit of the phonon GF, has been described in an earlier paper (Tewary, 1973). The GF techniques have been extensively applied in the continuum model of a solid as described in a very good book by Ting (1996). These techniques have contributed to the multiscale Green's function (MSGF) method described in this chapter for nanomaterials.

The plan of the chapter is as follows: Section 2.1 introduces the topic and outlines the need for multiscale modeling, that is, for bridging length and time scales and for its application to graphene. The basic GF technique is described in Section 2.2. A review of the lattice model of a solid as relevant for lattice GFs is given in Section 2.3, and the lattice statics Green's function (LSGF) is described in Section 2.4. The MSGF method

*Contribution of the National Institute of Standards & Technology, an agency of the U.S. Government. Not subject to copyright in the USA.

Modeling, Characterization and Production of Nanomaterials. http://dx.doi.org/10.1016/B978-1-78242-228-0.00002-8

for length and time scales are described in Sections 2.5 and 2.6, respectively. Finally, the application of the MSGF method for graphene is presented in Section 2.7.

2.1.1 Need for bridging length scales

The challenges associated with the modeling of nanostructures arise because the material system usually contains "defects" at various length scales: (i) the core region of the nanostructure and lattice defects at the atomistic scale (sub-nano regime) where nonlinear effects may be important, (ii) free surfaces in the nanostructure and their interface with the host solid and the region of the host solid around the nanostructure (nano regime), and (iii) free surfaces and interfaces (with thin films) in the host solid (macro regime). It is therefore necessary that a model for nanostructures links not only the nano and macro regimes but also the sub-nano regime and is an integrated model in which each length scale seamlessly merges into the next scale.

Lattice defects can be classified in two broad categories—potential defects and structural defects. The potential defects are those that can be simulated by a change in the potential energy or the Hamiltonian of the crystal. Examples of potential defects are point defects such as vacancies and interstitials or their aggregates such as voids, precipitates, and hillocks. In contrast, the structural defects or extended defects consist of major rearrangements of atoms in the lattice and cannot be represented by a change in the crystal Hamiltonian alone. Examples of structural defects are dislocations, free surfaces, and interfaces. These defects affect the mechanical properties of all solids but are especially important for nanostructures because they can strongly degrade the functional performance of the nanostructure in many cases, for example, in its interaction with light.

For ordinary macroscopic solids lattice defects can be adequately modeled by using the anisotropic continuum theory, which can be used to calculate the stresses and strains in the solid. These two are the most important measurable parameters that characterize the mechanical behavior of a solid and are mutually related by the elastic constants of the solid. It is also necessary to account for piezoelectric effects and electric polarization effects associated with certain materials; this can be done by using the continuum model.

Free surfaces and interfaces play a relatively large role in nanomaterials as compared to their role in ordinary solids. Many physical properties of nanomaterials and nanostructures in thin films depend upon the strains near the free surfaces and the interfaces caused by point defects. For example, the formation of quantum dots and their arrays depends strongly upon the strains near the free surface of the substrate. Optical and electronic properties of quantum dots are also sensitive to strains. Electromigration in copper interconnects and the efficiency of GaN and other III-V LED devices depend upon the concentration profile of vacancies and other point defects.

It is generally accepted that the continuum theory is inadequate to describe the response of a crystal lattice close to a defect (Tewary, 1973). This region in which

the continuum model is not valid extends from sub-nano to a few nanometers. It then becomes necessary to model the discrete atomistic structure of the lattice in this region. On the other hand, the continuum theory is adequate to model the response of the solid at sufficiently large distances from the defects and also free surfaces and interfaces that are not too close to the point defects. At the macroscopic level, the continuum theory is a highly developed theory that has been very successful in modeling the macroscopic response of solids and for interpreting measurements of stresses and strains that are essentially the continuum model parameters. The problem is that the physical processes that determine the macroscopic stresses and strains, in particular, the energetics of interatomic displacements, occur at the atomistic or sub-nano scales. Hence, a multiscale model is needed to relate the physical processes to macroscopic parameters for the purpose of design and interpretation of measurements that are sensitive to atomic-scale phenomena.

Further, for reasons described earlier, the atomistic arrangements inside and around a nanostructure (its interface with the host solid) and near the point defects have to be modeled by using a discrete lattice theory. On the other hand, those regions of the free surfaces and the interfaces that are distant from the nanostructures and the point defects can be modeled by using the continuum theory. In fact, for structural applications the continuum theory may be preferable for modeling such regions. A pure lattice-theory model of the macroscopic free surfaces and interfaces of the host lattice is difficult because of uncertain factors such as surface reconstruction, presence of impurities, and a lack of knowledge of reliable interatomic potentials near the surface (Puzder et al., 2003). The interatomic potentials that may be reliable in the bulk of the solid may not be valid at or close to the surface because of factors such as electronic rearrangements. On the other hand, the continuum model gives at least a reasonably correct macroscopic representation of structural defects (Hirth and Lothe, 1992), which has been verified experimentally over the last several years. Moreover, measurements of the strains are mostly made at or near a free surface. Because strain is a continuum parameter, it is convenient to represent the free surfaces of the host solid away from the defect by using the continuum model.

2.1.2 Bridging the time scales

A large class of materials modeling problems deals with the simulation and understanding of time-dependent processes. Examples are diffusion, phonon transport, thermal conduction, crack propagation, and radiation damage. Presently various non-silicon materials such as carbon nanotubes and graphene are being considered as adjuncts or additions to the CMOS technology and other semiconductor applications. A huge amount of work has been published on temporal processes in conventional materials but not so much on graphene, nanotubes, and other nanomaterials. This is partly because the continuum model and the analytical and semianalytical formulae work reasonably well for bulk materials but not for nanomaterials that must be simulated at the atomistic scales.

To appreciate the problem of temporal modeling and the need to bridge the time scales, we consider radiation damage in solids as an example. Because of the obvious difficulties associated with the purely experimental investigation of the nanoscale phenomena, even more so when radiation damage is involved, it is necessary to develop reliable mathematical models for the effect of radiation on the new nanomaterials.

Radiation damage often results in lattice displacements (see, for example, Gibson et al., 1960) that lead to the creation of vacancies and interstitials (primary event). These lattice changes can agglomerate into clusters and, under certain conditions, form voids and hillocks/dislocations (secondary and higher events). They may also get distributed randomly to make the crystal amorphous. The charge distribution in the crystal is strongly perturbed due to the lattice defects, which may cause the device to fail. In order to model the reliability and performance of the device when exposed to high-energy radiation, it is therefore necessary to track the movement of vacancies and interstitials and determine the conditions under which they aggregate or settle randomly. A precise knowledge of atomic locations is also needed for calculating charge distribution and other processes such as transport of hydrogen in graphene and nanotubes that are important for estimating the reliability of those devices.

Radiation damage is just one of many physical processes where bridging time scales is crucial. The most challenging aspect of modeling these processes is that the primary event occurs over femtoseconds, whereas the accumulation of defects and other secondary events occur over several nano- or even microseconds. It is therefore necessary to develop models that can bridge the time scales from femto- to microseconds.

Atomistic modeling of materials and physical processes is presently done by use of molecular dynamics (MD) and its variations (Rapaport, 2004). A major stumbling block in classical as well as *ab initio* MD is the extremely limited time scale. Convergence requirements limit the time step in MD analysis to a few femtoseconds in most materials. In some idealized cases, the time step can be extended to at most a few picoseconds by using very elegant techniques (Voter et al., 2002). It would still require 10^6 to 10^9 time integration steps in the conventional MD analysis to model material processes at time scales of practical interest (nano- to microseconds). This is a formidable task even for modern computers but has been a long-sought goal. We will describe here a mathematical technique that is a hybrid of causal GF and MD that can accelerate the temporal convergence by several orders of magnitude (Tewary, 2009).

2.1.3 Application

We will illustrate the MSGF method by applying it to graphene for bridging the length scales as well as the temporal scales. Graphene is a 2D hexagonal lattice of covalently bonded carbon atoms (Geim and Novoselov, 2007). It is widely regarded as having a strong potential for application in revolutionary new devices (Novoselov et al., 2012). In order to develop graphene-based devices, an important requirement is to control the local curvature of graphene films. This would require an understanding of the mechanical deflection of graphene and developing techniques for its multiscale modeling ranging from the atomistic to the device level.

It has been only a few years since graphene was invented/discovered. In spite of its short history, so much work has been published on graphene that it is no longer treated as a new material. In fact, many more 2D materials have now been identified that may be even more promising than graphene such as boron nitride, molybdenum disulfide, silicene, and phosphorene (Novoselov et al., 2005; Mas-Balleste et al., 2011). It is apparent that a whole new class of materials is emerging with the potential to revolutionize the materials industry. Still, graphene remains the main prototype of this new class of materials because of the simplicity of its structure and very fascinating electronic and mechanical properties. The importance of understanding graphene therefore cannot be overemphasized.

The MSGF can be used to model the mechanical strength of graphene, which should be useful for developing, for example, flexible electronic devices. The temporal modeling is useful for developing new methods of characterizing graphene samples and understanding processes such as propagation of ripples (Fasolino et al., 2007) that play an important role in the stability of graphene.

2.2 Green's function method: the basics

In any scientific measurement process, we measure the response of a system to a probe. The mathematical function that defines the response is called the response function and is a characteristic of the system. We need to know the physical process that determines this function. The physical process is represented in terms of an equation or a mathematical relationship that may be an algebraic, differential, or an integral equation. The equation needs to be solved to obtain the response function. In general, the objective of modeling is to calculate this function, which will enable us to predict the response of the system to a probe. Green's function is essentially the response function of a system. Obviously, the choice of the GF would depend upon the nature of the response that we are trying to model.

We can write symbolically the following equation, which is the master equation for all scientific measurements:

$$\text{Response} = \text{Response function} * \text{Probe} \tag{2.1}$$

The so-called forward problem results when the response function and the probe are known and we want to find the response. The inverse problem is when the probe and the response are known and we want to obtain the response function.

For example, consider a simple experiment on a particle of mass m attached at the end of a massless spring of spring constant ϕ. The spring is attached to a wall as shown in Figure 2.1. We apply a force f on the spring and measure u, the displacement of the end of the spring. The physical process that gives the displacement of the point A is expressed in the terms of the following simple equation:

$$f = \phi u \tag{2.2}$$

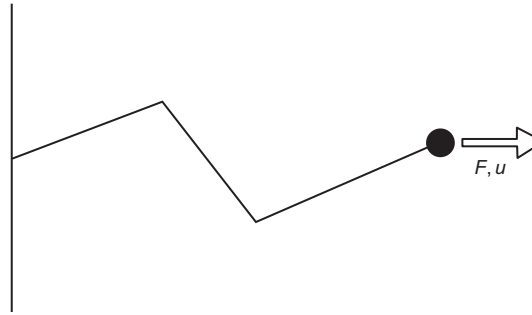

Figure 2.1 A particle attached to a spring. F is the applied force, and u is the displacement of the particle.

In this example, the applied force f is the probe and u, the displacement of the particle, is the response of the spring. In this one-dimensional (1D) case, f, u, and ϕ are all scalars. In general, they are vectors and tensors. In this chapter our interest is mainly in the calculation of the particle displacements in a multiparticle system. The displacement field, which gives the displacement of each particle, is the most important field quantity for modeling of elastic and thermal characteristics of a material system. Most of the elastic and thermal parameters of a material, such as stress and strain and heat diffusion, require calculation of the particle displacements.

We can write the solution of Eq. (2.2) as

$$u = Gf \tag{2.3}$$

where $G = 1/\phi$. In Eq. (2.3) G is the GF that gives the response of the spring to the applied probe f. Notice that G is independent of both f and u and is solely a characteristic of the spring. If we know G, we can obtain displacement for any applied force.

The GF obtained above is the static GF in contrast to the dynamic GF that is used for time-dependent problems. Now let us expand our example to include the time dependence. Suppose the probe is an applied force that is a function of time t. The equation of equilibrium in this case is given by

$$\phi u + M\partial^2 u/\partial t^2 = f(t) \tag{2.4}$$

where M is the mass of the particle A. We write Eq. (2.4) in the form of a linear operator equation as follows:

$$Pu(t) = f(t) \tag{2.5}$$

where the operator P is defined as

$$P = \left(\phi + M\partial^2/\partial t^2\right) \tag{2.6}$$

The formal solution of Eq. (2.5) is given by

$$u(t) = P^{-1}f = Gf(t) \tag{2.7}$$

where

$$G = P^{-1} \tag{2.8}$$

We identify G as the GF that is the inverse of the operator P. It is the particular solution of the equation

$$P_t G(t, t') = \delta(t - t') \tag{2.9}$$

where t' is also a time variable in the same space as t but is independent of t, and $\delta(t)$ is the Dirac delta function, which is zero for a nonzero argument. The delta function in Eq. (2.9) is defined by the following well-known integral relationship:

$$Z(t) = \int \delta(t - t') Z(t') \mathrm{d}t' \tag{2.10}$$

where $Z(t)$ is any arbitrary but integrable function of t and the integration is over all t-space. The subscript at P in Eq. (2.9) indicates that it operates only on the variable t and not on t'. We can now write the formal solution given by Eq. (2.7) in the following general form:

$$u(t) = \int G(t - t') f(t') \mathrm{d}t' \tag{2.11}$$

where the integration is over all t-space. It can be easily verified that Eq. (2.11) is the solution of Eq. (2.5) by substitution and using Eqs. (2.9) and (2.10). Note that we have written G as a function of single argument $t - t'$, which assumes that G depends upon t and t' only through their difference.

Now we derive an expression for G. We note that it is an operator so we need a representation for G. Let us try the Fourier representation and express all quantities in terms of their Fourier transforms defined as follows:

$$f(t) = (1/2\pi) \int f(\omega) \exp(\imath \omega t) \mathrm{d}\omega \tag{2.12}$$

$$u(t) = (1/2\pi) \int u(\omega) \exp(\imath \omega t) \mathrm{d}\omega \tag{2.13}$$

and

$$G(t) = (1/2\pi) \int G(\omega) \exp(\imath \omega t) \mathrm{d}\omega \tag{2.14}$$

where ω is the variable conjugate to t and $\imath = \sqrt{-1}$. The integration in Eqs. (2.12)–(2.14) is over all ω space. We now specify that both the variables t and ω range from $-\infty$ to $+\infty$.

The delta function has the following Fourier representation (Barton, 1989):

$$\delta(t) = (1/2\pi)\int_{-\infty}^{\infty} \exp(\iota\omega t)\mathrm{d}\omega \tag{2.15}$$

From Eq. (2.15) we can obtain the inversion relationship for the Fourier transforms. For example,

$$G(\omega) = \int_{-\infty}^{\infty} G(t)\exp(-\iota\omega t)\mathrm{d}\omega \tag{2.16}$$

Similar relationships can be derived for the Fourier transforms of other variables. Substitution of Eq. (2.14) in Eq. (2.9) and using Eqs. (2.6) and (2.15) gives the following result:

$$G(\omega) = 1/M\left(\omega_0^2 - \omega^2\right) \tag{2.17}$$

where

$$\omega_0 = \sqrt{(\phi/M)} \tag{2.18}$$

is the natural frequency of the spring. Equation (2.17) gives the desired GF in the frequency space. The GF in the time space can then be calculated from Eq. (2.14). Finally, we obtain by using Eqs. (2.11)–(2.15)

$$u(\omega) = G(\omega)f(\omega) \tag{2.19}$$

Equation (2.19) along with Eq. (2.13) yields Eq. (2.11), the desired particular solution of Eq. (2.5). The solution can also be written directly from Eq. (2.19) by taking the following convolution:

$$u(t) = \int G(t-t')f(t')\mathrm{d}t' \tag{2.20}$$

In a general case, the temporal GF $\mathbf{G}(t)$ is to be defined as retarded or advanced GF for positive and negative times to account for causality (Maradudin et al., 1971). The causal GFs that we consider in this chapter must obey the causality condition that the response cannot precede the cause. Hence,

$$G(t) = 0 \quad \text{for } t < 0 \tag{2.21}$$

Because $G(\omega)$ has a singularity on the real axis (Eq. 2.17), one has to take an appropriate contour for the integration to ensure causality.

For positive values, the variable ω can be identified as the frequency. In Eqs. (2.12)–(2.14) we have used the same symbol for the functions and Fourier

transform for notational brevity, the identifying feature being the functional dependence on t or ω.

The above derivation gives the basic features of the GF method. Although the example was rather trivial, it does bring out some of the main characteristics of the GF, summarized as follows:

1. GF is an operator being the inverse of an operator as defined by Eq. (2.9). We need a representation for calculating the GF. Fourier representation is one such representation, and other representations are possible. The choice of representation depends on the physical conditions to be simulated.
2. GF is linear so the solutions are additive as can be verified from Eq. (2.20). However, it is possible to include nonlinear effects in the probe.
3. GF has poles at the natural frequencies of the system. These poles can be identified as resonances.
4. GF is a characteristic of the system and is independent of the probe.
5. Once the GF is known, it can be used to obtain the solution (or the response) to any probe by using Eq. (2.20).
6. The static GF is the zero frequency limit of the dynamic GF and is independent of the mass of the particles.

2.3 Discrete lattice model of a solid

In this section we describe the main features of the lattice model of a solid that account for its discrete atomistic structure explicitly. We will include only those features that are directly relevant to the GF method. For details, please consult any textbook on solid state physics or lattice dynamics such as the excellent classics by Kittel (1996), Born and Huang (1954), or Maradudin et al. (1971). In this section we shall consider only a general 3D lattice. The special case of a two-dimensional (2D) graphene will be discussed in Section 2.5.

An important input to all the lattice calculations is the interatomic potential. All atomistic defect calculations are based upon minimizing the free enthalpy of the solid that consists of an ionic part, which gives the elastic contribution, and an electronic part. These are, of course, coupled. When a defect such as a vacancy is introduced in the lattice, the relaxed configuration depends upon the charge states of the defect (Lannoo and Bourgoin, 1981). The same applies to extended defects such as a quantum dot or a quantum well. A rigorous calculation of the relaxed configuration would require an *ab initio* quantum mechanical modeling of the coupled ion-electron system in the whole lattice. Such calculations are limited to very small model crystallites consisting of only a few hundred atoms (Parr and Yang, 1989). At the other extreme is the continuum model, in which the electron effects are totally neglected. The continuum model reproduces the bulk mechanical characteristics of the defect and has long been extensively used. It has the advantage of computational convenience but obviously has a limited validity.

The intermediate approach is to use models in which the effect of the electrons is included in an empirical and phenomenological manner by using an effective

interatomic potential (Tersoff, 1988, 1989; Brenner et al., 2002; Baskes, 1992, 1997; Tewary, 2011). This approximation has been used in almost all lattice statics/lattice dynamics/molecular dynamics defect calculations. See, for example, the review article by Stangl et al. (2004) and the monographs by Harrison (2002) and Bimberg et al. (1999) for application of phenomenological potentials to semiconductors. Such model potentials have been used in many atomistic calculations in Ge/Si and other semiconductors using MD. See, for example, the papers by Makeev and Madhukar (2001) and Swadener et al. (2005), which also give other references.

As discussed by Harrison (2002), the inherent assumptions in all these calculations include (i) tight binding approximation that allows us to treat atoms as separate entities, (ii) adiabatic approximation that assumes that the electrons respond adiabatically to the ionic displacements, and (iii) the independent electron approximation. These assumptions result in a separation of the crystal Hamiltonian into a part that corresponds to ionic interactions and another part that gives the energy of the electrons. Of course, the ionic interactions are also affected by the electrons. This contribution is included in a parametric model potential. Such models (Tersoff, 1988, 1989; Baskes, 1992, 1997; Tewary, 2011; Swadener et al., 2005; Cleri and Rosato, 1993; Balamane et al., 1992; Tersoff et al., 1996) give correct values for many observable parameters, including the energy of vacancies and other defects, which lends credence to the validity of the model potential. The potentials (Tersoff, 1988, 1989; Baskes, 1992, 1997; Cleri and Rosato, 1993) to which we refer in this paper belong to this class of models. Some other potentials are available in the literature (Balamane et al., 1992; Cai et al., 2005; Cheng et al., 2005; Mishin et al., 2001; Yavari et al., 2007; Zhigilei and Dongare, 2002), which all have comparable advantages. We have used the Tersoff potential for some applications to graphene because of its computational convenience. It reproduces the correct energy of the defect and has been widely used in defect calculations on covalent solids.

The GF method described in this chapter is based upon the Born von Karman (BvK) model (Maradudin et al., 1971; Kittel, 1996; Born and Huang, 1954) of a lattice. This model fully accounts for the discrete structure of the lattice. The basic assumptions of the BvK model are as follows:

1. Adiabatic approximation: As described above, it implies that the contribution of the electrons to the crystal Hamiltonian is additive. We therefore consider only the ionic interactions in the lattice model. The electronic energies can be calculated separately and added to the ionic energies to obtain the total energy of the crystal.
2. Cyclic boundary conditions: The whole crystal is assumed to be divided in identical supercells. This enables us to neglect the surface effects in a model lattice. This is, therefore, applicable only to large crystals in the regions far away from the surfaces. This assumption is obviously not valid for nanocrystals. In such cases the surfaces are modeled as defects in the ideal BvK lattice.
3. Harmonic approximation: The atomic displacements are assumed to be small enough such that their cubic and higher powers can be neglected in potential energy of the crystal.
4. Equilibrium and stability: The crystal is assumed to be in equilibrium in the absence of external forces so there is no net force at any atom in the lattice.

The lattice structure of a solid can be described in terms of its primitive real-space lattice vectors of the Bravais lattice and the corresponding reciprocal lattice vectors (see, for example, Kittel, 1996). The primitive lattice vectors define a unit cell. Each unit cell may contain one or more atoms. We consider a 3D lattice containing N unit cells with each unit cell containing p atoms. So the total number of degrees of freedom in our model are 3pN corresponding to three coordinates of pN atoms.

We assume a Cartesian frame of reference with the axes parallel to the crystallographic axes and its origin at a lattice site. The Z axis is assumed to be normal to the plane of the paper. We denote the lattice sites of the origin of the unit cells by the indices L, L', and so on, and the Cartesian coordinates x, y, and z by indices α, β, γ, and so on. The atoms inside each unit cell are labeled by the index κ. The atom at the origin of each unit cell is labeled as $\kappa=0$ and other atoms as $\kappa=1,2,p-1$. In all the cases considered in this paper p is either 1 or 2. For example, for a monoatomic Bravais lattice such as fcc Cu or Au, $p=1$. For semiconductors such as Si or Ge that have a diamond lattice structure and for 2D graphene, $p=2$.

We can label each atom by the index doublet $L\kappa$ and write its position vector as follows:

$$\mathbf{R}(L\kappa)=\mathbf{R}(L0)+\mathbf{r}(\kappa) \tag{2.22}$$

where $\mathbf{R}(L)$ is the position vector of the origin of the Lth unit cell and $\mathbf{r}(\kappa)$ is the position vector of the κth atom relative to the origin of its own unit cell. At equilibrium each atom is assumed to be located at its lattice site, and the energy at equilibrium is assumed to be zero.

We now introduce lattice distortion and denote the displacement of the atom $L\kappa$ by $\mathbf{u}(L\kappa)$. In time-dependent problems, $u(L\kappa)$ will also depend on t, and its Fourier transform over time will depend on the frequency ω. However, for brevity of notation, we will not show the explicit dependence of $u(L\kappa)$ on t or ω unless locally needed to avoid confusion.

We write the potential energy of the lattice in the form of a Taylor series as follows:

$$W=-\Sigma_{L\kappa\alpha}f_\alpha(L\kappa)u_\alpha(L\kappa)+(1/2)\Sigma_{L\kappa\alpha}\Sigma_{L'\kappa'\beta}\phi_{\alpha\beta}(L\kappa,L'\kappa')u_\alpha(L\kappa)u_\beta(L'\kappa') \tag{2.23}$$

where $-\mathbf{f}$ and $\boldsymbol{\phi}$ are the Taylor coefficients. They are defined by

$$f_\alpha(L\kappa)=-\partial W/\partial u_\alpha(L\kappa) \tag{2.24}$$

and

$$\phi_{\alpha\beta}(L\kappa,L'\kappa')=\partial^2 W/\partial u_\alpha(L\kappa)\partial u_\beta(L\kappa') \tag{2.25}$$

where the derivatives are evaluated at zero displacement. To clarify the notation, $\mathbf{f}(L\kappa)$ is a 3D vector that denotes the force at the atom $L\kappa$. Its three Cartesian components are denoted by $f_\alpha(L\kappa)$ where $\alpha=x$, y, or z. Similarly $\boldsymbol{\phi}(L\kappa,L'\kappa')$ is a 3×3 matrix called the

force-constant matrix between atoms at $L\kappa$ and $L'\kappa'$. Its nine elements are denoted by $\phi_{\alpha\beta}(L\kappa,L'\kappa')$ for α, $\beta = x$, y, or z.

The force and the force-constant matrices can be obtained from the interatomic potential (Maradudin et al., 1971). These matrices must obey the constraints imposed by the translation and rotation symmetry of the lattice, which determine the number of independent elements in the matrices (Maradudin et al., 1971). In addition, the equilibrium condition of zero net force on the solid imposes the following constraints:

1. For all α

$$\Sigma_{L\kappa} f_\alpha(L\kappa) = 0 \tag{2.26}$$

2. For all L, κ, α, and β

$$\Sigma_{L'\kappa'} \phi_{\alpha\beta}(L\kappa,L'\kappa') = 0 \tag{2.27}$$

At equilibrium, W must be minimum. By minimizing the right-hand side (RHS) of Eq. (2.23), we obtain the following equation for the displacements:

$$f_\alpha(Lk) = \Sigma_{L'\kappa'\beta} \phi_{\alpha\beta}(Lk,L'k') u_\beta(L'k') \tag{2.28}$$

Equation (2.28) is the generalized form of Eq. (2.2) for a many-particle system in which $\mathbf{f}$ is the probe and u is the response. For time-dependent problems, the Newtonian term has to be added to Eq. (2.28) as in Eq. (2.4). For a finite system, one can write a set of coupled equations for pN atoms as in Eq. (2.28) and solve it numerically for all u. This is essentially the technique used in MD. As mentioned in Section 2.1, solving Eq. (2.28) directly may become computationally too expensive for large N—say a few million or billion atoms. As we shall see in this section, the GF method offers a computationally efficient method for solving Eq. (2.28).

Using Eqs. (2.23) and (2.28), we can write the equation of motion for the atom $L\kappa$ for a perfect lattice as follows:

$$M_{L\kappa} \partial^2 u(L\kappa)/\partial t^2 = f_\alpha(L\kappa) - \sum_{L'\kappa'\beta} \phi_{\alpha\beta}(L\kappa,L'\kappa') u_\beta(L'\kappa') \tag{2.29}$$

For modeling of phonons, we take the Fourier transform of the displacement over time as given in Eq. (2.13). This will make $\mathbf{u}(L\kappa)$ a function of the frequency ω, which can be identified as the phonon frequency. The nonlinear terms in the potential, if any, will add terms on the right of Eq. (2.29) that will depend upon u. Alternatively, the nonlinear effects can be included by treating $\mathbf{f}$ and $\boldsymbol{\phi}$ as functions of $\mathbf{u}$ and hence t. In the harmonic approximation, $\mathbf{f}$ and $\boldsymbol{\phi}$ are independent of $\mathbf{u}$ and t. Further, in the harmonic approximation phonon frequencies are independent of $\mathbf{f}$. If $\mathbf{f}$ is nonzero, the equilibrium location of atoms will change and they will simply vibrate about their new position of equilibrium.

We define the discrete Fourier transform over space of the displacement vector as follows:

$$u_\alpha(L\kappa) = (1/N)\Sigma_k u_\alpha(\mathbf{k};\kappa)\exp[\imath\mathbf{k}.\mathbf{R}(L\kappa)] \tag{2.30}$$

where $\mathbf{k}$ is a vector in the reciprocal space of the lattice. The number of allowed $\mathbf{k}$ vectors in the first Brillouin zone is N equal to the number of unit cells in a supercell. For notational brevity, we follow the common convention and denote the matrix in real space and the Fourier (reciprocal) space by the same symbol. The distinguishing feature between the two is that the functional dependence on $\mathbf{k}$ will be shown explicitly for a matrix in reciprocal space. An equation similar to Eq. (2.30) can be written for the force vector defined by Eq. (2.24). Instead of Eq. (2.30), and an alternative definition of the Fourier transform has also been used in the literature in which $\mathbf{R}(L0)$ is used in the exponent instead of $\mathbf{R}(L\kappa)$. The two definitions differ only by a phase factor $\exp[\imath\mathbf{k}.\mathbf{r}(\kappa)]$.

Because of the orthogonality of the reciprocal and the direct-lattice vectors, the vector $\mathbf{k}$ can take only certain allowed discrete values (Maradudin et al., 1971; Tewary, 1973) and can be confined to the first Brillouin zone of the lattice. The inverse Fourier transform of Eq. (2.30) can be obtained by using the following relation (Maradudin et al., 1971):

$$\Sigma_L\exp[\imath\mathbf{k}.\mathbf{R}(L0)] = \delta_\mathrm{d}(\mathbf{k}) \tag{2.31}$$

and

$$\Sigma_k\exp[\imath\mathbf{k}.\mathbf{R}(L0)] = \delta_\mathrm{d}(L) \tag{2.32}$$

where δ_d is the discrete analog of the Dirac delta function defined by Eq. (2.10). It is 0 for the nonzero value of the argument and equal to N if the argument is 0. Strictly speaking, the sum in Eq. (2.31) is equal to N not just for $\mathbf{k}=0$ but whenever $\mathbf{k}$ is equal to a reciprocal lattice vector. However, in this paper, we will be concerned with only those cases when $\mathbf{k}$ is restricted to the first Brillouin zone of the lattice.

Using Eqs. (2.31) and (2.32) in Eq. (2.30), we find the following equation for the inverse transform of the displacement vector:

$$u_\alpha(\mathbf{k};\kappa) = \Sigma_L u_\alpha(L\kappa)\exp[-\imath\mathbf{k}.\mathbf{R}(L\kappa)] \tag{2.33}$$

Note the absence of the factor $(1/N)$ in Eq. (2.33) as compared to Eq. (2.30).

The above equations are valid for a perfect lattice as well as a lattice containing defects. A perfect infinite lattice or a perfect lattice with periodic boundary conditions has full translation symmetry. This, combined with the condition of invariance of the potential energy against rigid body translations, leads to the following additional constraints (Maradudin et al., 1971):

1. The Taylor coefficient $f_\alpha(L\kappa)=0$ for all $L\kappa$. Physically this condition implies that for a perfect lattice in equilibrium without any external forces, there cannot be any force on any

lattice site. Of course, if external forces are applied, then **f** can represent the applied external forces.

2. The force-constant matrix $\phi_{\alpha\beta}(L\kappa,L'\kappa')$ depends upon L and L' only through their difference. This is a consequence of translation symmetry. Because all atoms on one sublattice are equivalent, any atom can be chosen as the origin. The force-constant matrix can therefore be labeled by a single index as $\phi_{\alpha\beta}(0\kappa,L\kappa')$ that gives the force constant between any two atoms for which the unit cells are separated by $\mathbf{R}(L\kappa')-\mathbf{R}(0\kappa)$. This enables us to write the force-constant matrix in terms of its discrete Fourier transform as defined in the following equation:

$$\phi_{\alpha\beta}(0\kappa,L\kappa') = (1/N)\Sigma_k \phi_{\alpha\beta}(\mathbf{k};\kappa,\kappa')\exp[\imath\mathbf{k}.\{R(L\kappa')-R(0\kappa)\}] \tag{2.34}$$

where $\boldsymbol{\phi}(\mathbf{k})$ is the Fourier transform of the force-constant matrix. Its matrix elements are $\phi_{\alpha\beta}(\mathbf{k};\kappa,\kappa')$. As in Eq. (2.33), the inverse transform of $\boldsymbol{\phi}(\mathbf{k})$ is given by

$$\phi_{\alpha\beta}(\mathbf{k};\kappa,\kappa') = \Sigma_L \phi_{\alpha\beta}(0\kappa,L\kappa')\exp[-\imath\mathbf{k}.\{\mathbf{R}(L\kappa')-\mathbf{R}(0\kappa)\}] \tag{2.35}$$

Because κ and κ' can take p values, the matrix $\boldsymbol{\phi}(\mathbf{k})$ is $3p\times 3p$ square matrix. By generalizing the derivation given in Section 2.2 to 3D many-particle systems, it can be shown that the phonon frequencies ω are the eigenvalues of the dynamical matrix (Maradudin et al., 1971; Born and Huang, 1954) defined in terms of $\boldsymbol{\phi}(\mathbf{k})$ as follows:

$$D_{\alpha\beta}(\mathbf{k};\kappa,\kappa') = (M_\kappa M_{\kappa'})^{-1/2}\phi_{\alpha\beta}(\mathbf{k};\kappa,\kappa') \tag{2.36}$$

where M_κ is the mass of the atom κ. In view of the translation symmetry in a perfect lattice for which Eq. (2.36) is valid, M_κ is independent of L. The dynamical matrix $\mathbf{D}(\mathbf{k})$ is used extensively in the lattice dynamical calculations. Lattice statics for static problems are independent of the atomic masses. The relevant matrix for lattice statics is $\boldsymbol{\phi}(\mathbf{k})$ (Andreev et al., 1999).

The matrices $\mathbf{D}(\mathbf{k})$ and $\boldsymbol{\phi}(\mathbf{k})$ have $3p$ eigenvalues. From Eq. (2.36), their eigenvalues are related through a factor depending upon the atomic masses. By using Eq. (2.27) it can be shown that the determinant of $\mathbf{D}(\mathbf{k})$ is zero at $k=0$ and at least three of its eigenvalues vary as k^2 approach $k=0$ for a normal 3D solid. These are called the acoustic modes. The remaining $3p-3$ eigenvalues are, in general, finite at $k=0$ and are called the optical modes.

2.4 Lattice statics Green's function

First we consider a perfect lattice. The phonon GF of the lattice is defined as follows (Maradudin et al., 1971):

$$\mathbf{G}\left(\mathbf{k},\omega^2\right) = \left[-\omega^2\mathbf{I}+\boldsymbol{\phi}(\mathbf{k})\right]^{-1} \tag{2.37}$$

where $\mathbf{I}$ is the unit matrix. In steady state the displacements are independent of time so the steady state corresponds to $\omega=0$. We define the lattice statics Green's function

(LSGF) as the zero frequency limit of the phonon GF (Tewary, 1973). In the Fourier k-space, the LSGF is given by:

$$\mathbf{G}(\mathbf{k}) = [\boldsymbol{\phi}(\mathbf{k})]^{-1} \tag{2.38}$$

Because the determinant of $\boldsymbol{\phi}(\mathbf{k})$ is zero at $k=0$, $\mathbf{G}(\mathbf{k})$ is singular at $k=0$, which is consistent with the discussion in Section 2.2. Analogous to $\boldsymbol{\phi}(\mathbf{k})$, the matrix elements of the $3p \times 3p$ matrix $\mathbf{G}(\mathbf{k})$ are labeled as $G_{\alpha\beta}(\mathbf{k};\kappa,\kappa')$. The LSGF in the real space is defined by its inverse Fourier transform in analogy with Eq. (2.34) as follows:

$$G_{\alpha\beta}(0\kappa, L\kappa') = (1/N)\Sigma_k G_{\alpha\beta}(\mathbf{k};\kappa,\kappa')\exp[\imath\mathbf{k}.\{\mathbf{R}(L\kappa') - \mathbf{R}(0\kappa)\}] \tag{2.39}$$

Equation (2.39) provides a convenient and computationally efficient semianalytic representation for calculation of the LSGF. For a solid containing N atoms, it requires inversion of only $3p \times 3p$ matrices. In most cases of practical interest as considered here, p is a small number, that is, 1 or 2.

For real-space calculations, it is convenient to define a $3pN \times 3pN$ vector space in terms of the three coordinates of the pN atoms. In this representation we denote the real-space force constant and the GF matrices by $\boldsymbol{\Phi}$ and $\boldsymbol{\Gamma}$, respectively. These matrices will be $3pN \times 3pN$ square matrices, and their matrix elements are $\phi_{\alpha\beta}(L\kappa,L'\kappa')$ and $G_{\alpha\beta}(L\kappa,L'\kappa')$, respectively. Similarly, in the same vector space, we define $3pN$ dimensional column matrices $\mathbf{U}$ and $\mathbf{F}$ for the displacement and the force vectors with matrix elements $U_\alpha(L\kappa)$ and $f_\alpha(L\kappa)$, respectively. Using Eq. (2.38) it can be easily shown that in this representation

$$\boldsymbol{\Gamma} = \boldsymbol{\Phi}^{-1} \tag{2.40}$$

In the same representation, Eq. (2.23) can be written in the following compact form:

$$W = -\mathbf{F}\cdot\mathbf{U} + (1/2)\mathbf{U}^{\mathrm{T}}\cdot\boldsymbol{\Phi}\cdot\mathbf{U} \tag{2.41}$$

If defects are introduced in the lattice, then its translation symmetry is broken. Consequently, even in the absence of any external force, $\mathbf{f}$ becomes nonzero for at least some L and κ (Tewary, 1973). Further, $\boldsymbol{\Phi}$ and $\mathbf{G}$ depend upon L and L' separately and not merely on their difference (Maradudin et al., 1971). Hence, it is not possible to define their Fourier transform in terms of a single vector $\mathbf{k}$ as in Eqs. (2.34) and (2.39). In such cases, the defect LSGF, the GF for the lattice with defects, is calculated as follows (Tewary, 1973; Thomson et al., 1992).

We denote the force-constant matrix for the defective lattice and the defect LSGF by $\boldsymbol{\Phi}^*$ and $\boldsymbol{\Gamma}^*$ respectively. In the representation of lattice sites, $\boldsymbol{\Gamma}^*$ and $\boldsymbol{\Phi}^*$ are $3Np \times 3Np$ matrices. The GF is formally given by as in Eq. (2.40)

$$\boldsymbol{\Gamma}^* = [\boldsymbol{\Phi}^*]^{-1} \tag{2.42}$$

We write

$$\mathbf{\Phi}^* = \mathbf{\Phi} - \mathbf{\Delta\Phi} \tag{2.43}$$

where $\mathbf{\Delta\Phi}$ denotes the change in the force-constant matrix $\mathbf{\Phi}$ caused by the defect(s). From Eqs. (2.40), (2.42), and (2.43), we obtain the following equation:

$$\mathbf{\Gamma}^* = \mathbf{\Gamma} + \mathbf{\Gamma\Delta\Phi\Gamma}^* \tag{2.44}$$

Equation (2.44) is the Dyson equation for calculation of the defect GF. This equation shows that in order to calculate $\mathbf{G}^*$, we have to first define a reference state and calculate $\mathbf{G}$ and the corresponding $\mathbf{\Delta\Phi}$. The change $\mathbf{\Delta\Phi}$ is obtained by the interatomic potential between the defect and the host atoms. In quantum mechanical problems, $\mathbf{\Delta\Phi}$ gives the change in the system Hamiltonian. Methods for solving the Dyson equation have been discussed in detail in references (Maradudin et al., 1971; Tewary, 1973; Yang and Tewary, 2004).

In the present case we have taken the perfect lattice with full translation symmetry as the reference state. In practice, any state can be chosen to be the reference state for which $\mathbf{G}$ can be calculated and $\mathbf{\Delta\Phi}$ can be conveniently defined (Yang and Tewary, 2004; Yang and Tewary, 2006; Yang and Tewary, 2005). Further, although $\mathbf{G}$ for the reference state is calculated using the harmonic or the linear approximation, $\mathbf{\Delta\Phi}$ can include nonlinear terms (Read and Tewary, 2007; Tewary and Read, 2004).

For a defect lattice, Eq. (2.41) is modified as follows:

$$W^* = -\mathbf{F}\cdot\mathbf{U} + (1/2)\mathbf{U}^{\mathrm{T}}\cdot\mathbf{\Phi}^*\cdot\mathbf{U} \tag{2.45}$$

where $\mathbf{U}$ and $\mathbf{F}$ are now identified as the displacement and the force vectors in the defect lattice. The solution of Eq. (2.45) gives the displacement field:

$$\mathbf{U} = \mathbf{\Gamma}^*\mathbf{F} \tag{2.46}$$

A very useful form of Eq. (2.46) has been derived in Tewary (1973). It is shown that Eq. (2.46) is exactly equivalent to

$$\mathbf{U} = \mathbf{\Gamma F}^* \tag{2.47}$$

where

$$\mathbf{F}^* = \mathbf{F} + \mathbf{\Delta\Phi U} \tag{2.48}$$

Equations (2.46) and (2.47) are the main equations of the LSGF method. They are used to calculate the atomic displacements, which give the lattice distortion or the lattice relaxation caused by the defect. In this method the defect is characterized by $\mathbf{\Delta\Phi}$. Equation (2.46) gives the displacement in terms of the defect GF and the forces on the atoms at the lattice sites of the reference state. Equation (2.47), the alternative form

of Eq. (2.46), gives the displacement in terms of the perfect lattice GF and an effective force denoted by **F***, as defined by Eq. (2.48).

The effective force **F*** is called the Kanzaki force (Tewary, 1973). From Eq. (2.48), we can identify it as the force due to the defect on the relaxed lattice sites, in contrast to **F,** which denotes the force at the original lattice site.

2.5 Multiscale Green's function

The LSGF method provides a convenient and computationally efficient mathematical technique for multiscale modeling of nanomaterials. We need multiscale models of nanomaterials for bridging length scales as well as temporal scales. In this section we will discuss only the length scales. The problem of multitime scales will be discussed in the next section.

The coupling between the lattice and the continuum models in the GF method is achieved by using the Born's method of long waves (Born and Huang, 1954). This method establishes the correspondence between the force constants and the elastic constants. Using the Born's method, it has been shown in Tewary (1973) that the LSGF varies as $1/R$ for large R and reduces asymptotically to the continuum GF (CGF) for 3D lattices. The case of 2D graphene is, however, different and will be described in Section 2.7.

To establish the correspondence between the LSGF and the CGF, we make $\mathbf{R}(\mathbf{L}\boldsymbol{\kappa})$ and $\mathbf{k}$ continuous variables and replace the summation in Eq. (2.39) by integration over the reciprocal space. In conformity with the continuum model notation, we replace $\mathbf{R}(\mathbf{L}\boldsymbol{\kappa})$ by the continuous variable $\mathbf{x}$ for large $R(L\kappa)$ and the discrete wave vector $\mathbf{k}$ by the continuous wave vector $\mathbf{q}$, which spans all space from $-\infty$ to ∞.

$$\mathbf{G}(\mathbf{x}) \cong (1/2\pi)^3 \int \mathbf{G}(\mathbf{q}) \exp(\imath \mathbf{q}\cdot\mathbf{x}) \mathbf{dq} \tag{2.49}$$

We obtain the asymptotic limit of $\mathbf{G}(\mathbf{x})$ by using Duffin's lemma (see, for example, Tewary, 1973). In the limit $x \to \infty$, smaller values of q make more significant contribution to the integral in Eq. (2.49). Accordingly, we expand $\mathbf{G}(\mathbf{q})$ in powers of q as given in the following equation:

$$\mathrm{Lim}_{q\to 0}\mathbf{G}(\mathbf{q}) = \mathrm{Lim}_{q\to 0}[\boldsymbol{\Phi}(\mathbf{q})]^{-1} \tag{2.50}$$

For low values of q, $\boldsymbol{\Phi}(\mathbf{q})$ has the following behavior (Maradudin et al., 1971) for the acoustic modes:

$$\phi(q) \sim O\left(q^2\right) + O\left(q^4\right) \tag{2.51}$$

Using the expansion given in Eq. (2.51), in Eq. (2.50), we can carry out the integral in Eq. (2.49) term by term, which gives the asymptotic expansion of the LSGF.

The leading term in $\boldsymbol{\phi}(\mathbf{q})$ as $q \to 0$ is the q^2 term. This term is identical to the Christoffel matrix in the continuum model. Keeping only this term, we can show (Tewary, 1973) that

$$\mathrm{Lim}_{\mathrm{q}\to 0}\mathbf{G}(\mathbf{q}) = \mathrm{Lim}_{\mathrm{q}\to 0}[\boldsymbol{\phi}(\mathbf{q})]^{-1} = [\Lambda(\mathbf{q})]^{-1} \tag{2.52}$$

where $\boldsymbol{\Lambda}$ is the well-known Christoffel matrix of the continuum model (Ting, 1996), which is defined in terms of $\mathbf{c}$, the elastic constant tensor, as follows:

$$\Lambda_{ij}(\mathbf{q}) = c_{ikjl}q_k q_l \tag{2.53}$$

and i, j, k, l are Cartesian components in the continuum model. Summation over repeated Cartesian indices is assumed. The CGF $\mathbf{G_c}(\mathbf{q})$ in q space is defined as the Christoffel matrix. Thus we get

$$\mathrm{Lim}_{\mathrm{q}\to 0}\mathbf{G}(\mathbf{q}) = \mathbf{G_c}(\mathbf{q}) = [\Lambda(\mathbf{q})]^{-1} = O\left(1/q^2\right) \tag{2.54}$$

In view of Eq. (2.54), the integrand in Eq. (2.49) has a $1/q^2$ singularity at $q = 0$. It is integrated out in 3D because the integral element in 3D is proportional to q^2. It can be shown (Tewary, 1973) that the integral is proportional to $1/|x|$, which is the continuum GF in 3D. The subscript c on $\mathbf{G}$ in Eq. (2.49) denotes the GF for the continuum model. It has been extensively used in modeling solids using the boundary element analysis and provides a powerful technique for solving the boundary value problems for solids with and without defects. See, for example, Pan (2002), Yang and Tewary (2003), Tewary (2004a), and Berger and Tewary (2001).

It is important to note that the asymptotic relation given by Eq. (2.49) is valid only for the perfect lattice GF $\mathbf{G}$. It is generally not valid for the defect GF $\mathbf{G^*}$ defined by Eq. (2.44) unless the term containing $\boldsymbol{\Delta\Phi}$ is negligible (Tewary, 2004b). In most cases of practical interest, it is not negligible. For example, in the case of a vacancy $\boldsymbol{\Delta\Phi} = \boldsymbol{\Phi}$. Moreover, if the effect of $\boldsymbol{\Delta\Phi}$ is negligible, then the information about the defect is lost. Calculations in this region are therefore not of interest for studying the properties of the defect.

The advantage of writing the displacement in the form of Eq. (2.47) is now obvious. We can use the full power of continuum mechanics by using the continuum model GF for $\mathbf{G}$ where needed while retaining the discrete lattice effects and all the characteristics of the defect exactly in $\mathbf{F}^*$.

Equation (2.47) is the master equation of our MSGF method. The displacement of the atom at $L\kappa$, which is a matrix element of $\mathbf{U}$, is given by

$$u_\alpha(Lk) = \sum\nolimits_{L'k'\beta} G_{\alpha\beta}(Lk,L'k')\mathbf{f}^*{}_\beta(L'k') \tag{2.55}$$

where $\mathbf{f^*}$ is the Kanzaki force given, which is the corresponding matrix element of $\mathbf{F^*}$ given by Eq. (2.48) . For $L\kappa$ close to the defect we use $\mathbf{G}$ to be the LSGF, whereas for large values $|\mathbf{R(L\kappa)} - \mathbf{R(L'\kappa')}|$ we choose $\mathbf{G} = \mathbf{G_c}$, the CGF. Because $\mathbf{G_c}$ is the asymptotic limit of G for large $|\mathbf{R(L\kappa)} - \mathbf{R(L'\kappa')}|$, the linkage is seamless.

It must be emphasized that even with G_c, we use the discrete lattice value of **f*** (or **F***) as defined by Eq. (2.48) near the defect in terms of $\mathbf{\Delta\Phi}$. The Kanzaki force retains all the characteristics of the defect through $\mathbf{\Delta\Phi}$. Thus Eq. (2.55) is the multiscale representation of the lattice distortion or strains due to the defect because it relates the discrete lattice parameters through **f*** to the continuum model parameters through $\mathbf{G_c}$.

The advantage of writing the displacement in the form of Eq. (2.47) is now obvious. We can access the full power of continuum mechanics by using the continuum-model GF G_c for **G** where needed, while retaining the discrete lattice effects and all the characteristics of the defect exactly in **F***.

Further, nonlinear effects associated with the defect host interaction can be incorporated in the MSGF method through $\mathbf{\Delta\Phi}$ while still retaining the linear simplicity of the GFs. A convenient technique for including nonlinear effects is to calculate the atomic displacements in a zone near the defect by using MD and use these values to calculate **f***. MD accounts for the nonlinear forces. The displacements outside the zone are then calculated by using Eq. (2.55) by using LSGF or CGF for **G**, depending upon the value of $|\mathbf{R(L\kappa)} - \mathbf{R(L'\kappa')}|$. This method has been applied to model realistic-size Ge quantum dots in Si and Au islands in Cu (Read and Tewary, 2007; Tewary and Read, 2004). A somewhat different version of the MSGF method has been applied to quantum nanostructures in semiconductors (Yang and Tewary, 2005, 2007).

One important advantage of the MSGF method is that continuum parameters such as strain and stresses are uniquely defined in this method. In a pure discrete lattice model, the atomic displacements are defined at discrete lattice points. In many applications, one needs elastic strains, which are also measured experimentally. Strain is a continuum parameter defined in terms of the derivatives of the displacement field and cannot be defined as such for discrete values of the displacements. In practice, one has to assume some averaging scheme in order to define the derivatives. Although elegant techniques (Cormier et al., 2001) have been developed for this purpose, the averaging process is not unique and requires careful attention to various conservation laws. In the MSGF method, the variable x in Eq. (2.49) is continuous so the derivatives of **u** with respect to x are uniquely defined.

2.6 Causal Green's function for temporal modeling

We have developed a new temporal modeling technique (Tewary, 2009) by incorporating causal GF in MD. We refer to this method as the GFMD method. At least in some idealized cases, it has been shown that GFMD can model time scales over six to nine orders of magnitude at the atomistic level. So far this technique has been applied to only a few idealized cases, but it clearly has the potential for a much wider and realistic applications in all physical, chemical, and biological systems where MD is used.

In a certain class of problems in which atoms vibrate about an equilibrium site, GFMD gives exact results in the harmonic approximation. Even for nonlinear

vibrational problems, GFMD has been shown to accelerate the MD by up to 8 orders of magnitude (Tewary, 2009). This enables modeling processes up to microseconds. Examples of such problems are phonon transport and thermal conduction. In problems involving itinerant atoms, such as diffusion or crystal growth, GFMD should also be able to accelerate MD substantially.

The GFMD method has been described in detail in Tewary (2009). Here we will only quote the highlights of the technique given in Tewary (2009). Consider the equation of motion for the atom $L\kappa$ as given by Eq. (2.29). The symbols in this section will have a slightly more general meaning. The time-dependent displacement and the velocity vectors of the atom $L\kappa$ will be denoted by $\mathbf{u}(L\kappa,t)$ and $\mathbf{c}(L\kappa,t)$, respectively. We assume that at time $t=0$, $\mathbf{u}(L\kappa,0)$ and $\mathbf{f}(L\kappa)$ denote the values of displacement and force for the atom $L\kappa$. As in classical MD, we need to solve the following equation for $\mathbf{u}$:

$$\begin{aligned} M_{L\kappa}\frac{\partial^2 u_\alpha(L\kappa,t)}{\partial t^2} &= -\frac{\partial W}{\partial u_\alpha(L\kappa,t)} \\ &= f_\alpha(L\kappa) - \sum_{L'\beta}\phi_{\alpha\beta}(L\kappa,L'\kappa')u_\beta(L'\kappa',t) + \Delta f_\alpha(L\kappa) \end{aligned} \tag{2.56}$$

where $\Delta\mathbf{f}$ represents higher than harmonic terms in the expansion of W. This term depends upon $\mathbf{u}$ and hence on t.

As in Eq. (2.45), we define $3pN$-dimensional vectors $\mathbf{U}(t)$, $\mathbf{C}(t)$, $\mathbf{F}$, and $\Delta\mathbf{F}(t)$, and $3pN\times 3pN$ matrices $\mathbf{\Phi}$ and $\mathbf{D}$. However, in the present time-dependent case, for brevity of notation, their elements are denoted by the corresponding lowercase quantities weighted with atomic masses. For example, the $(\alpha,L\kappa)$ element of $\mathbf{U}(t)$ is $\sqrt{M_{L\kappa}}u_\alpha(L\kappa,t)$ and of $\mathbf{F}$ is $(1/\sqrt{M_{L\kappa}})f_\alpha(L\kappa)$. The formal solution of Eq. (2.56) in the operator form is then given by

$$\mathbf{U}(t) = \left(\mathbf{I}\frac{\partial^2}{\partial t^2} - \mathbf{D}\right)^{-1}\mathbf{F}_{\text{eff}}(t) \tag{2.57}$$

where $\mathbf{I}$ is the unit matrix, $\mathbf{M}$ is a diagonal matrix with atomic masses as its elements,

$$\mathbf{D} = \mathbf{M}^{-1/2}\mathbf{\Phi}\mathbf{M}^{-1/2} \tag{2.58}$$

and

$$\mathbf{F}_{\text{eff}}(t) = \mathbf{F} + \Delta\mathbf{F}(t) \tag{2.59}$$

The inverse operator in Eq. (2.57) is the GF. We solve Eq. (2.57) by using Laplace transform that gives the causal GF (Maradudin et al., 1971), which is 0 for $t<0$, to ensure causality. Using the numerical approximation $\mathbf{F}_{\text{eff}}(t)=\mathbf{F}$, we obtain the exact result (Tewary, 2009):

$$\mathbf{U}(t) = \mathbf{V}\mathbf{U}^*(t) \tag{2.60}$$

where

$$U_i^*(t) = -\left(F_i^*/E_i^2\right)[\cos(E_i t) - H(t)] + \left(C_{0i}^*/E_i\right)\sin(E_i t) + U_{0i}^*\cos(E_i t) \tag{2.61}$$

$\mathbf{U}^*$, $\mathbf{F}^*$, $\mathbf{C}_0^*$, and $\mathbf{U}_0^*$ are $\mathbf{V}^{\mathrm{T}}(\mathbf{U}, \mathbf{F}, \mathbf{C}_0$, and $\mathbf{U}_0)$, respectively, $\mathbf{V}$ is the matrix of eigenvectors of $\mathbf{D}$, E_i $(I = 1 \ldots 3pN)$ is an eigenvalue of $\mathbf{D}$, and $H(t)$ is the Heaviside step function, which is 0 for $t < 0$, and 1 for $t > 0$.

Equation (2.60) can be used as stated for phonons in systems where the harmonic approximation is valid but the analytical lattice dynamics cannot be used due to lack of translational symmetry. To account for anharmonic effects in a multiparticle system, we use the MD type iterative approach. We expand W locally at each time step. We calculate $\mathbf{U}(t)$ from Eq. (2.60) in steps of Δt. We keep Δt small so that $\Delta\mathbf{F}(t)$ is negligible at each step. This introduces a constraint on the step size Δt, which is much less severe than that in the conventional MD.

The convergence of GFMD is much faster than MD because in the basic MD only the first term on the right of Eq. (2.56) is retained whereas GFMD retains up to quadratic terms in the expansion of W, and the GFMD gives an exact solution of the temporal equation for any value of t. The constraint on t or Δt arises because of the necessity to keep $\Delta\mathbf{F}(t)$ small. The basic MD can of course be accelerated somewhat by using more refined numerical techniques that partly account for the second order terms by iteration.

We can compare the convergence of the GFMD and the MD techniques by estimating the errors in the two techniques as follows. We denote the displacement variable in the expansion of W in Eq. (2.23) by ξ. Suppose the actual normalized value of a displacement is unity, which we calculate in S_{MD} steps in the MD and S_{GFMD} in the GFMD technique. Then $\xi_{\mathrm{MD}} = 1/S_{\mathrm{MD}}$ for MD and $1/S_{\mathrm{GFMD}}$ for GFMD. In the conventional MD, second and higher powers of ξ_{MD} are neglected so the error in each step is of the order of $(\xi_{\mathrm{MD}})^2$. The corresponding error in GFMD is $(\xi_{\mathrm{GFMD}})^3$. For MD to be at least as accurate as GFMD, we must have

$$(\xi_{\mathrm{MD}})^2 = (\xi_{\mathrm{GFMD}})^3 \tag{2.62}$$

or

$$S_{\mathrm{MD}} \approx (S_{\mathrm{GFMD}})^{3/2} \tag{2.63}$$

Considering that in practical cases $S_{\mathrm{GFMD}} \approx 10^6$, Eq. (2.63) shows that the number of iterations needed in the conventional MD to attain the same accuracy as the GFMD technique approaches a factor of 1000.

Finally, we remark that the GFMD technique is particularly efficient for modeling of phonons and elastic properties of nanomaterials. This is because it is specifically the u^2 term in Eq. (2.23) that defines the phonon and elastic response of a solid (Maradudin et al., 1971). This term is exactly included in the GFMD technique. In conventional MD the u^2 term is included only through additional iterations that is a relatively inefficient process.

2.7 Application to 2D graphene

As we have seen in Section 2.5, a multiscale model of a solid can be constructed if we can establish a correspondence between its lattice and continuum GFs. Such a correspondence was rigorously proved for normal 3D solids in Section 2.5. Unfortunately, that does not apply to 2D graphene or any solid that is strictly 2D. The reason for this discrepancy will be apparent from Eq. (2.49). The integration volume element is proportional to q^2 in 3D, which integrates out the q^2 singularity at $q=0$. The corresponding element in 2D is proportional to q. Hence the singularity in the integral survives as $1/q$. This is responsible for the long-range logarithmic behavior of the GF and size effect in the static as well as dynamic response of graphene (Tewary and Yang, 2009a; Yang and Tewary, 2008).

However, it is still possible to set up a correspondence between lattice and continuum models for a 2D graphene film in deflection mode. The displacement field in the deflection mode is normal to the plane of graphene. For small displacements, in the harmonic approximation, the out-of-plane displacements are not coupled with the in-plane displacements. Consequently, the GF for the deflection mode is a scalar. Moreover, the q^2 term in Eq. (2.51) is identically zero (Yang and Tewary, 2008) in the deflection mode for graphene. Hence the leading term in $\phi(q)$ in the deflection mode is $O(q^4)$ for graphene.

The integral for the $O(q^4)$ term in Eq. (2.49) can be carried out analytically. This shows that the continuum limit of the LSGF of a graphene sheet in the deflection mode corresponds to the GF for an elastically stable Kirchhoff plate but not the GF for two-dimensional Christoffel equations. This correspondence demonstrates the mechanical stability of graphene in deflection and is necessary for relating its mechanical parameters to its lattice parameters. Using this approach, an explicit expression has been derived (Yang and Tewary, 2008; Tewary and Yang, 2009b, 2010) for relating the continuum flexural rigidity to the force constants of graphene. This relationship can be used to measure flexural rigidity of graphene directly from experimentally observed phonon dispersion. However, a more rigorous calculation or measurement of rigidity will involve some more contributions.

Now we consider the force constants for graphene that are the most important parameters for the lattice GFs. For multiscale applications, force constants give the elastic constants. This relation ensures that the LSGF is seamlessly linked with the CGF. The force constants can be obtained from the interatomic potential. A popular choice of potential for graphene is the Tersoff potential and its variations. This potential, which is essentially a bond-order potential, extends to second-neighbor distances. It is convenient for MD simulations and has been used for calculations of strains, friction, and many other physical characteristics of graphene (Deng et al., 2012; Smolyanitsky and Killgore, 2012; Smolyanitsky et al., 2012; Smolyanitsky and Tewary, 2011a, 2011b, 2013; Smolyanitsky et al., 2014) and many other solids.

The second-neighbor Tersoff-type potential does not seem to be a good choice for phonon calculations and those properties of graphene that are sensitive to details of the

phonon spectrum. An optimized Tersoff Brenner potential seems to be more suitable for modeling of phonons in graphene (Lindsay and Broido, 2010). The main point is that to obtain a good fit between the calculated and the experimental values of the phonon dispersion for graphene, interatomic interactions have to be included at least up to fourth-neighbor atoms (Tewary and Yang, 2009b, 2010; Wirtz and Rubio, 2004; Zimmermann et al., 2008; Mohr et al., 2007). However, if only the harmonic GF is needed, a detailed knowledge of the potential is not required. The force constants can be obtained by parametric fitting (Maradudin et al., 1971) of the calculated phonon dispersion with measured values.

For phonon applications, we give the 3×3 force-constant matrices for graphene as defined by Eq. (2.25). A graphene unit cell contains two nonequivalent atoms C1 and C2 as shown in Figure 2.2. This figure also shows the nearest neighbors of C1 and C2. All these atoms are in the plane of the graphene lattice. The force constants depend upon the choice of coordinate axes, which is shown in Figure 2.2. The Z axis is assumed to be normal to the plane of graphene.

We denote a lattice site $L\kappa$ by its 2D position vector $\mathbf{l}$, where l_x and l_y are its x and y coordinates, respectively. The coordinates of the atoms are given in the units of a where $2a =$ distance between C1 and A2, and is the lattice constant. The Z-coordinate of each atom in Figure 2.2 is zero. The force-constant matrices $\boldsymbol{\phi}(0;\mathbf{l})$ between C1 and its first four nearest neighbors identified by different values of $\mathbf{l}$ are written below. The form of the matrices is most general for the hexagonal symmetry of graphene:

$$f(0;2s,0) = -\begin{pmatrix} \alpha_1 & 0 & 0 \\ 0 & \beta_1 & 0 \\ 0 & 0 & \delta_1 \end{pmatrix} \tag{2.64}$$

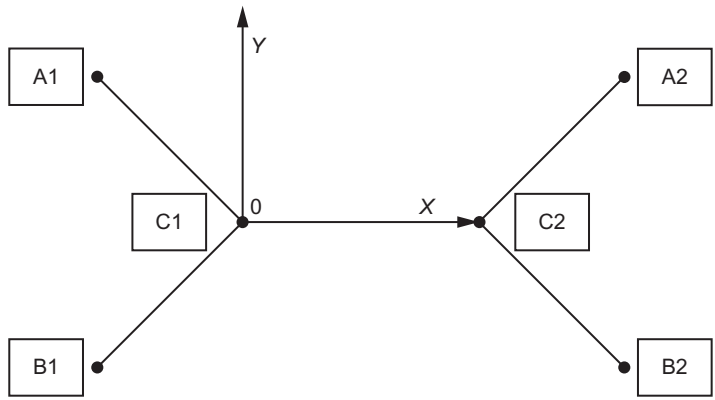

Figure 2.2 The bond structure of hexagonal graphene and the coordinate axes. The dots show the lattice sites occupied by carbon atoms A1, B1, C1, A2, B2, and C2. The origin of coordinates is at C1.

$$f(0;0,2) = -\begin{pmatrix} \alpha_2 & \gamma_2 & 0 \\ -\gamma_2 & \beta_2 & 0 \\ 0 & 0 & \delta_2 \end{pmatrix} \tag{2.65}$$

$$f(0;-4s,0) = -\begin{pmatrix} \alpha_3 & 0 & 0 \\ 0 & \beta_3 & 0 \\ 0 & 0 & \delta_3 \end{pmatrix} \tag{2.66}$$

$$f(0;5s,1) = -\begin{pmatrix} \alpha_4 & \gamma_4 & 0 \\ \gamma_4 & \beta_4 & 0 \\ 0 & 0 & \delta_4 \end{pmatrix} \tag{2.67}$$

where $s = 1/\sqrt{3}$. The form of the force-constant matrices between C1 and other atoms in the same neighbor shell and also between C2 and its neighbors can be obtained from symmetry. Note that the matrix elements corresponding to *xz* and *yz* are 0 for each atom. This shows that the displacements in the plane of the lattice are not coupled with the out-of-plane displacements. This decoupling is valid only in the harmonic approximation.

In the multiscale method based upon Born's method of long waves as described in Section 2.5, we compare the phonon frequencies with the frequencies given by the Christoffel matrix as in Eq. (2.51). This yields the following relations between the force constants and the elastic constants for graphene:

$$\begin{aligned} c11 = C_u[&2{\alpha_1}^2 + \alpha_1(6\alpha_2 + 19\alpha_3 + 35\alpha_4 + 54\alpha_5 + 6\beta_1 + 18\beta_2 + 3\beta_3 + 33\beta_4 + 18\beta_5 \\ &+ 14\sqrt{3}\gamma_4) + \alpha_2(6\alpha_3 + 12\alpha_4 + 6\beta_1 + 6\beta_3 + 12\beta_4) + 8\alpha_3^2 + \alpha_3(83\alpha_4 + 54\alpha_5 \\ &+ 9\beta_1 + 18\beta_2 + 24\beta_3 + 21\beta_4 + 18\beta_5 + 2\sqrt{3}\gamma_4) + 53{\alpha_4}^2 + \alpha_4(108\alpha_5 + 51\beta_1 \\ &+ 36\beta_2 + 27\beta_3 + 162\beta_4 + 36\beta_5 + 40\sqrt{3}\gamma_4) + \alpha_5(54\beta_1 + 54\beta_3 + 108\beta_4) \\ &+ \beta_1(18\beta_2 + 9\beta_3 + 9\beta_4 + 18\beta_5 + 6\sqrt{3}\gamma_4) + \beta_2(18\beta_3 + 36\beta_4) + \beta_3(45\beta_4 \\ &+ 18\beta_5 + 18\sqrt{3}\gamma_4) + 9\beta_4^2 + 36\beta_4\beta_5 - 12\gamma_4^2] \end{aligned} \tag{2.68}$$

$$\begin{aligned} c66 = C_u[&2{\beta_1}^2 + \beta_1(6\beta_2 + 19\beta_3 + 35\beta_4 + 54\beta_5 + 6\alpha_1 + 18\alpha_2 + 3\alpha_3 + 33\alpha_4 + 18\alpha_5 \\ &- 14\sqrt{3}\gamma_4) + \beta_2(6\beta_3 + 12\beta_4 + 6\alpha_1 + 6\alpha_3 + 12\alpha_4) + 8{\beta_3}^2 + \beta_3(83\beta_4 + 54\beta_5 \\ &+ 9\alpha_1 + 18\alpha_2 + 24\alpha_3 + 21\alpha_4 + 18\alpha_5 - 2\sqrt{3}\gamma_4) + 53{\beta_4}^2 + \beta_4(108\beta_5 + 51\alpha_1 \\ &+ 36\alpha_2 + 27\alpha_3 + 162\alpha_4 + 36\alpha_5 - 40\sqrt{3}\gamma_4) + \beta_5(54\alpha_1 + 54\alpha_3 + 108\alpha_4) \\ &+ \alpha_1(18\alpha_2 + 9\alpha_3 + 9\alpha_4 + 18\alpha_5 - 6\sqrt{3}\gamma_4) + \alpha_2(18\alpha_3 + 36\alpha_4) + \alpha_3(45\alpha_4 \\ &+ 18\alpha_5 - 18\sqrt{3}\gamma_4) + 9\alpha_4^2 + 36\alpha_4\alpha_5 - 12\gamma_4^2] \end{aligned} \tag{2.69}$$

where

$$C_u = 1/\left[4c\sqrt{3}(\alpha_1 + \alpha_3 + 2\alpha_4 + \beta_1 + \beta_3 + 2\beta_4)\right] \tag{2.70}$$

and $c = 3.355$ Angstrom is the interplanar separation in graphite and $2a = 2.462$ is the lattice constant of graphene. In deriving the above equations, we have used the fact that the volume per atom is equal to $a^2c\sqrt{3}$.

The values of the force constants reported in Tewary and Yang (2009b) were derived from the interatomic potential reported in that paper. Unfortunately, the potential is incorrect and actually unstable (Tewary and Yang, 2010). However, the values of the force constants given in that paper are correct in the sense that they can be treated as independent parameters for fitting the phonon dispersion relations. The force constants certainly give an excellent agreement between the calculated and the observed dispersion curves (Tewary and Yang, 2009b). Of course, they are related only with the derivatives of the potential at equilibrium lattice sites and are not meant to give the detailed interatomic potential.

The values of the force constants are given below in N/m:

$$\begin{aligned}
&\alpha_1 = 409.705;\ \ \beta_1 = 145.012;\ \ \delta_1 = 98.920;\ \ \alpha_2 = -40.8;\\
&\beta_2 = 74.223;\ \ \gamma_2 = -9.11;\ \ \delta_2 = -8.191;\ \alpha_3 = -33.203;\\
&\beta_3 = 50.10;\ \ \delta_3 = 5.802;\ \ \alpha_4 = 10.539;\\
&\beta_4 = 4.993;\ \ \gamma_4 = 2.184;\ \ \delta_4 = -5.213
\end{aligned} \tag{2.71}$$

The values of the two elastic constants calculated by using Eqs. (2.68) and (2.69) are $c11 = 1060$ GPa and $c66 = 440$ GPa, which fit exactly with the experimental values for graphite given by Blakslee et al. (1970). Because the interplanar interaction in graphite is much weaker than the intraplanar interactions, $c11$ and $c66$ of graphene should be approximately equal to those for graphite.

Using the method described earlier in this section, the flexural rigidity of graphene for the present fourth-neighbor interaction model is given by the following expression (Tewary and Yang, 2009b):

$$D = -\left(\sqrt{3}/36\right)(\delta_1 + 18\delta_2 + 16\delta_3 + 98\delta_4 + 162\delta_5)a^2 = 2.13\,\text{eV} \tag{2.72}$$

This value is in the range of values as reported in the literature (Lindahl et al., 2012; Wei et al., 2013). There is some confusion in the literature about the actual value of the rigidity, and a wide range of values have been reported. In any case, the derivation as given here shows that the rigidity is very sensitive to the range of the interatomic potential: The farther neighbors contribute more than the nearer neighbors. The rigidity may also be size dependent. Hence it is difficult to assess the validity of the calculated value.

Finally, we quote the result (Tewary, 2009) obtained by using GFMD method for propagation of elastic pulses or ripples in graphene. Propagation of pulses is an important characteristic of a material and is useful in understanding its elastic response and phonon transport. Such a calculation for a finite lattice cannot be done analytically even in the harmonic approximation.

The model used in Tewary (2009) is particularly simple and only serves the purpose of illustration. The origin and the system of axes is same as given in Figure 2.2. The model consists of about 1100 carbon atoms located at the equilibrium graphene lattice sites at time $t=0$. As in Yang and Tewary (2008), the outer atoms within the second-neighbor distance of the outermost vibrating atoms are constrained so that their displacement is zero at all times. The size of the active lattice along the X-axis is about 5.52 nm. Propagation is initiated by imposing an initial displacement d in the Z direction on the central atom.

We consider only the atomic displacements in the Z direction. Only the Z components f_z, Δf_z, and ϕ_{zz} in Eq. (2.56) contribute to these displacement. To account for the anharmonic effects in the Z direction, the MD-type iterative approach is used. The quantities f_z and ϕ_{zz} are calculated for each atom at each time step. These components change at each step due to anharmonicity. A major approximation in these calculations is that the displacements in the Z direction and in the XY plane are not coupled. This is strictly valid only in the harmonic approximation. It is, therefore, to keep d small so that the coupling between the ZZ and the planar components of $\boldsymbol{\Phi}$ can be neglected at all times. In these calculations, d was taken to be $0.01a$ and the results are normalized to this initial value.

The results are illustrated in Figure 2.3, which shows a snapshot of the ripples or the instantaneous displacements of all atoms in the lattice at about 20 ms. It is important to realize that, as stated earlier, the GFMD approach described here can reproduce the rippling dynamics of graphene in the case of infinitesimally small displacements. At sufficiently high lattice temperatures, however, it is expected that the long-wavelength flexural modes (Fasolino et al., 2007) will be significantly suppressed (private communication from Dr Alex Smolyanitsky).

An important test of the numerical convergence of the model is the invariance of the total energy of the system at all times. It was found that change in the energy of the system at each time step was less than $10^{-4}\%$. This shows that the results had

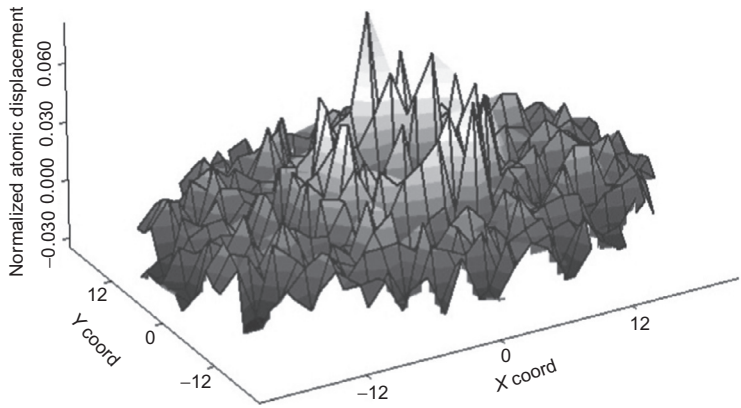

Figure 2.3 Snapshot of normalized atomic displacements in graphene at about 20 ms. Coordinates X and Y are in units of half lattice constant.

converged even up to microseconds and GFMD has extended and bridged the time scales at least in this model problem by eight orders of magnitude—from femto- to microseconds.

In the basic MD the lack of energy conservation results in an increase of the crystal temperature. This necessitates quenching of temperature that may introduce errors in the displacements. This problem should be substantially reduced in the GFMD calculations because the energy is very well conserved. An additional advantage of the GFMD is that the same formulation can be used to bridge the length scales by taking the asymptotic limit of the static part of the GF as described in Section 2.5.

2.8 Conclusions and future work

The MSGF and the GFMD techniques are computationally very efficient, and the next step is to combine them into a unified technique that can be applied to static as well as dynamic problems. These techniques have so far been applied to only symmetric lattices. They need to be developed for unsymmetric, disordered, and finite systems such as amorphous solids, polymers, and liquids. One interesting application in which these techniques will be useful is model plasmonics in graphene that is sensitive to mechanical strains (Rast et al., 2013). One reason why the MSGF and the GFMD techniques are not very widespread is the lack of efficient software. It would be useful, therefore, to develop efficient and freely available software for these techniques.

Finally, the GFMD technique should be useful for solving time-dependent problems that are very difficult to solve by using existing methods. So far this technique has been applied only to an idealized case of graphene. This technique should be applicable to modeling of time-dependent processes in various physical, chemical, and bio systems for which presently which MD is used. In particular, this technique should be useful in simulation of protein folding and unfolding, which has been of great interest for many years (Shea and Brooks, 2001).

Acknowledgments

The author thanks Drs. Lauren Rast, David Read, and Alex Smolyanitsky for helpful discussions.

References

Andreev, A.D., Downes, J.R., Faux, D.A., O'Reilly, E.P., 1999. Strain distributions in quantum dots of arbitrary shape. J. Appl. Phys. 86, 297–305.

Balamane, H., Halicioglu, T., Tiller, W.A., 1992. Comparative-study of silicon empirical interatomic potentials. Phys. Rev. B 46, 2250–2279.

Barton, G., 1989. Elements of Green's Functions and Propagation. Clarendon Press, Oxford.

Baskes, M.I., 1992. Modified embedded-atom potentials for cubic materials and impurities. Phys. Rev. B 46, 2727–2742.
Baskes, M.I., 1997. Determination of modified embedded atom method parameters for nickel. Mater. Chem. Phys. 50, 152–158.
Berger, J.R., Tewary, V.K., 2001. Greens functions for boundary element analysis of anisotropic bimaterials. Eng. Anal. Boundary Elements 25, 279–288.
Bimberg, D., Grundmann, M., Ledentsov, N., 1999. Quantum Dot Heterostructures. John Wiley, New York.
Blakslee, O.L., Proctor, D.G., Seldin, E.J., Spence, G.B., Weng, T., 1970. Elastic constants of compression-annealed pyrolytic graphite. J. Appl. Phys. 41, 3373.
Born, M., Huang, K., 1954. Dynamical Properties of Crystal Lattices. Oxford University Press, London.
Brenner, D.W., Shenderova, O.A., Areshkin, D.A., Schall, J.D., Frankland, S.J.V., 2002. Atomic modeling of carbon-based nanostructures as a tool for developing new materials and technologies. Comput. Model. Eng. Sci. 3, 643–673.
Cai, W.S., Lin, Y., Shao, X.G., 2005. Interatomic potential function in cluster research. Prog. Chem. 17, 588–596.
Cheng, D., Huang, S., Wang, W., 2005. The structure of 55-atom Cu-Au bimetallic clusters: Monte Carlo study. Eur. Phys. J. D 39, 41–48.
Cleri, F., Rosato, V., 1993. Tight-binding potentials for transition-metals and alloys. Phys. Rev. B 48, 22–33.
Cormier, J., Rickman, J.M., Delph, T.J., 2001. Stress calculation in atomistic simulations of perfect and imperfect solids. J. Appl. Phys. 89, 99–104.
Deng, Z., Smolyanitsky, A., Li, Q.Y., Feng, X.Q., Cannara, R.J., 2012. Adhesion-dependent negative friction coefficient on chemically modified graphite at the nanoscale. Nat. Mater. 11, 1032–1037.
Fasolino, A., Los, J.H., Katsnelson, M.I., 2007. Intrinsic ripples in graphene. Nat. Mater. 6, 858–861.
Geim, A.K., Novoselov, K.S., 2007. The rise of graphene. Nat. Mater. 6, 183–191.
Gibson, J.B., Goland, A.N., Milgram, M., Vineyard, G.H., 1960. Dynamics of radiation damage. Phys. Rev. 120, 1229–1253.
Harrison, P., 2002. Quantum Wells, Wires, and Dots: Theoretical and Computational Physics. John Wiley, New York.
Hirth, J.P., Lothe, J., 1992. Theory of Dislocations, second ed. Krieger Publishing Company, Florida.
Kittel, C., 1996. Introduction to Solid State Physics, seventh ed. John Wiley, New York.
Lannoo, M., Bourgoin, J., 1981. Point Defects in Semiconductors. I. Springer Series in Solid-State Sciences, vol. 22. Springer Verlag, New York.
Lindahl, N., Midtvedt, D., Svensson, J., Nerushev, O.A., Lindvall, N., Isacsson, A., Campbell, E.E.B., 2012. Determination of the bending rigidity of graphene via electrostatic actuation of buckled membranes. Nano Lett. 12, 3526–3531.
Lindsay, L., Broido, D.A., 2010. Optimized Tersoff and Brenner empirical potential parameters for lattice dynamics and phonon thermal transport in carbon nanotubes and graphene. Phys. Rev. B 81, 205441.
Makeev, M.A., Madhukar, A., 2001. Simulations of atomic level stresses in systems of buried Ge/Si islands. Phys. Rev. Lett. 86, 5542–5545.
Maradudin, A.A., Montroll, E.W., Weiss, G.H., Ipatova, I.P., 1971. Theory of lattice dynamics in the harmonic approximation. In: Ehrenreich, H., Seitz, F., Turnbull, D. (Eds.), second ed. In: Solid State Physics, vol. Suppl. 3. Academic Press, New York.

Mas-Balleste, R., Gomez-Navarro, C., Gomez-Herrero, J., Zamora, F., 2011. 2D materials: to graphene and beyond. Nanoscale 3, 20–30.
Mishin, Y., Sorensen, M.R., Voter, A.F., 2001. Calculation of point-defect entropy in metals. Philos. Mag. A 81, 2591–2612.
Mohr, M., Maultzsch, J., Dobardzic, E., Reich, S., Milosevic, I., Damnjanovic, M., Bosak, A., Krisch, M., Thomsen, C., 2007. Phonon dispersion of graphite by inelastic X-ray scattering. Phys. Rev. B 76, 035439.
Morse, P.M., Feshbach, H., 1953. Methods of Theoretical Physics, vol. 1, first ed. McGraw-Hill Publishing Company, New York, p. 1939.
Novoselov, K.S., Jiang, D., Schedin, F., Booth, T.J., Khotkevich, V.V., Morozov, S.V., Geim, A.K., 2005. Two-dimensional atomic crystals. Proc. Natl. Acad. Sci. U. S. A. 102, 10451–10453.
Novoselov, K.S., Fal'ko, V.I., Colombo, L., Gellert, P.R., Schwab, M.G., Kim, K., 2012. A roadmap for graphene. Nature 490, 192–200.
Pan, E., 2002. Mindlin's problem for an anisotropic piezoelectric half-space with general boundary conditions. Proc. R. Soc. Lond. Ser. A 458, 181–208.
Parr, R.G., Yang, W., 1989. Density-functional theory of atoms and molecules. In: Breslow, R., et al. (Ed.), In: International Series of Monographs on Chemistry, Oxford Science Publications, Oxford.
Puzder, A., Williamson, A.J., Reboredo, F.A., Galli, G., 2003. Structural stability and optical properties of nanomaterials with reconstructed surfaces. Phys. Rev. Lett. 91, 157405.
Rapaport, D.C., 2004. The Art of Molecular Dynamics Simulation, second ed. Cambridge University Press, Cambridge, UK.
Rast, L., Sullivan, T.J., Tewary, V.K., 2013. Stratified graphene/noble metal systems for low-loss plasmonics applications. Phys. Rev. B 87, 045428.
Read, D.T., Tewary, V.K., 2007. Multiscale model of near-spherical germanium quantum dots in silicon. Nanotechnology 18, 105402.
Shea, J.E., Brooks, C.L., 2001. From folding theories to folding proteins: a review and assessment of simulation studies of protein folding and unfolding. Annu. Rev. Phys. Chem. 52, 499–535.
Smolyanitsky, A., Killgore, J.P., 2012. Anomalous friction in suspended graphene. Phys. Rev. B 86, 125432.
Smolyanitsky, A., Tewary, V.K., 2011a. Simulation of lattice strain due to a CNT-metal interface. Nanotechnology 22, 085703.
Smolyanitsky, A., Tewary, V.K., 2011b. Atomistic simulation of a graphene-nanoribbon-metal interconnect. J. Phys. 23, 355006.
Smolyanitsky, A., Tewary, V.K., 2013. Manipulation of graphene's dynamic ripples by local harmonic out-of-plane excitation. Nanotechnology 24, 055701.
Smolyanitsky, A., Killgore, J.P., Tewary, V.K., 2012. Effect of elastic deformation on frictional properties of few-layer graphene. Phys. Rev. B 85, 035412.
Smolyanitsky, A., Zhu, S.Z., Deng, Z., Li, T., Cannara, R.J., 2014. Effects of surface compliance and relaxation on the frictional properties of lamellar materials. Res. Adv. 4, 26721–26728.
Stangl, J., Holy, V., Bauer, G., 2004. Structural properties of self-organized semiconductor nanostructures. Rev. Mod. Phys. 76, 725–783.
Swadener, J.G., Baskes, M.I., Nastasi, M., 2005. Stress-induced platelet formation in silicon: a molecular dynamics study. Phys. Rev. B 72, 201202.
Tersoff, J., 1988. Empirical interatomic potential for silicon with improved elastic properties. Phys. Rev. B 38, 9902–9905.

Tersoff, J., 1989. Modeling solid-state chemistry—interatomic potentials for multicomponent systems. Phys. Rev. B 39, 5566–5568.
Tersoff, J., Teichert, C., Lagally, M.G., 1996. Self-organization in growth of quantum dot superlattices. Phys. Rev. Lett. 76, 1675–1678.
Tewary, V.K., 1973. Green-function method for lattice statics. Adv. Phys. 22, 757–810.
Tewary, V.K., 2004a. Elastostatic Green's function for advanced materials subject to surface loading. J. Eng. Math. 49, 289–304.
Tewary, V.K., 2004b. Multiscale Green's-function method for modeling point defects and extended defects in anisotropic solids: application to a vacancy and free surface in copper. Phys. Rev. B 69, 13.
Tewary, V.K., 2009. Extending the time scale in molecular dynamics simulations: propagation of ripples in graphene. Phys. Rev. B 80, 161409(R).
Tewary, V.K., 2011. Phenomenological interatomic potentials for silicon, germanium and their binary alloy. Phys. Lett. A 375, 3811–3816.
Tewary, V.K., Read, D.T., 2004. Integrated Green's function molecular dynamics method for multiscale modeling of nanostructures: application to Au nanoisland in Cu. Comput. Model. Eng. Sci. 6, 359–371.
Tewary, V.K., Yang, B., 2009a. Singular behavior of the Debye-Waller factor of graphene. Phys. Rev. B 79, 125416.
Tewary, V.K., Yang, B., 2009b. Parametric interatomic potential for graphene. Phys. Rev. B 79, 075442.
Tewary, V.K., Yang, B., 2010. Parametric interatomic potential for graphene (vol. 79, 075442, 2009). Phys. Rev. B 81, 039904.
Thomson, R., Zhou, S.J., Carlsson, A.E., Tewary, V.K., 1992. Lattice imperfections studied by use of lattice Green-functions. Phys. Rev. B 46, 10613–10622.
Ting, T.C.T., 1996. Anisotropic Elasticity: Theory and Applications. Oxford University Press, New York.
Voter, A.F., Montalenti, F., Germann, T.C., 2002. Extending the time scale in atomistic simulation of materials. Annu. Rev. Mater. Res. 32, 321–346.
Wei, Y.J., Wang, B.L., Wu, J.T., Yang, R.G., Dunn, M.L., 2013. Bending rigidity and Gaussian bending stiffness of single-layered graphene. Nano Lett. 13, 26–30.
Wirtz, L., Rubio, A., 2004. The phonon dispersion of graphite revisited. Solid State Commun. 131, 141–152.
Yang, B., Tewary, V.K., 2003. Formation of a surface quantum dot near laterally and vertically neighboring dots. Phys. Rev. B 68, 6.
Yang, B., Tewary, V.K., 2004. Continuum Dyson's equation and defect Green's function in a heterogeneous anisotropic solid. Mech. Res. Commun. 31, 405–414.
Yang, B., Tewary, V.K., 2005. Green's function-based multiscale modeling of defects in a semi-infinite silicon substrate. Int. J. Solids Struct. 42, 4722–4737.
Yang, B., Tewary, V.K., 2006. Efficient Green's function modeling of line and surface defects in multilayered anisotropic elastic and piezoelectric materials. Comput. Model. Eng. Sci. 15, 165–177.
Yang, B., Tewary, V.K., 2007. Multiscale modeling of point defects in Si-Ge(001) quantum wells. Phys. Rev. B 75, 144103.
Yang, B., Tewary, V.K., 2008. Multiscale Green's function for the deflection of graphene lattice. Phys. Rev. B 77, 245442.
Yavari, A., Ortiz, M., Bhattacharya, K., 2007. A theory of anharmonic lattice statics for analysis of defective crystals. J. Elast. 86, 41–83.

Zhigilei, L.V., Dongare, A.M., 2002. Multiscale modeling of laser ablation: applications to nanotechnology. Comp. Model. Eng. Sci. 3, 539–555.

Zimmermann, J., Pavone, P., Cuniberti, G., 2008. Vibrational modes and low-temperature thermal properties of graphene and carbon nanotubes: minimal force-constant model. Phys. Rev. B 78, 104426.

Numerical simulation of nanoscale systems and materials

3

A. Smolyanitsky[1,2], *V.K. Tewary*[1]
[1]National Institute of Standards and Technology, Boulder, CO, USA; [2]NIST Center for Nanoscale Science and Technology (CNST), Gaithersburg, MD, USA

3.1 Introduction

As current studies of nanoscale devices and materials are in full swing at exploring Richard Feynman's famous words regarding the "room at the bottom," one wonders if the theoretical and numerical methods for studying physics at the nanoscale have sufficiently evolved for the task. More specifically, is there much room left for the traditional continuum and element-based approaches in the case of nanoscale systems? This is an especially relevant question today, when carbon nanotubes and graphene, along with various other atomically thin membranes, have become a mainstay of experimental exploration.

When electronic, thermal, and mechanical properties at the nanoscale differ vastly from their macroscopic counterparts, one can no longer expect to attain a comprehensive understanding of such systems through a continuum approach. As a simple example, if one were to study the mechanical properties of a free-standing graphene membrane, what should be the effective "thickness" of its continuum model? Experimental (Novoselov et al., 2004; Nemes-Incze et al., 2008; Gupta et al., 2006) and theoretical (Yakobson et al., 1996; Chang and Huajian, 2003) studies suggest various values, which are often contradictory and almost never directly correspond to the general idea of graphene being one carbon atom thick. In fact, it appears that the effective thickness of an atomically thin layer in the mechanical sense may differ from that in the thermal or electronic sense, especially given the quantum-mechanical effects (Fogler et al., 2008; Klimov et al., 2012) on its properties. Moreover, as we demonstrate further in this chapter, the problem of the effective thickness of graphene is far more complex due to the thermally induced out-of-plane dynamic rippling that naturally occurs at any nonzero temperature. A great many similar examples of the insufficiency of the continuum approach can be found among systems ranging from solid-state to biomolecules.

As a result of the demands imposed by nanoscale systems on theoretical and numerical methods, many new approaches have emerged. These include numerous semianalytical techniques; numerically efficient, although still computationally intensive, *ab initio* density functional theory for studying electronic and optical properties; and particle-based methods, including molecular dynamics (MD), molecular statics (MS), and Monte Carlo. These numerical methods have been strongly fueled by

Modeling, Characterization and Production of Nanomaterials. http://dx.doi.org/10.1016/B978-1-78242-228-0.00003-X

the rapid increase of computing power at the hardware level in the last two decades and especially by parallelization of computations.

In this chapter, we focus mainly on an overview of MD and MS, as well as some of their uses for studying the thermomechanical and (indirectly) electronic properties at the nanoscale. We first introduce the general idea behind these methods. We then consider the use of MS in determining the strains that arise in single-wall carbon nanotubes (SWCNTs) and graphene nanoribbons (GNRs) interfaced with a metal surface in various geometric configurations, as well as the effect of these strains on the local electronic properties. We proceed to describe the use of MD in studying dynamic frictional properties of multilayer graphene. In the last example, we describe the use of MD in studying the dynamic thermal ripples in free-standing graphene. The scope of this chapter is to provide specific examples of the use of particle-based simulation methods and to discuss a number of subtle points usually omitted in the journal article format. Our first aim is to inform the reader of the exciting possibilities provided by particle-based simulation methods in studying nanoscale systems and devices. Our second aim is to provide the correct context by elucidating the effect of numerical factors on the results obtained from simulations. These two aims may appear to be somewhat contradictory; however, we strongly believe that one is truly prepared to utilize a theoretical or a numerical method successfully when there is a strong awareness of both its range of applicability, as well as its fundamental limitations.

3.2 Molecular statics and dynamics: an overview

Simply put, MS and MD are numerical algorithms that describe the interaction of particles with their surroundings in terms of energy and explicitly describe the evolution of the system either in terms of energy or simulated time. To better explain the description above, let us consider a total of N interacting particles. Let V_i be the total potential energy of interaction between the ith particle and the rest of the system. This potential energy V_i is determined by the functional expression specific to the system (briefly discussed later), as well as the relative positions of the ith particle and its environment. We then have

$$V_{\text{tot}} = \sum_{N} V_i \tag{3.1}$$

which is the total potential energy of the system. The total force exerted upon the ith particle by the rest of the system is then

$$\overrightarrow{F}_i = -\nabla_i V_{\text{tot}} \tag{3.2}$$

where ∇_i represents the gradient with respect to the position of the ith particle in the three-dimensional space. Starting from Eq. (3.2), one can clearly describe the

difference between MS and MD. In case of MS, a static configuration that minimizes V_{tot} is found iteratively. Such a static configuration is usually achieved by artificially displacing particles along the $\overrightarrow{F}_i$ vectors from Eq. (3.2), for instance, with use of conjugate gradients, until V_{tot} reaches a minimum. The presence of local and global minima is determined by the starting geometry of the system, as well as the functional form of V_i. In case of MD, the force $\overrightarrow{F}_i$ is applied to each particle to iteratively solve the equation representing Newton's second law of motion:

$$\frac{\mathrm{d}^2\overrightarrow{r}_i}{\mathrm{d}t^2} = \frac{\overrightarrow{F}_i}{m_i} \tag{3.3}$$

where $\overrightarrow{r}_i$ and m_i are the position and mass of the ith particle, respectively. Equation (3.3) is solved iteratively with a small time step, during which the vector $\overrightarrow{F}_i$ is assumed constant. The time step is generally determined by the lightest particle present in the system. Usually, Eq. (3.3) is solved by intermediately determining the velocity $\overrightarrow{v}_i$ for each particle at every time step. Therefore, MD describes the time evolution of the system, while MS determines its final state in terms of potential energy. If no damping is present in the system and a global potential energy minimum is conveniently present, one can see that the system simulated by MD will oscillate around the minimum determined by MS. Therefore, MS is used for determining the static properties of a system (e.g., lattice constant, interatomic binding energy in a crystal), while MD is utilized for studying the dynamic properties of a lattice (e.g., phonon spectra without the assumption of linear response, thermal conductivity).

The convergence of Eq. (3.3) during an iterative procedure is affected by many factors (e.g., geometry, particle velocities), and usually small time steps are required. For instance, a standard time step is on the order of a femtosecond, while the total simulated time in MD is often in the nanoseconds to hundreds of nanoseconds, which means the number of iterations can reach hundreds of millions. Determining whether the system has converged at the level of a single particle is nontrivial and may be even impossible for very large systems, while at the "macroscopic" level (involving all N particles), one can check whether the Hamiltonian (total energy) of the system remains constant. Unfortunately, even with today's wide use of double-precision variables in scientific computing, energy conservation is not guaranteed, due to round-off errors that arise from numerical integration over a large number of steps. As a result, the total energy slowly increases and the simulated system essentially undergoes self-heating. In order to mitigate this apparent problem, one utilizes a numerical thermostat to impose a desired temperature upon the system.

Thermostatic control is usually achieved by augmenting the velocity calculations, either via a velocity rescaling term, or with an artificial damper/accelerator term that serves to speed up atoms that are slower than desired, while slowing down those that are faster. Let us give a more detailed description of the latter, in this case called the Nosé-Hoover thermostat algorithm (Nosé, 1984). The particle velocities are augmented by introducing an artificial time-dependent damping factor $\alpha(t)$; rewriting Eq. (3.3):

$$\frac{\mathrm{d}\overrightarrow{v}_i}{\mathrm{d}t} = \frac{1}{m_i}\left(\overrightarrow{F}_i - \alpha(t)\overrightarrow{v}_i\right) \tag{3.4}$$

while the following differential equation is solved concurrently to determine $\alpha(t)$:

$$\frac{\mathrm{d}\alpha}{\mathrm{d}t} \propto \frac{1}{\tau}(T(t) - T_0) \tag{3.5}$$

where $T(t) = (1/3k_\mathrm{b})\sum_N m_i v_i^2(t)$ is the system temperature at the current simulated time t. In Eq. (3.5), k_b is the Boltzmann constant, T_0 is the prescribed system temperature, and τ is a time-constant parameter, which determines how fast the thermostat responds to thermal perturbation. Given such a form of thermal control, a canonical velocity distribution is achieved and maintained at steady-state (Nosé, 1984).

A similar artificial augmentation may be applied not only to the velocities, but often to the particle positions as well, in order to keep the effective pressure in the system close to a prescribed value. In case the system is thermostatted at a constant volume without pressure control, the simulation is usually addressed as *NVT* (the variables conserved being the number of particles N, volume V, and the temperature of the system T), while with pressure control it is addressed as *NPT* (N and T as in *NVT*, P stands for pressure). Both *NVT* and *NPT* systems are usually set up either with solid (reflective) boundaries or with periodic boundaries, which can be implemented in a straightforward manner (Schlick, 2002). Once the computational framework described above has been established and the system is believed to conserve the desired parameters, additional computational modules are added to calculate a variety of properties, for example, thermal conductivity and other properties arising from atomic vibrations. It is worth noting that, although MS and MD simulations were initially designed to simulate systems close to equilibrium, simulations of externally perturbed (thermally, Muller-Prathe, 1997; Wang et al., 2007; mechanically, Smolyanitsky and Tewary, 2011b; Smolyanitsky and Killgore, 2012; electrically, Marreiro et al., 2007; Joshi et al., 2010) have been reasonably successful. As we show further, one needs to be careful in general when applying a thermostat to an externally driven system.

The potential energy of interaction V_i is without a doubt the most important component of particle-based simulations, because it represents the core of the simulated physics. It includes interactions arising from chemical bonds, electrostatic interactions, and Van der Waals interactions. In its simplest form, V_i is only a function of the pairwise distances between the ith particle and its neighbors $r_{ij}, j \neq i$:

$$V_i = \sum_{j \neq i} \varphi(r_{ij}) \tag{3.6}$$

where φ is the pairwise interaction potential, for example, Lennard-Jones (Jones, 1924), or Morse (Morse, 1929) potential.

In general, for example, for bonding in crystals the functional form of φ can be very complex and contain various parameters, because it is not a function of

merely the pairwise distance between the neighboring particles, but includes the local environments of both *i*th and *j*th particle in terms of the relative bonding alignment. Great examples of nonpairwise bonding potentials are the modified embedded atom method (MEAM) (Baskes, 1992; Lee and Baskes, 2000) and Tersoff-Brenner potential (Brenner, 1990; Lindsay and Broido, 2010), developed primarily for covalent crystals. Later in this chapter, we make extensive use of both of these potentials, described in great detail in the provided references. We would like to emphasize that, in general, the potential parameterization is the most important, material-specific, source of parameterization for particle-based simulations. Potentials such as MEAM or Tersoff-Brenner contain dozens of parameters adjusted in such a way that experimentally measured bulk properties of known crystals are reproduced. Such agreement with experimental data is crucial for the potential to be even considered for use in the particle-based simulations, such as MS or MD.

It is important to note that, although we earlier stated that V_i is calculated for the interactions between the *i*th particle and the rest of the system, the interactions in Eq. (3.6) are often spatially short-range. Therefore, the summation can be performed over a significantly smaller region surrounding the *i*th particle, which provides a tremendous gain in computational efficiency. The reason for this is that the gradient in Eq. (3.2) is often impossible to calculate analytically and therefore it is implemented numerically, which is one of the primary sources of computational burden, depending very strongly on the number of neighbors of the *i*th particle.

Although the authors of this chapter designed, implemented, and used their own MS/MD framework for their research, we point out that numerous open-source options are available. Discussing all of these options in detail would be outside the scope of this chapter; however, we choose to briefly mention two simulators excellent in terms of sophistication and feature set: LAMMPS MD Simulator (Bazari et al., 1988) and GROMACS (Apol et al., 2010). LAMMPS is distributed by Sandia National Laboratories and features interaction potentials for biomolecular and solid-state systems, as well as a great level of flexibility in terms of simulation design. GROMACS is distributed by the University of Groningen (The Netherlands) and is designed for biomolecular simulations. Both simulators are computationally efficient and offer well-optimized parallelization options.

3.3 Static calculations of strain due to interface

A popular use of static calculations is determining the geometry of a nanoscale solid-state system, such that the total potential energy of the system is minimized, that is, finding a possible stable state. The starting atomistic configuration is selected to be experimentally relevant, and the interatomic interactions are usually parameterized according to known empirical data. Here, we present the use of MS in studying interfaces between nanoscale objects, as well as the effect of interfaces on the lattice structure away from the interface.

Our first example is an interface between an uncapped SWCNT and the crystallographic 001 surface of nickel, as shown in the left pane of Figure 3.1 and described in Smolyanitsky and Tewary (2011b).

This system is generally relevant to nanoelectronics, for which carbon nanotubes show promise as high-performance nanoscale via-contacts due to their intrinsically low electrical resistance. Our goal here is to determine whether a low-energy state for the interface exists, what the geometry of such an interface is, and, finally, how the atomic configuration at the interface may affect the electrical properties of the entire interconnect.

The atoms restrained at the free end of the nanotube in Figure 3.1 (right) represent a fixed boundary. The interatomic interactions were set with MEAM potential selection rules for C-C, Ni-Ni, and Ni-C, as described in Smolyanitsky and Tewary (2011b) and the literature cited therein. The total energy of the system during energy minimization is shown as a function of the number of intermediate energy minimization steps in the right pane of Figure 3.1. This is a reasonably representative curve, demonstrating rapid convergence within 70 steps obtained with use of the steepest-descent algorithm. We must note that such fast convergence is usually indicative of a system that was initially close to an energy minimum, although in all cases our starting configurations were selected at random.

Shown in Figure 3.2 are the representative final bonding configurations obtained for SWCNTs of armchair and zigzag chirality. These configurations result from a combined effect of the disrupted bonding coordination at the SWCNT side, making the uncapped region prone to local deformation (both in the radial and in the axial direction) and the bonding interaction with the nickel atoms. A more detailed analysis of these configurations is provided in Smolyanitsky and Tewary (2011b), while here we focus on how these configurations may affect the electrical properties of such an interconnect.

In order to obtain meaningful quantitative data on the local lattice distortions (compared to bulk SWCNTs), we mapped the local changes in the C—C bond lengths onto a continuum grid (Smolyanitsky and Tewary, 2011b) and plotted these changes in the radial and axial directions of the nanotube as a function of distance from the interface with the nickel surface, as shown in Figure 3.3. The results are striking: In the radial direction, the strains are spatially short lived away from the interface, while in the axial direction, the strains are not only high, averaging 1%, but extend over a distance of almost 10 nm from the interface, especially for the SWCNTs with zigzag chirality. Effectively, this means that an almost 10-nm-long portion of the nanotube adjacent to the interface experiences a significant anisotropic strain.

The effect of anisotropic strain on the electronic band structure of a planar hexagonal lattice, given the results in Figure 3.3, is straightforward to estimate. In the case of electronic properties of the SWCNTs in Smolyanitsky and Tewary (2011b), we used the Landauer formalism (Datta, 1995) applied to the axially strained region to determine the effective electrical resistance R:

$$R = R_0\left(1 + e^{E_{\text{gap}}/kT}\right) \tag{3.7}$$

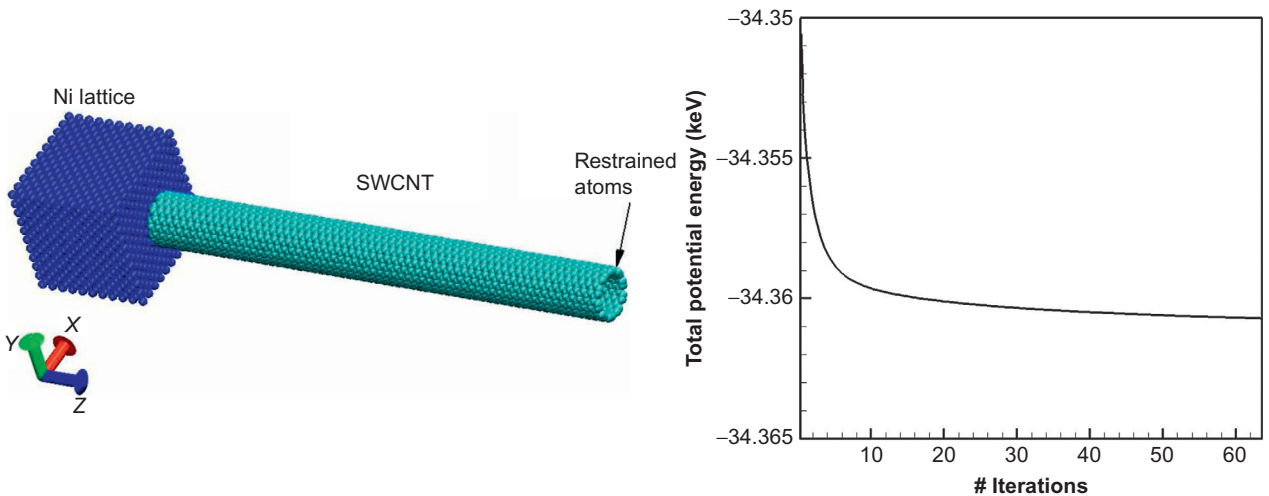

Figure 3.1 Atomistic assembly of the SWCNT-Ni system (left) and typical potential energy evolution as a function of the number of iterations (right). The nanotube length in all simulations was approximately 15 nm.

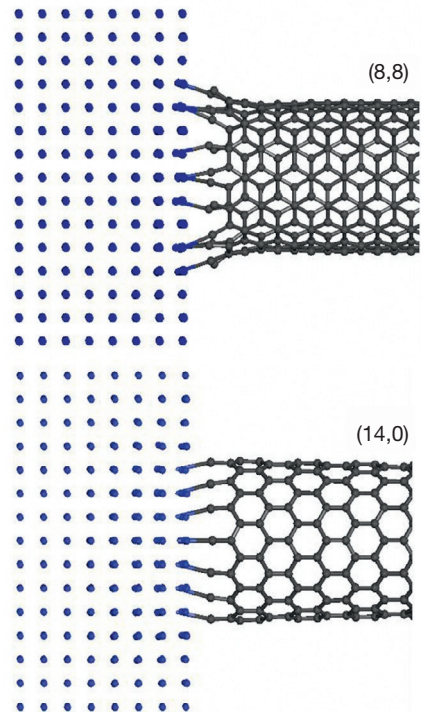

Figure 3.2 Representative final structures for SWCNT-Ni interconnect with an armchair (top) and zigzag (bottom) SWCNT.

where R_0 is the intrinsic resistance of a bulk metallic SWCNT, and the strain-induced bandgap is

$$E_{\text{gap}} \propto (\epsilon_{\text{A}} - \epsilon_{\text{R}}) \tag{3.8}$$

where ϵ_{A} and ϵ_{R} are the axial and the radial strain, respectively. We find that, for an average axial strain of 1% and zero radial strain, R increases by an order of magnitude compared to R_0. Therefore, the mere presence of an interface described above increases the effective electrical resistance of the SWCNT by an order of magnitude *within 10 nm of the interface*, which is completely separate from the tunneling resistance expected to be present directly at the interface, and can be comparable to R. This observation is in general agreement with previous theoretical predictions for a metal-CNT contact (Li et al., 2003; Quoc et al., 2004). We can now see how a particle-based static simulation can provide a reasonable insight into the properties of an electronic interconnect in an implicit manner, assuming the interatomic interactions are representative of the physical reality.

To bring out the question of validity of the interatomic interactions, we consider a similar example. Here, we performed static calculations for a GNR placed between two nickel electrodes, as shown in Figure 3.4. The graphene lattice was exposed to the crystallographic 111 surface of nickel. This structure is relevant to the way graphene is synthesized in a carbon-vapor-deposition (CVD) process. The GNR length

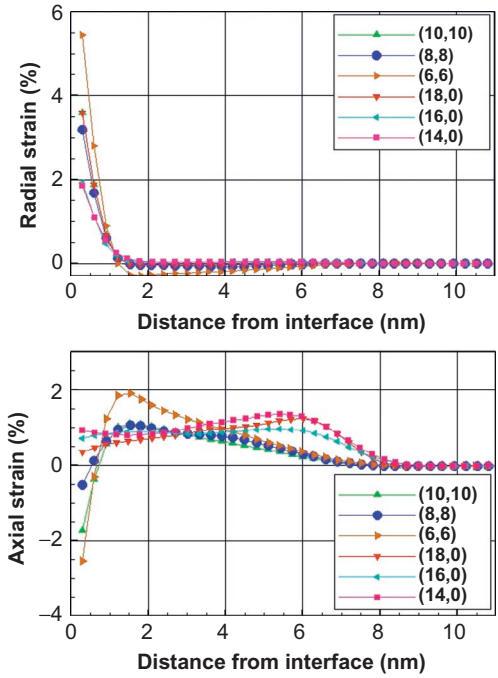

Figure 3.3 Radial (top) and axial (bottom) strains as a function of distance from the interface for various SWCNT chiralities.

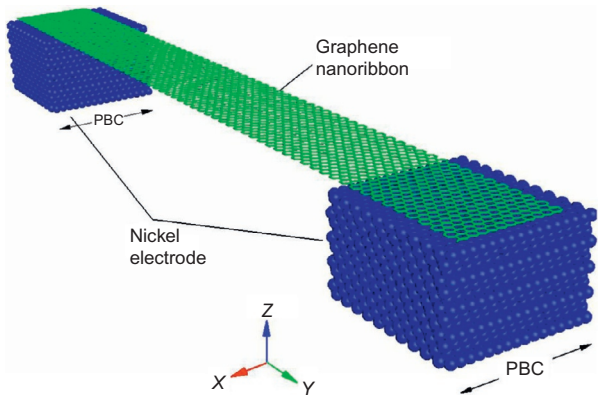

Figure 3.4 Atomistic assembly of the GNR-Ni system; the nanotube length in all simulations was approximately 15 nm.

in all simulations was approximately 30 nm. Note that the periodic boundary conditions were applied to the nickel electrodes in the *X* direction, essentially representing an infinite array of interconnects along the *X*-axis. The purpose of this boundary condition is to minimize the deformation of the electrodes, which in reality may be significantly larger, especially in the *X* direction.

The MEAM interatomic potential was used here as well for the C—C and Ni—Ni interactions. The Ni—C interaction, as described by default MEAM parameterization,

was unfortunately unsuitable for the simulation. Several translational intersurface configurations between graphene and Ni-111 are possible from both theoretical and experimental observations (Vanin et al., 2010; Xu and Buehler, 2010; Rosei and Crescenzi, 1983; Gamo et al., 1997; Deng et al., 2012; Fuentes-Cabrera et al., 2008) and none of the intersurface configurations appear to be properly represented in terms of adhesion energy and local stability (Smolyanitsky and Tewary, 2011a). As a result, we devised and implemented a custom potential term for the Ni-C interaction based on the Morse potential. It contained terms to account for the local environments of the nickel and carbon atoms at the interface and yielded reasonable agreement with existing empirical and theoretical data (Smolyanitsky and Tewary, 2011a). Once at least a locally satisfactory interaction potential was established, we proceeded with the production simulations. We found that the top-fcc intersurface configuration shown in figure 1 (a) of Smolyanitsky and Tewary (2011a) was the most stable; thus, all production simulations were performed for this intersurface configuration.

Shown in Figure 3.5 are the grid-mapped (similar to the example above) strains and out-of-plane graphene lattice distortions for a stand-alone GNR (left) and a GNR attached to electrodes (right). The comparison between cases with and without electrodes is made to determine the effect of the electrodes, which act as the local substrate. We see that a stand-alone GNR is virtually unstrained in the long (Y) direction, while showing significant (1.5%) in-plane strain in the short direction, resulting in a significant strain-induced bandgap, as explained earlier. This is caused solely by the presence of edges with highly disrupted bonding coordination. At the same time, the GNR is nearly flat, owing once again to the in-plane strain. For the GNR placed on electrodes, a significant change is observed throughout the entire GNR and not only the electrode-interfaced regions. First, the in-plane strain in the Y direction remains low. Second, the in-plane strain in the X direction decreases from 1.5% to 0.25%. At the same time, the GNR now ripples out of plane throughout the free-standing region of the GNR. Therefore, one can say that the electrodes, in their current intersurface configuration with the graphene lattice, clearly act as in-plane strain suppressors due to artificial passivation, while causing some rippling in the free-standing region. If the stand-alone GNR was semiconducting due to high anisotropic strain, the electrode-interfaced GNR is close to metallic. Moreover, because the Ni-GNR intersurface binding energy is significant, the interconnect may in fact be stable at room temperature and above (Smolyanitsky and Tewary, 2011a).

The described results suggest the possibility of engineering strains (and thus electronic properties of the GNR-metal interconnect) in terms of electrode shapes and the GNR length. Does the simulated result provide an exhaustive explanation of what may be observed experimentally? The answer is not necessarily. Compared to the fabrication process resulting in contamination, lack of geometry control, and many other issues, our system (as well as the Ni-CNT system above) is highly idealized. The purpose of the simulations here is to point out possible mechanisms leading to modification of the electronic properties of the interconnect, such as the effects of CNT or GNR edges and local graphene-substrate interactions. Our simulations in essence represent highly simplified systems, which we consider in atomistic detail within a static approximation. As mentioned in the introduction, a static calculation provides a

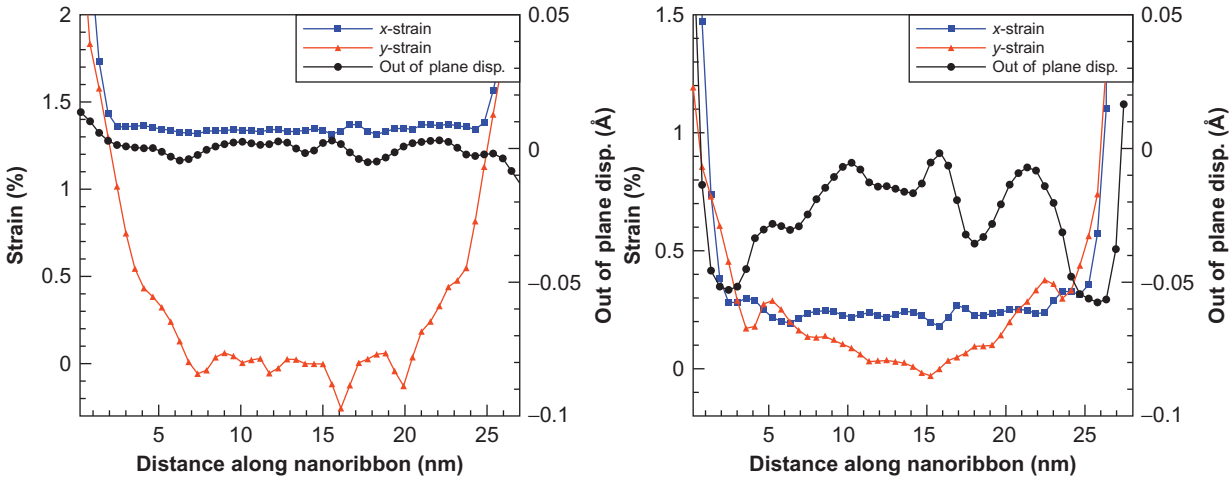

Figure 3.5 Strains and out-of-plane lattice distortions along the *Y*-centerline for a stand-alone GNR (left) and a GNR placed on electrodes as shown in Figure 3.4 (right).

way to determine a possible energetically stable state, as well as the geometry of the lattice in that state. Thermal effects may play a significant role as well, and in this sense a static calculation provides only low-temperature approximation of the state of the lattice. However, the described results are important, because they provide a qualitative insight, which should be taken into account when designing further theoretical calculations as well as experimental studies. In our next example, we consider a dynamic simulation designed to study kinetic friction in graphene, a topic of great interest in the last several years.

3.4 Dynamic calculations of kinetic frictional properties

Frictional properties of atomically thin layers at the nanoscale have become an important research topic, both in terms of the observed phenomena and their theoretical and numerical descriptions. Recent experimental studies utilizing atomic force microscopy (AFM) reported observations of very low friction for substrate-bound monolayer and bilayer graphene (Filleter et al., 2009), while free-standing regions of few-layer atomically thin layers exhibited a general trend of quantized decrease in friction with an increasing number of layers (Lee et al., 2010). These results suggested the use of graphene and other atomically thin layers as a family of nanoscale solid-state lubricants. A variety of interpretations of the experimental findings was suggested, ranging from a graphene-specific type of damping caused by electron-phonon scattering (Filleter et al., 2009) to puckering deformations in front of the AFM tip during lateral scanning (Lee et al., 2010). However, we still lack a comprehensive understanding of friction in atomically thin layers and layered materials at the nanoscale.

Our simulations were designed to model AFM lateral friction force scanning and were assembled as shown in Figure 3.6 and described in detail in Smolyanitsky et al. (2012) and Smolyanitsky and Killgore (2012). The number of graphite-like stacked layers varied from one to four, and the X-boundary atoms were fixed in position, while a periodic boundary was applied in the Y direction, which was also the direction of the lateral scan. Such a boundary configuration removed all edge effects when the simulated tip approaches the Y-boundary, that is, the scans were performed along a trench periodic in the direction of the scan. The Z position of the AFM tip (represented by a capped single-wall nanotube) was feedback controlled to maintain a prescribed contact force (load) between the tip and the sample. The interatomic interactions within each graphene sheet, as well as in the nanotube, were set by the Tersoff-Brenner potential (Brenner, 1990; Lindsay and Broido, 2010), while the tip-sample interactions and the interlayer van der Waals interactions were described by the appropriately parameterized Lennard-Jones potential (Jones, 1924). We applied the Langevin thermostat (Schlick, 2002) separately to the tip and the sample to control the local temperature during the lateral scan, which is expected to inherently add energy to the system due to continuous breakage of the van der Waals bonds between the tip and the sample. The important feature of such temperature control is that the damping term in Eq. (3.4) is actually an adjustable parameter, which presents somewhat of a

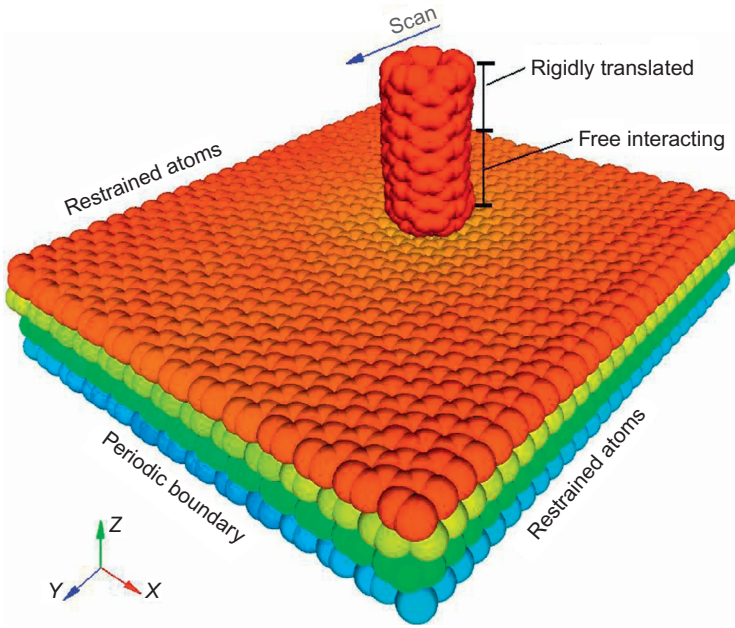

Figure 3.6 Assembly for the AFM scanning probe simulation.

scientific challenge, as we discuss further. The scan velocity was 5 nm/ns in all simulations, unless stated otherwise. In addition to few-layer samples, we also simulated a "bulk" sample consisting of four layers placed on a rigid fifth layer. This "bulk" system was used to represent a three-dimensional sample of material, which is a limiting case for the number of layers, as described in detail in Smolyanitsky et al. (2012) and the supporting information thereof.

Shown in Figure 3.7 are the friction averages obtained for various samples as a function of the tip-sample load. The shown behavior is qualitatively similar to that observed experimentally (Lee et al., 2010), yet the simulations revealed no puckering beyond the expected indenting deformation of the sample produced by the tip. As considered in detail in Smolyanitsky et al. (2012) and Smolyanitsky and Killgore (2012), the effect is caused by the viscoelastic deformation induced in the sample by the tip, commonly addressed in tribology as the ploughing friction with elastic return (Lafaye et al., 2006). This additional source of frictional resistance comes from the energy spent on laterally displacing the indented region. However, when more layers are stacked, the overall out-of-plane stiffness of the sample increases in a quantized fashion, that is, at the same tip-sample load, the depth of the indentation decreases, and so does the ploughing contribution to friction.

Our observation of ploughing at the nanoscale has led to the following prediction: If there is van der Waals adhesion between the tip and a monolayer graphene sample, upward (pulling) loads can be applied to the tip, resulting in a local "bulge" instead of the conventional indentation of the sample. Displacing such a bulge should then

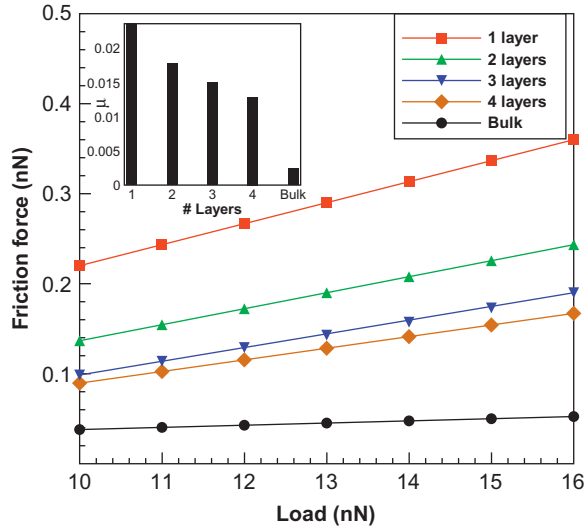

Figure 3.7 Friction force as a function of tip-sample load for few-layer graphene samples. The inset shows the effective slope of each line.

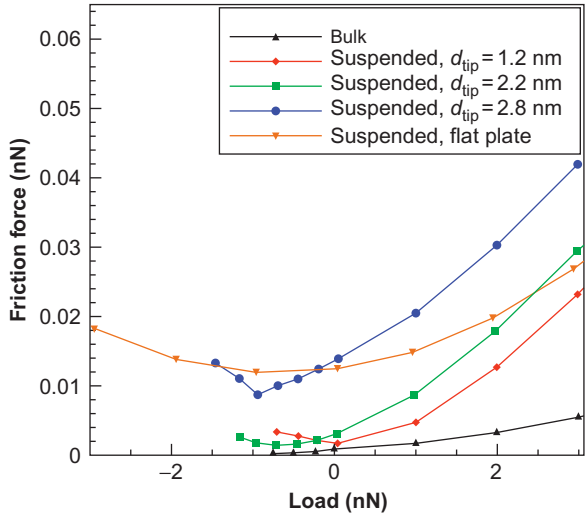

Figure 3.8 Friction force as a function of tip-sample load for monolayer graphene samples for various scanning tip diameters.

produce a ploughing contribution, because energy will be spent on laterally displacing the bulge during a scan. An increasing pulling force (before the tip and the sample lose contact, usually addressed as the pull-off) would then result in a greater local deformation, possibly leading to a greater ploughing contribution. Our subsequent simulations of AFM scans on graphene under negative applied loads clearly reveal this seeming anomaly, as shown in Figure 3.8. At negative loads, further retracting the tip (before a pull-off occurs) results in higher friction. We therefore have found a case, in which the kinetic friction increases when two objects are pulled further away from each other.

Interestingly, similar behavior was observed experimentally and also supported by particle-based simulations for chemically modified graphite (Deng et al., 2012). Although the anomalous trend was also observed for positive loads experimentally, this qualitative agreement between simulation and experiment for just the negative loads may indicate that the effect of ploughing at the nanoscale indeed plays an important role in the frictional properties of atomically thin layers and layered materials.

However, qualitative agreement is never a sufficient condition to definitively claim that the simulation indeed represents reality. An important issue here is the use of the Langevin thermostat, which was selected over the Nosé-Hoover thermostat because of the better local temperature control it provides in case of such a nonequilibrium system, compared to other methods (Smolyanitsky et al., 2012). In the Langevin dynamics framework, the effective viscosity of the atomically layers is essentially prescribed (and in our case was approximately equal to that of water at room temperature, Smolyanitsky et al., 2012). However, the actual viscoelastic properties of graphene are not empirically known, and therefore this important simulation parameter remains relatively free to adjust. Thus, if the effective viscoelasticity is experimentally found to be considerably lower than that in the simulations, the ploughing effects described here will have to be reconsidered, both quantitatively and qualitatively. This particular issue highlights the fine and crucial interplay between theory and simulation: If the initial parameterization of the simulation does not reproduce known empirical data, the results of the simulation must be considered with the known gaps in prior knowledge in mind. At the same time, the interesting results produced by the simulation parameterized without empirically known properties immediately demand that experimental measurements are performed to validate the results of the simulation and hopefully fill the existing parameterization gap. Such interplay is not always as obvious as in this case, and we believe that the described situation is an excellent example.

Another important issue in studying kinetic friction with use of MD is the fundamental timescale limitation. Because the simulated time reaches only nanoseconds, the scan velocity needs to be sufficiently high to allow considerable lateral displacement of the tip (necessary to collect statistically significant data for the friction force average). For instance, in the simulations described above, the simulated times were 1 ns, while the scanning rate was 5 nm/ns, resulting in a total lateral displacement of 5 nm, which is approximately 20 times the lattice constant of graphene. In an experiment, the scanning rates are of the order of nanometers per second, which is roughly nine orders of magnitude lower than in the simulation. First, combined with the significant effective viscoelasticity of the samples in the simulation, this high scanning rate may result in gross overestimation of the ploughing contribution. Second, the effective rate at which the van der Waals energy is pumped into the system during lateral scanning is linearly proportional to the scanning velocity. This means that in the experiment, the heating rate is extremely low compared to the simulation, where the local temperature of the contact may be higher than the temperature away from the contact, despite the thermostatting (Smolyanitsky et al., 2012). Given that friction is strongly affected by the contact temperature (Tomlinson, 1929), one must be strongly aware of the corresponding differences between experiment and simulation.

Provided that the experimental AFM scans are effectively static from the simulation standpoint, series of static replica simulations to probe the static friction at the nanoscale are becoming popular (Uberuaga et al., 2007; Martini et al., 2009). These simulations essentially reduce to probing the overall contact area as a result of the local deformation, but not the amount of energy that is spent on laterally displacing the deformed region. Therefore, we believe that the particular questions we attempted to answer in the simulations described above demand the dynamic approach. In the next section, we provide another example of dynamic simulations capable of revealing qualitatively interesting phenomena, given that we are well aware of the approximations made, as well as their effect on the possible differences between theory and experiment.

3.5 Fundamental properties of dynamic ripples in graphene

Over the past few years, we have come to accept as common knowledge that graphene is a two-dimensional material, because its remarkable electronic properties are a result of two-dimensional confinement. Is it, however, a perfectly flat two-dimensional crystal in its free-standing form? The Mermin-Wagner theorem suggests that a true two-dimensional crystal is impossible even in principle, and long-range crystalline order must be broken in the out-of-plane direction in order for phonons to propagate through the lattice in a manner that satisfies the Bose-Einstein statistics (Mermin, 1968). This theorem is closely related to and stems from the fact that boson statistics diverges in two dimensions. If a perfectly flat two-dimensional crystal is impossible, then how does graphene (along with other atomically thin membranes) exist? The answer is that it is not strictly two-dimensional.

Atomically thin membranes are flexible and are now understood to ripple out-of-plane for a variety of reasons. Both experimental and theoretical studies indicate that free-standing graphene is statically rippled, caused by strains (Bao et al., 2009), boundary effects (Thompson-Flagg et al., 2009), defects (Thompson-Flagg et al., 2009; Smolyanitsky and Tewary, 2011a), and rolling (Raux et al., 2010). What if the edges of a free-standing graphene sample are well passivated and no defects are present? In an important recent work, it was suggested by the results obtained with a particle-based simulation that at a finite temperature graphene is intrinsically covered with random dynamic waves (snapshot shown in the right pane of Figure 3.9). These dynamic waves were quantified and analyzed in detail from the standpoint of the theory of fluctuating membranes (Fasolino et al., 2007). Such dynamic rippling provides the fundamental reconciliation between the basic properties of crystal lattice vibrations and the ability of low-dimensional crystals to exist in three-dimensional space. In this sense, graphene is not a two-dimensional crystal, but a quasi-two-dimensional one, due to the fact that the third (out-of-plane) dimension is significantly suppressed relative to the in-plane dimensions. The effect of the third dimension on graphene's electronic properties, however, is important (Fogler et al., 2008),

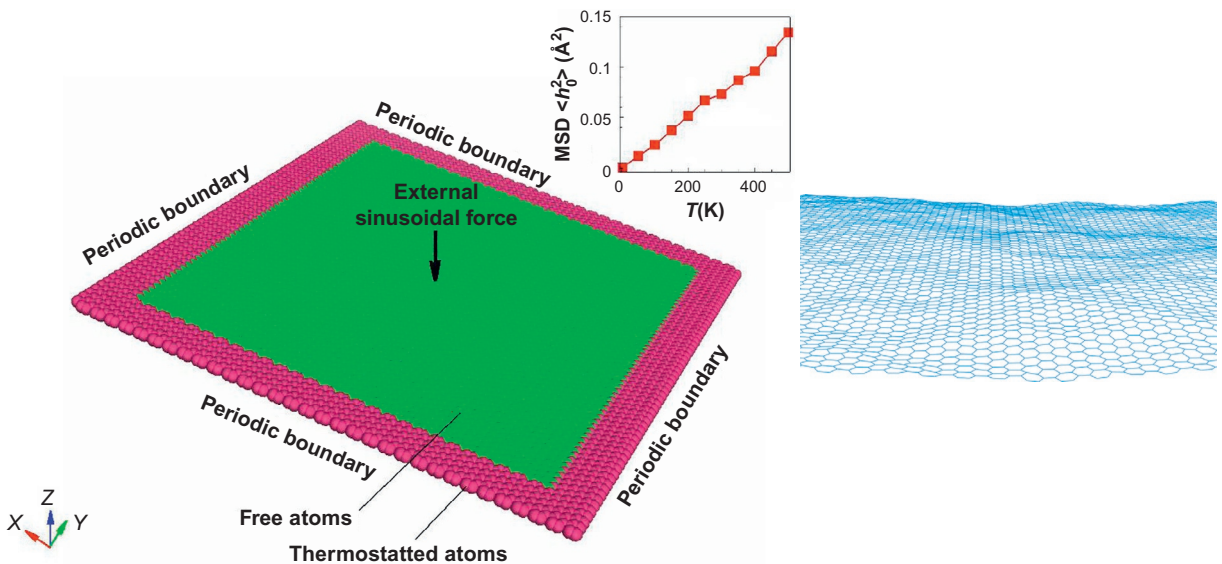

Figure 3.9 Simulated system (left) and snapshot of rippled graphene at 450 K (right). The inset on the left shows the out-of-plane rippling MSD as a function of temperature.

and recent studies indicate that local modulation of graphene static morphology results in controllable quantum dots (Klimov et al., 2012).

In our recent work (Smolyanitsky and Tewary, 2013), we considered dynamic modulation of graphene in the presence of thermal vibrations. The purpose of our investigation was to study externally induced local out-of-plane excitation of free-standing graphene and to understand the interaction between the externally excited ripples with those intrinsically present at a finite temperature.

Shown in the left pane of Figure 3.9 is the simulated system. A graphene membrane approximately 14 nm × 16 nm in size was thermostatted with use of the Nosé-Hoover algorithm throughout a 1-nm-wide region along the perimeter, with periodic boundaries applied in both X and Y directions. The temperature during external excitation was maintained at 300 K. An external excitation in the form of a sinusoidal force was applied to a small region at the geometric center of the membrane. All quantities of interest were calculated for the atoms *not subject* to direct thermal control. The primary reason for such care when applying thermal control is that we intended to simulate a thermally isolated free-standing membrane placed in a rectangular holder, which provided heat dissipation represented by the thermostat. The thermal control along the perimeter was also aimed at avoiding the effect of the thermostat on the response of the membrane to an external excitation via explicit damping terms, as shown in Eq. (3.4). The necessary initial test in determining the validity of the simulation setup was to plot the out-of-plane mean-square-displacement as a function of temperature, which is known to have a linear dependence (Nelson et al., 2004; Fasolino et al., 2007). The results of this validation are shown in the inset of Figure 3.9 (left). In addition, we successfully confirmed that the normal-normal correlations reduce to the continuum theory limit at long phonon wavelengths and also reproduce the corresponding Bragg peaks reasonably well for the wavelengths comparable to the lattice constant of graphene. These results are in accord with previous work (Nelson et al., 2004; Fasolino et al., 2007), and a more detailed discussion is available in the supplementary information of Smolyanitsky and Tewary (2013).

One of the key desired quantities was the normalized (with respect to the root-mean-square displacement, RMSD, of the out-of-plane ripples without external excitation) externally excited ripple RMSD as a function of the forcing frequency. The curves for various forcing amplitudes are shown in the left pane of Figure 3.10. We find that at low (below 5 THz) and high (above 30 THz) forcing frequencies the rippling magnitudes are in qualitative agreement with the established continuum theory (Smolyanitsky and Tewary, 2013). Despite the low excitation magnitudes (relative to the energy associated with the thermal portion), reasonably stable dynamic patterns are possible without thermal smearing for low excitation frequencies, similar to the pattern shown for 8 nN forcing amplitude and 1 THz frequency in the right pane of Figure 3.10.

An intriguing flattening effect takes place around forcing frequencies of 10 and 22 THz for the membrane of this size. This seeming anomaly can be explained in terms of the interplay between energies of the intrinsic thermal ripples and the externally excited ripples, assuming a low level of nonlinear effects. Once these energies become comparable, the presence of an active heat sink results in low-magnitude, fast

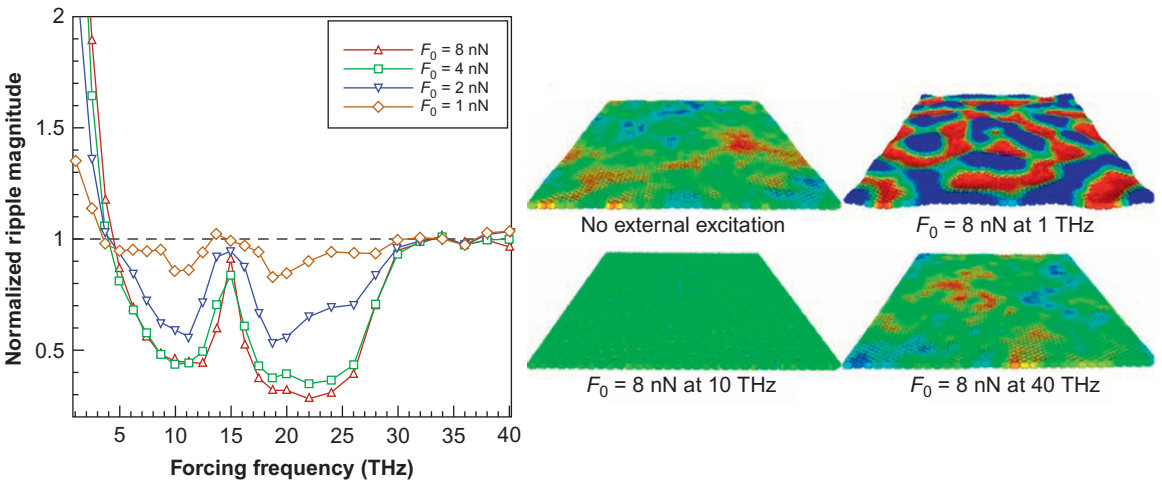

Figure 3.10 Normalized externally excited ripple magnitude as a function of the forcing frequency for various excitation amplitudes (left) and dynamic rippling snapshots (right). The color on the right is determined by the out-of-plane atomic position.

ripples replacing the higher-magnitude slower modes responsible for the intrinsic rippling, as explained in detail analytically in Smolyanitsky and Tewary (2013). This is a direct result of thermostatting in the simulation. However, if strict temperature control is imposed upon an experimental system, one may expect the same type of flattening. An additional important source of flattening is the presence of nonlinear effects, which result in self-stiffening of the membrane as a result of external excitation (Nelson et al., 2004). In general, our results suggest a possibility of generating dynamic rippling patterns, which are stable in terms of rippling spatial periodicity, as well as amplitude, and may strongly affect optical and electronic properties of graphene membranes at various timescales.

An important question arises from the discussion above: Is the use of terahertz frequencies for the simulation of external excitation appropriate? Such a choice is clearly less than compatible with the experiment and is dictated by the timescale limitations of MD, together with the small size of the simulated membrane. Fortunately, however, it presents less of a scientific challenge, because it can be shown that in the qualitative sense the properties of a nanometer-sized membrane excited by terahertz frequencies are equivalent to those of a micron-sized membrane excited by gigahertz frequencies (Smolyanitsky and Tewary, 2013). This qualitative equivalence follows from the fundamental properties of vibrating membranes, which includes the thermal ripple propagation.

Importantly, here we can see that the timescale limitation of the MD methodology affects the physical interpretation of the obtained results to a smaller degree than in our previous examples. In case of vibrating membranes, one can indeed claim qualitative correspondence between the simulation results, continuum-based theory, and possible experimental observation. One notes that both here and in other examples, it clearly follows that the principal difference between simulation and reality depends greatly on the system and the simulated properties of interest.

3.6 Conclusions and general remarks

In this chapter, we introduced particle-based simulation methodologies for studying static and dynamic lattice properties of nanoscale solid-state systems. We demonstrated the use of MS in determining the local lattice structure in nanoscale interconnects, as well as simulations of dynamic phenomena, such as kinetic friction and thermal fluctuations of the graphene lattice. It is our hope that these examples provide a glimpse at the power of these methodologies and thus the overall impact particle-based simulations can have on the entire field of nanoscale physics. It is very important to note that, although we did not give specific examples of the use of particle-based simulations in biophysics and biochemistry, the impact on those fields has been staggering, ranging from describing the dynamics of protein folding (Bazari et al., 1988) to drug discovery (Durrant and McCammon, 2011).

Simulation of biomolecules can also be used as a great example of one of the most important fundamental limitations of particle-based methods: the timescaling issue. In

addition to the examples presented here, consider the following: Proteins fold in milliseconds, or even seconds, while standard MD simulations can describe protein dynamics on the order of tens to hundreds of nanoseconds. As a result, the dynamic process can be simulated only within time intervals that are a small fraction of the total time interval required for the process of interest to take place. The timescale gap in this case is so significant that a recent MD simulation of a millisecond-long protein folding process with use of a supercomputer specifically designed for MD (Shaw et al., 2010) received major attention in the scientific community.

Despite the great advances in computing hardware and parallelization through effective domain decomposition, as well as strong effort to perform scientific computations with use of graphics-rendering hardware (Liu et al., 2007), the timescaling issue is expected to persist for at least the next decade for any system, where the physical process of interest takes place on a timescale significantly longer than hundreds of nanoseconds to microseconds. It is especially true for simulations of the solid-state systems, where interatomic potentials are significantly more complex than those used for biomolecules.

A variety of ways has been suggested to bring the simulated and experimental timescales closer. Suggested approaches range from use of Green's function (Tewary, 2009) to combining multiple approaches in a single simulation (Nielsen et al., 2010) and use of concurrent atomic-scale and coarse-grained representations of the same system. Each of these timescale extension approaches has its own merit and its own range of applicability, as can be seen in the corresponding literature.

In addition to future developments aimed at extending the timescale of MD simulations, several very important extensions to MD have been introduced recently. One extension is the combination of MD with a concurrent solution of Maxwell's equations on a three-dimensional grid to which electrically charged particles are assigned (Muralidharan et al., 2003). This provides a great opportunity to accurately model electromagnetic wave scattering in a nanoscale solid-state system, as opposed to finite-element methodology, which requires assigning questionable parameters to the elements prior to simulation. Another promising idea is the implementation of quantum-mechanical corrections to the motion of particles, which can be crucial for nanoscale systems at low temperatures. Previous methods of quantum-mechanical correction included representing each atom by a swarm of nonlocally interacting lighter particles (Feynman and Hibbs, 1965), which presents an additional computational burden, or direct application of the Feynman-Hibbs correction (Feynman and Hibbs, 1965; Hammou et al., 2005), which is suitable only for pairwise interactions. In the currently proposed approach, Newtonian dynamics is effectively replaced by quantized Hamilton dynamics (QHD), which utilizes the Heisenberg's equation of motion with some approximations to make the computations feasible (Prezhdo and Pereverzev, 2002). Combining the two extensions described above suggests the very exciting possibility of simulating the optical properties of nanoscale systems and devices at low temperatures, thus greatly expanding the range of problems that can be addressed.

It is often stated that particle-based simulations are, to a large degree, art. The authors of this chapter believe that, although the researchers' creativity is a must, the key to successfully representing a system in a simulation and providing a

reasonable physical interpretation of the simulated processes is to have a clear understanding of the applicability range of the existing tools. Given the current multitude of methods, algorithms, and extensions, it is far from straightforward to set up a simulation in a physically sound manner. It is, however, also an exciting task. It is our hope that the reader shares the authors' excitement about the vast opportunities such a great variety of methods provide within a single computational framework.

Disclaimer

Certain commercial equipment, instruments, or materials are identified in this paper in order to specify the experimental procedure adequately. Such identification is not intended to imply recommendation or endorsement by the National Institute of Standards and Technology, nor is it intended to imply that the materials or equipment identified are necessarily the best available for the purpose.

Acknowledgments

The authors thank Lawrence Robins, Lauren Rast, and Jason Killgore for illuminating and helpful discussions. This research was performed while the A.S. held a PREP appointment in collaboration with the University of Colorado at Boulder. This work represents an official contribution of the National Institute of Standards and Technology and is not subject to copyright in the USA.

References

Apol, E., Apostolov, R., Berendsen, H.J.C., Buuren, A.V., Bjelkmar, P., Rudi Van Drunen, Feenstra, A., Groenhof, G., Peter Kasson, Larsson, P., Meulenhoff, P., Teemu Murtola, Pall, S., Pronk, S., Schulz, R., Shirts, M., Sijbers, A., Tieleman, P., Hess, B., Spoel, D.V.D., Lindahl., E., 2010. GROMACS 4.5.6 manual.

Bao, W., Miao, F., Chen, Z., Zhang, H., Jang, W., Dames, C., Lau, C.N., 2009. Controlled ripple texturing of suspended graphene and ultrathin graphite membranes. Nat. Nanotechnol. 4, 562–566.

Baskes, M.I., 1992. Modified embedded-atom potentials for cubic materials and impurities. Phys. Rev. B 46, 2727–2742.

Bazari, W.L., Matsudaira, P., Wallek, M., Smeal, T., Jakes, R., Ahmed, Y., 1988. Villin sequence and peptide map identify six homologous domains. PNAS 85.

Brenner, D.W., 1990. Empirical potential for hydrocarbons for use in simulating the chemical vapor deposition of diamond films. Phys. Rev. B 42, 9458–9471.

Chang, T., Huajian, G., 2003. Size-dependent elastic properties of a single-walled carbon nanotube via a molecular mechanics model. J. Mech. Phys. Solids 51.

Datta, S., 1995. Electron Transport in Mesoscopic Systems. Cambridge University Press, Cambridge.

Deng, Z., Smolyanitsky, A., Li, Q., Feng, X.-Q., Cannara, R.J., 2012. Adhesion-dependent negative friction coefficient on chemically modified graphite at the nanoscale. Nat. Mater. 11, 1032–1037.

Durrant, J.D., Mccammon, J.A., 2011. Molecular dynamics simulations and drug discovery. BMC Biol. 9.

Fasolino, A., Los, J.H., Katsnelson, M.I., 2007. Intrinsic ripples in graphene. Nat. Mater. 6, 858–861.

Feynman, R.P., Hibbs, A.R., 1965. Quantum Mechanics and Path Integrals. McGraw-Hill, New York.

Filleter, T., Mcchesney, J.L., Bostwick, A., Rotenberg, E., Emtsev, K.V., Seyller, T., Horn, K., Bennewitz, R., 2009. Friction and dissipation in epitaxial graphene films. Phys. Rev. Lett. 102, 08610.

Fogler, M.M., Guinea, F., Katsnelson, M.I., 2008. Pseudomagnetic fields and ballistic transport in a suspended graphene sheet. Phys. Rev. Lett. 101.

Fuentes-Cabrera, M., Baskes, M.I., Melechko, A.V., Simpson, M.L., 2008. Bridge structure for the graphene/Ni(111) system: a first principles study. Phys. Rev. B 77.

Gamo, Y., Nagashima, A., Wakabayashi, M., Terai, M., Oshima, C., 1997. Atomic structure of monolayer graphite formed on Ni(111). Surf. Sci. 374, 61–64.

Gupta, A., Chen, G., Joshi, P., Tadigadapa, S., Eklund, P.C., 2006. Raman scattering from high-frequency phonons in supported n-graphene layer films. Nano Lett. 6, 2667–2673.

Hammou, Z., Lebsir, F., Krallafa, A., Hadjadj, A., Bormann, D., 2005. Feynman-Hibbs correction in classical molecular dynamics simulations of solid C60 under a progressively raised pressure and temperature. Model. Simul. Mater. Sci. Eng. 13.

Jones, J.E., 1924. On the determination of molecular fields. II. From the equation of state of a gas. Proc. R. Soc. Lond. A 106, 463–477.

Joshi, P., Smolyanitsky, A., Petrossian, L., Goryll, M., Saraniti, M., Thornton, T.J., 2010. Field effect modulation of ionic conductance of cylindrical silicon-on-insulator nanopore array. J. Appl. Phys. 107.

Klimov, N.N., Jung, S., Zhu, S., Li, T., Wright, C.A., Solares, S.D., Newell, D.B., Zhitenev, N.B., Stroscio, J.A., 2012. Electromechanical properties of graphene drumheads. Science 336, 1557–1561.

Lafaye, S., Gauthier, C., Schirrer, R., 2006. The ploughing friction: analytical model with elastic recovery for a conical tip with a blunted spherical extremity. Tribol. Lett. 21, 95–99.

Lee, B.-J., Baskes, M.I., 2000. Second nearest-neighbor modified embedded-atom-method potential. Phys. Rev. B 62, 8564–8567.

Lee, C., Li, Q., Kalb, W., Liu, X.-Z., Berger, H., Carpick, R.W., Hone, J., 2010. Frictional characteristics of atomically thin sheets. Science 328, 76–80.

Li, J., Ye, Q., Cassell, A., Hou Tee, N.G., Stevens, R., Han, J., Meyyappan, M., 2003. Bottom-up approach for carbon nanotube interconnects. Appl. Phys. Lett. 82.

Lindsay, L., Broido, D.A., 2010. Optimized Tersoff and Brenner empirical potential parameters for lattice dynamics and phonon thermal transport in carbon nanotubes and graphene. Phys. Rev. B 81.

Liu, W., Schmidt, B., Voss, G., Müller-Wittig, W., 2007. In: Molecular Dynamics Simulations on Commodity GPUs with CUDA. Lecture Notes in Computer Science, vol. 4873. Springer, Heidelberg, pp. 185–196.

Marreiro, D., Saraniti, M., Aboud, S., 2007. Brownian dynamics simulation of charge transport in ion channels. J. Phys. Condens. Matter 19, 215203.

Martini, A., Dong, Y., Perez, D., Voter, A.F., 2009. Low-speed atomistic simulation of stick-slip friction using parallel replica dynamics. Tribol. Lett. 36, 63–68.

Mermin, N.D., 1968. Crystalline order in two dimensions. Phys. Rev. 176, 250–254.
Morse, P.M., 1929. Diatomic molecules according to the wave mechanics. II. Vibrational levels. Phys. Rev. 34, 57–64.
Muller-Prathe, F., 1997. A simple nonequilibrium molecular dynamics method for calculating the thermal conductivity. J. Chem. Phys. 106.
Muralidharan, K., Deymier, P.A., Simmons, J.H., 2003. A Concurrent multiscale finite difference time domain/molecular dynamics method for bridging an elastic continuum to an atomic system. Model. Simul. Mater. Sci. Eng. 11.
Nelson, D., Weinberg, S., Piran, T. (Eds.), 2004. Statistical Mechanics of Membranes and Surfaces. World Scientific, Singapore.
Nemes-Incze, P., Osváth, Z., Kamarás, K., Biró, L.P., 2008. Anomalies in thickness measurements of graphene and few layer graphite crystals by tapping mode atomic force microscopy. Carbon 46.
Nielsen, S.O., Moore, P.B., Ensing, B., 2010. Adaptive multiscale molecular dynamics of macromolecular fluids. Phys. Rev. Lett. 105, 237802.
Nosé, S., 1984. A unified formulation of the constant temperature molecular dynamics methods. J. Phys. Chem. 81, 511–519.
Novoselov, K.S., Geim, A.K., Morozov, S.V., Jiang, D., Zhang, Y., Dubonos, S.V., Grigorieva, I.V., Firsov, A.A., 2004. Electric field effect in atomically thin carbon films. Science 306, 666–669.
Prezhdo, O.V., Pereverzev, Y.V., 2002. Quantized Hamilton dynamics for a general potential. J. Chem. Phys. 116, 4450–4461.
Quoc, N.G.O., Shoba Krishnan, D.P., Cassell, A.M., Ye, Q., Li, J., Meyyappan, M., Yang, C.Y., 2004. Electron transport through metal-multiwall carbon nanotube interfaces. IEEE Trans. Nanotechnol. 3, 311.
Raux, P.S., Reis, P.M., Bush, J.W.M., Clanet, C., 2010. Rolling ribbons. Phys. Rev. Lett. 105.
Rosei, R., Crescenzi, M.D., 1983. Structure of graphitic carbon on Ni(111): a surface extended-energy-loss fine-structure study. Phys. Rev. B 28, 1161–1164.
Schlick, T., 2002. Molecular Modeling and Simulation: An Interdisciplinary Guide. Springer, New York.
Shaw, D.E., Maragakis, P., Lindorff-Larsen, K., Piana, S., Dror, R.O., Eastwood, M.P., Bank, J.A., Jumper, J.M., Salmon, J.K., Shan, Y., Wriggers, W., 2010. Atomic-level characterization of the structural dynamics of proteins. Science 330, 341–346.
Smolyanitsky, A., Killgore, J.P., 2012. Anomalous friction in suspended graphene. Phys. Rev. B 86.
Smolyanitsky, A., Tewary, V.K., 2011a. Atomistic simulation of a graphene-nanoribbon-metal interconnect. J. Phys. Cond. Matter 23, 355006.
Smolyanitsky, A., Tewary, V.K., 2011b. Simulation of lattice strain due to a CNT-metal interface. Nanotechnology 22.
Smolyanitsky, A., Tewary, V.K., 2013. Manipulation of graphene's dynamic ripples by local harmonic out-of-plane excitation. Nanotechnology 24.
Smolyanitsky, A., Killgore, J.P., Tewary, V.K., 2012. Effect of elastic deformation on frictional properties of few-layer graphene. Phys. Rev. B 85, 035412.
Tewary, V.K., 2009. Extending the time scale in molecular dynamics simulations: propagation of ripples in graphene. Phys. Rev. 80.
Thompson-Flagg, R.C., Moura, M.J.B., Marder, M., 2009. Rippling of graphene. Europhys. Lett. 85.
Tomlinson, G.A., 1929. A molecular theory of friction. Philos. Mag. 7, 905–939.

Uberuaga, B.P., Stuart, S.J., Voter, A.F., 2007. Parallel replica dynamics for driven systems: derivation and application to strained nanotubes. Phys. Rev. B 75.

Vanin, M., Mortensen, J.J., Kelkkanen, A.K., Garcia-Lastra, J.M., Thygesen, K.S., Jacobsen, K.W., 2010. Graphene on metals: a van der Waals density functional study. Phys. Rev. B 81.

Wang, Z., Gao, F., Crocombette, J.-P., Zu, X.T., Yang, L., Weber, W.J., 2007. Thermal conductivity of GaN nanotubes simulated by nonequilibrium molecular dynamics. Phys. Rev. B 75.

Xu, Z., Buehler, M.J., 2010. Interface structure and mechanics between graphene and metal substrates: a first-principles study. J. Phys. Condens. Matter 22.

Yakobson, B.I., Brabec, C.J., Bernholc, J., 1996. Nanomechanics of carbon tubes: instabilities beyond linear response. Phys. Rev. Lett. 76, 2511–2514.

TEM studies of nanostructures

4

K. Wang, B. Cao, J. Chen, W. Zhou
University of New Orleans, New Orleans, LA, USA

4.1 Introduction

The field of one-dimensional (1D) nanomaterials, such as nanowires, nanobelts, nanotubes, and nanoribbons, has become one of the most active research areas in nanoscience and nanotechnology (Li et al., 2006; Yang et al., 2010; Kempa et al., 2013). Because of their small diameters, 1D nanomaterials can have very high surface-to-bulk ratios. More significantly, the conduction of quantum particles, such as electrons, phonons, and photons, in these 1D nanostructures is confined in the planes normal to their longitudinal directions. This so-called 2D confinement endows 1D nanomaterials with unique chemical and physical properties that are quite different from those of their bulk materials. For instance, nanowire conductivity can be described as the sum of the transport by separate channels of different quantized energy levels, and it is strongly influenced by edge effects. When illuminated by light, semiconducting nanowires can exhibit size-dependent absorption similar to that observed in quantum dots (QDs). More evidently, as a nanowire shrinks in size, its chemical activities can be greatly enhanced because the surface atoms outnumber the atoms within the nanowire. Consequently, 1D nanostructures, and particularly semiconducting nanowires, have been considered as the ideal building blocks for fabricating novel devices that exhibit superior performance than their thin film or bulk counterparts (Zimmler et al., 2010; LaPierre et al., 2013; Espinosa et al., 2012). It has been revealed that the properties of nanostructures vary with respect to their general morphology, diameter, crystallinity, growth direction, polarity, defect structures, interfaces, and compositions. Undoubtedly, structure analysis is of great importance to correlate the structure and the novel properties observed in nanomaterials, and, ultimately, to achieve a more controllable synthesis and device performance.

Ever since the discovery of the transmission electron microscope (TEM), it has played an important role in revealing the crystal structure and surface and chemical composition of materials (Edington, 1976). These capabilities become increasingly important in characterizing nanomaterials toward an atomic-level control of structure and composition. In addition to the bright field (BF) imaging of nanowire morphology, TEM allows for determination of crystallinity and growth direction of nanowires by analyzing the select-area electron diffraction (SAED) patterns, assignment of surface polarizations by studying the convergent beam electron diffraction (CBED), and identification of planar defects with atomic resolution via high-resolution

Modeling, Characterization and Production of Nanomaterials. http://dx.doi.org/10.1016/B978-1-78242-228-0.00004-1
Copyright © 2015 Elsevier Ltd. All rights reserved.

transmission microscopy (HRTEM) imaging. Dark-field (DF) imaging can be used to visualize crystalline defects such as twinning and secondary phase precipitates and determine the interfaces in nanoheterostructures. As a well-established compositional analysis technique, energy-dispersive X-ray spectroscopy is capable of identifying and quantifying nanowire composition with heavier elements. A more chemically sensitive spectroscopic technique, electron energy loss spectroscopy (EELS), can provide better identification and qualification of low atomic number elements, such as oxygen and carbon. Beyond these conventional TEM techniques, Z-contrast or high angle annular dark-field (HAADF) images obtained in scanning transmission electron microscope (STEM) mode can offer good composition contrast, for instance, of nanowire superlattice with elements comprising of differentiable atomic numbers or noble-metal nanoparticles decorated nanowires (Pennycook and Nellist, 2011). Despite the limitations in imaging elements with low atomic numbers, TEM enables us to map compositional variations on the nanoscale along or across the growth direction of nanowires when combined with energy dispersive X-ray spectroscopy (EDS) or EELS. However, because of the effects of spherical aberration (*Cs*) in the electromagnetic lens, further achieving atomic resolution imaging and analysis in a conventional STEM is limited by the probe size and electron-beam current density. By applying the *Cs*-correction technology, one can expect a higher signal-to-noise ratio and a reduced probe broadening effect (Kotaka et al., 2010). Consequently, performance for the analysis of structure, composition, and physical properties on the atomic scale can be significantly improved. For instance, newly developed annular bright-field (ABF) imaging technique in a *Cs*-corrected STEM equipment allows for the direct visualization of oxygen and nitrogen atom columns, opening new routes for the fine characterization of oxide and nitride nanostructures (Findlay et al., 2011). Moreover, electron tomography in STEM mode can retrieve 3D structure information, such as shape and morphology, of nanostructures by multiple-angle imaging and tomographic reconstruction (Ding et al., 2013). Additionally, *in situ* TEM techniques provide opportunities to probe the nucleation and growth, transformation, measurement, and function of 1D nanomaterials in real time (Petkov, 2013).

TEM investigation is an essential part in structure analysis of 1D nanostructures, thus the application of TEM (STEM) in 1D nanomaterials has been reviewed (Pennycook and Nellist, 2011; Ding and Wang, 2004). Therefore, the principal and technical details of TEM (STEM) imaging and spectroscopies on 1D nanostructures are beyond the scope of this chapter. The goal of this chapter is to illustrate the capabilities of TEM techniques in 1D nanomaterial structural analysis with a number of semiconducting nanostructures. The main focus will be on the growth mechanism discussion based on TEM analysis. In the first section of this chapter, polarity-driven and stacking-faults-induced growth will be exemplified with double-tip ZnO nanoneedles and ultrathin ZnO nanobelts. In the second section, a polytypoid SnO_2 (ZnO:Sn) nanowire will be demonstrated to highlight the application of HAADF and ABF imaging in analyzing superlattice nanowires. The third section will focus on TEM characterization of nanowire heterostructures, including axially heterostructured nanowire, core-shell nanowire, and surface functionalized

nanowires, to demonstrate the strategies of fabricating these complex structures. Finally, a brief summary of TEM in 1D nanomaterials characterization will be presented.

4.2 Polarity determination and stacking faults of 1D ZnO nanostructures

1D nanostructures are commonly grown by vapor-liquid-solid (VLS) (Wagner and Ellis, 1964), vapor-solid (Hsu and Lu, 2005), template-assisted electrochemical deposition (Zhao et al., 2004), and solution growth (Ye and Qi, 2008). The VLS mechanism, where metallic nanoparticles catalyze the anisotropic growth, offers more controllability in nanowire diameters, locations, and density and has attracted special interest (Fortuna and Li, 2010). However, the shape and the composition uniformity of the nanostructure are strongly associated with the growth conditions and the intrinsic crystallographic features, such as polarity and planar defects. Note that incorporating a metal particle in the nanowire generally degrades the nanowire's physical properties (Fasoli et al., 2011). In this manner, the polarity-driven or defect-induced growth becomes more intriguing in the case where the 1D nanostructure growth is governed by a self-catalyzed mechanism (i.e., without catalysts).

4.2.1 Polarity determination in 1D ZnO nanostructures

Most of the II-VI and III-V compound semiconductors adopt either hexagonal wurtzite (WZ) or cubic zinc blende (ZB) structures. The lack of a center of symmetry in both crystal structures, that is, the crystal polarity, may induce spontaneous polarization in WZ or piezoelectric polarization in ZB, which strongly impacts the impurity incorporation, etch rate, defect formation, and surface roughness of the crystals. This impact becomes more significant when the size reduces to nanoscale, partially owing to the high surface-to-volume ratio and quantum confinement effects. In fact, the crystal polarity influences the spontaneous nucleation and growth of nanoarchitectures, and it is strongly correlated with the optoelectronic and transport properties of the nanowire devices (de la Mata et al., 2012). Therefore, polarity determination in nanowires is essential for understanding the growth mechanism. With a low spatial resolution, the polarity of surfaces or layers can be determined by various methods including chemical or thermal etching, resonant X-ray diffraction (XRD), and high energy ion channeling, hemispherically scanned X-ray photoelectron diffraction. In contrast, as a microscopic technique, TEM allows for investigating the polarity even with unit cell resolution, defining itself as a better choice for determining the polarity of nanowires. Various TEM-based methods are used to determine the polarity of layers or surfaces, including CBED, spectrum imaging

by EELS and EDS, and HAADF and ABF performed in STEM mode. The relative merits and demerits in their capability of polarity determination depend highly on the crystals and the corresponding morphologies. Among them, CBED is a well-established and more widely used methodology to determine the polarity. Fundamentally, it uses the breakdown of Friedel's law caused by the electron dynamical diffraction to determine the polarity. CBED patterns vary depending upon different factors, such as incident direction and absorption of the electrons, sample thickness, accelerating voltage, and the observation temperature (Williams and Carter, 2009). Here, we use 1D ZnO nanoneedles as an example to demonstrate the polarity determination through CBED. The growth mechanism will also be discussed based on the CBED results.

The ZnO nanoneedles were synthesized on a silicon substrate by chemical vapor deposition (Li et al., 2010). Briefly, mixed powders of zinc oxide, manganese oxide, and graphite were used as the precursor. The entire system was naturally cooled down to room temperature after the reaction. This slow cooling was believed to be crucial to achieve nanoneedle morphology. A low-magnification TEM image, as shown in Figure 4.1a, revealed that the collected sample exhibited a needle-like morphology with two opposite tips. Figure 4.1b and c illustrates the CBED patterns taken from the areas marked by cycles in Figure 4.1a, respectively. The corresponding simulated CBED patterns were shown in Figure 4.1d and e. The nanoneedle is a *c*-axis-grown WZ structure described as a number of alternating planes composed of fourfold tetrahedral-coordinated O^{2-} and Zn^{2+} ions, stacked alternatively along the *c*-axis. The (0001) and (000-1) surfaces are terminated with Zn and O, respectively, giving rise to positively and negatively charged polar surfaces. The intensity distributions in the (0002) and the (000-2) disks are significantly different, which is due to the non-central symmetric structure of ZnO. Experimental and simulated CBED patterns are in excellent agreement, indicating that the two tips of nanoneedles grow out of the positively charged (0001)-Zn surfaces.

A close investigation of the double tip nanoneedles by TEM reveals that some of the double-tip nanoneedles have a kink in the middle as shown in the rectangular region of Figure 4.1f, implying the possibility that two single-tip nanoneedles fused together and formed a double-tip nanoneedle during the growth. The corresponding enlarged DF image is presented in Figure 4.1g and the projection of interface is clearly seen, ensuring that the two single-tip nanoneedles were fused together to form a double-tip nanoneedle. Possible models revealing the growth of the single-tip and double-tip nanoneedles are given in Figure 4.1h. Initially, the system reaches a critical value, and ZnO nanorods were formed by the effect of a temperature gradient and air flow. When the temperature started to descend during the cooling period, the nanorods still grew, but thinner than the original rod, forming tips until the temperature reached a critical value, which was compared with synthesis condition of the nanorods formed under a fast cooling speed. The tips formed along the [0001] direction by the effect of the molecular polarity, resulting in the formation of many single-tip nanoneedles. Meanwhile, some single-tip nanoneedles encountered and aligned, growing into double-tip nanoneedles with kinks in the middle.

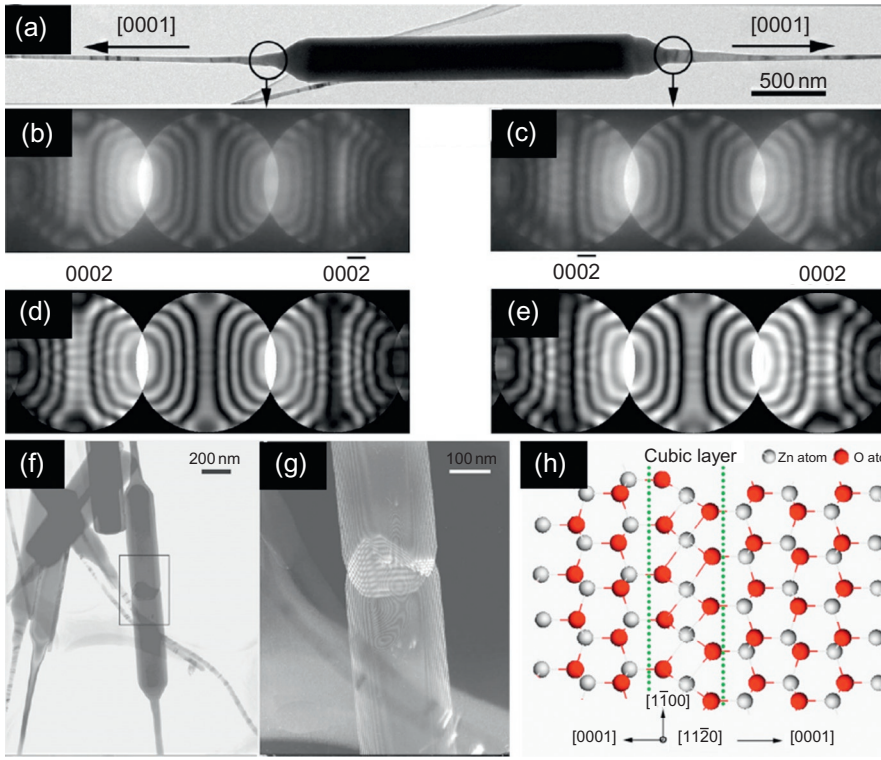

Figure 4.1 (a) TEM image showing a double tip nanoneedle. (b and c) CBED patterns gained from the zone marked by cycles in (a). (d and e) The corresponding simulated CBED pattern with the CBED in (b) and (c), respectively. (f) TEM bright field image showing a double tip nanoneedle which originated from the two single tip nanoneedles. (g) Magnified dark-field image of the zone marked by a rectangle in (f). (h) The schematic illustration of the stacking sequence of atoms and the growth direction of the perfect ZnO nanoneedles with a thin pseudo-cubic layer.
Adapted with permission from Li et al. (2010). Copyright © 2010 American Scientific Publishers.

However, CBED is not very straightforward because it requires image simulations associated with an accurate measure of defocus and sample thickness. Moreover, a certain volume of crystals is needed to obtain accurate CBED patterns. This limits its capability of polarity determination in ultrathin nanostructures. Additionally, its pattern is very sensitive to the defects in the illuminated area, possibly causing misleading interpretations when high-density stacking faults exist in the nanostructure. HAADF-STEM, also called Z-contrast imaging, provides a direct and robust imaging mode for determining the location of heavy atoms and thus can be used to assign the polarity of nanostructures composed by heavy elements. Contrary to CBED, no image simulation is involved in this technique, and more importantly, it is insensitive to sample thickness and defocus. However, it is limited in visualizing the light atoms, such as, Li, O, and N, which imposes difficulties in determining the polarity of

nitride and oxide nanostructures. Fortunately, the recently established ABF-STEM technique enables the direct imaging of both lighter and heavier atomic columns simultaneously, providing a reliable and efficient approach in assigning polarities in compound semiconductor nanostructures that consist of lighter elements (de la Mata et al., 2012).

It should be noted that TEM is a microscopic method, providing information on individual nanowires but not the whole population. The polarity determination in nanostructures is more accurate when one combines TEM with other macroscopic techniques, for instance, resonant XRD.

4.2.2 Stacking-fault-induced growth of ultrathin ZnO nanobelts

As one type of planar defects, stacking faults are formed by a change in stacking sequence of atomic planes. They are commonly observed in nanowire and nanobelts and play important roles in determining the physical properties of the nanostructures. Theoretically, an appropriate number of stacking faults or nanoscale twins in metal nanowires may give rise to ultrahigh yield strengths and flow stresses in metals. However, the presence of stacking faults in functional semiconducting nanostructures generally results in reduced carrier mobility and thus a degraded performance in corresponding nanodevices. Therefore, great effort has been dedicated to achieving stacking-fault-free nanostructures, such as III-V nanowires by molecular beam epitaxy (Huang et al., 2010b; Shtrikman et al., 2009). From a growth perspective, the formation of stacking faults in nanostructures can stabilize the high-energy surfaces and influence a preferred growth direction. HRTEM imaging, along with image simulation, is in high demand to probe the nature of stacking faults, allowing for an increased understanding the nanowire growth.

Ultrathin ZnO nanobelts were synthesized via a vapor transport technique, and no catalyst was introduced (Wang et al., 2010a). The as-synthesized ZnO nanobelt has a width of $\sim$5.5 nm, evident in the HRTEM image taken along the $\langle$2-1-10$\rangle$ zone axis (Figure 4.2a). The inset shows the corresponding SAED pattern, suggesting that the thin ZnO nanobelts grow along the $\langle$01-10$\rangle$ direction, with top/bottom {2-1-10} surfaces and {0001} side surfaces. Interestingly, the thin ZnO nanobelt exhibits stacking-fault contrast along its {0002} basal plane, as denoted by white arrows in Figure 4.2a. An enlarged HRTEM image of the {0002} stacking fault plane is shown in Figure 4.2b. The {01-10} lattice planes on both sides of the {0002} stacking fault share one-third $\langle$01-10$\rangle$ with each other, which is the projection of one-sixth $\langle$2-203$\rangle$ Frank partial dislocation on the {0002} basal plane in ZnO. It is believed that the terminating partial dislocations glide out of the thin nanobelts, leaving the {0002} stacking-fault plane penetrating through entire length of the thin nanobelts.

In the case of the ionic compound ZnO, in order to maintain nearest-neighbor bonding across the stacking-fault plane, intrinsic and extrinsic stacking faults arrive at the same structure of the stacking-fault plane by a simple shear, as shown in the schematics of Figure 4.2c. The stacking sequence is $A\alpha B\beta A\alpha B\beta A\alpha|B\gamma C\alpha B\gamma C\alpha B\gamma$, where the Roman and Greek letters denote Zn and O atoms in the {0002} double planes respectively. It is apparent that the electronic environment across the stacking fault

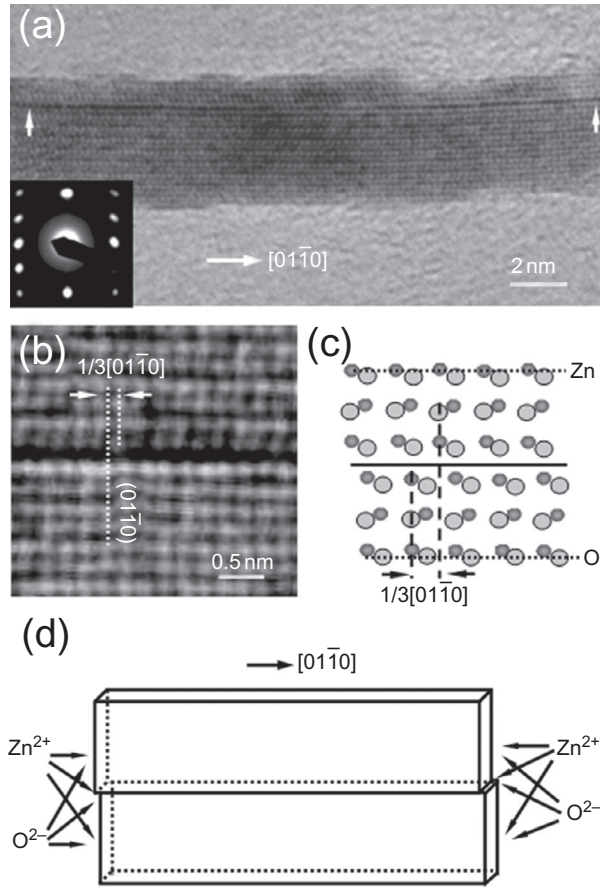

Figure 4.2 (a) Representative HREM image of a thin ZnO nanobelt taken along the ⟨2-1-10⟩ zone axis. Inset in the left bottom corner is the corresponding SAED pattern. The white arrows denote the {0002} stacking fault. (b) Enlarged HREM image of the {0002} stacking fault plane. (c) Schematic drawing of the projection of the atomic structure along the ⟨2-1-10⟩ direction. The solid line denotes the stacking fault position. (d) Schematic drawing of the preferential deposition steps at the {01-10} growth fronts of the thin ZnO nanobelts.
Adapted with permission from Wang et al. (2010a). Copyright © 2010 American Scientific Publishers.

plane is dramatically disturbed, which might be the reason for the formation of the dark contrast along the {0002} stacking-fault plane.

Crystallographically, the {0002} stacking faults plane would result in a step with a translation of one-third ⟨01-10⟩ at each side of the {01-10} growth fronts, as shown in Figure 4.2d. The steps might provide preferential deposition sites for the reactants Zn^{2+} and O^{2-} ions during the growth process of the thin ZnO nanobelt, which could result in fast axial growth of the thin ZnO nanobelt. Consequently, the stacking fault induced much faster axial growth along ⟨01-10⟩ than the lateral {0002} growth, under assumption that the reactant supplies are constant. In fact, constant supplies of the reactants Zn^{2+} and

O^{2-} ions were reasonable since all of the synthesis parameters were carefully maintained without variations during the synthesis process. Thus, it is believed that the {0002} stacking faults caused the formation of the thin ZnO nanobelt in our experiment.

4.3 Structure analysis of superlattice nanowire by TEM: a case of SnO_2 $(ZnO:Sn)_n$ nanowire

Superlattice is a periodic (strict) or aperiodic (broad) structure that consists of alternate layers of two (or more) different materials or two phases of a single material. It can help maintain the stoichiometry of the materials and manipulate the carrier concentration down to the intrinsic level, making it a very versatile and powerful candidate in electronic and photonic applications. In the last decade, 1D superlattice nanomaterials have attracted great attention for their potential quantum confinement effects on both circumferential and axial directions. Generally, superlattice nanowires can be prepared via two approaches: artificial growth and natural self-assembly. The former method applies to group III-V and IV materials, such as GaP/GaAs (Gudiksen et al., 2002; Borgstrom et al., 2006), InAs/InP (Bjork et al., 2002), and Si/SiGe (Wu et al., 2002), by the alternate introduction of vapor phase reactants that react with the same catalyst. While the latter method mostly works for a specific group of homologous compounds $InMO_3(ZnO)_n$ (M = In, Ga, Fe, Al, etc.), superlattice structures will form naturally when the compositional elements reach a specific ratio.

Compared with superlattice nanowires of group III-V and IV materials, the structure of homologous compounds $InMO_3(ZnO)_n$ is more complicated, consisting of slabs of WZ M-doped ZnO ($M/Zn_nO_{n+1}^+$) separated by octahedrally coordinated InO_2^- (In-O) layers (Da Silva et al., 2008). Because two segments have the same amount of positive and negative charges, the nanowire itself is charge-balanced. The In ions in the In-O layer occupy the octahedral sites, while the M and Zn ions in the M/Z-O layer take the tetrahedral or trigonal bipyramidal ones. These In-O layers induce a polarity inversion in the two adjacent ZnO layers forming an inverse domain boundary (Yan et al., 1998). Zigzag-shaped contrast polarity inversion boundaries would form between two In-O layers in some $InMO_3(ZnO)_n$ nanowires with a larger n ($n > 6$) (Huang et al., 2010a; Wang et al., 2010c) to relax the strain energy. Although $InMO_3(ZnO)_n$ has been extensively studied in the forms of bulk and thin film structures, it was not until 2004 that $In_2O_3/(ZnO)_n$ superlattice nanowires were synthesized with diverse compositions ($n = 5, 7, 18$) (Jie et al., 2004), followed by the synthesis of $In_2O_3(ZnO)_4$ and $In_2O_3(ZnO)_5$ nanowires, doped with 6-8% Sn (Na et al., 2005). In addition to $In_2O_3(ZnO)_n$ nanowires, $InGaO_3(ZnO)_n$ (Andrews et al., 2011; Li et al., 2009a), $InAlO_3(ZnO)_n$ (Li et al., 2009b), and $InFeO_3(ZnO)_n$ (Huang et al., 2010a) superlattice nanowires were successively reported later on.

A new superlattice nanowire was found when we tried to substitute In with Sn during the growth, which has never been observed in bulk form. It has similar features of layered structures, but the distribution of Sn atoms among the nanowires is not clear.

Figure 4.3a is a typical TEM image of the new nanowire mentioned above that shows modulated contrast along its entire length with no obvious amorphous shell attached. The inset is the corresponding SAED pattern taken from the [100] zone axis.

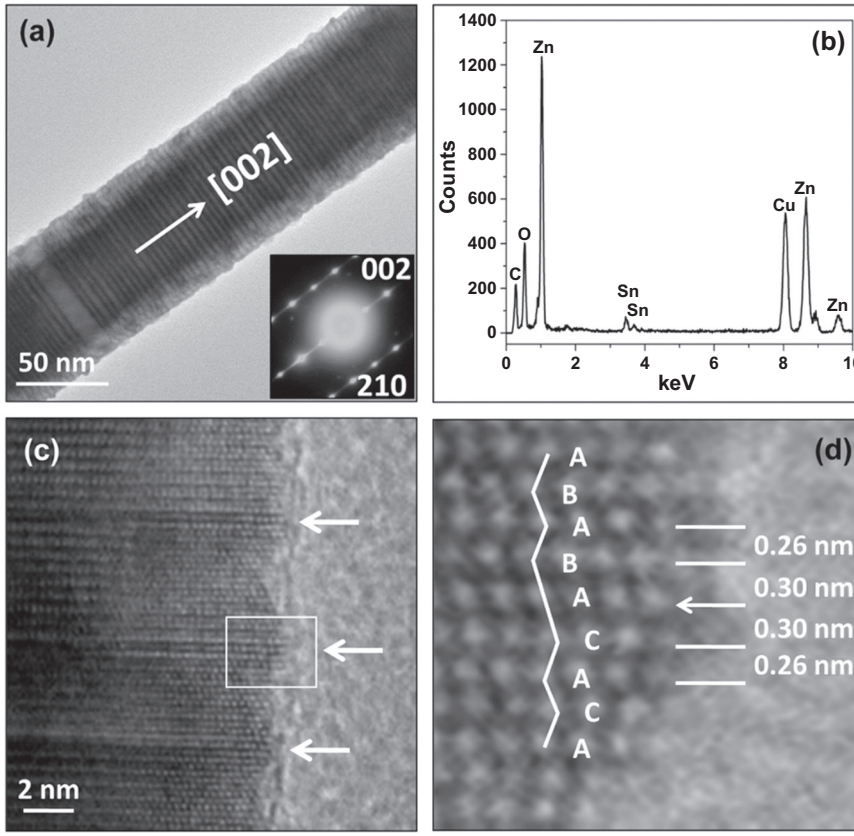

Figure 4.3 TEM image (a) of the $SnO_2(ZnO:Sn)_n$ nanowire with [002] growth direction. Inset is the [100] electron diffraction pattern. (b) EDS shows the presence of Sn. (c–d) HRTEM images reveal that modulated contrast comes from those individual atomic planes which separate the nanowire into slabs.
Adapted with permission from Cao et al. (2012). Copyright (2012) American Chemical Society.

Notice that, in addition to the main diffraction spots of the normal ZnO phase, a series of streaks can be seen along the [001] direction, which is the typical sign of planar defects. The EDS measurement (Figure 4.3b) indicates the presence of Sn in the nanowire, and the average Sn content in the nanowire, defined as atomic ratio of Sn/(Zn + Sn), is identified to be about 23.8%. Figure 4.3c is a high-resolution TEM image taken at the edge of a nanowire. It turns out that the black contrast under low magnification comes from many individual atomic layers as illustrated by white arrows, separating the body of nanowires into a series of slabs. Evidently, these isolated layers are also the origin of the streaks in the diffraction pattern. The highlighted area in the white square is enlarged in Figure 4.3d. It is found that the atomic layers' stacking sequence switches from *BABA* to *ACAC* over the marked layer.

Moreover, the interplanar distances within the slab are measured as 0.26 nm, corresponding to the characteristic d-spacing of the ZnO (002) plane, while the distance

between the arrow-marked layer and its neighboring layers is 0.30 nm, which is larger than 0.26 nm. It is known that the radius of the ion is correlated with its coordination number (CN). Sn^{4+} ions have two possible radii, 69 pm for CN = 4 and 83 pm for CN = 6 (Shannon, 1976). Because the Zn^{2+} ions have a radius of 74 pm, the bigger Sn^{4+} ion (83 pm) with octahedral coordination should result in a thicker atomic layer. Thus, it is conceivable that these isolated atomic layers are composed of an octahedral Sn-O plane. However, it is challenging to discriminate Sn atoms from Zn atoms under conventional TEM investigation.

Z-contrast imaging under the STEM-HAADF mode is very sensitive to atomic weight, making it effective for discriminating Sn and Zn atoms. The intensity of the atomic image is approximately proportional to the mean square of the atomic number of the constituent atoms (Z^2). The position of Sn atomic columns should be able to be unambiguously determined, because Sn ($Z = 50$) is much heavier than Zn ($Z = 30$). Thus, an advanced *Cs*-corrected JEM-2100 F scanning TEM was applied to further study the fine structure of this nanowire. Figure 4.4a is a Z-contrast image of a typical superlattice nanowire, clearly showing the presence of Sn atomic layers (bright lines). Sn columns are well resolved with obviously higher contrast compared with Zn columns, and individual planes of Sn atoms are clearly separated by ZnO slabs. The numbers of Zn-O layers inside each slab are in the range of 11 to 18, and the average is 12. The stacking sequence of Zn-O slabs exhibits no periodicity, thus as a broad definition, it can be considered as an aperiodic superlattice nanowire. If we assume there are no Sn atoms in ZnO slabs, then the ratio of Sn/(Sn + Zn) should be about 1:13, which is significantly smaller than the Sn/(Sn + Zn) ratio of 23.8% measured by EDS. Therefore, a certain amount of Sn should exist in ZnO slabs, which was confirmed further by nanoscale EDS (not shown here). Figure 4.4b shows a HAADF image of the nanowire with a higher magnification, from which zigzag-shaped contrast has been clearly observed. Because it is not energetically favorable for Sn atoms in ZnO slabs to locate near the SnO_2 octahedral layers, the wave-like contrast caused by doped Sn atoms does not get touched with the Sn-O layers, which is different from $InMO_3(ZnO)_n$ systems where the top of the zigzag contrast is connected with the In-O layer (Cao et al., 2012).

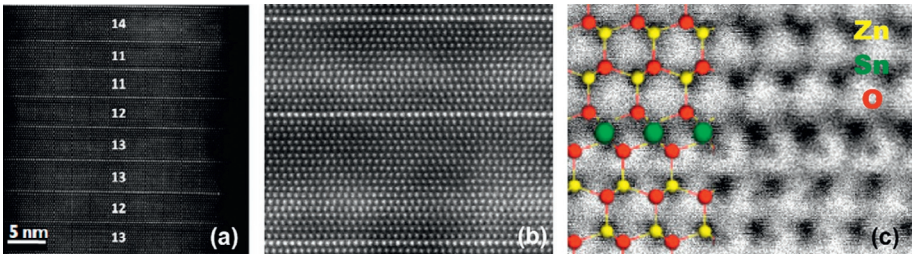

Figure 4.4 HAADF image resolves Sn atomic layer. (b) White zigzag-like contrast indicates a certain amount Sn atoms is doped into ZnO slabs. (c) ABF image shows position of O column, presenting the detailed configuration of O around Zn (tetrahedral) and Sn (octahedral).
Adapted with permission from Cao et al. (2012). Copyright (2012) American Chemical Society.

Although HAADF imaging can distinguish Sn and Zn atoms, it does not offer any information about O atom distribution, which is also crucial to determine the coordination of Zn atoms in the slab and Sn atoms in the interface layer. The structure model of the superlattice oxide has been well established in previous works (Da Silva et al., 2008), and the distribution of In and Zn/M atoms has been confirmed with Z-contrast imaging. Direct visualization of O atoms in the structure has not been provided due to the limitation of HAADF in detecting light elements. Figure 4.4c shows the ABF image collected between 7 and 33 mrad, in which O atoms (gray spots) are visualized around Sn (bigger dark spots) and Zn atoms (smaller dark spots). Each Sn atom is surrounded by four O atoms, which is actually a two-dimensional projection of an Sn-centered octahedron (6 O atoms at the vertex). Analogously, each Zn atom is surrounded by three O atoms, providing a 2D projection of the Zn-centered tetrahedron (4 O atoms at the vertices). The proposed model (yellow, Zn; green, Sn; red, O) is overlaid on the left part of the ABF image, showing a perfect match.

4.4 TEM analysis of 1D nanoheterostructure

Based on single-component 1D nanostructure, one can fabricate simple nanodevices, such as resistors, transistors, and optical waveguides, to extract fundamental physical parameters of the nanostructures or attain basic device functionality in applications (Colinge et al., 2010). Nonetheless, most semiconductor devices require junctions to manipulate the transport of electrons, phonons, and photons for exploring broader applications, which inspires numerous works on growth, assembly, and property studies of 1D nanoheterostructures. Here, 1D heterostructures can be defined as structures that consist of two or more geometrically 1D components. These junctions, including homojunctions, type-I and type-II heterojunctions, and Schottky junctions, in nanoheterostructures are generally present at the interfaces between different 1D components. These interfaces can allow or block the carrier transport, tolerate the strains and defects, and create new band structures, eventually determining the material's properties and device performance. From a materials prospective, acquiring structure and composition information across the interfaces is the major interest in characterizing 1D nanoheterostructures. On the other hand, surface modification of a single-component 1D nanostructure is an efficient way to enhance the device properties, as well as providing an ideal platform for investigating the interaction between materials with different dimensionalities. For example, loading nanocrystals (0D) on wide-bandgap oxide nanowires (1D) facilitates carrier injection for photovoltaics (Leschkies et al., 2007). The size distribution and faceting of the nanocrystals, along with the interface quality between the nanocrystals and nanowire, can significantly impact the final device behavior.

TEM has played an indispensable role in the structure analysis of 1D nanoheterostructures, such as identifying the interfaces, mapping the strain and composition, and imaging the extended defects and dopants. To simplify the discussion, here we divide 1D nanoheterostructures into three categories: axially heterostructured nanowire, radial core-shell nanowire, and surface-decorated 1D nanostructures. For each of these categories, we will present one or a few examples to describe the TEM analysis.

4.4.1 Axially heterostructured nanowires

Compared to radial heterojunction growth, synthesis of axial heterojunction is relatively challenging mainly due to more stringent requirements of crystallographic relationships and reactant atmospheres during growth. Thus, understanding crystallographic relationships between two components is quite crucial to predict or design a new axial heterojunction growth. Here is an example of growing a new ternary/binary oxide axial nanowire heterojunction based on the detailed structure analysis between Zn_2GeO_4 nanowire and a small segment of ZnO residue formed during the growth of Zn_2GeO_4 nanowire array. Controllable growth of ZnO with various lengths onto the Zn_2GeO_4 nanowire was realized based on the proposed epitaxial growth relationship and growth mechanism.

The ternary Zn_2GeO_4 nanowires were synthesized using a typical chemical vapor deposition method with a mixture of ZnO, GeO_2, and graphite powder as precursor (Cao et al., 2011). During the conventional TEM examination of as-grown ternary Zn_2GeO_4 nanowires, it is interesting to notice that a tiny unknown segment around 20 nm (see Figure 4.5a) is always observed between the Zn_2GeO_4 nanowire and Au catalyst, which is seldom seen in other VLS-grown ternary nanowires. The high-resolution TEM image of the interface area is displayed in Figure 4.5b, revealing that the interplanar d-spacings on two sides are 0.41 and 0.28 nm, corresponding to Zn_2GeO_4 (300) plane and ZnO (100) plane, respectively. Generally, selected area electron diffraction (SAED) at a large tilting range is a good way for phase

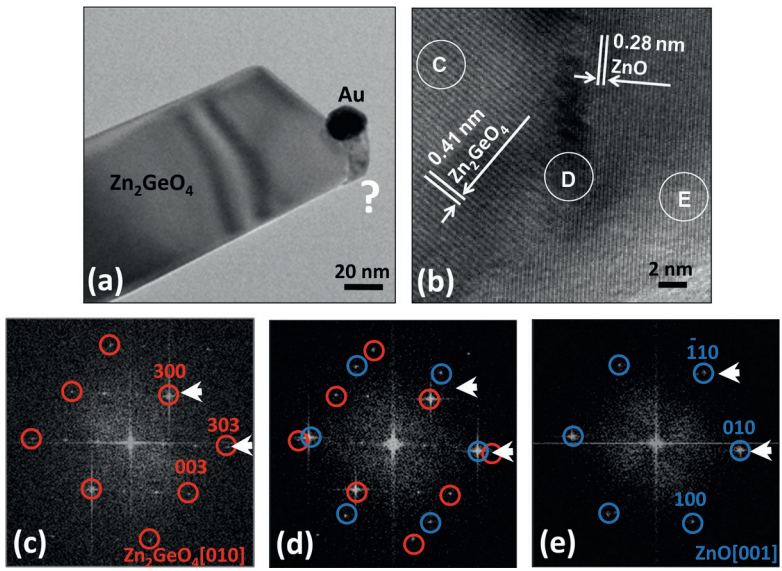

Figure 4.5 (a and b) Low-magnification and high-resolution TEM image of a junction area. (c–e) FFT diffraction patterns of marked locations (C, D, and E) in (b), respectively, indicating Zn_2GeO_4-[010]//ZnO-[001].

identification. However, for a nanoparticle around 20 nm, it is very hard to obtain a diffraction pattern. Therefore, fast Fourier transformations (FFT) are performed at locations of C, D, and E, as shown in Figure 4.5c and d, respectively. The FFT pattern of the unknown segment has the same typical hexagonal pattern as ZnO in the [001] zone axis. So this mysterious section could very likely be ZnO. The FFT pattern collected at the interface is a superimposed pattern from both Zn_2GeO_4 and ZnO phases, suggesting a crystallographic relationship of Zn_2GeO_4[010]//ZnO[001].

Only one FFT pattern is insufficient for confirming the ZnO phase, but compositional information will help validate the presumption of ZnO. The energy dispersive X-ray spectroscopy (EDS) mappings, using a probe size of 0.1 nm, were conducted to further study the junction part, as seen in Figure 4.6b–e, from which we can see that the region of unknown particles is majorly composed of Zn and O. Based on both the structural and compositional information, it is concluded that this particle residue is the ZnO phase. Thus, at the tip of Zn_2GeO_4 nanowire, a Zn_2GeO_4/ZnO heterojunction is formed. Because Zn_2GeO_4 and ZnO have absolutely different crystal structures, this heterojunction strongly suggest possible epitaxial growth relationships between these two phases. However, due to the small size of the ZnO section, the FFT pattern achieved is limited to a small range. Based on the rotation angle between two FFT patterns from Zn_2GeO_4 and ZnO phases, an interface model is built using Mac Tempas to simulate the superimposed electron diffraction pattern (EDP), as presented in Figure 4.7. This gives us a bigger view of the overlapped FFT of the two phases. The FFT pattern in Figure 4.5d is only within the range of the blue circle, beyond which more orientation relationships are indicated by green circles and dashed lines. It is found that diffraction spots of Zn_2GeO_4 ($3m$, 0, 0) and (0, 0, $3n$) are almost aligned with diffraction spots of ZnO (, h, 0) and (k, k, 0), respectively, indicating orientation

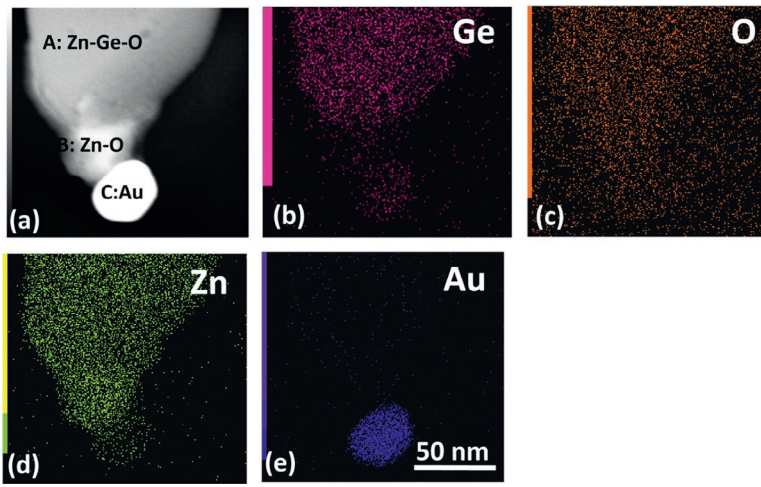

Figure 4.6 (a) Dark field TEM image of a junction area. (b–e) Ge, O, Zn, and Au elemental mapping, showing unknown section is composed of Zn and O.
Adapted with permission from Cao et al. (2011) with permission from Elsevier.

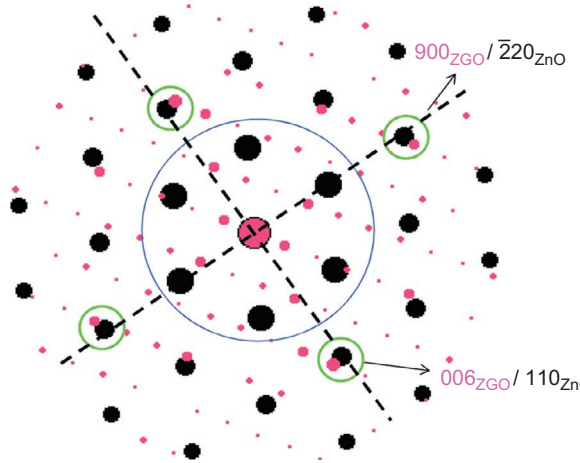

Figure 4.7 Simulated superimposed diffraction patterns from Zn_2GeO_4/ZnO interface imply more orientation relationships beyond experimental FFT pattern (within the blue circle).

relationship of Zn_2GeO_4 (300)//ZnO (10), and Zn_2GeO_4 (003)//ZnO (110), where *m*, *n*, *h*, and *k* are integers. Moreover, the diffraction spots of Zn_2GeO_4 (9, 0, 0) and (0, 0, 6) are found nearly overlapped with those of ZnO (, 2, 0) and (1, 1, 0), respectively. This implies good lattice matching along these two sets of planes with small mismatches of 2.7% and 2.3%; it also confirms the epitaxial growth of the heterojunction.

Based on the close relationships between these two phases, possible epitaxial growth may lead to a longer heterojunction if more Zn vapor is provided. In order to grow a longer ZnO segment, a second synthesis was conducted by extending growth time from 1 to 2 h without changing other experimental conditions. It was observed that the ZnO segment grew much longer (500 nm), forming the typical Zn_2GeO_4/ZnO heterojunction as shown in Figure 4.8a and b (enlarged). The SAED patterns in Figure 4.8c–e were recorded from the ZnO junction area and Zn_2GeO_4 region (denoted by C, D, and E in Figure 4.8b, respectively). Two sets of diffraction patterns, highlighted by rectangles and rhombohedra in Figure 4.8d, were observed at the junction region D, which correspond to the [001] zone axis of ZnO (C) and [010] zone axis of Zn_2GeO_4 (E) in Figure 4.8c and e, respectively, indicating that Zn_2GeO_4 [010] is parallel to ZnO [001]. Figure 4.8d matches the simulated diffraction pattern in Figure 4.7 very well.

From the above experimental results, we proposed a possible VLS growth mechanism. First, the Zn and Ge vapors from precursors dissolve into the melted gold catalyst downstream and form into an Au-Zn-Ge droplet. With the increasing content of Zn and Ge, a Zn_2GeO_4 nanowire grows out from the oversaturated Au-Zn-Ge droplet with assistance of residual oxygen in the furnace tube. Due to the higher proportion of ZnO in the source material (Zn: Ge > 2: 1), the GeO_2 source runs out first, resulting in the ending of the Ge vapor supply during the growth of ternary Zn_2GeO_4 nanowire. While excess ZnO source material continues to provide Zn vapor downstream, Au-Zn oversaturated droplets form, and the ZnO nanowires start to nucleate. By changing growth time, the length of ZnO segment can be manipulated along axial direction of the Zn_2GeO_4 nanowire.

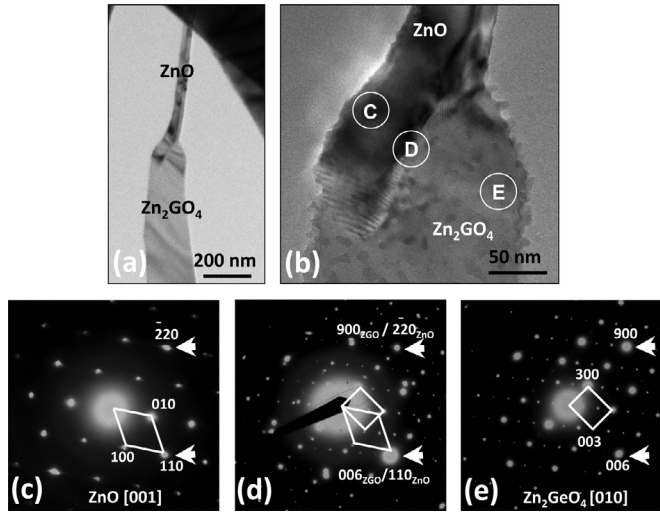

Figure 4.8 (a) Typical morphology of a Zn_2GeO_4/ZnO axial heterojunction in the second synthesis. (b) Enlarged heterojunction area where the ZnO section, interface region, and Zn_2GeO_4 section is denoted as C, D, and E, respectively. (c) SAED pattern of ZnO [001] (region C). (d) Superimposed SAED pattern from interface region D, where ZGO denotes Zn_2GeO_4. (e) SAED pattern of Zn_2GeO_4 [010] (region E).
Adapted with permission from Cao et al. (2011) with permission from Elsevier.

4.4.2 Coaxial core-shell nanowires

Compared to axially heterostructured nanowires, coaxial core-shell nanowires, namely radial heterostructured nanowires, promise more exotic applications because of their unique geometry-induced properties. First, the shell can act as a sidewall passivation layer to tune the emission of the core nanowire. This is a well-known strategy for improving the luminescence for core-shell QDs (Reiss et al., 2009), and it also holds true for the 1D quantum core-shell nanowire system. Second, alignment of energy states at the interface between the two components (core and shell) generally facilitates an efficient charge separation by isolating charge carriers from the impurities and defects on both surfaces and interfaces. This, along with the extended light absorption profile through type-II interfacial transition, makes the core-shell nanowires useful for solar-energy applications such as solar cells and hydrogen generation via photoelectrochemical water splitting and thermoelectrics (Zhang et al., 2007). Additionally, a nanowire surrounded by a radial shell can function as a wrap-gate structure, which provides better controllability over the conducting channel (Xiang et al., 2006). Finally, this unique coaxial geometry allows for significant relaxation of lattice mismatching strains that would lead to incoherent growth in the planar structure (Wang et al., 2008a).

Despite the possibility for growing coaxial nanowires by a one-step technique (Moore et al., 2008), one can usually fabricate core-shell nanowires by depositing

a material (shell) on the template nanowire (core). Multiple depositions in a modulated growth condition produce complex radial heterostructures (Lauhon et al., 2002). To pursue a high-performance device, of particular importance in the fabrication process is achieving an abrupt interface between the core and shell. Nevertheless, interfacial diffusion and incoherent growth can block the way. The former can result in the occurrence of a transition layer and has to be minimized by modulating the growth conditions. The latter, mostly arising from lattice mismatching between two materials, can also be related to the side facets of the template nanowire, and it likely induces an inhomogeneous shell thickness.

Structural and compositional analysis provided by TEM can help to clarify these issues. Here, we demonstrate the TEM analysis on two different cases of core-shell nanowires, according to the lattice mismatching between the materials: (i) highly lattice-mismatched ZnO/ZnSe and ZnO/ZnS core-shell nanowires and (ii) nearly lattice-matched CdSe/ZnTe core-shell nanowire.

4.4.2.1 *Highly lattice-mismatched ZnO/ZnSe and ZnO/ZnS core-shell nanowires*

The lattice mismatch strain in planar heterostructures allows for a critical thickness and composition, thus limiting the exploration of high-performance planar devices. The nanowire geometry provides new strain relaxation mechanisms that facilitate heteroepitaxy at unusually high lattice mismatch between dissimilar materials, enabling strain-induced band structure engineering (Hyun et al., 2013).

The ZnO/ZnSe core-shell nanowires were synthesized by using a two-step technique, combining chemical vapor deposition of ZnO and pulsed laser deposition (PLD) of ZnSe (Wang et al., 2008b). Figure 4.9a shows a lowmagnification TEM image of a ZnO/ZnSe core/shell nanowire with a rough external surface, but a sharp interface between the core and shell. The ZnSe shell grows directly in the radial direction from the surface of ZnO nanowire with a thickness of ~5 to 8 nm. A HRTEM image taken from the interface region between the ZnO core and ZnSe shell (specified in the rectangular area in Figure 4.9a), as shown in Figure 4.9b, reveals that ZnO and ZnSe are of WZ and ZB crystal structures, respectively. At the interface, an epitaxial growth of ZnSe from ZnO core is observed. The interface is smooth, and no transitional layer is found in between. The axis of the ZnO nanowire is identified to be the WZ *c*-axis. The epitaxial growth relationship of the WZ ZnO core and ZB ZnSe shell has been identified as [0001]ZnO//[001] ZnSe and (2-1-10)ZnO//(011)ZnSe. Inset in Figure 4.9b are the fast Fourier transform (FFT) patterns of ZnO core and ZnSe shell, indexed as WZ and ZB structure with zone axis of [2-1-10] and [011], respectively, which also confirms the above epitaxial growth relationship. Defects were also observed in the interface along the *c*-axis of ZnO due to the large lattice mismatch (8.8%) along the nanowire axis between $c = 0.521$ nm for ZnO and $a = 0.567$ nm for ZnSe. Note that the lattice mismatch along the nanowire axis would be much larger (~25%) if ZnO and ZnSe were both in the WZ phase. The spatial distributions of the atomic composition across the ZnO/ZnSe core/shell nanowire were obtained by a nanoprobe EDS line-scan analysis (marked by a line in Figure 4.9a),

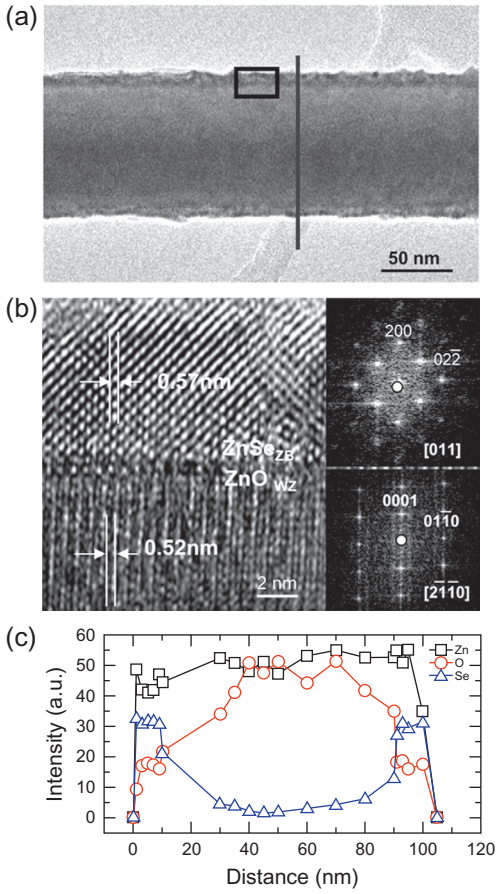

Figure 4.9 (a) Low-magnification TEM micrograph of a ZnO/ZnSe core/shell nanowire. A thin layer of ZnSe was coated on the ZnO nanowire. (b) High-resolution TEM image of the interface of the core/shell heterostructure, enlarged from the rectangular area in (a), showing the epitaxial growth relationship of the ZnO wurtzite core and ZnSe zinc blende shell. Inset shows fast Fourier transfer (FFT) patterns of rectangular areas in (b). (c) EDS nanoprobe line-scan on elements Zn, Se, and O, across the ZnO/ZnSe core/shell nanowire, indicated by a line shown in (a). Adapted with permission from Wang et al. (2008b). Copyright © 2008 WILEY-VCH Verlag GmbH & Co. KGaA, Weinheim.

showing that the ZnO nanowire was homogeneously coated, as shown in Figure 4.9c. It is also found that epitaxial growth only occurred during high-temperature deposition, and no epitaxial growth was found at room temperature deposition, indicating the epitaxial growth between ZnO and ZnSe demands favorable thermodynamic as well as kinetic conditions.

An even higher lattice mismatched system, ZnO/ZnS core-shell nanowire, was also synthesized using the same two-step technique (Wang et al., 2010b). Figure 4.10a is a representative low-magnification TEM image for a ZnO/ZnS core-shell nanowire, showing sharp interfaces and a shell layer of ~12 nm. The HRTEM image taken from the area labeled as b in Figure 4.10a reveals the detailed interface structure between the core and shell. Despite the presence of lattice distortion and stacking faults, both the core and shell exhibit lattice fringes and can be further identified as WZ and zinc blende (ZB) structures, respectively, thus indicating that the ZnS shell layer was grown over the ZnO core. The magnified HRTEM image of the core and shell taken from rectangles c and d in Figure 4.10a and their corresponding fast Fourier transform

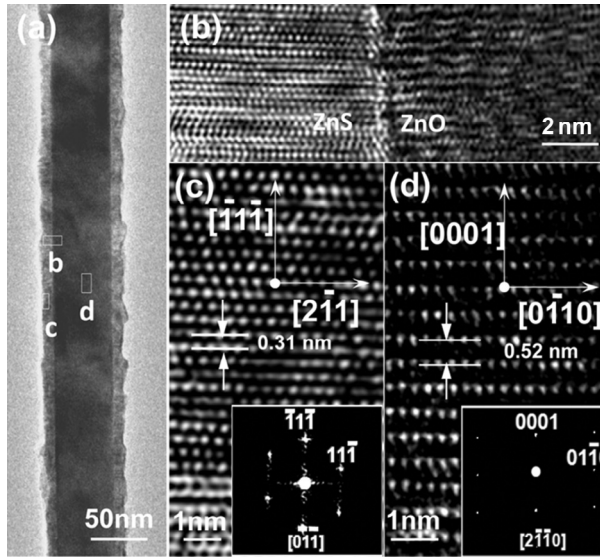

Figure 4.10 (a) Low-magnification TEM micrograph of a ZnO/ZnS core/shell nanowire, showing a thin layer of ZnS coated on the ZnO nanowire. (b) High-resolution TEM image of the interface of the core/shell heterostructure, enlarged from the rectangular area in (a), showing the epitaxial growth relationship of ZnO wurtzite core and ZnS zinc blende shell. (c and d) Atomic resolution images of the core and shell areas taken from the rectangular areas in (c), respectively. The insets in (c and d) represent the corresponding fast Fourier transfer patterns. Reprinted with permission from Wang et al. (2010b). Copyright 2010, AIP Publishing LLC.

(FFT) patterns are also shown in Figure 4.10c and d. The marked interplanar d spacings of 0.31 and 0.52 nm correspond, respectively, to the (-11-1) lattice plane of ZB ZnS with the [011] zone axis and the (0001) lattice plane of WZ ZnO with the [2-1-10] zone axis. Thus, the core and shell are determined as epitaxial growth with the growth relationship of $[0001]_{ZnO}//[-11-1]_{ZnS}$ and $[01-10]_{ZnO}//[21-1]_{ZnS}$, in contrast to that for the previously studied ZnO/ZnSe system, where $[0001]_{ZnO}//[001]_{ZnSe}$ was observed.

The epitaxial growth of WZ ZnS and ZnO has been reported in many nanoheterostructures in the planar form even though a large lattice mismatch (~20%) exists (Lu et al., 2009; Wu et al., 2007). In our case, although the lattice mismatch between the WZ ZnO and ZB ZnS is still fairly large (~19%), it appears that various factors, including perhaps the geometry of the "substrate" (the ZnO nanowire), size of the core, growth temperature, and nonthermal equilibrium condition, play roles in successfully growing such an epitaxial core/shell heterostructure. However, due to the large lattice mismatch, structure defects, such as stacking faults and lattice distortion as shown in Figure 4.10b, inevitably exist in order to release strain energy when the shell layer grows thicker. Further shell growth results in roughening and grain formation that provides additional strain relief. This could explain the rough external surface of the ZnS shell.

4.4.2.2 Nearly lattice-matched CdSe/ZnTe core-shell nanowires

The unique geometric feature of the core-shell nanowires offers great flexibility to release the strain at epitaxial interfaces. Nonetheless, the extended defects, such as dislocation and stacking faults, in the core-shell nanowire could still negatively impact the electronic and optical properties. CdSe and ZnTe stand out as an optimal combination in the II-VI semiconductor materials for constructing a high-quality heteroepitaxial junction because of their small lattice mismatch, similar thermal expansion coefficients, and well-established doping capability (Phillips et al., 1991).

Figure 4.11a shows a low-magnification TEM image of several CdSe/ZnTe nanowires. The morphology of coated nanowires presented some nanoparticles on the surface. The presence of these nanoparticles could be attributed to the emission of microscopic particulates from solid targets when irradiated by a laser beam. One representative lower-magnification TEM image of a single coated nanowire in

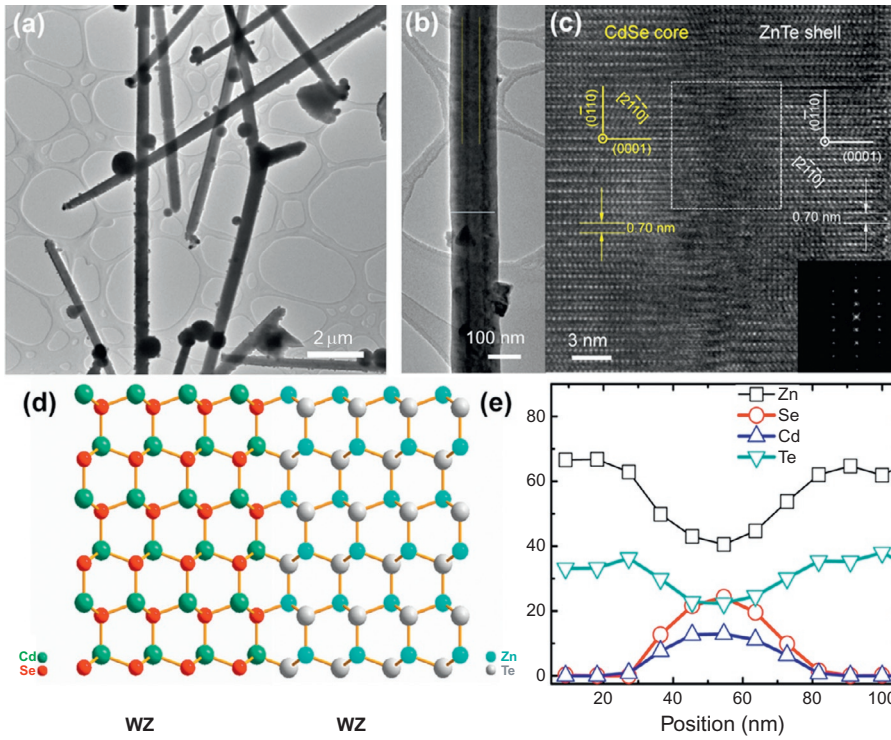

Figure 4.11 (a) Low-magnification TEM image of CdSe/ZnTe core-shell nanowires. (b) A representative TEM image of an individual CdSe/ZnTe core-shell nanowire, clearly showing the smooth surface and core-shell geometry. (c) HRTEM images of a typical core-shell interface manifesting the epitaxial growth relationship of $CdSe_{WZ}$ and $ZnTe_{WZ}$; Inset shows the FFT of the area marked as a dashed frame. (d) Ball and stick model of the relaxed CdSe (WZ) /ZnTe (WZ) structure. (e) Nanoprobe EDS scanning along the line marked in (b), suggesting the conformal shelling and absence of interfacial diffusion.

Figure 4.11b revealed that the nanowire exhibited core-shell geometry, if we neglect the microscopic particulates on the surface. The interface of the core and shell can be easily distinguished by the phase contrast, as highlighted by the dash lines. The core had a diameter of 80 nm, and the thickness of the shell was around 20 nm. To obtain detailed information about the interface, a high-resolution TEM image was recorded at the interface, shown in Figure 4.11c. Most of the lattice fringes of the core and shell along the interface of the nanowire were well matched and continuous, despite a few dislocations. Further structural analysis revealed that both the core and shell were crystallized in WZ structures, and an epitaxial growth relationship could be assigned as $(0001)_{CdSe}//(0001)_{ZnTe}$ and $(01\ \bar{1}0)_{CdSe}//(01\ \bar{1}0)_{ZnTe}$. The FFT of the dashed rectangular area across the interface shows one set of diffraction patterns, further confirming the epitaxial growth between the core and shell. An atomistic model of a WZ/WZ heterostructure was illustrated in Figure 4.11d. The Cd and Se atoms have been marked in green and red for WZ CdSe, respectively, while Zn and Te atoms have been marked in cyan and gray, respectively, for WZ ZnTe. Owing to the same WZ crystal structure and close lattice parameters, nearly identical atom arrangements were demonstrated. A special concern in fabricating core-shell nanowires is the interfacial diffusion between the core and shell. To clarify this in CdSe/ZnTe core-shell nanowires, we employed nanoprobe EDS line scanning along the white line marked in Figure 4.11a. The element dispersive distribution data, as shown in Figure 4.11e, verified that there was no interfacial diffusion occurring between the core and shell in this synthesis condition. Additionally, this result also further confirmed the conformal coating of ZnTe on CdSe nanowires.

4.4.3 TEM characterization of surface coating of gas-sensing layers and light absorption QDs on nanowires

Besides coating of epitaxial shell layer on the surface of single crystal nanowire, polycrystalline coatings on single nanowires or nanowire arrays are also desired for various applications. For instances, the core nanowires can provide structural templates to support 3D functional layers for gas sensing (Chen et al., 2010, 2011) or high-performance conduction channels for charge collection in photovoltaic devices (Chen and Wang, 2013), while the polycrystalline shell can capture targeting gas molecules or harvest photons.

4.4.3.1 Structural characterization of polycrystalline SnO_2-coated ZnO nanowires with Pd decoration

Polycrystalline SnO_2-coated ZnO nanowires with Pd decoration have been proven as high performance nanomaterials that can detect low concentrations of industrial gases (i.e., H_2S, NO_2, NH_3) at room temperature. A polycrystalline coating is preferred for gas sensor applications. First, the polycrystalline film has a larger surface area to capture gas molecules. Second, the energy barriers between the nanocrystals can be tuned by surface gas adsorption, which induces device conductivity changes (Shimizu and Egashira, 1999). In this study, the Pd decoration was used to further enhance the

sensitivity by helping the dissociation of oxygen molecules during the transduction process (Kolmakov et al., 2005).

A typical fabrication process for coating of SnO_2 nanocrystals and Pd-nanoparticles on ZnO nanowires is shown in Figure 4.12a. The ZnO nanowire arrays were first grown by a hydrothermal method (Vayssieres, 2003) or chemical vapor deposition (Wang et al., 2008b). Physical vapor deposition methods, such as PLD or RF sputtering, were used to deposit the SnO_2 shell layer on the ZnO nanowire surfaces. In the last step, well-controlled DC sputtering was employed to apply isolated Pd nanoparticles on the SnO_2 surface. The electrical measurements (Chen et al., 2010) confirmed that the ZnO nanowires play the role of structural templates, and the electrical current mostly flowed through the polycrystalline SnO_2 shell layers. To understand the structures of the SnO_2 coating, a fundamental TEM technique was used to separate the SnO_2 phase from ZnO nanowires. In Figure 4.12c, a high-contrast BF image was formed using the direct electron beam that was selected by the objective aperture. Although we can identify the particulate nature of the surface coating in the BF image, we cannot fully separate the shell layer coating from the ZnO core. To highlight the SnO_2 phase, a DF image (Figure 4.12e) was formed using a portion of the Bragg diffracted beam. In such a DF image, only the SnO_2 phase showed the bright

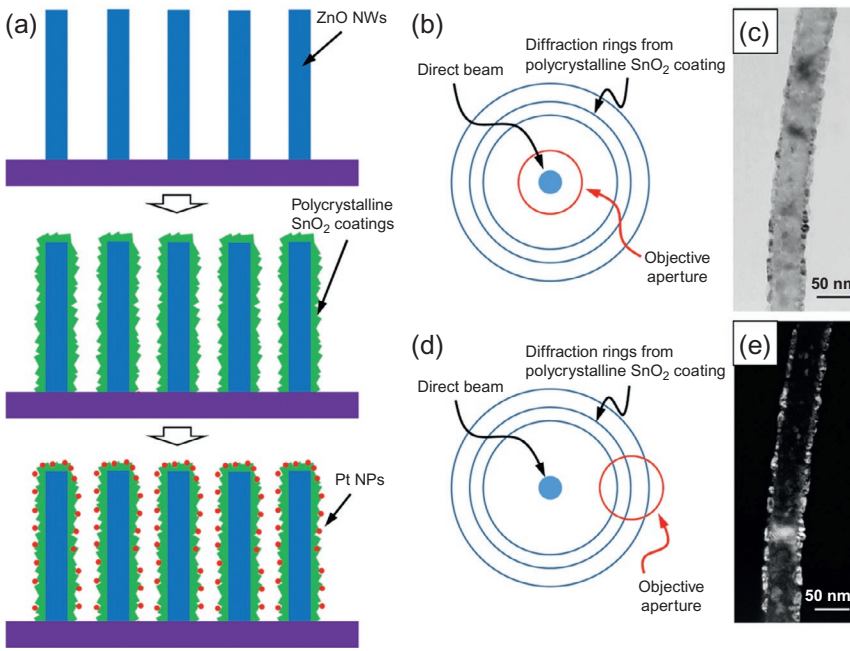

Figure 4.12 (a) Schematic diagrams of nanowire cross sections showing the growth processes of polycrystalline Pd/SnO_2 nanowire using a ZnO-nanowire template. (c) and (e) Conventional BF and DF images of a Pd/SnO_2-coated ZnO nanowire. The diagrams (b) and (d) show the selection of electron beam for forming BF and DF images, respectively. Diffraction from single-crystal ZnO is not shown in the diagrams.

contrast, which clearly highlighted the polycrystalline SnO_2 coating on the nanowire. Although DF imaging is a very simple method, it is very effective in characterizing this type of core/shell structures.

However, it is difficult to identify the Pd decorations using conventional imaging techniques in TEM because of the much smaller size of Pd nanoparticles (~2-3 nm). The HRTEM image can provide the lattice fringes of the whole structure, including the single-crystal core and polycrystalline shell, as shown in Figure 4.13a, but it is difficult to separate Pd from SnO_2 nanoparticles. Fortunately, Pd has a much higher atomic number compared to Sn or Zn, which can be highlighted by Z-contrast imaging.

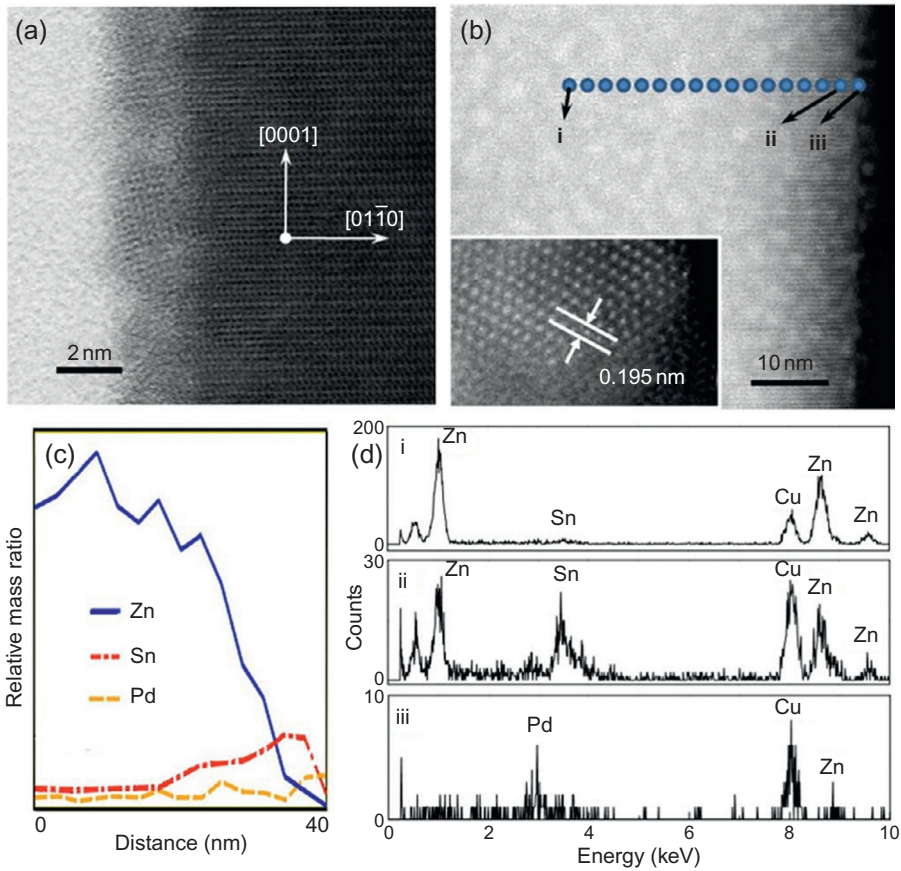

Figure 4.13 (a) High-resolution TEM image showing the ZnO nanowire with polycrystalline SnO_2 and Pd-nanocrystal coating. (b) HAADF Z-contrast image taken under a *Cs*-corrected field-emission TEM highlighting the Pd-nanocrystal distribution. Inset shows the lattice image of a Pd nanocrystal taken by HAADF-STEM through [110] zone. (c) Composition distribution obtained by nanoprobe XEDS linescan across the nanowire. The sampling points are indicated in (b). (d) Three EDS spectra obtained at the (i) ZnO core, (ii) SnO_2 layer, and (iii) outermost Pd coating. Adapted with permission from Chen et al. (2010). Copyright (2010) IEEE.

Z-contrast images can be formed by HAADF detector under the STEM mode. Using the forward-scattered electron at high angle (>3 degrees) can avoid the signal of Bragg scattering from crystalline specimens and maintain the contrast signal associated with the atomic number (Williams and Carter, 2009). One important advantage of HAADF images is that, compared with phase contrast images, the contrast is generally unaffected by small changes in objective lens defocus and specimen thickness (Williams and Carter, 2009). As shown in Figure 4.13b, the HAADF-STEM image of the nanowire has high brightness of Pd nanoparticles. These nanoparticles were homogeneously dispersed on the surface of the nanowire with a size of about 2 to 3 nm and interparticle distance of 2 nm. Because the Z-contrast image resolution is close to the probe diameter, the atomic resolution of HAADF-STEM image is possible in TEM with a field-emission gun (FEG) with a probe size of <0.3 Å or a *Cs*-corrected lens with a sub-Angstrom probe. The inset of Figure 4.13b is a HAADF-STEM image of a single Pd nanoparticle attached on SnO_2 surface collected with *Cs*-corrected TEM. It clearly showed the bright lattice fringes of Pd, which can be easily distinguished from the background SnO_2 lattice. This method is extremely useful for the identification of noble metal catalysts in metal oxides for gas-sensing applications, because the structures and distributions of the catalysts determine the performance of the sensing layers. By taking advantage of the sub-Angstrom probe in *Cs*-corrected FEG-TEM, high-resolution X-ray energy dispersion spectroscopy can also be done (Figure 4.13c and d), which further confirmed the structures of the nanowires.

4.4.3.2 Structural characterization of nanowire-based quantum-dot-sensitized solar cells (QDSSC)

Nanowire-based QDSSCs may work as the platform for low-cost high-efficiency solar energy conversion. There are multiple advantages to directly attach QDs on the nanowire surface for sunlight absorption and conversion. First, the energy bandgap of QDs can be tuned by adjusting the QD size to match the sunlight spectrum for efficient light absorption. Second, multi-exciton-generation (Sambur et al., 2010a) in QDs may circumvent the Shockley-Queisser limit of conventional *p-n* junction-based solar cells. Third, the single-crystalline nanowires provide direct fast electron transport channels for efficient charge collection. The performance of QDSSCs highly relies on the structural configuration of the QDs and the metal oxide nanowires. The structure of the contacts between the QDs and the metal oxide is one of the important factors for efficient electron transfer from QDs to metal oxides (Robel et al., 2006). The surface condition of the QDs also determines the hole-harvesting process between the QDs and electrolyte (Shen et al., 2008).

We use solar cells based on CdSe QD-sensitized Zn_2SnO_4 nanowires as an example to explain how the detailed structural characterization with a TEM can help our understanding of the relation between the structure and solar cell performance. The QDSSC photoanodes were prepared with a two-step method (Dai et al., 2012). The single-crystal Zn_2SnO_4 nanowires were first grown by conventional CVD through a VLS mechanism and transferred onto transparent conducting metal oxide using a printing method (Chen et al., 2012). The CdSe QDs were directly grown on the Zn_2SnO_4

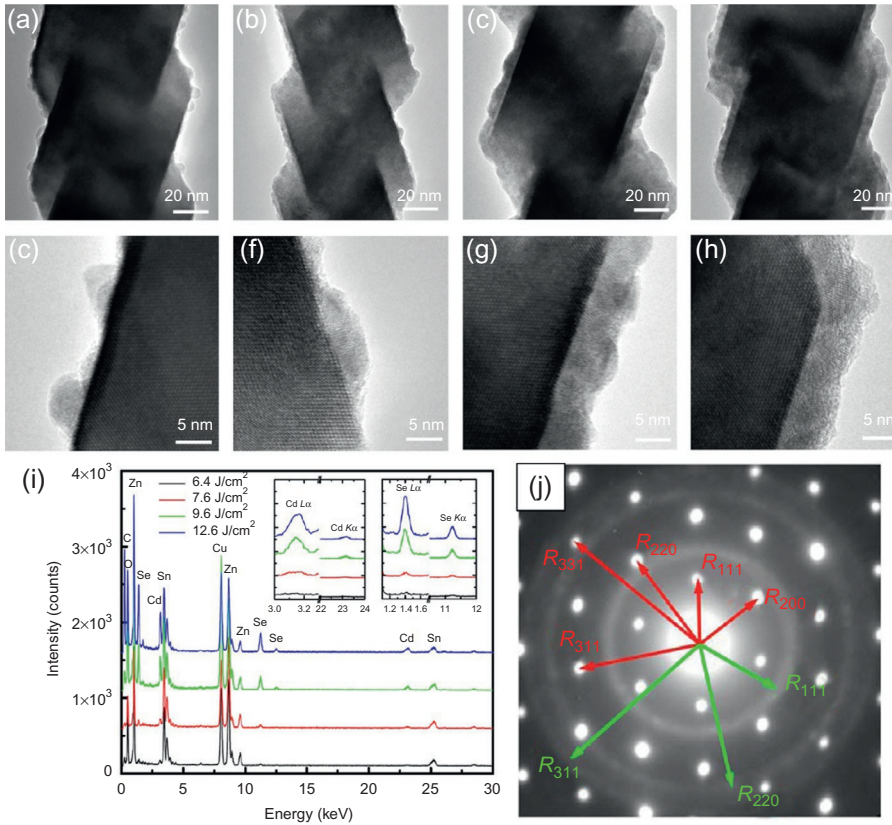

Figure 4.14 Low and high magnification TEM images of CdSe QDs-coated Zn_2SnO_4 nanowires coated using PLD with different laser energies: (a and e) 6.4 J/cm^2; (b, f) 7.6 J/cm^2; (c, g) 9.6 J/cm^2; (d, h) 12.6 J/cm^2. (i) XEDS spectra of Zn_2SnO_4 nanowires after PLD coating of CdSe QDs with different laser energy densities. The insets are enlarged peaks for Cd and Se. The spectra are shifted for clarification. (j) SAED patterns of Zn_2SnO_4 nanowire coated with CdSe QDs along $[011]_{ZTO}$ zone axis.
Adapted with permission from Nano Lett. 2012, 12, 4718. Copyright (2012) American Chemical Society.

nanowire surface by PLD. Figure 4.14a–h show a series of TEM images of CdSe QDs-coated Zn_2SnO_4 nanowires prepared under different laser fluences. These low-magnification images indicated that the CdSe QDs sparsely distributed on the nanowire surfaces when a low laser fluence was used but started forming dense QD layers when the laser fluence increased. Interestingly, the QDs have a similar size (∼5 nm) that is independent of the fluence. The deposition of CdSe QDs on different substrates also showed that the size of QDs is self-limited (Donnelly et al., 2007) and independent of the substrate's material. The XEDS measurements (Figure 4.14i) further confirmed the amount of CdSe QDs coating increased as the laser fluence

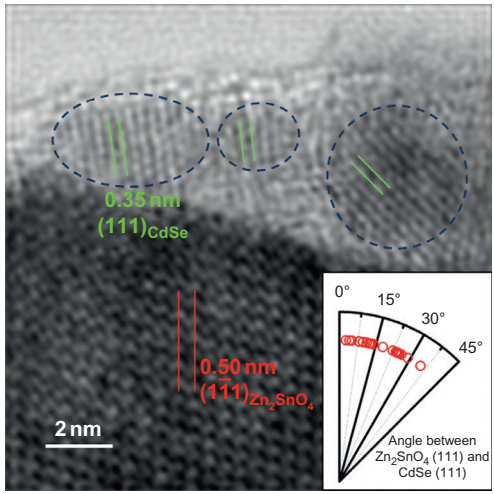

Figure 4.15 A typical HRTEM image of CdSe QDs coated on Zn_2SnO_4 nanowires by pulsed laser deposition observed along Zn_2SnO_4 [011] zone axis. The (111) planes of each CdSe QDs and (1-11) planes of Zn_2SnO_4 were labeled by green and red color, respectively. The inset shows the angles between CdSe (111) planes and (1-11) planes were measured from HRTEM images. Twenty-four CdSe QDs were examined.
Adapted with permission from Nano Lett. 2012, 12, 4718. Copyright (2012) American Chemical Society.

increased. However, despite the thicker coating of CdSe QDs for higher absorption of sunlight, the QDSSCs coated with higher laser fluences had lower efficiency (Dai et al., 2012), which may be explained by the bandgap change and the lower hole harvesting for inner layers of QDs as QDs stack on each other (Guijarro et al., 2009). The SAED shown in Figure 4.14j also indicated that the QDs were randomly attached onto the Zn_2SnO_4 nanowires without specific orientation. To further understand the interfaces of QD-to-nanowire and QD-to-electrolyte, HRTEM image (Figure 4.15) was taken at the Zn_2SnO_4 surface. An amorphous shell layer was clearly shown on the surface of CdSe QDs. The role of this amorphous layer in the electron transfer from QDs to metal oxide or hole harvesting from QDs to electrolyte is still unclear, although a number of studies (Sambur et al., 2010b; Shen et al., 2008; Robel et al., 2006) have been conducted to investigate the effects of surface ligands or inorganic coatings. But this observation on the surface structures provides a valuable reference for future characterization of solar cell performance. Additionally, the measurement of the angles between the lattice fringes of CdSe and Zn_2SnO_4 confirmed that there is no epitaxial relation between the QDs and the nanowire.

In summary, TEM observation is a very important technique to characterize the surface structures of nanowire-based gas sensors and solar cells, where the surface condition determines the final device performance. Even the very fundamental techniques (i.e., BF, DF imaging, SAED, HRTEM) in a conventional TEM can provide very useful information for the optimization of device performance.

4.5 Concluding remarks

TEM investigations accompany almost every publication regarding 1D nanostructure growth and play an increasingly important role in studying the structure-property relationship. In this chapter, we have demonstrated the capabilities of TEM on the

structure analysis of 1D nanostructures with imaging, diffraction, and spectroscopies. Taking ZnO nanoneedles as an example, we have showed the polarity determination by CBED and proposed the rational growth mode. TEM analysis in ultrathin ZnO nanobelts revealed that the growth of such a thin nanobelt was induced by the stacking faults. In addition, we have given a comprehensive TEM analysis on nanowire superlattice and heterostructured nanowires, aiming at highlighting the capabilities of TEM in growth mechanism studies, interface investigations, and composition mapping in complex nanoheterostructures. The *in situ* TEM techniques, although not covered in this chapter, provide the opportunity to investigate the nanowire growth and response to external stimuli in a real-time manner, facilitating the basic understanding of the growth mechanism and the surface energetics of 1D nanostructures.

On the other hand, 1D nanostructure research provides an excellent platform for fundamental science research for epitaxial growth, interface, and surface sciences. In terms of material synthesis, 1D single-crystal materials can be easily grown through simple CVD or solution methods without the strict requirements of high vacuum and substrate lattice match for the single crystal thin film growth. Moreover, the specimen preparation of 1D nanostructure samples for TEM observations is much easier than thin films, allowing easy evaluation of the surfaces and interfaces of the structures while avoiding structural damages or contamination from sample preparation.

In conclusion, the full spectrum of the TEM characterization has already shown significant impact in the field of materials science and nanotechnology and will continue to benefit the scientific and industry communities.

Acknowledgments

The authors acknowledge the collaboration with colleagues who have been cited in the references. This work was supported by the DARPA Grant No. HR0011-09-1-0047, research grants from Louisiana Board of Regents Contract Nos. LEQSF(2007-12)-ENH-PKSFI-PRS-04, LEQSF(2008-11)-RD-B-10, and LEQSF(2011-13)-RD-B-08, and American Chemical Society Petroleum Research Fund under PRF No 48796-DN110.

References

Andrews, S.C., Fardy, M.A., Moore, M.C., Aloni, S., Zhang, M.J., Radmilovic, V., Yang, P.D., 2011. Atomic-level control of the thermoelectric properties in polytypoid nanowires. Chem. Sci. 2, 706–714.

Bjork, M.T., Ohlsson, B.J., Sass, T., Persson, A.I., Thelander, C., Magnusson, M.H., Deppert, K., Wallenberg, L.R., Samuelson, L., 2002. One-dimensional steeplechase for electrons realized. Nano Lett. 2, 87–89.

Borgstrom, M.T., Verheijen, M.A., Immink, G., De Smet, T., Bakkers, E., 2006. Interface study on heterostructured GaP-GaAs nanowires. Nanotechnology 17, 4010–4013.

Cao, B., Chen, J., Huang, R., Ikuhara, Y.H., Hirayama, T., Zhou, W., 2011. Axial growth of Zn_2GeO_4/ZnO nanowire heterojunction using chemical vapor deposition. J. Cryst. Growth 316, 46–50.

Cao, B., Shi, T., Zheng, S., Ikuhara, Y.H., Zhou, W., Wood, D., Al-Jassim, M., Yan, Y., 2012. New polytypoid $SnO_2(ZnO:Sn)_m$ nanowire: characterization and calculation of its electronic structure. J. Phys. Chem. C 116, 5009–5013.

Chen, J.J., Wang, W.Y., 2013. Carrier transport processes in dye sensitized solar cells based on Zn_2SnO_4 nanostructures studied by intensity modulated photocurrent/photovoltage spectroscopy. Appl. Phys. Lett. 102, 213904.

Chen, J.J., Wang, K., Huang, R., Saito, T., Ikuhara, Y.H., Hirayama, T., Zhou, W.L., 2010. Facile route to polycrystalline Pd/SnO_2 nanowires using ZnO-nanowire templates for gas-sensing applications. IEEE Trans. Nanotechnol. 9, 634–639.

Chen, J.J., Wang, K., Zhou, W.L., 2011. Vertically aligned ZnO nanorod arrays coated with SnO_2/noble metal nanoparticles for highly sensitive and selective gas detection. IEEE Trans. Nanotechnol. 10, 968–974.

Chen, J.J., Lu, Y., Wang, W.Y., 2012. Zn_2SnO_4 nanowires as photoanode for dye-sensitized solar cells and the improvement on open-circuit voltage. J. Phys. Chem. C 116, 10841–10847.

Colinge, J.P., Lee, C.W., Afzalian, A., Akhavan, N.D., Yan, R., Ferain, I., Razavi, P., O'Neill, B., Blake, A., White, M., Kelleher, A.M., McCarthy, B., Murphy, R., 2010. Nanowire transistors without junctions. Nat. Nanotechnol. 5, 225–229.

Da Silva, J.L.F., Yan, Y.F., Wei, S.H., 2008. Rules of structure formation for the homologous InMO(3)(ZnO)(n) compounds. Phys. Rev. Lett. 100.

Dai, Q.L., Chen, J.J., Lu, L.Y., Tang, J.K., Wang, W.Y., 2012. Pulsed laser deposition of CdSe quantum dots on Zn_2SnO_4 nanowires and their photovoltaic applications. Nano Lett. 12, 4187–4193.

De La Mata, M., Magen, C., Gazquez, J., Utama, M.I.B., Heiss, M., Lopatin, S., Furtmayr, F., Fernandez-Rojas, C.J., Peng, B., Morante, J.R., Rurali, R., Eickhoff, M., Morral, A.F.I., Xiong, Q.H., Arbiol, J., 2012. Polarity assignment in ZnTe, GaAs, ZnO, and GaN-AlN nanowires from direct dumbbell analysis. Nano Lett. 12, 2579–2586.

Ding, Y., Wang, Z.L., 2004. Structure analysis of nanowires and nanobelts by transmission electron microscopy. J. Phys. Chem. B 108, 12280–12291.

Ding, Y., Zhang, F., Wang, Z.L., 2013. Deriving the three-dimensional structure of ZnO nanowires/nanobelts by scanning transmission electron microscope tomography. Nano Res. 6, 253–262.

Donnelly, T., Krishnamurthy, S., Carney, K., McEvoy, N., Lunney, J.G., 2007. Pulsed laser deposition of nanoparticle films of Au. Appl. Surf. Sci. 254, 1303–1306.

Edington, J.W., 1976. Practical Electron Microscopy in Materials Science. Van Nostrand Reinhold Co, Herndon.

Espinosa, H.D., Bernal, R.A., Minary-Jolandan, M., 2012. A review of mechanical and electromechanical properties of piezoelectric nanowires. Adv. Mater. 24, 4656–4675.

Fasoli, A., Colli, A., Martelli, F., Pisana, S., Tan, P.H., Ferrari, A.C., 2011. Photoluminescence of CdSe nanowires grown with and without metal catalyst. Nano Res. 4, 343–359.

Findlay, S.D., Azuma, S., Shibata, N., Okunishi, E., Ikuhara, Y., 2011. Direct oxygen imaging within a ceramic interface, with some observations upon the dark contrast at the grain boundary. Ultramicroscopy 111, 285–289.

Fortuna, S.A., Li, X.L., 2010. Metal-catalyzed semiconductor nanowires: a review on the control of growth directions. Semicond. Sci. Technol. 25, 024005.

Gudiksen, M.S., Lauhon, L.J., Wang, J., Smith, D.C., Lieber, C.M., 2002. Growth of nanowire superlattice structures for nanoscale photonics and electronics. Nature 415, 617–620.

Guijarro, N.S., Lana-Villarreal, T., Mora-Seró, I.N., Bisquert, J., Gómez, R., 2009. CdSe quantum dot-sensitized TiO_2 electrodes: effect of quantum dot coverage and mode of attachment. J. Phys. Chem. C 113, 4208–4214.

Hsu, Y.J., Lu, S.Y., 2005. Vapor-solid growth of Sn nanowires: growth mechanism and superconductivity. J. Phys. Chem. B 109, 4398–4403.

Huang, D.L., Wu, L.L., Zhang, X.T., 2010a. Size-dependent $InAlO_3(ZnO)(m)$ nanowires with a perfect superlattice structure. J. Phys. Chem. C 114, 11783–11786.

Huang, H., Ren, X.M., Ye, X., Guo, J.W., Wang, Q., Yang, Y.S., Huang, S.W., Cai, Y.Q., 2010b. Growth of stacking-faults-free zinc blende GaAs nanowires on Si substrate by using AlGaAs/GaAs buffer layers. Nano Lett. 10, 64–68.

Hyun, J.K., Zhang, S., Lauhon, L.J., 2013. Nanowire heterostructures. Annu. Rev. Mater. Res. 43, 451–479.

Jie, J.S., Wang, G.Z., Han, X.H., Hou, J.G., 2004. Synthesis and characterization of ZnO: In nanowires with superlattice structure. J. Phys. Chem. B 108, 17027–17031.

Kempa, T.J., Day, R.W., Kim, S.-K., Park, H.-G., Lieber, C.M., 2013. Semiconductor nanowires: a platform for exploring limits and concepts for nano-enabled solar cells. Energy Environ. Sci. 6, 719–733.

Kolmakov, A., Klenov, D.O., Lilach, Y., Stemmer, S., Moskovits, M., 2005. Enhanced gas sensing by individual SnO_2 nanowires and nanobelts functionalized with Pd catalyst particles. Nano Lett. 5, 667–673.

Kotaka, Y., Yamazaki, T., Kataoka, Y., 2010. Atomic-resolution imaging and analysis with C-s-corrected scanning transmission electron microscopy. Fujitsu Sci. Tech. J. 46, 249–256.

Lapierre, R.R., Chia, A.C.E., Gibson, S.J., Haapamaki, C.M., Boulanger, J., Yee, R., Kuyanov, P., Zhang, J., Tajik, N., Jewell, N., Rahman, K.M.A., 2013. III-V nanowire photovoltaics: review of design for high efficiency. Phys. Status Solidi (RRL) Rapid Res. Lett. 7, 815–830.

Lauhon, L.J., Gudiksen, M.S., Wang, C.L., Lieber, C.M., 2002. Epitaxial core-shell and core-multishell nanowire heterostructures. Nature 420, 57–61.

Leschkies, K.S., Divakar, R., Basu, J., Enache-Pommer, E., Boercker, J.E., Carter, C.B., Kortshagen, U.R., Norris, D.J., Aydil, E.S., 2007. Photosensitization of ZnO nanowires with CdSe quantum dots for photovoltaic devices. Nano Lett. 7, 1793–1798.

Li, Y., Qian, F., Xiang, J., Lieber, C.M., 2006. Nanowire electronic and optoelectronic devices. Mater. Today 9, 18–27.

Li, D.P., Wang, G.Z., Han, X.H., Jie, J.S., Lee, S.T., 2009a. Synthesis and characterization of in-doped ZnO planar superlattice nanoribbons. J. Phys. Chem. C 113, 5417–5421.

Li, D.P., Wang, G.Z., Yang, Q.H., Xie, X., 2009b. Synthesis and photoluminescence of $InGaO_3(ZnO)(m)$ nanowires with perfect superlattice structure. J. Phys. Chem. C 113, 21512–21515.

Li, Y., Xing, Q.F., Yan, Y., Zhou, W.L., 2010. A large quantity synthesis of ZnO nanoneedles and their polarity determination. J. Nanosci. Nanotechnol. 10, 2023–2027.

Lu, M.Y., Song, J.H., Lu, M.P., Lee, C.Y., Chen, L.J., Wang, Z.L., 2009. ZnOZnS heterojunction and ZnS nanowire arrays for electricity generation. ACS Nano 3, 357–362.

Moore, D., Morber, J.R., Snyder, R.L., Wang, Z.L., 2008. Growth of ultralong ZnS/SiO_2 core-shell nanowires by volume and surface diffusion VLS process. J. Phys. Chem. C 112, 2895–2903.

Na, C.W., Bae, S.Y., Park, J., 2005. Short-period superlattice structure of Sn-doped $In_2O_3(ZnO)(4)$ and $In_2O_3(ZnO)(5)$ nanowires. J. Phys. Chem. B 109, 12785–12790.

Pennycook, S.J., Nellist, P.D., 2011. Scanning Transmission Electron Microscopy Imaging and Analysis. Springer, New York.

Petkov, N., 2013. In situ real-time TEM reveals growth, transformation and function in one-dimensional nanoscale materials: from a nanotechnology perspective. ISRN Nanotechnol. 2013, 893060.

Phillips, M.C., Yu, E.T., Rajakarunanayake, Y., Mccaldin, J.O., Collins, D.A., Mcgill, T.C., 1991. Characterization of CdSe/ZnTe heterojunctions. J. Cryst. Growth 111, 820–822.

Reiss, P., Protiere, M., Li, L., 2009. Core/shell semiconductor nanocrystals. Small 5, 154–168.

Robel, I., Subramanian, V., Kuno, M., Kamat, P.V., 2006. Quantum dot solar cells. Harvesting light energy with CdSe nanocrystals molecularly linked to mesoscopic TiO_2 films. J. Am. Chem. Soc. 128, 2385–2393.

Sambur, J.B., Novet, T., Parkinson, B.A., 2010a. Multiple exciton collection in a sensitized photovoltaic system. Science 330, 63–66.

Sambur, J.B., Riha, S.C., Choi, D., Parkinson, B.A., 2010b. Influence of surface chemistry on the binding and electronic coupling of CdSe quantum dots to single crystal TiO_2 surfaces. Langmuir 26, 4839–4847.

Shannon, R.D., 1976. Revised effective ionic-radii and systematic studies of interatomic distances in halides and chalcogenides. Acta Crystallogr. A 32, 751–767.

Shen, Q., Kobayashi, J., Diguna, L.J., Toyoda, T., 2008. Effect of ZnS coating on the photovoltaic properties of CdSe quantum dot-sensitized solar cells. J. Appl. Phys. 103, 084304.

Shimizu, Y., Egashira, M., 1999. Basic aspects and challenges of semiconductor gas sensors. MRS Bull. 24, 18–24.

Shtrikman, H., Popovitz-Biro, R., Kretinin, A., Heiblumf, M., 2009. Stacking-faults-free zinc blende GaAs nanowires. Nano Lett. 9, 215–219.

Vayssieres, L., 2003. Growth of arrayed nanorods and nanowires of ZnO from aqueous solutions. Adv. Mater. 15, 464–466.

Wagner, R.S., Ellis, W.C., 1964. Vapor-liquid-solid mechanism of single crystal growth. Appl. Phys. Lett. 4, 89–90.

Wang, H.L., Upmanyu, M., Ciobanu, C.V., 2008a. Morphology of epitaxial core-shell nanowires. Nano Lett. 8, 4305–4311.

Wang, K., Chen, J.J., Zhou, W.L., Zhang, Y., Yan, Y.F., Pern, J., Mascarenhas, A., 2008b. Direct growth of highly mismatched type IIZnO/ZnSe core/shell nanowire arrays on transparent conducting oxide substrates for solar cell applications. Adv. Mater. 20, 3248–3253.

Wang, K., Chen, J.J., Chen, Y.X., Zhou, W.L., 2010a. A large quantity synthesis of ultra-thin ZnO nanobelts induced from stacking faults. J. Nanosci. Nanotechnol. 10, 2257–2260.

Wang, K., Chen, J.J., Zeng, Z.M., Tarr, J., Zhou, W.L., Zhang, Y., Yan, Y.F., Jiang, C.S., Pern, J., Mascarenhas, A., 2010b. Synthesis and photovoltaic effect of vertically aligned ZnO/ZnS core/shell nanowire arrays. Appl. Phys. Lett. 96, 123105.

Wang, N.W., Yang, Y.H., Chen, J., Xu, N.S., Yang, G.W., 2010c. One-dimensional Zn-doped In_2O_3-SnO_2 superlattice nanostructures. J. Phys. Chem. C 114, 2909–2912.

Williams, D.B., Carter, C.B., 2009. Transmission Electron Microscopy: A Textbook for Materials Science. Springer, New York.

Wu, Y.Y., Fan, R., Yang, P.D., 2002. Block-by-block growth of single-crystalline Si/SiGe superlattice nanowires. Nano Lett. 2, 83–86.

Wu, X., Jiang, P., Ding, Y., Cai, W., Xie, S.S., Wang, Z.L., 2007. Mismatch strain induced formation of ZnO/ZnS heterostructured rings. Adv. Mater. 19, 2319–2323.

Xiang, J., Lu, W., Hu, Y.J., Wu, Y., Yan, H., Lieber, C.M., 2006. Ge/Si nanowire heterostructures as high-performance field-effect transistors. Nature 441, 489–493.

Yan, Y., Pennycook, S.J., Dai, J., Chang, R.P.H., Wang, A., Marks, T.J., 1998. Polytypoid structures in annealed In_2O_3-ZnO films. Appl. Phys. Lett. 73, 2585–2587.

Yang, P., Yan, R., Fardy, M., 2010. Semiconductor nanowire: what's next? Nano Lett. 10, 1529–1536.

Ye, J.F., Qi, L.M., 2008. Solution-phase synthesis of one-dimensional semiconductor nanostructures. J. Mater. Sci. Technol. 24, 529–540.

Zhang, Y., Wang, L.W., Mascarenhas, A., 2007. "Quantum coaxial cables" for solar energy harvesting. Nano Lett. 7, 1264–1269.

Zhao, Y.C., Chen, M., Xu, T., Liu, W.M., Liu, X., 2004. Preparation of porous anodic oxide film on aluminum and its application in synthesis of 1-dimensional nanomaterials. Chin. J. Chem. Phys. 17, 369–374.

Zimmler, M.A., Capasso, F., Muller, S., Ronning, C., 2010. Optically pumped nanowire lasers: invited review. Semicond. Sci. Technol. 25, 024001.

Characterization of strains and defects in nanomaterials by diffraction techniques

5

D. Balzar
University of Denver, Denver, CO, USA

5.1 Introduction

X-ray diffraction was first used over a century ago to identify a crystal structure of kitchen salt. Since that day, diffraction by X-rays, neutrons, and electrons has become one of the major tools for the determination of not only the crystal structure but other properties of condensed matter as well. Diffraction is among the selected few techniques that give valuable information about the materials at multiple scales: crystal structure and defects at the nanoscale (nanometers), orientation and distribution of grains (hundreds to thousands of nanometers) at the microscale, and phase composition and macrostresses (hundreds of nanometers to centimeters) at the macroscale.

The aim here is to focus on the characterization of crystalline defects and strains in materials. In general, any deformation of a perfect three-dimensional crystalline lattice will affect the diffraction pattern. Therefore, a comparison with a diffraction pattern of a "standard" sample without significant crystalline defects is a key to deducing information on the type and density of defects. There is an extensive literature on the subject; here, we cite a review article by Balzar (1999).

The defects and strains affect the diffraction pattern in two ways: Bragg reflections (profiles) can be shifted and/or (asymmetrically) broadened, and the intensity between the Bragg profiles (background) can be increased due to diffuse scattering. Here, we focus on the former effect. In the first part, we discuss diffraction profile shift due to a change of interplanar spacing caused by residual strains/stresses at the macroscale. In the second part, we focus on the diffraction profile broadening, due to both size and strain broadening, at the microscale level.

5.2 Section 1: diffraction profile shift due to residual strains/stresses

5.2.1 Introduction

One of the oldest applications of powder diffraction is the investigation of the elastic macro strain and stress state in polycrystalline samples. A recent review of the main theoretical approaches in this field can be found in the book chapter by Popa (2008).

Modeling, Characterization and Production of Nanomaterials. http://dx.doi.org/10.1016/B978-1-78242-228-0.00005-3
Copyright © 2015 Elsevier Ltd. All rights reserved.

According to the definitions and notations from that article, the elements of strain and stress tensors dependent on the crystallite orientation, called also *strain* and *stress orientation distribution functions* (*SODF*), are $e_i(g), s_i(g), (i=1,6)$, in the sample orthogonal reference system $(\mathbf{y}_1, \mathbf{y}_2, \mathbf{y}_3)$, and $\varepsilon_i(g), \sigma_i(g), (i=1,6)$, in the crystal reference system $(\mathbf{x}_1, \mathbf{x}_2, \mathbf{x}_3)$, where $g=(\phi_1, \Phi_0, \phi_2)$ is the triplet of Euler angles transforming $(\mathbf{y}_i)$ into $(\mathbf{x}_i)$. The SODF are connected by the single crystal Hooke equations that in the system $(\mathbf{x}_i)$ are the following:

$$\sigma_i(g) = \sum_{j=1}^{6} C_{ij}\rho_j\varepsilon_j(g) \tag{5.1a}$$

$$\varepsilon_i(g) = \sum_{j=1}^{6} S_{ij}\rho_j\sigma_j(g) \tag{5.1b}$$

Here C_{ij} and S_{ij} are the single crystal stiffness and compliance elastic constants and (ρ_i) is the vector $(1,1,1,2,2,2)$. In the sample system $(\mathbf{y}_i)$ the Hooke equations and the single crystal elastic constants follow as:

$$s_i(g) = \sum_{j=1}^{6} C_{ij}(g)\rho_j e_j(g) \tag{5.2a}$$

$$e_i(g) = \sum_{j=1}^{6} S_{ij}(g)\rho_j s_j(g) \tag{5.2b}$$

$$C_{ij}(g) = \rho_j^{-1}\sum_{m=1}^{6}\sum_{k=1}^{6} P_{im}(g)C_{mk}\rho_k Q_{kj}(g) \tag{5.3a}$$

$$S_{ij}(g) = \rho_j^{-1}\sum_{m=1}^{6}\sum_{k=1}^{6} P_{im}(g)S_{mk}\rho_k Q_{kj}(g) \tag{5.3b}$$

By P_{ij} and Q_{ij} were denoted the matrices of transformation of strain/stress tensors from crystal into sample reference system and inversely:

$$(e_i, s_i) = \sum_{j=1}^{6} P_{ij}(\varepsilon_j, \sigma_j) \tag{5.4a}$$

$$(\varepsilon_i, \sigma_i) = \sum_{j=1}^{6} Q_{ij}(e_j, s_j) \tag{5.4b}$$

The quantity measured in a diffraction experiment on polycrystal is the mean value of the strain along the reciprocal lattice vectors $\pm\mathbf{H}$ fulfilling the Laue equations

$\mathbf{Q} = \pm\mathbf{H}$; here $\mathbf{Q}$ is the wave vector transfer. If $\mathbf{h}$ and $\mathbf{y}$ are the unit vectors of $\mathbf{H}$ and $\mathbf{Q}$ in $(\mathbf{x}_i)$ and $(\mathbf{y}_i)$, respectively, the measured strain can be written in two equivalent ways:

$$\langle \varepsilon_{\mathbf{h}}(\mathbf{y}) \rangle = P_{\mathbf{h}}^{-1}(\mathbf{y}) \sum_{i=1}^{6} E_i \rho_i \frac{1}{2\pi} \int_{\pm\mathbf{h}||\mathbf{y}} \mathrm{d}\omega \varepsilon_i\left(g^{\pm}\right) f\left(g^{\pm}\right) \tag{5.5a}$$

$$\langle e_{\mathbf{h}}(\mathbf{y}) \rangle \equiv \langle \varepsilon_{\mathbf{h}}(\mathbf{y}) \rangle = P_{\mathbf{h}}^{-1}(\mathbf{y}) \sum_{i=1}^{6} F_i \rho_i \frac{1}{2\pi} \int_{\pm\mathbf{h}||\mathbf{y}} \mathrm{d}\omega e_i\left(g^{\pm}\right) f\left(g^{\pm}\right) \tag{5.5b}$$

The brackets $\langle \ldots \rangle$ denote the averaging only over the crystallites satisfying condition for Bragg reflection and the symbol $(\pm)$ denotes the average of the two terms, $\mathbf{h}||\mathbf{y}$ and $-\mathbf{h}||\mathbf{y}$. The function $f(g)$ is the orientation distribution function (ODF) and $P_{\mathbf{h}}(\mathbf{y})$ is the *reduced pole distribution*: $P_{\mathbf{h}}(\mathbf{y}) = \frac{1}{2\pi} \int_{\pm\mathbf{h}||\mathbf{y}} \mathrm{d}\omega f\left(g^{\pm}\right)$. Analogously, the function $\langle \varepsilon_{\mathbf{h}}(\mathbf{y}) \rangle$ can be called *the strain pole distribution*. The vectors (E_i) and (F_i) in Eqs. (5.5a) and (5.5b) are defined as follows:

$(E_1, \ldots, E_6) = (a_1^2, a_2^2, a_3^2, a_2a_3, a_1a_3, a_1a_2)$, $(F_1, \ldots, F_6) = (b_1^2, b_2^2, b_3^2, b_2b_3, b_1b_3, b_1b_2)$, where $(a_1, a_2, a_3) = (\cos\beta \sin\Phi, \sin\beta \sin\Phi, \cos\Phi)$ are the direction cosines of $\mathbf{h}$ in $(\mathbf{x}_i)$ and $(b_1, b_2, b_3) = (\cos\gamma \sin\Psi, \sin\gamma \sin\Psi, \cos\Psi)$ are the direction cosines of $\mathbf{y}$ in $(\mathbf{y}_i)$, the pairs (Φ, β) and (Ψ, γ) being the corresponding polar and azimuthal angles.

Each elastic strain/stress tensor has two components: *the averaged* macro strain/stress tensor $\bar{\mathbf{t}} = (8\pi^2)^{-1} \iiint \mathrm{d}g f(g) \mathbf{t}(g)$ and the *intergranular* tensor $\Delta\mathbf{t}(g) = \mathbf{t}(g) - \bar{\mathbf{t}}$. Here $\mathbf{t}$ stands for any of the tensors $\mathbf{e}, \mathbf{s}, \varepsilon, \sigma$. The elastic intergranular strains/stresses have various origins but can be grouped in only two terms, namely the elastically induced and the plastically induced intergranular strain/stress. The principal aim of stress analysis for many years was to determine only the average tensors. The determination was based on the assumption that the plastically induced strains/stresses are zero and the elastically induced strain/stress tensor elements dependent on the crystallite orientation are given as linear combinations of the averaged macro stress/strain tensor elements. The intergranular strains/stresses have various origins (see, e.g., Behnken, 2000): elastic and plastic deformations, phase transformations, thermal treatments, mismatch of d-spacing in composite materials and differences in the coefficients of thermal expansion. These elastic intergranular strains/stresses can be grouped in only two terms, $\Delta\tau_i^{\text{elastic}}$ and $\Delta\tau_i^{\text{plastic}}$, then the SODF can be written as follows:

$$t_i(g) = \bar{t}_i + \Delta t_i^{\text{elastic}}(g) + \Delta t_i^{\text{plastic}}(g) \tag{5.6}$$

The first two terms in the right-hand side of Eq. (5.6) describe the elastically induced part of SODF. Although the diffraction is able, in principle, to determine both, the averaged strain/stress tensors $\bar{t}_i$, as well as the intergranular strain/stress $\Delta t_i(g)$, the principal aim for many years was to determine only the averaged tensors. The determination was based on the assumption that only the first term in the right-hand side of

Eq. (5.6) should be included into the right-hand side of Eqs. (5.2a) and (5.2b). In some approaches, the second term of Eq. (5.6) can be added to the resulting expression if this term has the form $\Delta e_i^{\text{elastic}}(g) = \sum_j t_{ij}(g)\rho_j \bar{s}_j$ and respectively $\Delta s_i^{\text{elastic}}(g) = \sum_j u_{ij}(g)\rho_j \bar{e}_j$ with the constraints $\bar{t}_{ij} = 0$ and $\bar{u}_{ij} = 0$, which means that there are no elastic grain interactions if the averaged strains/stresses are zero. With this assumption, in place of equations (Eqs. (5.2a) and (5.2b)), we have:

$$e_i(g) = \sum_{j=1}^{6} \left[S_{ij}(g) + t_{ij}(g)\right]\rho_j \bar{s}_j \tag{5.7a}$$

$$s_i(g) = \sum_{j=1}^{6} \left[C_{ij}(g) + u_{ij}(g)\right]\rho_j \bar{e}_j \tag{5.7b}$$

The fourth-rank tensors [. . .] in these equations express the elastic behavior of the crystallites in the polycrystalline materials. Now substituting Eq. (5.7a) into Eq. (5.5b), the strain pole distribution becomes:

$$\langle \varepsilon_{\mathbf{h}}(\mathbf{y}) \rangle = \sum_{j=1}^{6} R_j(\Psi, \gamma; \Phi, \beta)\bar{s}_j \tag{5.8}$$

The coefficients R_j are called *diffraction stress factors* and can be calculated analytically or numerically. This formula is typical for classical models, such as Voigt (1928), Reuss (1929), and Kroner (1958). For isotropic (not-textured) samples, this formula becomes linear in $\sin^2 \Psi$ and $\sin 2\Psi$ and is the basic equation of the traditional "$\sin^2 \Psi$" method (Hauk, 1952; Christenson and Rowland, 1953). This method is appropriate to process most of the experimental data.

For textured samples, the relation between the peak shifts and $\sin^2 \Psi$ becomes nonlinear but occasionally, especially in metals after plastic deformation, the departure from linearity cannot be explained only by texture. To explain such large departure, the whole intergranular strain/stress must be accounted for and the exact relations (Eqs. (5.2a) and (5.2b)) between strain and stress tensors considered. One possibility is to calculate the plastically induced part of the stress starting from the models of the plastic flow of crystallites. The second possibility is to obtain directly SODF by inverting the strain pole distributions $\langle \varepsilon_{\mathbf{h}}(\mathbf{y}) \rangle$ measured for several peaks in a large number of sample directions. In this case, no model is necessary to assume for the elastic or plastic interactions of crystallites.

The representation of SODFs by generalized spherical harmonics has been proposed as a method for inverting the strain pole distribution. Three different approaches were reported: by Wang et al. (1999, 2001, 2003), by Behnken (2000), and by Popa and Balzar (2001). Wang et al. represented by spherical harmonics the stress tensor in the sample reference system $s_i(g)$, and separately the ODF, and also used the Clebsch-Gordon coefficients to express the product of the SODF and ODF. Behnken

(2000) proposed expanding in spherical harmonics both $e_i(g)$ and $s_i(g)$ independently and calculating numerically the integrals in Eq. (5.5b). For determination of the coefficients of expansion, both Wang et al. (1999, 2001, 2003) and Behnken (2000) used a stabilized least-square method.[1] Finally, these authors considered only the case of the cubic crystal symmetry and orthorhombic sample symmetry. The third approach reported by Popa and Balzar (2001) is similar to those of Wang et al. (1999, 2001, 2003) and Behnken (2000), but with an important difference that makes the problem of determination of the strain tensor equivalent to the texture problem. In place of SODF, $e_i(g)$ and $s_i(g)$, the analysis by spherical harmonics was performed on the product between $\varepsilon_i(g)$, the SODF in the crystal reference system, and ODF; in other words, on SODF weighted by texture (WSODF). Equations (5.5a) and (5.5b) express the projection of the WSODF with the condition $\pm\mathbf{h}||\mathbf{y}$ from the Euler space $g=(\phi_1,\Phi_0,\phi_2)$ into the space (Ψ,γ). WSODF is the quantity measured in an experiment, because the d spacings can be measured only along the grain orientations present in the sample. On the other hand, the ODF can be derived independently from the integrated intensities of the diffraction peaks. Therefore, once WSODF is known, SODF can be readily calculated from it. The major advantage of expanding WSODF in place of SODF is that the integrals in Eqs. (5.5a) and (5.5b) are solved analytically, resulting in an open (convergent infinite series) analytical expression for the strain pole distribution, similar to the texture pole distribution (see Von Dreele, 1997), and thus appropriate for easy implementation into the Rietveld programs (Rietveld, 1969), allowing constraints during the refinements. Finally, such expressions were derived for all crystal and sample symmetries.

5.2.2 New developments in macro strain/stress analysis by spherical harmonics

In terms of the mathematical nomenclature, the *open* representation of a function, in other words, by an infinite convergent series, appears as a *perturbation* of the *ground state* represented by the coefficient of order zero. As far from ground state as is the function, the larger the number of terms necessary to reach the convergence. If more open representations are known for a given function, it is rational to use the "shortest" for its calculation. The strain pole distribution supports multiple open spherical harmonics representations. As was proven by Popa (2008), the ground state of representation derived by Popa and Balzar (2001), starting from the WSODF formed with the strain tensor in the crystal reference system $\varepsilon_i(g)$, is the hydrostatic strain/stress state of isotropic polycrystal. The ground state will be of the Voigt (1928) and Reuss (1929) type if the object of spherical harmonics analysis is the WSODF formed with the strain and the stress tensor in the sample reference system, respectively. In comparison to already existent Wang et al. (1999) and Behnken (2000) approaches, these new representations are analytical, extended to any sample and crystal symmetries and implementable in the Rietveld programs (Rietveld 1969).

[1]The constrained least-squares method was used for preventing the effect of the ill-posed character of the inversion problem; in place of "chi square," a Lagrange function constructed as a weighted sum of this quantity with the elastic free energy, or with the SODF index, is minimized.

5.2.3 Hydrostatic and Voigt ground state spherical harmonics representation; the strain pole distribution

Similarly to Popa and Balzar (2001), the WSODF defined by the elements of the macro strain tensor in the sample reference system is expanded in generalized spherical harmonics:

$$f(g)e_i(g) = \sum_{l=0}^{\infty} \sum_{m=-l}^{l} \sum_{n=-l}^{l} c_{il}^{mn} \exp(im\phi_2) P_l^{mn}(\Phi_0) \exp(in\phi_1) \tag{5.9}$$

Here, $P_l^{mn}(\Phi_0)$ are Legendre functions defined according to Bunge (1982) and c_{il}^{mn} are complex coefficients fulfilling the condition resulting from the real character of the series:

$$c_{il}^{-m,-n} = (-1)^{m+n} c_{il}^{mn*} \tag{5.10}$$

The definitions and properties of the Legendre functions P_l^{mn} and P_l^m are reviewed in Popa and Balzar (2001). Integrating Eq. (5.9) in the Euler space and using the orthogonality of spherical harmonics, one obtains $\overline{e}_i = c_{i0}^{00}$; therefore, the free term of expansion is the strain given by the Voigt model of isotropic polycrystal.

The next step in calculating the strain pole distribution is to substitute Eq. (5.9) into Eq. (5.5b) and to integrate according to formula (5.1) from Popa and Balzar (2012). For the average of the two terms (±), this formula becomes:

$$\frac{1}{2\pi} \int_{\pm \mathbf{h} \| \mathbf{y}} d\omega \exp\left(im\phi_2^{\pm}\right) P_l^{mn}\left(\Phi_0^{\pm}\right) \exp\left(in\phi_1^{\pm}\right) = \begin{cases} [2/(2l+1)] \exp(-im\beta) P_l^m(\Phi) \exp(in\gamma) \\ \times P_l^n(\Psi) \cdot (-1)^n \quad \text{for } l = \text{even} \\ 0 \quad \text{for } l = \text{odd} \end{cases}$$

In the resulting expression, the sums are permuted to have the following sequence of indices: (l, i, n, m). This sequence is imposed by the derivation of the selection rules, involving in this case the direction cosines of $\mathbf{y}$ in the reference system $\mathbf{y}_i$. Finally, rearranging to have only positive indices, accounting for the condition (Eq. (5.10)) and using some properties of the Legendre functions P_l^m, one obtains:

$$\langle e_{\mathbf{h}}(\mathbf{y}) \rangle P_{\mathbf{h}}(\mathbf{y}) = \sum_{l=0}^{\infty} [2/(2l+1)] I_l(\mathbf{h}, \mathbf{y}), \quad l = \text{even} \tag{5.11}$$

Here, the hydrostatic ground state is defined by the strain tensor in the crystal reference system (x_i) and the Voigt ground state by the strain tensor in the sample reference system (y_i), that is,

$$I_l(\mathbf{h},\mathbf{y}) = \sum_{i=1}^{6} E_i(\mathbf{h})\rho_i t_{il}(\mathbf{h},\mathbf{y}) \quad \text{for hydrostatic ground state} \tag{5.12a}$$

and

$$I_l(\mathbf{h},\mathbf{y}) = \sum_{i=1}^{6} F_i(\mathbf{y})\rho_i t_{il}(\mathbf{h},\mathbf{y}) \quad \text{for Voigt ground state} \tag{5.12b}$$

The definitions are:

$$t_{il}(\mathbf{h},\mathbf{y}) = A_{il}^{0}(\mathbf{h})P_l^0(\Psi) + \sum_{n=1}^{l}\left[A_{il}^{n}(\mathbf{h})\cos\ n\gamma + B_{il}^{n}(\mathbf{h})\sin\ n\gamma\right]P_l^n(\Psi) \tag{5.13}$$

$$A_{il}^{n}(\mathbf{h}) = \alpha_{il}^{0n}P_l^0(\Phi) + \sum_{m=1}^{l}\left(\alpha_{il}^{mn}\cos\ m\beta + \beta_{il}^{mn}\sin\ m\beta\right)P_l^m(\Phi) \quad (n=0,l) \tag{5.14}$$

$$B_{il}^{n}(\mathbf{h}) = \gamma_{il}^{0n}P_l^0(\Phi) + \sum_{m=1}^{l}\left(\gamma_{il}^{mn}\cos\ m\beta + \delta_{il}^{mn}\sin\ m\beta\right)P_l^m(\Phi) \quad (n=1,l) \tag{5.15}$$

The coefficients $\alpha_{il}^{mn}, \beta_{il}^{mn}, \gamma_{il}^{mn}, \delta_{il}^{mn}$ are obtained from $c_{il}^{mn} = a_{il}^{mn} + ib_{il}^{mn}$ by the relations given in Table 5.1. They can be refined in any least-square program, including Rietveld refinement (Rietveld, 1969), fitting the strain pole distribution measured for a number of peaks in a number of sample directions by the parameterized Eqs. (5.11)–(5.15). The refinement is performed by taking into account the selection rules for coefficients imposed by sample and/or crystal symmetries higher than triclinic and truncating the series (Eq. (5.11)) at a value $l = l_0$. Finally, gathering the coefficients $\alpha_{il}^{mn}, \beta_{il}^{mn}, \gamma_{il}^{mn}, \delta_{il}^{mn}$ into a vector $\mathbf{g}_{il}$ in the sequence given by Eq. (5.16) below, Eqs. (5.13)–(5.15) can be written in the compact form (Eq. (5.17)):

Table 5.1 The relations between the coefficients $\alpha_{il}^{mn}, \beta_{il}^{mn}, \gamma_{il}^{mn}, \delta_{il}^{mn}$ and $c_{il}^{mn} = a_{il}^{mn} + ib_{il}^{mn}$

$\alpha_{il}^{00} = a_{il}^{00}$	$\alpha_{il}^{m0} = 2a_{il}^{m0}$	$\beta_{il}^{m0} = 2b_{il}^{m0}$
$\alpha_{il}^{0n} = 2(-1)^n a_{il}^{0n}$	$\alpha_{il}^{mn} = 2[(-1)^n a_{il}^{mn} + (-1)^{m+n} a_{il}^{-m,n}]$	$\beta_{il}^{mn} = 2[(-1)^n b_{il}^{mn} - (-1)^{m+n} b_{il}^{-m,n}]$
$\gamma_{il}^{0n} = -2(-1)^n b_{il}^{0n}$	$\gamma_{il}^{mn} = -2[(-1)^n b_{il}^{mn} + (-1)^{m+n} b_{il}^{-m,n}]$	$\delta_{il}^{mn} = 2[(-1)^n a_{il}^{mn} - (-1)^{m+n} a_{il}^{-m,n}]$

$$\mathbf{g}_{il} = \left(\alpha_{il}^{0,0}, \alpha_{il}^{1,0}, \beta_{il}^{1,0}, \ldots, \alpha_{il}^{l,0}, \beta_{il}^{l,0}; \ldots; \right.$$
$$\left. \alpha_{il}^{0,n}, \alpha_{il}^{1,n}, \beta_{il}^{1,n}, \ldots, \alpha_{il}^{l,n}, \beta_{il}^{l,n}; \gamma_{il}^{0,n}, \gamma_{il}^{1,n}, \delta_{il}^{1,n}, \ldots, \gamma_{il}^{l,n}, \delta_{il}^{l,n}; \ldots\right) \quad (n = 1, l) \tag{5.16}$$

$$t_{il}(\mathbf{h}, \mathbf{y}) = \sum_{\nu=1}^{(2l+1)^2} g_{il}^{\nu} T_l^{\nu}(\Phi, \beta; \Psi, \gamma) \tag{5.17}$$

The functions $T_l^{\nu}(\Phi, \beta; \Psi, \gamma)$ are paired with the coefficients g_{il}^{ν} according to Table 5.2.

5.2.4 The selection rules

The number of the coefficients for triclinic crystal and sample symmetries is $\sum_{l=0}^{l_0} 6(2l+1)^2$, $l =$ even and decreases for higher symmetries. The selection rule for a given symmetry operation is derived from the invariance of $I_l(\mathbf{h}, \mathbf{y})$ to this operation. This quantity has a structure identical to those for spherical harmonic expansion of hydrostatic ground state but with the dependences on the vectors **h** and **y** permuted, as can be seen comparing Eqs. (5.12a)–(5.15) with (5.17)–(5.20) from Popa and Balzar (2001).[2] Consequently, to obtain the selection rules for the actual expansion, the selection rules derived in that paper for crystal and sample symmetries should be interchanged, taking care to set correctly the indices m, n. For sample Laue groups $2/m$ and mmm, the selection rules are given in Tables 5.3 and 5.4, with higher sample symmetry being improbable. The selection rules for crystal, noncubic Laue groups are given in Tables 5.5 and 5.6 for the cubic groups.

Table 5.2 Assignment of functions $T_l^{\nu}(\Phi, \beta; \Psi, \gamma)$ to the coefficients g_{il}^{ν}

g_{il}^{ν}	$\leftarrow$	$T_l^{\nu}(\Phi, \beta; \Psi, \gamma)$
α_{il}^{mn}	$\leftarrow$	$\cos m\beta P_l^m(\Phi) \cos n\gamma P_l^n(\Psi)$
β_{il}^{mn}	$\leftarrow$	$\sin m\beta P_l^m(\Phi) \cos n\gamma P_l^n(\Psi)$
γ_{il}^{mn}	$\leftarrow$	$\cos m\beta P_l^m(\Phi) \sin n\gamma P_l^n(\Psi)$
δ_{il}^{mn}	$\leftarrow$	$\sin m\beta P_l^m(\Phi) \sin n\gamma P_l^n(\Psi)$

Table 5.3 The selection rules for sample Laue class $2/m$

$i = 1, 2, 3, 6$:	$\begin{cases} A_{il}^0 \\ A_{il}^n, B_{il}^n, \ n = 2k, \ 1 \le k \le l/2 \end{cases}$
$i = 4, 5$:	$A_{il}^n, B_{il}^n, \ n = 2k-1, \ 1 \le k \le l/2$

[2] In this paper the direction cosines of **h** in $\mathbf{x}_i$ are denoted by capital letters. A_1, A_2, A_3.

Table 5.4 The selection rules for sample Laue class *mmm*

$i=1,2,3:$	A_{il}^{n},	$n=2k$,	$0\le k\le l/2$
$i=4:$	B_{il}^{n},	$n=2k-1$,	$1\le k\le l/2$
$i=5:$	A_{il}^{n},	$n=2k-1$,	$1\le k\le l/2$
$i=6:$	B_{il}^{n},	$n=2k$,	$1\le k\le l/2$

Table 5.5 The selection rules for crystal not cubic Laue classes; $r=2,3,4,6$

$$2/m,\bar{3},4/m,6/m:\quad \begin{cases} \alpha_{il}^{0n};\gamma_{il}^{0n} \\ \alpha_{il}^{mn},\beta_{il}^{mn};\gamma_{il}^{mn},\delta_{il}^{mn},\ m=rk,\ 1\le k\le l/r \end{cases}$$

$$mmm,\bar{3}m,4/mmm,6/mmm:\quad \begin{cases} \alpha_{il}^{0n};\gamma_{il}^{0n} \\ \alpha_{il}^{mn};\gamma_{il}^{mn},\ m=rk=even,\ 1\le k\le l/r \\ \beta_{il}^{mn};\delta_{il}^{mn},\ m=rk=odd,\ 1\le k\le l/r \end{cases}$$

Table 5.6 The selection rules for crystal cubic Laue classes for $l\le 8$: the following constraints should be added to the selection rules for *mmm* and 4/*mmm*

$$m\bar{3}\quad \begin{cases} \left(\alpha_{i2}^{mn},\gamma_{i2}^{mn}\right)=0,\ (m=0,2) \\ \left(\alpha_{i4}^{4n},\gamma_{i4}^{4n}\right)=(10/7)^{1/2}\left(\alpha_{i4}^{0n},\gamma_{i4}^{0n}\right) \\ \left(\alpha_{i6}^{4n},\gamma_{i6}^{4n}\right)=-(14)^{1/2}\left(\alpha_{i6}^{0n},\gamma_{i6}^{0n}\right),\ \left(\alpha_{i6}^{6n},\gamma_{i6}^{6n}\right)=(5/11)^{1/2}\left(\alpha_{i6}^{2n},\gamma_{i6}^{2n}\right) \\ \left(\alpha_{i8}^{4n},\gamma_{i8}^{4n}\right)=(56/99)^{1/2}\left(\alpha_{i8}^{0n},\gamma_{i8}^{0n}\right),\ \left(\alpha_{i8}^{8n},\gamma_{i8}^{8n}\right)=(130/99)^{1/2}\left(\alpha_{i8}^{0n},\gamma_{i8}^{0n}\right) \end{cases}$$

$$m\bar{3}m\quad \begin{cases} \left(\alpha_{i2}^{0n},\gamma_{i2}^{0n}\right)=0 \\ \left(\alpha_{i4}^{4n},\gamma_{i4}^{4n}\right)=(10/7)^{1/2}\left(\alpha_{i4}^{0n},\gamma_{i4}^{0n}\right) \\ \left(\alpha_{i6}^{4n},\gamma_{i6}^{4n}\right)=-(14)^{1/2}\left(\alpha_{i6}^{0n},\gamma_{i6}^{0n}\right) \\ \left(\alpha_{i8}^{4n},\gamma_{i8}^{4n}\right)=(56/99)^{1/2}\left(\alpha_{i8}^{0n},\gamma_{i8}^{0n}\right),\ \left(\alpha_{i8}^{8n},\gamma_{i8}^{8n}\right)=(130/99)^{1/2}\left(\alpha_{i8}^{0n},\gamma_{i8}^{0n}\right) \end{cases}$$

5.2.5 WSODFs and the averaged strain and stress tensors

According to Popa et al. (2014), the strain tensor weighted by texture in terms of generalized spherical harmonics in real space is the following:

$$f(g)e_i(g)=\sum_{l=0}^{l_0}\sum_{v=1}^{(2l+1)^2} g_{il}^{v}R_l^{v}(g),\quad l=\text{even} \tag{5.18}$$

The stress tensor weighted by texture is obtained by substituting Eq. (5.18) into Eq. (5.2a):

$$f(g)s_i(g) = \sum_{l=0}^{l_0} \sum_{v=1}^{(2l+1)^2} \sum_{j=1}^{6} C_{ij}(g)\rho_j R_l^v(g) g_{jl}^v, \quad l = \text{even} \tag{5.19}$$

Here $C_{ij}(g)$ are the single crystal elastic stiffness constants in the sample reference system given by Eq. (5.3a).

Integrating Eqs. (5.18) and (5.19) in the Euler space, we find the averaged strain and stress tensors. Because the spherical harmonics are orthogonal, $\overline{R}_l^v = 1$ for $l = 0, v = 1$ and $\overline{R}_l^v = 0$ for the rest, we have:

$$\overline{e}_i = g_{i0}^1 = \alpha_{i0}^{00} \quad (i = 1,6) \tag{5.20}$$

Let us now introduce the Fourier coefficients of $C_{ij}(g)$ in the basis $R_l^v(g)$:

$$\overline{C}_{ijl}^v = \left(8\pi^2\right)^{-1} \iiint \mathrm{d}g C_{ij}(g) R_l^v(g) \tag{5.21}$$

Because the elements of the matrices P_{ij} and Q_{ij} in Eq. (5.3a) are sums of products of two Euler matrix elements, one expects that $\overline{C}_{ijl}^v \neq 0$ for $l = 0, 2, 4$ and for some values of i, j, v but $\overline{C}_{ijl}^v = 0$ for $l > 4$ and then:

$$\overline{s}_i = \sum_{l=0}^{4} \sum_{v=1}^{(2l+1)^2} \sum_{j=1}^{6} \overline{C}_{ijl}^v \rho_j g_{jl}^v, \quad l = \text{even} \tag{5.22}$$

The matrix $\overline{C}_{ijl}^v$ of 3852 elements is very sparse, but it is not possible to predict what elements are different from zero. The matrix can be calculated by numerical integration, requiring the single crystal stiffness constants as input data. Note that the elements of the matrix $\overline{C}_{ij0}^1$ represent the Voigt averaged stiffness constants for isotropic polycrystal $\overline{C}_{ij}^V$. Keeping only the term $l = 0$, Eq. (5.22) becomes the basic Hooke equation in the Voigt model: $\overline{s}_i = \sum_{j=1}^{6} \overline{C}_{ij}^V \rho_j \overline{e}_j$.

5.2.6 Implementation in Rietveld programs

To obtain a smoothed solution, it is worthwhile to implement Eqs. (5.11)–(5.15) into a Rietveld program allowing constraints. In these programs, the Lagrange function $(1-\lambda)\chi^2 + \lambda\Lambda$ is minimized. A simple choice for Λ is the WSODF index J, defined as follows:

$$J = \sum_{i=1}^{6} \sum_{j=1}^{6} \left(8\pi^2\right)^{-1} \iiint \mathrm{d}g \left[f(g)e_i(g)\right]\left[f(g)e_j(g)\right] \tag{5.23}$$

By using Eq. (5.18) and the orthogonality conditions of the functions R_l^v, this equation becomes:

$$J = \sum_{i=1}^{6}\sum_{j=1}^{6}\rho_i\rho_j\sum_{l=0}^{\infty}\sum_{v=1}^{(2l+1)^2} g_{il}^v g_{jl}^v \left(r_l^v\right)^2 \tag{5.24}$$

5.3 Section 1: conclusions

A method for the determination of the elastic strain and stress in textured polycrystals has been presented. The approach is based on the expansion of the texture-weighted strain orientation distribution function (WSODF) in generalized spherical harmonics. The ground (unperturbed) state can be chosen either as the hydrostatic strain/stress state of isotropic sample or the state of isotropic sample described by the Voigt model (Voigt, 1928). The choice of model being employed will depend on the actual strain/stress state in the sample and can be established only by trials. The main advantage of this method over other existing approaches for the determination of strain and stress is that the model is applicable for an arbitrary crystal symmetry and texture. Moreover, it can be easily incorporated into whole diffraction pattern fitting programs, including Rietveld refinement (Rietveld, 1969).

5.4 Section 2: diffraction profile broadening due to crystalline defects and strains and their influence on ferroelectric thin films

5.4.1 Introduction

Most crystalline defects cause broadening of diffraction lines. In particular, line defects (i.e., dislocations) manifest themselves through so-called strain broadening, and planar defects (subgrain structures, stacking, and twin faults) cause size-related broadening. Point defects (particularly vacancies and interstitials) generally result in diffuse scattering but some arrangements of point defects can also broaden diffraction profiles. Here, we look at the determination of defect densities and associated inhomogeneous strains by the analysis of diffraction profile broadening and its influence on the dielectric properties of ferroelectric thin films. Lattice parameters are also used to deduce elastic (homogeneous) strains and associated misfit dislocation densities.

Thin-film ferroelectric (FE) materials have received considerable attention because of their growing use in electronic, electro-optical, optical, and acoustic devices. Potential applications include integrated, nonvolatile, and dynamic random access memories, pyroelectric detectors, and acoustic transducers (Auciello et al., 1998). These materials also exhibit nonlinear dielectric properties under an external

electric field, which is exploited in tunable microwave devices, such as microstrip line phase shifters, high-Q resonators, and tunable filters (Hermann et al., 1993). For these applications, it is imperative that the films exhibit a high dielectric constant and tunability and low dielectric loss. While reasonable success has been achieved with tunability, the major challenge has been lowering the dielectric loss and in particular understanding its mechanism. It was elucidated that losses depend on substrate and post annealing treatments (Chang et al., 1999a,b) and the film thickness (Li et al. 1998a), in that the free-standing films generally have low losses (Dalberth et al., 1998) and that crystalline $SrRuO_3$, YBCO (Li et al., 1998b), and amorphous (Chang et al., 1999a) buffer layers decrease losses. This indicates that minimizing lattice misfit between the film and the substrate is of utmost importance. Indeed, dielectric losses depend on residual stresses of both intrinsic (caused by optical-phonon interaction with the applied electric field) and extrinsic (caused by lattice defects) nature. The latter is an especially important and complicated process because many possible defects can be involved, such as ferroelectric domains, grain boundaries, stacking faults, dislocations, vacancies, and vacancy complexes. Of the various ferroelectric materials, perovskite oxide thin films are considered as potential candidates for tunable microwave devices because of their high dielectric constant. Materials investigated widely are based on solid solutions of $Ba_xSr_{1-x}TiO_3$ that exhibit high tunability and easily controlled Curie temperature by varying chemical composition. Losses can be controlled by doping very small percentages (<4%) of ions such as Mn, W, Ca, Mg, and Zr (Chang et al., 1999b).

Our previous studies on doped BSTO films (Hermann et al., 2000) indicate that the ferroelectric transition temperature and the extrinsic dielectric losses depend on the internal stresses and defects. Thus it is evident that lattice strain plays a crucial role in influencing the dielectric and ferroelectric properties. To understand this further, we attempted to investigate the effect of doping on the ferroelectric properties. Here, we report on the correlation between Curie-Weiss temperature and residual elastic strain (stress) and defect concentration.

5.4.2 Theory

A comprehensive treatment of the influence of homogeneous strain due to the misfit in lattice parameter and thermal expansion coefficients on the ferroelectric transition temperature and electrical permittivity was reported by Pertsev et al. (1998). They start with the expression for the Gibbs free energy, close to the transition temperature and appearance of polarization P:

$$
\begin{aligned}
G = {} & a_1\left(P_1^2 + P_2^2 + P_3^2\right) + a_{11}\left(P_1^4 + P_2^4 + P_3^4\right) + a_{12}\left(P_1^2P_2^2 + P_1^2P_3^2 + P_2^2P_3^2\right) \\
& + a_{111}\left(P_1^6 + P_2^6 + P_3^6\right) \\
& + a_{112}\left[P_1^4\left(P_2^2 + P_3^2\right) + P_3^4\left(P_1^2 + P_2^2\right) + P_2^4\left(P_1^2 + P_3^2\right)\right] + a_{123}P_1^2P_2^2P_3^2 \\
& - Q_{11}\left(\sigma_1P_1^2 + \sigma_2P_2^2\right) - Q_{12}\left[\sigma_1\left(P_2^2 + P_3^2\right) + \sigma_2\left(P_1^2 + P_3^2\right)\right] - Q_{44}P_1P_2\sigma_6 \\
& - 1/2s_{11}(\sigma_1^2 + \sigma_2^2) - s_{12}\sigma_1\sigma_2 - 1/2s_{44}\sigma_6^2
\end{aligned}
$$

Here, $a_{i,j,k}$ are dielectric stiffness coefficients, s_{ij} is the elastic compliance tensor, Q_{ij} is the electrostrictive tensor, and σ_i is the mechanical stress tensor, all in the Voigt condensed tensor notation.

In the approximation of the single-domain two-dimensional thin film constrained by the substrate, we can write the additional term to the Gibbs free energy due to elastic-strain e_i contribution as (Lines and Glass, 2001):

$$G' = G + \sum_i e_i \sigma_i$$

This expression considers only elastic strains. However, crystalline defects (e.g., oxygen vacancies) will affect the polarization of a ferroelectric. We proposed (Balzar et al., 2004) that the internal crystalline defects induce similar changes of the Gibbs free energy

$$G'' = G' + \sum\nolimits_i \varepsilon_i T_i$$

through the inhomogeneous strain ε_i (e.g., strain of the III kind that influences the diffraction line width) and the stress of the III kind T_i.

On the assumption that the spontaneous polarization axis is perpendicular to the film surface and isotropy of inhomogeneous strain, we have (Balzar et al., 2004):

$$G'' = a_3^* P_3^2 + a_{33}^* P_3^4 + a_{111} P_3^6 + \frac{e_m^2}{s_{11} + s_{12}} + \frac{3}{2} \frac{\varepsilon_m^2}{s_{11} + 2s_{12}} \tag{5.25}$$

where the renormalized coefficients a^* were given elsewhere (Balzar et al., 2004). The last term in Eq. (5.25) is given by the inhomogeneous strain. Note that its contribution is always positive, unlike that of the elastic-strain term that can be either positive or negative, depending on whether the film is in tension or compression parallel to its surface. Similarly, the Curie-Weiss temperature is renormalized (Balzar et al., 2004):

$$\Delta T_{\mathrm{C-W}} = \max \left\{ 2C\varepsilon_0 \left(\frac{2Q_{12}}{s_{11} + s_{12}} e_m + \frac{Q_{11} + 2Q_{12}}{s_{11} + 2s_{12}} \right) \right.$$
$$\left. 2C\varepsilon_0 \left(\frac{Q_{11} + Q_{12}}{s_{11} + s_{12}} e_m + \frac{Q_{11} + 2Q_{12}}{s_{11} + 2s_{12}} \varepsilon_m \right) \right\} \tag{5.26}$$

Here, C and ε_0 are the Curie-Weiss constant and the permittivity of the vacuum, respectively.

5.4.3 Experimental

The pristine $Ba_{0.6}Sr_{0.4}TiO_3$ (BSTO) and Mn,W-doped and co-doped $Ba_{0.6}Sr_{0.4}Ti_{0.99}M_{0.01}O_3$ (M = Mn,W) thin films were deposited on (001) $LaAlO_3$ (LAO) substrate using a KrF eximer laser (248 nm) at 700 °C at oxygen partial pressures

of 300 mTorr (Balzar et al., 2002). During deposition, the stoichiometric BSTO targets with densities of 98% were used. The energy density was about 1.5-2 J/cm^2. The films were postannealed in flowing oxygen at 950 °C for 6 h.

Dielectric measurements were carried out on these films using a four-capacitor shadow mask design with interdigitated capacitors. The mask has six terminal pads for contact, with finger widths of 125 μm and finger separation of 75 μm. The interdigitated capacitor configurations were obtained by thermal evaporation of silver to a thickness of 150 nm. Fine-gauge copper leads were then attached to each capacitor using silver paste. The whole assembly was then annealed at 300 °C in Ar to ensure good electrical contact and to decompose the organic matter present in the silver paste.

The capacitance and dielectric loss (tan δ) were measured using an HP 4192A LCR meter at a constant frequency of 1 MHz. For temperature variation, a closed cycle He refrigerator was used. Automated data acquisition was achieved by the LABVIEW program. A standard 2 pF capacitor was used to calibrate the instrument, which gave $<1\%$ error in the frequency range studied.

The optical properties were measured with a dual mode automatic ellipsometer model L116A at room temperature. The ellipsometer measurements can be used for determining the film thickness and refractive index of optically transparent and absorbing layers in the range between a few Å and a few μm. The film thickness was relatively nonuniform due to the deposition technique used and varied in the range of 1000-3500 Å.

X-ray diffraction data were collected using Scintag four-circle and two-circle double-axis diffractometers with Cu K_α radiation excited at 45 kV and 40 mA. To thoroughly study the misfit relationship at the film-substrate interface, we recorded reciprocal space maps for all films. Reciprocal space maps discern differences between different types of defects in epilayers, in particular mosaicity parallel to the film surface and strain variations perpendicular to the film surface. Reciprocal space maps of asymmetric reflections (013) were used to obtain both parallel and perpendicular (to the film surface) lattice parameters. All films showed relatively small broadening of various amounts as compared to the substrate. Broadening was evident both parallel to the surface, thus indicating somewhat increased mosaicity, and perpendicular to it, which could be caused by small correlation lengths, inhomogeneous strain, and the through-depth stoichiometry variations. To investigate this point further, we conducted a careful study of line broadening perpendicular to the film surface. The analysis took into consideration multiple Bragg reflections, thus allowing for an unequivocal separation of correlation-length and inhomogeneous-strain effects on line broadening (Balzar, 1999). Our experimental setup was a low resolution one without the incident-beam (Bartels) monochromator. To account for wavelength dispersion, we corrected the measured profiles for effects of instrumental broadening. This correction was accomplished by measurements of line profiles of the bare $LaAlO_3$ substrate reflections and also includes corrections for additional instrumental effects (Balzar, 1999).

5.4.4 Results and discussion

Figure 5.1 shows a plot of relative permittivity and dielectric loss (tan δ), measured at 1 MHz frequency with both zero and 35 V bias in order to estimate tunability as a function of temperature for the pristine BSTO thin film (Balzar et al., 2002). Relative permittivity shows a relatively broad ferroelectric transition around room temperature. The temperature at the curve maximum was taken as a ferroelectric transition temperature $T_{C\text{-}W}$. Because the measurements were taken at a frequency lower than the microwave region, we do not discuss the influence of strains and defects on dielectric loss and relative permittivity here.

X-ray diffraction measurements were used to confirm the epitaxial relationship between the films and substrate and to calculate lattice parameters. Coupled $\theta/2\theta$ scans perpendicular to the surface showed only 00l Bragg reflections for all films that confirm preferential [001] growth perpendicular to the surface. A good BSTO [001] || LAO (pseudo) [001] epitaxy with the substrate was confirmed by the scans parallel to the film surface (ϕ scans), which showed four maxima 90° apart for all the films. Figures 5.2(a) and 5.2(b) show the $\theta/2\theta$ and ϕ scans for the pristine BSTO film.

At room temperature, there is a large misfit (up to 5%) between the (pseudocubic) lattice parameter of the substrate and that of the epilayer. Such a large difference is accommodated through the introduction of misfit dislocations mainly at the growth temperature. An incomplete misfit relaxation at growing temperature and different thermal expansion coefficients of the film and substrate may cause tetragonal distortion of the film, although the bulk BSTO with this composition is cubic at room temperature.

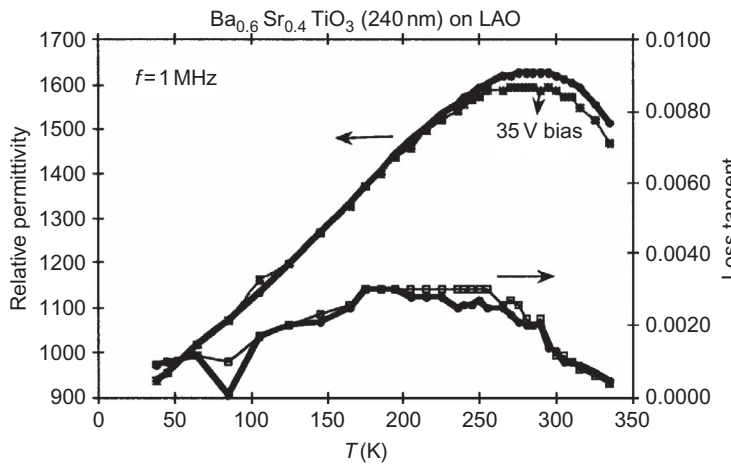

Figure 5.1 Dielectric permittivity and loss, measured at 1 MHz frequency at zero and 35 V bias, as a function of temperature for undoped $Ba_{0.60}Sr_{0.40}TiO_3$ thin film on the $LaAlO_3$ substrate.

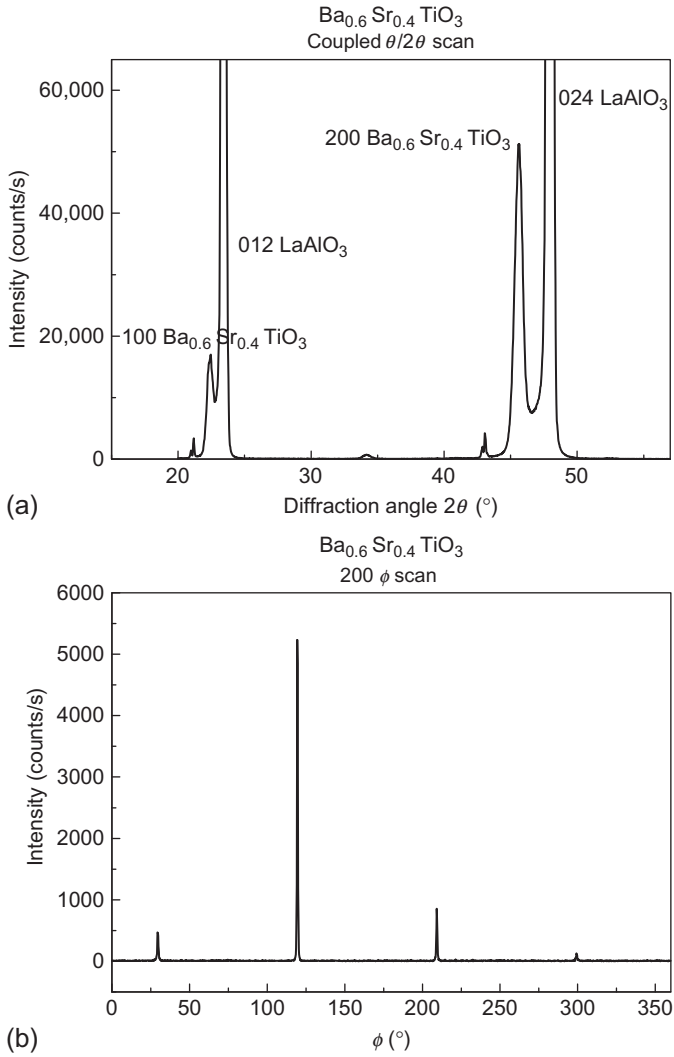

Figure 5.2 X-ray diffraction scans of the undoped $Ba_{0.60}Sr_{0.40}TiO_3$ thin film on the $LaAlO_3$ substrate: (a) perpendicular to the film surface and (b) parallel to the film surface.

For our thin films, the epilayer dimension parallel to the epilayer-substrate interface (designated as a) stayed in compression and that perpendicular to it, in tension (designated as c). If the "relaxed" cubic lattice parameter of an epilayer is defined as

$$a^R = \frac{c + 2a(v/(1-v))}{1 + 2v/(1-v)}$$

where v is the Poisson ratio (approximately taken as 1/3), the relaxed lattice parameter is estimated to be the same for all the samples within the single standard uncertainty. The value, $a = 3.957(6)$ Å, is slightly lower than the value for bulk BSTO reported in the literature, $a = 3.965$ Å (ICDD). It may indicate that the actual stoichiometry of the thin films, which we did not measure, is richer in Sr than the nominal target composition.

From the values of relaxed and measured lattice parameters, we calculated elastic strains:

$$e_a = a/a^R - 1; \quad e_c = c/a^R - 1$$

They are presented in Figure 5.3 for all the films. Although the elastic strain varies between samples, the relaxation of the films is above 90%, as estimated from the difference of the relaxed and measured lattice parameters, relative to the substrate lattice parameter a_s:

$$R = \frac{a - a_s}{a^R - a_s} 100$$

The relaxation process is greatly dependent on the geometry of misfit dislocations and misfit between the film and the substrate lattice parameter, which define the

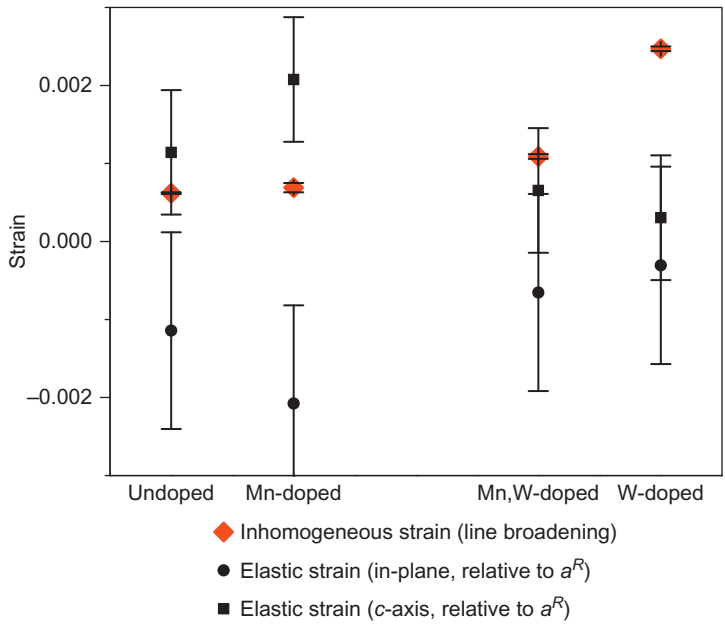

Figure 5.3 Elastic and inhomogeneous strain for four thin films: undoped $Ba_{0.60}Sr_{0.40}TiO_3$ single-doped and co-doped $Ba_{0.60}Sr_{0.40}Ti_{0.99}M_{0.01}O_3$ (M = Mn,W). Error bars were estimated from the counting statistics of diffraction measurements through the propagation of errors.

critical thickness for introduction of misfit dislocations. For this large misfit, the critical thickness is estimated as being below 100 Å (Speck and Pompe, 1994). Because the thickness of both thin films was determined to be larger than 1000 Å by ellipsometry measurements, the relaxation should be complete at the growth temperature, and any residual elastic strain should stem from differences in thermal expansion coefficients between the film and the substrate. However, because the doping at a 1% level cannot appreciably change thermal expansion coefficients, the difference in lattice parameters between the pristine and the doped samples cannot be explained entirely by cooling effects. This might indicate that the doping influences the relaxation mechanism at the deposition temperature. The relaxation degree yields information about the linear density of misfit dislocations ρ_I

$$a/a_s - 1 = b\rho_I$$

where b is the magnitude of the Burger's vector. For all films, the misfit dislocation density is on the order of 10^6/cm.

Threading dislocation densities, which do not affect lattice parameters, can be determined through the analysis of diffraction line breadths (Hordon and Averbach, 1961). Generally, dislocations broaden diffraction lines of epitaxial thin films for three principal reasons: (i) Dislocations define both twist (in-plane rotations) and tilt (perpendicular rotations) boundaries between grains, (ii) dislocations cause inhomogeneous strain fields and thus local changes in the d spacing and the additional line broadening, (iii) dislocation configurations may subdivide columnar grains into subgrain domains. Following Ayers (1994), dislocation density due to (i) was estimated to about 8×10^8/cm^2, and it is approximately equal for all the samples, being somewhat different for the W-doped film (see Figure 5.4). To estimate the effect of domain size according to (iii) perpendicular to the film surface, we followed the broadening analysis formalism described elsewhere (Balzar, 1999). Domain size

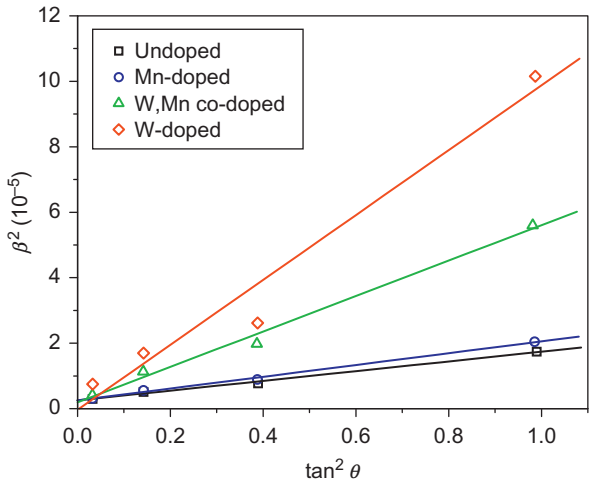

Figure 5.4 The square of the integral breadth of the thin-film diffraction lines, corrected for the effects of instrumental broadening, as a function of $\tan^2\theta$ for all four thin films. The intercept yields threading dislocation density and the slope inhomogeneous strain.

varies from 850 to 1550 Å and is close to the measured thickness of the films. The values differ because diffraction measures the dimension of grains perpendicular to the substrate and is therefore reduced because of grain tilts and possible extended defects parallel to the surface. The inhomogeneous-strain values resulting from (ii) are given in Figure 5.3. There is a large increase in inhomogeneous strain for the co-doped but especially for the W-doped sample. It appears that the W doping on the Ti site strongly influences the defect concentration, either because the relaxation mechanism at growth temperature is affected, which would influence the dislocation density, or because the W doping affects the point defect concentration. There is a possibility that both effects are at work because the diffusion of point defects seems to be essential to the kinetic process of dislocation reactions, as showed for the $BaTiO_3/SrTiO_3$ system (Suzuki et al., 1999). It is expected that doping with W on the Ti site should partially compensate oxygen vacancies, which would have an opposite effect on strain. However, at the same time, the doping might increase the density of Ti interstitials, which is then expected to increase inhomogeneous strain if interstitials are nonrandomly distributed at the preferential crystallographic sites. This point warrants a careful study of point defect concentration and distribution, which is the focus of the future study.

The difference in inhomogeneous strain is responsible for the relatively large contribution to the change of ferroelectric properties. Following Eq. (5.26), in Figure 5.5 we plot the shift of the Curie-Weiss temperature for both models, that is, when only elastic-strain contribution is considered and when both elastic and inhomogeneous strain are taken into account. It is evident that the latter shows a much better correlation. Figure 5.3 indicates that the elastic and inhomogeneous strains are most often of a complementary magnitude. For instance, if a relief of elastic strain by introduction of misfit dislocations at the growth temperature was smaller, this would cause a larger elastic strain in the lattice, and vice versa. This implies that minimizing dielectric loss through the relief of only elastic strains might not yield the desired effect because the

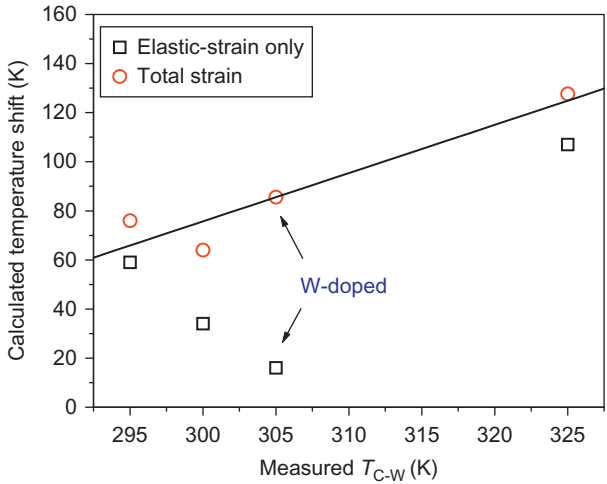

Figure 5.5 Temperature shift of the Curie-Weiss temperature, calculated by Eqs. (5.2a) and (5.2b) for both elastic strain and total (elastic and inhomogeneous) strain contribution to the Gibbs free energy as a function of Curie-Weiss temperature determined from the dielectric measurements (compare Figure 5.1). Note an especially large influence on the result for the W-doped film.

total strain—that is, both elastic and defect-related inhomogeneous strain—should instead be used to estimate effects on the ferroelectric and dielectric properties of thin films.

5.5 Section 2: conclusions

The results indicate that the doping at the Ti site influences the microstructure of $Ba_{0.6}Sr_{0.4}TiO_3$ epitaxial thin films grown on the (001) $LaAlO_3$ substrate. The misfit relaxation is suppressed in the case of Mn but increases when doping with W. Both compressive in-plane elastic strains (stresses) and in particular inhomogeneous strains influence the observed increase in Curie-Weiss temperature. This seems to corroborate the assumption that the Curie-Weiss temperature and extrinsic dielectric losses strongly depend on internal stresses and defects. For a good agreement with the thermodynamic theory, it is necessary to consider the contribution of inhomogeneous strains.

Acknowledgments

Nicolae C. Popa (National Institute of Materials Physics, Romania), Allen Hermann, Padmanabhan Ramakrishnan, Priscila Spagnol, and Sugantha Mani (all University of Colorado-Boulder) have contributed to the different parts of this chapter and are greatly acknowledged for their contributions.

References

Auciello, O., Scott, J.F., Ramesh, R., 1998. The physics of ferroelectric memories. Phys. Today 51, 22.

Ayers, J.E., 1994. The measurement of threading dislocation densities in semiconductor crystals by X-ray diffraction. J. Cryst. Growth 135, 71.

Balzar, D., 1999. Defect and microstructure analysis by diffraction. In: Snyder, R.L., Bunge, H.J., Fiala, J. (Eds.), International Union of Crystallography Monographs on Crystallography No. 10. Oxford University Press, New York, p. 94.

Balzar, D., Ramakrishnan, P.A., Spagnol, P., Mani, S., Hermann, A.M., Matin, M.A., 2002. Influence of strains and defects on ferroelectric and dielectric properties of thin-film barium-strontium titanates. Jpn. J. Appl. Phys. 41, 6628.

Balzar, D., Ramakrishnan, P.A., Hermann, A.M., 2004. Defect-related lattice strain and the transition temperature in ferroelectric thin films. Phys. Rev. B 70, 92103.

Behnken, H., 2000. Strain-function method for the direct evaluation of intergranular strains and stresses. Phys. Stat. Sol. A177, 401–418.

Bunge, H.J., 1982. Texture Analysis in Material Science. Butterworth, London.

Chang, W., Horwitz, J.S., Carter, A.C., Pond, J.M., Kirchoefer, S.W., Gilmore, C.M., Chrisey, D.B., 1999a. The effect of annealing on the microwave properties of $Ba_{0.5}Sr_{0.5}TiO_3$ thin films. Appl. Phys. Lett. 74, 1033.

Chang, W., Horwitz, J.S., Kim, W.J., Pond, J.M., Kirchoefer, S.W., Gilmore, C.M., Qadri, S.B., Chrisey, D.B., 1999b. Pulsed laser deposition of $Ba_xSr_{1-x}TiO_3$ films on MgO, $LaAlO_3$ and $SrTiO_3$ for tunable microwave applications. Mater. Res. Soc Symp. 541, 693.

Christenson, A.L., Rowland, E.S., 1953. Trans. A.S.M. 45, 638–676.

Dalberth, M.J., Price, J.C., Rogers, C.T., 1998. Epitaxial lift-off of strontium titanate thin films and the temperature dependence of the low frequency dielectric properties of the films. In: Ferroelectric Thin Films VI Symposium, Mater. Res. Soc, p. 371.

Hauk, V., 1952. Arch. Eisenhüttenwesen 23, 353–361.

Hermann, A.M., Price, J.C., Scott, J.F., Yandrofski, R.M., Naziripour, A., Galt, D., Duan, H.M., Paranthaman, M., Tello, R., Cuchiaro, J., Ahrenkiel, R.K., 1993. Deposition and characterization of low-loss epitaxial nonlinear dielectric thin films for microwave devices. Bull. Am. Phys. Soc. 38, 689.

Hermann, A.M., Veeraraghavan, B., Balzar, D., Fickett, F.R., 2000. Integr. Ferroelect. 29, 161–173.

Hordon, M.J., Averbach, B.L., 1961. X-ray measurements of dislocation density in deformed copper and aluminum single crystals. Acta Metall. 9, 237.

Kroner, E., 1958. Berechnung der Elastischen Konstanten des Vielkristalle aus dem Konstanten des Einkristalls. Z Phys. 151, 504–518.

Li, H.-C., Si, W., Wang, R.-L., Xuan, Y., Liu, B.-T., Xi, X.X., 1998a. Mater. Sci. Eng. B 56, 218.

Li, H.-C., Si, W., West, A.D., Xi, X.X., 1998b. Appl. Phys. Lett. 73, 464.

Lines, M.E., Glass, A.M., 2001. Principles and Applications of Ferroelectrics and Related Materials. Clarendon Press, Oxford, p. 112.

Pertsev, N.A., Zembilgotov, A.G., Tagantsev, A.K., 1998. Effect of mechanical boundary conditions on phase diagrams of epitaxial ferroelectric thin films. Phys. Rev. Lett. 80, 1988.

Popa, N.C., 2008. Microstructural properties: texture and macrostress effects. In: Dinnebier, R. E., Billinge, S.J.L. (Eds.), Powder Diffraction, Theory and Practice. RSC, Cambridge, pp. 332–375 (Chapter 12).

Popa, N.C., Balzar, D., 2001. Elastic strain and stress determination by Rietveld refinement: generalized treatment for textured polycrystals for all Laue classes. J. Appl. Cryst. 34, 187–195.

Popa, N.C., Balzar, D., 2012. Elastic strain and stress determination by Rietveld refinement: generalized treatment for textured polycrystals for all Laue classes. Corrigenda. J. Appl. Cryst. 45, 838–839.

Popa, N.C., Balzar, D., Vogel, S.C., 2014. Strain and stress tensors of rolled uranium plate by Rietveld refinement of TOF neutron-diffraction data. J. Appl. Crystallogr. 47, 154–159. http://dx.doi.org/10.1107/S1600576713029208.

Reuss, A., 1929. Berechnung der Fliessgrenze von Mischkristallen auf Grund derPlastizitäsbendingung für Einkristalle. Z. Angew. Math. Mech. 9, 49–58.

Rietveld, H.M., 1969. A profile refinement method for nuclear and magnetic structures. J. Appl. Cryst. 2, 65–71.

Speck, J.S., Pompe, W., 1994. Domain configurations due to multiple misfit relaxation mechanisms in epitaxial ferroelectric thin films. I. Theory. J. Appl. Phys. 76, 466.

Suzuki, T., Nishi, Y., Fujimoto, M., 1999. Analysis of misfit relaxation in heteroepitaxial $BaTiO_3$ thin films. Philos. Mag. A 79, 2461.

Voigt, W., 1928. Lehrbuch der Kristallphysik. Teubner Verlag, Berlin-Leipzig.

Von Dreele, R.B., 1997. Quantitative texture analysis by Rietveld refinement. J. Appl. Cryst. 30, 517–525.

Wang, Y.D., Lin Peng, R., McGreevy, R., 1999. High anisotropy of orientation dependent residual stress in austenite of cold rolled stainless steel. Scripta Mater. 9, 995–1000.

Wang, Y.D., Lin Peng, R., McGreevy, R., 2001. A novel method for constructing the mean field of grain-orientation-dependent residual stress. Philos. Mag. Lett. 81, 153–163.
Wang, Y.D., Wang, X.L., Stoica, A.D., Richardson, J.W., Lin Peng, R., 2003. Determination of the stress orientation distribution function using pulsed neutron sources. J. Appl. Cryst. 36, 14–22.

Recent advances in thermal analysis of nanoparticles: methods, models and kinetics*

6

E. Mansfield
National Institute of Standards and Technology, Boulder, CO, USA

6.1 Introduction

Nanoparticles are an important and diverse class of materials with applications in all major areas of the economy, including manufacturing, medicine, and energy. The use of engineered nanoparticles in consumer products increases dramatically each year. The Project on Emerging Nanotechnologies reports over 1600 nano-containing consumer products on the market as of October 2013, as compared to 54 products in 2005 (Project on Emerging Nanotechnologies, 2013). The main classes of nanoparticles utilized in products include carbon-based (nanotubes and fullerenes), metal nanoparticles (including gold, silver, iron, and copper nanoparticles), metal oxide nanoparticles (iron oxide, ZnO, TiO_2, CeO_2, SiO_2, among others), and quantum dots (Hornyak et al., 2009). There are endless possibilities for nanoparticle coatings that can be applied to the surface of these particles in order to improve solubility, improve biocompatibility, target interactions with other molecules, or prevent interactions with the nanoparticle's environment (Richman and Hutchison, 2009). In fact, most nanoparticles used in commercial products have surface functionalizations of some sort. More complex nanoparticles, such as core-shell nanoparticles for medical applications, are being developed. All of these nanoparticle systems will require analytical characterization. Complete characterization of the material, including the core, coatings, and any other factors affecting nanoparticle use are essential to understanding its potential as a commercial product, evaluating the effects of its release into the environment, or developing it for biological or medical applications.

Nanoparticle characterization is not a trivial task (Richman and Hutchison, 2009). The methods available for bulk-scale analysis of materials are not necessarily applicable to nanoparticles. Because of these and sample preparation challenges, complementary analytical techniques are used to confirm the values of specific measurements (Decker et al., 2009). Some of the most common methods for analysis include microscopy (scanning electron microscopy, transmission electron microscopy, fluorescence), spectroscopy (Raman, UV/visible, Fourier-transform infrared

*Contribution of NIST, an agency of the U.S. government; not subject to copyright in the United States.

Modeling, Characterization and Production of Nanomaterials. http://dx.doi.org/10.1016/B978-1-78242-228-0.00006-5

spectroscopy (FTIR), fluorescence), elemental characterization (neutron activation analysis, inductively coupled plasmon techniques), and particle-sizing methods (dynamic light scattering, field flow fractionation) (Hornyak et al., 2009). In general, microscopy methods provide a means for visualizing the sample's size, shape, and morphology. Spectroscopy and elemental characterization are often used to identify the nanoparticles' elemental and structural characteristics, and particle-sizing methods yield information about size and shape to some degree. Development of these techniques for nanoparticle analysis is a growing area, because many have to be adapted to address the unique challenges of small particle size and limited sample volumes that come with nanoparticle analysis. The above list is not a complete list of techniques or results that can be obtained from those techniques, but it is an introduction to the analytical data most commonly reported.

Thermal analysis methods, which measure the properties of the sample as a result of change in temperature, have been used historically for analyzing filler particles in composites. Thermoanalytical measurements are often used to provide quick information on nanoparticles in the manufacturing or laboratory setting, including inferring the composition of the materials and nanoparticle coating composition, as well as structural information about the material (crystallinity) and kinetics of formation. The most common of the thermal analysis methods utilized for nanoparticle work are discussed here in more detail, including thermogravimetric analysis (TGA), calorimetry, and differential scanning calorimetry (DSC). The application of these methods to nanomaterials in some cases can be direct, using the same methods developed for bulk-scale materials. In some cases, sample preparation is minimal. However, it may be necessary to concentrate and dry a sample to ensure that the minimum sample volume for the analytical technique is met (typically $\sim$10 mg). Modifications to traditional thermal analysis methods have been made to accommodate nanomaterial samples. This usually results in the development of new methods that minimize sample volume to accommodate laboratory-scale samples, which may be produced in limited quantities or obtained from the environment. Future applications of thermal analysis methods for nanoparticle samples are discussed at the end of this chapter.

6.2 Thermal analysis methods

6.2.1 Thermogravimetric analysis

For most thermal analysis methods, a sample is heated and undergoes physical and chemical changes that can yield more information about the material. TGA describes the process in which the sample mass of a material is monitored with heating. The sample is introduced onto a balance within a furnace and heated using a specific temperature program. The atmosphere in which the sample is heated is controlled by introducing vacuum, and/or inert (argon, nitrogen) or reactive (oxygen, air) gases. As a result of the heating, the mass of the sample will either increase or decrease as a result of changes in the material. The major data outputs are thermograms, either the percentage mass loss with time or the percentage mass loss with temperature.

Some of the most commonly observed transitions include loss of water (i.e., desorption or vaporization) or oxidation (i.e., uptake of oxygen from a reactive environment). Decomposition of the material, whether through combustion (an exothermic event in a reactive environment) or pyrolysis (an endothermic event in an inert environment), is one of the most common chemical phenomena studied with TGA. Further information can be obtained by coupling the TGA to an evolved-gas analysis technique, such as FTIR, mass spectrometry (MS), or gas chromatography mass spectrometry (GC-MS). A key TGA measurement is the residual mass of the sample at a given temperature, usually given as a percentage of the original sample mass:

$$M\text{res}(\%) = \frac{M_{\text{r},T}}{M_{\text{s}}} 100\%$$

where Mres (%) is the residual mass expressed as a percentage, $M_{\text{r},T}$ is the mass remaining at as specific temperature (T) in grams, and M_{s} is the initial mass of the sample in grams. At the end of an oxidizing sample run, the residual mass is often referred to as the ash content. Other important TGA metrics are the temperatures in which events occur. Temperatures of importance can be determined by taking the first derivatives of the thermogram and identifying the peaks. This can show features that may not be easily discerned or quantified in the thermogram to be identified (i.e., shoulders). The onset temperature at which major transitions occur may also be quantified.

6.2.2 Differential scanning calorimetry

Calorimetry is the general term for the measurement of thermodynamic changes in material due to chemical reactions, phase transitions, and other physical changes. Many types of calorimetry can be applied to nanoparticle samples. Thermodynamic data (heat capacity, enthalpy, and entropy) and kinetic data (rate of reactions, activation energies) can be measured with DSC. The difference in heat flow between the sample (T_{S}) and a reference material (T_{R}) is monitored and recorded as a function of temperature. In DSC, the sample and reference cells are heated independently so that $\Delta T = T_{\text{S}} - T_{\text{R}} = 0$; the heat flow difference is monitored as a function of temperature. As a material undergoes a phase transition, more or less heat will be needed to maintain the sample temperature, depending on whether the transition is endothermic or exothermic. The difference in energy needed to match the sample temperature to the reference is the amount of excess heat released or absorbed as a result of sample transitions. In the most basic form, the information from DSC can be described by the following equation:

$$\frac{\mathrm{d}H}{\mathrm{d}t} = mC_p \frac{\mathrm{d}T}{\mathrm{d}t}$$

where $\mathrm{d}H/\mathrm{d}t$ is the DSC heat flow signal, m is the sample mass, C_p is the sample heat capacity, and $\mathrm{d}T/\mathrm{d}t$ is the heating rate (O'Neill, 1966). Physical changes in the

material, such as melting, crystallizing, and transitioning through glass transitions, can all be observed using DSC. A similar technique to DSC is differential thermal analysis, or DTA, which measures the difference in temperature between the sample and the reference, not the heat flow. STA, or simultaneous thermal analysis, is an extension of the technique that allows for DSC and TGA measurements to occur simultaneously.

6.2.3 Other calorimetry methods

Other calorimetry methods are used to determine different thermodynamic parameters of nanoparticle systems. Isothermal titration calorimetry (ITC) can be used to measure enthalpy changes and interactions between nanoparticles and materials binding to the surface, including binding affinities and stoichiometry. ITC is well suited for measurements in biological and/or nanoparticle solutions for drug delivery because it allows for solution-based measurements (Bouchemal, 2008). Nanocalorimetry is a general term being used for traditional calorimetric measurements that are currently being scaled to smaller sample sizes and faster rates appropriate for nanoparticles (Yi and La Van, 2012) and will be discussed in detail.

6.3 Thermal analysis of nanoparticle purity and composition

Nanoparticle purity and composition are two of the most important parameters to consider prior to deploying nanomaterials in other systems. Thermal analysis is a rapid technique for determining composition and purity of nanoparticles through the material's decomposition, with minimal sample preparation. Modifications made to nanomaterials before and after chemical reactions, such as the addition of surface chemistry, can also be measured.

An important aspect of assessing nanomaterial purity and composition is determining the chemical components of a nanoparticle, especially during formation and synthesis. Some nanoparticles are made through solution-based processes, in which solution components react to form the material; nanoparticles grow as the material precipitates. Other nanoparticles are synthesized using chemical vapor deposition or physical vapor deposition pathways. Some methods rely on the entrapment of other molecules during the nanoparticle synthesis process and can lead to nanoparticle populations of unknown compositions. For example, hollow nanoparticle populations synthesized via sol-gel methods encapsulate some of the suspension solution within the nanoparticle (Sarmento et al., 2006). This is a common method for assembling drug-delivery nanoparticles, especially with a mechanism for slowly leaching drug moieties or targeted delivery to a specific location (Castelli et al., 2005). In these cases, it is important to know exactly how much of each component is present. TGA can be used to evaluate the components of nanoparticles to determine how much of a certain component is present in the final mixture (mass percentage of each

component). Nanoparticles must first be isolated from the encapsulating solution through centrifugation or other means of separation, after which, the nanoparticle sample components can be analyzed. The chemical composition is determined by heating the nanoparticle sample and comparing to the oxidation temperature transitions to those of the pure components (Dong and Feng, 2005). The mass loss at each temperature is used to quantitatively determine chemical constituents. TGA and DSC have also been used to validate protein encapsulation in nanoparticles by measuring the mass percent composition and exo/endothermic results from the sample with encapsulated proteins versus the pure nanoparticle samples. The difference in the thermograms provides evidence of protein encapsulation and can give an estimate of the mass of protein per nanoparticle (Ma et al., 2004). TGA and DSC are bulk-scale techniques, so information about the size and morphology of the nanoparticles may be needed to relate total mass loss to mass loss per nanoparticle. Such data includes the average size of the nanoparticle (measured with particle-sizing instrumentation) and/or the mass per nanoparticle. Similarly, the mass of nanoparticles loaded into other systems, such as liposomal membranes, can be evaluated using similar TGA methods (Amstad et al., 2011). DSC can be used to evaluate crystallization behaviors and interactions of drugs with the nanoparticle drug-delivery systems (Siekmann and Westesen, 1994). DSC has been used to evaluate interactions between indomethacin, a lipophilic drug, and solid lipid nanoparticles prepared for pharmaceutical drug delivery. Kinetic studies in the DSC were used to evaluate if the indomethacin was associated with the lipid system and how it was migrating through the bulk of the nanoparticle (Castelli et al., 2005). Microemulsion synthetic methods also benefit from calorimetric determination of the nanoparticles and synthesis matrix to garner information about how changes in the synthetic process may impact nanoparticle composition (Fini et al., 2003). By measuring changes in the experimental molar enthalpies as nanoparticles are formed, the general impact on the size of cadmium sulfide (CdS) nanocrystals formed and the energetic contributions of structural changes that occurred during nanoparticle synthesis could be determined (Fini et al., 2003). From measurements such as these, the synthesis of the nanomaterials could be tuned to obtain particles of desired sizes.

By comparison to standards, the purity of synthesized nanomaterials can be measured by DSC and TGA. TGA can provide composition information for non-metal-based nanoparticles. One example of this is the application of TGA for the analysis of carbon nanotubes (CNTs) (Hornyak et al., 2009). CNT samples typically consist of amorphous carbons, structured CNTs, and metal catalyst particles used to grow the CNTs. By heating the CNT powder in an oxidizing environment, CNTs will decompose at a given temperature characteristic of the nanomaterial, with individual transitions observable for each component. The observed oxidation temperatures are around 200 °C for amorphous carbons, 400 °C for single-wall CNTs, 600 °C for multiwall CNTs, and anything over 650 °C is attributed to a metal catalyst and its oxidation products (Mansfield et al., 2010a). The use of TGA in the case of CNTs can provide a measure of purity for CNT material, as measured by the percentage of the sample that degrades in the temperature range of interest. Furthermore, TGA is one of the fastest methods to measure relative percentages of single-walled versus

multiwalled CNTs in a sample (Mansfield et al., 2010a). The purity of other organic nanoparticles, such as polymer-based particles or lipid nanoparticles, can also be measured with TGA. In addition to composition, the interactions between components that comprise the nanoparticles can be measured using DSC (Sarmento et al., 2006). For example, nanoparticles made from polyelectrolytes with opposite electrical charges form more complex mixtures than just the physical mixture of the two components. Alginate, a negatively charged polyelectrolyte, is often combined with chitosan, with a positively charged amine-containing polyelectrolyte, which yields a distinct broad exothermic peak in the DSC (Sarmento et al., 2006). When the two components are mixed but do not interact significantly, two distinct exothermic peaks (one for alginate, one for chitosan) are observable. These typically occur at the same temperatures as those for the pure components. Mixtures that interact with each other usually have a different thermal signature, often with one broad peak that defines the mixture. By utilizing TGA to evaluate the composition of the particle, one can distinguish if particles are a mixture of the two components or a more complex, thermally stable system. This technique is also commonly used to demonstrate miscible and immiscible polymer blends.

Chemical composition is also important for determining what is attached to the core of a nanoparticle. These coatings can be attached through noncovalent or covalent means. STA can be used to validate the attached coating, as can TGA and DSC individually. In some systems, composition is theoretically known but needs to be validated after a synthesis. In a $[Ni(en)_3](NO_3)_2$ nanoparticle population (Farhadi and Roostaei-Zaniyani, 2011) two major transitions were observed in the thermogram that validated the theoretical calculated weights of each ligand (en, or ethylenediamine, and NO_3) from the complex, indicating the nanoparticle population was the expected composition. The DTA curve showed that these mass losses consisted of an endothermic event (release of ethylenediamine) followed by exothermic decomposition of the complex, giving additional information about the kinetics of the reactions to form the nanoparticles (Farhadi and Roostaei-Zaniyani, 2011). Another example for which this may be useful is metal-conjugated dendrimer nanoparticles, where dendrimers are covalently attached to the core and the nanoparticle composition can be calculated theoretically (Gopidas et al., 2003). The mass loss measurements, as determined by TGA, can be used to obtain ligand:nanoparticle ratios for lesser known ligand-stabilization methods (Woehrle et al., 2005; Sebby and Mansfield, 2010). Ratios in these systems can be validated by other measurement techniques, including X-ray photoelectron spectroscopy and nuclear magnetic resonance to further confirm TGA results.

Other nanoparticle coatings, such as adsorbed noncovalent polymer or protein coatings, are particularly important to study, because these can be naturally occurring and lead to dramatic changes in how the nanoparticle interacts with the environment. Adsorbed coatings are often added to protect the nanoparticle from the environment or improve solubility in the given environment. Adventitious coatings may develop as a nanoparticle travels through a natural environment. Measuring these adsorbed coatings is complex, because many factors of the nanoparticle (surface properties such as size, charge) and properties of the adsorbed moiety (charge, hydrophobicity)

govern these interactions. Some examples include protein coronas, which form as a result of exposure to protein systems, and adsorbed natural organic matter in water samples. Measuring the number of associated proteins on the nanoparticle surface under biological conditions is of importance as more and more nanomaterials get introduced into biological systems for therapeutic or inadvertent means (Sebby and Mansfield, 2010). ITC has been used to measure stoichiometric affinity and enthalpy of protein-nanoparticle interactions (Cedervall et al., 2007).

Proteins adsorbed to nanoparticle solutions can be assessed for dried samples. The nanoparticle concentration, protein concentration, and surface area are used to calculate the number of proteins per nanoparticle. Surface coverage can be estimated through simple surface-packing models (Cedervall et al., 2007). TGA is also used to determine the ratio of adsorbed protein mass or ligands to the nanoparticle surface (Sebby and Mansfield, 2010; Cedervall et al., 2007; Wang et al., 2012; Mansfield et al., 2014). Mass loss due to decomposition of nanoparticles at specific temperatures can be used to determine (i) dehydration of the nanoparticle or associated protein, (ii) mass loss due to decomposition of the surface ligands/associated proteins, and (iii) mass loss due to decomposition of the nanoparticle. In some cases, it may be necessary to correct the mass measurements for the loss of water to obtain the mass loss due only to surface coatings (Wang et al., 2012). The corrected mass measurements can then be used to estimate functional group density and coverage on the nanoparticle surface. Changes in nanoparticle sizes, charges, and other properties can be used to understand adsorption behaviors of proteins using TGA.

6.4 Evaluation of nanoparticle-containing composites

Nanocomposites include materials in which nanoparticles are added to a matrix material to tailor the optical, mechanical, magnetic, electrical, or thermal properties. Thermal analysis methods are often used to validate the differences between the initial composite versus one that incorporates nanoparticles. Changes in the thermal performance of composites with the addition of nanoparticles can be monitored using DSC and TGA. Shifts to higher decomposition temperatures, as measured by TGA, indicate increased thermal stability of the composite material (Hasan et al., 2006). The measurement of glass transition temperatures and melting points with DSC can be used to evaluate differences in degree of crystallinity and heat of fusion (Hasan et al., 2006; Rittigstein and Torkelson, 2006; Shah et al., 2005). Mass loss profiles via TGA can also be used in conjunction with MS to determine what is being released from the composite at a given time (water, decomposition products), which can provide further information of the composite composition (Kanniah et al., 2012). Using the information obtained from TGA and DSC, any enhancements or negative changes from the original composite structure can be evaluated. Not only does thermal analysis give information about the bulk properties that may affect the process ability of the composites, but it also can give information about how the particles are integrated into the composite network.

6.5 Monitoring kinetics of thermal transitions

Thermal analytic techniques can be used to monitor kinetic phenomena of nanoparticle systems. One of the major kinetic systems that thermal analysis can be used to monitor is properties within nanocomposites. Cure kinetics of nanocomposites can be affected by nanoparticle composition and density within the composite. DSC can also provide glass transition temperatures, which can be used to predict nanoparticle mobility within the matrix (Shah et al., 2005). The kinetics of curing can be measured by monitoring the evolution of heat with DSC and the activation energy. The degree of cure is defined as the heat at a certain time during a cure divided by the total heat of reaction. Assuming the heat released during the cure process is proportional to the reaction rate, the rate of cure is calculated as:

$$\frac{d\alpha}{dt} = \frac{1}{H_g}\frac{dH}{dt}$$

where the $d\alpha/dt$ is the reaction rate, H_g is the total heat of the reaction, and dH/dt is the heat evolved during the cure at a certain time (Rosso and Ye, 2007).

Calorimetry provides a means for the measurement of many types of nanoparticle kinetics. Direct measurement via a micromechanical calorimeter of particle energies opened up the field for nanoparticle energetic measurements via thermal analysis (Bachels et al., 2000). After nanoparticle samples were sorted by size, the heat released was measured using the calorimeter. Formation energies, a particle size-dependent quality, were measurable using this method, and the capabilities were extended to allow for measurement of nanoparticle energetics in catalyst sintering applications (Campbell et al., 2002). Calorimetry, in this case, gave size-dependent energy changes of metal atoms in nanoparticles, as predicted by theory. Sintering of nanoparticle metal catalysts was also possible after the initial calorimetry measurements (Campbell et al., 2002). Heat of adsorption obtained from calorimetry can also be used to predict energetics of nanoparticle oxide formation (Navrotsky, 2003).

Nanoparticle energetic state and the growing process as a result of reactant concentrations are measurable through calorimetric means. Experimental enthalpies are obtained by integrating the area under a calorimeter signal versus time plot while reactants are mixed in a reaction chamber. Many different microemulsion-synthesized nanoparticle systems have been studied using this method. Rate equations can also be determined from the work if the time constants used are greater than that of the calorimeter (Aliotta et al., 1995). Rates of reactions for kinetic processes, such as thermal dehydration of nanoparticle populations, have been measured by constructing Arrhenius plots from DSC thermograms (Al-Kady et al., 2011). The Arrhenius plots can be used to determine the energy of activation for the hydration process. In one case, the higher activation energy indicated a chemical reaction rather than diffusion-controlled reaction (hematite nanoparticles (Al-Kady et al., 2011)), and there was a highly ordered transition state in the dehydration process. Other aspects, such as reactivity of nanoparticles, have been studied using nonisothermal TGA measurements (Park et al., 2005).

6.6 Trends in development of thermal analysis for nanoparticles

There is room for improvement for today's thermoanalytical techniques to become more appropriate for nanoparticle systems. Smaller sample sizes, ability to increase sensitivity, and monitoring nanomaterial-matrix interactions are of importance. Recent developments in thermoanalytical methods have made nanoparticle analysis on small scales possible.

One method making strides in the application of nanomedical-based products is the advancement of nanocalorimetry. Nanocalorimetry is a microchip-based system capable of measuring samples on the order of nanoliter in volume or micrograms to nanograms in mass (Yi and La Van, 2012) that has a resolution below 5 nW when measuring heats of reactions (Lee et al., 2009). The small sample volumes allow for the measurement of as-produced samples and their interactions with the environment, as well as interactions between nanomaterials and cells, which is of importance in the area of nanomedicine (Yi and La Van, 2012). As with any thermoanalytical technique, accurate temperature, power, and mass measurements are needed. The measurements of these small-scale interactions are difficult because the compensation for heat loss in these systems is not as controlled as in large-scale instrumentation. Overall, the application of nanocalorimetry has led to advances in understanding binding reactions between biological systems and nanoparticles, crystallization and melting behaviors of particles, and size-dependent thermodynamics and kinetics. Further development to push toward femtowatt measurements (Burke and LaVan, 2013), improved uncertainty analysis, and aqueous environmental analysis will yield the next phase of nanocalorimeters (Yi and La Van, 2012).

TGA has also been advanced significantly to provide decomposition information on nanotechnology-relevant scales. In the late 1970s, the use of more sensitive balances for TGA, specifically utilizing quartz crystal microbalances, was suggested as a potential improvement. Recent work at the National Institute of Standards and Technology has led to the development of a microscale-TGA instrument that requires 1000-fold less sample than traditional instrumentation (Mansfield et al., 2010b) and overcomes previous challenges associated with use of quartz crystal microbalances. TGA has been limited by sensitivity of the microbalance, with commercial instruments requiring at least 1 mg of sample. Because nanoparticle applications require tighter controls on nanoparticle compositions, often the yield from synthesis is far below the 1 mg size limit for traditional instruments. The microscale-TGA method replaces microbalances in traditional instruments with piezoelectric quartz crystal microbalances to allow for analysis on sample masses of 1-10 μg and sensitivities of mass detection on the order of nanogram (Johnson et al., 2012). After a correction for thermal changes in quartz at elevated temperatures (which previously limited use of quartz crystal microbalances), decomposition data has been obtained for a number of materials (Mansfield et al., 2010b). CNT decomposition can be monitored using microscale-TGA, as well as quantitative measurement of coatings on gold and silica nanoparticles (Sebby and Mansfield, 2010; Mansfield et al., 2014; Mansfield et al., 2010b), all of which could

be compared to conventional TGA or other analytical results. This new TGA instrumentation will enable measurements of limited nanoparticle populations, such as those that may be obtained from environmental or biological samples without complex sample preparation or tedious sample analysis. Further development of the microscale-TGA measurements for nanomaterial analysis would include the linking of microscale-TGA to secondary detection instrumentation (Raman, MS) to yield more information about the decomposition products, improving sensitivity and commercialization of the instrumentation (Mansfield and Quinn, 2011).

6.7 Conclusions

Thermoanalytical methods are now widely used for the study of nanomaterials and products containing nanoparticles. Thermal analysis has many advantages that complement other nanoparticle analysis techniques. In most cases, preparation of the nanoparticle sample is minimal (i.e., concentration of the sample) and no additional modifications (i.e., fluorescent labeling) are needed to complete the analysis. A wide range of techniques can be used, including TGA, DSC, and other calorimetric systems. Commercial instrumentation is available, and interpretation of results is often easy enough that thermal analysis can be applied in the manufacturing setting to compare batch-to-batch reproducibility (Mansfield et al., 2010a). Nanoparticle purity and composition can be assessed quickly on the laboratory scale with minimal sample preparation, and results can be compared to other analytical methods to provide further certainty of the composition. Interactions that may influence nanoparticle coatings can also be determined using thermal methods, including those in which the nanoparticle may be exposed to environmental systems such as water or biological media. Kinetics of nanoparticle energetics is increasingly important as more complex synthetic methods are used. Nanoparticle systems, such as nanocomposites, can be characterized for composition and kinetics of reactions as related to nanoparticle content.

References

Aliotta, F., et al., 1995. Calorimetric investigation on the formation of gold nanoparticles in water/AOT/n-heptane microemulsions. Thermochim. Acta 265, 15–23.

Al-Kady, A.S., et al., 2011. Structural and fluorescence quenching characterization of hematite nanoparticles. Spectrochim. Acta A 83, 398–405.

Amstad, E., et al., 2011. Triggered release from liposomes through magnetic actuation of iron oxide nanoparticle containing membranes. Nano Lett. 11, 1664–1670.

Bachels, T., Schäfer, R., Güntherodt, H.-J., 2000. Dependence of formation energies of tin nanoclusters on their size and shape. Phys. Rev. Lett. 84 (21), 4890–4893.

Bouchemal, K., 2008. New challenges for pharmaceutical formulations and drug delivery systems characterization using isothermal titration calorimetry. Drug Discov. Today 13 (21–22), 960–972.

Burke, B.G., LaVan, D.A., 2013. Laser heating and detection of bilayer microcantilevers for non-contact thermodynamic measurements. Appl. Phys. Lett. 102, 021916.
Campbell, C.T., Parker, S.C., Starr, D.E., 2002. The effect of size-dependent nanoparticle energetics on catalyst sintering. Science 298, 811–814.
Castelli, F., et al., 2005. Characterization of indomethacin-loaded lipid nanoparticles by differential scanning calorimetry. Int. J. Pharm. 304, 231–238.
Cedervall, T., et al., 2007. Understanding the nanoparticle-protein corona using methods to quantify exchange rates and affinities of proteins for nanoparticles. Proc. Natl. Acad. Sci. 104, 2050–2055.
Decker, J.E., et al., 2009. Sample preparation protocols for realization of reproducible characterization of single-walled carbon nanotubes. Metrologia 46 (6), 682–692.
Dong, Y., Feng, S.-S., 2005. Poly(D, L-lactide-co-glycolide)/montmorillonite nanoparticles for oral delivery of anticancer drug. Biomaterials 26, 6068–6076.
Farhadi, S., Roostaei-Zaniyani, Z., 2011. Preparation and characterization of NiO nanoparticles from thermal decomposition of the $[Ni(en)_3](NO_3)_2$ complex: a facile and low-temperature route. Polyhedron 30, 971–975.
Fini, P., et al., 2003. Calorimetric study of CdS nanoparticle formation in w/o microemulsions. Mater. Sci. Eng. C 23, 1077–1081.
Gopidas, K.R., Whitesell, J.K., Fox, M.A., 2003. Synthesis, characterization, and catalytical applications of a palladium-nanoparticle-cored dendrimer. Nano Lett. 3 (12), 1757–1760.
Hasan, M.M., et al., 2006. Effect of SiO_2 nanoparticle on thermal and tensile behavior of nylon-6. Mater. Sci. Eng. A 429, 181–188.
Hornyak, G.L., et al., 2009. Introduction to Nanoscience & Nanotechnology. CRC Press, Boca Raton, FL.
Johnson, W.L., Mansfield, E., et al., 2012. Thermogravimetric analysis with a heated quartz crystal microbalance. In: Frequency Control Symposium (FCS), 2012 IEEE International.
Kanniah, V., et al., 2012. Graphite functionalization for dispersion in a two-phase lubricant oligomer mixture. J. Appl. Polym. Sci. 125, 165–174.
Lee, W., et al., 2009. High-sensitivity microfluidic calorimeters for biological and chemical applications. Proc. Natl. Acad. Sci. 106 (36), 15225–15230.
Ma, D., et al., 2004. Fabrication of protein/silica core-shell nanoparticles by microemulsion-based molecular wrapping. Adv. Mater. 16 (20), 1838–1841.
Mansfield, E., Quinn, T.P., 2011. Microscale thermogravimetric device analyzes nanoparticle purity and coatings. SPIE Newsroom. http://dx.doi.org/10.1117/2.1201102.003528.
Mansfield, E., Kar, A., Hooker, S.A., 2010a. Applications of TGA in quality control of SWCNTs. Anal. Bioanal. Chem. 396, 1071–1077.
Mansfield, E., et al., 2010b. Quartz crystal microbalances for microscale thermogravimetric analysis. Anal. Chem. 82 (24), 9977–9982.
Mansfield, E., et al., 2014. Determination of nanoparticle surface coatings and nanoparticle purity using microscale thermogravimetric analysis. Anal. Chem. 86 (3), 1478–1484.
Navrotsky, A., 2003. Energetics of nanoparticle oxides: interplay between surface energy and polymorphism. Geochem. Trans. 4 (6), 34–37.
O'Neill, M.J., 1966. Measurement of specific heat functions by differential scanning calorimetry. Anal. Chem. 38 (10), 1331–1336.
Park, K., et al., 2005. Size-resolved kinetic measurements of aluminum nanoparticle oxidation with single particle mass spectrometry. J. Phys. Chem. B 109, 7290–7299.
Project on Emerging Nanotechnologies, 2013. Available from: http://www.nanotechproject.org/.
Richman, E.K., Hutchison, J.E., 2009. The nanomaterial characterization bottleneck. ACS Nano 3 (9), 2441–2446.

Rittigstein, P., Torkelson, J.M., 2006. Polymer-nanoparticle interfacial interactions in polymer nanocomposites: confinement effects on glass transition temperature and suppression of physical aging. J. Polym. Sci. B Polym. Phys. 44, 2935–2943.

Rosso, P., Ye, L., 2007. Epoxy/silica nanocomposites: nanoparticle-induced cure kinetics and microstructure. Macromol. Rapid Commun. 28, 121–126.

Sarmento, B., et al., 2006. Characterization of insulin-loaded alginate nanoparticles produced by ionotropic pre-gelation through DSC and FTIR studies. Carbohydr. Polym. 66, 1–7.

Sebby, K.B., Mansfield, E., 2010. The stability and surface coverage of polymer stabilized gold nanoparticles. eCells Mater. 20 (Suppl. 3), 234.

Shah, D., et al., 2005. Effect of nanoparticle mobility on toughness of polymer nanocomposites. Adv. Mater. 17 (5), 525–528.

Siekmann, B., Westesen, K., 1994. Thermoanalysis of the recrystallization process of melt-homogenized glyceride nanoparticles. Colloids Surf. B: Biointerfaces 3 (3), 159–175.

Wang, B., et al., 2012. Influence of surface charge on lysozyme adsorption to ceria nanoparticles. Appl. Surf. Sci. 258, 5332–5341.

Woehrle, G.H., Brown, L.O., Hutchison, J.E., 2005. Thiol-functionalized, 1.5-nm gold nanoparticles through ligand exchange reactions: scope and mechanism of ligand exchange. J. Am. Chem. Soc. 127, 2172–2183.

Yi, F., La Van, D.A., 2012. Nanoscale thermal analysis for nanomedicine by nanocalorimetry. WIREs Nanomed. Nanobiotechnol. 4, 31–41.

Raman spectroscopy and molecular simulation studies of graphitic nanomaterials

7

D. Casimir, R. Garcia-Sanchez, P. Misra
Howard University, Washington, DC, USA

7.1 Introduction

Many new crystalline forms of carbon were discovered experimentally in the last few decades. These crystalline graphitic materials or allotropes include exotic materials such as C60 buckyballs, carbon nanotubes, and graphene, to name a few. These newer forms of carbon have significantly different properties compared to the more common forms of C in graphite and diamond (Wong and Akinwande, 2011). As a rough guide, the dimensions involved in carbon nanotubes are about 10,000 times thinner than a strand of hair, while graphene is approximately 300,000 times thinner than a single paper sheet. In addition, all three of the low-dimensional carbon allotropes mentioned above—buckyballs, CNTs, and graphene—share a common sp2 covalently bonded, hexagonal arrangement of C-atoms.

7.1.1 CNT synthesis

The three primary modes of producing carbon nanotubes are through chemical vapor deposition (CVD), the arc discharge (AD) method, and laser ablation. While a multitude of varieties of each of these techniques now exist, leading to more subcategories of nanotube manufacturing methods, the above broad categorization serves to highlight the similarities shared by essentially all modes of CNT synthesis. The majority of industrially practical methods of CNT production basically involve the thermal decomposition of a carbon-containing source material in a sealed chamber that is heated to very high temperatures. Metal catalysts present in the chamber serve as nucleation sites for nanotube growth, with empirically determined pressure and temperature conditions that result in the desired nanotube type and diameter distribution.

(a) *Chemical vapor deposition*: In CVD carbon nanotube production, CH_4, CO, or some other carbon-containing gas is decomposed by metal catalysts in a high-temperature chamber at pressures at or below 1 atm. The dissociated carbon atom from the gaseous material that is flowed into the chamber nucleates on the metal catalysts, and self-assembles into cylindrical CNTs. The resultant CNT material is then removed from the furnace after being allowed to cool in order to prevent damage to the tubes due to oxidation.

Modeling, Characterization and Production of Nanomaterials. http://dx.doi.org/10.1016/B978-1-78242-228-0.00007-7
Copyright © 2015 Elsevier Ltd. All rights reserved.

(b) *Arc discharge*: In this technique a graphite electrode with a gap of a few mm is used to produce carbon plasma. Again the process takes place in a sealed chamber that is cooled at or below 1 atm pressure, where the vapor then condenses on metal catalyst particles as the plasma travels toward the cathode. This technique is usually applied in the production of C60 and hence various graphitic materials may be present in the resultant material, leading to postproduction purification and separation of CNTs.

(c) *Laser ablation*: This method refers to the use of a laser in the vaporization of graphite contained in a highly heated chamber. The graphitic target material is usually mixed with catalyst metals, resulting in nanotube formation as the vapor of ablated material condenses on the cooled surface of the chamber.

In all of these nanotube production techniques the exact growth mechanism of these tubular nanostructures are still unclear. Therefore, at present, production of specific chirality or diameter nanotubes is virtually impossible, leaving one to rely on the use of optimized arrangements and densities of catalyst particles to produce statistically correlated distributions of nanotube diameters.

7.1.2 Graphene

Graphene is an allotrope of carbon that consists of covalently bonded atoms arranged in a planar hexagonal structure depicted in Figure 7.1. This two-dimensional material is considered as the conceptual base material for all other carbon allotropes, where single graphite planes can be rolled into cylinders, spheres, or stacked one atop the other to form 0D buckyballs, 1D carbon nanotubes, or graphite, respectively. Graphene was experimentally isolated and studied in 2004 and has arguably rapidly

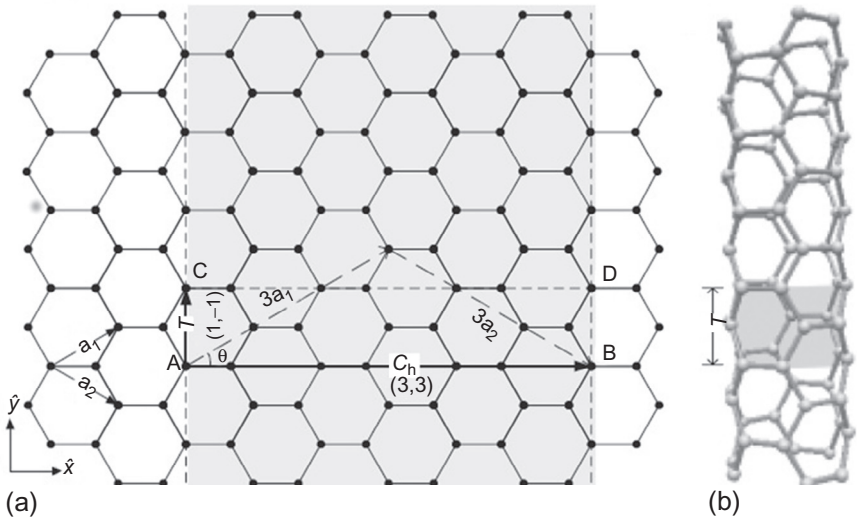

Figure 7.1 (a) Graphene lattice and (b) resulting single-wall nanotube. Adapted from Wong and Akinwande (2011).

become the most researched topic in materials science, as evidenced by the Nobel Prize recognition awarded to its discoverers 6 years later in 2010. This one-atom-thick material has provided avenues in the study of low-dimensional physics, where its unique band structure has been and is still being used as a testing ground of quantum relativistic effects in materials science in addition to other "basic physics" (Geim and Novoselov, 2007).

In carbon, a group IV element, the four valence electrons in the 2s and 2p atomic orbitals of neighboring atoms mix with each other, or "hybridize," into sp2 orbitals, resulting in very strong σ bonded electrons confined along the planar graphene surface and 2pz electrons that form weaker π bonds through electron clouds that are distributed perpendicular to the graphene plane. A few of the remarkable properties of graphene follow.

Owing to its 2D structure, the behavior of charge carriers in graphene is governed more closely by the relativistic 3D Dirac equation instead of Schrodinger's equation. Hence π electrons in graphene mimic relativistic massless Dirac fermions, with speeds just two orders of magnitude less than the speed of light. Two other interesting effects that have been demonstrated are the appearance of new quantum Hall effects, and the anomalous minimum of the conductivity of graphene in zero-field. In contrast to its remarkable properties, some of which were mentioned above, the first successful technique used in the isolation of single graphene layers is the simple micromechanical cleavage of graphite layers through the repeated use of scotch tape.

7.2 Literature review

Before specifically discussing thermal expansion solely, this section presents a more general overview of the study of the carbon nanotubes' mechanical properties, including properties of all sorts, such as elastic constants, Poisson's ratios, and Young's moduli of carbon nanotubes of the single-walled and multiwalled variety, and also bundles or "ropes" of these nano-objects. The dependence of these structural properties' dependence on chirality and diameter were discussed in some of the earliest such studies, which relied heavily on continuum elasticity theory. Ruoff and Lorents (1995) early on realized that "[t]he thermal conductivity and thermal expansion of carbon nanotubes are also fundamentally interesting and technologically important properties." They were also two of the few initial investigators to exploit the structural similarities between graphite/graphene in their studies. Regarding the tensile strength of nanotubes, for example, Ruoff and Lorents (1995) obtained the stiffness constant of carbon nanotubes in the axial dimension, shown in Eq. (7.1), by scaling the intraplanar Young's modulus of graphite with an estimate of the cross-sectional area of a carbon nanotube. Earlier estimates of the latter dimension were the interplanar spacing in graphitic layers, approximately 0.34 nm. The use of this estimate as the "thickness" of a nanotube has been and still proves problematic, especially with regard to the wide scatter in the reported values of the structural properties mentioned at the top of the introduction.

$$K = \frac{E_0\left(r_o^2 - r_i^2\right)}{r_o^2} \tag{7.1}$$

The tensile stiffness value computed by Ruoff and Lorents (1995) was ~800 GPa, nearly three-quarters of the ideal in plane graphite value of 1060 GPa. They also show that the behavior of the thermal expansion of carbon nanotubes differs significantly from that of graphite and carbon fibers, noting that the radial expansion coefficient for not only single-walled carbon nanotubes but also multiwalled types would also be similar to the in-plane axial values. Their topologically based reasoning was that although multiwalled tubes have multiple tubes with separations and van der Waals interactions similar to graphite, the tubes making up the MWCNT wrap around onto themselves, in which case the van der Waals forces between individual tubes does not play a critical role in radial thermal expansion.

Tersoff and Ruoff (1994) examined ordered hexagonal arrays of carbon nanotubes modeled as cylinders in their calculations, resulting again in some of the earlier predictions of the unique unexpected mechanical properties of CNTs. Their early modeling, for example, predicted the energetically favorable flattening of the sides of nanotubes against each other in nanotube bundles for tubes with diameters of 0.25 nm or greater, due to van der Waals interactions. Tubes with 0.1 nm diameters or smaller were shown to behave essentially as rigid cylinders. Tersoff and Ruoff (1994) also noted the unexpected strange behavior of the rigidity of nanotube bundles. The expectation is for rigidity to decrease as the diameter of the tubes in the bundle increase, because materials soften with lower density, and density in the case of nanotube bundles varies inversely with diameter. However, they predicted nanotube bundle material initially stiffens, then softens, and eventually settles at a compressibility value that does not depend on any additional decrease of the density.

Robertson et al. (1992) used empirical potentials in their study of the mechanical properties of nanotubes, where they established the inverse squared relationship between the strain energy and nanotube radius. The same relationship between radius and strain energy is also derivable from continuum mechanics, thus showing the applicability of continuum elasticity theory to the study of carbon nanotubes early on. In Robertson et al.'s study, interactions were modeled with the many-body potentials developed by Tersoff and Ruoff (1994) and Brenner et al. (2002), which were parameterized by the lattice constant, binding energy and elastic constants of various carbon lattices. Robertson et al. (1992) also verified their findings with *ab initio* calculations.

Experimental attempts at measuring the Young's modulus of carbon nanotubes also occurred concurrently with the above modeling/atomistic studies. One experimental method adopted in initial nanotube investigations was the use of transmission electron microscopy (TEM) imaging of the thermally induced vibrations of the free end of carbon nanotubes in bulk roped samples. Krishnan et al. (1998) employed this technique to measure the Young's modulus of 27 single-walled carbon nanotubes, reporting an average value of 1.25 TPa. Krishnan's study was one of the early few ones using this technique to obtain a carbon nanotube Young's modulus close to the in-plane C11 elastic constant of graphite. More importantly, however, it added more support to the initial claims of the remarkable mechanical properties of SWCNTs. Krishnan performed a least-squares analysis on the TEM images of the nanotubes to determine the various dimensions of the sample tubes, which also involved analyzing the "blur" of the free vibrating end of the tubes to determine

the vibrational amplitude. The Young's moduli were then calculated by basing the behavior of the nanotubes on that of homogeneous cylindrical shells of a suitably chosen thickness.

X-ray diffraction (XRD) of bundled SWCNT samples was also another experimental method in the determination of nanotube mechanical properties. Yosida (2000), after applying XRD to carbon nanotubes produced by the direct current arc discharge method, reported that the triangular lattice constant of SWCNT bundles L0 shrank over an entire temperature range of 290-1600 K. Values of the lattice constant were obtained from the (10) reflection Bragg angle at 2θ, approximately equal to 6°. A coefficient of linear thermal expansion perpendicular to the tube bundle axis over the temperature ranges of 290-330 and 1300-1550 K was -1.52×10^{-6}, and $-2.48 \times 10^{-6}\,\mathrm{K}^{-1}$, respectively.

Atomic force microscopy, which is probably one of the more costly methods, is also used in investigating nanotube mechanical properties (Yamamoto et al., 2008). Salvetat et al. (1999) used an AFM probe to apply lateral forces on bundles of single-walled nanotubes or isolated multiwalled tubes whose sections were lying across 0.4 μm diameter holes on a porous membrane. Based on the nanotube deflection, Salvetat et al. (1999) concluded with Young's moduli of 0.87 and 0.755 TPa for unpurified nanotube samples and samples that underwent thermal treatment, respectively. Last, Salvetat et al.'s study also demonstrated the ease with which nanotubes can slide pass one another, revealing a significantly low shear modulus for bundles of SWCNTs, which was not surprising to the authors considering how easily graphite is cleaved, using scotch tape, for example, in the mechanical cleavage technique used in the successful isolation of graphene.

While being stretched at high temperatures, $\sim 10^3$ K, nanotubes were also discovered to display "a superplastic behavior." Both single- and multiwalled nanotubes, while being stretched axially at extreme temperatures through the use of two AFM tips connected at both ends, suffered fractional increases in length of almost 300%, while concurrently undergoing more than 10-fold decreases in their diameter. This extremely elastic response of nanotubes at high temperatures was in stark contrast to the brittle behavior they displayed in the same type of experiments at room temperature, with multiwalled and single-walled nanotube bundles fracturing at 3-12% and 3.1-5.3% strains, respectively. Some possible explanations of this "super plastic" behavior have been proposed over time, with one example being the 5/7/7/5 defect mechanism (Nardelli et al., 1998), which refers to the formation of defects consisting of two pentagons and two heptagons in the hexagonal CNT lattice through induced Stone-Wales rotations of certain bonds. This defect formation is an endothermic process when no stress is applied to the CNT; it becomes exothermic after a specific amount of applied stress. The resulting 5/7/7/5 defect then traverses the length of the nanotube as two pairs of pentagons and heptagons, appearing as a distorted kink in the nanotube. The overview in this section shows some of the exciting mechanical properties of carbon nanotubes and also the promise of significant advances that are yet to be made in understanding the behavior of these objects under mechanical stress and at high temperatures and pressures.

7.3 Methodology

In this section we will discuss the Raman spectroscopy setup and molecular dynamics parameterization employed to carry out thermal analysis of purified single-walled carbon nanotubes.

7.3.1 Raman spectroscopy

The Raman spectroscopic analysis will help determine which type of model nanotubes to use in the MD simulations, where expansion coefficients and other elastic constants for individual representative nanotube models will be calculated based on the adaptive intermolecular reactive empirical bond order (AIREBO) interatomic potential and is given by the following equation:

$$E = \frac{1}{2}\sum_i \sum_{i \neq j} \left[E_{ij}^{\text{REBO}} + E_{ij}^{\text{LJ}} + \sum_{k \neq i} \sum_{l \neq i,j,k} E_{kijl}^{E_{kijl}^{\text{Torsion}}} \right] \tag{7.2}$$

The REBO term of the potential shown in Eq. (7.2) refers to the precursor of the AIREBO potential, the reactive empirical bond order (REBO) potential formulated by Brenner et al. (2002). This part of the AIREBO potential is switched on for short-ranged (less than $\sim$2 Å separations) interactions between C—C, H—H, and C—H interactions. It is responsible for covalently bonded interactions such as those between C-atoms in graphene and nanotubes, for example. A variety of chemical influences on the bond strength between two neighbor atoms, such as coordination numbers, conjugation effects, bond angles, are accounted for in the term b_{ij} in Eq. (7.3).

$$E^{\text{REBO}} = V_{ij}^{R}\left(r_{ij}\right) + b_{ij} V_{ij}^{A}\left(r_{ij}\right) \tag{7.3}$$

The Lennard-Jones contribution to the AIREBO potential, denoted as ELJ, takes into account van der Waals and dispersion interactions, based on the 6-12 potential.

The third contribution to the AIREBO potential denoted, as $E_{kijl}^{\text{Torsion}}$, calculates the energy of dihedral angles present in the modeled system. This contribution was an added improvement to the AIREBO potential's predecessor, the REBO potential, which did not take into account the energetics of four-body torsional interactions around individual bonds (Stuart et al., 2000). The rule governing the switching on and off of the long-range Lennard-Jones interactions between two atoms is what gives this potential the "reactive" nature embodied in its name. The decision to include L-J interactions depends on the nonbonded separation between two atoms, the strength of the bonds between bonded atoms, and the network of intermediate bonds between two interacting atoms. For example, atoms commonly experience L-J repulsion at close separations only if they are not 1-4 neighbor atoms between two consecutive bonds or if there is a negligible chance of the two atoms bonding themselves.

These rules governing the rules for switching on the long-range L-J interactions make the AIREBO potential better suited to take into account the chemical nature of the modeled system and are handled by the universal switching function shown in Eq. (7.4), which varies continuously between 0 and 1,

$$S(t) = \Theta(-t) + \Theta(t)\Theta(1-t)(1-t)\left[1 - t^2(3-2t)\right] \tag{7.4}$$

where $\Theta(t)$ is the Heaviside step function $\Theta(t) = \begin{cases} 0, & t < 0 \\ 1, & t \geq 0 \end{cases}$.

Scanning electron microscopy (SEM) analysis was also used in order to identify candidate nanotube models to be used in simulations. The temperature dependent shift of peak location, corrected and uncorrected intensities, peak widths, and other spectral variations obtained from this data will serve as the means for experimental verification of the atomistic/MD simulation results.

Raman spectral data was collected on the CNT samples under thermal loading, from room temperature up to 200 °C in steps of 10 °C. The sample analyzed was carbon nanotube powder from Unidym™ carbon nanotubes. The SWCNTs were produced by the high-pressure carbon monoxide (HiPco) process, followed by purification. According to the manufacturer, the diameter range of the nanotubes was from 0.8 to 1.2 nm, and the lengths varied from ~100 to 1000 nm. After thermogravimetric analysis, the manufacturers also claimed to have less than 15% residual Fe catalyst by weight (Misra et al., 2013).

The instrument used to carry out Raman spectroscopy of our samples is a Thermo-Scientific DXR Smart Raman Spectrometer, with a 780 nm wavelength laser and $M^2 \leq 1.5$ beam quality. A laser power setting of 6 mW was used for all spectra collections.

Figure 7.2 shows the internal setup for the instrument. The laser module is focused on the sample via lenses, and the scattering that results from the laser striking the sample is sent back into the CCD detector and a Raman signature is obtained. The spectrometer resolution using a 25-μm slit is ~1.93 cm^{-1}. The temperature-controlled environmental chamber used, the Ventacon Heated Cell, houses the sample on its surface (for solid samples such as plates) or within (as is the case for nanopowder and carbon nanotubes) and can heat the sample from room temperature to 200 °C.

The experimental method carried out the collection of spectra at a constant laser power, with the sample heated externally with a heat cell up to 200 °C. All data so far were collected only on the purified batch of SWCNT, with much more data collection needed. The initial analysis of the peak shift variation of the various Raman features of the externally heated SWCNT shown in Figures 7.3–7.7 and Table 7.1 agrees with Raravikar et al. (2002) and Gregan (2009).

Temperature-dependent Raman data is one type of experimental data that can be reproduced using the bond order-length-strength (BOLS) correlation mechanism developed by Yang et al. (2013). Using the data from the atomistic MD simulations as input to the BOLS mechanism to reproduce the measured temperature-dependent Raman data will serve as the connection between the computational atomistic results and mechanical properties of actual CNTs.

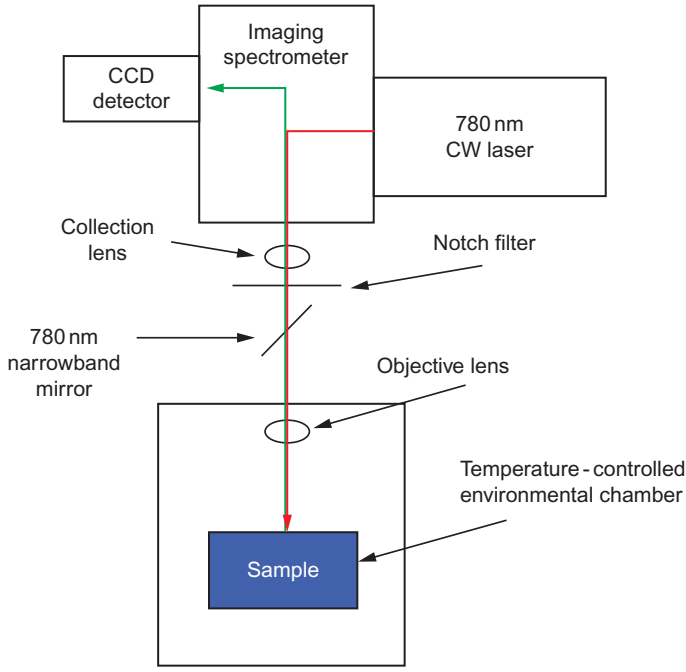

Figure 7.2 Raman spectroscopy instrument setup.

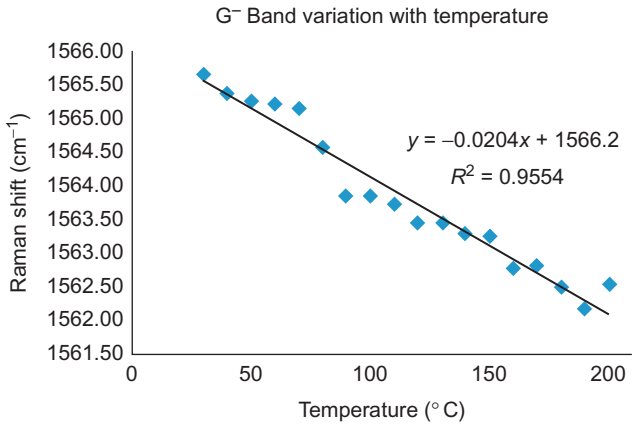

Figure 7.3 Linear frequency downshift with temperature of the G^- Raman peak of purified bundled SWCNT.

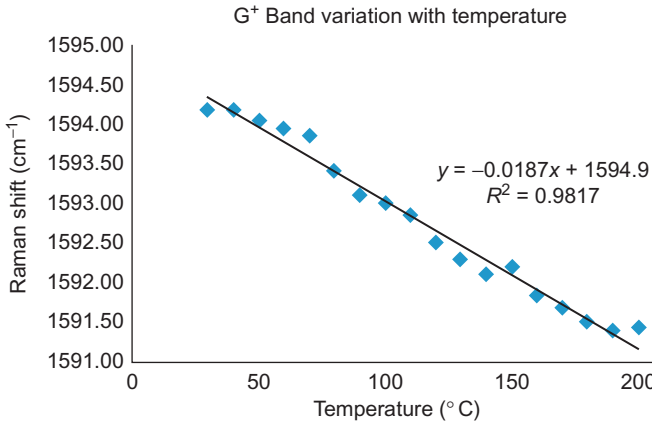

Figure 7.4 Linear frequency downshift with temperature of the G^+ Raman peak of purified bundled SWCNT.

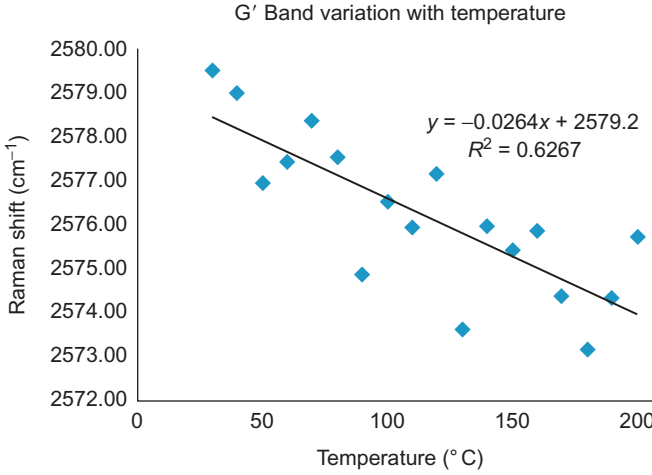

Figure 7.5 Linear frequency downshift with temperature of the G′ Raman peak of purified bundled SWCNT.

7.3.2 MD simulations

Molecular dynamics (MD) simulation is one of the primary atomistic/simulation techniques used in modeling the thermal/structural properties of SWCNTs. In this classic technique, the trajectory of a model of the nanosystem is generated according to Newton's equations of motion and equilibrium, and transport properties are subsequently computed from averages over the time-evolution of the model system (Rafii-Tabar,

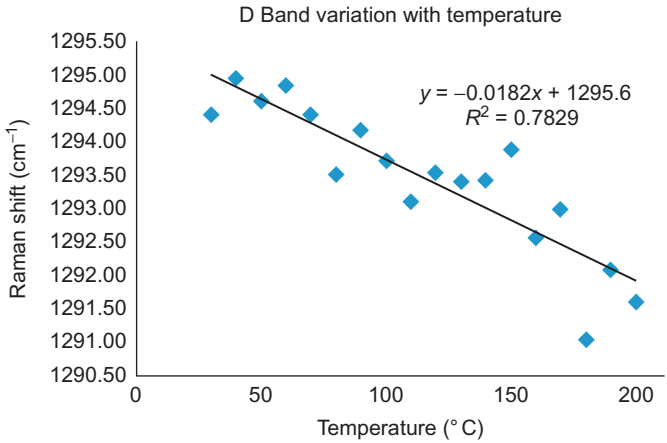

Figure. 7.6 Linear frequency downshift with temperature of the D Raman peak of purified bundled SWCNT.

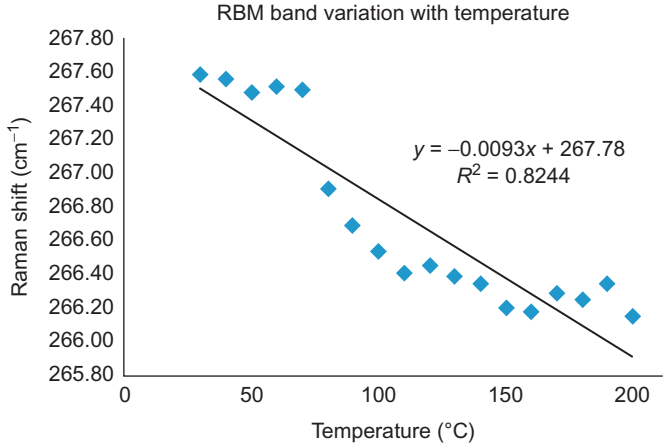

Figure 7.7 Linear frequency downshift with temperature of the RBM Raman peak of purified bundled SWCNT.

2008). In MD simulations of any complexity, the algorithm of the simulations is usually some variation of the following five steps (A–E) (Frenkel and Smith, 2002).

7.3.2.1 Initialization of the model system

Initial conditions and parameters of the simulation are read in, such as the initial positions, velocities/temperature, particle number, volume, and time-step. Particles are usually positioned on a lattice that corresponds as closely as possible with the structure

Table 7.1 Temperature slopes of the various Raman peaks of bundled single-walled carbon nanotubes, measured and compared to two other references

Temperature slope	Results (ours) $\frac{\Delta\omega}{\Delta T}$ (cm^{-1}/°C) 780 nm excitation wavelength	Raravikar et al. (2002) $\frac{\Delta\omega}{\Delta T}$ (cm^{-1}/K) 514.5 nm excitation wavelength	Gregan (2009) $\frac{\Delta\omega}{\Delta T}$ (cm^{-1}/K) 514.5 nm excitation wavelength
G^+ Peak	−0.0187	−0.0189	−0.016
G^- Peak	−0.0204	−0.0238	−0.016
G′ Peak	−0.0264	–	–
"Defect" D Peak	−0.0182	–	–
RBM ~267 cm^{-1}	−0.0093	–	–

being studied. This also helps to avoid extremely large initial forces caused by overlapping of cores of representative atoms or molecules. The velocities of the constituent atoms are randomly selected from a uniform distribution, followed by a removal of the center of mass velocity of the model system.

7.3.2.2 Force computation

The calculation of the potential and energy and total pairwise forces for the particular model is considered the most important part of any MD routine, because it's the intermolecular potentials that are used to understand the physics of the nanomaterial. This MD simulation step is also most computationally demanding of all the others. If only pairwise interactions and no other optimization techniques are used, the time required to examine all pair distances for this calculation scales as the square of the total number of particles, N^2.

7.3.2.3 Equations of motion

Using the computed forces on all particles from the previous step, the trajectory is developed based on Newton's second law. The particle trajectory is developed by using finite difference methods based on the discrete time-step Δt. The most popular method is the Verlet method and its slightly modified variant known as the "leap frog" method. The central idea in the basic Verlet method is the addition of the Taylor series of the positions of the particles $x(t)$ around the time-step Δt in order to generate the trajectory (Haile, 1997). The accelerations, of course can be determined from the forces calculated in the previous step.

$$x(t+\triangle t) = x(t) + \frac{\mathrm{d}x(t)}{\mathrm{d}t}\triangle t + \frac{1}{2}\frac{\mathrm{d}^2x(t)}{\mathrm{d}t^2}\triangle t^2 + \frac{1}{3!}\frac{\mathrm{d}^3x(t)}{\mathrm{d}t^3}\triangle t^3 + O\left(\triangle t^4\right) \tag{7.5}$$

$$x(t-\triangle t)=x(t)-\frac{\mathrm{d}x(t)}{\mathrm{d}t}\triangle t+\frac{1}{2}\frac{\mathrm{d}^2x(t)}{\mathrm{d}t^2}\triangle t^2-\frac{1}{3!}\frac{\mathrm{d}^3x(t)}{\mathrm{d}t^3}\triangle t^3+O\left(\triangle t^4\right) \tag{7.6}$$

$$x(t+\triangle t)=2x(t)-x(t-\triangle t)+\frac{\mathrm{d}^2x(t)}{\mathrm{d}t^2}\triangle t^2+O\left(\triangle t^4\right) \tag{7.7}$$

7.3.2.4 Computation of thermal properties

Calculate thermal quantities as time averages of the model system. Thermodynamic quantities that can be expressed as the average of functions of coordinates and momenta are one set of quantities derivable from MD simulations. Below is a simple example of the temperature in terms of the mean kinetic energy according to the equipartition theorem:

$$T(t)=\sum\nolimits_{i=1}^{N}\frac{m_iv_i^2(t)}{k_{\mathrm{B}}N_f} \tag{7.8}$$

Other thermodynamic quantities such as entropy and the Gibbs and Helmholtz free energies are not derivable from such simple averages and require specialized techniques for their derivation from MD simulations.

7.3.2.5 Interatomic potential

The energetics of the model nanosystem in MD simulations is handled by empirical interatomic potentials. Also dependent on the interatomic potentials are the calculated structural/thermal properties of interest in this chapter, such as elastic constants and thermal expansion. The form and parameters of these potentials are derived from many sources, such as quantum-mechanical calculations and experimental data, with the empirical potential undergoing continual refinement. The potential used in this study is the AIREBO potential developed by Stuart et al. (2000) specifically for modeling chemical reactions and interactions of hydrocarbons. It is one of the latest variants of many-body potentials that employ Tersoff's original bond-order concept, which refers to the modification of the strength of bonded interactions based on the local environment of the bonded interaction being calculated.

7.4 Temperature-dependent Raman spectra

The differences between bulk and individual SWCNTs and the BOLS mechanism are some of the concepts that explain the behavior of temperature effects on the Raman spectra of the SWCNTs. In this section we will discuss the linear downshift behavior of the Raman spectra of such materials when exposed to temperature changes.

7.4.1 Bulk versus individual SWCNT

Three studies, Huong et al. (1995), Huang et al. (1998), and Iliev et al. (2000), were some of the earliest to observe and investigate the possible use of the temperature-induced frequency shift of the Raman bands of carbon nanotubes and other allotropes. In these initial and subsequent studies, such as that of Gregan (2009), the extent of aggregation of the nanotube samples and effect of intertube interactions on temperature studies were also recognized and taken into account. In her study on SWCNTs, Gregan collected Raman spectra at increasingly greater temperatures using both highly bundled SWCNT powdered samples and samples dispersed in 1,2 dichloroethane (DCE) at concentrations both below and above the dispersion limit, thus ensuring adequate de-bundling of the SWCNTs. Further information on the use of discontinuities in the absorption spectra of SWCNT samples dispersed in DCE and other organic solvents to determine the level of aggregation of nanotube samples is available in Gregan (2009).

Gregan's temperature Raman study on dispersed debundled single-walled nanotubes elucidated two differences in the temperature-induced shift of peak position compared with bulk bundled samples, supporting the conclusion that not only temperature, but the level of bundling and intertube interactions play a role in the peak positions in Raman spectra of SWCNTs. 514.5 nm excitation was used to collect spectra in the temperature range of 83-343 K. The nanotubes used in our study and Gregan's were produced through the HiPco technique, with Gregan's samples being cooled and heated on a Linkham THMS600 stage. The first effect of debundling on the temperature-induced Raman peak shift observed in Gregan (2009) was the frequencies being greater in magnitude compared to bundled bulk samples. This result is not surprising, because the upshift in the Raman bands of SWCNTs after aggregating into bundled "ropes" has been known for some time (Gregan, 2009). More importantly, Gregan (2009) showed a significant change in the temperature coefficient itself of debundled SWCNTs compared to the case of bundled tubes, up to one order of magnitude.

Iliev et al. (2000) settled an important issue regarding Raman spectroscopy applied to macroscopic bundled SWCNT samples. The peaks from the Raman spectra of bundled nanotubes are dominated by the diameters that are resonant with the excitation wavelength (Saito et al., 1998). Because of this resonant enhancement, it is important in the analysis of Raman spectra of bulk samples to know if the bands observed are homogeneous peaks primarily from the resonant tubes or are complicated inhomogeneously broadened peaks composed of contributions from several different tubes with very similar diameters (Iliev et al., 2000). Iliev et al. (2000) concluded that the latter is the case based again on the temperature variation of band components, only this time it was the temperature variation of peak width, not peak location, that was used. Nanotube samples used by Iliev et al. (2000) were produced by the laser arc method, and spectra were collected with 632.8 nm He—Ne laser excitation at temperatures from 5 to 500 K.

$$\triangle(T) = \gamma + \Gamma_0\left(1 + \frac{2}{e^x - 1}\right) \tag{7.9}$$

In Iliev et al. (2000) the authors show that the application of Eq. (7.9), which expresses the variation of the phonon line width Δ with temperature due to phonon scattering, did not reproduce the experimental line-width temperature variation based on the assumption of a homogeneous band. The temperature behavior of the line width was able to be modeled only after multiple simulations of various nearly similar diameter tubes with line widths that behaved according to Eq. (7.9).

Huong et al. (1995), in one of the earliest known temperature-dependent Raman studies of SWCNT, were able to identify a significant structural property of carbon nanotubes, namely hemispherical end caps that contained pentagons in the sp^2 skeleton of carbon fullerenes. The Raman peak at 1470 cm^{-1} observed in C60 buckyballs exhibited resistance to increased temperatures in SWCNT samples compared to the latter fullerene type. Huong et al. (1995) concluded that the resilient behavior of the pentagon containing end caps on nanotubes was due to the constraint of their being attached to the cylindrical walls, while the spherical C60 fullerenes would more easily "explode" under laser-induced heating due to thermal expansion. Carbon nanotubes produced by the arc-discharge method and 514.5 nm wavelength excitation from an Ar ion laser were used in this micro-Raman study. Like the subsequent similar studies, the increase in frequency observed in carbon nanotube samples under thermal loading was attributed to lengthening of C—C distances.

A third and final study of the temperature dependence of the Raman bands of SWCNT is that of Huang et al. (1998). The authors subject single-walled carbon nanotubes, highly ordered pyrolytic graphite (HOPG), and "Active-Carbon," a mixture of amorphous carbon and crystalline graphite, to increasing power levels (0.2-4.0 mW) of a 632.8 nm He—Ne lasers to demonstrate the linear frequency downshift of the Raman bands with increasing temperature in all samples except for the HOPG. Huang et al. (1998) also noted the need for caution when comparing the temperature behavior of the Raman peaks of carbon nanotubes, especially for the still not fully understood, dispersive D, "Defect" band and its overtones. Huang et al. (1998) suggest that the defects present in the amorphous carbon and nanotube samples allow for the flexibility necessary for bond elongation in these samples and that such defects are not sufficiently present in crystalline HOPG to allow for the resulting temperature-induced peak shift in the latter. The Raman shift with temperature is a significant identifying feature in the mechanical properties and vibration dynamics of carbon fullerenes. An alternative to the previously mentioned disorder-induced flexibility cause in the explanation for the temperature behavior of Raman bands is the BOLS mechanism (Yang et al., 2013).

7.4.2 Bond order-length-strength mechanism

In this section the bond order-length-strength (BOLS) correlation mechanism developed by Sun (2007) and its use in Yang et al. (2013) and Sun (2007) will be discussed. Only relevant results are presented. The BOLS correlation mechanism is based on Pauling and Goldschmidt's premise that the reduction in the coordination number of certain atoms in nanomaterials—for example, near grain boundaries or at other terminations of the periodic lattice—results in the spontaneous contraction of the

associated bonds and increase in the associated bond energy (Sun, 2007). The resulting modification of the atomic coherency, given by the product of the number of bonds and energy of one bond, Hamiltonian, work function, and electro-affinity of the nanosolid, means that measurable physical properties of the nanosolid, such as the Stokes shift, can be described as functions of any one of the above quantities or combination thereof (Sun, 2007).

The results of Yang et al.'s (2013) use of BOLS in the reproduction of the response of the Raman spectra of various carbon allotropes, including SWCNTs, under external pressure and temperature variation similar to the measurements in Section 7.4.3 follows. Yang et al. note that information on the physical basis of the interatomic bond vibration and phonon relaxation for the temperature shift of the Raman frequency should be obtainable from the latter data, but such correlation was actually lacking until the development of the BOLS mechanism. Earlier reliance on the use of fitted polynomial relations such as in Eq. (7.9) provided no information on Gruniesen constants or any other phonon-related scattering mechanisms involved (Yang et al., 2013). The contraction of the bond-length of undercoordinated atoms and gain in bond energy, according to Yang et al. (2013), are given by Eqs. (7.10) and (7.11) respectively.

$$C_z = \frac{d_z}{d_b} = \frac{2}{1 + e^{(12-z)/8z}} \tag{7.10}$$

$$C_z^{-m} = \frac{E_z}{E_b} \tag{7.11}$$

where C_z^{-m} is the bond contraction coefficient, d is the bond-length, and E represents the bond energy. The subscripts z and b refer to quantities involving atoms with z-coordination numbers and in the bulk phase respectively; m is the bond-nature index, which describes the variation of the bond energy with bond-length, which according to Yang et al. (2013) has a value of 2.56 for carbon. The final expression relating the observed Raman frequency shift and mechanical property of the nanomaterial, the thermal expansion coefficient in this case, according to BOLS theory, is given by the following equation:

$$\frac{\omega(z,T) - \omega(1,T_0)}{\omega(z_b,T_0) - \omega(1,T_0)} \cong \sqrt{(1 - \triangle^T)} \times e^{\int_{T_0}^{T} \alpha dt} \tag{7.12}$$

where $\omega(1,T_0)$ is the respective Raman peak under some standard condition(s) before the application of external stimuli leading to the peak shift, with such stimuli being temperature and pressure, either individually or together. $\omega(z_b,T_0)$ is the measured Raman peak in the bulk case, $\triangle^T$ is the thermally depressed bond energy, and α is the volume thermal expansion coefficient. The value of α used in Yang et al.'s reproduction of the Raman shift data was 8.0×10^{-06}, which was the value of the thermal expansion coefficient of the triangular lattice in bundles of SWCNT obtained through X-ray diffraction (Maniwa et al., 2001).

7.4.3 Linear frequency downshift with increasing temperature

Two separate Raman spectrum collections were performed every 10 °C in the range of 30-200 °C, with an exposure time of 10.00 s averaged over three exposures for each collection. Spectra were also collected after allowing enough time for a maximum temperature fluctuation of ±0.1 °C as displayed by the heat cell's electronic display.

Numerous studies have shown the effect of increased temperature is to red-shift the different mode frequencies of the Raman peaks of carbon allotropes, including SWCNT (Dresselhaus and Eklund, 2000). This highly visible temperature shift of the Raman bands of carbon nanotubes is the focus of this section; it also serves as one of the many examples of the earlier stated usefulness of Raman spectroscopy in probing the structural/mechanical properties of carbon nanotubes. According to Dresselhaus and Eklund (2000), the cause of this temperature-induced peak shift can be decomposed into an exclusively thermal effect and a volume effect due to thermal expansion of the lattice, represented by the first and second terms respectively in the following equation:

$$\triangle\omega = \left(\frac{\partial\omega}{\partial T}\right)_V \triangle T + \left(\frac{\partial\omega}{\partial V}\right)_T \left(\frac{\partial V}{\partial T}\right)_P \triangle T \tag{7.13}$$

Such studies, however, have also demonstrated the prediction that this frequency shift, $\triangle\omega$, is dominated by the temperature effect, with a negligible volume-related effect term, based on actual measurements. In terms of empirical polynomials such as Eq. (7.14), where ω_0 is the fitted frequency at 0 K and a_1 and a_2 represent first- and second-order temperature coefficients, the previously mentioned "temperature effect" dominance expresses itself as a negligible second-order term $a_2 \approx 0$, with the temperature variation in fact being linear, which is also the case for us (Gregan, 2009).

$$\omega = \omega_0 - a_1 T - a_2 T^2 \tag{7.14}$$

The temperature coefficients obtained have magnitudes comparable to literature values as shown in Table 7.1. Each peak location in the ω versus temperature plots, Figures 7.3–7.7 show the linear frequency downshift slope as temperature increases, utilizing the average of the values from both separate Raman collections.

In Figures 7.3–7.7 we were able to reproduce the same linear red-shift with increasing temperature for the major Raman peaks in bundled samples of SWCNTs, namely the G+, G-, D, G′ and RBM peaks. The G′ linear plot of peak location versus temperature has the most scattering compared to the other Raman bands, as evidenced by its R^2 value. It should be noted that this is the only second-order Raman band included in Figures 7.3–7.7, and while the cause of the strong nonlinearity in the red-shift trend is unknown, this feature is a highly dispersive band that is very sensitive to electronic and photonic perturbations (Jorio et al., 2011).

7.5 Application of MD to SWCNT structural analysis

The examination of the thermomechanical properties of carbon nanotubes is deeply linked with computational nanoscience (Rafii-Tabar, 2004). This broad field, which consists of numerical modeling and MD simulation, provides an integral avenue in the

research of the extremely reduced time, length, and energy scale processes occurring with these objects.

Much information on the mechanical properties is derivable from the interatomic potentials used to model them. The atomic-level stress tensor, for example, which is obtained by the method of finite strain, involves the first derivative of the potential, whereas the elastic constants and bulk moduli are based on the second derivative. The usual course of action to help meet the challenge of limited computing resources is referred to as a "multiscale" technique by (Rafii-Tabar, 2008), where data from quantum calculations and/or continuum mechanics acts as input to MD simulations or vice versa. The results of Bao et al.'s (2004) MD analysis of the Young's modulus demonstrates this fact and was chosen because of Bao's use of the REBO potential. Based on MD simulations using Verlet time integrations with a 1 fs time-step, Bao et al. calculated Young's moduli of 1026.176 and 929.8 ± 11.5 GPa for graphite and SWCNTs respectively. Both these values are close to experimental values and also to those from quantum calculations.

The MD simulations of nanotube models are currently in the equilibration phase. The MD simulations are done using the large-scale atomic/molecular massively parallel simulator program (Plimpton, 1995). They are also being run remotely on the computing clusters at the National Energy Research Scientific Computing Center (NERSC), a division of the Lawrence Berkley National Laboratory, in order to meet the very large computational and time demands of the simulations. The sampling phase of the simulations, where structural data will be collected after the simulations, will then follow.

As mentioned at the end of the previous section, the value of the volume thermal expansion coefficient used in the fitting of the experimental thermal Raman peak shift in Yang et al. (2013) came from the expansion coefficient of the triangular lattice constant of SWCNT ropes, as determined by X-ray diffraction. An often used method in the determination of the structural/thermomechanical properties of carbon nanotubes has been the use of continuum elasticity theory that simulates the behavior of SWCNT responses using a hollowed cylinder or cylindrical shell going through SWCNT deformations and resulting in a reduction of MD simulation data (Batra and Gupta, 2008). However, although macroscopic continuum theory applied to SWCNTs happened to be surprisingly relevant and useful, as noted by Harik and Gates (2002) and many others during the early days of nanotube structural analysis, extreme caution is still required in approaches based on macroscopic continuum mechanics because "... its relevance for a covalent bonded system of only a few atoms in diameter is far from obvious" (Harik and Gates, 2002). In fact, the determination of the cross-sectional thickness of carbon nanotubes is still an active research issue (Batra and Gupta, 2008). In Batra and Gupta (2008) the structural properties of the "Equivalent Continuum Structure," represented by isotropic shells used to elucidate the properties of the corresponding SWCNT they represented, were determined by equating the first Rayleigh mode and RBM frequencies of the two structures. Another technique based on the axial, twisting, and first Love vibrational modes of an elastic shell and its corresponding model SWCNT was also used. Batra and Gupta (2010) were then able to derive the Young's modulus, Poisson's ratio, and an expression for the thickness of a SWCNT as a function of radius and the bond-length in the equilibrated SWCNT

model used in MD simulations. The key results of Batra and Gupta (2010) were the SWCNT thickness calculated at 0.88 Å when the nanotube radius is ~3.68Å. This wall thickness value increased to and remained at approximately 1.37Å when the diameter is at or greater than 15Å; both values are much smaller than the interplanar spacing between graphitic planes, ~3.4Å, often used as a first approximation.

Based on initial Raman analysis, SEM visualization, and manufacturer data, representative nanotube types with reasonable probabilities of being present in the samples used in the simulations have been modeled. Large portions of the script that will be used to perform the MD simulations at increasing temperatures have been developed. The sampling geometry and other geometrical parameters of the nanotube models have been incorporated into the simulation script that will be used to compute thermal expansion data.

Some initial data are available on an MD simulation of a (10,2) chirality SWCNT, the dominant chiral species present in the purified nanotube sample based on the Raman spectra presented earlier. The vibrations of a 200 Å long SWCNT are based on the AIREBO potential discussed previously. A nonbonded Lennard-Jones cutoff of 3 Å was used in addition to the other default parameterized constants in Table 7.2 (Stuart et al., 2000). Nonperiodic boundaries were used in all three dimensions of the simulation box with x, y, and z dimensions of $100.0 \times 100.0 \times 240.0$ Å. A 0.5 fs time-step and 100,000 total time-steps were used. Simple velocity rescaling was also used to achieve a mean temperature of 300.0 K over the course of the run. The sampling geometry used to describe the length variation of the nanotube was based on the summation of the center of mass between consecutive cylindrical disk sections of the model nanotube as shown in Figure 7.8 the behavior of the axial dimension in this case of an initial room temperature MD simulation exhibits the anomalous thermal expansion behavior also observed in other MD studies.

Table 7.2 Average length decreases over 10,000 time-steps, over the course of a 100,000 time-step MD simulation

Time-step	Average length, L_{ave} (each length averaged over 10^4 time-steps) (Å)
10,000	177.341
20,000	177.226
30,000	177.288
40,000	177.035
50,000	176.963
60,000	176.618
70,000	176.992
80,000	176.618
90,000	176.803
100,000	176.355

Initial sampling length $L_0 = 179.93161$ Å.

Figure 7.8 Axial sampling geometry of a model (10,2) chiral SWCNT used in Molecular Dynamics (MD) simulations.

7.6 Conclusion

Investigation of the mechanical properties of carbon nanotubes is one of the most actively studied aspects in nanotube research (Rafii-Tabar, 2008). In Rafii-Tabar (2008) a "multiscale" approach where quantum *ab initio* calculation results, continuum elasticity theory, and atomistic/MD simulations are used concurrently, with data from one of these techniques being used as input in any of the other methods just listed. Our investigation is based on such an approach, using experimental Raman spectroscopic data, specifically the temperature-induced red-shifting of the various peaks, and classical molecular dynamics.

A review of the findings from the earliest days to more recently regarding the remarkable properties of nanotubes was presented in Section 7.2 while far from being an exhaustive review, the major findings on the superlatives and unexpected results on the stiffness and other mechanical properties of SWCNTs were covered, which was the aim of this section. Also captured in this section was the varied array of methods used in both experimental and computational methods and the inevitable mixing of these techniques in the study of carbon nanotube mechanical properties. The parameters and attributes of our own classical MD simulations, most importantly basing the intra-nanotube energetics on the robust AIREBO many-body potential, were discussed in Section 7.3. The Raman spectra of actual SWCNT samples collected under increasing temperature, and our reproduction of the linear downshift of frequency with temperature, are a key part of Section 7.4. Also very important in this same section is a discussion of the BOLS theory/mechanism, the proposed link between the Raman spectral data and MD simulation results. Last, initial MD simulations based on the AIREBO potential have already provided promising results by reproducing the anomalous axial contraction of SWCNTs at this early stage of the investigation.

Much progress still remains in examining SWCNTs' mechanical properties and responses to stresses and temperature gradients. Some of the extreme elastic properties of SWCNTs were also discussed and exhibited through SEM imaging. Also, such data on the mechanical properties of actual carbon nanotube samples are extremely important for comparison with computational studies, which is becoming the preferred method of study of this subject in lieu of more expensive *ab initio* and scanning probe method techniques.

References

Bao, W.X., Zhu, C.C., Cui, W.Z., 2004. Simulation of Young's modulus of single-walled carbon nanotubes by molecular dynamics. Physica B 352, 156–163. http://dx.doi.org/10.1016/j.physb.2004.07.005.

Batra, R.C., Gupta, S.S., 2008. Wall thickness and radial breathing modes of single-walled carbon nanotubes. J. Appl. Mech. 75, 061010-1–061010-6. http://dx.doi.org/10.1115/1.2965370.

Batra, R.C., Gupta, S.S., 2010. Wall thickness and elastic moduli of single-walled carbon nanotubes from frequencies of axial, torsional and inextensional modes of vibration. Comput. Mater. Sci. 47, 1049–1059. http://dx.doi.org/10.1016/j.commatsci.2009.12.007.

Brenner, D.W., et al., 2002. A second-generation reactive empirical bond order (REBO) potential expression for hydrocarbons. J. Phys. Cond. Matter. 14, 783–802. http://dx.doi.org/10.1088/0953-8984/14/4/312.

Dresselhaus, M.S., Eklund, P.C., 2000. Phonons in carbon nanotubes. Adv. Phys. 49 (6), 705–814. http://dx.doi.org/10.1080/000187300413184.

Frenkel, D., Smith, B., 2002. Understanding Molecular Simulation: From Algorithms to Applications. Academic Press, New York. http://dx.doi.org/10.1063/1.881812.

Geim, A.K., Novoselov, K.S., 2007. The rise of graphene. Nat. Mater. 6, 183–191. http://dx.doi.org/10.1038/nmat1849.

Gregan, E., 2009. The use of Raman spectroscopy in the characterization of single walled carbon nanotubes (Doctoral dissertation), Dublin Institute of Technology, School of Physics.

Haile, J.M., 1997. Molecular Dynamics Simulation: Elementary Methods. Wiley, New York. http://dx.doi.org/10.1002/adma.19930050319.

Harik, V.M., Gates, T.S., 2002. Applicability of the continuum-shell theories to the mechanics of carbon nanotubes, NASA/CR-2002-211460 ICASE Report No. 2002-7.

Huang, F., Yue, K.T., Tan, P., Zhang, S.L., Shi, Z., Zhou, X., Gu, Z., 1998. Temperature dependence of the Raman spectra of carbon nanotubes. J. Appl. Phys. 84 (7), 4022–4024. http://dx.doi.org/10.1063/1.368585.

Huong, P.V., Cavagnot, R., Ajayan, P.M., Stephan, D., 1995. Temperature dependent vibrational spectra of carbon nanotubes. PRB 51 (15), 10048–10051. http://dx.doi.org/10.1103/PhysRevB.51.10048.

Iliev, M.N., Litvinchuk, A.P., Arepalli, S., Nikolaev, P., Scott, C.D., 2000. Fine structure of the low-frequency Raman phonon bands of single-wall carbon nanotubes. Chem. Phys. Lett. 316, 217–221. http://dx.doi.org/10.1016/S0009-2614(99)01293-2.

Jorio, A., Saito, R., Dresselhaus, G., Dresselhaus, M., 2011. Raman spectroscopy in graphene related systems. Wiley-VCH Verlag GmbH & Co. KGaA, Weinheim.

Krishnan, A., et al., 1998. Young's Modulus of single-walled carbon nanotubes. Phys. Rev. B 58 (20), 14013–14019. http://dx.doi.org/10.1103/PhysRevB.58.14013.

Maniwa, Y., et al., 2001. Thermal expansion of single-walled (SWNT) bundles: X-ray diffraction studies. Phys. Rev. B 64, 241402-1–241402-3. http://dx.doi.org/10.1103/PhysRevB.64.241402.

Misra, P., Casimir, D., Garcia-Sanchez, R., 2013. Thermal expansion properties of single-walled carbon nanotubes, by Raman spectroscopy at 780 nm wavelength. In: Annual International Conference on Opto Electronics, Photonics & Applied Physics (OPAP), pp. 52–55.

Nardelli, M.B., Yakobson, B.I., Bernhole, J., 1998. Mechanism of strain release in carbon nanotubes. Phys. Rev. B. (57), R4277. http://dx.doi.org/10.1103/PhysRevB.57.R4277.

Plimpton, S., 1995. Fast parallel algorithms for hort-range molecular dynamics. J. Comp. Phys. 117, 1–19. http://dx.doi.org/10.1006/jcph.1995.1039.

Rafii-Tabar, H., 2004. Computational modelling of thermomechanical and transport properties of carbon nanotubes. Phys. Rep. 390, 235–452. http://dx.doi.org/10.1016/j.physrep.2003.10.012.

Rafii-Tabar, H., 2008. Computational Physics of Carbon Nanotubes. Cambridge University Press, Cambridge.

Raravikar, N.R., et al., 2002. Temperature dependence of radial breathing mode Raman frequency of single-walled carbon nanotubes. Phys. Rev. B 66, 235424-1–235424-9. http://dx.doi.org/10.1103/PhysRevB.66.235424.

Robertson, D.H., Brenner, D.W., Mintmire, J.W., 1992. Energetics of nanoscale graphitic tubules. Phys. Rev. B 45 (21), 12592–12595. http://dx.doi.org/10.1103/PhysRevB.45.12592.

Ruoff, R.S., Lorents, D.C., 1995. Mechanical and thermal properties of carbon nanotubes. Carbon 33 (7), 925–930.

Saito, R., Dresselhaus, G., Dresselhaus, M.S., 1998. Physical Properties of Carbon Nanotubes. Imperial College Press, London.

Salvetat, J.P., Briggs, G.A.D., Bonard, J.M., Basca, R.R., Kulik, A.J., 1999. Elastic and shear moduli of singlewalled carbon nanotube ropes. Phys. Rev. Lett. (82), 944. http://dx.doi.org/10.1103/PhysRevLett.82.944.

Stuart, S.J., Tutein, A.B., Harrison, J.A., 2000. A reactive potential for hydrocarbons with intermolecular interactions. J. Chem. Phys. (112), 6472. http://dx.doi.org/10.1063/1.481208.

Sun, C.Q., 2007. Size dependence of nanostructures: impact of bond order deficiency. Prog. Solid State Chem. 35, 1–159. http://dx.doi.org/10.1002/chin.200719203.

Tersoff, J., Ruoff, R.S., 1994. Structural properties of a carbon-nanotube crystal. Phys. Rev. Lett. 73 (5), 676–679. http://dx.doi.org/10.1103/PhysRevLett.73.676.

Wong, H.S.P., Akinwande, D., 2011. Carbon Nanotube and Graphene Device Physics. Cambridge University Press, New York. http://dx.doi.org/10.1017/CBO9780511778124.

Yamamoto, T., Watanabe, K., Hernandez, E.R., 2008. Mechanical properties, thermal stability and heat transport in carbon nanotubes. In: Jorio, A., et al., (Ed.), Carbon Nanotubes: Advanced Topics in the Synthesis Structure Properties and Applications. Springer, Heidelberg, pp. 165–194. http://dx.doi.org/10.1007/978-3-540-72865-8_5.

Yang, X.X., Zhou, Z.F., Wang, Y., Li, J.W., Guo, N.G., Zheng, W.T., Peng, J.Z., Sun, C.Q., 2013. Raman spectroscopic determination of the length, energy, Debye temperature, and compressibility of the C-C bond in Carbon allotropes. Chem. Phys. Lett. 575, 86–90. http://dx.doi.org/10.1016/j.cplett.2013.05.008.

Yosida, Y., 2000. High-temperature shrinkage of single-walled carbon nanotube. J. Appl. Phys. 87 (7), 3338–3341. http://dx.doi.org/10.1063/1.372345.

Carbon-based nanomaterials

8

P. Pillai, M.M. De Souza
University of Sheffield, Sheffield, UK

8.1 Introduction

The technological achievements of the electronics sector are a result of miniaturization and improved performance derived from scaling (Davari et al., 1995). As geometrical scaling continues, to reduce the lateral electric field (electric field $E \propto V_{DD}/L_G$) and the power density, $V_{DD} \times I_{ON}/A$ (where A is the area of the device), the supply voltage should also be scaled. Ultimately, new strategies are required to keep the gate overdrive sufficiently high to avoid high OFF current and switching delay. Because silicon cannot sustain these requirements, the search is therefore on for a replacement material and device for the semiconductor industry. Among the various graphitic nanostructures, single-walled carbon nanotubes (CNTs) invite special attraction for digital logic due their structural simplicity and tunable electronic properties arising from a finite semiconducting bandgap. Carbon-based devices are also being touted for RF applications: Where the transistor on/off current ratio is not of relevance, the transistor here is never switched off, and a small signal is superimposed on the transistor characteristics at a predesigned bias condition. Good RF performance requires high cutoff frequency, achieved via a high mobility of carriers. High mobility of carriers in graphene as compared to nanotubes/graphene nanoribbon (GNR) makes it more suitable for RF applications.

8.2 Outline

In this chapter, fundamental details of the atomic and electronic structure of CNTs are introduced from the nearest neighbor tight binding approximation. The importance of 1D electrostatics in various carbon-based device geometries is discussed. An overview of state-of-the-art developments in CNTFET technology is presented and the performance compared with rivaling III-V technologies. Technological issues in implementing these materials in the mainstream CMOS are briefly reviewed. Using nonequilibrium Green's function-based quantum mechanical device simulations, the performance of CNT and GNR tunnel FETs is benchmarked using the requirements

Modeling, Characterization and Production of Nanomaterials. http://dx.doi.org/10.1016/B978-1-78242-228-0.00008-9
Copyright © 2015 Elsevier Ltd. All rights reserved.

for ITRS-2024, and an advantageous diameter and width range for a CNT and a GNR to meet the proposed ITRS requirements are identified.

8.3 Electronic structure of graphite

Graphite is a well-known allotropic form of carbon composed of layers of sp^2-bonded atoms in a honeycomb arrangement. The electronic structure of individual layers of graphite, called *graphene*, was first discussed by Wallace (1947). Single-atom-thick graphite sheets (graphene) and their seamlessly rolled up form (CNTs) (Castro Neto et al., 2009) consist of a hexagonal structure with each atom forming three σ bonds with each of its nearest neighbors (Figure 8.1). These covalent bonds are nearly equivalent to those holding a diamond together, giving graphene similar mechanical and thermal properties as diamond. The fourth valence electron does not participate in covalent bonding. It lies in the $2P_z$ orbital oriented perpendicular to the sheet of graphite and forms a conducting π band. Overlap of the P_z orbitals of neighboring atoms results in the formation of delocalized π-bonds that determine the electronic properties of the material (Charlier et al., 2007).

A graphene unit cell composed of two atoms per unit cell is fully described by a wave function corresponding to the individual atoms and a coupling term that denotes their interaction with nearest neighbors (Charlier et al., 2007). The dispersion relation

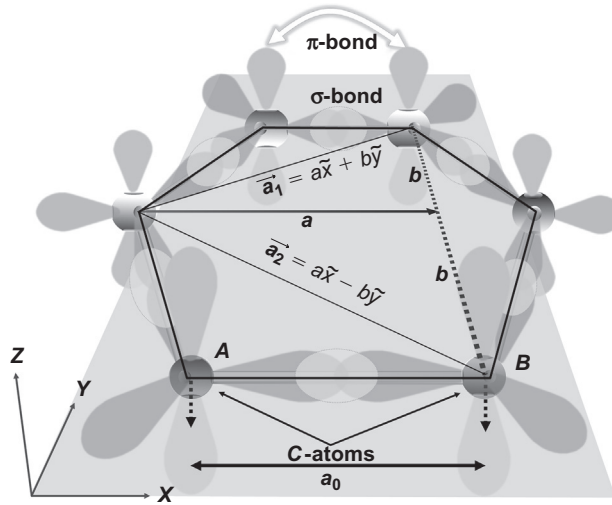

Figure 8.1 Schematic representation of σ- and π-bonding in graphene responsible for its elastic and electronic properties where each corner of the hexagon represents a carbon atom. The vector distances between two identical nearest neighbors of an atom are represented as $\vec{a_1} = a\,\tilde{x} + b\,\tilde{y}$ and $\vec{a_2} = a\,\tilde{x} - b\,\tilde{y}$, where the distances a and b are connected to a_0 as $a = \frac{3}{2}a_0$ and $b = \frac{\sqrt{3}a_0}{2}$.

can be obtained by solving the general time-independent Schrodinger equation as follows:

$$E\{\phi(r)\} = \left(\frac{-\hbar^2}{2m}\nabla^2 + V(r)\right)\{\phi(r)\} \tag{8.1}$$

where $\frac{-\hbar^2}{2m}\nabla^2 + V = H$ is the Hamiltonian, $\phi(r)$ corresponds to the wave function, and $V(r)$ is the confining potential due to the $2P_z$ orbitals of each carbon atom. For a periodic solid, the wave function can be expressed by the sum of basis functions as $\phi(r) = \sum_m \phi_m U_m(r)$, where $U_m(r)$ is the basis function at point m in the lattice and ϕ_m is the coefficient of the basis function at m. Thus one can convert the Schrodinger equation into its matrix form as

$$E\begin{bmatrix}\phi_1\\ \phi_2\\ .\\ .\\ \phi_N\end{bmatrix} = [H]\begin{bmatrix}\phi_1\\ \phi_2\\ .\\ .\\ \phi_N\end{bmatrix} \tag{8.2}$$

The above matrix represents N algebraic equations and for an arbitrary unit cell n,

$$E\{\phi_n\} = \sum\nolimits_m [H_{nm}]\{\phi_m\} \tag{8.3}$$

where $\{\phi_n\}$ is a matrix that includes the basis functions of the unit cell at point n, which consists of two basis functions corresponding to the "A" and "B" lattice sites in that unit cell. H_{nm} is the Hamiltonian at the nth unit cell due to the neighboring m unit cells.

Considering the periodicity of the lattice, one can express the wave function of the nth unit cell as $\{\phi_n\} = \{\phi_1\}e^{i\vec{k}\cdot\vec{d_n}}$ where d_n is the distance to the nth unit cell from the first unit cell, k is the reciprocal lattice vector, and ϕ_1 is the wave function of the first unit cell. Using this expression for $\{\phi_n\}$ in Eq. (8.3) results in

$$E\{\phi_1\} = [h]\{\phi_1\} \tag{8.4}$$

where $h = \sum_m [H_{nm}]e^{i\vec{k}\cdot\left(\vec{d_m}-\vec{d_n}\right)}$.

In the case of graphene, the position of every other unit cell from a given unit cell can be easily obtained by defining the vector distances as a linear combination of $\vec{a_1}$ and $\vec{a_2}$ given by $n\vec{a_1} + m\vec{a_2}$ (Figure 8.1). The Hamiltonian corresponding to any arbitrary unit cell and the derivation of the energy dispersion relation from there (shown in Eq. (8.16)) have been discussed by Datta (2008). Datta's approach begins with Hamiltonian of the unit cell as

$$h\left(\vec{k}\right)=\begin{bmatrix}\varepsilon & t\\ t & \varepsilon\end{bmatrix}+\begin{bmatrix}0 & 0\\ t & 0\end{bmatrix}e^{i\cdot\vec{k}\cdot\vec{a_1}}+\begin{bmatrix}0 & 0\\ t & 0\end{bmatrix}e^{i\cdot\vec{k}\cdot\vec{a_2}}+\begin{bmatrix}0 & t\\ 0 & 0\end{bmatrix}e^{-i\cdot\vec{k}\cdot\vec{a_1}}+\begin{bmatrix}0 & t\\ 0 & 0\end{bmatrix}e^{-i\cdot\vec{k}\cdot\vec{a_2}} \tag{8.5}$$

where ε is the self-energy term and t is the nearest neighbor coupling term in graphene. The first term arises from the unit cell under consideration and the subsequent four terms from each of its nearest neighbors. Adding all the terms yields

$$\left|h\left(\vec{k}\right)\right|=\begin{bmatrix}\varepsilon & t(1+e^{-i\cdot\vec{k}\cdot\vec{a_1}}+e^{-i\cdot\vec{k}\cdot\vec{a_2}}\\ t(1+e^{i\cdot\vec{k}\cdot\vec{a_1}}+e^{i\cdot\vec{k}\cdot\vec{a_2}} & \varepsilon\end{bmatrix} \tag{8.6}$$

The Eigen value of this matrix is given by

$$E=\varepsilon\pm|h_0| \tag{8.7}$$

where

$$h_0=t\left(1+e^{i\cdot\vec{k}\cdot\vec{a_1}}+e^{i\cdot\vec{k}\cdot\vec{a_2}}\right) \tag{8.8}$$

From Figure 8.1, the following vectors can be expressed in their component form as

$$\vec{k}=\tilde{x}k_x+\tilde{y}k_y \tag{8.9}$$

$$\vec{a_1}=\tilde{x}\frac{3a_0}{2}+\tilde{y}\frac{\sqrt{3}a_0}{2} \tag{8.10}$$

$$\vec{a_2}=\tilde{x}\frac{3a_0}{2}-\tilde{y}\frac{\sqrt{3}a_0}{2} \tag{8.11}$$

Assuming the distance $\frac{3a_0}{2}=a$ and $\frac{\sqrt{3}a_0}{2}=b$t, the expression for h_0 yields

$$h_0=t\left(1+2e^{ik_xa}\cos k_yb\right) \tag{8.12}$$

here $|h_0|^2=h_0h_0^*=t^2(1+4\cos k_xa\cos k_yb+4\cos^2k_yb)$ and hence

$$\left|h_0\left(\vec{k}\right)\right|=t\sqrt{1+4\cos k_xa\cos k_yb+4\cos^2k_yb} \tag{8.13}$$

This energy eigenvalue E can be expressed as the dispersion relation for valence and conduction bands from Eq. (8.7) as

$$E^{\pm}=\varepsilon\pm t\sqrt{1+4\cos k_xa\cos k_yb+4\cos^2k_yb} \tag{8.14}$$

where the + and − signs represent the conduction and valence band energies, respectively.

The energy dispersion curve has minima in reciprocal space when

$$(k_x, k_y) = \left(0, \frac{2\pi}{3b}\right), \left(0, -\frac{2\pi}{3b}\right), \left(\frac{\pi}{a}, \frac{\pi}{3b}\right), \left(\frac{\pi}{a}, -\frac{\pi}{3b}\right), \left(-\frac{\pi}{a}, \frac{\pi}{3b}\right), \text{and} \left(-\frac{\pi}{a}, -\frac{\pi}{3b}\right)$$

which corresponds to the valley points of the Brillouin zone in k-space.

The value of the function $h_0\left(\vec{k}\right) = t\left(1 + 2e^{ik_x a}\cos k_y b\right)$ around one of the valley points $((k_x a, k_y b) = \left(0, \frac{2\pi}{3}\right)$ can be evaluated by considering the Taylor series expansion of $h_0\left(k_x, k_y\right) = t\left(1 + 2e^{ik_x a}\cos k_y b\right)$ as

$$h_0\left(k_x, k_y\right) = h_0\left(0, \frac{2\pi}{3}\right) + \left[\frac{\partial h_0}{\partial k_x}\right]_{\left(0, \frac{2\pi}{3}\right)} (k_x - 0) + \left[\frac{\partial h_0}{\partial k_y}\right]_{\left(0, \frac{2\pi}{3}\right)} \left(k_y - \frac{2\pi}{3}\right) \tag{8.15}$$

where $\left[\frac{\partial h_0}{\partial k_x}\right]_{\left(0, \frac{2\pi}{3}\right)} = -iat$ and $\left[\frac{\partial h_0}{\partial k_y}\right]_{\left(0, \frac{2\pi}{3}\right)} = -\sqrt{3}tb = -at$, taking $\sqrt{3}b = a$ so $h_0\left(k_x, k_y\right) = -iatk_x - at\left(k_y - \frac{2\pi}{3}\right) = -iat\left[k_x - i\beta_y\right]$ where $\beta_y = k_y - \frac{2\pi}{3}$.

Therefore, the energy eigenvalue around the valley point is given by

$$E\left(k_x, k_y\right) = \varepsilon \pm |h_0| = \varepsilon \pm at\sqrt{k_x^2 + \beta_y^2} \tag{8.16}$$

This is the energy dispersion relation in graphene around the valley points $(k_x, k_y) = \left(0, \frac{2\pi}{3b}\right)$ and the energy dispersion relation over the entire Brillouin zone can be represented as shown in Figure 8.2b. The conduction (π^*) band and the valence (π) bands meet at these six points—known as Dirac points—giving the Fermi level in undoped graphene at these six points (Wallace, 1947; Castro Neto et al., 2009; Charlier et al., 2007). Each valley is shared between three adjacent Brillouin zones and effectively only one-third belongs to the first Brillouin zone.

8.4 Types of CNTs

CNTs are labeled in terms of a pair of integers (n, m) defining their chiral vector $C_h = na_1 + ma_2$ that describes the circumference ($C_h = \pi d_{\text{CNT}}$), where a_1 and a_2 are the unit vectors of the graphene honeycomb lattice. The vector distances are given by Eqs. (8.10) and (8.11), respectively, and are represented in simple terms as $\vec{a_1} = a\tilde{x} + b\tilde{y}$ and $\vec{a_2} = a\tilde{x} - b\tilde{y}$. The periodic boundary condition along the circumference forces the boundary condition $\vec{k}.\vec{C}_h = 2\pi\vartheta$ where $\vec{k} = k_x\tilde{x} + k_y\tilde{y}$. Hence, $\vec{k}\cdot\vec{C}_h = k_x a(m+n) + k_y b(m-n) = 2\pi\vartheta$. At the valley point $\left(k_x, k_y\right) = \left(0, \frac{2\pi}{3b}\right)$,

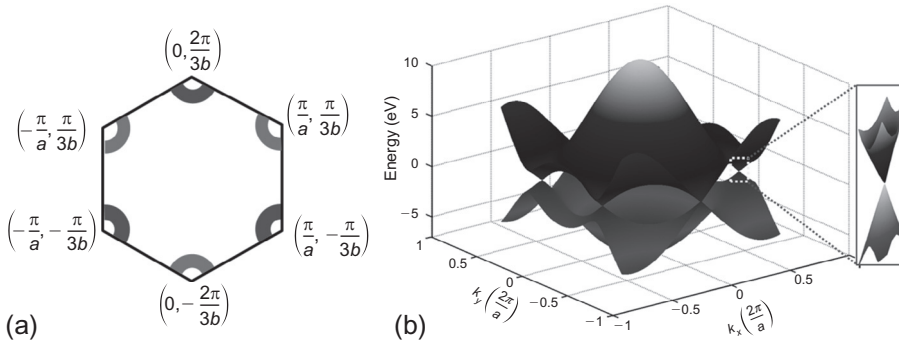

Figure 8.2 (a) Illustration of the six Brillouin valley points of graphene. Because each vertex is shared between two other neighboring Brillouin zones, an effective contribution of only one-third per corner point can be considered. To represent the states belonging to the first Brillouin zone, $13*6=2$ valley points are adequate (Datta, 2005). (b) 3D electronic band dispersion of graphene with valence (red) and conduction (blue) bands shown in the first Brillouin zone. A zoom of the bands near the K point or Dirac point where the two bands meet is highlighted.

$\vec{k}\cdot\vec{C}_h=\frac{2\pi}{3}(m-n)=2\pi\vartheta\Rightarrow\frac{(m-n)}{3}=\vartheta$, an integer. In a nanotube, a series of lines that follow the equation $\vec{k}\cdot\vec{C}_h=k_x a(m+n)+k_y b(m-n)=2\pi\vartheta$ are called its subbands (Charlier et al., 2007; Datta, 2008).

The chiral angle θ, i.e., the angle between C_h and a_1 is estimated as

$$\cos\theta=\frac{C_h\cdot a_1}{|C_h||a_1|}=\frac{2n+m}{2\sqrt{n^2+m^2+nm}} \tag{8.17}$$

The hexagonal symmetry of graphene restricts the value of θ to the range $0\le|\theta|\le30\,^\circ$. In armchair tubes, wrapped along the x direction, the circumferential vector $\vec{C}=2am$, where m is an integer (the equivalent points along the x-direction of the nanotube are separated by a distance $2a$ as shown in Figure 8.3b). These types of tubes are of type (n, n) $(\theta=30^\circ)$ and their bonds are perpendicular to the tube axis. Their periodic boundary conditions result in $k_\vartheta\cdot2am=2\pi\vartheta$, $\Rightarrow k_\vartheta=\frac{2\pi}{2am}\vartheta$.

Every value of the integer ϑ defines a k_ϑ at which the dispersion relation becomes

$$\epsilon_\vartheta(k_y)^{\pm}=\pm at\sqrt{k_\vartheta^2+\left(k_y-\frac{2\pi}{3b}\right)^2} \tag{8.18}$$

At $\vartheta=0$,

$$\epsilon_0(k_y)^{\pm}=\pm at\left|k_y-\frac{2\pi}{3b}\right| \tag{8.19}$$

For tubes wrapped along the x-direction (armchair tubes), a linear dispersion relation is always valid and results in metallic nanotubes.

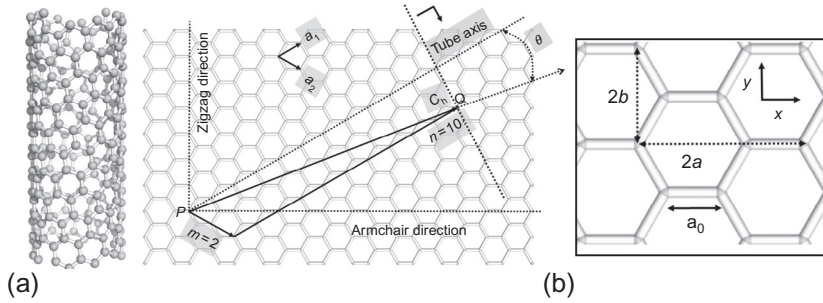

Figure 8.3 (a) Illustration of geometrical construction of (10,2) nanotube from a 2D sheet of graphene. A rolled up (10,2) tube is shown on the left. (b) The minimum distance corresponds to periodic boundary conditions for tube wrapping along x and y directions. The vectors $2a$ and $2b$ connect equivalent points of an nanotube and hence periodic boundary conditions apply so that $k_\vartheta \cdot 2am = 2\pi\vartheta$ (along x) or $k_\vartheta \cdot 2bm = 2\pi\vartheta$ (along y) where m is the chiral index and ϑ, an integer.

For tubes wrapped along the y direction, the circumferential vector $\vec{C} = 2bm$ and such nanotubes are called zigzag. Their indices are described as $(n, 0)$ $(\theta = 0°)$, and they display bonds parallel to the nanotube axis. The periodic boundary conditions in their case results in $k_\vartheta \cdot 2bm = 2\pi\vartheta \Rightarrow k_\vartheta = \frac{2\pi}{2bm}\vartheta - \frac{2\pi}{3b} = \frac{2\pi}{2bm}\left(\vartheta - \frac{2m}{3}\right)$.

This implies that the lowest subbands derived from the dispersion relation

$$\epsilon_\vartheta(k_x)^{\pm} = \pm at\sqrt{k_x^2 + (k_\vartheta)^2} \tag{8.20}$$

where $k_\vartheta = \frac{2\pi}{2bm}\left(\vartheta - \frac{2m}{3}\right)$ has a linear E-K relationship only when the chiral index m becomes an integer multiple of 3, the condition for metallic nanotubes (Charlier et al., 2007). That is, zigzag nanotubes become metallic only when $m = 3 * \vartheta$. Chiral nanotubes have indices $n \neq m \neq 0$.

In Figure 8.4, the electronic band structures of metallic and semiconducting nanotubes are shown, where the subbands cross at $k_x = 0$ for metallic nanotubes, resulting in a finite density of states (DOS) around the K point, while semiconducting nanotube exhibits nearly zero DOS around K.

8.5 Types of nanoribbons

Rather than rolling graphene sheets to form nanotubes, it is also possible to achieve semiconducting properties by controlling the width and edge structure of a graphene sheet. Such GNRs are classified into armchair-edge (AGNR) and zigzag-edge ribbons (ZGNR), and both categories exhibit a width-dependent bandgap (Yang et al., 2007). The dispersion relation in GNRs is different from the nearest neighbor tight binding dispersion relation in graphene due to the presence of edge states that stem from the π electron network at the edges (Yang et al., 2007; Nakada et al., 1996). But one can have reasonable agreement with *ab initio* band structure calculations by including an

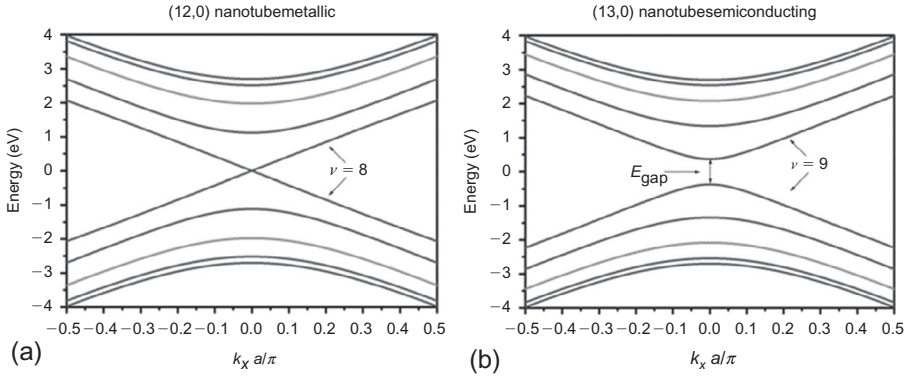

Figure 8.4 Electronic band structure of a (12,0) metallic nanotube (a) and a (13,0) semiconducting nanotube (b) calculated using atomic P_z orbital tight binding method (using CNTbands, Purdue University) (Seol et al., 2011). The band structure of a metallic nanotube showing subband crossing at the "valley" point ($x=0$) and hence a nonzero density of states at the valley point.

edge-bond distortion and third nearest neighbor interaction in the tight binding description (Gunlycke and White, 2008). Using this modified TB model, the expression for the tight binding bandgap in AGNR is given by (Gunlycke and White, 2008; Zhao et al., 2008)

$$E_g \approx -2\pi(t_1 - 2t_3)/\sqrt{3}(m+1) \pm 6(t_3 + \triangle t_1)/(m+1) \tag{8.21}$$

where t_1 and t_3 are first nearest neighbor and third nearest neighbor hopping energies, $\triangle t_1$ is the edge-bond relaxation energy and $m=3p$ or $3p+1$, where p is an integer. The plus (minus) sign in Eq. (8.21) applies to $m=3p$ ($m=3p+1$) family types. The width relation in AGNR is $W=(m-1)a/2$, where $a=0.246$ nm and in ZGNR is $\left(\frac{3m}{2}-1\right)a_{cc}$, where $a_{cc}=1.42$ Å.

8.6 DOS and quantum capacitance

The DOS is defined as a measure of the number of energy eigenstates per unit energy governed by the *E-K* relationship. Considering a system in equilibrium with Fermi function $f_0(E)$ at energy E, the total number of electrons over the entire energy range can be assumed as (Datta, 2005, 2008)

$$N = \int dE D(E) f_0(E) \tag{8.22}$$

where $D(E)$ is considered as the DOS of the material at energy E. Alternately, one can assume the total number of electrons as a summation of the Fermi functions at each energy $\in \left(\vec{k}\right)$, i.e.,

$$N = \sum_{\vec{k}} f_0\left(\in\left(\vec{k}\right)\right) \tag{8.23}$$

For the validity of the above two equalities, the DOS can be assumed as

$$D(E) = \sum_{\vec{k}} \delta\left(E - \in\left(\vec{k}\right)\right) \tag{8.24}$$

i.e., $N = \int dE\, D(E) f_0(E) = \sum_{\vec{k}} \int dE\, \delta\left(E - \in\left(\vec{k}\right)\right) f_0(E) = \sum_{\vec{k}} f_0\left(\in\left(\vec{k}\right)\right) = N$. Here the property of delta function $\int dx\, \delta(x-a) f(x) = f(a)$ has been utilized.

For a 2D solid with periodic boundary conditions along the x and y directions, the allowed k states in x and y are spaced by $\frac{2\pi}{L}$ and $\frac{2\pi}{W}$, where L and W are the length and width of the solid. Hence, over an energy range dE, the number of available states are $\frac{dk_x}{2\pi/L} * \frac{dk_y}{2\pi/W}$ (Figure 8.5).

Therefore, the total DOS of the system (Eq. (8.30)) can be evaluated as previously shown by Datta (2008) as

$$D(E) = \int\int \frac{dk_x}{\frac{2\pi}{L}} * \frac{dk_y}{\frac{2\pi}{W}} \delta\left(E - \in\left(\vec{k}\right)\right) \tag{8.25}$$

Using another property of delta function, i.e., $\delta\left(E - \in\left(\vec{k}\right)\right) = \delta\left(\in\left(\vec{k}\right) - E\right)$, as discussed in Datta (2008) one can write

$$D(E) = \int\int \frac{dk_x}{2\pi/L} * \frac{dk_y}{2\pi/W} \delta\left(\in\left(\vec{k}\right) - E\right) \tag{8.26}$$

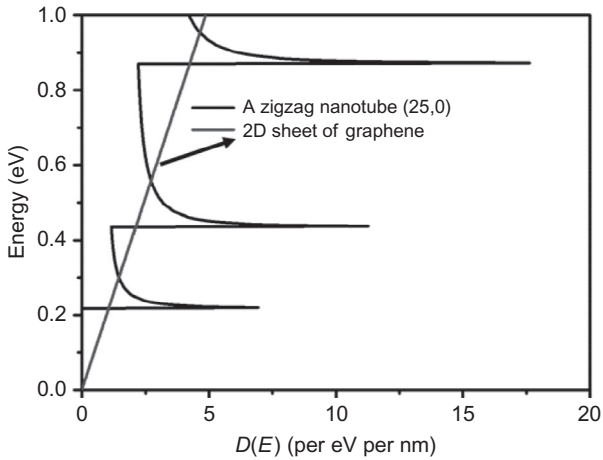

Figure 8.5 Density of states comparison between a (25,0) zigzag nanotube and a 2D graphene sheet calculated using Eqs. (8.30) and (8.32) for graphene sheet and zigzag nanotube, respectively.

This integral in circular coordinates can be written as

$$D(E) = \frac{LW}{4\pi^2}\int_{-\pi}^{\pi} \mathrm{d}\theta \int \mathrm{d}k \cdot k\,\delta\left(\in\left(\vec{k}\right) - E\right) \tag{8.27}$$

$$\Rightarrow D(E) = \frac{LW}{4\pi^2} * 2\pi * \int \mathrm{d}k \cdot k\,\delta\left(\in\left(\vec{k}\right) - E\right) \tag{8.28}$$

But the energy eigenvalue around the valley point for graphite is

$$\in\left(\vec{k}\right) = \varepsilon \pm |h_0| = \varepsilon \pm at\sqrt{k_x^2 + \beta_y^2} = \varepsilon \pm at|k| \tag{8.29}$$

Assuming zero site energy (i.e., $\varepsilon = 0$), $\in\left(\vec{k}\right) = \pm at|k|$ and considering only the positive value, $\mathrm{d}\in\left(\vec{k}\right) = at * \mathrm{d}k \Rightarrow \mathrm{d}k = \mathrm{d}\left[\in\left(\vec{k}\right)\right]/at$,

$$D(E) = \frac{LW}{4\pi^2} * 2\pi * \int \mathrm{d}\frac{\left[\in\left(\vec{k}\right)\right]}{at} * \in\frac{\left(\vec{k}\right)}{at} * \delta\left(\in\left(\vec{k}\right) - E\right) = \frac{A}{2\pi}\frac{|E|}{(at)^2} \tag{8.30}$$

where A is the area of the 2D conductor.

Therefore, the DOS in a 2D conductor (i.e., graphene) is linearly proportional to the energy E. Because both the length (L) and the width (W) of the conductor are large, the allowed k states are spaced very close to each other, and the summation over k can be replaced by an integral as shown in Eqs. (8.24) and (8.25).

On the other hand, in the case of a 1D material such as a CNT whose length spans over the x-direction, the distance in the y-direction is the diameter, which is very small. Hence, states along k_y are finitely spaced, and one cannot use integration to sum up the number of states. Therefore, the expression for the DOS becomes (Datta, 2008)

$$D(E) = \sum\nolimits_{\vec{\beta}_y} \int \frac{\mathrm{d}k_x}{2\pi/L} * \delta\left(E - \in\left(\vec{k}\right)\right) \tag{8.31}$$

From the general dispersion relation, Eq. (8.16), we have $\epsilon^2 = (at)^2(k_x^2 + \beta_y^2)$. Taking the differential with respect to k_x yields $\epsilon\,\mathrm{d}\epsilon = (at)^2 * k_x * \mathrm{d}k_x$ and $k_x = \sqrt{\frac{\epsilon^2 - a^2t^2\beta_y^2}{a^2t^2}}$. Replacing k_x and $\mathrm{d}k_x$ and using the property of delta function, the expression for 1D DOS becomes (Datta, 2005)

$$D(E) = \frac{L}{2\pi at}\sum\nolimits_{\vec{\beta}_y} \frac{E}{\sqrt{E^2 - a^2t^2\beta_y^2}} \tag{8.32}$$

That is, corresponding to the energy values $E^2 = a^2t^2\beta_y^2$, the DOS exhibits a series of spikes, which are typical signatures of 1D materials called Van-Hove singularities (Van Hove, 1953).

For a nanotube of sufficiently large length L, the discrete energy levels in momentum space separated by a distance $\delta k = {}^{2}\pi/_{L}$ are close enough to form a continuum of states, and the DOS can alternatively be expressed as

$$D(E) = \int \delta\left(E - \in\left(\vec{k}\right)\right) \mathrm{d}E = \int \frac{\mathrm{d}k}{{}^{2\pi}/_{L}} \delta\left(E - \in\left(\vec{k}\right)\right) \tag{8.33}$$

$$= \frac{L}{2\pi} \int \mathrm{d}\varepsilon \frac{\mathrm{d}k}{\mathrm{d}\varepsilon} \delta\left(E - \in\left(\vec{k}\right)\right) = \frac{L}{2\pi} \left| {}^{1}\Big/ {}_{\mathrm{d}\varepsilon/\mathrm{dk}} \right|_{\varepsilon = E} \tag{8.34}$$

i.e.,

$$\left|\mathrm{d}\varepsilon/\mathrm{dk}\right|_{\varepsilon = E} = \frac{L}{2\pi * D(E)} \tag{8.35}$$

The energy required to add an additional electron to the nanotube at the Fermi energy is given by

$$\delta E = \delta k \left|\mathrm{d}\varepsilon/\mathrm{dk}\right|_{\varepsilon = E_{\mathrm{F}}} = \frac{1}{2\pi * D(E_{\mathrm{F}})} \delta k \tag{8.36}$$

where $D(E_{\mathrm{F}})$ is the DOS per unit length at Fermi energy. Substituting δk yields $\delta E = \frac{1}{D(E_{\mathrm{F}})L}$. This energy is equal to the capacitive energy $CV^2 \equiv e^2/LC$, i.e.,

$$\delta E = e^2/LC \tag{8.37}$$

And the capacitance per unit length in the case of the nanotube is given by

$$C_{\mathrm{Q}} = e^2 D(E_{\mathrm{F}}) \tag{8.38}$$

This term C_{Q} is called the intrinsic or quantum capacitance of a nanotube, representing the charge occupied in the quantized energy levels (Léonard, 2009).

In a conventional MOSFET structure, which has been the main driver of CMOS over the last half century or so, this capacitance corresponds to that of the layer of quantized carriers confined in the inversion layer at the surface of the channel. The electrical behavior of the conventional MOSFET device is determined by the maximum potential ($\delta\phi$) in the channel that controls the flow of carriers from the source into the channel via an applied gate bias (Figure 8.6).

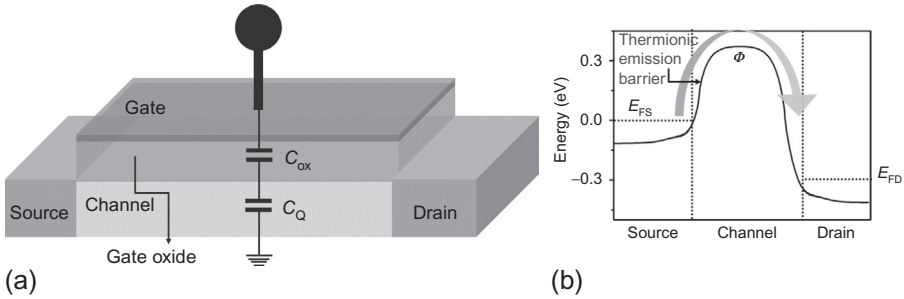

Figure 8.6 Schematic representation of a conventional MOSFET device and the relevant capacitances (a). The conduction band profile of the device (b) shows the channel potential far from the contacts (Φ). E_{FD} represents the chemical potential of the drain terminal.

The potential applied at the gate terminal is dropped across the oxide and semiconductor surface to create an inversion layer of quantized electrons. A change in channel potential ($\delta\Phi$) in the device with respect to change of gate potential ($\delta\Phi_G$) can be assumed as (Auth and Plummer, 1997; Knoch and Appenzeller, 2006, 2008)

$$\delta\Phi = \delta\Phi_G \frac{C_{OX}}{C_{OX} + C_Q + C_S + C_D} \tag{8.39}$$

where C_{OX}, C_Q, C_S, C_D are the oxide, quantum, source, and drain capacitances (C_S and C_D are neglected in the following for simplicity, although C_D plays a part in short channel effects).

In a MOSFET, it is very well known that the total gate capacitance for a metal gate consists of a series combination of C_{OX} and C_Q (Datta, 2005):

$$C_G = \frac{C_{OX} * C_Q}{C_{OX} + C_Q} \tag{8.40}$$

The charge in the channel is described (by definition of a capacitor) as Q_{ch},

$$C_G = \frac{\delta Q_{ch}}{\delta V_G} = q * \frac{\delta Q_{ch}}{\delta\Phi} * \frac{\delta\Phi}{\delta\Phi_G} \tag{8.41}$$

From Eq. (8.39), $\frac{\delta\Phi}{\delta\Phi_G} = \frac{C_{OX}}{C_{OX}+C_Q}$, and comparing the above two equations reveals that $q * \frac{\delta Q_{ch}}{\delta\Phi} = C_Q$. Therefore, the quantum capacitance of a conventional MOSFET of bulk material as discussed by Knoch and Appenzeller (2008), Knoch and Appenzeller (2006) can be written as

$$C_Q^{3D} = q\frac{\partial Q_{ch}}{\partial\Phi} \propto -q^2 tWLD^{3D}(E_{FS} - \Phi) \propto \sqrt{E_{FS} - \Phi} \tag{8.42}$$

In the on state, C_Q^{3D} increases with the change in surface potential and finally beyond the threshold voltage (quantified by an equal amount of band bending below and above the Fermi level) reaches a stage where the surface potential hardly moves with increase in gate voltage. In this situation, $C_Q \gg C_{OX}$ because of the bulk DOS of the channel, thus limiting the scaling capacitance of the bulk MOSFET. In the device off state $C_{OX} \gg C_Q$ and $C_{OX} \gg C_D$. The relative contribution of C_Q with respect to C_{OX} determines the nature of the turn-on characteristic (called inverse subthreshold slope), which is given by the number of carriers that are thermally excited over the source/channel potential barrier. The number of electrons changes exponentially with gate voltages and N can be written as

$$N \approx N_0 \exp\left(\frac{\Phi}{k_B T}\right) \Rightarrow \log_{10}\left(\frac{N}{N_0}\right) \approx \left(\frac{\Phi}{2.3 * k_B T}\right) \tag{8.43}$$

where N_0 is the charge density corresponding to the neutral potential, i.e., the number of electrons increases by a decade with an increase in gate potential of $2.3 * k_B T = 60$ meV at room temperature as shown in Figure 8.7a (Taur and Ning, 1998). Application of a positive gate voltage lowers the overall DOS in the channel region and increases the electron density in the channel. Inverse subthreshold swing S in terms of device I-V is therefore defined by $S = \ln(10)\left(\frac{\partial I_{DS}}{\partial V_{GS}} \frac{1}{I_{DS}}\right)^{-1}$.

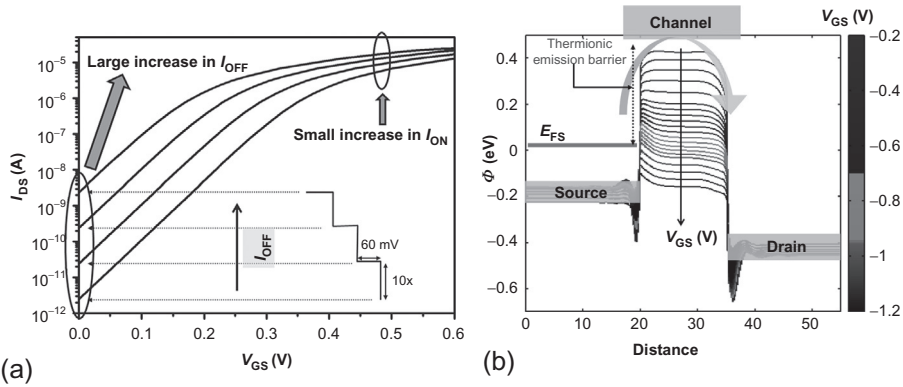

Figure 8.7 (a) Reduction of the threshold voltage and subsequent reduction of minimum current in a MOSFET device. Each curve in the figure is left shifted by 60 mV. The figure shows a typical scenario in a conventional MOSFET where a small increase in ON-current by reduction of the threshold voltage of 60 mV results in a tenfold increase in OFF-current. (b) Modulation of conduction band profile of an *n*-channel CNTFET by applied gate voltage interval of 0.05 V. As the gate voltage is increased in the negative direction, the barrier height is reduced, which allows a flow of electrons from the source side. The gate voltage continues to modify the surface potential in the device on-state in contrast to bulk MOSFETs (beyond threshold).

Contrary to bulk solids, the DOS in 1D solids such as CNTFETs equals the DOS $\propto {}^{1}\Big/_{\sqrt{E_{FS}-\Phi}}$. Appenzeller et al. have previously shown that the quantum capacitance per unit length in such materials is proportional to the tunneling probability of the carriers across the potential barrier in the device (Knoch and Appenzeller, 2006), i.e.,

$$C_Q = e\frac{\partial Q_{ch}}{\partial \Phi} \approx e\frac{\partial}{\partial \Phi}\int_0^{\triangle \varnothing} dE T_{WKB} D(E)(1 - f(E - E_{FS})) \tag{8.44}$$

Hence, in the quantum capacitance limit $C_Q \leq C_{OX}$ can be achieved in 1D systems with ultrathin gate oxides and/or high-k dielectrics as shown by Guo et al. (2002). In this case, the gate capacitance is dominated by C_Q (rather than C_{OX}) and consequently $\frac{\delta \Phi}{\delta \Phi_G}$ approaches unity, which means that the gate voltage continues to modify the surface potential in the device on-state (beyond threshold). In Figure 8.7b, it is shown that one-dimensional FETs have a superior ability for electrostatic control thereby eliminating short-channel effects.

8.7 CNT tunnel FETs

Because MOSFETS are limited in their switching by an $S = 60$ mV/dec, a possible way for a faster turn-on at room temperature is by modifying the current injection mechanism at the source contact through tunneling rather than thermionic emission (Leburton et al., 1988; Reddick and Amaratunga, 1995; Aydin et al., 2004; Choi et al., 2005; Bhuwalka et al., 2006; Nirschl et al., 2007). Figure 8.8 shows the on-state and off-state band bending in a CNT tunnel FETs (CNT-TFET). At $V_{GS} > 0$ V, the channel conduction band is below the source valence band; this makes it easier for carriers to tunnel from the source valence band to the channel conduction band. At $V_{GS} < 0$ V, the band bending at the channel drain results in a tunneling current between source and drain terminals. The tunneling mechanism depicted in Figure 8.8b shows that only electrons within an energetic window of $\triangle \varnothing$ contribute to the current (I_d) because the tunneling probability is finite only within an energy window of $\triangle \varnothing$.

The interband tunneling probability across the contact-channel junction T_{WKB} is given by the WKB approximation as (Sze, 1981)

$$T_{WKB} \approx \exp\left(-\frac{4\Lambda\sqrt{2m^*}\sqrt{E_g{}^3}}{3q\hbar\left(E_g + \Delta\Phi\right)}\right) \tag{8.45}$$

where E_g is the bandgap of the nanotube, m^* is the effective mass, Λ is the width of the interband potential barrier assumed at the source-channel interface region, and $\Delta\Phi$ is the energetic difference between the channel conduction band and the source valence band (Figure 8.8b).

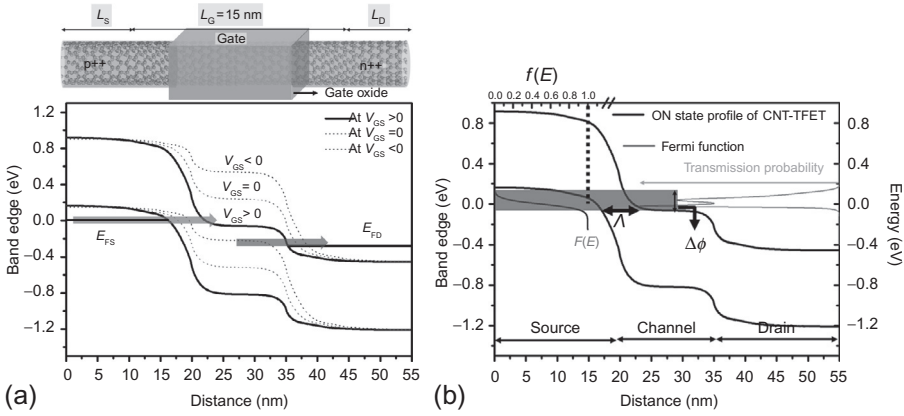

Figure 8.8 (a) A schematic band bending in a CNT-TFET under gate voltage $V_{GS} = 0$ V (red dotted line), $V_{GS} > 0$ V (solid line), and $V_{GS} < 0$ V (black dotted line). (b) Band-to-band tunneling at the source-channel interface where the width of the barrier is represented as Λ and the energetic difference between the channel conduction band and source valence band in the on-state is denoted as $\Delta\phi$. The Fermi distribution function plotted along with the band energy indicates that the low and high energy tails of the Fermi distribution function are cut off when the interband tunnel probability is high across the barrier. Only the red-shaded part of Fermi distribution is involved in device operation.

The band-to-band tunneling (BTBT) current in a CNT-TFETs can be ascertained using the NEGF or an analytic approach. The latter is given by (Sze, 1981; Knoch et al., 2007)

$$\begin{aligned} I_d &= \frac{4e}{h}\int_0^{\Delta\varnothing} dE T_{WKB}(1 - f(E - E_{FS})) \\ &= \frac{4e}{h} T_{WKB} k_B T \left(\ln\left(e^{\frac{\Delta\varnothing - E_{FS}}{k_B T}} + 1 \right) - \ln\left(e^{\frac{-E_{FS}}{k_B T}} + 1 \right) \right) \end{aligned} \tag{8.46}$$

When the interband tunnel distance Λ is small, the tunneling probability at the interface can be considered as unity. Then, the inverse subthreshold slope for CNT-TFET in the case of 1D CNT-TFETs can be obtained from its general form $S = \ln(10)\left(\frac{\partial I_{DS}}{\partial V_{GS}}\frac{1}{I_{DS}}\right)^{-1}$. Equation (8.46) as discussed by Knoch et al. (2007)

$$S \approx \frac{\ln(10)}{|e|}\frac{3q\hbar\left(\Delta\varnothing + E_g\right)^2}{4\Lambda\sqrt{2m^*}E_g^{3/2}} \tag{8.47}$$

In 1D TFETs the quantum capacitance is significantly smaller than conventional MOSFETs due to the dependence of the quantum capacitance on T_{WKB} (Knoch and Appenzeller, 2006, 2008). For $\Lambda \ll L$, where L is the channel length, the gate capacitance $C_G = \frac{C_{OX} C_Q}{C_{OX} + C_Q}$. The quantum capacitance per unit length is given by (Knoch et al., 2007)

$$C_Q = e\frac{\partial Q_{ch}}{\partial \Phi} \approx e\frac{\partial}{\partial \Phi}\int_0^{\Delta\varnothing} dE T_{WKB} D(E)(1 - f(E - E_{FS})) \tag{8.48}$$

For devices working in the limit $C_{OX} \gg C_Q$, the total capacitance is dominated by C_Q, which reduces the requirement of aggressive scaling of oxide thickness.

8.8 ITRS requirements—2024

Materials that can act as alternate channels for beyond CMOS device applications are expected to enable continued scaling of integrated circuits with improved energy efficiency for applications where no solutions are currently known. The ITRS roadmap targets major parameters such as saturation current, on-off ratio, and device delay in the timeframe of 2024 and beyond, where carbon-based materials can be considered viable (Table 8.1).

The 14 nm node of the ITRS roadmap is projected to operate with 0.7 V supply (http://www.itrs.net/Links/2012ITRS/Home2012.htm) with a power consumption 25× higher than a V_{DD} of 0.14 V (as power consumption $\propto V_{DD}^2$). The minimum required on-off ratio of four orders (for HP technology) demands the subthreshold swing of 35 mV/dec for the operating voltage of $V_{DD} = 0.14$ V. A number of strategies/device architectures have been explored to realize subthreshold operation <60 mV/dec for various TFETs. A few of them are summarized in Table 8.2.

A comparison between the predicted and experimentally reported tunnel FETs reveals a significant gap in the on-state current and inverse subthreshold slope. In TFETs, for high on-state current, the tunneling probability at the source/channel interface should be nearly one; this requires an abruptly varying doping profile (four to five orders of magnitude) between source and intrinsic channel region within a distance of few nanometers (Ionescu and Riel, 2011; Ionescu et al., 2011). High trap density (D_{it}) at the channel-gate dielectric interface in experimental TFETs is detrimental to realize the steep subthreshold slope because it results in tunneling of carriers from the valence band in the p-doped source region to mid-gap trap states and a subsequent thermal emission into the conduction band that degrades S (Mookerjea et al., 2010). In order to realize the full potential of TFET devices, parasitic access resistance at the contact region also needs to be minimized to improve the on-current (Zhou et al., 2011). Ambipolarity in TFETs is another major issue in designing n-type and p-type TFETs. Asymmetry

Table 8.1 ITRS-2024 targeted values for various parameters

Parameter	High-performance logic technology (low operating power technology)
Saturation current (μA/μm)	2152 (666)
On-Off ratio	$\sim 2 \times 10^4$
Intrinsic device delay (fs)	130 (280)
Supply voltage (V)	0.61 (0.46)

Source: http://www.itrs.net/Links/2012ITRS/Home2012.htm.

Table 8.2 Summary of TFET performance demonstrated using experiment and theory and its comparison with recently experimentally reported MOSFET performance

Device type	Device technology	Inverse subthreshold swing (mV/dec)	I_{ON} (μA/μm)	ON-OFF ratio	EOT (nm)	Gate length (nm)	References
Experimental TFETs	InGaAs/InP TFETs	93	20	6×10^5 (@ $\lvert V_{GS}\rvert=1.75$ V, $\lvert V_{DS}\rvert=0.5$ V)	~1.3	70,000	Zhou et al. (2012)
	GaSb/InAs(Sb) NW-TFETs	~235	62	>143 (@ $\lvert V_{GS}-V_r\rvert=0.5$ V, $\lvert V_{DS}\rvert=0.3$ V)	1.3	290	Dey et al. (2013)
	InAs-Si nanowire TFET	150	2.4	10^6 (@ $\lvert V_{DD}\rvert=1$ V)	~3.25	~550	Moselund et al. (2012)
	Si-tunneling green transistor	46	1.2	7×10^7 (@ $\lvert V_{GS}\rvert=\lvert V_{DS}\rvert=1$ V)	–	20,000	Hu et al. (2010)
Projected TFETs	InGaAs/AlGaAsSb heterojunction TFETs	–	400	10^4 (@ $\lvert V_{DD}\rvert=0.3$ V)	0.6	100	Wang et al. (2010)
	InAs/InGaAs vertical TFETs	16	~1000	~10^6 (@ $\lvert V_{GS}\rvert=0.6$ V, $\lvert V_{DD}\rvert=0.4$ V)	0.3	20	Ganapathi and Salahuddin, 2011
	InGaAs-InAlAs superlattice FETs	13	4500	~4.5×10^4 (@ $\lvert V_{DD}\rvert=0.4$ V)	1	40	Gnani et al. (2011)
Experimental MOSFETs	InGaAs/InP/InAlAs/InGaAs core-multishell NWFETs	75	1000	>10^6 (@ $\lvert V_{GS}\rvert=\lvert V_{DS}\rvert=0.5$ V)	2.75	200	Tomioka et al. (2012)
	InGaAs gate-all-around NW MOSFETs	91	1000	~10^4 (@ $\lvert V_{GS}\rvert=\lvert V_{DS}\rvert=0.5$ V)	1.2	20	Gu et al. (2012)

Source: Zhou et al. (2012), Dey et al. (2013), Moselund et al. (2012), Hu et al. (2010), Wang et al. (2010), Ganapathi and Salahuddin (2011), Gnani et al. (2011), Tomioka et al. (2012) and Gu et al. (2012). The grey shaded cells represent the best values for ON- current and inverse sub-threshold slope.

in the doping profile in the source/drain extensions and using a small bandgap at the source region and high bandgap at drain side (heterojunction TFETs) to minimize the BTBT at the channel/drain region are considered as suitable ways to suppress ambipolarity (Wang et al., 2010; Jang and Choi, 2011; Boucart and Ionescu, 2007).

Since the first demonstration of a CNTFET by Dekker and coworkers (Tans et al., 1998), the potential of carbon-based materials for electronic applications was explored by many groups and IBM in particular (Martel et al., 1998, 2001; Wind et al., 2002; Avouris et al., 2003, 2007; Appenzeller, 2008; Appenzeller et al., 2002, 2005; Franklin et al., 2012a,b). In 2004, Ali Javey et al. demonstrated a combination of top- and bottom-gated, doped source/drain CNTFETs with an on-current up to 20 μA and a conductance of $0.1 \times 4e^2/h$ ($4e^2/h$ is the ballistic conductance in semiconducting nanotubes) for long-channel devices (Javey et al., 2004). Eight years later, in 2012, a sub 10 nm channel Schottky barrier CNTFET of diameter 1.3 nm with subthreshold slope (S) 94 meV/dec and on-current of 2410 μA/μm at a $V_{DD} = 0.5$ V, much higher than Si-based FETs, was reported (Franklin et al., 2012a). A short-channel ($L_{ch} = 30$ nm) gate all-around n-type CNTFET, also demonstrated by IBM researchers, showed an on-state current >1000 μA/μm @ $V_{DD} = 0.5$ V and on-off ratio $>10^3$ (Franklin et al., 2012b). Figure 8.9 summarizes the ON- and OFF-state performance of these best-reported Schottky barrier CNTFETs by the IBM research group (Franklin et al., 2012a,b). However, the ON-OFF ratio falls short of requirements for various ITRS technologies (http://www.itrs.net/Links/2012ITRS/Home2012.htm). The main reason for the poor off-state current is the leakage current through the Schottky barrier

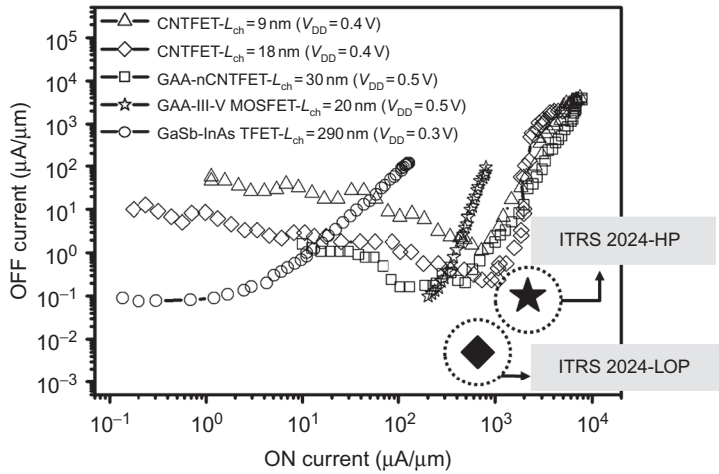

Figure 8.9 A comparison of ON- and OFF-state performance of best reported short channel CNT (Franklin et al., 2012a,b) and III-V devices (Gu et al., 2012; Dey et al., 2013) (Zhou et al., 2012; Dey et al., 2013; Moselund et al., 2012; Hu, 2008; Wang et al., 2010; Ganapathi and Salahuddin, 2011; Gnani et al., 2011; Tomioka et al., 2012). The ITRS targeted values for low operating power (LOP) and high performance (HP) technologies are highlighted (http://www.itrs.net/Links/2012ITRS/Home2012.htm).

present at the metal-CNT interface, which needs to be addressed (Appenzeller et al., 2002). A comparison of the experimentally demonstrated performance of Schottky barrier CNTFETs with III-V MOSFET and T-FETs in Figure 8.9 reveals that today CNTFETs exhibit better on-state performance as compared to the rivaling III-V technologies (Zhou et al., 2012; Dey et al., 2013; Moselund et al., 2012; Hu, 2008; Wang et al., 2010; Ganapathi and Salahuddin, 2011; Gnani et al., 2011; Tomioka et al., 2012; Gu et al., 2012), however, the poor on-off ratio exhibited by the SB-CNTFETs reveals the need for short-channel carbon-based FETs with minimum off-state leakage.

A number of obstacles need to be overcome before introducing CNTs into the mainstream manufacturing technology. CNTs can be metallic or semiconducting in nature and statistical analysis reveals that 33% of the nanotube chiralities are metallic. In the case of 7 nm channel devices targeted for the year 2024 by ITRS, completely eliminating metallic chiralities in devices is considered of paramount importance, and a targeted impurity concentration of metallic nanotubes by year 2020 is expected to be 0.0001% (Franklin, 2013). Another important aspect is achieving high parallel packing density with a minimum pitch between the nanotubes to produce high on-state current. The targeted packing density for the year 2020 is 125 nanotubes/μm (Franklin, 2013), although a packing density of 250 nanotubes/μm with a pitch of 4 nm (distance between two nanotubes) is essential to surpass silicon CMOS technology (Patil et al., 2009a). A number of methods have been explored for the purification of nanotubes such as ultracentrifugation (Arnold et al., 2006; Green and Hersam, 2011); chromatographic separation of semiconducting chiralities (Zheng and Semke, 2007; Liu et al., 2011); alternating current dielectrophoresis, where an opposite movement of metallic and semiconducting tubes is established along the electric field gradient (Krupke et al., 2003); and DNA-assisted separation and purification (Tu et al., 2009). The main drawback of these methods is that the resulting nanotubes are short (∼1 μm) or coated with molecules/DNA so that their well-controlled parallel assembly becomes technically challenging. Perfectly aligned growth (>99.9% of SWNTs within 0.01° of perfect alignment) of CNTs has been realized in CVD growth on quartz substrate, but this suffers from the limitation that includes metallic CNTs (Patil et al., 2009b; Zhou et al., 2008). However, a recently reported CMOS-compatible method in which an effective method for selective removal of metallic nanotubes has been demonstrated (Jin et al., 2013). A long parallel array of CNTs is coated with a special organic thin film (resist) that is sensitive to thermal fluctuations. By turning off the semiconducting nanotubes by applying a suitable gate bias, current flow is achieved only through metallic nanotubes there by locally breaking down the resist around the metallic nanotubes and creating a surrounding trench. These exposed metallic nanotubes are removed by oxygen plasma treatment, giving a purity of 99.9%, semiconducting nanotubes with a packing density ∼4 nanotubes/μm in a chip, exhibiting devices with on-off ratio of $\sim 10^4$ and mobility exceeding 1000 $cm^2\ V^{-1}\ s^{-1}$ (Jin et al., 2013). However, the packing density in this approach needs to be significantly improved to meet the targeted values for 2024.

CNTs exhibit a diameter-dependent bandgap; hence, it is necessary to identify suitable diameter (bandgap) nanotubes that can be used to realize FETs of targeted performance proposed by ITRS for various technologies. Direct measurement of electronic bandgap from spectrofluorimetric measurements is challenging because

the recorded energies account not only for the electronic bandgaps but also for the exciton binding energies. Tunneling spectroscopic measurements underestimate the bandgaps due to screening arising from the image charge in metal substrates (Dukovic et al., 2005; Lin et al., 2010). Hence, more accurate approaches are necessary to establish a bandgap relation with diameter in nanotubes (Figure 8.10).

In this section the performance of tunnel FETs consists of CNT diameter from 0.55 to 1.25 nm are analyzed via modeling.

The TFETs IVs are evaluated using NANOTCAD ViDES in which the electron-hole concentration in the device is computed by solving the Schrödinger equation with open boundary conditions by means of the NEGF formalism (Fiori et al., 2006). An intrinsic channel length of 15 nm and doped source/drain regions of length 20 nm, an effective gate oxide thickness (EOT) of 0.5 nm, and a $V_{DS} = 0.3$ V are used. A tight binding Hamiltonian with atomistic (P_z orbitals) basis has been used in the mode space approach. Transport is calculated using the GW-bandgaps of the nanotubes (Umari et al., 2012) with corresponding DOS and effective mass for various diameters are incorporated using an effective tight parameter of $\gamma = -5.2$ eV. Analyzing the tunnel FET performance of various diameter CNTs in Figure 8.11 reveals that low-diameter nanotubes (<0.8 nm) are unsuitable for the technology due to their low ON-state current (<0.1 μA/nanotube), while large-diameter nanotube devices (>1.3 nm) exhibit poor ON-OFF ratios ($<10^3$) due to the high off-state leakage in those devices. A (11,0) TFET shows an advantage in the case of ON-state current (~2-3 μA/nanotube) while exhibiting an on-off ratio $>10^6$.

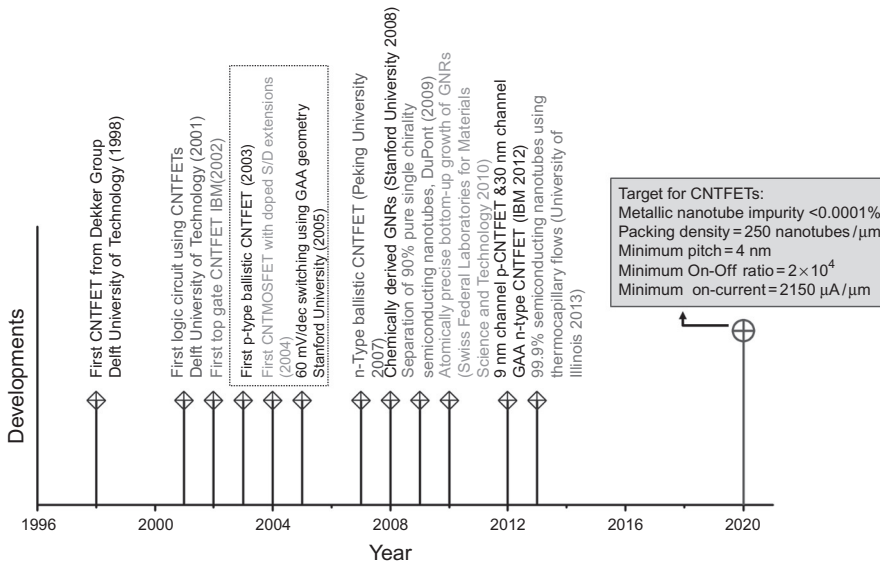

Figure 8.10 Progress in carbon-based electronics since their first demonstration in a FET geometry (Tans et al., 1998; Bachtold et al., 2001; Wind et al., 2002; Franklin et al., 2012a; Javey et al., 2003, 2004; Franklin, 2013; Tu et al., 2009; Jin et al., 2013; Lu et al., 2006; Zhang et al., 2007; Wang et al., 2008; Cai et al., 2010).

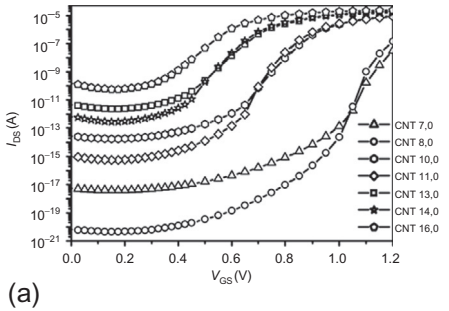

(a)

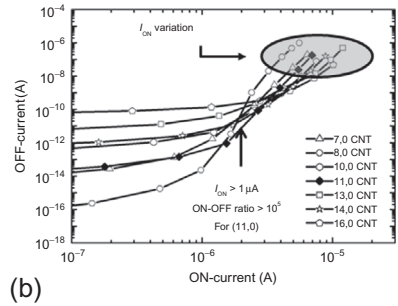

(b)

Nanotube chirality	GW-band gap (eV)	Effective mass	Channel length (nm)	EOT (nm)	Drain bias (V)
(7,0)	2.69	0.092	15	0.5	0.3
(8,0)	2.38	0.080			
(10,0)	1.89	0.064			
(11,0)	1.72	0.058			
(13,0)	1.45	0.050			
(14,0)	1.34	0.046			
(16,0)	1.18	0.040			

(c)

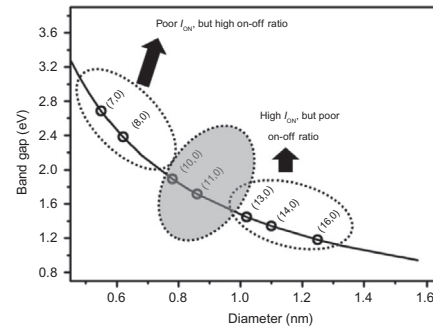

(d)

Figure 8.11 (a) Simulated transfer characteristics of carbon nanotube TFETs with CNT diameters from 0.55 nm (7,0) to 1.25 nm (16,0) using a nonequilibrium Green's function-based quantum transport simulation tool, NANOTCAD ViDES, from Fiori et al. (2006). The bandgaps of the nanotubes used in the study are calculated via GW-approach as reported in Umari et al. (2012). (b) Comparison of ON- and OFF-current variation (at a $V_{DD} = 0.3$ V) with bandgap. The effective masses and other device parameters used in the simulation are summarized in the table shown in (c). (d) An analysis shows that low-diameter (<0.8 nm) nanotube TFET devices exhibit poor on-current, while large-diameter (>1.25 nm) TFET devices suffer from low ON-OFF ratio.

8.9 Comparison between a CNT-MOSFET and TFET

A comparison of CNTFETs using a (11,0) nanotube (diameter ≈0.85 nm) with bandgap ≈1.4 eV, an effective oxide thickness of 0.5 nm and drain bias of 0.3 V, and channel length of 15 nm in the MOSFET and tunnel FET geometries are investigated in this section.

Analyzing the on-off and subthreshold performance reveals a strong device geometry dependence that stems from the fundamental differences in their operation (Figures 8.12 and 8.13). As explained in the previous sections, for CNTMOSFETs, thermionic emission over the source-channel potential barrier limits their S value at 60 mV/dec, while a highly gate-dependent tunneling probability in TFETs presents $S < 60$ mV/dec.

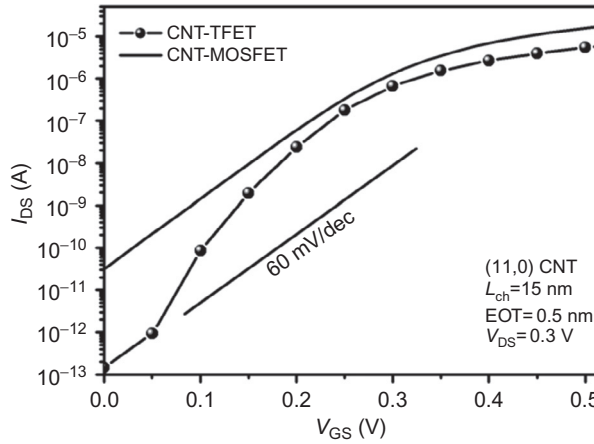

Figure 8.12 Simulated transfer characteristics of a CNT-MOSFET, and a tunnel FET using an EOT = 0.5 nm, $V_{DS} = 0.3$ V, $L_{ch} = 15$ nm for a (11,0) nanotube with GW-bandgap of 1.4 eV. The gate voltage corresponding to minimum drain current (~0.1 pA in TFET) is adjusted to 0 V using a gate work function of 3.5 eV.

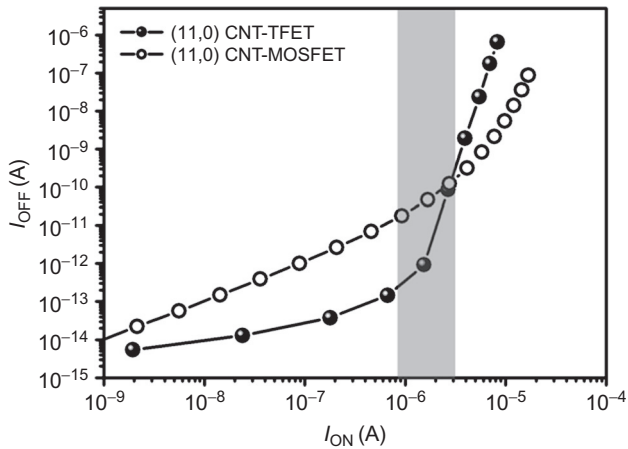

Figure 8.13 On-Off ratio comparison in CNT-TFETs and MOSFETs. The gray shaded part represents the advantageous region where the devices deliver on-current values between 1 and 10 μA, which is beneficial for both high-performance and low-operating-power technologies. In this region, the tunnel FETs offer maximum performance by providing off-current as low as 10^{-5} μA. Device parameters EOT = 0.5 nm, $V_{DS} = 0.3$ V, $L_{ch} = 15$ nm for a (11,0) nanotube with GW-BG ≈ 1.4 eV.

8.10 Carbon nanotube vs. graphene nanoribbon

Despite the recent interest in GNRs, the best reported GNRFET (Wang et al., 2008) displays an inferior performance in terms of on-off ratio ($<10^{-3}$) and inverse subthreshold slope (~210 mV/dec) at a V_{DD} of 0.5 V, and their short-channel performance may not be easily ascertained in the absence of ultra-narrow GNRs with atomically smooth edges (Jiao et al., 2010). Transfer characteristics of different family

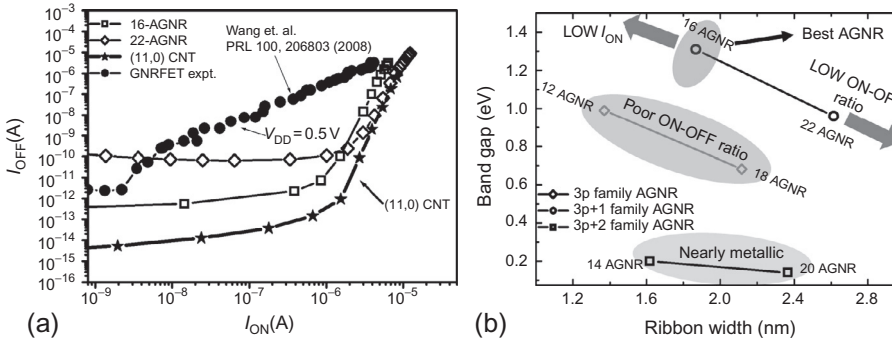

Figure 8.14 (a) On-Off ratio in GNR tunnel FETs and its comparison to a (11,0) TFET evaluated using device parameters, $L_{ch} = 15$ nm, $V_{DS} = 0.3$ V, EOT = 0.5 nm, *S/D* doping = 0.8/nm. (b) GW-bandgap in GNR vs. various family types showing the ideal chirality to realize high-performance TFETs is a 16AGNR (width = 1.87 nm) with bandgap ≈ 1.4 eV.

type GNRs in the TFET geometry are investigated using NEGF-based quantum transport simulations with NANOTCAD ViDES (Fiori et al., 2006) to identify suitable ribbon width and family type offering high ON-state current. Among different types of GNRs, the $3p+1$ family offers comparable ON-current and ON-OFF ratio with a best identified (11,0) CNT TFET. A 16AGNR TFET shows an ON-OFF ratio $>10^6$ with an ON-state current of ∼1 μA. Narrower ribbons that considered in Figure 8.14 from $3p+1$ family type exhibit lower ON-current and hence are not shown here.

In the following discussion a (11,0) nanotube with GW bandgap of 1.4 eV and 16AGNR of bandgap ≈1.4 eV is chosen for comparison. The diameter of 11,0 nanotube is ≈0.85 nm and the width of 16AGNR is 1.87 nm.

The identical bandgap of the (11,0) CNT and 16AGNR in MOSFET geometries exhibits comparable performance (Figure 8.15), but in TFET geometry (11,0) CNT exhibits better off-state and subthreshold properties as compared to 16AGNR (Figure 8.14). The higher on-current in CNTs is due to the difference in quantum capacitance arising from a difference in the DOS. A 15 nm long (11,0) CNT has higher number of atoms (∼1552) than a similar length 16AGNR (∼1129). It should be noted that the above comparative performance holds only for an unoptimized TFET geometry.

8.11 Summary

CNTs and GNR FETs are appealing materials for use in TFET applications due to their desirable bandgap and low effective mass of the carriers; however, small-diameter CNT devices are still limited by low on-currents, and large-diameter CNT devices suffer from poor on-off ratios.

Moreover, intrinsic CNTs/graphene directly connected to metal electrodes also tend to form Schottky barriers at the contact regions. Current flow through these

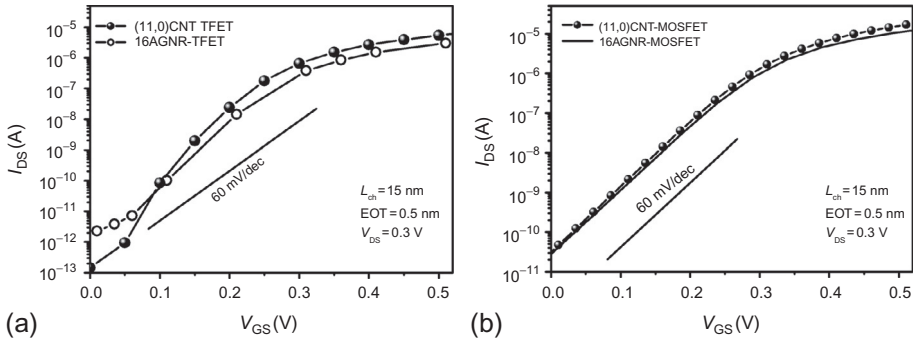

Figure 8.15 Comparison of GNR vs. CNTs. A 11,0 CNT and 16AGNR ribbon are considered in (a) tunnel-FET and (b) MOSFET geometries. Device parameters EOT = 0.5 nm, V_{DS} = 0.3 V, L_{ch} = 15 nm. The gate voltage corresponding to minimum drain current is adjusted to 0 V using a gate work function of 3.5 eV (Pillai et al., 2013).

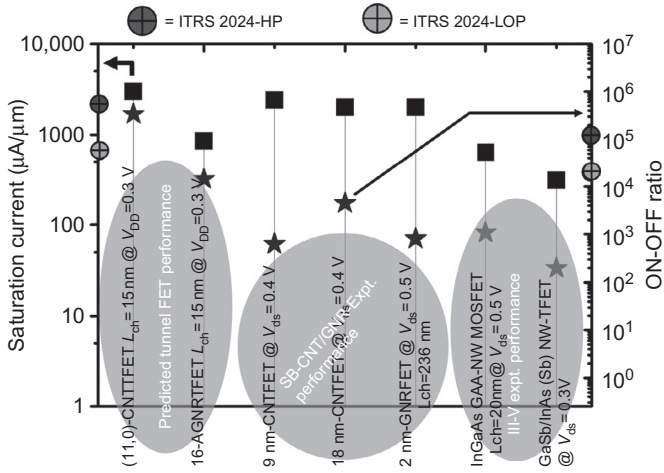

Figure 8.16 Summary of the predicted TFET performance for CNTs and GNRs along with experimentally reported performance of Schottky barrier FETs consisting of 1.3 nm CNT and ~2 nm wide GNR (Dey et al., 2013; Gu et al., 2012; Franklin et al., 2012a; Wang et al., 2008).

devices is modulated by the barrier width and height using the gate electric field. Large off-state leakage in experimentally demonstrated Schottky barrier CNTFETs results in a poor ON-OFF ratio, although the approximated ON-state current meets the ITRS targeted values for 2024 technology (Figure 8.16). To achieve MOSFET-type or TFET characteristics requires doped source/drain regions, which are still somewhat difficult to achieve and control with uniformity in carbon-based systems.

References

Appenzeller, J., 2008. Carbon nanotubes for high-performance electronics—progress and prospect. Proc. IEEE 96, 201. http://dx.doi.org/10.1109/JPROC.2007.911051.

Appenzeller, J., Knoch, J., Derycke, V., Martel, R., Wind, S., Avouris, P., 2002. Field-modulated carrier transport in carbon nanotube transistors. Phys. Rev. Lett. 89, 126801. http://dx.doi.org/10.1103/PhysRevLett.89.126801.

Appenzeller, J., Lin, Y.M., Knoch, J., Chen, Z., Avouris, P., 2005. Comparing carbon nanotube transistors—the ideal choice: a novel tunneling device design. IEEE Trans. Electron Dev. 52, 2568. http://dx.doi.org/10.1109/TED.2005.859654.

Arnold, M.S., Green, A.A., Hulvat, J.F., Stupp, S.I., Hersam, M.C., 2006. Sorting carbon nanotubes by electronic structure using density differentiation. Nat. Nanotechnol. 1, 60. http://dx.doi.org/10.1038/nnano.2006.52.

Auth, C.P., Plummer, J.D., 1997. Scaling theory for cylindrical, fully-depleted, surrounding-gate MOSFET's. IEEE Trans. Electron Device Lett. 18, 74. http://dx.doi.org/10.1109/55.553049.

Avouris, P., Appenzeller, J., Martel, R., Wind, S.J., 2003. Carbon nanotube electronics. Proc. IEEE 91, 1772. http://dx.doi.org/10.1109/JPROC.2003.818338.

Avouris, P., Chen, Z., Perebeinos, V., 2007. Carbon-based electronics. Nat. Nanotechnol. 2, 605. http://dx.doi.org/10.1038/nnano.2007.300.

Aydin, C., Zaslavsky, A., Luryi, S., Cristoloveanu, S., Mariolle, D., Fraboulet, D., Deleonibus, S., 2004. Lateral interband tunneling transistor in silicon-on-insulator. Appl. Phys. Lett. 84, 1780. http://dx.doi.org/10.1063/1.1668321.

Bachtold, A., Hadley, P., Nakanishi, T., Dekker, C., 2001. Logic circuits with carbon nanotube transistors. Science 294, 1317. http://dx.doi.org/10.1126/science.1065824.

Bhuwalka, K.K., Born, M., Schindler, M., Schmidt, M., Sulima, T., Eisele, I., 2006. P-channel tunnel field-effect transistors down to sub-50 nm channel lengths. Jpn. J. Appl. Phys. 45, 3106. http://dx.doi.org/10.1143/JJAP.45.3106.

Boucart, K., Ionescu, A.M., 2007. Double-gate tunnel FET with high-κ gate dielectric. IEEE Trans. Electron Dev. 54, 1725. http://dx.doi.org/10.1109/TED.2007.899389.

Cai, J., Ruffieux, P., Jaafar, R., Bieri, M., Braun, T., Blankenburg, S., Muoth, M., Seitsonen, A.P., Saleh, M., Feng, X., Müllen, K., Fasel, R., 2010. Atomically precise bottom-up fabrication of graphene nanoribbons. Nature 466, 470. http://dx.doi.org/10.1038/nature09211.

Castro Neto, A.H., Guinea, F., Peres, N.M.R., Novoselov, K.S., Geim, A.K., 2009. The electronic properties of graphene. Rev. Mod. Phys. 81, 109. http://dx.doi.org/10.1103/RevModPhys.81.109.

Charlier, J.C., Blase, X., Roche, S., 2007. Electronic and transport properties of nanotubes. Rev. Mod. Phys. 79, 677. http://dx.doi.org/10.1103/RevModPhys.79.677.

Choi, W.Y., Song, J.Y., Lee, J.D., Park, Y.J., Park, B.G., 2005. 70-nm impact-ionization metal-oxide-semiconductor (I-MOS) devices integrated with tunneling field-effect transistors (TFETs). In: In: Tech. Dig.—Int. Electron Devices Meet, p. 955.

Datta, S., 2005. Quantum Transport: Atom to Transistor. Cambridge University Press, UK, ISBN: 9780521631457.

Datta, S., 2008. ECE 495N: Fundamentals of Nanoelectronics. http://nanohub.org/resources/5346.

Davari, B., Dennrad, R.H., Shahidi, G.G., 1995. CMOS scaling for high performance and low power—the next ten years. Proc. IEEE 83, 595. http://dx.doi.org/10.1109/5.371968.

Dey, A.W., Borg, B.M., Ganjipour, B., Ek, M., Dick, K.A., Lind, E., Thelander, C., Wernersson, L.E., 2013. High-current GaSb/InAs(Sb) nanowire tunnel field-effect transistors. IEEE Electron Dev. Lett. 34, 211. http://dx.doi.org/10.1109/LED.2012.2234078.

Dukovic, G., Wang, F., Song, D., Sfeir, M.Y., Heinz, T.F., Brus, L.E., 2005. Structural dependence of excitonic optical transitions and band-gap energies in carbon nanotubes. Nano Lett. 5, 2314. http://dx.doi.org/10.1021/nl0518122.

Fiori, G., Iannaccone, G., Klimeck, G., 2006. A three-dimensional simulation study of the performance of carbon nanotube field-effect transistors with doped reservoirs and realistic geometry. IEEE Trans. Electron Dev. 53, 1782. http://dx.doi.org/10.1109/TED.2006.878018.

Franklin, A.D., 2013. Electronics: the road to carbon nanotube transistors. Nature 498, 443. http://dx.doi.org/10.1038/498443a.

Franklin, A.D., Luisier, M., Han, S.J., Tulevski, G., Breslin, C.M., Gignac, L., Lundstrom, M.S., Haensch, W., 2012a. Sub-10 nm carbon nanotube transistor. Nano Lett. 12, 758. http://dx.doi.org/10.1021/nl203701g.

Franklin, A.D., Koswatta, S.O., Farmer, D., Tulevski, G.S., Smith, J.T., Miyazoe, H., Haensch, W., 2012b. Scalable and fully self-aligned n-type carbon nanotube transistors with gate-all-around. In: IEDM, p. 4.5.1. http://dx.doi.org/10.1109/IEDM.2012.6478979.

Ganapathi, K., Salahuddin, S., 2011. Heterojunction vertical band-to-band tunneling transistors for steep subthreshold swing and high on current. IEEE Electron Dev. Lett. 32, 689. http://dx.doi.org/10.1109/LED.2011.2112753.

Gnani, E., Maiorano, P., Reggiani, S., Gnudi, A., Baccarani, G., 2011. Performance limits of superlattice-based steep-slope nanowire FETs. In: In: IEDM, p. 5.1.1. http://dx.doi.org/10.1109/IEDM.2011.6131491.

Green, A.A., Hersam, M.C., 2011. Nearly single-chirality single-walled carbon nanotubes produced via orthogonal iterative density gradient ultracentrifugation. Adv. Mater. 23, 2185. http://dx.doi.org/10.1002/adma.201100034.

Gu, J.J., Wang, X.W., Wu, H., Shao, J., Neal, A.T., Manfra, M.J., Gordon, R.G., Ye, P.D., 2012. Nearly single-chirality single-walled carbon nanotubes produced via orthogonal iterative density gradient ultracentrifugation. In: IEDMp. 27.6.1. http://dx.doi.org/10.1109/IEDM.2012.6479117.

Gunlycke, D., White, C.T., 2008. Tight-binding energy dispersions of armchair-edge graphene nanostrips. Phys. Rev. B 77, 115116. http://dx.doi.org/10.1103/PhysRevB.77.115116.

Guo, J., Datta, S., Lundstrom, M., Brink, M., McEuen, P., Javey, A., Dai, H., Kim, H., McIntyre, P., 2002. Assessment of silicon MOS and carbon nanotube FET performance limits using a general theory of ballistic transistors. In: IEDM, p. 711. http://dx.doi.org/10.1109/IEDM.2002.1175937.

Hu, C., 2008. Green transistor as a solution to the IC power crisis. In: Proc. Int. Conf. Solid-State Integr. Circuit Technol, p. 16. http://dx.doi.org/10.1109/ICSICT.2008.4735116.

Hu, C., et al., 2010. Electron Devices Meeting (IEDM), 2010 IEEE International. Date of Conference: 6-8 December 2010, pp. 16.1.1–16.1.4. http://dx.doi.org/10.1109/IEDM.2010.5703372.

Ionescu, A.M., Riel, H., 2011. Tunnel field-effect transistors as energy-efficient electronic switches. Nature 479, 329. http://dx.doi.org/10.1038/nature10679.

Ionescu, A.M., Boucart, K., Moselund, K.E., Pott, V., 2011. Small Swing Switches. Cambridge Univ. Press, Cambridge.

Jang, J.-S., Choi, W.-Y., 2011. Ambipolarity factor of tunneling field-effect transistors (TFETs). J. Semicond. Technol. Sci. 11, 272. http://dx.doi.org/10.5573/JSTS.2011.11.4.272.

Javey, A., Guo, J., Wang, Q., Lundstrom, M., Dai, H., 2003. Ballistic carbon nanotube field-effect transistors. Nature 424, 654. http://dx.doi.org/10.1038/nature01797.

Javey, A., Guo, J., Farmer, D.B., Wang, Q., Wang, D., Gordon, R.G., Lundstrom, M., Dai, H., 2004. Carbon nanotube field-effect transistors with integrated ohmic contacts and high-κ gate dielectrics. Nano Lett. 4, 447. http://dx.doi.org/10.1021/nl035185x.

Jiao, L., Wang, X., Diankov, G., Wang, H., Dai, H., 2010. Facile synthesis of high-quality graphene nanoribbons. Nat. Nanotechnol. 5, 321. http://dx.doi.org/10.1038/nnano.2010.54.

Jin, S.H., Dunham, S.N., Song, J., Xie, X., Kim, J., Lu, C., Islam, A., Du, F., Kim, J., Felts, J., Li, Y., Xiong, F., Wahab, M.A., Menon, M., Cho, E., Grosse, K.L., Lee, D.J., Chung, H.U., Pop, E., Alam, M.A., King, W.P., Huang, Y., Rogers, J.A., 2013. Using nanoscale thermocapillary flows to create arrays of purely semiconducting single-walled carbon nanotubes. Nat. Nanotechnol. 8, 347. http://dx.doi.org/10.1038/nnano.2013.56.

Knoch, J., Appenzeller, J., 2006. Carbon nanotube field-effect transistors—the importance of being small. In: Mukherjee, S., Aarts, R.M., Roovers, R., Widdershoven, F., Ouwerkerk, M. (Eds.), AmIware Hardware Technology Drivers of Ambient Intelligence. Philips Research, vol. 5. p. 371. ISBN: 978-1-4020-4197-6 (Print) 978-1-4020-4198-3 (Online).

Knoch, J., Appenzeller, J., 2008. Tunneling phenomena in carbon nanotube field-effect transistors. Phys. Status Solidi A 205, 679. http://dx.doi.org/10.1002/pssa.200723528.

Knoch, J., Mantl, S., Appenzeller, J., 2007. Impact of the dimensionality on the performance of tunneling FETs: bulk versus one-dimensional devices. Solid State Electron. 51, 572. http://dx.doi.org/10.1016/j.sse.2007.02.001.

Krupke, R., Hennrich, F., van Löhneysen, H., Kappes, M.M., 2003. Separation of metallic from semiconducting single-walled carbon nanotubes. Science 301, 344. http://dx.doi.org/10.1126/science.1086534.

Leburton, J.P., Kolodzey, J., Briggs, S., 1988. Bipolar tunneling field-effect transistor: A three-terminal negative differential resistance device for high-speed applications. Appl. Phys. Lett. 52, 1608. http://dx.doi.org/10.1063/1.99056.

Léonard, F., 2009. The Physics of Carbon Nanotube Devices. William Andrew Inc., USA.

Lin, H., Lagoute, J., Repain, V., Chacon, C., Girard, Y., Lauret, J.-S., Ducastelle, F., Loiseau, A., Rousset, S., 2010. Many-body effects in electronic bandgaps of carbon nanotubes measured by scanning tunnelling spectroscopy. Nat. Mater. 9, 235. http://dx.doi.org/10.1038/nmat2624.

Liu, H., Nishide, D., Tanaka, T., Kataura, H., 2011. Large-scale single-chirality separation of single-wall carbon nanotubes by simple gel chromatography. Nat. Commun. 2, 1. http://dx.doi.org/10.1038/ncomms1313.

Lu, Y., Bangsaruntip, S., Wang, X., Zhang, L., Nishi, Y., Dai, H., 2006. DNA functionalization of carbon nanotubes for ultrathin atomic layer deposition of high κ dielectrics for nanotube transistors with 60 mV/decade switching. J. Am. Chem. Soc. 128, 3518. http://dx.doi.org/10.1021/ja058836v.

Martel, R., Schmidt, T., Shea, H.R., Hertel, T., Avouris, P., 1998. Single- and multi-wall carbon nanotube field-effect transistors. Appl. Phys. Lett. 73, 2447. http://dx.doi.org/10.1063/1.122477.

Martel, R., Derycke, V., Lavoie, C., Appenzeller, J., Chen, K., Tersoff, J., Avouris, P., 2001. Ambipolar electrical transport in semiconducting single-wall carbon nanotubes. Phys. Rev. Lett. 87, 256805. http://dx.doi.org/10.1103/PhysRevLett.87.256805.

Mookerjea, S., Mohata, D., Mayer, T., Narayanan, V., Datta, S., 2010. Temperature-dependent I-V characteristics of a vertical $In_{0.53}Ga_{0.47}As$ tunnel FET. IEEE Electron Dev. Lett. 31, 564. http://dx.doi.org/10.1109/LED.2010.2045631.

Moselund, K.E., Schmid, H., Bessire, C., Björk, M.T., Ghoneim, H., Riel, H., 2012. InAs-Si nanowire heterojunction tunnel FETs. IEEE Electron Dev. Lett. 33, 1453. http://dx.doi.org/10.1109/LED.2012.2206789.

Nakada, K., Fujita, M., Dresselhaus, G., Dresselhaus, M.S., 1996. Edge state in graphene ribbons: nanometer size effect and edge shape dependence. Phys. Rev. B 54, 17954. http://dx.doi.org/10.1103/PhysRevB.54.17954.

Nirschl, T., Weis, M., Fulde, M., Schmitt-Landsiedel, D., 2007. Correction to "Revision of tunneling field-effect transistor in standard CMOS technologies". IEEE Electron Dev. Lett. 28, 315. http://dx.doi.org/10.1109/LED.2007.893272.

Patil, N., Deng, J., Mitra, S., Wong, H.-S.P., 2009a. Circuit-level performance benchmarking and scalability analysis of carbon nanotube transistor circuits. IEEE Trans. Nanotechnol. 8, 37. http://dx.doi.org/10.1109/TNANO.2008.2006903.

Patil, N., Lin, A., Myers, E.R., Ryu, K., Badmaev, A., Zhou, C., Wong, H.-S.P., Mitra, S., 2009b. Wafer-scale growth and transfer of aligned single-walled carbon nanotubes. IEEE Trans. Nanotechnol. 8, 498. http://dx.doi.org/10.1109/TNANO.2009.2016562.

Pillai, P., De Souza, M.M., Umari, P., 2013. Are carbon nanotubes still a viable option for ITRS 2024? In: IEEE International Electron Devices Meeting (IEDM), pp. 32.2.1–32.2.4. http://dx.doi.org/10.1109/IEDM.2013.6724735.

Reddick, W.M., Amaratunga, G.A.J., 1995. Silicon surface tunnel transistor. Appl. Phys. Lett. 67, 494. http://dx.doi.org/10.1063/1.114547.

Seol, G., Yoon, Y., Fodor, J.K., Guo, J., Matsudaira, A., Kienle, D., Liang, G., Klimeck, G., Lundstrom, M., Saeed, A.I., 2011. http://nanohub.org/resources/cntbands-ext.

Sze, S.M., 1981. Physics of Semiconductor Devices. John Wiley and Sons, Inc., New York.

Tans, S.J., Verschueren, A., Dekker, C., 1998. Room-temperature transistor based on a single carbon nanotube. Nature 393, 49. http://dx.doi.org/10.1038/29954.

Taur, Y., Ning, T., 1998. Fundamentals of Modern VLSI Devices. Cambridge University Press, UK.

Tomioka, K., Yoshimura, M., Fukui, T., 2012. A III-V nanowire channel on silicon for high-performance vertical transistors. Nature 488, 189. http://dx.doi.org/10.1038/nature11293.

Tu, X., Manohar, S., Jagota, A., Zheng, M., 2009. DNA sequence motifs for structure-specific recognition and separation of carbon nanotubes. Nature 460, 250. http://dx.doi.org/10.1038/nature08116.

Umari, P., Petrenko, O., Taioli, S., De Souza, M.M., 2012. Communication: electronic band gaps of semiconducting zig-zag carbon nanotubes from many-body perturbation theory calculations. J. Chem. Phys. 136, 18101. http://dx.doi.org/10.1063/1.4716178.

Van Hove, L., 1953. The occurrence of singularities in the elastic frequency distribution of a crystal. Phys. Rev. 89, 1189. http://dx.doi.org/10.1103/PhysRev.89.1189.

Wallace, P.R., 1947. The band theory of graphite. Phys. Rev. 71, 622. http://dx.doi.org/10.1103/PhysRev.71.622.

Wang, X., Ouyang, Y., Li, X., Wang, H., Guo, J., Dai, H., 2008. Room-temperature all-semiconducting sub-10-nm graphene nanoribbon field-effect transistors. Phys. Rev. Lett. 100, 206803. http://dx.doi.org/10.1103/PhysRevLett.100.206803.

Wang, L., Yu, E., Taur, Y., Asbeck, P., 2010. Design of tunneling field-effect transistors based on staggered heterojunctions for ultralow-power applications. IEEE Electron Dev. Lett. 31, 431. http://dx.doi.org/10.1109/LED.2010.2044012.

Wind, S., Appenzeller, J., Martel, R., Derycke, V., Avouris, P., 2002. Vertical scaling of carbon nanotube field-effect transistors using top gate electrodes. Appl. Phys. Lett. 80, 3817. http://dx.doi.org/10.1063/1.1480877.

Yang, L., Park, C., Son, Y., Cohen, M.L., Louie, S.G., 2007. Quasiparticle energies and band gaps in graphene nanoribbons. Phys. Rev. Lett. 99, 186801. http://dx.doi.org/10.1103/PhysRevLett.99.186801.

Zhang, Z., Liang, X., Wang, S., Yao, K., Hu, Y., Zhu, Y., Chen, Q., Zhou, W., Li, Y., Yao, Y., Zhang, J., Peng, L.M., 2007. Doping-free fabrication of carbon nanotube based ballistic CMOS devices and circuits. Nano Lett. 7, 3603. http://dx.doi.org/10.1021/nl0717107.

Zhao, P., Choudhury, M., Mohanram, K., Guo, J., 2008. Analytical theory of graphene nanoribbon transistors. In: Proc. Intl. Workshop on Design and Test of Nano Devices, Circuits and Systems, p. 3. http://dx.doi.org/10.1109/NDCS.2008.22.

Zheng, M., Semke, E.D., 2007. Enrichment of single chirality carbon nanotubes. J. Am. Chem. Soc. 129, 6084. http://dx.doi.org/10.1021/ja071577k.

Zhou, W., Rutherglen, C., Burke, P., 2008. Wafer scale synthesis of dense aligned arrays of single-walled carbon nanotubes. Nano Res. 1, 158. http://dx.doi.org/10.1007/s12274-008-8012-9.

Zhou, G., Lu, Y., Li, R., Zhang, Q., Hwang, W.S., Liu, Q., Vasen, T., Chen, C., Zhu, H., Kuo, J.-M., Koswatta, S., Kosel, T., Wistey, M., Fay, P., Seabaugh, A., Xing, H., 2011. Vertical InGaAs/InP tunnel FETs with tunneling normal to the gate. IEEE Electron Dev. Lett. 32, 1516. http://dx.doi.org/10.1109/LED.2011.2164232.

Zhou, G., Lu, Y., Li, R., Zhang, Q., Liu, Q., Vasen, T., Zhu, H., Kuo, J.M., Kosel, T., Wistey, M., Fay, P., Seabaugh, A., Xing, H., 2012. InGaAs/InP tunnel FETs with a subthreshold swing of 93 mV/dec and I_{ON}/I_{OFF} ratio near 10^6. IEEE Electron Dev. Lett. 33, 782. http://dx.doi.org/10.1109/LED.2012.2189546.

Atomic behavior and structural evolution of alloy nanoparticles during thermodynamic processes

9

G. Li, Q. Wang, K. Wang
Northeastern University, Shenyang, China

9.1 Introduction

Nanoparticles are aggregates containing a few to many millions of atoms. In general, alloy nanoparticles include two metal elements and exhibit many fascinating potential applications in heterogeneous catalysts, sensors, and microelectronic and optoelectronic devices (Wang, 2003). Their chemical and physical properties can be tuned by varying their size, composition, and atomic distribution (Ferrando et al., 2008). The surface energies between two random elements are different, and atoms with lower surface energy segregate to the nanoparticle surface to decrease the system free energy. Segregation usually exists during the formation of all alloy nanoparticles. Nanoparticle structures are generally formed by the surface-induced or surface-reconstruction mechanism (Nam et al., 2002; Rodriguez-Lopez et al., 2004). Therefore, surface layers formed from heteroatoms can affect the alloy nanoparticle structure.

A number of alloy nanoparticle properties are influenced by atomic behavior:

(1) *Surface segregation pattern*. Competition between thermodynamic and geometric effects leads to different Cu surface segregation patterns in Cu-Ni nanoparticles. Furthermore, composition and size thresholds exist for Cu atom segregation (Mainardi and Balbuena, 2001a,b).

(2) *Atomic distribution*. Nanoparticles containing Pd (Kim et al., 2007; Kim et al., 2008) or Co (Wang et al., 2009) atoms embedded in the subsurface layer of Ag-based alloy nanoparticles of Ag-Pd or Ag-Co form by Ag atom segregation. Special nanoparticle configurations with different atomic distributions, such as core-shell (Van Hoof and Hou, 2005), onion-like (Baletto et al., 2003), and Janus-like (Parsina and Baletto, 2010) distributions, have also been fabricated by Ag atom segregation in bimetallic clusters.

(3) *Crystal structure*. The coating layer, which is formed by the segregated atoms, can induce the formation of some structures, such as Co-Ag core-shell with hcp core (Dorfbauer et al., 2006).

Results indicate that nanoparticle structure is affected by the hetero coating layer on the alloy nanoparticles. In fact, the segregation process results in the formation of a coating layer as well as the dynamic behavior of atomic segregation. Both can

Modeling, Characterization and Production of Nanomaterials. http://dx.doi.org/10.1016/B978-1-78242-228-0.00009-0
Copyright © 2015 Elsevier Ltd. All rights reserved.

influence the structural formation of alloy nanoparticles. Similar segregation phenomena always exist during alloy nanoparticle fabrication by physical vapor deposition (Binns, 2001). Furthermore, experimental results show that the formation of decahedral structures in bimetallic clusters is easier than icosahedral structures (Stappert et al., 2003; Tan et al., 2006; Pauwels et al., 2001), even though the latter has the lowest free energy.

Research into atomic behavior and structural evolution of alloy nanoparticles during thermodynamic processes therefore plays a key role in studying the abovementioned phenomena and in exploring new nanostructural materials. We have used molecular dynamics simulations to study the effect of atomic segregation on thermodynamic processes and the structural evolution of alloy nanoparticles.

9.2 Simulation method

9.2.1 Molecular dynamics procedure

A fifth-order predictor-corrector algorithm was used to integrate the Newton equations in the molecular dynamics simulation. A canonical ensemble without external stress and with periodic boundary conditions was used. A velocity scaling method was used to control the system temperature.

9.2.2 Interaction potential

The embedded atom method (EAM) potential was used as interatomic force (Zhou et al., 2001). The potential assumes that the crystal energy is the sum of a pair energy and an embedding energy, which is required to embed an atom into a local medium with given electron density. In the EAM, the total energy E of the crystal can be expressed as

$$E = \frac{1}{2}\sum_{i,j,i\neq j}\varphi_{ij}(r_{ij}) + \sum_{i}F_i(\rho_i) \tag{9.1}$$

where $\varphi_{ij}(r_{ij})$ is the pair energy between atoms i and j separated by r_{ij}, and $F_i(\rho_i)$ is the embedding energy required to embed an atom i into an electron density ρ_i. ρ_i can be calculated from

$$\rho_i = \sum_{j(j\neq i)} f_j(r_{ij}) \tag{9.2}$$

where $f_j(r_{ij})$ is the electron density at the i atomic site arising from j atom at a distance of r_{ij}. $f(r)$ can be expressed as

$$f(r)=\frac{f_e \exp\left[-\beta\left(\frac{r}{r_e}-1\right)\right]}{1+\left(\frac{r}{r_e}-\lambda\right)^{20}} \tag{9.3}$$

where f_e is the scaling factor ($f_e=1$ for pure metals). For alloys, $f_e=(E_C/\Omega)^{\gamma_1}$. r_e is the equilibrium spacing between nearest neighboring atoms.

The generalized pair potentials have the form

$$\varphi(r)=\frac{A\cdot\exp\left[-\alpha\left(\frac{r}{r_e}-1\right)\right]}{1+\left(\frac{r}{r_e}-\kappa\right)^{20}}-\frac{B\cdot\exp\left[-\beta\left(\frac{r}{r_e}-1\right)\right]}{1+\left(\frac{r}{r_e}-\lambda\right)^{20}} \tag{9.4}$$

A, B, α, β, κ, and λ are adjustable parameters. For the alloy model, the pair potential between different species a and b is defined using the alloy model proposed by Johnson (1990)

$$\varphi^{ab}(r)=\frac{1}{2}\left(\frac{f^b(r)}{f^a(r)}\varphi^{aa}(r)+\frac{f^a(r)}{f^b(r)}\varphi^{bb}(r)\right) \tag{9.5}$$

To ensure the embedding energy functions are effective over a range of electron density, they are split into three equations:

$$F(\rho)=\begin{cases}\sum_{i=0}^{3}F_{ni}\left(\frac{\rho}{\rho_n}-1\right)^i, & \rho<\rho_n,\ \rho_n=0.85\rho_e\\ \sum_{i=0}^{3}F_i\left(\frac{\rho}{\rho_e}-1\right)^i, & \rho_n\le\rho<\rho_o,\ \rho_o=1.15\rho_e\\ F_e\left[1-\ln\left(\frac{\rho}{\rho_e}\right)^\eta\right]\cdot\left(\frac{\rho}{\rho_e}\right)^\eta, & \rho_o\le\rho\end{cases} \tag{9.6}$$

The parameters for this model are given by Zhou et al. (2001).

9.2.3 Selection of alloy elements in nanoparticles

In this study, alloy elements are selected according to the difference in their surface energies (Nanda et al., 2002). Because Ag has a lower surface energy (1065 mJ m^{-2}) than Pd (1805 mJ m^{-2}), Ag atoms are more likely to segregate to the surface layer of Pd-Ag nanoparticles. To compare the effect of segregation ability of alloy elements on structural evolution, Co, Cu, and Ni were selected to form different alloy nanoparticles for the following reasons:

(1) Difference in surface energy. Cu (1592 mJ m^{-2}) has a much lower surface energy than Co (2197 mJ m^{-2}), while that of Ni (2104 mJ m^{-2}) is similar to that of Co. This difference in atomic behavior leads to a different segregation ability for Cu and Ni atoms in Co-based nanoparticles and is useful in the study of influence of atomic behavior on structure.
(2) The small differences in atomic radii of Co (0.1385 nm), Cu (0.1412 nm), and Ni (0.1378 nm) can prevent the formation of amorphous structure in the nanoparticles because of the large lattice mismatch (Wang et al., 2009).

9.3 Results and discussion

9.3.1 Effect of atomic segregation on melting and structural evolution of Pd-Ag nanoparticles

The initial nanoparticles were icosahedral and contained 561 atoms. Small atomic segregation can induce a large energy decrease with an increase in temperature for this size making these particles suitable for observing the effect of atomic segregation on melting. Two kinds of Ag distributions were produced. In the first, all Ag atoms were located at the nanoparticle core (Ag-core nanoparticle), and almost all Ag atoms would segregate to the surface layer with an increase in temperature. In the other, all Ag atoms were on the surface (Ag-surface nanoparticle), and no Ag atom segregation existed. The effect of atomic segregation on melting can therefore be explored by comparing difference in melting of the Ag-core and Ag-surface nanoparticles. The Ag-core and Ag-surface alloy nanoparticles were constructed by randomly substituting Pd atoms in the core or surface with Ag atoms to concentrations of 45% and 15% Ag (Li et al., 2012c).

The thermodynamic process was as follows. Nanoparticles were heated from 300 to 1300 K (temperature step of 100 K and relaxation time of 0.3 ns per temperature step). This temperature step was reduced to 10 K to approach the melting point with shorter relaxation time (0.03 ns) at a constant cooling rate. The time step was 1.0 fs.

The temperature-energy curves of the Ag-core and Ag-surface nanoparticles with 45% and 15% Ag concentrations (Figure 9.1) show that their melting is different. Before melting, the energy of the Ag-surface nanoparticle is lower than that of the Ag-core nanoparticle at the same temperature. This is because the Ag atoms have a lower surface energy, and their distribution in the surface layer ensures they remain in a low free-energy state. After melting, the energies at the same temperature were almost identical for both nanoparticle types, indicating that the atomic distributions are similar. These results indicate that melting is strongly related to Ag atom distribution but the concentration effect is different. For the 45% Ag-core nanoparticle, the energy decreases with an increase in temperature from 400 to 800 K. After 800 K, the atomic energy increases with an increase in temperature. The gradual increase in energy indicates that the nanoparticle melted. For the 15% Ag-core nanoparticle, the atomic energy always increases with an increase in temperature. At 960 K, a sharp

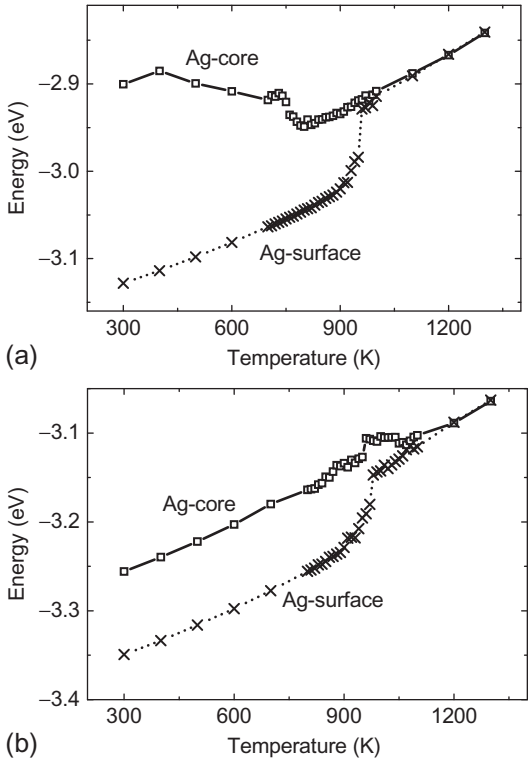

Figure 9.1 Heating curves of clusters with different Ag distributions and concentrations. (a) 45% Ag and (b) 15% Ag.

increase in energy indicates that the nanoparticle melted. Melting is therefore affected not only by Ag atom distribution, but also by Ag concentration. The melting point of the 45% Ag-surface nanoparticle is 960 K, which is lower than that of the 15% Ag-surface nanoparticle (980 K). This occurs because higher melting points exist for lower Ag concentrations.

To define the relationship between melting and Ag atom segregation, the atomic numbers (N_{Seg}) of the Ag that segregated to the surface layer or Pd that diffused to the core were calculated at different temperatures. The Pd atoms on the surface are also discussed. Results are shown in Figure 9.2. For the 45% Ag-core nanoparticle, there is no Ag atom segregation and the energy increases with an increase in temperature from 300 to 400 K. Ag atom segregation occurred at 500 K, and the N_{Seg} for Ag increased with an increase in temperature. The increase of N_{Seg} for Ag is consistent with the decrease in atomic energy and decrease of N_{Seg} for Pd. Ag atom segregation therefore leads to a decrease in atomic energy. After 800 K, the increase in N_{Seg} is small. The atomic energy increases with an increase in temperature. Ag atom segregation therefore plays a key role in melting. Not all of the 252 atoms segregated to the surface layer. For the 15% Ag-core nanoparticle, the N_{Seg} of Ag increases with an increase in temperature to above 700 K. At 1100 K, all 84 atoms segregated to the surface layer. The energy also decreases with an increase in temperature for

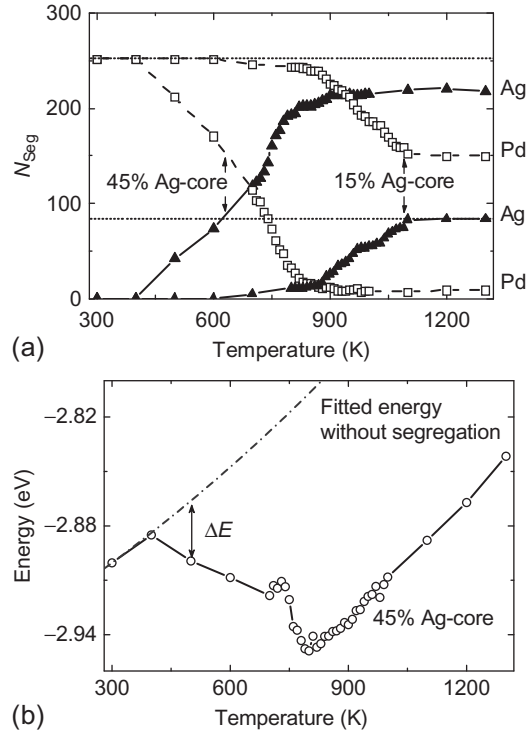

Figure 9.2 Comparison of energy and atomic numbers N_{Seg} of Ag segregated to surface layer or Pd diffused to core (a) for 15% and 45% Ag-core clusters and definition of segregated energy ΔE (b). Dotted lines are total Ag atomic numbers for 15% and 45% Ag-core clusters. Dash dot line is fitted energy curve without atomic segregation.

the 45% Ag, but not for the 15% Ag despite the Ag atom segregation for both nanoparticles. There is a concentration threshold as the irregular phenomenon of melting induced by Ag atom segregation does not occur until the segregated atomic number reaches a critical value.

To determine the effect of Ag atom segregation on the decrease in energy with an increase in temperature during Ag-Pd melting, the segregated energy ΔE was calculated. $\Delta E = N_{Seg} E_{Seg}$ where E_{Seg} is the decrease in energy from segregating one Ag atom from the core to the surface layer. As shown in Figure 9.2b, there is no atomic segregation at 400 K for the 45% Ag-core nanoparticle. The energy decreases sharply at 500 K but there is no structural transformation and lattice distortion at this temperature. Only 42 Ag atoms segregated to the surface layer ($N_{Seg} = 42$), and the energy decrease was therefore induced by Ag atom segregation. The calculated value of E_{Seg} is 0.789 meV. The fitted energies were calculated by combining N_{Seg} at each temperature with E_{Seg} (see Figure 9.3). The fitted results are almost identical to the simulated results at 500-700 K. After 700 K, the fitted energy is slightly lower than the simulated energy at the same temperature. This is because there is no obvious lattice distortion before 700 K. After 700 K, the lattice distortion induced by Ag atom segregation becomes obvious and will increase the atomic energy of the nanoparticles. However, the fitted energy disregards the energy change because of lattice distortion. Therefore, the fitted energy is lower than the simulated energy.

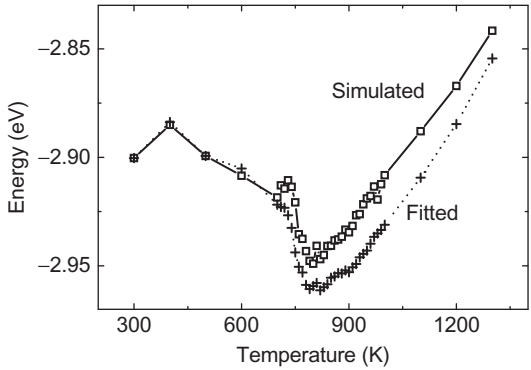

Figure 9.3 Comparison of simulated energy and fitted energy for 45% Ag-core cluster.

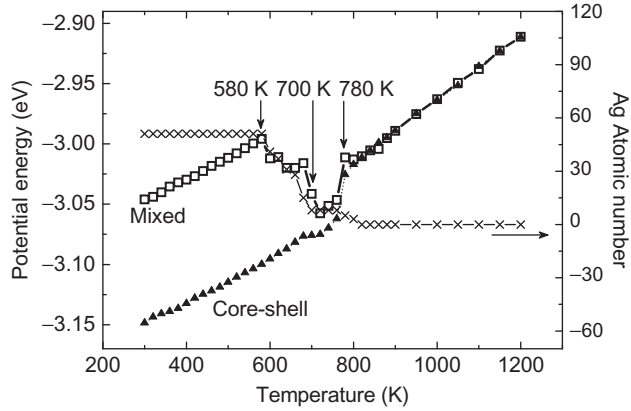

Figure 9.4 Temperature dependence of atomic potential energy and Ag atomic number inside mixed and core-shell $(PdAg)_{309}$ clusters.

The influence of atomic segregation on structural evolution was examined using 309 atoms (Li et al., 2012b). The structural transformation of the nanoparticle is dependent on the release of excess energy. For the $(PdAg)_{309}$ nanoparticle, a large release in excess energy by Ag atom segregation can easily induce structural transformation. The time step was 1 fs and the thermodynamic process was simulated as follows:

(1) Nanoparticles were heated to 900 K from 300 K with a 20 K temperature and 0.5 ns time step.
(2) The nanoparticles were heated to 1200 K from 900 K with a 50 K temperature and 0.5 ns time step.

Figure 9.4 gives the temperature dependence of the atomic energy in the mixed and core-shell $(PdAg)_{309}$ and the Ag atomic number inside the mixed $(PdAg)_{309}$. The melting points of both nanoparticles are the same (780 K). The atomic energies are almost the same with an increase in temperature after the nanoparticles melted. However,

their energy-temperature curves are different before melting. The energy of the mixed $(PdAg)_{309}$ is higher than that of the core-shell $(PdAg)_{309}$ at the same temperature. This is because the atomic energy will decrease when the Ag atoms distribute on the surface layer of the nanoparticle because Ag has a lower surface energy than that of Pd. The atomic energy does not increase linearly with an increase in temperature from 580 to 760 K. The inner Ag atomic number (Figure 9.4) is closely related to the decrease in Ag atomic number. Ag atom segregation therefore causes this phenomenon. The atomic energy increases from 660 to 680 K despite Ag atom segregation because the lattice distortion between Pd and Ag changes the nanoparticles to a disordered state and leads to an increase in atomic energy. In addition, there is no atomic segregation from 700 to 720 K, while the energy decreases with an increase in temperature. A structural transformation most likely leads to a decrease in energy. There is no atomic segregation from 720 to 760 K, and the energy increases with an increase in temperature. The atomic energy of the mixed $(PdAg)_{309}$ is higher than that of the core-shell $(PdAg)_{309}$ because not all Ag atoms segregate to the surface layer. All Ag atoms segregated to the surface layer after the cluster melted.

The bond order parameter W_6 was used to study structural evolution in the mixed $(PdAg)_{309}$. The W_6 values of the core-shell $(PdAg)_{309}$, Pd_{309}, and Ag_{309} were also calculated, as shown in Figure 9.5, while the standard W_6 values for liquid, icosahedra, and decahedra are depicted by dotted lines. The initial W_6 values of all nanoparticles are near the icosahedral value because of their initial icosahedral structure. After the nanoparticles melted, the W_6 values are the same as the liquid value. The W_6 values of the other nanoparticles were almost unchanged before melting except for the

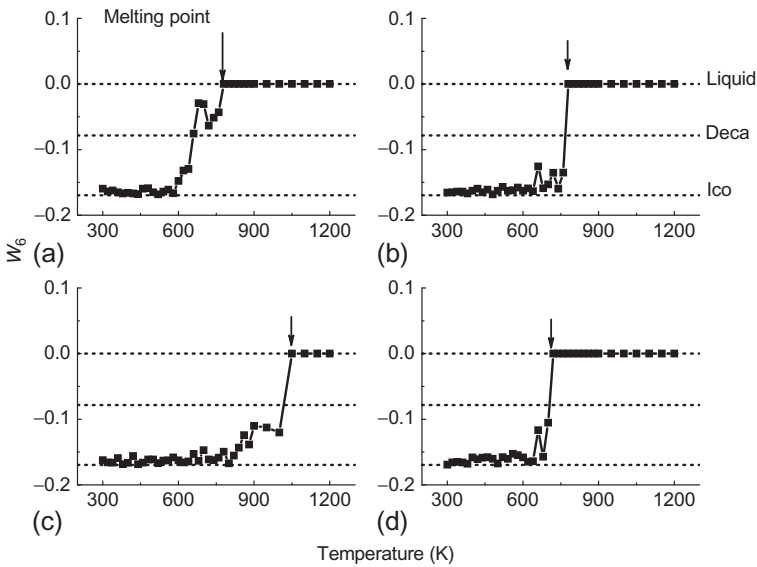

Figure 9.5 Variation of W_6 for mixed (a), core-shell $(PdAg)_{309}$ (b), Pd_{309} (c), and Ag_{309} (d) with temperature.

temperature near their melting points. When these three nanoparticles melted, there was a sharp increase in W_6. The variation in W_6 is different in the mixed $(PdAg)_{309}$. After 580 K, lattice distortion induced by Ag atom segregation leads to an increase in W_6. At 680 and 700 K, the W_6 values almost approach the liquid value. This indicates that the nanoparticles have a disordered state like that of liquid. At 720 K, the W_6 values decrease sharply and approach the decahedral value. The nanoparticles transform to form a decahedron. Because there is surface premelting in the nanoparticle, the W_6 value at 720 K is higher than that of the decahedral value. The nanoparticle remains decahedral until the nanoparticle melts. A comparison of the structural transformation and energy-temperature variation shows that the energy decrease occurs during the structural transformation process.

An icosahedral-decahedral structural transformation occurred in the mixed $(PdAg)_{309}$, but not in the Pd_{309} and Ag_{309}. The transformation was therefore induced by doping the alloy element and may be tuned by doping with alloy elements. The transformation occurs at 720 K in the mixed $(PdAg)_{309}$ but not in the core-shell $(PdAg)_{309}$. At this temperature, an Ag coating layer was formed for both nanoparticles, indicating that there is no influence of the Ag coating layer on the transformation. The only difference is the Ag atom segregation during heating, which indicates that Ag atom segregation leads to structural transformation.

9.3.2 Influence of atomic behavior on freezing structure of alloy nanoparticles

Cuboctahedral nanoparticles were constructed from a $30a_0 \times 30a_0 \times 30a_0$ fcc bulk sample (a_0 is the bulk lattice constant). The number of atoms in the clusters at specific increasing times were 561 (2.47 nm), 923 (2.93 nm), 1289 (3.2 nm), 2057 (4.08 nm), and 3871 (4.85 nm), respectively. Alloy nanoparticles were constructed by randomly substituting Co atoms with Ni (Cu) atoms up to 50% (Li et al., 2012a). These nanoparticles were heated to 1700 from 200 K and then cooled to 200 K with a time step of 1.6 fs. The equilibration time for each temperature cycle (20 K) was 0.1 ns. The influence of initial structure on frozen structure can almost be ignored because the nanoparticles were frozen from the liquid state. In addition, the temperature and time dependence of the frozen structures can also be excluded because they exhibit the same thermodynamic properties. Therefore, variations in frozen structure were mainly related to their size and composition. The bond order parameter W_6 was used to define the structural evolutions.

Figure 9.6 shows snapshots of the frozen clusters at 200 K for Co, Co-Ni, and Co-Cu nanoparticles of different size. Frozen morphologies of the Co nanoparticles are different for different sizes. The frozen structures of Co_{561} and Co_{923} are icosahedral and were formed by six fivefold symmetry axes and a quasispherical shape with 20 (111)-like facets. Nanoparticles of other sizes were constructed by packing the (111) planes. Frozen morphologies of Co are different from the alloy nanoparticles. Atoms with low surface energy segregate to form a shell on the surface and inhibit the formation of some structures (Li et al., 2008; Chushak and Bartell, 2003). Differences

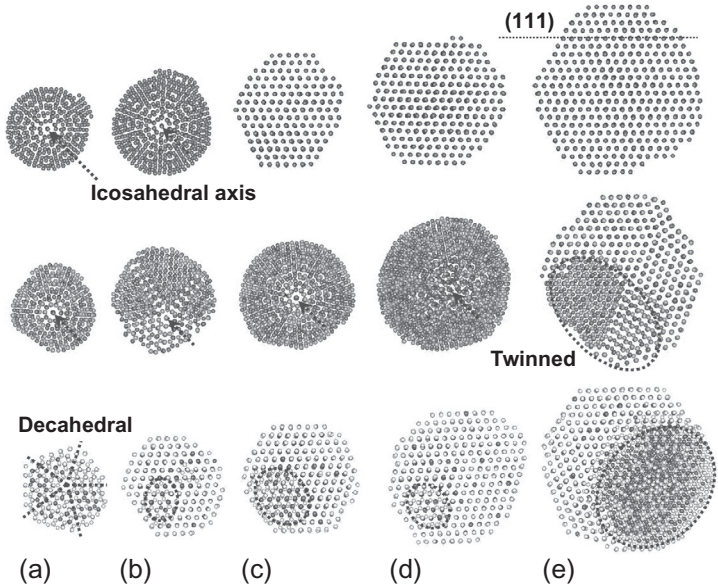

Figure 9.6 Snapshot overviews of frozen clusters at 200 K. Number of atoms in clusters are 561 (a), 923 (b), 1289 (c), 2057 (d), and 3871 (e). Top to bottom row shows clusters of Co, Co-Ni, and Co-Cu, respectively.

in surface energies for Cu, Ni, and Co will result in different segregations and result in nanoparticles of various structures. In the Co-Cu, the Cu atoms prefer to segregate to the surface layer and the cluster remains at a low energy state, while the case for the Ni-Co nanoparticles is different. Therefore, the surface layer is almost capped by Cu atoms in the Co-Cu nanoparticles. The surface layer of the Co-Ni nanoparticles consists of almost equiatomic Co and Ni. The difference in segregation leads to differences in the frozen structure of Co-Cu and Co-Ni nanoparticles at various sizes. For the Co-Ni nanoparticles (with the exception of Co_{3871}) all other sizes were icosahedral. For the Co-Cu nanoparticles, the influence of segregation on frozen structures was obvious. No icosahedron was formed for all sizes, and only $(CoCu)_{561}$ formed a decahedron. For the other sizes, the twinned case as shown by the elliptical zone in Figure 9.6 occurs because of different atomic diffusion in the alloy nanoparticles. It can be concluded that the frozen morphologies are closely related to the nanoparticle size and can be affected by atomic segregation.

Figure 9.7 shows the W_6 parameter of the nanoparticles during freezing. When the nanoparticles are liquid, their W_6 values fluctuate near the zero value at a large range. After being frozen, the W_6 values remain almost unchanged with decrease in temperature. This indicates that the frozen structure was formed at the freezing point and not during cooling. Figure 9.7a illustrates the W_6 parameters of the Co nanoparticles. The W_6 values of Co_{561} and Co_{923} are almost identical and are similar to standard icosahedral values (-0.169754) (Sankaranarayanan et al., 2005). Co nanoparticles with small size ($\leq$2.93 nm) therefore froze to form icosahedra. Furthermore, for Co_{1289}, Co_{2057},

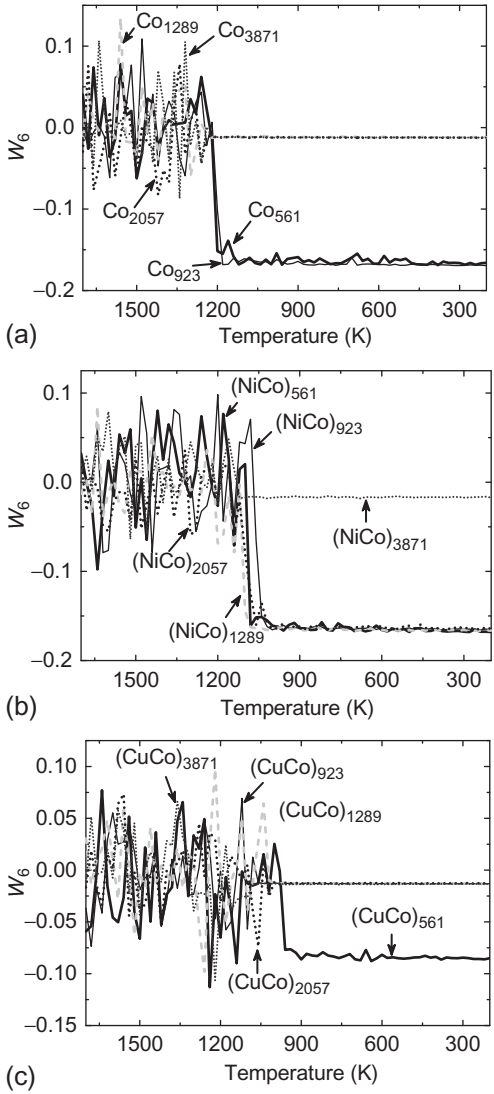

Figure 9.7 Temperature-dependent bond order parameter W_6 of clusters with different sizes during freezing. (a) Co, (b) Co-Ni, and (c) Co-Cu clusters.

and Co_{3871}, the W_6 values are the same as those of the hcp structure (−0.012442), which is similar to the Co bulk. This means that nanoparticles with large size (≥3.2 nm) froze to form a Co bulk-like structure.

With the exception of $(CoNi)_{3871}$, which formed an fcc bulk-like structure, the Co-Ni nanoparticles of other sizes in Figure 9.7b froze to form icosahedra. Therefore, size-dependent frozen structures also existed for the Co-Ni nanoparticles, but the size at which the particles froze to form an icosahedron is larger than that of the Co nanoparticles. Because structural evolution is related strongly to the release of energy, the variation in energy of the nanoparticles from the disordered structure at 1700 K to

the icosahedron at 200 K was calculated. It was found that the released energy of $(CoNi)_{561}$ is larger than that of Co_{561}. Thus, the Co-Ni nanoparticles can form icosahedra in a large size range. Regarding the Co-Cu nanoparticles, only the W_6 value of $(CoCu)_{561}$ exhibits features of the decahedron, and others froze to form the fcc structure. These frozen structures are different from Co and Co-Ni because the icosahedron is formed using a surface-induced mechanism (Nam et al., 2002). Cu atoms segregated to the Co-Cu surface layer because of the lower Cu surface energy. Segregated Cu atoms on the surface layer would change the formation of the surface layer and influence nanoparticle nucleation. Icosahedron formation was inhibited by the Cu shell. However, for the small size, energy released because of Cu atom segregation can drive Co-Cu nanoparticles to form decahedra.

9.3.3 Effect of atomic behavior on coalesced structures of alloy nanoparticles

Cu and Co were selected as the elements of focus because (1) a structural transformation occurs from fcc to hcp for Co and it is easy to obtain new structures by manipulating atomic behaviors, and (2) the surface energy of Cu (1592 mJ m^{-2}) is lower than that of Co (2197 mJ m^{-2}) and Cu atoms prefer to migrate to the surface and influence the structural evolution.

Initial nanoparticles were constructed from a bulk sample by using various spherical cutoff radii centered at a random atom site. The Cu_{369} nanoparticle had an fcc structure by truncation from an fcc bulk sample while Co_{605} had an hcp structure. The Cu-Co alloy nanoparticle structures were obtained by randomly substituting Co atoms with Cu atoms. Therefore, the structure of the $Cu_{369}Co_{605}$ nanoparticle was hcp. The Cu_{369} and Co_{605} coalescence nanoparticle was constructed by placing Cu_{369} and Co_{605} at the center of a large simulation box ($30a_0 \times 30a_0 \times 30a_0$, Cu bulk lattice constant a_0 is 0.3615 nm), as shown in Figure 9.8 (Li et al., 2008).

The time step was 1.6 fs. Cooling of Cu_{369}, Co_{605}, and $Cu_{369}Co_{605}$ was simulated as follows. Nanoparticles were relaxed for 2 ns at 1300 K to ensure the initial structure relaxed adequately before being cooled to 200 K. The temperature step was 50 K with 0.2 ns relaxation time. The cooling rate remained constant at 250 K/ns. The coalesced cooling of Cu_{369} and Co_{605} was similar to the abovementioned cooling processes, with the only difference being that the nanoparticle was cooled to 200 K after coalescing for 2 ns at 1300 K.

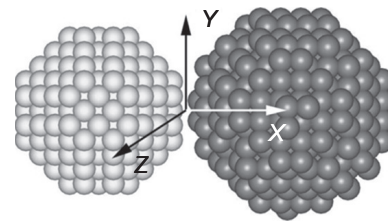

Figure 9.8 Initial setup of Cu_{369} (gray sphere) and Co_{605} coalescence nanoparticle (black sphere).

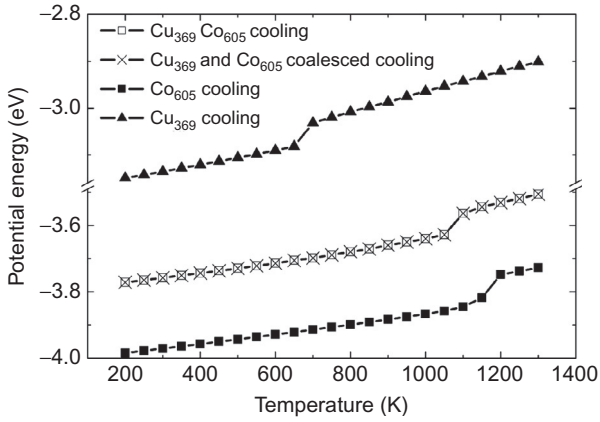

Figure 9.9 Potential energy as a function of temperature for cooling and coalesced cooling of various nanoparticles.

The temperature-dependent atomic energy of the nanoparticles for the cooling and coalesced cooling processes is shown in Figure 9.9. The freezing points of Cu_{369}, Co_{605}, and $Cu_{369}Co_{605}$ were 650, 1150, and 1050 K, respectively. The freezing point of the coalesced cooling of Cu_{369} and Co_{605} was 1050 K.

Temperatures of 1300 and 1000 K were selected as initial cooling temperatures based on the above freezing points because these temperatures cause the atoms to exhibit different atomic behavior. Liquid atoms can diffuse freely at 1300 K, which is higher than the freezing point of $Cu_{369}Co_{605}$. However, the temperature of 1000 K is lower than the freezing point of $Cu_{369}Co_{605}$, and atomic diffusion by substitution is difficult. For the coalescence nanoparticles, both Cu_{369} and Co_{605} are liquid at 1300 K, and the nanoparticles coalesce by atomic convection (Hawa and Zachariah, 2006). When the initial cooling temperature is 1000 K, Cu_{369} is liquid and Co_{605} is solid. Liquid Cu atoms diffuse along the solid Co_{605} surface during coalescence. The different atomic behavior of Cu and Co may result in different structures. The following contents were calculated:

(1) Cooling of $Cu_{369}Co_{605}$ from 1300 to 200 K (1300-200 K cooling).
(2) Cooling of $Cu_{369}Co_{605}$ from 1000 to 200 K (1000-200 K cooling).
(3) Cu_{369} coalesces with Co_{605} for 2 ns at 1300 K and is then cooled to 200 K (1300-200 K coalesced cooling).
(4) Cu_{369} coalesces with Co_{605} for 2 ns at 1000 K and is then cooled to 200 K (1000-200 K coalesced cooling).

Figure 9.10 shows the final morphologies of nanoparticles at 200 K under different cooling conditions. The top row shows the outer view and the bottom row shows the cross section through the center. The nanoparticle morphology for the 1300-200 K cooling in Figure 9.10a is spherical. The surface layer is composed mostly of Cu atoms, and the inner layer is composed mostly of Co atoms. Because the Cu surface energy is lower than that of Co, the Cu atoms form a capping layer on the Co surface. This capping layer is unable to form an entire surface shell because the Cu content in the alloy nanoparticle is not high enough. When the initial cooling

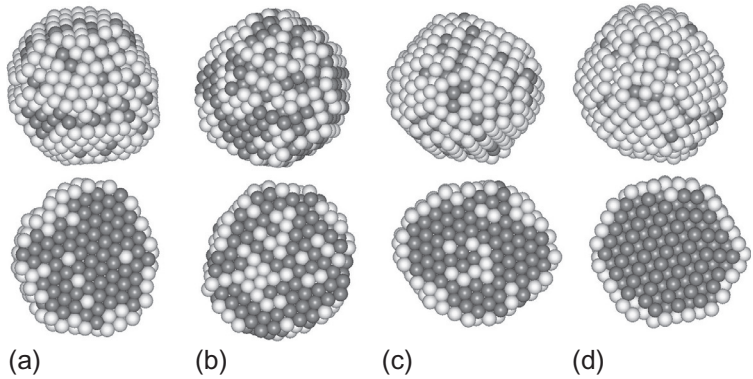

Figure 9.10 Final cluster morphologies at 200 K for different cooling conditions: (a) 1300-200 K cooling, (b) 1000-200 K cooling, (c) 1300-200 K coalesced cooling, and (d) 1000-200 K coalesced cooling. Top row shows outer view and bottom row shows cross section.

temperature is 1000 K, diffusion occurs by substitutional diffusion because the atomic radius of Cu (0.128 nm) is similar to that of Co (0.126 nm). Therefore, large atomic segregation is difficult and leads to the uniform distribution of Cu and Co inside the nanoparticle, as shown in Figure 9.10b. During the 1300-200 K coalesced cooling process, the nanoparticles first coalesce to form a liquid sphere at 1300 K while Cu atoms segregate to the surface. The nanoparticle morphology (Figure 9.10c) of the 1300-200 K coalesced cooling is similar to that of the 1300-200 K cooling. For the 1000-200 K coalesced cooling process, because 1000 K is higher than the freezing point of Cu_{369} but lower than that of Co_{605}, liquid Cu_{369} and solid Co_{605} coalesce. Liquid Cu atoms therefore diffuse along the Co surface. When the nanoparticle relaxes for 2 ns at 1000 K, the atoms have sufficient time to diffuse. Therefore, Cu atoms form a capping layer on the Co surface, resulting in a core-shell morphology as shown in Figure 9.10d.

The pair distribution function (PDF) was used to analyze the nanoparticle structure. The PDF of Cu_{959} after relaxing for 0.2 ns at 200 K was calculated from the standard peaks, as shown in Figure 9.11. Figure 9.11a shows that the special peaks of Cu_{959} are consistent with those of the nearest fcc neighbors (can be calculated using $\sqrt{2n}a_0/2$, where n is the nth nearest neighbor and a_0 is the lattice constant). This implies that Cu_{959} has an fcc structure. The PDF of the 1000-200 K cooling is similar to that of Cu_{959}. Typical hcp peaks appear for the 1300-200 K cooling of $Cu_{369}Co_{605}$ at 0.41 and 0.48 nm, as shown by the black arrows in Figure 9.11a. The 1300-200 K cooling structure is hcp-like. However, the PDF for the 1300-200 K cooling nanoparticle is not the same as that for a perfect hcp. This is because many dangling positions exist for the surface atoms. The PDFs of the coalesced cooling nanoparticles are shown in Figure 9.11b. The peaks of the 1300-200 K coalesced cooling nanoparticle are similar to those of Cu_{959}. This indicates that the 1300-200 K coalesced cooling nanoparticle has an fcc structure. The peak at 0.48 nm is slightly higher than that of Cu_{959}. Furthermore, a special phenomenon appears to exist in the PDF of the 1000-200 K coalesced cooling case, which has special peaks for both fcc and hcp.

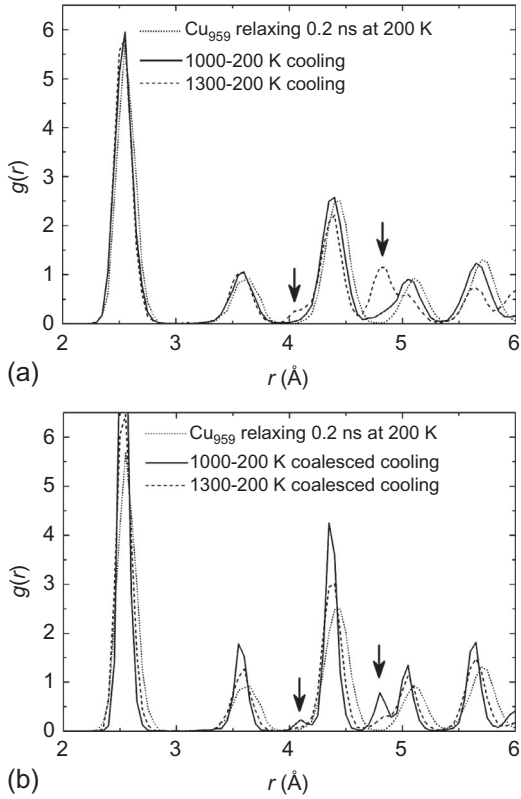

Figure 9.11 Comparison of pair distribution functions between Cu_{959} after relaxing for 0.2 ns at 200 K and final structures: (a) 1000-200 and 1300-200 K cooling, (b) 1000-200 and 1000-200 K coalesced cooling.

Final snapshots of the nanoparticles at 200 K were analyzed to define variations in cooling and coalesced cooling structures. An fcc structure shows an ABC stacking order, and an hcp structure exhibits an AB order. Figure 9.12a-c gives snapshots of the 1300-200 K cooling, 1000-200 K cooling, and 1300-200 K coalesced cooling, respectively, along the direction parallel to the closed-packing plane. The stacking planes are arranged in an orderly fashion. The stacking order of the closed-packing planes is AB (Figure 9.12a) for the 1300-200 K cooling and ABC for the 1000-200 K cooling (Figure 9.12b). The stacking order of the 1300-200 K coalesced cooling is also ABC. The atoms, as shown by the dashed line in Figure 9.12c, do not lie along the closed-packing plane. This leads to a peak PDF at 0.48 nm, which is a little higher than that of Cu_{959}. All results agree well with those of the PDFs. A similar stacking arrangement as above is not observed for the 1000-200 K coalesced cooling cluster for the snapshot in any direction. Figure 9.12d gives a snapshot of the nanoparticle from a random direction. The closed-packing planes are arranged in an orderly fashion. The stacking order is composed mostly of AB in one section, while the other part is different. Therefore, the 1000-200 K coalesced cooling includes two different stacking types. The hexagonal part in Figure 9.12d is cut and rotated such that the closed-packing plane shows a stacking order of ABC, as shown in Figure 9.12e. The structure of

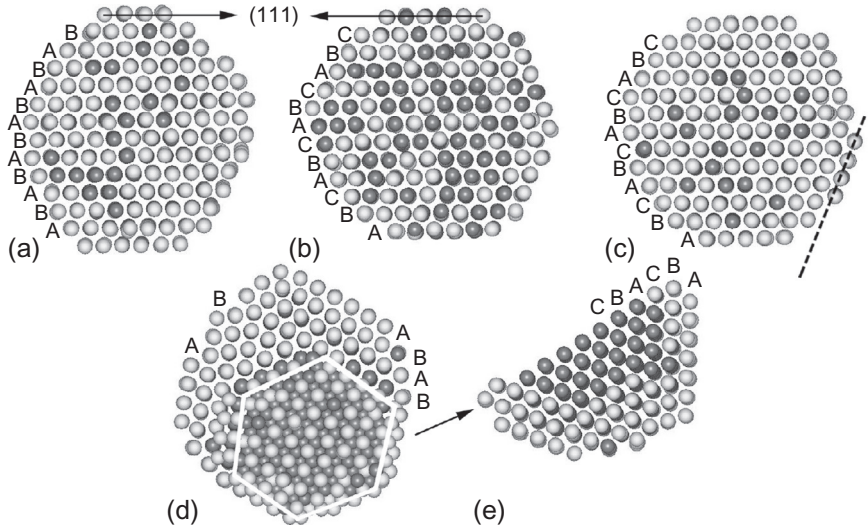

Figure 9.12 Final structures of cooling clusters: (a) 1300-200 K cooling cluster with AB stacking, (b) 1000-200 K cooling cluster with ABC stacking, (c) 1300-200 K coalesced cooling cluster with ABC stacking, (d) 1000-200 K coalesced cooling cluster with twinned crystalline form of AB and ABC stacking, and (e) snapshot after rotating from cutting part of (d).

the 1000-200 K coalesced cooling nanoparticle is twinned crystalline formed by the stacking orders of AB and ABC. Therefore, the special peaks in PDF show fcc and hcp character. This nanoparticle is therefore twinned crystalline formed by fcc and hcp structures.

In this study we obtained Cu-Co nanoparticles with different structures and morphologies. The structural variation is a consequence of the following contributions by overall analysis of the structures under different conditions:

(1) Cu content and atomic distribution in the nanoparticle. For example, the distributions of Cu and Co are uniform in the 1000-200 K cooling and form an fcc structure. In the 1300-200 K cooled nanoparticle, Cu segregates to the surface, resulting in an inner composed mostly of Co and a nanoparticle with hcp structure.

(2) Mode of controlling the synthesis process. For example, both Cu and Co restructure by convection during coalescence at 1300 K. Therefore, the final structure exhibits an fcc character despite Cu segregation. For coalescence at 1000 K, Cu atoms diffuse along the Co nanoparticle surface. The Co atoms surrounded by Cu atoms at the beginning of coalescence form an hcp structure, because the Co atoms do not have enough time to restructure. The Co atoms restructure to form an fcc structure. Therefore, twinned crystalline fcc and hcp structures are obtained in the nanoparticle.

Thus, the desired particle morphology and structure can be obtained by controlling the constitution and distribution of alloy atoms during coalescence and cooling.

9.4 Conclusions and future outlook

Differences in surface energies of elements in alloy nanoparticles lead to atoms with a lower surface energy segregating to the surface layer to decrease the system energy. Atomic behaviors differ with changes in thermodynamic parameters and alloy elements. During the heating of Pd-Ag nanoparticles, the atomic energy variation with an increase in temperature is strongly related to Ag atom segregation. The atomic energy increases, remains unchanged, or decreases with an increase in temperature. Ag atom segregation induces an icosahedral-decahedral transformation in the Pd-Ag nanoparticles. Nanoparticle structures were formed by using a surface-induced or surface-reconstruction mechanism. Segregation to the surface layer changes the formation conditions of alloy nanoparticles. Thus, fcc, hcp, or twinned fcc and hcp structures were fabricated by manipulating the cooling and coalesced cooling of Co-Cu. Atomic segregation ability was influenced by variations in size and composition of alloy nanoparticles and leads to large-sized nanoparticles freezing to form bulk-like structures. However, frozen structures for small sizes are generally related to their composition. Icosahedral nanoparticles are formed for Co nanoparticles ($\leq$3.2 nm diameter), and also for Co-Ni nanoparticles, but in a larger size range ($\leq$4.08 nm). A decahedral structure is obtained for a small size (2.47 nm) on the Co-Cu nanoparticles. These results indicate that preformed nanoparticles with special structures can be tuned by controlling atomic behaviors, namely, composition, size, and formation processes.

In the future, significant improvements can be made by controlling experimentally the atomic behavior during the fabrication of alloy nanoparticles by using advanced formation methods. Nanoparticles may be formed atom by atom. Furthermore, the development of high-resolution measurement methods allows one to obtain structural information as well as electron, magnetic, or optical properties at the atomic scale. High-level quantum mechanical calculations on larger systems can be simulated at the experimental scale. This is required to accelerate the combination of experiment and simulation. Furthermore, research on supported nanoparticles is essential in applications of alloy nanoparticles.

References

Baletto, F., Mottet, C., Ferrando, R., 2003. Growth of three-shell onionlike bimetallic nanoparticles. Phys. Rev. Lett. 90, 135504.

Binns, C., 2001. Nanoclusters deposited on surfaces. Surf. Sci. Rep. 44, 1–49.

Chushak, Y.G., Bartell, L.S., 2003. Freezing of Ni-Al bimetallic nanoclusters in computer simulations. J. Phys. Chem. B 107, 3747–3751.

Dorfbauer, F., Schrefl, T., Kirschner, M., Hrkac, G., Suess, D., Ertl, O., Fidler, J., 2006. Nanostructure calculation of CoAg core-shell clusters. J. Appl. Phys. 99, 08G706.

Ferrando, R., Jellinek, J., Johnston, R.L., 2008. Nanoalloys: from theory to applications of alloy clusters and nanoparticles. Chem. Rev. 108, 845–910.

Hawa, T., Zachariah, M.R., 2006. Coalescence kinetics of unequal sized nanoparticles. J. Aerosol Sci. 37, 1–15.

Johnson, R.A., 1990. Phase stability of fcc alloys with the embedded-atom method. Phys. Rev. B 41, 9717–9720.

Kim, H.Y., Kim, H.G., Ryu, J.H., Lee, H.M., 2007. Preferential segregation of Pd atoms in the Ag-Pd bimetallic cluster: density functional theory and molecular dynamics simulation. Phys. Rev. B 75, 212105.

Kim, D.H., Kim, H.Y., Kim, H.G., Ryu, J.H., Lee, H.M., 2008. The solid-to-liquid transition region of an Ag-Pd bimetallic nanocluster. J. Phys. Condens. Matter 20, 035208.

Li, G.J., Wang, Q., Li, D.G., Lü, X., He, J.C., 2008. Structure evolution during the cooling and coalesced cooling processes of Cu-Co bimetallic clusters. Phys. Lett. A 372, 6764–6769.

Li, G.J., Wang, Q., Cao, Y.Z., Du, J.J., He, J.C., 2012a. Size and composition dependence of the frozen structures in Co-based bimetallic clusters. Phys. Lett. A 376, 534–537.

Li, G.J., Wang, Q., Cao, Y.Z., Wang, K., Du, J.J., He, J.C., 2012b. Icosahedral-decahedral transformation in the (PdAg)309 cluster induced by Ag atomic segregation. CMC-Comput. Mater. Con. 30, 195–206.

Li, G.J., Wang, Q., Liu, T., Wang, K., Wu, C., He, J.C., 2012c. Controllable irregular phenomenon induced by Ag atomic segregation on the melting of (AgPd)561 bimetallic clusters. J. Nanopart. Res. 14, 1068.

Mainardi, D.S., Balbuena, P.B., 2001a. Monte Carlo simulation of Cu-Ni nanoclusters: surface segregation studies. Langmuir 17, 2047–2050.

Mainardi, D.S., Balbuena, P.B., 2001b. Surface segregation in bimetallic nanoclusters: geometric and thermodynamic effects. Int. J. Quantum Chem. 85, 580–591.

Nam, H.S., Hwang, N.M., Yu, B.D., Yoon, J.K., 2002. Formation of an icosahedral structure during the freezing of gold nanoclusters: surface-induced mechanism. Phys. Rev. Lett. 89, 275502.

Nanda, K.K., Sahu, S.N., Behera, S.N., 2002. Liquid-drop model for the size-dependent melting of low-dimensional systems. Phys. Rev. A 66, 013208.

Parsina, I., Baletto, F., 2010. Tailoring the structural motif of AgCo nanoalloys: core/shell versus Janus-like. J. Phys. Chem. C 114, 1504–1511.

Pauwels, B., Tendeloo, G.V., Zhurkin, E., Hou, M., Verschoren, G., Kuhn, T., Bouwen, W., Lievens, P., 2001. Transmission electron microscopy and Monte Carlo simulations of ordering in Au-Cu clusters produced in a laser vaporization source. Phys. Rev. B 63, 165406.

Rodriguez-Lopez, J.L., Montejano-Carrizales, J.M., Pal, U., Sanchez-Ramirez, J.F., Troiani, H. E., Garcia, D., Miki-Yoshida, M., Jose-Yacaman, M., 2004. Surface reconstruction and decahedral structure of bimetallic nanoparticles. Phys. Rev. Lett. 92, 196102.

Sankaranarayanan, S.K.R.S., Bhethanabotla, V.R., Joseph, B., 2005. Molecular dynamics simulation study of the melting of Pd-Pt nanoclusters. Phys. Rev. B 71, 195415.

Stappert, S., Rellinghaus, B., Acet, M., Wassermann, E.F., 2003. Gas-phase preparation of $L1_0$ ordered FePt nanoparticles. J. Cryst. Growth 252, 440–450.

Tan, C.Y., Chen, J.S., Liu, B.H., Chow, G.M., 2006. Microstructure of FePt nanoparticles produced by nanocluster beam. J. Cryst. Growth 293, 175–185.

Van Hoof, T., Hou, M., 2005. Structural and thermodynamic properties of Ag-Co nanoclusters. Phys. Rev. B 72, 115434.

Wang, G.H., 2003. Cluster Physics. Shanghai Science & Technology Press, Shanghai.

Wang, Q., Li, G.J., Li, D.G., Lü, X., He, J.C., 2009. Evolution of three-shell onion-like and core-shell structures in $(AgCo)_{201}$ bimetallic clusters. Chin. Phys. B 18, 1843–1849.

Zhou, X.W., Wadley, H.N.G., Johnson, R.A., Larson, D.J., Tabat, N., Cerezo, A., Petford-Long, A.K., Smith, G.D.W., Clifton, P.H., Martens, R.L., Kelly, T.F., 2001. Atomic scale structure of sputtered metal multilayers. Acta Mater. 49, 4005–4015.

Metallic nanoparticles for catalysis applications

10

S. Shan, J. Luo, N. Kang, J. Wu, W. Zhao, H. Cronk, Y. Zhao, Z. Skeete, J. Li, P. Joseph, S. Yan, C.-J. Zhong
State University of New York at Binghamton, Binghamton, NY, USA

10.1 Introduction

The exploration of the unique surface and structural properties and the large surface-area-to-volume ratios is one of the major driving forces for the surge of interest in nanocatalysts. Design, synthesis, and characterization of metal nanoparticles, especially alloy nanoparticles ranging from subnanometer to a few nanometers, are now in the center of nanotechnology in heterogeneous catalysis (Zhong and Regalbuto, 2013; Wu and Yang, 2013; Singh and Xu, 2013; Guo et al., 2013). It is the nanoscale size range over which metal nanoparticles undergo a transition from metallic to atomic properties, leading to unique electronic and catalytic properties different from their bulk counterparts. Significant advances have been made in harnessing the nanoscale catalytic properties in the energy and environmental fronts (Wu and Yang, 2013; Singh and Xu, 2013; Guo et al., 2013; Long et al., 2013). However, challenges remain, especially in preparation and characterization of active, robust, low-cost nanocatalysts with controllable sizes, shapes, compositions and structures.

An alloy is a mixture of two or more metallic species, which can exist either in a complete solid solution state exhibiting a single phase characteristics or in a partial or phase-segregated solid solution state with two or more phases. A nanoalloy (NA) differs from a bulk alloy in several significant aspects in terms of mixing patterns and geometric shapes (Ferrando et al., 2008). Considering both binary and ternary nanoalloys (Figure 10.1), there are different types of mixing patterns, two of which include completely phase-segregated nanoalloys, where the different phases share either an extended mixed interface or a very limited number of heterometal bonds, and mixed nanoalloys with chemically ordered or random structures. The degree of segregation, mixing, and atomic ordering depends on a number of factors (Ferrando et al., 2008), including relative strengths of homoatomic versus heteroatomic bonds, surface energies of the component elements, differences in atomic sizes, charge transfer between the different atomic species, and strength of binding to surface ligands or support materials. The observed atomic arrangement, and geometric shape as well, for a particular NA depends critically on the balance of these factors and on the preparation and usage conditions. In addition, the surface structures of nanoalloys could be very complex due to the enrichment of certain elements in the core or shell. In the case of metal dissolution ("dealloying") in the presence of acidic

Modeling, Characterization and Production of Nanomaterials. http://dx.doi.org/10.1016/B978-1-78242-228-0.00010-7
Copyright © 2015 Elsevier Ltd. All rights reserved.

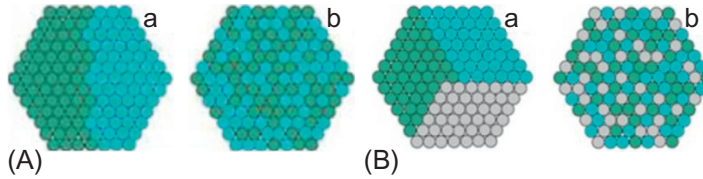

Figure 10.1 Schematic illustrations of a few types of nanoalloys in terms of mixing patterns for binary (A) and ternary (B) systems: phase-segregated or multiparticle structures (a) and ordered or random alloy structures (b).

electrolytes, often referred to Pt-skin structure formation (Gasteiger et al., 2005; Brouzgou et al., 2012; Wang et al., 2012; Jeon et al., 2012; Watanabe et al., 2012; Cui and Yu, 2013), the details of the noble metal skin could be influenced strongly by the structural types of the nanoalloys, the understanding of which in terms of structural evolution, noble metal skin, or d-band structure has attracted increasing interest in catalysis and electrocatalysis.

Nanocatalysts based on naked metal nanoparticles on supporting materials from traditional preparation methods have been well demonstrated for various catalytic reactions (Long et al., 2013; Aiken and Finke, 1999; Klabunde and Mulukutla, 2001). In the last decade, new approaches to the synthesis of metal nanoparticles capped in molecular monolayers, dendrimers, and polymers have been rapidly emerging. While some of the catalysts exploit the functional groups at the capping shell of the nanoparticles (Li et al., 1999; Ingram and Murray, 1998), most explore the surface sites on the metal nanoparticles either after removing the capping layers (Aiken and Finke, 1999; Klabunde and Mulukutla, 2001; Zhong and Maye, 2001) or through open channels of the capping layers (Qian et al., 2012; Philip et al., 2012; Cliffel et al., 2000). In addition, nanoscale facet is an important factor in catalysis. For a noble metal (e.g., Pt, Pd) alloyed with other transition metals (e.g., Ni, Cu, Co), a volcano curve has been observed for certain metal ratios (e.g., 1:1, 1:3, or 3:1) in binary nanocatalysts (Singh and Xu, 2013; Liu et al., 2013a; Kusada et al., 2014; Liao et al., 2013; Duchesne et al., 2013). Moreover, the strong metal-support interaction is shown to play a key role in the catalytic reactions (Bauer et al., 2013; Geukens and De Vos, 2013; Liu et al., 2013b). In addition to various nanostructural design parameters (Khanal et al., 2013; Leppert et al., 2013; Ting et al., 2013), the understanding of how the activation of oxygen on alloy catalysts plays an important role in different catalytic reactions such as CO oxidation and alcohol oxidation reactions remains elusive.

One area of increasing interests in the study of nanoalloy catalysts involves oxidation of alcohols. Alcohol fuel cells, such as direct methanol fuel cells (DMFCs) and direct ethanol fuel cells (DEFCs), become attractive because of high conversion efficiency, low pollution, light weight, high power density, and applications from small power supplies for electronic devices such as PCs, notebooks, and cellular phones. In a typical alcohol fuel cell, oxidation reaction of methanol (for DMFC) or ethanol (for DEFC) occurs at the anode, where oxygen reduction reaction occurs at the cathode.

In DMFCs, the oxidation of methanol on a catalyst layer in the presence of water forms carbon dioxide. Protons (H^+) are transported across the proton exchange membrane (e.g., Nafion) to the cathode where they react with oxygen to produce water. Electrons (six electrons) are transported through an external circuit, providing power to the connected load. The thermodynamic potential is 1.21 V. Both the methanol oxidation reaction (MOR) at the anode and the oxygen reduction reaction at the cathode are highly irreversible, thus there is a loss of about 0.2 V at the anode for DMFC under open-circuit conditions and an enhanced loss of about 0.1 V at the oxygen electrode because of the crossover of methanol from the anode to the cathode (Shukla and Raman, 2003). In DEFCs, ethanol is used instead of the more toxic methanol. Ethanol is a biofuel and an attractive alternative to methanol. In comparison with methanol, ethanol is a hydrogen-rich liquid with a higher energy density (8.0 kWh/kg) compared to methanol (6.1 kWh/kg), which means ethanol has a 33% higher energy density than methanol. Ethanol can be obtained from renewable resources such as sugar cane, wheat, or corn.

There are many unique features in exploring nanoalloys for the above catalysis applications, some of which are also supported in theoretical simulation considerations. In a modeling study of ternary PtVFe particles (Wang et al., 2011) in terms of molecular chemisorption configurations, the O_2 bond is found to be weakened the most with the Yeager configuration, followed by the Griffith and the Pauling configurations. The charge transfer and the adsorption energy are dependent on the metal and adsorption site. The modeled PtVFe clusters happened to be most effective in transferring electrons to oxygen species and thus weakening the O_2 bonds when the oxygen atoms bind to non-Pt atoms, providing useful hints for the design of trimetallic nanoalloys. Similarities have also been found for O_2 adsorption and dissociation on $Pt_4V_2Fe_7$. Another important fundamental aspect on the ternary nanoalloy's electrocatalytic activity and stability is related to the oxophilicity for different metals (Fernandez et al., 2005; Norskov et al., 2004). It is hypothesized that the removal of O-containing intermediates (—O, —OH, —OOH) resulting from the O═O breaking on the Pt-bridge sites that recovers the catalytically active sites is possibly more effective by alloying Pt with two different metal components (M and M′) than with a single metal component. There are several recent studies supporting this hypothesis. EXAFS and XPS characterizations of Pt-trimetallic alloy electrocatalysts for oxygen reduction reaction (ORR) prepared by electrodeposition (Hwang et al., 2011) showed that the electronic states such as the d-band centers, geometric factors, as well as Pt-Pt distance change with the composition. Fe and Co might play bifunctional roles: adsorption and desorption of oxygen species, respectively, due to their different electronic properties. Also, recent density functional theory (DFT) calculation of oxygen and hydroxyl adsorption energies showed that there is an approximate linear trend in oxygen reduction activity versus O- or OH-binding energy for a large number of different transition and noble metals (Norskov et al., 2004). Another DFT study of a Pt_3Ni surface doped with a third transition metal (V, Fe, Co, Ir, etc.) found negative Pt surface segregation energies, whereas doping with Pd, Ag, and Au was found to completely suppress the Pt segregation (Zhang et al., 2011). There are a number of relevant critical issues, including how the initial structure of an as-prepared nanoalloy catalyst impacts the structural

evolution (e.g., Pt-skin or d-band shift) and how the structural integrity can be sustained by the alloying components and processing strategies.

In this chapter, some of the recent findings from structural characterizations of nanoalloy catalysts and selected examples of catalytic oxidation reactions in gas phase and in electrolytes (Yang et al., 2012; Shan et al., 2013, 2014; Petkov et al., 2012, 2014; Wanjala et al., 2012a; Yin et al., 2012a; Loukrakpam et al., 2013) are discussed. One important emphasis is placed on understanding atomic-scale chemical and structural ordering and coordination in correlation with the catalytic or electrocatalytic properties, which can be obtained based on synchrotron X-ray characterizations such as high energy X-ray diffraction coupled to atomic pair distribution functions (HE-XRD/PDFs) and X-ray absorption fine structure (XAFS).

10.2 Synthesis of nanoalloys and preparation of nanocatalysts

10.2.1 Synthesis of nanoalloys

The synthesis of molecularly capped metal nanoparticles as building blocks for engineering the nanoscale catalytic materials takes advantage of diverse attributes, including monodispersity, processability, solubility, stability, and self-assembly capability in terms of size, shape, composition, and surface properties. Indeed, the preparation of nanoparticles capped in monolayers, polymers, or dendrimers is rapidly emerging, demonstrating remarkable parallels to catalytic activities for supported nanoparticles (Aiken and Finke, 1999; Li et al., 1999; Zhong and Maye, 2001; Peng et al., 1997; Galow et al., 2002). One important approach involves core-shell type synthesis (Brust et al., 1994; Templeton et al., 2000; Schmid et al., 1996; Paulus et al., 2000). The core-shell type nanostructure can be broadly defined as core and shell of different matters in close interaction, including inorganic/organic and inorganic/inorganic combinations (Zhong and Maye, 2001; Whetten et al., 1996; El-Sayed, 2001; Caruso, 2001; Storhoff and Mirkin, 1999; Sun et al., 2000; Chen and Nikles, 2002). The synthesis of metal nanoparticles in the presence of organic capping agents to form encapsulated metal nanoparticles has demonstrated promise for preparing nanocatalysts with controllable size, shape, composition, and surface properties (Zhong and Maye, 2001; Paulus et al., 2000; El-Sayed, 2001; Caruso, 2001; Storhoff and Mirkin, 1999; Sun et al., 2000; Chen and Nikles, 2002).

The use of capping agents in the synthesis is perhaps one of the most effective strategies to control the size, shape, and composition of metal nanoparticles (Wang et al., 2008; Kang and Murray, 2010; Zhong et al., 2010; Niu and Crooks, 2003; Narayanan and El-Sayed, 2003; Zhang et al., 2007; Lim et al., 2009). An increasing number of examples demonstrate that the metal nanoparticles synthesized by this strategy display intriguing catalytic properties for a number of chemical reactions. Among many synthesis methods, wet chemical synthesis is very effective in producing monodispersed nanoparticles (Klabunde and Mulukutla, 2001; Templeton et al., 2000; Caruso, 2001;

Sun et al., 2001). The two-phase synthesis reported first by Brust et al. (1994) is now widely used for fabricating stable and soluble gold and many other metal nanoparticles of a few nm core sizes. Further modifications of the synthetic protocols or processing of the produced nanoparticles have been shown to produce a variety of chemically tunable nanoparticles in terms of size, shape, and surface properties (Hostetler et al., 1998). Perhaps one of the most important attributes of these nanoparticles is the reactivity of both the metal nanoparticles and the capping molecules that allows re-engineering or assembly of nanoparticles. The capping molecules can be reconstituted to impart the desired functional properties, which was first demonstrated in a place-exchange reaction by Murray's group (Hostetler et al., 1999). For example, the synthesis of AuPt nanoparticles involves transfer of $AuCl_4^-$ and $PtCl_6^-$ from aqueous to organic solution by a phase transfer reagent followed by the reduction in the presence of thiols and/or amines, producing thiolate (or amine)-capped gold-platinum (AuPt) nanoparticles of a few nm sizes (Figure 10.2) (Brust et al., 1994; Zhong et al., 2010).

Briefly, $AuCl_4^-$ and $PtCl_6^{2-}$ were first transferred from aqueous solution into toluene solution using a phase-transfer reagent (tetraoctylammonium bromide). Thiols (e.g., decanethiol, DT) or amine compounds (e.g., oleylamine, OAM) were added to the organic solution as capping agents. An excess of aqueous $NaBH_4$ was slowly added for the reduction reaction. The resulting DT/OAM-encapsulated AuPt nanoparticles in toluene were collected by removing the solvent and cleaned using ethanol. The control of the bimetallic composition in the entire bimetallic composition range and the particle size with high monodispersity (<0.5 nm) was achieved by manipulating the precursor feeding ratio (Zhong et al., 2010). The as-synthesized Au_mPt_{100-m} nanoparticles with different compositions are capped with thiol/amine monolayer shells. Varying the feeding ratio of the metal precursors to capping agents used in the synthesis controls the bimetallic composition and sizes of the nanoparticles. Bimetallic nanoparticles in which the nanocrystal core consists of one metal core and another metal shell (core@shell) such as Au@Pt and Pt@Au could also be synthesized by the seeded growth method (Luo et al., 2008). A similar approach was used for synthesizing other binary nanoparticles, such as AuAg (Kariuki et al., 2004), core-shell AuAg (Nishimura et al., 2012), and Cu nanoparticles (Mott et al., 2007a, 2010).

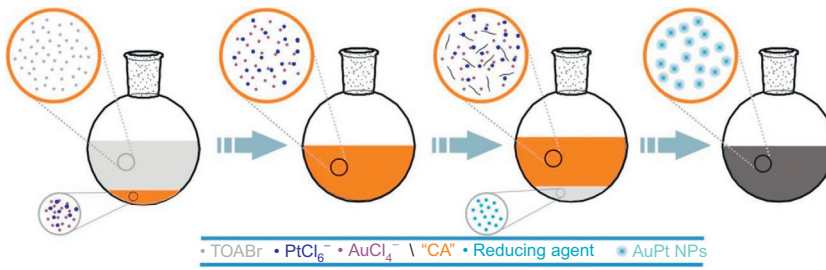

Figure 10.2 Illustration of two-phase synthesis of AuPt nanoparticles in terms of phase transfer and chemical reduction.

Similar strategies in terms of molecular encapsulation have also been used for the synthesis of other binary and ternary nanoparticles under controlled reaction conditions, such as AuM (M = Cu, Ag, etc.), PdM, PtM, and PtMM′ (M,M′ = Ni, Co, Fe, V, Cu, etc.) (Zhang et al., 2011; Yang et al., 2012; Shan et al., 2013, 2014; Petkov et al., 2012, 2014; Wanjala et al., 2012a; Yin et al., 2012a, 2013; Loukrakpam et al., 2013; Kariuki et al., 2004; Nishimura et al., 2012). The synthesis of these nanoalloy particles is in contrast to traditional approaches for preparing supported nanoparticle catalysts, which involve, for example, coprecipitation, deposition-precipitation, ion-exchange, impregnation, successive reduction, and calcination (Klabunde and Mulukutla, 2001; Paulus et al., 2002; Antolini, 2003; Yang et al., 2004; Feldheim and Foss, 2002; Waszczuk et al., 2002; Schmidt et al., 1999; Raja et al., 2001), and often have limited ability to control the size and composition due to the propensity of aggregation.

10.2.2 Preparation of nanocatalysts

A key strategy in our approaches to the preparation of nanocatalysts involves molecularly mediated synthesis of the nanoparticles and postsynthesis thermochemical processing under controlled temperatures and atmospheres (Figure 10.3). The removal of the organic encapsulation from metal nanoparticles is also an important step in the catalyst preparation. Among different strategies (Zhong and Regalbuto, 2013), thermochemical processing strategy has demonstrated not only effectiveness in removing

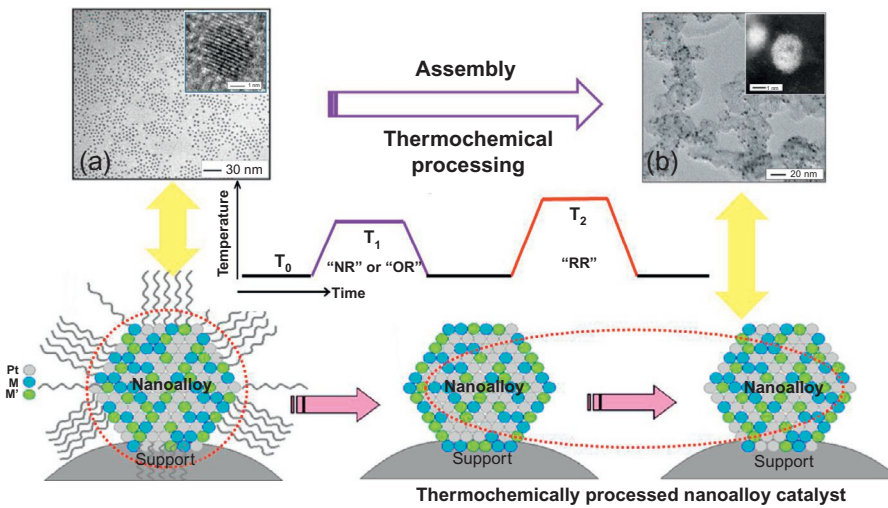

Figure 10.3 A schematic illustration of molecularly engineered synthesis and thermochemical processing of nanoalloy catalysts under nonreactive (N_2) ("NR"), oxidative (O_2) reaction ("OR"), and reductive (H_2) reaction ("RR") atmosphere. Example TEM/HR-TEM images showing as-synthesized $Pt_{39}Ni_{22}Co_{39}$ nanoparticles (3.4 ± 0.4 nm, (a)), and thermochemically treated carbon-supported $Pt_{39}Ni_{22}Co_{39}$ nanoparticles (4.4 ± 0.5 nm, (b)).

the encapsulation, but also in refining the nanostructural parameters (Figure 10.3). The combination of the molecular encapsulation-based synthesis and thermochemical processing strategies thus involves a sequence of steps for the preparation of nanoalloy catalysts: (1) chemical synthesis of the metal nanocrystal cores capped with ligands, (2) assembly of the encapsulated nanoparticles on supporting materials (e.g., carbon powders, TiO_2 or SiO_2) (Liu et al., 2013a,b; Yang et al., 2012; Shan et al., 2014; Haruta et al., 1993), and (3) thermal treatment of the supported nanoparticles (Luo et al., 2006a,b; Han et al., 2004). In the molecularly engineered synthesis and thermochemically controlled processing of nanoalloy catalysts, the understanding of whether alloying or phase-segregation in multimetallic nanoparticles is different from bulk-scale materials, and how the catalytic activity and stability are influenced by size, composition, morphology, support, and phases has been an important focus of the recent research activities.

The size and composition of the nanoparticles produced by thermochemical processing are controllable, as demonstrated for a series of binary and ternary nanoparticles supported on carbon (Yang et al., 2012; Shan et al., 2013, 2014; Wanjala et al., 2012a; Zhong et al., 2010). One example is shown in Figure 10.3 for PtNiCo nanoparticles in as-synthesized and carbon-supported forms (Yang et al., 2012; Zhong et al., 2010; Wanjala et al., 2012b). The as-synthesized $Pt_{39}Ni_{22}Co_{39}$ nanoparticles are highly monodispersed with a good crystallinity. The subtle increase of the particle sizes for the thermochemically treated carbon-supported $Pt_{39}Ni_{22}Co_{39}$ nanoparticles was due to thermal sintering of the nanoparticles. Two binary nanoalloy examples are shown in Figure 10.4 for AuPt and PdCu nanoalloys (Yin et al., 2013; Petkov et al., 2012; Wanjala et al., 2010a, 2011).

These nanoparticles display crystalline characteristics and largely uniform distributions of the two metal components. The AuPt nanoparticles are fully alloyed with uniform bimetallic distribution in the nanoparticles (Figure 10.4a). The observation of the indicated lattice fringes of 0.235 nm indicates that the carbon-supported nanoparticles are highly crystalline with a subtle difference in interatomic distance between catalysts treated under H_2 at 400 and 800 °C. In our recent studies (Luo et al., 2006a; Wanjala et al., 2010a, 2011), carbon-supported AuPt nanoparticles have been shown to exhibit single-phase alloying characteristics but also a controllable degree of partial alloying or phase segregation depending on the thermochemical processing conditions. The fully alloyed AuPt nanoparticles have a uniform distribution of the two metals across the nanoparticles. The bimetallic nanoparticles are not only crystalline with highly faceted surfaces but also have a uniform distribution of Au and Pt. Similar nanocrystalline features and relatively uniform bimetallic distribution have also been observed for PdCu nanoparticles (Figure 10.4b) (Yin et al., 2013), revealing that the bimetallic nanoparticle is basically a uniform alloy across the entire nanoparticle.

As will be discussed in later sections, the catalytic or electrocatalytic properties of the nanoalloy catalysts prepared by the combination of molecular encapsulation-based synthesis and thermochemical processing strategies depend on the detailed synthesis and thermochemical processing parameters, showing synergistic correlation with the atomic-scale structural evolution of the nanoalloys.

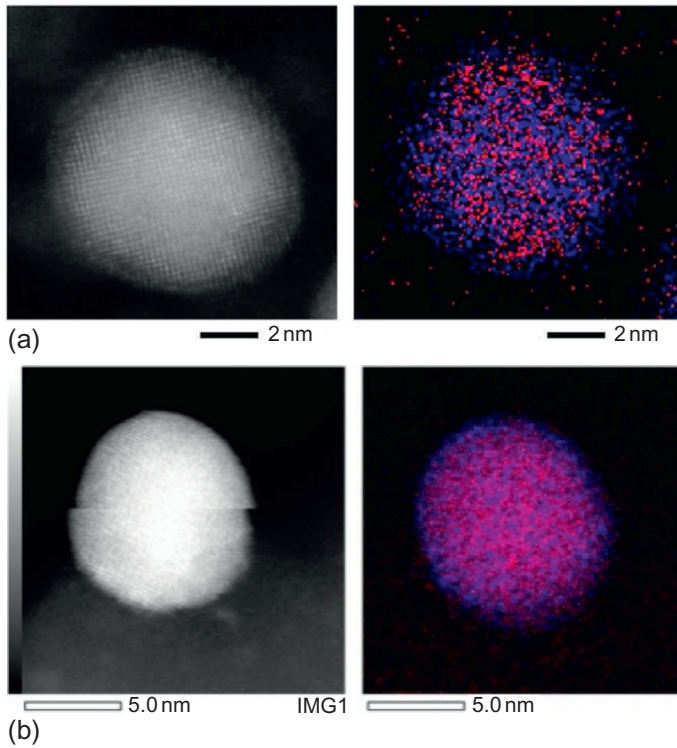

Figure 10.4 HRTEM and EDS composition mapping for $Au_{22}Pt_{78}/C$ (red: Pt, blue: Au) (a) and $Pd_{21}Cu_{79}/C$ (red: Cu, blue: Pd) (b) nanoparticles.
(a) Reproduced from Petkov et al. (2012) with permission. Copyright 2012, American Chemical Society. (b) Reproduced from Yin et al. (2013) with permission. Copyright 2013, American Chemical Society.

10.3 Structural characterizations of nanoalloy catalysts

The understanding of the atomic-scale chemical and structural ordering of the nanoalloys in either as-synthesized or thermochemically processed state is central to the exploration of catalytic properties. In addition to TEM, HRTEM, and EDX imaging techniques, there are many analytical techniques that have been used to characterize the nanoalloy structures. In particular, synchrotron X-ray techniques, including HE-XRD/PDFs and XAFS, have proven powerful for gaining insights into both extended and local atomic structures of nanoalloys (Figure 10.5). The HE-XRD/PDF study can be coupled with 3D simulations for determining the overall atomic-scale structure across the nanoalloy, including details of the chemical ordering. XANES/EXAFS has been demonstrated as a powerful technique for determining the near-neighbor metal-metal coordination, metal oxide content, electronic properties, and charge transfer phenomena in the studied alloys, including the effect of support providing

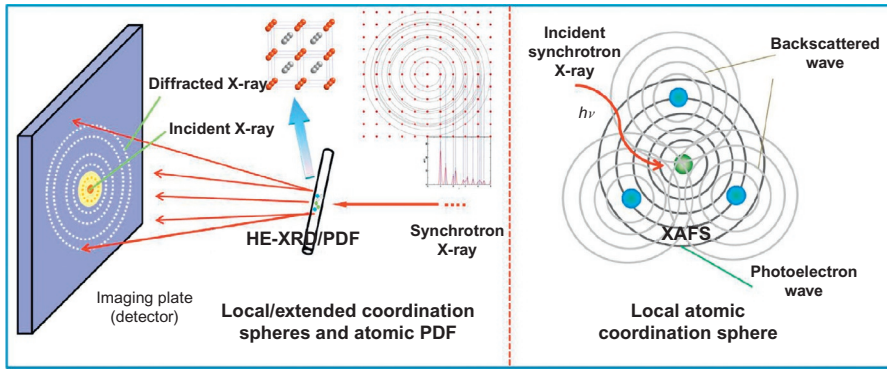

Figure 10.5 Schematic illustrations of structural characterizations of nanoalloys using synchrotron X-ray based techniques: average structure sensitive HE-XRD (Yang et al., 2012; Shan et al., 2014; Petkov et al., 2012), and local structure sensitive XAFS.

valuable information for assessing O_2 activation on the nanoalloy binding sites in terms of local structural configurations. EXAFS provides structural information on the coordination environment around each component for assessing the alloy formation in terms of coordination number (CN) of M or M′ around Pt. Metal oxide contents can be estimated from XANES spectra using a linear combination fitting. In addition, the Pt L-edge absorption edge peak (or white line) is sensitive to the particles size, shape, and support type (Behafarid et al., 2012; Bazin et al., 1997). The understanding of how both local and extended atomic ordering parameters, including structural/chemical alloying degree, interatomic distances, CNs, and oxophilicity, correlate with the nanoalloy catalyst's activity and stability is important for the design of nanoalloy catalysts.

Using high-energy X-rays (80-1000 keV, about one order of magnitude higher than conventional X-rays), the unique advantages of HE-XRD include high penetration into materials, no radiation damage of the sample, and many other qualities enabling the characterization of the nanoscale materials and detail structures. Both *ex situ* and *in situ* HE-XRD coupled to atomic pair distribution function (PDFs) analysis could be used to obtain fundamental insight into atomic-scale structure of nanoparticle in various gas atmospheres (Figure 10.5). The PDF technique has emerged recently as a powerful and unique tool for the characterization and structure refinement of crystalline materials with intrinsic disorder (Petkov et al., 2000). The strength of the technique stems from the fact that it takes into account the total diffraction—that is, Bragg as well as diffuse scattering—thus it can be applied to both crystalline (Petkov et al., 1999) and amorphous materials (Waseda, 1980). In contrast, other techniques used to study polycrystalline samples (e.g., Rietveld) (Rietveld, 1969) use only the Bragg scattering portion of the pattern and therefore any information originating from the disorder present is lost. A reactor-type cell (Oxford et al., 2010) can be used in the *in situ* experiments (Figure 10.5 inset).The XRD diffraction data can be reduced to the so-called structure factors, $S(q)$, and then Fourier transformed to atomic PDFs

$G(r)$. The wave vector q is defined as $q = 4\pi\sin(\theta)/\lambda$, where θ is half of the scattering angle and λ is the wavelength of the X-rays used. The atomic PDFs $G(r)$ are experimental quantities that oscillate around zero and show positive peaks at real space distance; r, where the local atomic density $\rho(r)$ exceeds the average one ρ_o. The PDF $G(r)$ can be expressed by the equation: $G(r) = 4\pi r\rho_o[\rho(r)/\rho_o - 1]$. High-energy XRD and atomic PDFs have already proven to be very efficient in studying the atomic-scale structure of nanosized materials (Egami and Billinge, 2003; Petkov, 2008).

In comparison with XRD technique, XAFS (Figure 10.5) is a spectroscopic technique that uses X-rays to probe the physical and chemical structure of matter at an atomic scale. XAFS is element-specific, in that X-rays are chosen to be at and above the binding energy of a particular core electronic level of a particular atomic species. Unlike regular diffraction-based techniques for studying atomic structure of matter, XAFS does not require a crystalline sample. XAFS provides information on how X-rays are absorbed by an atom at energies near and above the core-level binding energies. Because XAFS spectra are very sensitive to the formal oxidation state, coordination chemistry, and the distances, CN, and species of the atoms immediately surrounding the selected element. It provides a relatively simple way to determine the chemical state and local atomic structure for a selected atomic species. Because XAFS is an atomic probe, all atoms have core-level electrons, and importantly, crystallinity is not required for XAFS measurements, making it one of the few structural probes available for noncrystalline and highly disordered materials, including solutions. Because X-rays are fairly penetrating in matter, XAFS is not inherently surface-sensitive, although special measurement techniques can be applied to enhance its surface sensitivity (Newville, 2004). As discussed in the next two subsections, these two techniques provide information for short-range interatomic bonding and coordination structure about a specific atom as well as more extended structural/chemical ordering across the entire nanoparticle, regardless of whether the particle is crystalline or amorphous (Evans, 1989; Antoniak, 2011).

10.3.1 Synchrotron X-ray-based techniques

A series of binary PtM and ternary PtMM′ (M/M′ = Co, Fe, V, Ni, etc.) have been studied to understand the structure-activity correlation (Yang et al., 2012; Shan et al., 2013, 2014; Wanjala et al., 2012a). Consider PtVCo nanoalloys (Wanjala et al., 2012a) as an example to illustrate the structural evolution by thermochemical processing treatments of oxidation reaction in O_2 ("OR") followed by reduction reaction in H_2 ("RR") at different temperatures (Figure 10.6). There is a clear structural evolution for the catalyst treated in an "OR"-"RR" treatment atmosphere (Wanjala et al., 2012a). A hypothetical fcc lattice inferred from the increase of the major Bragg peaks showed a gradual decrease (Figure 10.6). The appearance of the low-intensity peaks for $T > 600$ °C suggests that the particle's structure rearranges away from the fcc type at higher temperatures. This rearrangement transforms the fcc-type structure of the as-prepared particles into particles with a face-centered tetragonal (fct)-type structure (Watanabe et al., 1994), bearing some resemblance to phase transitions observed in binary alloy particles such as PtCo and PtV (Koh et al., 2007a,b; Petkov, 2009).

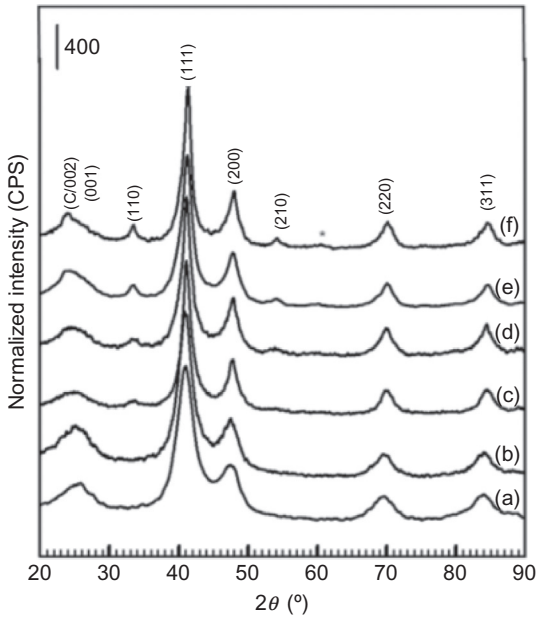

Figure 10.6 Regular XRD patterns for $Pt_{45}V_{18}Co_{37}$/C treated by "OR" followed by "RR" treatment at different temperatures: 400 (a), 500 (b), 600 (c), 700 (d), 800 (e), and 926 °C (f).
Reproduced from Wanjala et al. (2012a) with permission. Copyright 2012, American Chemical Society.

The use of regular XRD for determining the detailed structures of nanoparticles has limitations largely because of the fact that small-size nanoparticles do not exhibit extended crystalline structures. In contrast, the HE-XRD/PDF technique can provide insights into the atomic scale details of the phase state and structures, especially for small-sized nanoparticles. One example is to study the phase state of PtVCo/C nanoalloys (Wanjala et al., 2012a). To reveal the nature of the atomic ordering in $Pt_{45}V_{18}Co_{37}$/C and its temperature-driven evolution in more detail we conducted HE-XRD experiments coupled to atomic PDFs analysis that is very well suited for nanosized particles (Petkov, 2009; Wanjala et al., 2010b). HE-XRD patterns for $Pt_{45}V_{18}Co_{37}$/C catalysts treated by "OR" followed by "RR" at 400, 600, and 926 °C are shown in Figure 10.7A. Atomic PDFs extracted from the HE-XRD patterns are shown in Figure 10.7B together with that for pure Pt particles used here as a standard. The PDFs exhibit a series of well-defined peaks reflecting the presence of a sequence of well-defined coordination spheres in the ternary catalysts. In the PDF for pure Pt particles the first peak is positioned at 2.76 Å, which is very close to the Pt-Pt distance in the respective bulk metal. The first peak in the experimental PDFs for PtVCo/C catalysts is positioned at 2.70 Å indicating a shortening of the metal-metal distances in the alloy particles due to the smaller size of the Co/V atoms as compared to Pt atoms. All features in the PDF for pure Pt can be very well fit with a structure model featuring an fcc-type structure with a parameter of 3.92 Å. The results revealed a random alloy fcc-type or chemically ordered alloy fct-type structure for 400 °C treated catalyst. The chemically ordered fct lattice model, however, becomes increasingly a better match to the experimental PDFs for the particles annealed at >400 °C. Indeed, only the fct-type model can explain well the fine features of the

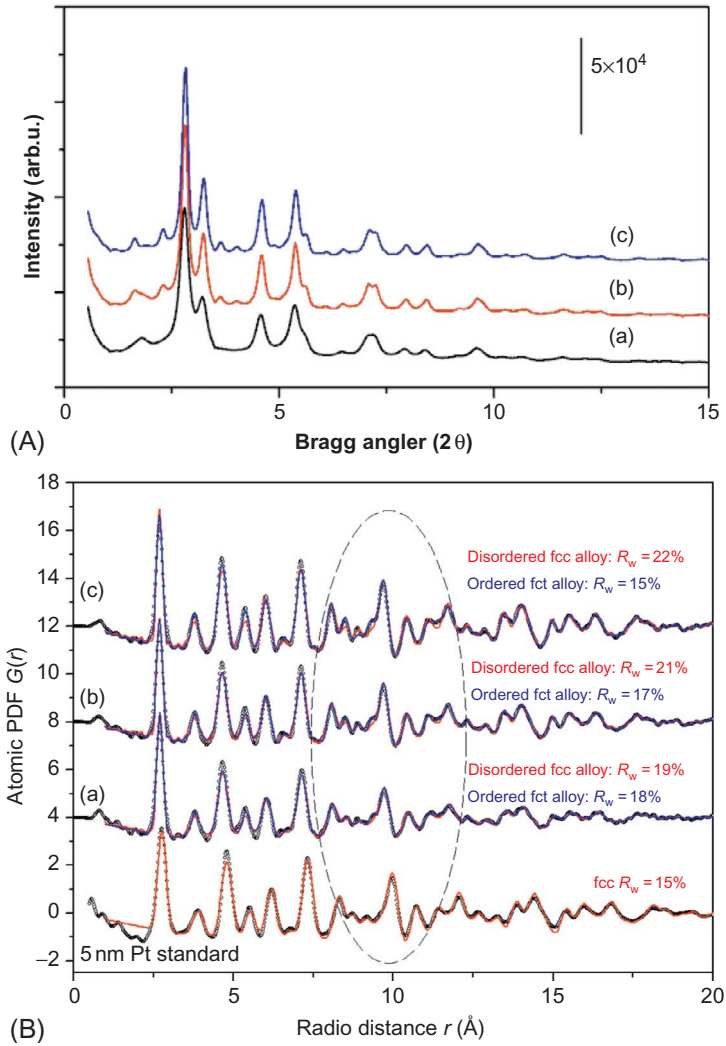

Figure 10.7 (A) HE-XRD patterns for $Pt_{45}V_{18}Co_{37}$/C catalysts treated by "OR" followed by "RR" treatment as a function of treatment temperature: 400 (a), 600 (b), and 926 °C (c) and (B) atomic PDFs extracted from the HE-XRD diffraction patterns for $Pt_{45}V_{18}Co_{37}$/C catalysts at "RR" annealing temperature: 400 (a), 600 (b), and 926 °C (c). The PDF for 5 nm Pt particles is shown for comparison.
Reproduced from Wanjala et al. (2012a) with permission. Copyright 2012, American Chemical Society.

experimental PDF data (see the encircled region) that are characteristic benchmarks of a chemically ordered structure where Pt, Co, and V atoms are not randomly distributed within the nanoparticles but assume preferential ordering with respect to each other. The PDF refined fct lattice parameters change from $a = 2.710$ Å and $c = 3.776$ Å for

the sample annealed at 400 °C to $a = 2.700$ Å and $c = 3.773$ Å at 600 °C and then to $a = 2.698$ Å and $c = 3.770$ Å at 926 °C. If Pt and $Pt_{45}V_{18}Co_{37}$ samples are compared on the basis of a hypothetical fcc model, the respective lattice parameters change from $a = 3.82$ Å (400 °C) to $a = 3.809$ Å (600 °C) and then to $a = 3.803$ Å (926 °C). The synchrotron-based PDF studies unambiguously show that with increasing the temperature, the catalyst undergoes a phase transition from a random alloy to a chemically ordered alloy-type structure, which is accompanied by a shrinking of the distances between the metal atoms.

In addition to HE-XRD/PDF data, EXAFS data have also shown that the formation of oxygenated metal species in the nanoalloys is highly dependent on the thermal treatment condition. The atomic M-M coordination in $Pt_{45}V_{18}Co_{37}$/C catalysts was analyzed by EXAFS on selected samples annealed under H_2 atmosphere at 400 and 800 °C (Wanjala et al., 2012a). The understanding of the structural changes between these two temperatures provides information for assessing how the change in activity with annealing temperature is related to the structural change of the catalysts. The data can be analyzed by fitting of the Pt EXAFS data using PtCo and PtV models. As summarized in Table 10.1 for the structural parameters from fitting Pt L3 edge EXAFS data using the PtCo model and the Co K edge data using the CoCo model for a $Pt_{45}V_{18}Co_{37}$/C catalyst, the results clearly show a significant presence of Co/V neighbors around Pt and Pt neighbors around Co, which is direct evidence of the formation of PtVCo alloy in the samples studied here. Also, the EXAFS data indicate a

Table 10.1 Structural parameters from fitting Pt L3 edge EXAFS data using PtCo model and Co K edge data using CoCo model for $Pt_{45}V_{18}Co_{37}$/C catalysts

Sample	Scattering path	*N*	*R* (Å)
Pt L3 edge			
400 °C	Pt-O	0.5 ± 0.1	1.99 ± 0.03
	Pt-Co/V	2.3 ± 0.7	2.64 ± 0.01
	Pt-Pt	5.7 ± 0.7	2.70 ± 0.01
800 °C	Pt-O	0.4 ± 0.1	1.99 ± 0.03
	Pt-Co/V	3.1 ± 0.5	2.64 ± 0.01
	Pt-Pt	5.4 ± 0.6	2.69 ± 0.00
Co K edge			
400 °C	Co-O	2.3 ± 0.3	1.99 ± 0.01
	Co-Co/V	1.2 ± 0.5	2.62 ± 0.01
	Co-Pt	4.1 ± 0.5	2.64 ± 0.01
800 °C	Co-O	1.8 ± 0.2	1.99 ± 0.01
	Co-Co/V	1.8 ± 0.8	2.62 ± 0.01
	Co-Pt	4.9 ± 0.6	2.64 ± 0.01

Note: *R*-factor: 0.0088 for Pt L3 edges, 0.0127 for Co K edges; *N*: coordination number; *R*: bond length; DWF: Debye-Waller factor.
Reproduced from Wanjala et al. (2012a) with permission. Copyright 2012, American Chemical Society.

higher probability of Pt bonding with transition metal atoms for the catalyst treated at 800 °C as compared to the catalyst treated at 400 °C. For example, the CN of Pt-Co/V atomic pairs changes from 2.3 for the 400 °C treated sample to 3.1 for the 800 °C sample while the corresponding change in CN of Pt-Pt is insignificant (from 5.7 to 5.4). Although increase in particle size may lead to an increase of total CN, the more significant increase in CN of Pt-Co/V than that of Pt-Pt suggests better alloying between Pt and Co/V. The EXAFS results in Table 10.1 also indicate a clear reduction of the oxide content (e.g., reduction in the metal-oxygen CNs) for the 800 °C treated sample.

Other ternary or binary nanoalloys have also been studied using HE-XRD/PDFs and EXAFS techniques, especially under *in situ* conditions for the thermochemical treatments of the catalysts (Yang et al., 2012; Shan et al., 2013, 2014; Wanjala et al., 2012a). A comparison of the structural evolutions of PtVCo and PtNiCo nanoalloys under both oxidative (O_2) and reductive (H_2) atmosphere (Shan et al., 2013) reveals differences in the changes of the lattice parameters in the oxidation-reduction cycles between the two systems (Figure 10.8). One intriguing finding is that the changes in the lattice parameter of the PtVCo catalyst are only half of those observed for the PtNiCo system. In other words, PtVCo maintains a more stable lattice parameter—i.e., a more stable atomic scale structure—than the PtNiCo system in the catalytic reaction process. The PtVCo/C nanoalloy's interatomic distances increase when the catalyst is treated in the oxidizing atmosphere and shrink uniformly when the catalyst is treated in the reducing atmosphere. The nanoalloy particles remain "expanded" when cooled back to room temperature (RT) in an oxidizing atmosphere and "shrunk" if cooled back to RT in a reducing atmosphere. The expansion of the interatomic distances upon oxidation is consistent with the enhanced interaction of oxygen with the particle's surface that is favored by the oxophilicity of the base transition metal. The overall shrinking of the interatomic distances in the nanoalloy particles treated in a reducing atmosphere is consistent with freeing their surface from the oxygen species. Interestingly, ternary nanoparticles show a great degree of tunability in lattice parameters. For the PtVCo nanoalloy, there is a clear lattice expansion upon oxidation ($\delta a/a = 0.9\%$), and lattice shrinking upon reduction ($\delta a/a = -1.0\%$). In comparison, the lattice expansion upon oxidation ($\delta a/a = 1.4\%$) and shrinking upon

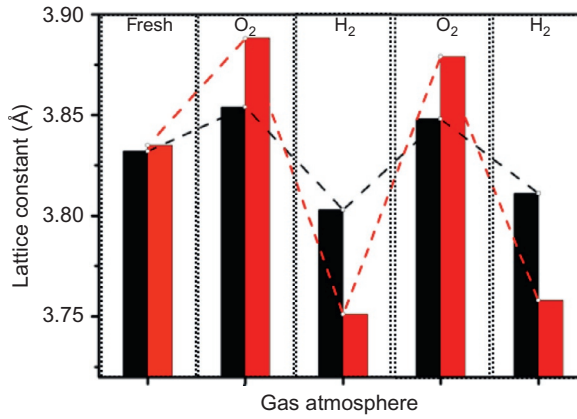

Figure 10.8 A comparison of the fcc-lattice parameters for $Pt_{45}V_{18}Co_{37}$ (black bar) and $Pt_{25}Ni_{16}Co_{59}$ (red bar) in the thermochemical treatment cycles in O_2 (at 240 °C) and H_2 (400 °C) atmosphere, as denoted on the horizontal axis, then cooled down to room temperature.
Reproduced from Shan et al. (2013) with permission. Copyright 2013, American Chemical Society.

reduction ($\delta a/a = -3.6\%$) are somewhat larger for that of PtNiCo nanoalloy (Figure 10.8). The introduction of a third transition metal ($M' = V$, Ni, Ir, etc.) into PtCo nanoalloys minimizes or suppresses changes in the lattice parameters of the nanoparticle during the catalytic processes, consistent with the order of oxophilicity of these metals.

The results from the recent detailed characterization of AuPt nanoparticles (Petkov et al., 2012) provide another example demonstrating the power of HE-XRD/PDFs in gaining atomic-scale insights into the nanoalloy structure. AuPt nanoalloys are analyzed using an element-specific resonant HE-XRD technique. Both HE-XRD (Figure 10.9a) coupled with atomic PDFs (Figure 10.9b) and computer simulations prove the formation of Pt-Au alloys in particles less than 10 nm in size.

The bond lengths in the alloys differing in 0.1 Å leads to extra structural distortion as compared to pure Pt and Au particles. In the nanoalloys, Au-Au and Pt-Pt bond lengths differing by 0.1 Å are revealed. The results demonstrate the presence of an extra structural distortion for AuPt nanoparticles as compared to pure Pt and Au nanoparticles. Pt-Pt and Pt-Au pairs were identified in the first coordination shell of Pt atoms, providing atomic-scale insights into the alloy characteristic for the AuPt nanoparticles. Reverse Monto Carlo (RMC) refined models are also used to aid the analysis of the alloy structures. Pure Au and Pt nanoparticles (NPs) are used to produce model configurations for Au_mPt_{100-m} NPs where Au and Pt atoms show various patterns of chemical order-disorder effects. All peaks in the partial Au-Au PDFs for Au_mPt_{100-m} NPs are accompanied by largely diminished areas corresponding to reduced Au-Au CNs that are characteristic of random type Pt-Au alloys. The alloying of Pt and Au occurs not only within a wide range of Pt-Au concentrations but is also stable in NPs of different sizes. Importantly, the alloying characteristics of the less than 5-nm-sized AuPt particles were found to remain unchanged for a long period of time under ambient conditions, demonstrating structural stability of the nanoalloy.

Synchrotron X-ray techniques have also been used to monitor the formation of nanoalloys from mixed single-component nanoparticles during thermochemical evolution processes. One example involves the formation of AuCu nanoalloy from Au and Cu nanoparticles (Yin et al., 2012a). Figure 10.10a and b shows the behavior of the wide-angle XRD patterns during uniform heating from 25 to 225 °C of a binary solution of 2 nm Au and 0.5 nm Cu cast on a planar Si substrate. The temperature evolution of the binary sample is compared with the evolution of unary Cu and unary Au nanoparticles (Figure 10.10b). Due to the smaller size and lower melting point, the Cu particles start to aggregate immediately after heating above 60 °C. In sharp contrast, the Au nanoparticles restructure significantly only above 140 °C. In terms of the "halfway" temperature for the increase of the integrated intensity, the temperature for Cu + Au (~115 °C) falls in between those for Au (~160 °C) and Cu (~90 °C). Because this temperature is relatively low compared to the melting temperature of 2 nm Au nanoparticles, the restructuring process likely involves solid-phase sintering and recrystallization. The physical mixture exhibits an intermediate behavior, but it is clear that the particles restructure at considerably lower temperatures than pure Au nanoparticles, indicating a significant effect of the Cu nanoparticles.

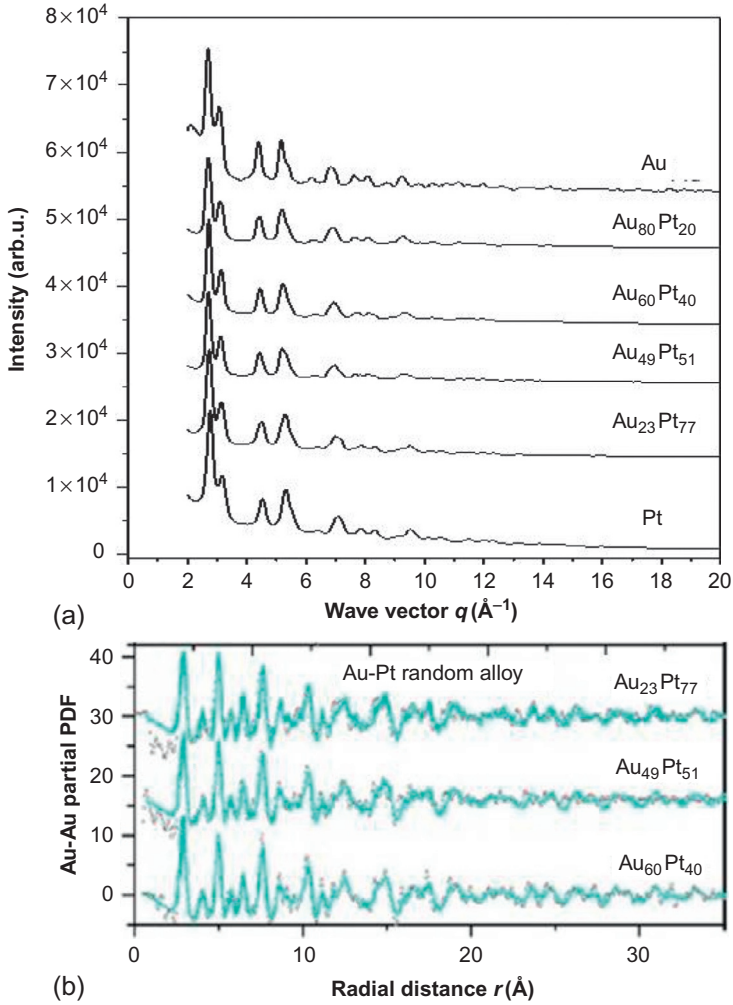

Figure 10.9 Background corrected experimental XRD patterns of Au_mPt_{100-m} particles annealed at 400 °C (a) and experimental (symbols) and model (line in cyan) Au-Au partial PDFs (b) for 5.1 nm Pt-Au particles. The data sets are shifted by a constant factor for clarity. Au-core/Pt-shell model Au-Au PDFs show first peaks that are too strong in intensity than the peaks in the respective experimental Au-Au PDFs and also decay to zero much faster than the experimental data. Peaks in the Au-Au PDFs for Pt-core/Au-shell model show characteristic step-down loss in intensity at short interatomic distances that is inconsistent with the behavior of the experimental data. Au-Pt random alloy model Au-Au PDFs agree with the experimental data in very good detail.
Reproduced from Petkov et al. (2012) with permission. Copyright 2012, American Chemical Society.

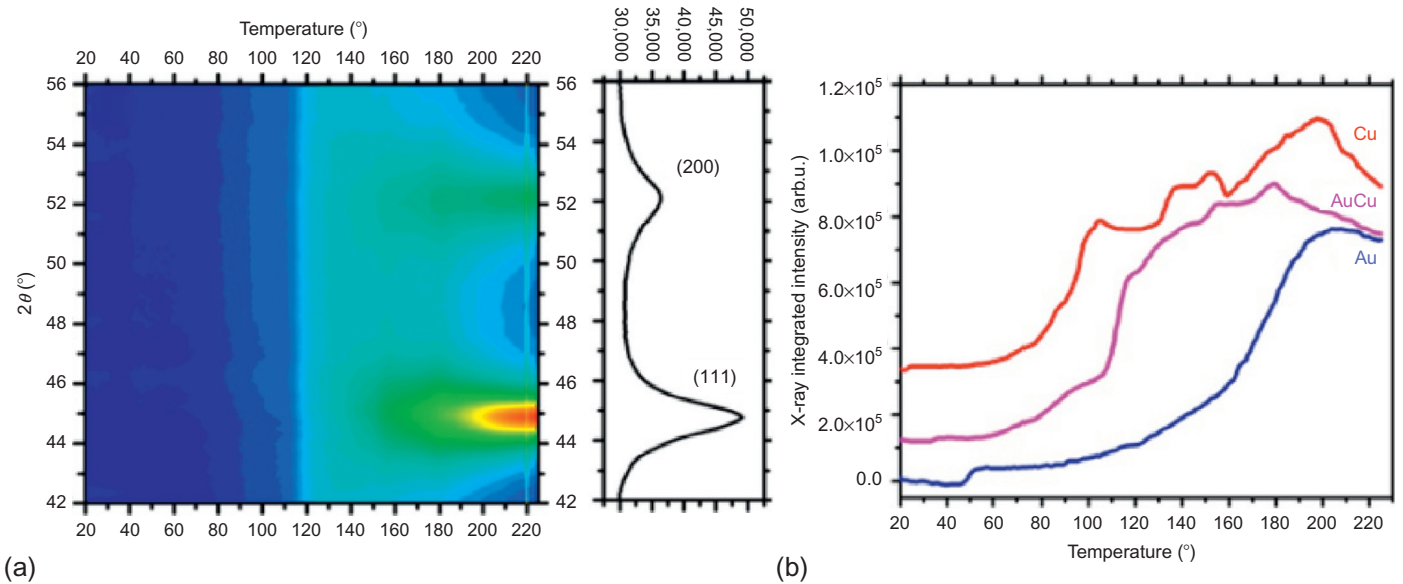

Figure 10.10 *In situ* real-time synchrotron XRD. (a) A map showing evolution during uniform ramping from 25 to 225 °C for binary Au nanoparticles (2 nm) and Cu nanoclusters with a Cu:Au molar ratio of 8.5 cast on a Si surface, and a snapshot of XRD pattern at 220 °C. (b) Comparison of temperature evolution of (111)-intensity for Au, Cu, and binary (1:1) Au and Cu (X-ray energy: 6.9 keV).
Reproduced from Yin et al. (2012a) with permission. Copyright 2012, American Chemical Society.

10.3.2 Computational modeling

For supported Au_mPt_{100-m} nanoparticles, the nanoscale alloying or phase segregation is also found to depend on the composition, support, and thermal treatment temperature (Wanjala et al., 2010b; Luo et al., 2005a). Currently, two aspects of the fundamental insights are considered in supporting some of these alloying or phase-segregation states. One involves the theoretical finding of a negative heat of formation for AuPt nanoparticles smaller than ~6 nm, which constitutes a thermodynamic basis for favoring the formation of alloyed phase (Xiao et al., 2006). The other involves the theoretical finding of a possible phase segregation of AuPt particles as a result of the combination of larger surface free energy of Pt (2.48 J/m^2) than Au (1.50 J/m^2) (Xiao et al., 2006) and the lower melting point of smaller-sized nanoparticles than larger-sized particles ($\Delta T \propto 1/r_{(\text{particle radius})}$) (Maye et al., 2000; Schadt et al., 2006, Maye and Zhong, 2000). The nanoscale phase of Au_mPt_{100-nm} nanoparticles is a very important parameter for the exploration of nanoscale bimetallic functional properties. The lattice constants of the bimetallic nanoparticles were found not only to scale linearly with Pt%, in contrast to the bulk AuPt counterparts that display a miscibility gap at 20-90% Au, but also to be smaller than those of the bulk counterparts (Luo et al., 2005a; Mott et al., 2007b,c). This finding was the first example demonstrating that the nanoscale AuPt nanoparticles could exhibit single-phase character and reduced interatomic distances in the entire bimetallic composition range in contrast to the bulk counterparts (Luo et al., 2005a; Mott et al., 2007b,c). In addition to the latest HE-XRD/PDFs evidence (Petkov et al., 2012), results from theoretical modeling and DFT computation for small AuPt nanoparticles (~1.2 nm) have also revealed a difference in the lattice constant-composition relationship between the nanoscale and the bulk systems in agreement with the experimental data (Wanjala et al., 2010a, 2011). In theoretical modeling of realistic particle sizes, a negative heat is revealed for the formation for AuPt particles smaller than ~6 nm (Xiao et al., 2006), thermodynamically favoring the formation of alloyed phase (Xiao et al., 2006). The atomic distributions of Au and Pt are also shown to change in distance from the center of mass in the nanoparticle depending on temperature and support (Morrow and Striolo, 2010). The complex phase properties are also supported by *in situ* time-resolved X-ray diffraction study of phase change kinetics at high temperature (Luo et al., 2008). The nanoscale phase evolution has a significant impact on the surface alloying or segregation (Wanjala et al., 2010b; Mott et al., 2007b,c; Malis et al., 2009), as supported by FTIR probing of CO adsorption as a function of the bimetallic composition (Mott et al., 2007b,c) and XPS analysis of the relative surface composition as a function of the treatment temperature (Wanjala et al., 2010b, 2012a).

DFT computation of small AuPt nanoparticles (~1.2 nm) has provided some insights into the phase properties (Wanjala et al., 2010a). Seventeen 55-atom AuPt nanoparticles (~1.2 nm), six $Au_{24}Pt_{76}$ (13 Au atoms and 42 Pt atoms), five $Au_{49}Pt_{51}$ (27 Au atoms and 28 Pt atoms), and six $Au_{76}Pt_{24}$ (42 Au atoms and 13 Pt atoms) were studied using DFT calculations. These calculations were carried out using the spin-polarized DFT method that is implemented in Vienna *Ab initio* Simulation Package (Xiao et al., 2006; Kresse and Hafner, 1993; Kresse and Furthmuller, 1996a). The structures and the corresponding stability of these nanoparticles are shown in Figure 10.11.

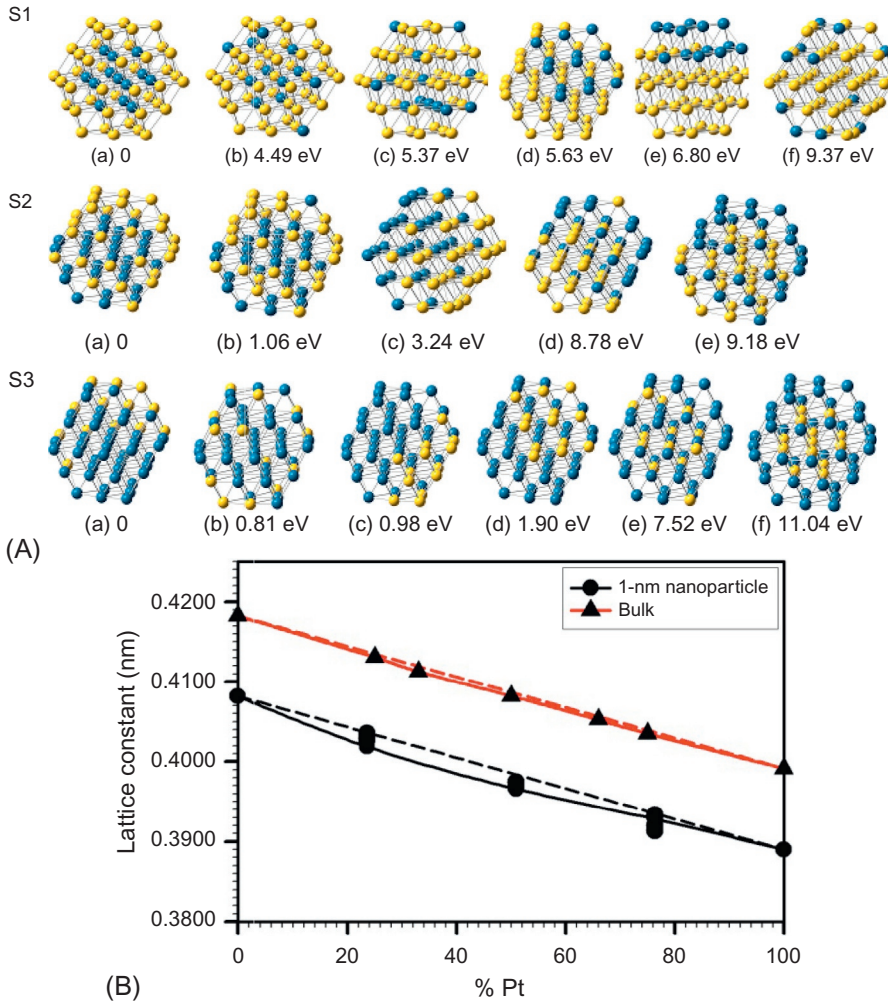

Figure 10.11 Computation results in terms of structures and relative energies: (A) S1: $Au_{76}Pt_{24}$ nanoparticles. A positive number means that the corresponding structure is less stable than structure (a). S2: $Au_{49}Pt_{51}$ nanoparticles. A positive number means that the corresponding structure is less stable than structure (a). S3: $Au_{24}Pt_{76}$ nanoparticles. A positive number means that the corresponding structure is less stable than structure (a). (B) DFT-calculated lattice constant-composition relationship for the nanoscale and bulk bimetallic systems. Reproduced from Wanjala et al. (2010a) with permission. Copyright 2010, American Chemical Society.

The stability of alloy structures was found to lie between the core-shell structures. The complete Pt-core/Au-shell structure is the most stable among all isomers. The least stable isomer has the least number of surface Au atoms. When temperature increases, the alloy nanoparticles evolve in such a way that the outer shell Pt atoms migrate into the inner shell. This is further supported by molecular dynamics

simulations (Kresse and Furthmuller, 1996b), where upon heating above 600 K such Pt migration takes place in an alloy nanoparticle of ~3.6 nm. The computational results further indicate that thermal treatments of alloy AuPt nanoparticles should be below certain temperatures to prevent the loss of outer shell Pt atoms. Figure 10.11 shows the DFT-calculated lattice constants, which are indeed smaller than those of bulk. This finding is in agreement with our earlier finding of the nanoscale phase properties for the alloyed AuPt/C catalysts (Luo et al., 2005b). The computation results supported the observed overall lattice shrinking of the metal and bimetallic nanoparticles in comparison with the bulk counterparts and showed the possibility of an evolution of the alloy nanoparticles in such a way that the outer shell Pt atoms migrate into the inner shell when temperature increases, which is qualitatively consistent with the XRD analysis results. There are many recent examples on DFT computational modeling of AuPt nanoparticle structures in terms of composition and structures (Bochicchio et al., 2013). For example (Bochicchio et al., 2013), the study of AuPt nanoalloys with 55 atoms with an intermediate composition range by a procedure combining global optimization searches within an atomistic potential model with DFT relaxation of the lowest energy isomers identified two structural motifs in close competition: the Mackay icosahedron and an asymmetric capped decahedron.

10.4 Applications in heterogeneous catalysis

10.4.1 Catalytic oxidation of carbon monoxide

In comparison with the study of nanoalloys for reactions in electrolytes, which is complex due to possible Pt-skin formation as a result of dealloying, the study in gas-phase reactions allows probing the structural characteristics in the absence of dealloying. This condition facilitates the study of how the catalytic activity and stability of the nanoalloys can be correlated with the detailed structure by design. Under gas phase catalytic conditions, one important reaction involves water gas shift reaction (Senanayake et al., 2013), which is important to hydrogen energy production. A key challenge is to remove CO trace, which is a poison for some catalysts used downstream, from hydrogen fuel. The typical process of CO removal is catalytic oxidation of CO at low temperatures:

$$2CO(g) + O_2(g) \rightarrow 2CO_2(g) \tag{10.1}$$

Catalytic CO oxidation has been an important subject of interest (Yang et al., 2012; Shan et al., 2013; Evans, 1989), which is often used as a probe molecule to nanoalloy catalysts (Singh and Xu, 2013; Bauer et al., 2013; Yang et al., 2012; Shan et al., 2013) for understanding catalytic synergy in relation to atomic surface structure, phase properties, and nanoalloy-support interactions.

In a recent study of CO oxidation over PtNiCo nanoalloys on different supports (Yang et al., 2012), both supports and thermochemical treatment conditions were

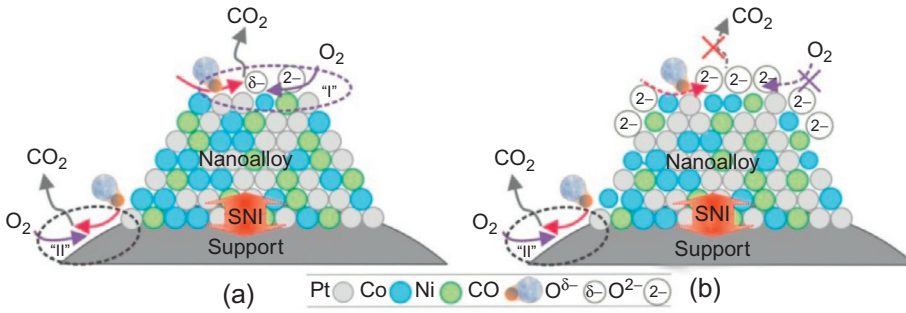

Figure 10.12 Illustration of catalytic CO reaction over supported nanoalloy catalyst in either reduced nanoalloy (a) or oxidized nanoalloy (b) state.
Reproduced from Yang et al. (2012) with permission. Copyright 2012, American Chemical Society.

found to substantially affect the overall atomic-scale structure of the nanoalloy particles and the surface-oxygenated Ni/Co species. It is the combination of the particle's atomic-scale structural/chemical ordering and the surface chemistry that determines the nanoalloy's catalytic activity. As illustrated in Figure 10.12, there are two types of catalytic surface sites for supported nanoalloys. The nanoalloy particles alone can provide Type-I sites (Co-Pt-Ni sites) involving Pt atoms for activating CO and base transition metal atoms (Ni/Co) for assisting the oxygen activation. Supports such as titania can provide catalyst-support perimeter sites (Type-II sites), which are inactive in the case of silica supports and hardly available in the case of carbon supports. The catalytic properties of Type-I sites depend on whether the nanoalloy is in reduced or oxidized state and the support-nanoalloy interaction, both of which are significantly influenced by the atomic-scale ordering and phase structures of the nanoalloy. The surface of the nanoalloy involves oxygen storage and release capacity where the transition base metals Ni/Co provide sites for the activated O^{2-} and $O^{\delta-}$ species. While both reduced and oxidized surfaces may involve Type-II sites for O_2 activation, the Type-I site for O_2 activation exists only on a reduced nanoalloy surface (a) and does not exist on the oxidized nanoalloy surface where the surface is completely blocked by the oxide species (b).

The presence of the surface sites was supported by data for CO oxidation over PtCoM (M = Ni,V) nanoalloys (Figure 10.13) (Yang et al., 2012). In Figure 10.13A, the catalytic CO reaction rates of the ternary PtNiCo/C catalyst are compared with those of the binary PtNi/C and PtCo/C in an as-prepared state. For the as-prepared catalyst, which is likely partially oxidized at the surface by air, PtNiCo has an activity higher than PtCo and PtNi. PtCo's activity is slightly higher than Pt, whereas PtNi shows almost no improvement in activity. Similar results were also obtained for the H_2-reduced catalysts. Upon reactivation *in situ* by H_2, which reduces the particles back to alloy state, the activity for the ternary catalyst shows an increase by factor of 2-3. PtCo shows the largest increase in activity (by a factor of 10-20), although this is still lower than the ternary catalyst, especially at the high reaction temperature. In contrast, PtNi shows practically no change in activity, similar to Pt.

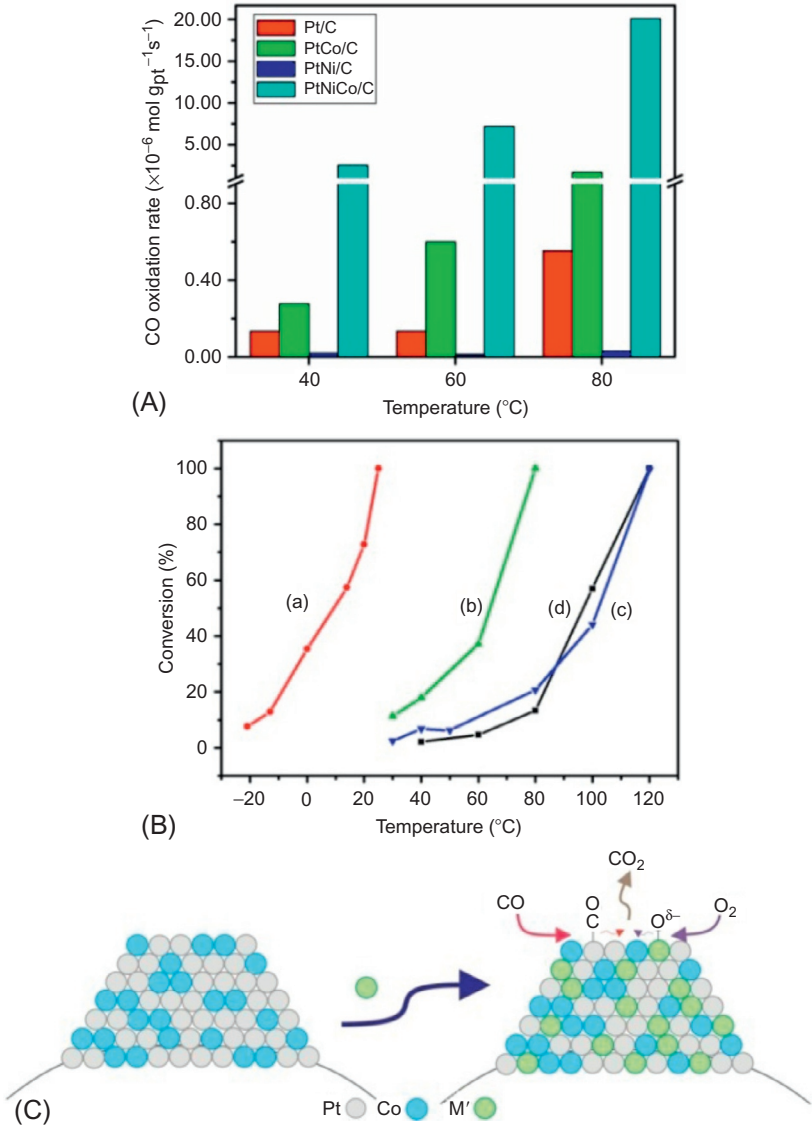

Figure 10.13 (A) Comparisons of Pt mass specific CO oxidation rates of $Pt_{39}Ni_{22}Co_{39}$/C with those of $Pt_{64}Ni_{36}$/C, $Pt_{45}Co_{55}$/C, and Pt/C catalysts in the as-prepared state.* The Pt mass-specific CO oxidation rate is normalized against the metal loading on carbon and the Pt composition in the nanoparticles. (*The as-prepared catalyst underwent "OR"-"RR" or "NR"-"RR" treatment by exposure to ambient air for an extensive period of time before catalytic measurement.) (B) Comparison of CO conversion percentage over $Pt_{45}V_{18}Co_{37}$/C (red, a), $Pt_{39}Ni_{22}Co_{39}$/C (green, b), and $Pt_{23}Ir_{29}Co_{48}$/C (blue, c) with $Pt_{55}Co_{45}$/C (black, d) catalysts. (C) A schematic illustration of the introduction of a third transition metal (M′) into PtCo nanoalloy, forming PtCoM′ nanoalloy for formation/removal of —O or —CO species in CO oxidation. Reproduced from Yang et al. (2012) and Shan et al. (2013, 2014) with permission. Copyright 2012, American Chemical Society.

Another intriguing example involves catalytic CO oxidation over PtVCo nanoalloy in comparison with those over different binary and ternary nanoalloys (Shan et al., 2013). The catalytic activity of PtVCo/C catalyst is compared with those for PtNiCo/C and PtIrCo/C catalysts (Figure 10.13B). It is evident that the PtVCo/C exhibits the highest activity, in the order PtVCo $\gg$ PtNiCo > PtIrCo $\geq$ PtCo. At RT, the activity of PtVCo/C is greater than that of PtNiCo/C by a factor of 10-20. In comparison with PtCo/C, the addition of V into the binary system leads to an increase in the activity by a factor of 10^2-10^3, whereas the addition of Ni into the binary system leads to an increase in the activity by a factor of 10-20. The addition of Ir into the binary system showed the smallest increase in the catalytic activity. The catalytic activity order appears to be consistent with the order of oxophilicity of the third transition metal (M′) in PtCoM′ (M′ = Ni, V, and Ir), which is in the order of V > Ni > Ir. The introduction of M′ with oxophilicity larger (i.e., V) than Co results in a greater enhancement to the activity than introducing a metal (i.e., Ni) with oxophilicity close to Co (Figure 10.13B). The understanding of this type of Pt-based nanoalloy properties in terms of M or M′ (Figure 10.13B) is useful for creating a bifunctional or multifunctional synergy for effectively maneuvering surface CO or oxygenated species over the M/M′ sites through structural or compositional effect.

To understand the self-tunable oxophilicity and structural integrity of PtVCo nanoalloy in comparison with PtNiCo nanoalloy catalysts, the detailed analysis of the *in situ* HE-XRD/PDF results revealed some insights. For $Pt_{45}V_{18}Co_{37}$/C nanoalloys, the fits to the atomic PDFs reveal (1) little change in lattice parameter for the CO + O_2 mixed gas, as evidenced by 3.842 Å at RT, 3.845 Å at 80 °C, and 3.844 Å when the sample is cooled back down to RT; and (2) a considerable shrinking of the lattice constant from 3.850 Å at RT to 3.848 Å at 400 °C, and to 3.831 Å when the sample is cooled back to RT under the reducing gas (H_2). A similar *in situ* experiment was performed for $Pt_{25}Ni_{16}Co_{59}$/C catalyst. Little structural change was seen when the catalyst was subjected to a gas mixture of CO and O_2 at 80 °C. In particular, the change in the lattice constant was relatively small when the temperature was changed from RT (3.885 Å) to 80 °C (3.887 Å) and then back to RT (3.886 Å). However, upon exposing to H_2 gas atmosphere at 400 °C, the change was noticeable, as evidenced by the difference of the respective lattice constants: from 3.861 Å at RT to 3.856 Å at 100 °C, then to 3.851 Å at 200 °C, 3.846 Å at 300 °C, 3.828 Å at 400 °C, and to 3.851 Å when the sample is cooled to RT. Under CO reaction conditions (80 °C, CO + O_2), the change in the lattice parameter is very small (<0.1%). Upon reductive treatment following the catalytic reaction, there is a small lattice parameter shrinking (−0.5%). It may be conjectured that the insignificant change of the lattice parameter under the catalytic reaction condition is indicative of a surface self-regulation of the oxygenated species by the second and third transition metals (V and Co) in the PtVCo nanoalloy.

The insignificant change in the lattice parameter may be one of the important factors for the significant enhancement of the catalytic activities for CO oxidation. The introduction of a third transition metal (M′ = V, Ni, Ir, etc.) into PtCo nanoalloys minimizes or suppresses changes in the lattice parameters of the nanoparticle during the catalytic processes, leading to an activity enhancement in the order of V > Ni > Ir, consistent with the order of oxophilicity of these metals. There is a significant contrast of the

lattice expansion and shrinking between $M' = V$ and Ni in the nanoalloys under the oxidation/reductive and catalytic reaction conditions. The lattice expansion and shrinking under CO oxidation condition are very small for PtVCo and PtNiCo catalysts.

10.4.2 Catalytic and electrocatalytic oxidation of alcohols

In DMFCs, a key catalytic reaction is the anode reaction, i.e., MOR:

$$CH_3OH(l) + H_2O(l) \rightarrow CO_2(g) + 6H^+(l) + 6e^- \tag{10.2}$$

In DEFCs, the key catalytic reaction is the ethanol oxidation reaction (EOR):

$$CH_3CH_2OH(l) + 3H_2O(l) \rightarrow 2CO_2(g) + 12H^+(l) + 12e^- \tag{10.3}$$

In comparison with 6 electrons for MOR in DMFCs, twelve electrons are transported through an external circuit, though the thermodynamic potential (1.15 V) is similar to that for DMFC (1.21 V). The higher energy density has the potential to significantly increase the fuel utilization and fuel cell performance, lower the cost, improve the safety, and enhance fuel sustainability.

The design and control of spatial arrangement of Au and Pt in AuPt nanoparticles are critical for exploiting the nanoscale bifunctional catalytic activity where Pt provides a site for catalyzing methanol oxidation or oxygen reduction reactions and Au provides a site for adsorption of hydroxide groups or oxidation of CO to CO_2 (Luo et al., 2008; Senanayake et al., 2013; Zhong et al., 2008). The understanding of the synergistic electrocatalytic activity of AuPt/C in MOR has been an important focus of interests in this bimetallic system (Mott et al., 2007b,c; Subhramannia and Pillai, 2008). For MOR, one of the most significant findings is that the mass activity in the alkaline electrolyte exhibits a maximum around 65-85%Au (Figure 10.14a). Considering the modeling results for CO adsorption on small clusters of AuPt for CO adsorption, the Au atoms surrounding Pt atoms in the AuPt alloy are believed to have played an important role in either removing the intermediate CO-like species and/or providing oxygenated species in the methanol oxidation process (see Figure 10.14b). This assessment is consistent with the known facts that the nanoscale Au is highly active for CO oxidation and produces surface oxygenated species in basic electrolytes. A further analysis using HE-XRD/PDF techniques (Petkov et al., 2012) has demonstrated: (i) the unchanged Pt-Pt bond distances in nanoalloy for the adsorption of methanol on Pt-Pt sites which favor the dehydrogenation; (ii) the unchanged Au-Au bond distances which help the adsorption or addition of hydroxyl groups to the intermediate CO species; and (iii) the presence of Pt-Au sites which facilitates the transfer of intermediate species from Pt and Au.

In terms of a relative Pt-specific mass activity for MOR in alkaline solution, a maximum activity is observed at Au concentration of 60-80%. Note pure Au NPs are not active for this reaction, there is no apparent indication of size and shape effect (Miller et al., 2006), and no change in Au-Au and Pt-Pt bond lengths (Kang et al., 2006; Mukarjee et al., 1995; Chou et al., 1976). Because of the difference in their

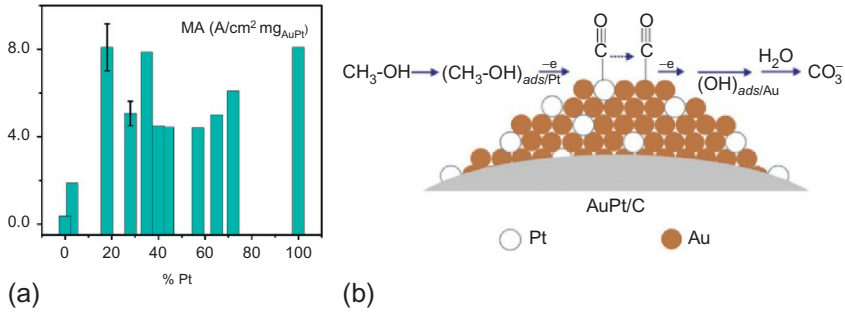

Figure 10.14 Plots of mass activity as a function of composition in alkaline electrolytes (Petkov et al., 2012; Wanjala et al., 2010a) (a) and a scheme for catalytic oxidation of methanol on carbon-supported PtAu alloy particles (b) in terms of a surface adsorption and hydrogenation of methanol (CH_3-OH)ads on Pt sites, an intermediate reaction step of C≡O transfer (marked with an arrow) from Pt to neighboring Au sites, and the addition of hydroxyl (OH) and water (H_2O) from the latter sites to the C≡O species resulting in the formation of the final carbonate product $(CO_3^{=})_{soln}$.
Reproduced from Wanjala et al. (2010a) with permission. Copyright 2010, American Chemical Society.

electronegativity, mixing of Pt and Au atoms results in small but not negligible Pt-to-Au net charge transfer (Rajasekharan and Seshubai, 2012; Tedsree et al., 2011; Berg et al., 1998). Such charge transfer will occur throughout the alloy NPs, modifying the electron density distribution of all atoms involved (Mott et al., 2007b,c; Ge et al., 2006; Galvagno and Parravano, 1979; Selvarani et al., 2009; Dai and Balasubramanian, 1994; Tian et al., 2006; Pedersen et al., 1999; Skulason et al., 2010). Note that alloying throughout the NPs is important because studies (Moussounda et al., 2010) show that not only the very top NP's layer but at least three atomic layers close to the NP's surface influence the catalytic properties. With NPs a few nm in size about 30-50% of the total numbers of atoms are in those layers. Because of the Pt-to-Au partial charge transfer, there will be an increase of the d-band vacancy at the Pt sites that may facilitate the removal of intermediate CO-like species from them toward the neighboring Au sites, greatly facilitating the formation of the carbonate ($CO_3^{=}$) product of the oxidative dehydrogenation of methanol. This synergistic effect (Figure 10.14) involves adsorption and hydrogenation of methanol (CH_3OH) on Pt sites, an intermediate step of transferring C≡O from Pt sites to neighboring Au sites, and the addition of hydroxyl and water from the latter to C≡O, resulting in the formation of the final carbonate $CO_3^{=}$ reaction product. The presence of Pt-Pt and Pt-Au pairs in the first coordination shell of Pt atoms (i.e., the complete alloying of Pt and Au) is believed to play an important role in this mechanism. In particular, the unchanged Pt-Pt bond distances in the alloy particles ensures the adsorptive dehydrogenation of methanol molecules that tend to line up with Pt-Pt bonds (Frenkel, 2012). On the other hand, the unchanged Au-Au bond distances help the adsorption and addition of hydroxyl groups to the intermediate CO-like

species. In addition, the increased d-band vacancy on the Pt sites and respective electron enrichment on Au sites facilitates the transfer of those intermediate species from Pt sites to the neighboring Au sites.

For ethanol-based fuel cells, one of the key problems is the need for highly effective catalysts, which is considered to be much more challenging than the study of catalysts for DMFCs (Zhou et al., 2004; Tadanaga et al., 2010). This is largely due to the difficulty in C-C bond cleavage for the complete oxidation of ethanol to CO_2. In addition to the extensively studied platinum catalysts, palladium-based systems have received an increased interest. The mechanism of the EOR on Pd in alkaline media is believed to involve the removal of the adsorbed ethoxi by the adsorbed hydroxyl as the rate-determining step (Dimos and Blanchard, 2010; Liang et al., 2009). Despite increasing demonstrations of the catalysts for ethanol oxidation, the understanding of the catalyst design and structures for achieving C-C cleavage of ethanol in its electrooxidation remains elusive. Two examples demonstrating the C-C bond cleavage include oxidation of ethanol to CO_2 over Pt/Rh/SnO_2 electrocatalysts in an acidic electrolyte (Kowal et al., 2009) and in alkaline solutions containing Pb(IV) acetate as a co-catalyst of Pt electrode (He et al., 2012). These studies have provided some useful information for the design of catalysts for achieving C-C bond cleavage.

The viability of catalytic activation of C-C and C-H bonds and oxygenation by PdCu alloy catalysts for EOR has recently been demonstrated (Yin et al., 2013). In the gas phase, the Pd/C catalyst shows higher catalytic activities for ethanol conversion than the PdCu/C catalyst. The activity drops upon the oxidation treatment of the catalysts. However, the alloyed catalyst shows a lower degree of decrease upon the oxidation treatment, suggesting that the fresh alloy catalyst is likely partially oxidized. The catalytic selectivity data are compared in terms of CO_2 and CH_3CHO products detected for the catalytic oxidation of ethanol over Pd/C and $Pd_{21}Cu_{79}$/C catalysts. For Pd/C, the selectivity for forming CO_2 is about the same as for forming CH_3CHO for both fresh and oxidized states. Note, however, that a significant fraction of CH_3COOH (over 50%) was detected in the gas phase along with CO_2 and CH_3CHO. In comparison, a similar trend is observed for $Pd_{21}Cu_{79}$/C, but at a higher temperature range, indicating a lower catalytic activity. However, almost no CH_3COOH was detected when CO_2 and CH_3CHO were detected. While the catalytic conversion rate is higher for Pd/C than PdCu/C, the selectivity appears to be quite different. It is evident that while aldehyde is involved in both cases, the alloy PdCu catalyst appears to suppress the formation of acetic acid, which is the significant portion of the product in the case of Pd catalyst. These differences are indicated by the relative percentages of products detected in the following reaction schemes for both oxidized catalysts (at 200 °C).

$$CH_3CH_2OH \xrightarrow{Pd/C} CO_2\,(\sim 6\%) + CH_3CH=O\,(\sim 17\%) + CH_3COOH\,(\sim 77\%) \tag{10.4}$$

$$CH_3CH_2OH \xrightarrow{PdCu/C} CO_2\,(\sim 6\%) + CH_3CH=O\,(\sim 94\%) + CH_3COOH\,(\sim 0\,(<5\%)) \tag{10.5}$$

The reaction product distribution showed a clear difference between the Pd/C and PdCu/C catalysts. No CO and H_2 were detected for PdCu catalysts.

The electrocatalytic activities for ethanol and methanol oxidation over PdCu/C catalysts are also compared. For MOR, the forward peak was at ∼−0.19 V and the backward peak was located at ∼−0.37 V. The current intensity of forward peak was four times larger than backward peak. For PdCu/C for EOR, the forward peak was at ∼−0.21 V and backward peak was located at ∼−0.30 V. The current intensity of the backward peak was about two times larger than the forward one. It is evident that the PdCu alloy catalyst showed a higher electrocatalytic activity than Pd/C for EOR but slightly lower MOR activity. This finding is intriguing because the operation of the synergy as a result of the surface enrichment of Pd on the alloy.

CO_2 was detected by analyzing the gas sample from the sealed top compartment of an electrolysis cell with a PdCu/C catalyst supported on a high-surface-area vitreous carbon electrode. The electrolysis was performed in 0.5 M KOH/0.5 M EtOH for 20-22 h. Control experiments were performed to ensure that the detected CO_2 was not from ambient air. Preliminary results from two different detection trials of CO_2 product released from the electrocatalytic oxidation of ethanol over $Pd_{21}Cu_{79}$ nanoalloy catalyst are shown in Figure 10.15.

While CO_2 was detected in both the electrolysis and control cells, the CO_2 concentration was found to be much higher from the electrolysis cell than that in the control cell. This difference was substantiated by the similar amount of water and ethanol being detected between the electrolysis and the control cells. The amount of catalysts loaded on the reticulated vitreous carbon (RVC) electrode for trial B was more than that in trial A by a factor of two. Almost no aldehyde was detected, but a trace of CH_3COOH was detected. Because CH_3COOH is soluble in the acid-treated electrolyte, the detected trace of CH_3COOH in the gas phase is a fraction of the total CH_3COOH produced, suggesting that CH_3COOH is part of the products. While quantitative aspects of the electrolysis data and the GC data are yet to be further delineated, the data did provide an indication of a CO_2 product being released from the electrolysis. This finding suggests that the electrocatalytic oxidation of ethanol involves C-C cleavage over the PdCu catalysts.

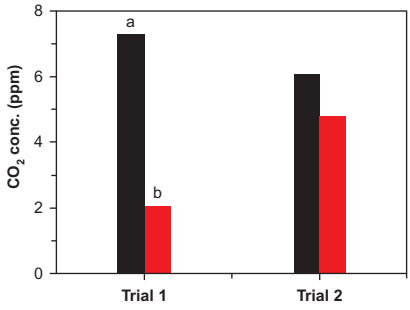

Figure 10.15 Results from two different trials (1 and 2) of detection of CO_2 product released (upon addition of acid into the electrolyte after electrolysis) from the electrocatalytic oxidation of ethanol over $Pd_{21}Cu_{79}$ nanoalloy catalyst in 0.5 M KOH/0.5 M EtOH at 0.24-0.26 V (vs. Ag/AgCl, saturated KCl) for 20-22 h. The data are determined from GC analysis of gas phase CO_2 (a, dark bar) and the charges consumed in the electrolysis (b, red bar).
Reproduced from Yin et al. (2013) with permission. Copyright 2013, American Chemical Society.

10.5 Summary and future perspectives

In summary, nanoalloy catalysts prepared by alloying Pt or Pd with a second (M) and/or third (M′) transition metal (PtM/M′) via molecularly encapsulated nanoparticle synthesis and thermochemical processing of the nanostructure exhibit enhanced catalytic activities for several reactions related to sustainable energy production and conversion, including catalytic oxidation of carbon monoxide in a gas phase and electrocatalytic reaction in a fuel cell reaction condition. In addition to the usual size, shape, and composition phenomena, the enhanced catalytic or electrocatalytic activities are linked to the unique nanoscale phenomena in terms of atomic-scale alloying, interatomic distances, metal coordination structures, structural/chemical ordering, and phase states that operate synergistically in activating oxygen and maneuvering surface oxygenated species. These structural details provide important information for the design of catalysts with high activity at significantly reduced use of noble metals (low cost), which is a sustainable pathway in green energy exploration. There are still technical issues yet to be addressed in the area of understanding how the structural synergy can be harnessed for the stability of base metals in the nanoalloy catalysts under harsh catalytic or electrocatalytic operation conditions. In addition to further investigations of the refinement of the synthesis and processing strategies, there is a clear need of *in situ* experiments for understanding the structural evolution processes such as dealloying in the electrolyte, poisoning of catalytic sites, and atomic-scale rearrangements leading to changes in size, shape, or surface energy by enrichment of certain elements in the core or shell. To determine the structural changes in these processes, studies using various *in situ* X-ray or spectroscopic techniques (Redmond et al., 2012), part of our ongoing investigation, are expected to generate some fresh insights for advancing our ability in achieving high stability of the nanoalloy catalysts by design. This ability will also be useful for creating new opportunities to explore the nanoalloy catalysts for a wide range of sustainable energy production, conversion, and storage, including oxygen evolution reaction in lithium-air batteries (Yin et al., 2012b), where the catalytic synergy of the nanoalloy plays an important role in the catalytic activity and stability.

Acknowledgments

The authors express their gratitude to former and current members of the Zhong Research Group and our collaborators who have made contributions in the last few years to the work described in this chapter. The research work was supported by the DOE-BES (DE-SC0006877), NSF (CBET-0709113, CMMI-1100736), Honda, and UTC Power.

References

Aiken, J.D., Finke, R.G., 1999. A review of modern transition-metal nanoclusters: their synthesis, characterization, and applications in catalysis. J. Mol. Catal. A: Chem. 145, 1–44.

Antolini, E., 2003. Formation of carbon-supported PtM alloys for low temperature fuel cells: a review. Mater. Chem. Phys. 78, 563–573.

Antoniak, C., 2011. Extended X-ray absorption fine structure of bimetallic nanoparticles. Beilstein J. Nanotechnol. 2, 237–251.

Bauer, J.C., Mullins, D.R., Oyola, Y., Overbury, S.H., Dai, S., 2013. Structure activity relationships of silica supported AuCu and AuCuPd alloy catalysts for the oxidation of CO. Catal. Lett. 143, 926–935.

Bazin, D., Sayers, D., Rehr, J.J., Mottet, C., 1997. Numerical simulation of the platinum L-III edge white line relative to nanometer scale clusters. J. Phys. Chem. B 101, 5332–5336.

Behafarid, F., Ono, L.K., Mostafa, S., Croy, J.R., Shafai, G., Hong, S., Rahman, T.S., Bare, S.R., Cuenya, B.R., 2012. Electronic properties and charge transfer phenomena in Pt nanoparticles on gamma-Al_2O_3: size, shape, support, and adsorbate effects. Phys. Chem. Chem. Phys. 14, 11766–11779.

Berg, C., Vevnik, H.J., Stisland, F., Ramstad, A., Borg, A., 1998. Nucleation and growth of Au overlayers on Pt(100)-hex-R0.7° studied by STM and photoelectron spectroscopy. Surf. Sci. 409, 1–15.

Bochicchio, D., Negro, F., Ferrando, R., 2013. Competition between structural motifs in gold-platinum nanoalloys. Comput. Theor. Chem. 1021, 177–182.

Brouzgou, A., Song, S.Q., Tsiakaras, P., 2012. Low and non-platinum electrocatalysts for PEMFCs: current status, challenges and prospects. Appl. Catal. B: Environ. 127, 371–388.

Brust, M., Walker, M., Bethell, D., Schiffrin, D.J., Whyman, R., 1994. Synthesis of thiol-derivatized gold nanoparticles in a 2-phase liquid-liquid system. J. Chem. Soc. Chem. Commun. 7, 801–802.

Caruso, F., 2001. Nanoengineering of particle surfaces. Adv. Mater. 13, 11–22.

Chen, M., Nikles, D.E., 2002. Synthesis, self-assembly, and magnetic properties of $Fe_xCo_yPt_{100-x-y}$ nanoparticles. Nano Lett. 2, 211–214.

Chou, T.S., Perlman, M.L., Watson, R.E., 1976. Electronegativity and electron binding in gold alloys. Phys. Rev. B 14, 3248–3250.

Cliffel, D.E., Zamborini, F.P., Gross, S.M., Murray, R.W., 2000. Mercaptoammonium-monolayer-protected, water-soluble gold, silver, and palladium clusters. Langmuir 16, 9699–9702.

Cui, C.H., Yu, S.H., 2013. Engineering interface and surface of noble metal nanoparticle nanotubes toward enhanced catalytic activity for fuel cell applications. Acc. Chem. Res. 46, 1427–1437.

Dai, D., Balasubramanian, K., 1994. Pt_3Au and PtAu clusters: electronic states and potential energy surfaces. J. Chem. Phys. 100, 4401–4407.

Dimos, M.M., Blanchard, G.J., 2010. Evaluating the role of Pt and Pd catalyst morphology on electrocatalytic methanol and ethanol oxidation. J. Phys. Chem. C 114, 6019–6026.

Duchesne, P.N., Chen, G.X., Zheng, N.F., Zhang, P., 2013. Local structure, electronic behavior, and electrocatalytic reactivity of CO-reduced platinum-iron oxide nanoparticles. J. Phys. Chem. C 117, 26324–26333.

Egami, T., Billinge, S.J.L. (Eds.), 2003. Underneath the Braggs Peak: Structural Analysis of Complex Material. Pergamon, Amsterdam, Netherlands.

El-Sayed, M.A., 2001. Some interesting properties of metals confined in time and nanometer space of different shapes. Acc. Chem. Res. 34, 257–264.

Evans, J., 1989. A specialist periodical report. In: Bond, G.C., Webb, G. (Eds.), Catalysis, vol. 8. The Royal Society of Chemistry, London, p. 1.

Feldheim, D.L., Foss Jr., C.A. (Eds.), 2002. Metal Nanoparticles: Synthesis, Characterization, and Applications. Marcel Dekker, Inc., New York.

Fernandez, J.L., Walsh, D.A., Bard, A.J., 2005. Thermodynamic guidelines for the design of bimetallic catalysts for oxygen electroreduction and rapid screening by scanning electrochemical microscopy. M-Co (M: Pd, Ag, Au). J. Am. Chem. Soc. 127, 357–365.

Ferrando, R., Jellinek, J., Johnston, R.L., 2008. Nanoalloys: from theory to applications of alloy clusters and nanoparticles. Chem. Rev. 108, 845–910.

Frenkel, A.I., 2012. Applications of extended X-ray absorption fine-structure spectroscopy to studies of bimetallic nanoparticle catalysts. Chem. Soc. Rev. 41, 8163–8178.

Galow, T.H., Drechsler, U., Hanson, J.A., Rotello, V.M., 2002. Highly reactive heterogeneous Heck and hydrogenation catalysts constructed through 'bottom-up' nanoparticle self-assembly. Chem. Commun. 10, 1076–1077.

Galvagno, S., Parravano, G., 1979. Supported Au-Pt catalysts: characterization and hydrogen transfer activity between benzene and cyclohexane. J. Catal. 57, 272–286.

Gasteiger, H.A., Kocha, S.S., Sompalli, B., Wagner, F.T., 2005. Activity benchmarks and requirements for Pt, Pt-alloy, and non-Pt oxygen reduction catalysts for PEMFCs. Appl. Catal. B Environ. 56, 9–35.

Ge, Q., Song, C., Wang, L., 2006. A density functional theory study of CO adsorption on Pt-Au nanoparticles. Comput. Mater. Sci. 35, 247–253.

Geukens, I., De Vos, D.E., 2013. Organic transformations on metal nanoparticles: controlling activity, stability, and recyclability by support and solvent interactions. Langmuir 29, 3170–3178.

Guo, S.J., Zhang, S., Sun, S.H., 2013. Tuning nanoparticle catalysis for the oxygen reduction reaction. Angew. Chem. Int. Ed. 52, 8526–8544.

Han, L., Wu, W., Kirk, F.L., Luo, J., Maye, M.M., Kariuki, N.N., Lin, Y.H., Wang, C.M., Zhong, C.J., 2004. A direct route toward assembly of nanoparticle-carbon nanotube composite materials. Langmuir 20, 6019–6025.

Haruta, M., Tsubota, S., Kobayashi, T., Kageyama, H., Genet, M.J., Delmon, B., 1993. Low-temperature oxidation of CO over gold supported on TiO_2, alpha-Fe_2O_3, and Co_3O_4. J. Catal. 144, 175–192.

He, Q., Shyam, B., Macounová, K., Krtil, P., Ramaker, D., Mukerjee, S., 2012. Dramatically enhanced cleavage of the C-C bond using an electrocatalytically coupled reaction. J. Am. Chem. Soc. 134, 8655–8661.

Hostetler, M.J., Zhong, C.J., Yen, B.K.H., Anderegg, J., Gross, S.M., Evans, N.D., Porter, M., Murray, R.W., 1998. Stable, monolayer-protected metal alloy clusters. J. Am. Chem. Soc. 120, 9396–9397.

Hostetler, M.J., Templeton, A.C., Murray, R.W., 1999. Dynamics of place-exchange reactions on monolayer-protected gold cluster molecules. Langmuir 15, 3782–3789.

Hwang, S.J., Yoo, S.J., Jang, S., Lim, T.H., Hong, S.A., Kim, S.K., 2011. Ternary Pt-Fe-Co alloy electrocatalysts prepared by electrodeposition: elucidating the roles of Fe and Co in the oxygen reduction reaction. J. Phys. Chem. C 115, 2483–2488.

Ingram, R.S., Murray, R.W., 1998. Electroactive three-dimensional monolayers: anthraquinone omega-functionalized alkanethiolate-stabilized gold clusters. Langmuir 14, 4115–4121.

Jeon, M.K., Lee, C.H., Park, G.I., Kang, K.H., 2012. Combinatorial search for oxygen reduction reaction electrocatalysts: a review. J. Power Sources 216, 400–408.

Kang, Y.J., Murray, C.B., 2010. Synthesis and electrocatalytic properties of cubic Mn-Pt nanocrystals (nanocubes). J. Am. Chem. Soc. 132, 7568–7569.

Kang, J.H., Menard, L.D., Nuzzo, R.G., Frenkel, A.I., 2006. Unusual non-bulk properties in nanoscale materials: thermal metal-metal bond contraction of γ-alumina-supported Pt catalysts. J. Am. Chem. Soc. 37, 12068–12069.

Kariuki, N.N., Luo, J., Han, L., Maye, M.M., Moussa, L., Patterson, M., Lin, Y.H., Engelhard, M.H., Zhong, C.J., 2004. Nanoparticle-structured ligand framework as electrode interfaces. Electroanalysis 16, 120–126.

Khanal, S., Casillas, G., Bhattarai, N., Velazquez-Salazar, J.J., Santiago, U., Ponce, A., Mejia-Rosales, S., Jose-Yacaman, M., 2013. CuS_2-passivated Au-core, Au_3Cu-shell nanoparticles analyzed by atomistic-resolution Cs-corrected STEM. Langmuir 29, 9231–9239.

Klabunde, K.J., Mulukutla, R.S., 2001. Chemical and catalytic aspects of nanocrytals. In: Klabunde, K.J. (Ed.), Nanoscale Materials in Chemistry. John Wiley & Sons, Inc., New York, p. 223.

Koh, S., Leisch, J., Toney, M.F., Strasser, P., 2007a. Structure-activity-stability relationships of Pt-Co alloy electrocatalysts in gas-diffusion electrode layers. J. Phys. Chem. C 111, 3744–3752.

Koh, S., Yu, C., Mani, P., Srivastava, R., Strasser, P., 2007b. Activity of ordered and disordered Pt-Co alloy phases for the electroreduction of oxygen in catalysts with multiple coexisting phases. J. Power Sources 172, 50–56.

Kowal, A., Li, M., Shao, M., Sasaki, K., Vukmirovic, M.B., Zhang, J., Marinkovic, N.S., Liu, P., Frenkel, A.I., Adzic, R.R., 2009. Ternary $Pt/Rh/SnO_2$ electrocatalysts for oxidizing ethanol to CO_2. Nat. Mater. 8, 325–330.

Kresse, G., Furthmuller, J., 1996a. Efficient iterative schemes for ab initio total-energy calculations using a plane-wave basis set. Phys. Rev. B 54, 11169–11186.

Kresse, G., Furthmuller, J., 1996b. Efficiency of ab-initio total energy calculations for metals and semiconductors using a plane-wave basis set. Comput. Mater. Sci. 6, 15–50.

Kresse, G., Hafner, J., 1993. Abinitio molecular-dynamics for liquid-metals. Phys. Rev. B 47, 558–561.

Kusada, K., Kobayashi, H., Ikeda, R., Kubota, Y., Takata, M., Toh, S., Yamamoto, T., Matsumura, S., Sumi, N., Sato, K., Nagaoka, K., Kitagawa, H., 2014. Solid solution alloy nanoparticles of immiscible Pd and Ru elements neighboring on Rh: changeover of the thermodynamic behavior for hydrogen storage and enhanced CO-oxidizing ability. J. Am. Chem. Soc. 136, 1864–1871.

Leppert, L., Albuquerque, R.Q., Foster, A.S., Kummel, S., 2013. Interplay of electronic structure and atomic mobility in nanoalloys of Au and Pt. J. Phys. Chem. C 117, 17268–17273.

Li, H., Luk, Y.Y., Mrksich, M., 1999. Catalytic asymmetric dihydroxylation by gold colloids functionalized with self-assembled monolayers. Langmuir 15, 4957–4959.

Liang, Z.X., Zhao, T.S., Xu, J.B., Zhu, L.D., 2009. Mechanism study of the ethanol oxidation reaction on palladium in alkaline media. Electrochim. Acta 54, 2203–2208.

Liao, M.Y., Hu, Q., Zheng, J.B., Li, Y.H., Zhou, H., Zhong, C.J., Chen, B.H., 2013. Pd decorated Fe/C nanocatalyst for formic acid electrooxidation. Electrochim. Acta 111, 504–509.

Lim, B., Jiang, M.J., Camargo, P.H.C., Cho, E.C., Tao, J., Lu, X.M., Zhu, Y.M., Xia, Y.N., 2009. Pd-Pt bimetallic nanodendrites with high activity for oxygen reduction. Science 324, 1302–1305.

Liu, L.C., Gu, X.R., Cao, Y., Yao, X.J., Zhang, L., Tang, C.J., Gao, F., Dong, L., 2013a. Crystal-plane effects on the catalytic properties of Au/TiO_2. ACS Catal. 3, 2768–2775.

Liu, X.Y., Wang, A.Q., Zhang, T., Mou, C.Y., 2013b. Catalysis by gold: new insights into the support effect. Nano Today 8, 403–416.

Long, N.V., Yang, Y., Thi, C.M., Minh, N.V., Cao, Y.Q., Nogami, M., 2013. The development of mixture, alloy, and core-shell nanocatalysts with nanomaterial supports for energy conversion in low-temperature fuel cells. Nano Energy 2, 636–676.

Loukrakpam, R., Shan, S.Y., Petkov, V., Yang, L.F., Luo, J., Zhong, C.J., 2013. Atomic ordering enhanced electrocatalytic activity of nanoalloys for oxygen reduction reaction. J. Phys. Chem. C 117, 20715–20721.

Luo, J., Han, L., Kariuki, N.N., Wang, L.Y., Mott, D., Zhong, C.J., He, T., 2005a. Synthesis and characterization of monolayer-capped PtVFe nanoparticles with controllable sizes and composition. Chem. Mater. 17, 5282–5290.

Luo, J., Maye, M.M., Petkov, V., Kariuki, N.N., Wang, L.Y., Njoki, P., Mott, D., Lln, Y., Zhong, C.J., 2005b. Phase properties of carbon-supported gold-platinum nanoparticles with different bimetallic compositions. Chem. Mater. 17, 3086–3091.

Luo, J., Njoki, P.N., Lin, Y., Wang, L.Y., Zhong, C.J., 2006a. Activity-composition correlation of AuPt alloy nanoparticle catalysts in electrocatalytic reduction of oxygen. Electrochem. Commun. 8, 581–587.

Luo, J., Kariuki, N., Han, L., Wang, L.Y., Zhong, C.J., He, T., 2006b. Preparation and characterization of carbon-supported PtVFe electrocatalysts. Electrochim. Acta 51, 4821–4827.

Luo, J., Wang, L., Mott, D., Njoki, P.N., Lin, Y., He, T., Xu, Z., Wanjana, B.N., Lim, I.I.S., Zhong, C.J., 2008. Core/shell nanoparticles as electrocatalysts for fuel cell reactions. Adv. Mater. 20, 4342–4347.

Malis, O., Radu, M., Mott, D., Wanjala, B., Luo, J., Zhong, C.J., 2009. An in situ real-time X-ray diffraction study of phase segregation in Au-Pt nanoparticles. Nanotechnology 20, 245708.

Maye, M.M., Zhong, C.J., 2000. Manipulating core-shell reactivities for processing nanoparticle sizes and shapes. J. Mater. Chem. 10, 1895–1901.

Maye, M.M., Lou, Y.B., Zhong, C.J., 2000. Core-shell gold nanoparticle assembly as novel electrocatalyst of CO oxidation. Langmuir 16, 7520–7523.

Miller, J., Kropf, A., Zha, Y., Regalbuto, J., Delannoy, L., Louis, C., Bus, E., Vanbokhoven, J., 2006. The effect of gold particle size on Au-Au bond length and reactivity toward oxygen in supported catalysts. J. Catal. 240, 222–234.

Morrow, B.H., Striolo, A., 2010. Supported bimetallic Pt-Au nanoparticles: structural features predicted by molecular dynamics simulations. Phys. Rev. B 81, 155437.

Mott, D., Galkowski, J., Wang, L.Y., Luo, J., Zhong, C.J., 2007a. Synthesis of size-controlled and shaped copper nanoparticles. Langmuir 23, 5740–5745.

Mott, D., Luo, J., Njoki, P.N., Lin, Y., Wang, L.Y., Zhong, C.J., 2007b. Synergistic activity of gold-platinum alloy nanoparticle catalysts. Catal. Today 122, 378–385.

Mott, D., Luo, J., Smith, A., Njoki, P.N., Wang, L.Y., Zhong, C.J., 2007c. Nanocrystal and surface alloy properties of bimetallic gold-platinum nanoparticles. Nanoscale Res. Lett. 2, 12–16.

Mott, D., Yin, J., Engelhard, M., Loukrakpam, R., Chang, P., Miller, G., Bae, I.T., Das, N.C., Wang, C.M., Luo, J., Zhong, C.J., 2010. From ultrafine thiolate-capped copper nanoclusters toward copper sulfide nanodiscs: a thermally activated evolution route. Chem. Mater. 22, 261–271.

Moussounda, P.S., Haroun, M.F., Legare, P., 2010. Adsorption of methanol and atomic oxygen on the Pt(100) surface: a first-principles periodic density functional theory study. Phys. Scr. 81, 045603–045605.

Mukarjee, S., Srinivasan, S., Soriaga, M., 1995. Role of structural and electronic properties of Pt and Pt alloys on electrocatalysis of oxygen reduction. J. Electrochem. Soc. 142, 1409–1422.

Narayanan, R., El-Sayed, M.A., 2003. Effect of catalysis on the stability of metallic nanoparticles: Suzuki reaction catalyzed by PVP-palladium nanoparticles. J. Am. Chem. Soc. 125, 8340–8347.

Newville, M., 2004. Fundamentals of XAFS, Consortium for Advanced Radiation Sources. University of Chicago, Chicago, IL.

Nishimura, S., Anh, D.T.N., Mott, D., Ebitani, K., Maenosono, S., 2012. X-ray absorption near-edge structure and X-ray photoelectron spectroscopy studies of interfacial charge transfer in gold-silver-gold double-shell nanoparticles. J. Phys. Chem. C 116, 4511–4516.

Niu, Y.H., Crooks, R.M., 2003. Preparation of dendrimer-encapsulated metal nanoparticles using organic solvents. Chem. Mater. 15, 3463–3467.

Norskov, J.K., Rossmeisl, J., Logadottir, A., Lindqvist, L., Kitchin, J.R., Bligaard, T., Jonsson, H., 2004. Origin of the overpotential for oxygen reduction at a fuel-cell cathode. J. Phys. Chem. B 108, 17886–17892.

Oxford, S.M., Lee, P.L., Chupas, P.J., Chapman, K.W., Kung, M.C., Kung, H.H., 2010. Study of supported PtCu and PdAu bimetallic nanoparticles using in-situ X-ray tools. J. Phys. Chem. C 114, 17085–17091.

Paulus, U.A., Endruschat, U., Feldmeyer, G.J., Schmidt, T.J., Bonnemann, H., Behm, R.J., 2000. New PtRu alloy colloids as precursors for fuel cell catalysts. J. Catal. 195, 383–393.

Paulus, U.A., Wokaun, A., Scherer, G.G., Schmidt, T.J., Stamenkovic, V., Radmilovic, V., Markovic, N.M., Ross, P.N., 2002. Oxygen reduction on carbon-supported Pt-Ni and Pt-Co alloy catalysts. J. Phys. Chem. B 106, 4181–4191.

Pedersen, M.O., Helveg, S., Ruban, A., Stensgaard, I., Legsgaard, E., Norskov, J.K., Besenbacher, F., 1999. How a gold substrate can increase the reactivity of a Pt overlayer. Surf. Sci. 426, 395–409.

Peng, X.G., Schlamp, M.C., Kadavanich, A.V., Alivisatos, A.P., 1997. Epitaxial growth of highly luminescent CdSe/CdS core/shell nanocrystals with photostability and electronic accessibility. J. Am. Chem. Soc. 119, 7019–7029.

Petkov, V., 2008. Nanostructure by high-energy X-ray diffraction. Mater. Today 11, 28–38.

Petkov, V., 2009. 3D structure of nanosized catalysts by high-energy X-ray diffraction. Synch. Rad. News 22, 29–33.

Petkov, V., Jeong, I.K., Chung, J.S., Thorpe, M.F., Kycia, S., Billinge, S.J.L., 1999. High real-space resolution measurement of the local structure of $Ga_{1-x}In_xAs$ using X-ray diffraction. Phys. Rev. Lett. 83, 4089–4092.

Petkov, V., Billinge, S.J.L., Heising, J., Kanatzidis, M.G., 2000. Application of atomic pair distribution function analysis to materials with intrinsic disorder. Three-dimensional structure of exfoliated-restacked WS2: not just a random turbostratic assembly of layers. J. Am. Chem. Soc. 122, 11571–11776.

Petkov, V., Wanjala, B.N., Loukrakpam, R., Luo, J., Yang, L.F., Zhong, C.J., Shastri, S., 2012. Pt-Au alloying at the nanoscale. Nano Lett. 12, 4289–4299.

Petkov, V., Ren, Y., Shan, S.Y., Luo, J., Zhong, C.J., 2014. A distinct atomic structure-catalytic activity relationship in 3-10 nm supported Au particles. Nanoscale 6, 532–538.

Philip, R., Chantharasupawong, P., Qian, H.F., Jin, R.C., Thomas, J., 2012. Evolution of nonlinear optical properties: from gold atomic clusters to plasmonic nanocrystals. Nano Lett. 12, 4661–4667.

Qian, H.F., Zhu, M.Z., Wu, Z.K., Jin, R.C., 2012. Quantum sized gold nanoclusters with atomic precision. Acc. Chem. Res. 45, 1470–1479.

Raja, R., Khimyak, T., Thomas, J.M., Hermans, S., Johnson, B.F.G., 2001. Single-step, highly active, and highly selective nanoparticle catalysts for the hydrogenation of key organic compounds. Angew. Chem. Int. Ed. 40, 4638–4642.

Rajasekharan, T., Seshubai, V., 2012. Charge transfer on the metallic atom-pair band, and the crystal structures adopted by intermetallic compounds. Acta Crystallogr. A 68, 68–76 (published online).

Redmond, E.L., Setzler, B.P., Juhas, P., Billinge, S.J.L., Fuller, T.F., 2012. In-situ monitoring of particle growth at PEMFC cathode under accelerated cycling conditions. Electrochem. Solid-State Lett. 15, B72–B74.

Rietveld, H.M., 1969. A profile refinement method for nuclear and magnetic structures. J. Appl. Crystallogr. 2, 65–71.

Schadt, M.J., Cheung, W., Luo, J., Zhong, C.J., 2006. Molecularly tuned size selectivity in thermal processing of gold nanoparticles. Chem. Mater. 18, 5147–5149.
Schmid, G., Maihack, V., Lantermann, F., Peschel, S., 1996. Ligand-stabilized metal clusters and colloids: properties and applications. J. Chem. Soc. Dalton Trans. 7, 589–595.
Schmidt, T.J., Gasteiger, H.A., Behm, R.J., 1999. Methanol electrooxidation on a colloidal PtRu-alloy fuel-cell catalyst. Electrochem. Commun. 1, 1–4.
Selvarani, G., Selvaganesh, S.V., Krishnamurthy, S., Kiruthika, G.V.M., Sridhar, P., Pitchumani, S., Shukla, A.K., 2009. A methanol-tolerant carbon-supported Pt-Au alloy cathode catalyst for direct methanol fuel cells and its evaluation by DFT. J. Phys. Chem. C 113, 7461–7468.
Senanayake, S.D., Stacchiola, D., Rodriguez, J.A., 2013. Unique properties of ceria nanoparticles supported on metals: novel inverse ceria/copper catalysts for CO oxidation and the water-gas shift reaction. Acc. Chem. Res. 46, 1702–1711.
Shan, S.Y., Petkov, V., Yang, L.F., Mott, D., Wanjala, B.N., Cai, F., Chen, B.H., Luo, J., Zhong, C.J., 2013. Oxophilicity and structural integrity in maneuvering surface oxygenated species on nanoalloys for CO oxidation. ACS Catal. 3, 3075–3085.
Shan, S., Petkov, V., Yang, L.F., Luo, J., Joseph, P., Mayzel, D., Prasai, B., Wang, L., Engelhard, M., Zhong, C.J., 2014. Atomic-structural synergy for catalytic CO oxidation over palladium-nickel nanoalloys. J. Am. Chem. Soc. 136, 7140–7151.
Shukla, A.K., Raman, R.K., 2003. Methanol-resistant oxygen-reduction catalysts for direct methanol fuel cells. Annu. Rev. Mater. Res. 33, 155–168.
Singh, A.K., Xu, Q., 2013. Synergistic catalysis over bimetallic alloy nanoparticles. ChemCatChem 5, 652–676.
Skulason, E., Tripkovic, V., Bjorketun, M.E., Gudmundsdottir, S., Karlberg, G., Rossmeisl, J., Bligaard, Th., Jonsson, H., Norskov, J.K., 2010. Modeling the electrochemical hydrogen oxidation reaction on the basis of density functional theory calculations. J. Phys. Chem. C 114, 18182–18197.
Storhoff, J.J., Mirkin, C.A., 1999. Programmed materials synthesis with DNA. Chem. Rev. 99, 1849–1862.
Subhramannia, M., Pillai, V.K., 2008. Shape-dependent electrocatalytic activity of platinum nanostructures. J. Mater. Chem. 18, 5858–5870.
Sun, S.H., Murray, C.B., Weller, D., Folks, L., Moser, A., 2000. Monodisperse FePt nanoparticles and ferromagnetic FePt nanocrystal superlattices. Science 287, 1989–1992.
Sun, S.H., Fullerton, E.E., Weller, D., Murray, C.B., 2001. Compositionally controlled FePt nanoparticle materials. IEEE Trans. Magn. 37, 1239–1243.
Tadanaga, K., Furukawa, Y., Hayashi, A., Tatsumisago, M., 2010. Direct ethanol fuel cell using hydrotalcite clay as a hydroxide ion conductive electrolyte. Adv. Mater. 22, 4401–4404.
Tedsree, K., Chan, C.W.A., Jones, S., Cuan, Q., Li, W.K., Gong, X.Q., Tsang, S.C.E., 2011. ^{13}C NMR guides rational design of nanocatalysts via chemisorption evaluation in liquid phase. Science 332, 224–228.
Templeton, A.C., Wuelfing, M.P., Murray, R.W., 2000. Monolayer protected cluster molecules. Acc. Chem. Res. 33, 27–36.
Tian, W.Q., Ge, M., Gu, F., Yamada, T., Aoki, Y., 2006. Binary clusters AuPt and Au6Pt: structure and reactivity within density functional theory. J. Phys. Chem. A 110, 6285–6293.
Ting, J.M., Navale, T.S., Bates, F.S., Reineke, T.M., 2013. Precise compositional control and systematic preparation of multimonomeric statistical copolymers. ACS Macro Lett. 2, 770–774.

Wang, C., Daimon, H., Onodera, T., Koda, T., Sun, S.H., 2008. A general approach to the size- and shape-controlled synthesis of platinum nanoparticles and their catalytic reduction of oxygen. Angew. Chem. Int. Ed. 47, 3588–3591.

Wang, L.C., Williams, J.I., Lin, T., Zhong, C.J., 2011. Spontaneous reduction of O_2 on PtVFe nanocatalysts. Catal. Today 165, 150–159.

Wang, C., Markovic, N.M., Stamenkovic, V.R., 2012. Advanced platinum alloy electrocatalysts for the oxygen reduction reaction. ACS Catal. 2, 891–898.

Wanjala, B.N., Luo, J., Loukrakpam, R., Fang, B., Mott, D., Njoki, P.N., Engelhard, M., Naslund, H.R., Wu, J.K., Wang, L.C., Malis, O., Zhong, C.J., 2010a. Nanoscale alloying, phase-segregation, and core-shell evolution of gold-platinum nanoparticles and their electrocatalytic effect on oxygen reduction reaction. Chem. Mater. 22, 4282–4294.

Wanjala, B.N., Loukrakpam, R., Luo, J., Njoki, P.N., Mott, D., Zhong, C.J., Shao, M.H., Protsailo, L., Kawamura, T., 2010b. Thermal treatment of PtNiCo electrocatalysts: effects of nanoscale strain and structure on the activity and stability for the oxygen reduction reaction. J. Phys. Chem. C 114, 17580–17590.

Wanjala, B.N., Luo, J., Fang, B., Mott, D., Zhong, C.J., 2011. Gold-platinum nanoparticles: alloying and phase segregation. J. Mater. Chem. 21, 4012–4020.

Wanjala, B.N., Fang, B., Shan, S.Y., Petkov, V., Zhu, P.Y., Loukrakpam, R., Chen, Y.S., Luo, J., Yin, J., Yang, L.F., Shao, M.H., Zhong, C.J., 2012a. Design of ternary nanoalloy catalysts: effect of nanoscale alloying and structural perfection on electrocatalytic enhancement. Chem. Mater. 24, 4283–4293.

Wanjala, B.N., Fang, B., Loukrakpam, R., Chen, Y.S., Engelhard, M., Luo, J., Yin, J., Yang, L. F., Shan, S.Y., Zhong, C.J., 2012b. Role of metal coordination structures in enhancement of electrocatalytic activity of ternary nanoalloys for oxygen reduction reaction. ACS Catal. 2, 795–806.

Waseda, Y., 1980. The Structure of Noncrystalline Materials: Liquid and Amorphous Solids. McGraw-Hill, New York.

Waszczuk, P., Lu, G.Q., Wieckowski, A., Lu, C., Rice, C., Masel, R.I., 2002. UHV and electrochemical studies of CO and methanol adsorbed at platinum/ruthenium surfaces, and reference to fuel cell catalysis. Electrochim. Acta 47, 3637–3652.

Watanabe, M., Tsurumi, K., Mizukami, T., Nakamura, T., Stonehart, P., 1994. Activity and stability of ordered and disordered Co-Pt alloys for phosphoric-acid fuel-cells. J. Electrochem. Soc. 141, 2659–2668.

Watanabe, M., Tryk, D.A., Wakisaka, M., Yano, H., Uchida, H., 2012. Overview of recent developments in oxygen reduction electrocatalysis. Electrochim. Acta 84, 187–201.

Whetten, R.L., Khoury, J.T., Alvarez, M.M., Murthy, S., Vezmar, I., Wang, Z.L., Stephens, P. W., Cleveland, C.L., Luedtke, W.D., Landman, U., 1996. Nanocrystal gold molecules. Adv. Mater. 8, 428–433.

Wu, J.B., Yang, H., 2013. Platinum-based oxygen reduction electrocatalysts. Acc. Chem. Res. 46, 1848–1857.

Xiao, S., Hu, W., Luo, W., Wu, Y., Li, X., Deng, H., 2006. Size effect on alloying ability and phase stability of immiscible bimetallic nanoparticles. Eur. Phys. J. B 54, 479–484.

Yang, H., Vogel, W., Lamy, C., Alonso-Vante, N., 2004. Structure and electrocatalytic activity of carbon-supported Pt-Ni alloy nanoparticles toward the oxygen reduction reaction. J. Phys. Chem. B 108, 11024–11034.

Yang, L.F., Shan, S.Y., Loukrakpam, R., Petkov, V., Ren, Y., Wanjala, B.N., Engelhard, M.H., Luo, J., Yin, J., Chen, Y.S., Zhong, C.J., 2012. Role of support-nanoalloy interactions in the atomic-scale structural and chemical ordering for tuning catalytic sites. J. Am. Chem. Soc. 134, 15048–15060.

Yin, J., Shan, S.Y., Yang, L.F., Mott, D., Malis, O., Petkov, V., Cai, F., Ng, M.S., Luo, J., Chen, B.H., Engelhard, M., Zhong, C.J., 2012a. Gold-copper nanoparticles: nanostructural evolution and bifunctional catalytic sites. Chem. Mater. 24, 4662–4674.

Yin, J., Fang, B., Luo, J., Wanjala, B., Mott, D., Loukrakpam, R., Ng, M.S., Li, Z., Hong, J., Whittingham, M.S., Zhong, C.J., 2012b. Nanoscale alloying effect of gold-platinum nanoparticles as cathode catalysts on the performance of a rechargeable lithium-oxygen battery. Nanotechnology 23, 305404.

Yin, J., Shan, S.Y., Ng, M.S., Yang, L.F., Mott, D., Fang, W.Q., Kang, N., Luo, J., Zhong, C.J., 2013. Catalytic and electrocatalytic oxidation of ethanol over palladium-based nanoalloy catalysts. Langmuir 29, 9249–9258.

Zhang, J., Sasaki, K., Sutter, E., Adzic, R.R., 2007. Stabilization of platinum oxygen-reduction electrocatalysts using gold clusters. Science 315, 220–222.

Zhang, Y.H., Duan, Z.Y., Xiao, C., Wang, G.F., 2011. Density functional theory calculation of platinum surface segregation energy in Pt_3Ni (111) surface doped with a third transition metal. Surf. Sci. 605, 1577–1582.

Zhong, C.J., Maye, M.M., 2001. Core-shell assembled nanoparticles as catalysts. Adv. Mater. 13, 1507–1511.

Zhong, C.J., Regalbuto, J.R., 2013. Schloegl, R., Niemantsverdriet, J.W. (Eds.), "Metal Nanoparticle Synthesis", Chapter in Comprehensive Inorganic Chemistry II, vol. 7. Elsevier, pp. 75–102 (Chapter 4).

Zhong, C.J., Luo, J., Njoki, P.N., Mott, D., Wanjala, B., Loukrakpam, R., Lim, S., Wang, L., Fang, B., Xu, Z.C., 2008. Fuel cell technology: nano-engineered multimetallic catalysts. Energy Environ. Sci. 1, 454–466.

Zhong, C.J., Luo, J., Fang, B., Wanjala, B.N., Njoki, P.N., Loukrakpam, R., Yin, J., 2010. Nanostructured catalysts in fuel cells. Nanotechnology 21, 062001.

Zhou, W.J., Zhou, B., Li, W.Z., Song, S.Q., Sun, G.Q., Xin, Q., Douvartzides, S., Goula, M., Tsiakaras, P., 2004. Performance comparison of low-temperature direct alcohol fuel cells with different anode catalysts. J. Power Sources 126, 16–22.

Physical approaches to tuning luminescence process of colloidal quantum dots and applications in optoelectronic devices

11

H. Wu[1], *L. Hu*[2]
[1]Zhejiang University, Hangzhou, PR China; [2]Jiangnan University, Wuxi, PR China

11.1 Introduction

Semiconductor colloidal quantum dots (CQDs) as fluorescent materials have attracted much attention in optoelectronics, biotechnology, and fundamental research because of their tunable small sizes, high quantum yields (QYs), and low fabrication cost. In the past two decades a number of semiconductor CQDs have been successfully synthesized, characterized, and applied. They include the II-VI semiconductor CQDs, CdX (Mattoussi et al., 2000; Qu et al., 2001; Xie et al., 2005; Gaponik et al., 2002), HgTe (Rogach et al., 1999), ZnX (X = S and O) (Chen et al., 2004; Wong and Searson, 1999; Radovanovic et al., 2002); the IV-VI semiconductor CQDs, PbX (Yang et al., 2013; Wehrenberg et al., 2002; Hines and Scholes, 2003; Murphy et al., 2006) (X = S, Se, and Te); the III-V semiconductor CQDs, InP (Micic et al., 1994), and InAs (Schaller et al., 2007); the IV semiconductor CQDs, Si (Biteen et al., 2006; Mangolini and Kortshagen, 2007; Beard et al., 2007), and Ge (Heath et al., 1994). Other typical chalcogenide semiconductor CQDs are $CuInS_2$ (Zhong et al., 2008; Kruszynska et al., 2010; Tan et al., 2011), $CuInGaSe_2$ (Tang et al., 2008), $CuZnSnS_4$ (Steinhagen et al., 2009; Khare et al., 2011), and Ag_2S (Brelle et al., 1999). Some reviews and books on the synthesis and chemical and physical properties of the semiconductor CQDs have been published (Murray et al., 2000; Efros and Rosen, 2000; Burda et al., 2005; Jun et al., 2006; Cozzoli et al., 2006; Rogach et al., 2007; Reiss et al., 2009; Gaponik et al., 2010). For example, the developments in the shape control of CQDs with a focus on the scientifically and technologically important semiconductor and metal oxide nanocrystals obtained by nonhydrolytic synthetic methods were reviewed by Jun et al. (2006). The advances in the synthesis of CQDs, with emphasis on the strategies followed for the fabrication of nano-heterostructures, as well as on their properties, were surveyed by Cozzoli et al. (2006). The reviews on synthesis, assembly, optical properties, and applications for infrared-emitting semiconductor CQDs, including HgTe, $Cd_xHg_{1-x}Te$, InP, InAs, PbX (X = S, Se, and Te) were made by Rogach et al. (2007). The fundamental properties and synthesis methods of core-shell and

Modeling, Characterization and Production of Nanomaterials. http://dx.doi.org/10.1016/B978-1-78242-228-0.00011-9
Copyright © 2015 Elsevier Ltd. All rights reserved.

core-multiple shell structures for the II-VI, IV-VI, and III-V semiconductors CQDs were reviewed by Reiss et al. (2009). Progress in the synthetic efforts to improve light emission efficiencies and stability of the CQDs was addressed by Eychmüller and coworkers (Gaponik et al., 2010).

In 1993, Murray et al. proposed a hot-injection route for the synthesis of CQDs, which has been widely used to fabricate monodisperse CQDs for 20 years (Murray et al., 1993). In this approach, the mixture of metal precursor dimethylcadmium ($CdMe_2$) and chalcogen precursor trioctylphosphine selenide (TOPSe) was swiftly injected into trioctylphosphine oxide at high temperature (more than 300 °C) for CdSe nucleation. The growth of the CQDs was controlled by changing the synthesis temperature and times. This approach facilely separated the size-focusing growth process from burst nucleation, which was considered as the key for the monodisperse products (Murray et al., 1995, 2000). In 1996, Hines and Guyot-Sionnest successfully overcoated the CdSe CQD's surface with a ZnS shell by adding the Zn and S precursors into the CdSe solution to form the ZnS on the present CdSe surface (Hines and Guyot-Sionnest, 1996). The ZnS shell well passivated the dangling bonds of the surface atoms of CdSe QDs, which strongly suppressed the surface defects of the CdSe cores. Because the ZnS material had wider bandgap than CdSe, the ZnS shell also provided energy barriers for the electrons and holes in the CdSe cores that enhanced the recombination of core excitons. Additionally, the wide bandgap ZnS shell has higher stability than the core material. The realized final CdSe/ZnS core-shell QDs demonstrated the luminescent QYs of ~50%, a huge improvement (~10-fold) compared to the initial CdSe cores. Beginning in 2001, Peng and coworkers used relatively low hazard CdO to form the Cd precursor (1-octadecene (ODE) as the noncoordinating solvents with a high boiling point) and introduced the successive ion layer adsorption and reaction route for preparing the CQDs with a high-quality core-shell structure (Peng and Peng, 2001, 2002; Yu and Peng, 2002; Li et al., 2003). Thereafter, the hot-injection routes of CQD preparation became more complete and mature, and various kinds of high-quality CQDs have been produced.

The semiconductor CQDs have been successfully applied in many fields since the hot-injection routes became mature, such as biomedical technologies, lighting, and display. Surveys of semiconductor CQDs for the applications in nano-biotechnology have already been conducted by some groups (Penn et al., 2003; Parak et al., 2003; Pellegrino et al., 2005; Qian and Nie, 2008). The CQDs as quantitation tags were reviewed by Penn et al. (2003). Surface enhanced Raman scattering CQDs tags have been developed that are capable of providing detailed spectroscopic information and are much brighter than semiconductor CQDs in the near-infrared spectral window (Qian and Nie, 2008). CQDs also demonstrated potential applications in the next generation of optoelectronic technologies. A review was made by Sargent on the progress and prospects for infrared photovoltaics made by CQDs, focusing on new insights into how QD solar cells operate and how these findings give guidance to optimizing their full performance potential (Sargent, 2009). The multiple exciton generation phenomenon recently discovered in semiconductor CQDs and its applications to third-generation photovoltaic solar cells were summarized by

Nozik et al. (2010). Tang et al. summarized progress both in device operation and in gaining new insights into materials properties and processing, including new electrical contact materials and deposition techniques, surface treatments, and film-forming technologies that underpin these rapid advances (Tang and Sargent, 2011). CQD tandem solar cells using the size-effect tuning of a single PbS CQD material was recently reported by Wang et al. in which a graded recombination layer was used to provide a progression of work functions from the hole-accepting electrode in the bottom cell to the electron-accepting electrode in the top cell, allowing matched electron and hole currents to meet and recombine (Wang et al., 2011). Stable and efficient CQD light-emitting diodes (LEDs) based on solution-processed multilayer structures have been realized by Qian et al. (2011). Zhang et al. (2011) reported on the design and fabrication of solution-processed white LEDs containing a bilayer of heavy metal-free CQDs and polymer in the device active region. Shirasaki et al. addressed the potential of optically and electrically excited QDs for high-color-quality lighting and display technologies, discussed the key advantages of using CQDs as luminophores in LEDs, and outlined the operating mechanisms of four types of QD-LED (Shirasaki et al., 2013).

As the most typical zero-dimension materials, the CQDs have large surface-to-volume ratio; consequently, CQD surface greatly impacts the optical and electric properties. The surface-related trap states (called surface states) located between the valence band and the conduction band of CQDs originate from the dangling bonds and the vacancies of surface atoms (Spanhel et al., 1987; Underwood et al., 2001; Jasieniak and Mulvaney, 2007; Smith and Nie, 2009). The surface states are the natural and intrinsic defect states in the electronic structure of CQDs, and they are usually regarded as nonradiative recombination centers in QD electron states. However, a portion of surface states, called surface states emission (SSE), are radiative. SSE usually displays a broad emission tail with longer wavelength relative to the band-edge emission (BEE), which has been observed in many CQDs. The broad SSE weakens the color purity of CQD emission, thus the radiative surface states are often purposely suppressed for high purity luminescence. On the contrary, the broad SSE combined with BEE can be used to form an expected emission color, such as white light emission (WLE) (Shirasaki et al., 2013; Hu and Wu, 2013). From this point of view, it is a key issue to precisely tune and control both BEE and SSE of CQDs in the postsynthesis and understand their behaviors.

In this chapter, three physical approaches for modifying of BEE and SSE of CQDs are presented, including thermal annealing, photooxidation, and surface plasmon coupling. The combination of these physical operations can be applied for designed luminescence color. Colloidal CdSe QDs that demonstrated intense BEE and SSE emissions were synthesized and embedded in PMMA. Results show that the CQDs-PMMA composites demonstrated evident enhancement of surface-state-related emissions while annealing of QDs-PMMA composites led to intensity quench of the band-band emission. The annealing process also caused the red shift of band-band emissions. By contrast, photooxidation of QDs-PMMA composites resulted in blue shifts accompanied by the remarkable enhancement of luminescence intensity

(Hu et al., 2011). Furthermore, it was found in the photooxidation process that the SSE was saturated earlier than the BEE, which renders it possible to tune the color of the emission. We then have synthesized the WLE CdSe QDs capped with oleic acid (OA) in ODE, a noncoordination solvent. The small CdSe QDs capped with OA have the BEE in blue light range and broad SSE spanning the whole visible spectrum. The thermal annealing effect of the CdSe QDs immobilized in PMMA (PMMA-QD composite) was also studied, and bimodal size-distribution properties were observed in photoluminescence (PL) spectra (Hu and Wu, 2013). The combination of annealing and photooxidation passivation could provide an effective way to precisely tune the colors of light-emitting devices that use CQDs. We will introduce distinct enhancement of the SSEs of CQDs via coupling the CQD emitters with localized plasmons (LPs) excited on silver (Ag) nanostructures (Hu et al., 2012a). It was found that the OA ligand on the CQDs plays a critical role in the intense luminescence enhancement of the CQDs/Ag nanostructures, and annealing of the CQDs/Ag hybrid structure greatly affects the features of SSEs. OA on the CQDs modifies the morphology of Ag films and leads to the formation of metal crystals. With this new approach of OA reshaping Ag particles and consequent realization of intense luminescence enhancement, the luminescence colors of CQDs layers could be changed selectively, and microscale luminescence color patterns were demonstrated (Hu et al., 2012b). Light-emitting diodes based on CQDs (QD-LEDs) were developed in which inorganic ZnSnO and organic TPD thin films were used as the electron-transporting layer (ETL) and hole-transporting layer (HTL), respectively (Liu et al., 2013).

11.2 Annealing effect on the luminescence of CQDs and WLE by single-size CQDs

It is known that small QDs have large surface/volume ratios, and surface defects greatly impact on the optoelectronic properties. Studies showed SSEs of CQDs could be potentially applied in white LEDs because the radiative emissions of surface states (SSs) are just at visible light region and display a variable broad emission band (Schreuder et al., 2010; Baker and Kamat, 2010; Bowers et al., 2005). Nizamoglu et al. synthesized CdS CQDs with a broad SSE that spanned the entire visible spectrum (Nizamoglu et al., 2008). Baker et al. tuned the SSEs and the intensity ratio of BEE to SSE of the CdSe CQDs via modulating the 3-mecaptopropionic acid (MPA) concentration, thereby obtaining different fluorescence colors (Baker and Kamat, 2010). In contrast, for other applications light emission from SSs of the CQDs should be avoided or suppressed carefully to obtain high radiative rates of conduction-band electron-valence band hole (BB) recombination and pure radiation colors. The fabrication of the devices commonly requires annealing process. Farva et al. found that annealing bare CdSe QDs in air and N_2 ambient could improve the crystallinity and PL intensity (Farva and Park, 2010). Hu et al. studied the effect of annealing and photooxidation on the recombination of both band-to-band (BB) and SSs of colloidal CdSe QDs in PMMA (Hu et al., 2011).

11.2.1 Experiments on chemical synthesis and physical treatment of CQDs

Materials used in the synthesis of CdSe QDs were cadmium oxide (CdO, 99.95%), selenium powder (Se, 99.999%), oleic acid (OA, 90%), 1-octadecane (ODE, 90%), tri-*n*-octyl phospine (TOP, 90%), and polymethylmethacrylate (PMMA, average MW 350,000) powders. Toluene, ethanol, tetrachloride, and acetone were used as received. The synthesis route were described as following: A mixture of 0.128 g CdO powder (0.1 mmol), 3.5 ml OA, and 30 ml ODE in a 50 ml flask were heated to 240 °C under the Ar gas flow. After the CdO powder was dissolved and the mixture of Cd precursor solution became transparent, 0.6 ml TOPSe (involved 1.2 mmol Se) was injected into the flask quickly and the mixture was stirred vigorously by the magnetron. Then the solution was removed from the heater and cooled down naturally. A minute later the flask was immersed in tap water for quick cooling to room temperature. The OA-capped CdSe QDs in the ODE were centrifuged with the ethanol in the ratio of 1:5. After a purification step, the precipitate was dispersed in toluene. A small part of the colloidal CdSe QDs/toluene solution was removed from the beaker and reserved for reference of PL measurement. The concentration of the CdSe QDs in the toluene was estimated to be about 0.05 mmol/ml in which a possible loss factor of QDs in the purifying process is considered.

There are two methods for the combination of PMMA polymer and CdSe QDs: The first is polymerizing the monomer QDs blend solution. After the prepolymerization step, the viscous liquid could be spin-coated on a substrate (Pang et al., 2005). The second way is directly spin-coating the polymer-QDs solution on a substrate (Tamborra et al., 2004; Pompa et al., 2006). The former method could fabricate block polymer-QDs composite materials while the latter could simply realize the polymer-QDs composite thin films because the viscosity could be easily adjusted according to the needs of polymer concentration. The latter method with slight alterations was adapted to this experiment. Fabrication of the polymer-QDs composite was as follows: The PMMA powders were added to the reddish CdSe QDs/toluene solution to form a PMMA/QDs/toluene solution with 3% weight concentration. It took several hours to dissolve PMMA powders in the toluene solution. Sonication processing could promote the dissolving speed, but it might produce heating effect on QDs. To avoid surface oxidation of QDs by heating, sonication was not applied here. Different size CQDs can be obtained by changing the injection temperature.

The PMMA/QDs/toluene solution was spin-coated on a cleaned Si substrate in open air. The uniformity of the coated films was easily checked by observing the film interference color changing. PMMA/QDs film samples were annealed in nitrogen gas ambient at different temperatures. Photooxidation experiments of the PMMA/QDs composites were conducted in ambient air. A ultraviolet (UV) laser was used for both the excitation line for PL measurements and the UV light source for surface passivation. The laser beam just stayed at the same area of the sample surface and recorded PL intensities for an interval.

11.2.2 Annealing effect on the luminescence of CQDs

Figure 11.1 shows the PL spectra for three different-sized CQDs. The BEEs are centered at 479, 524, and 560 nm, respectively. The average sizes in diameter of QDs are calculated from the BEEs (Wu et al., 2005). The PL spectrum of the smallest QDs (#1) shows the most intense SSE spanning nearly the whole visible band (centered at ~600 nm) because the smallest QDs have the largest surface/volume ratio, whereas other two groups have relatively weak SSEs located at 602 and 646 nm, respectively. Evidently, a larger surface/volume ratio related to smaller QDs presents higher density of SSs that lead to an enhanced SSE. The PL spectra for the thin film composed of bare CdSe QDs and the thin film of the QDs embedded in PMMA are primarily the same (Hu et al., 2011). Figure 11.1b illustrates the BB transition and SSs transition at longer wavelength.

To study the effect of annealing on the BB and SS recombination of the CdSe CQDs in PMMA and compare the luminescence properties, we annealed six ODs-PMMA film samples in nitrogen gas ambient with different temperatures. Sample #1 illustrates no annealing. The other five samples were annealed at 90, 120, 150, 180, and 210 °C for 1 h and called #2, #3, #4, #5, and #6, respectively. Figure 11.2a shows the comparison of PL spectra for the six samples. All the spectra except #6 consist of two main peaks in the wavelength regions of 500-600 and 700-800 nm, respectively. It is seen that the BEE peaks for samples #2 and #3 that were annealed at low temperatures remain almost unchanged (552 nm). However, as the annealing temperature rises, the BEE peaks show distinct red shifts from 552 to 556 nm and 573 nm for samples #4 and #5, respectively. After annealing at 210 °C, the BEE peak completely disappears, indicating possible degradation of

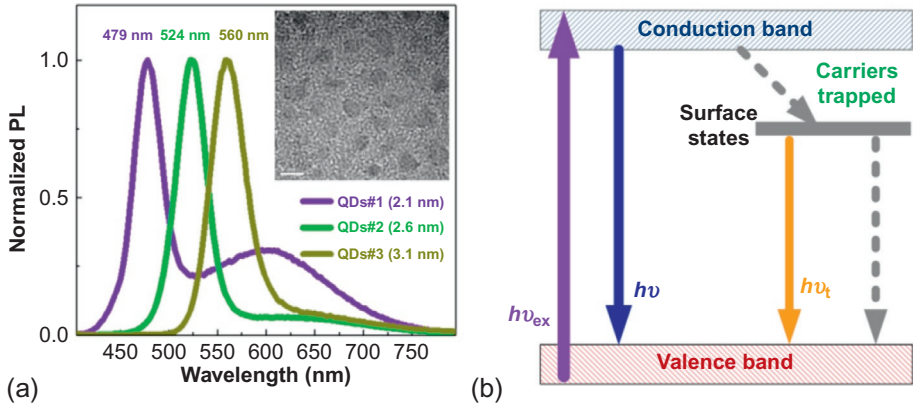

Figure 11.1 (a) PL spectra of the three groups of CdSe QDs. The average sizes of the QDs are 2.1, 2.6, and 3.1 nm for #1, #2, and #3 QDs, respectively. A transmission electron microscope (TEM) image of the #3 QDs is given in the inset. (b) The optical transitions of the CdSe QDs with BEE and SSE.
(a) Adapted from Hu et al. (2012a). (b) Adapted from Hu et al. (2011).

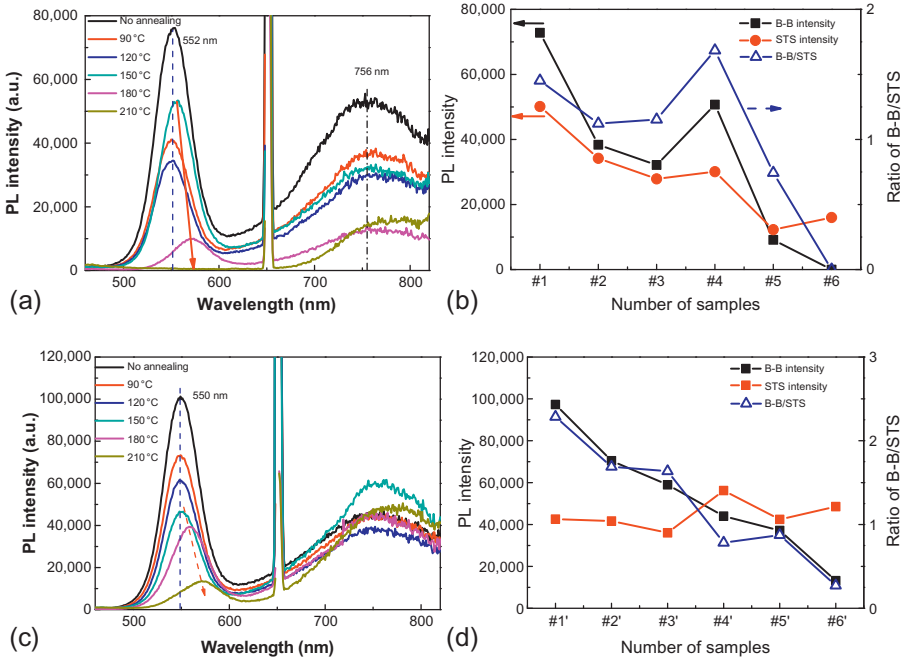

Figure 11.2 (a) PL spectra of CdSe QDs-PMMA film samples annealed at different temperatures; (b) the intensities of the BEE and SSE peaks and their ratio at different annealing temperatures corresponding to (a); (c) PL spectra of bare CdSe QDs film samples annealed at different temperatures; and (d) the intensities of the BEE and SSE peaks and their ratio at different annealing temperatures corresponding to (c).
Adapted from Hu et al. (2011).

structural quality of the PMMA and QDs caused by heating. Figure 11.2b plots the intensities of BEE and SSE peaks and their ratio versus annealing temperatures. We can see that all three curves show a similar trend with the rise of annealing temperatures. It is noticed that the BEE intensity first decreases after annealing at 90 and 120 °C. To the contrary, after annealing at 150 °C, the BEE peak intensity recovers notably. As annealing temperature is further raised to 180 and 210 °C, the BEE becomes quenched quickly. This interesting phenomenon is evidently different from the behaviors of other QDs reported in Farva and Park (2010) and Lee et al. (2005). To explore the effect of PMMA in the PL spectra, we compared the other six film samples (#1′, #2′, #3′, #4′, #5′, and #6′) that were composed of bare CdSe QDs using the same annealing process. Figure 11.2c shows the PL spectra of the six bare CdSe QD film samples with different annealing temperatures. In contrast to the QDs-PMMA samples, as the annealing temperature rises, the BEE peak intensities here decrease while the SSE intensities remain almost at the same level.

The annealing process can lead to breakdown of the surface ligand on CdSe CQDs, which lowers the confinement of the charge carriers in CQDs. Observation of the

normal decrement of the BEE and SSEs and their ratio for the annealed samples in reference to the unannealed sample sustains the argument. The interesting point is that annealing at 150 °C causes an abnormal rise in PL intensity for sample #4, which was interpreted as follows. When the blend of QDs-PMMA was heated in nitrogen gas ambient, on the one hand, the coalescence of the adjacent quantum dots caused the attenuation and red shift of the PL peaks; on the other hand, at a suitable annealing temperature (150 °C) the PMMA matrices around the QDs partially passivated the surface of the CQDs. These two contradictory processes made the PL spectrum undulating rather than varying monotonously.

11.2.3 WLE by single-size CQDs

Five batches of small CdSe QDs were synthesized for realization of WLE with single-size CQDs. In the synthesis of the small CdSe QDs, the quantities of precursors were different in the synthesis processes, for example, for QDs#D the quantities of CdO, Se, and OA are 2 mmol, 6 mmol, and 6 ml, respectively; for QDs#E the quantities are 3 mmol, 6 mmol, and 4 ml, respectively. All the SSE intensities are evident compared to the BEE peak, and the superposition of BEE and SSE always shows white luminescence. The small CdSe QDs (#A) with the BEE and SSE located in the blue (476 nm) and orange (~593 nm) bands are shown in Figure 11.3a. The mixture of the two emission peaks is white color, which is shown in the inset. The CIE 1931 coordinate of the PL spectrum is (0.30, 0.31), which is close to the pure white center (0.33, 0.33). The color render index of the PL spectrum is 69. Figure 11.3b shows the time resolved photoluminescence (TRPL) spectra of the dried CdSe QDs on a silicon wafer. The PL spectra of other four batches of small-size CdSe QDs are shown in Figure 11.3c-g. They are all distributed around the white-light center in the CIE 1931 coordinates. Although the PL spectra of the five batches show small differences in peak positions and intensities of BEE and SSE, the luminescence color of these QDs are all quasi-white. Therefore, we can conclude that this synthesis process for WLE CdSe QDs is stable and consistent.

11.3 Photooxidation effect on the luminescence of CQDs

Photooxidation improves the luminescence QY of CQDs by surface passivation. The effect of photooxidation on BB transition has been studied for bare CQDs (Hu et al., 2011; Cordero et al., 2000; Jung et al., 2010). Here, we introduce the photooxidation effect on luminescence of QDs-PMMA thin films by UV laser irradiation and an effective way to precisely tune the emission colors of QDs-PMMA thin films that could be used to fabricate bright LEDs.

11.3.1 Experiments on photooxidation of CQDs

The synthesized CdSe precipitates were dispersed in toluene, then the QDs/toluene solution was added with PMMA powders in a weight ratio of 30:1. The mixture was placed in a dark ambient for days to dissolve the PMMA powders. PMMA-QDs/toluene solution was coated on the Si wafers by spin coater.

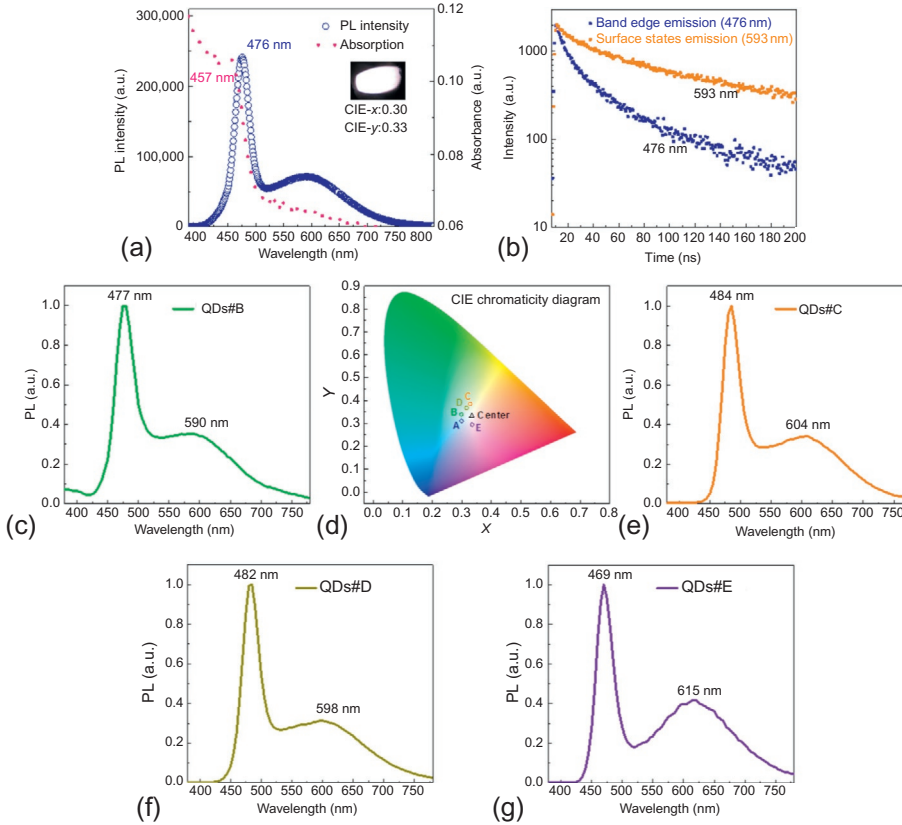

Figure 11.3 (a) The absorption spectrum and PL of the QDs shows that the absorption peak locates at 457 nm, inset in (a): digital photograph of the light spot under the irradiation of Xe lamp at 325 nm; (b) TRPL spectra of the dried CdSe QDs on silicon wafer; (c-g) the PL spectra of the four batches of small CdSe QDs. The CIE 1931 coordinates of these spectra are listed in the color space chromaticity diagram, in which they are all distributed around the white-light center. Adapted from Hu and Wu (2013).

Consequently, uniform and smooth PMMA-QDs films were prepared. In the photooxidation processing and PL measurements, an excitation laser beam ($\lambda = 325$ nm) was used as both of an excitation line for PL and an UV light source for photooxidation. The laser beam remained in the same area of the sample surface and recorded PL intensity for an interval. Photooxidation processing for the fabrication of color patterns was performed by UV light irradiation for different periods using a 20 W UV lamp (center wavelength $\lambda = 365$ nm). The photographs of the color luminescence patterns were taken by a digital camera under the UV spot of xenon lamp at 325 nm. The absolute QYs of the two groups of QDs-PMMA blends were measured by the FluoroMax-4, HORIBA. The QYs of the UV-irradiated samples and the annealing processed samples were obtained by quantitative comparison of the integrated areas of the PL spectra to the reference spectra area.

11.3.2 Photooxidation effect on the luminescence of CQDs

Figure 11.4 shows the PL spectra corresponding to the photooxidation processed PMMA-QDs blending thin films made by #1 and #2 CdSe CQDs. The PL spectra for the as-deposited films are also plotted in black lines in Figure 11.4a and c. Both samples display BEE blue shifts after photooxidation treatment in ambient air. The blue

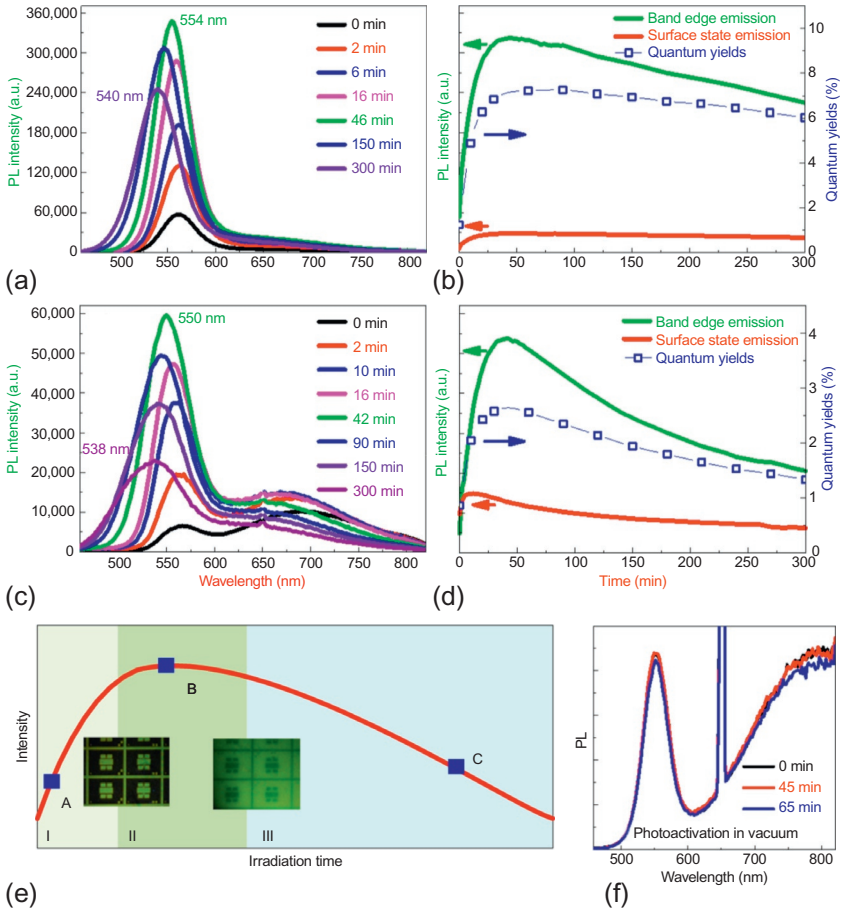

Figure 11.4 PL spectra of the PMMA-QDs films with different UV irradiation times. (a) #1 CdSe QDs; (c) #2 CdSe QDs; (b) and (d) the intensities of the band-edge emission and SSE intensities versus UV irradiation time for #1 and #2 QDs, respectively; (e) schematic diagram of the PL intensity versus irradiation time. The left inset in (e) is the fluorescent patterns corresponding to the UV irradiation with a glass photo mask and the right inset in (e) is the photo with wholly irradiation prior to the UV irradiation with the glass photo mask. (f) The PL spectra of CdSe QDs-PMMA with UV light irradiation in vacuum. Either BEE or SSE peak shows seldom variation.
Adapted from Hu et al. (2011).

shifts originated from photooxidation of QDs' surfaces, which generates Cd-OH and SeO_2 layers on the QDs' surfaces. The formed oxide layers by the photochemistry process can effectively reduce the size of QDs and isolate connection of QDs, which leads to an apparent blue shift and intensity enhancement in the PL spectra (Hu et al., 2011).

Because the fluorescent colors are determined by the spectral characteristics in the visible light range, the color of the #1 QD is green, which is dominated by the BEE, whereas the second one is orange as determined by both of the BEE and SSE. Figure 11.4b and d plots the PL intensity variations of BEE and SSE versus UV irradiation times. The QYs versus UV irradiation times are shown as well. There are obvious similarities between the two samples: As irradiation time is prolonged, the BEE intensities first rise, then fall, accompanied by peak blue shifts. The change of QYs for the two groups of QDs after photooxidation processing is consistent with the BEE. For #1 QDs, the QYs rise to 7.2% in 90 min and then fall slowly. For #2 QDs, the QYs are much lower and decrease faster than #1 QDs because a higher density of SSs is involved in #2 QDs. Figure 11.4e illustrates the schematic diagram of the PL intensity versus UV irradiation times and is divided into three regions: I, II, and III. High brightness contrast for color luminescence patterns can be realized by UV irradiation corresponding to point B, whereas point A (insufficient irradiation) or C (overexposure) corresponds to dark ones.

To intuitively illustrate the modulation of brightness contrast for fluorescent patterns by photooxidation, we chose the CQDs with weak SSE to fabricate periodic color patterns using a glass photo mask and irradiation of UV light (365 nm). The two insets in Figure 11.4e show the photos of fluorescent patterns after the UV irradiation. The dark area in the left color photo corresponds to nonirradiation (region I), whereas the bright green patterns fall into region II. When a PMMA-QDs film was wholly irradiated by the UV light for a suitable period, falling into region II prior to the UV irradiation with the glass photo mask, the overexposed area (patterns) became darker than the surrounding region. In the right color photo of Figure 11.4e, the light area corresponds to region II, whereas the dark patterns are the result of overexposure (region III). The tempered exposure and excessive exposure are similar to positive and negative photoresist technology.

To further explore the photooxidation effect on the luminescence of the CdSe QDs-PMMA, we set a sample in a vacuum sample holder and repeated surface passivation by 325 nm UV light irradiation. The sample holder with two optical windows was evacuated to 10^{-2} Torr by a vacuum pump. Figure 11.4(f) shows the PL spectra after the surface passivation in vacuum for different irradiation times. Notice that the UV irradiation up to 1 h did not cause evident PL spectrum changes either for BEE or SSE transitions. The PL difference between two surface passivation methods (in vacuum and ambient air) indicates that water vapor and oxygen in ambient air play an important role in the photooxidation process of the CdSe QDs-PMMA composites.

To explain the evident red shifts caused by annealing and the blue shifts by photooxidation in CdSe QDs-PMMA, a theoretical model is proposed, which is shown in Figure 11.5. As illustrated in Figure 11.5a, the surfaces of the CdSe CQDs in the as-deposited composites are encapsulated by ligand and surfactants. When annealed at a relatively high temperature, such as 180 °C, the loss of ligand and surfactants leads to

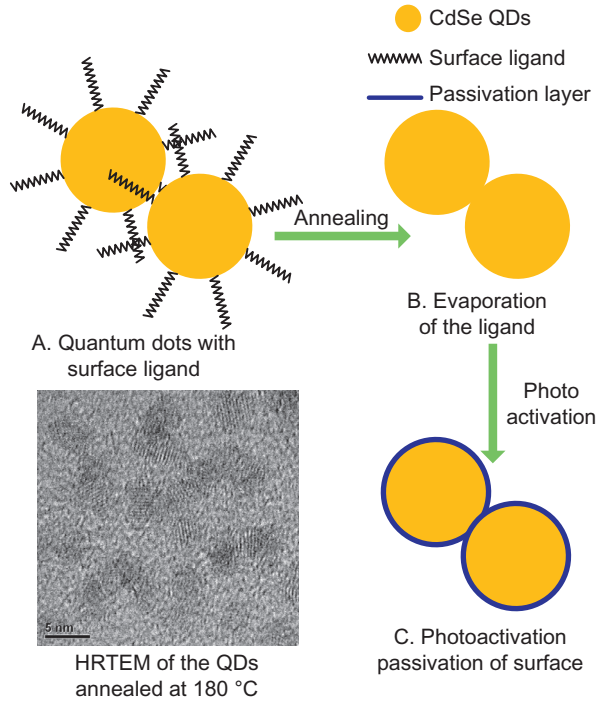

Figure 11.5 A model elucidates the effects of annealing and following photooxidation process. A HRTEM image of the QDs-PMMA composites after annealing at 180 °C shows coalescence of the adjacent quantum dots. Adapted from Hu et al. (2011).

coalescence of the adjacent quantum dots shown in Figure 11.5b, i.e., two or more QDs approached or contacted with each other. Consequently, electron coupling between these quantum dots became possible, which is equivalent to the effective increase of the QDs sizes (Eijt et al., 2009). The quantum size enlargement led to the distinct red shifts of BEE transitions and the intensity decrease due to weakening of carrier confinement. A high-resolution TEM image for a QDs-PMMA sample annealed at 180 °C is shown in Figure 11.5. The coalescence of the adjacent CdSe QDs can be clearly seen. Contrarily, the photooxidation process in ambient air isolates the connected QDs by photo-assisted oxidation, which generates Cd-OH and SeO_2 layers on the QDs surfaces. As illustrated in Figure 11.5c, the oxide layers created by the photochemistry process can effectively separate the joined one into two, which leads to an apparent blue shift and intensity enhancement in the PL spectra. Obviously, a combination of annealing and photooxidation can provide a new way to obtain tunable color with only one group of CQDs.

11.4 Plasmonic coupling effect on the luminescence of CQDs

Plasmon-exciton coupling in metal-semiconductor nanostructures could effectively enhance fluorescent intensity of QDs emitters because these hybrid systems have novel features beyond single components. Localized plasmons (LPs) in metal-semiconductor

nanostructures could influence the vicinal emitters. We present distinct enhancement of the SSEs of CdSe CQDs via coupling the CQD emitters with LPs excited on silver (Ag) nanostructures (Hu et al., 2012a,b). It is found that the OA ligand on the QDs plays a critical role in the intense luminescence enhancement of the CdSe QDs/Ag nanostructures, and annealing of the QDs/Ag hybrid systems greatly affects the features of SSEs. OA on the CdSe QDs modifies the morphology of Ag films and leads to the formation of the metal crystals. With this new approach of OA reshaping Ag particles and the consequent realization of intense luminescence enhancement, the luminescence colors of CdSe QD layers could be changed selectively, and microscale luminescence color patterns have been demonstrated.

The preparation of QDs-Ag coupling systems occurred as follows. Half the area of a Si wafer was coated with a 60-nm Ag film by thermal evaporation. The thickness was controlled by a crystal monitor. The CdSe QDs/toluene solution or PMMA-QDs blends was spin-coated on the wafer with half-coated Ag films. Each wafer was cleaved to two pieces along the orientation perpendicular to the boundary between the area with Ag and the area without Ag. Then one of the pieces was kept as a reference sample while the other one was annealed in air at 150 °C in an oven for 30 min. PL spectra were measured separately on the areas with and without Ag for all the samples.

11.4.1 Size effect of CQDs on the coupling with plasmons

Figure 11.6 shows the PL spectra for the QDs hybrid samples in which the CQDs layers (∼50 nm) were spin-coated only once. The left column of Figure 11.6 shows the PL spectra of the three groups of QDs on the Si area and Ag/Si area without annealing treatment, while right column shows the PL spectra of the annealed ones. Accordingly, Figure 11.7 shows the PL spectra of the hybrid samples with thicker QDs layers (∼100 nm) fabricated by three-time spin coating. As demonstrated in Figure 11.6, the radiative emissions from the area of QDs/Ag/Si are remarkably different from those from the QDs/Si area for all three groups of QDs. In Figure 11.6a and c, the SSEs of both #1 and #2 QDs on the Ag/Si area display distinct intensity enhancement compared to those of QDs/Si area (more than 10 times the peak heights), whereas the intensities of BEEs rarely change. For #1 QDs, the peak of the enhanced SSE from the QDs/Ag/Si area locates at 572 nm, which has an evident blue shift in reference to the SSE from the QDs/Si area (∼600 nm). The SSE peak intensity is about four times higher than the BEE peak intensity such that the SSE dominates the luminescence color of the QDs/Ag/Si area (yellow). For #2 QDs, the enhanced SSE peak locates at 612 nm as shown in Figure 11.6c. In Figure 11.6e, the PL peak intensity of the QDs/Ag/Si area is twice that of the QDs/Si area, while SSE changes little.

The BEE of the #1 QDs/Si structure shows a slight red-shift from 479 to 486 nm after annealing, which is ascribed to the coupling of the adjacent QDs resulted from annealing. Red shifts of 8 nm (#1 QDs), 5 nm (#2 QDs), and 2 nm (#3 QDs) were observed in the annealed samples. The decrease of red shift with increasing size indicates that smaller CQDs have stronger coupling between adjacent QDs after annealing. This could be explained in terms of chemical potential at the synthesis stage because the CQDs with smaller sizes have higher surface energy so that they

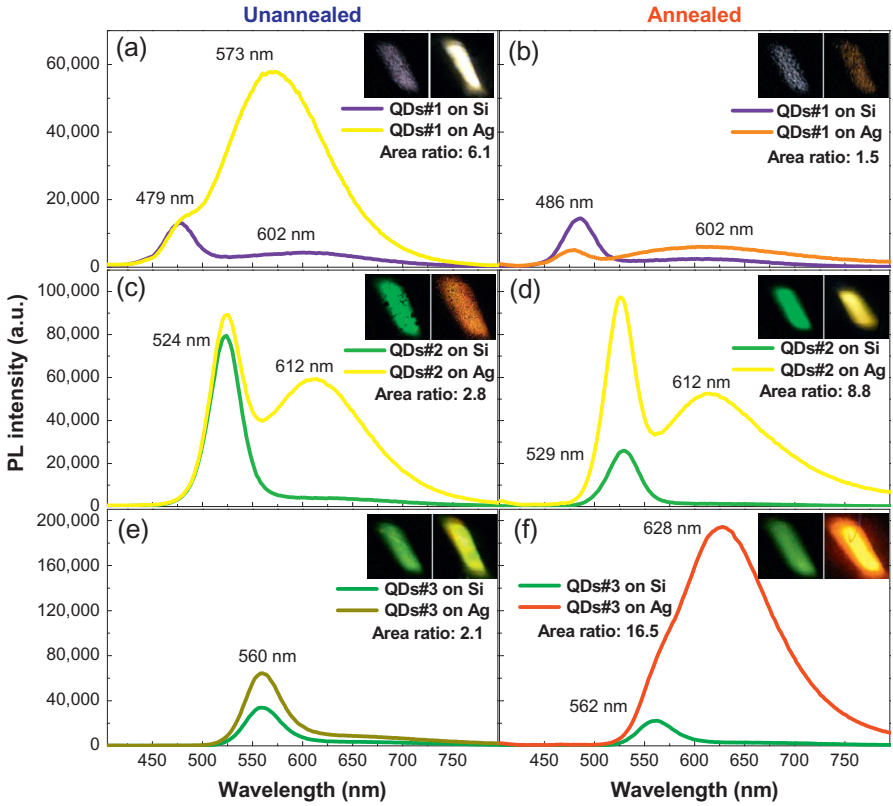

Figure 11.6 (a–f) PL spectra of the unannealed (left) and annealed (right) CdSe CQDs hybrid samples. Each row corresponds to one of the three groups of QDs (#1, #2, and #3 from top to bottom).
Adapted from Hu et al. (2012a).

have stronger coupling in the annealing process. For #1 QDs, after annealing treatment the emissions on the QDs/Ag/Si area is clearly quenched in comparison to the emissions of the QDs/Si area, as shown in Figure 11.6b. Figure 11.6d shows that the emissions of the #2 QDs/Ag/Si area change seldom after annealing. A spectrum area ratio (defined as the ratio of integrated PL intensity of QDs/Ag/Si to that of QDs/Si) changes from 2.8 to 8.8 after annealing due to a quench of BEE from the QDs/Si area. Figure 11.6f shows the most intensely enhanced SSE from the #3 QDs/Ag/Si area after annealing, and the spectrum area ratio reaches 16.5. As seen in Figure 11.6, there is an apparent discipline from top to bottom for the SSEs of all the QDs/Ag/Si samples: an opposite intensity variation trend of the SSE intensities before (left) and after (right) annealing, i.e., before annealing, SSE intensity decreases as CQD size increases, whereas the trend reverses after annealing. It indicates annealing can enhance the SSE of large-size CQDs (#3) more easily than that of the small-size ones.

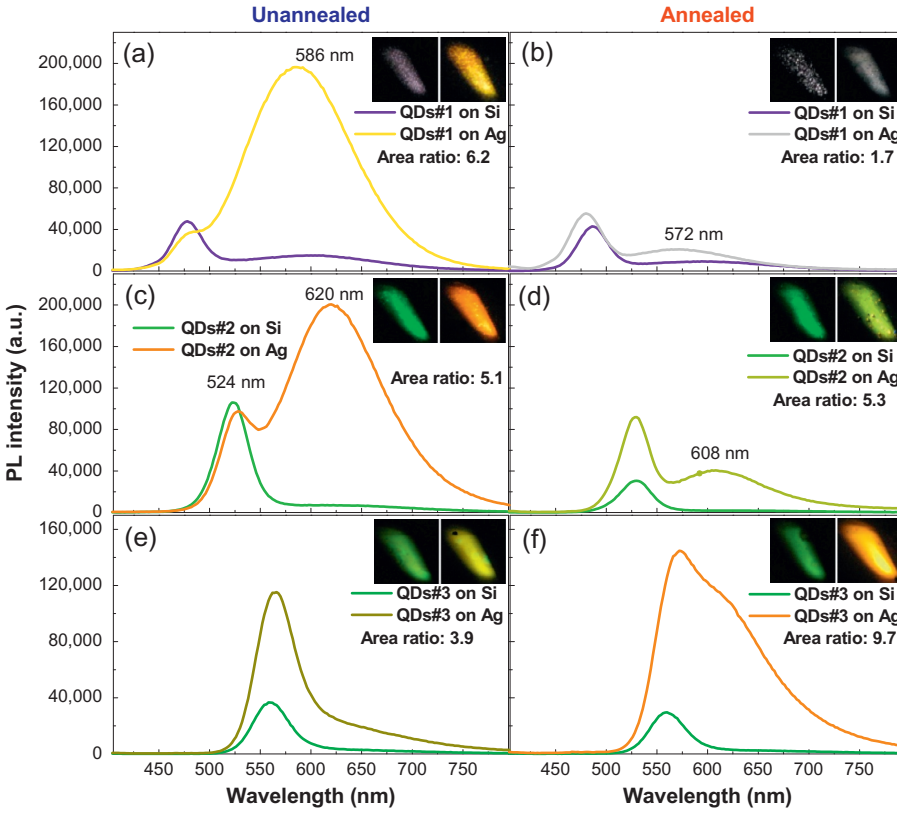

Figure 11.7 (a–f) PL spectra of the unannealed (left) and annealed (right) thick CdSe QDs hybrid samples that were spin-coated three times.
Adapted from Hu et al. (2012a).

11.4.2 Thickness of CQD layers on coupling with plasmons

Figure 11.7 shows the PL spectra of the samples with thick QDs layers that display similar PL spectra as the ones with thin layers shown in Figure 11.6. For the unannealed thick samples (left column in Figure 11.7), all the three groups of QDs/Ag/Si samples have evidently enhanced SSEs compared to those QDs/Si. Figure 11.7c shows that the SSE of the #2 QDs/Ag/Si is enhanced more intensely than that shown in Figure 11.6c, i.e., the intensity of SSE of #2 QDs is much higher than that of BEE. Here the ratio of the SSE intensity of QDs/Ag/Si to the BEE intensity of QDs/Si is defined as the relative intensity of SSEs, called peak ratio for short hereinafter.

The peak ratios and spectra area ratios (called area ratios for short) are plotted in Figure 11.8. Figure 11.8a corresponds to Figure 11.6, while Figure 11.8b corresponds to Figure 11.7. For the two sets of samples, similar ratio changes with size increase of QDs are observed in Figure 11.8, i.e., the monotonic decrease of the peak ratio and area ratio for the unannealed samples and the monotonic increase of the peak ratio

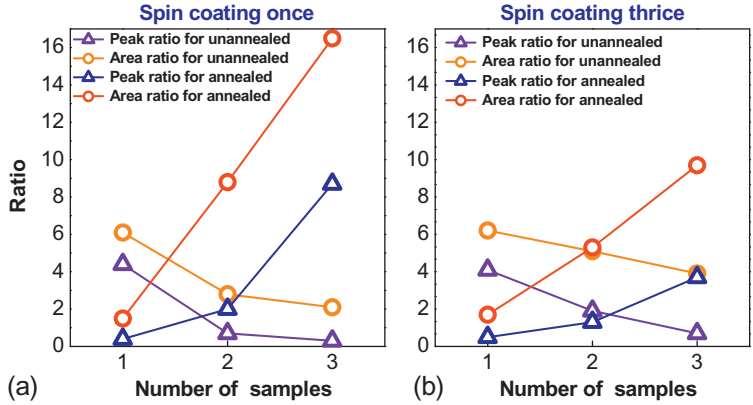

Figure 11.8 (a) The peak ratios and area ratios obtained from thin QDs layer samples shown in Figure 11.6 and (b) thick QDs layer samples shown in Figure 11.7. The annealed thin QDs layer samples demonstrate the higher peak ratios and area ratios than those of thick ones. Adapted from Hu et al. (2012a).

and area ratio for the annealed samples. The coherence of the ratios within the two sets of samples is due to the fact that the area ratio is dominated by the broad SSE rather than the BEE. It is seen that the SSE of the unannealed small-size CQDs is enhanced more notably, but the annealing treatment reverses this tendency (the purple and blue lines in Figure 11.8 have opposite trends). Comparison of Figure 11.8a with b indicates that the thickness of QD layers influences the enhancement strength of SSEs for both unannealed and annealed samples. Greater intensity enhancements of SSEs are observed in Figure 11.7c and e than that in Figure 11.6c and e, but after annealing, the enhancements of SSEs of QDs/Ag/Si shown in Figure 11.7d and f are smaller than those shown in Figure 11.6d and f. This indicates an as-deposited thick QD layer assists in the coupling of SSE with Ag, but after annealing, the SSE of a thin QD layer has a relatively higher enhancement effect than the thick layer.

11.4.3 OA role in the formation of Ag nanostructures

It is known that annealing decreases the density of ligands around CQDs, quenches the light emission of CQDs, and causes a red shift of CQD emission peaks (Hu et al., 2011). We find here that annealing of the QDs/Ag/Si hybrid structures clearly changes the surface morphology of the underneath Ag films and the contact between QDs and Ag. The possible variation of both QDs and Ag layers by annealing are illustrated in Figure 11.9a. Figure 11.9b, c, and d shows the scanning electron microscope (SEM) images of the Ag films in three different states. An as-deposited Ag film shown in Figure 11.9b is composed of myriad dense Ag particles with sizes of ~50 nm. The change of Ag surface morphology caused by annealing the QDs/Ag/Si hybrid structures can be revealed by removal of the QDs layer using toluene or chloroform. As shown in Figure 11.9c, after annealing, the dense Ag particles became bigger

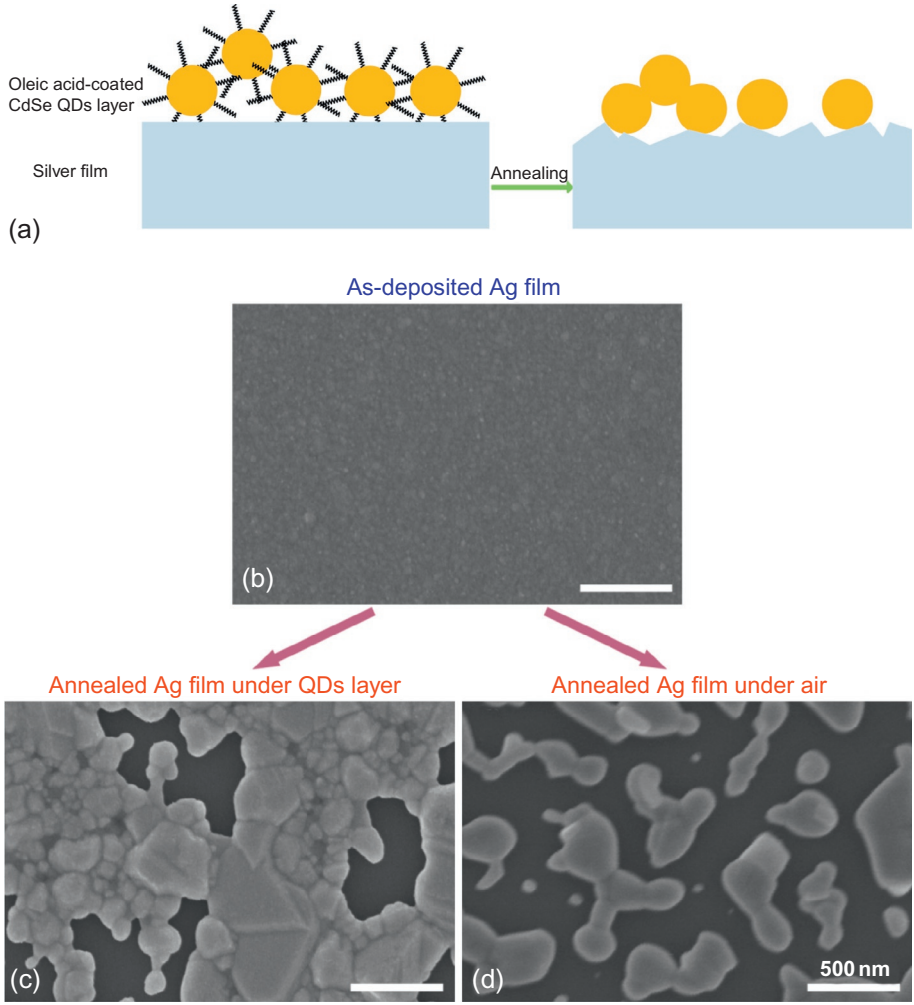

Figure 11.9 (a) The schematic diagram of the changes of a QDs layer and the underneath Ag film by annealing; (b) a SEM image of the surface of an as-deposited Ag/Si film; (c) a SEM image of the surface of Ag after annealing of #3 QDs/Ag/Si; and (d) a SEM image of the surface of bare Ag/Si after annealing in air.
Adapted from Hu et al. (2012a).

(>100 nm) and some of them display crystal facets and clear corners. X-ray diffraction (XRD) characterization observed a significant increase of diffraction intensity of the Ag (111) peak after annealing Ag films in OA ambient. However, annealing a bare Ag/Si sample in air leads to the well-known island morphology shown in Figure 11.9d, i.e., water-drop-like individual Ag islands with smooth boundaries, called the dewetting phenomenon. The dewetting caused by large-scale diffusion of Ag atoms on substrate surfaces has been well studied (Chatain et al., 1994; Ye and Thompson, 2011; Giermann

and Thompson, 2005). The different dewetting phenomena observed in the annealed QDs/Ag/Si in reference to the Ag/Si annealed in air are ascribed to the influence by a second material (OA-capped QDs) on the Ag surface, i.e., the placement of a QDs layer on Ag inevitably alters the surface diffusion process. It appears that the QDs layer inhibits the dewetting phenomenon while allowing grain growth. The realized different Ag morphology changes the interaction of QDs emitters with LPs in Ag nanostructures, or the modification of Ag films in the annealing process plays a critical role in the enhancement of SSE of QDs by LPs coupling.

The significant difference in morphologies between the annealed QDs/Ag/Si and Ag/Si structures (Figure 11.10) and consequently the much variation in enhancements of SSE (Figure 11.6f) indicate that the existence of a QDs layer on Ag in the annealing process is a key factor that causes these great changes. It is known that the main components in the QDs layer are OA-capped CdSe CQDs with a small fraction of residual toluene. The residual toluene on the Ag surface volatilizes quickly at room

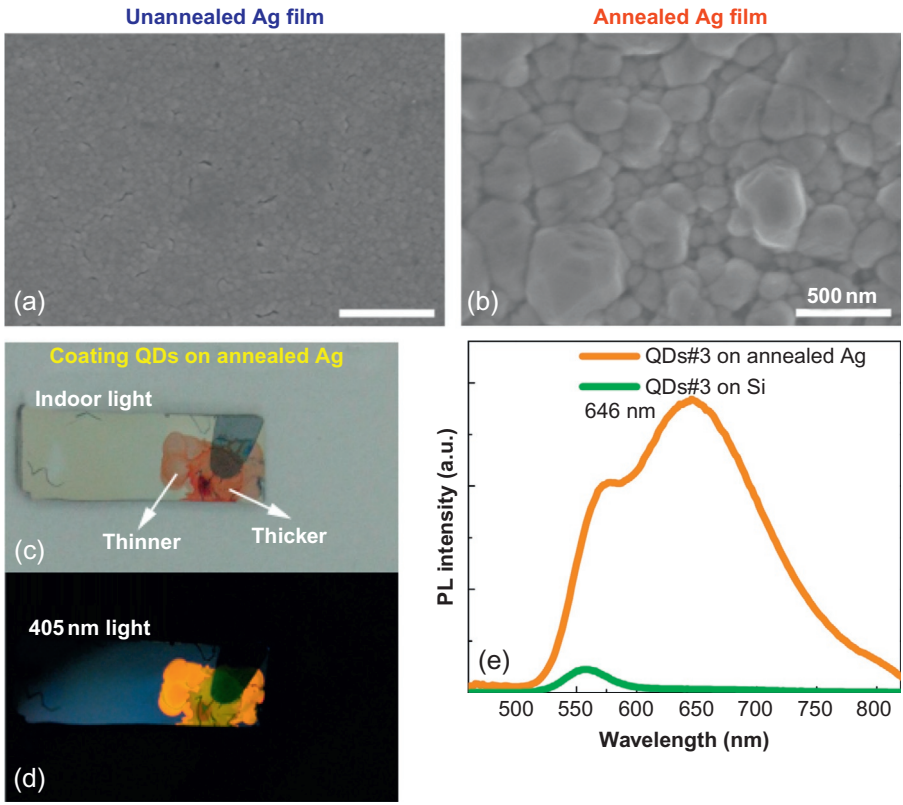

Figure 11.10 (a, b) SEM images of the Ag films without annealing and after annealing with OA. (c, d) Digital photographs of the Ag film coated with #3 QDs layer under the visible light and 405 nm purple light. (e) Comparison of PL spectra of #3 QDs layers on Si and on the annealed Ag/Si film.
Adapted from Hu et al. (2012a).

temperature and should be excluded as a modifier of Ag. On the other hand, OA as a surfactant or etchant could affect the morphology of nanomaterials (Mohamed et al., 2010; Han et al., 2010). Thus, we presume that the OA ligand on CdSe QDs modifies the Ag films in the annealing. To verify this hypothesis, we performed the following test: A piece of Ag/Si sample was annealed in OA at 150 °C for 30 min, and was then cleaned with toluene to remove the residual OA on the surface of Ag. The morphology of the Ag film was inspected by both SEM (Figure 11.10a and b) and a digital camera (Figure 11.10c and d). Afterward, the modified Ag film was coated with a #3 QDs layer for PL characterization as plotted in Figure 11.10e.

The SEM images shown in Figure 11.10a and b demonstrate that the annealed OA-Ag/Si surface is remarkably different from the unannealed sample. Interestingly, the morphology of the annealed Ag film in Figure 11.10b is very similar to that in Figure 11.9c: The sizes of the Ag particles become larger and their shapes are irregular. Here we can picture the morphology evolution of Ag films by annealing with OA: As temperature increased, myriad tiny Ag particles (Figure 11.10a) began to merge through the diffusion of Ag atoms while the OA etchant reacted with surface of Ag by selective etching, which led to the formation of large Ag particles with irregular shapes and improved crystallinity.

As observed in Figure 11.10d, the #3 QDs on the annealed OA-Ag/Si structure emits primarily orange light in a thickness-dependent manner, i.e., the thick part of the #3 QDs layer emits green-yellow light rather than orange from the thin part (see Figure 11.10c and d). The brighter orange color of the thin part also indicates that the SSE of a thin QDs layer is enhanced more intensely than that of a thick QDs layer. Therefore, we conclude that the OA ligand on CdSe QDs plays a critical role in modifying the Ag morphology during annealing and consequently impacts the coupling of QDs emitters with LPs in Ag nanostructures as observed in Figures 11.6f and 11.7f. Further, OA as a sort of ligand on CdSe CQDs provides rich surface states and a broad radiative SSE, which is favorable to the coupling of SSE with LPs in Ag nanostructures.

The assumption that the OA ligand on CdSe QDs as an etchant modifies the Ag films is further confirmed by the observations of Ag morphology change and corresponding PL spectra of the #3 QDs/Ag/Si hybrid structures at different storage periods. The #3 QDs/Ag/Si samples were stored at room temperature. As shown in Figure 11.11, after 6 months, neighboring grains of Ag merged and the surface became blurred in comparison to the as-deposited one. Consequently, PL spectra of the unannealed #3 QDs/Ag/Si sample also changed obviously with time lapse. However, the PL spectra measured at three different stages for the annealed sample (Figure 11.11d) rarely changed because OA evaporated during annealing process. These results verified that OA on QDs modifies Ag films by anisotropic etching even at room temperature.

11.4.4 Mechanism of plasmons in Ag nanostructures coupled with CQDs

The observation of intense enhancement of SSEs in Figures 11.6 and 11.7 can be explained by the resonant coupling of CdSe QDs with LPs in Ag nanostructures. Here, the resonance between SSs of CdSe CQDs and the LPs in Ag nanostructures possibly enhances the radiative decay rates of SSEs. As concluded in Section 11.4.3, OA

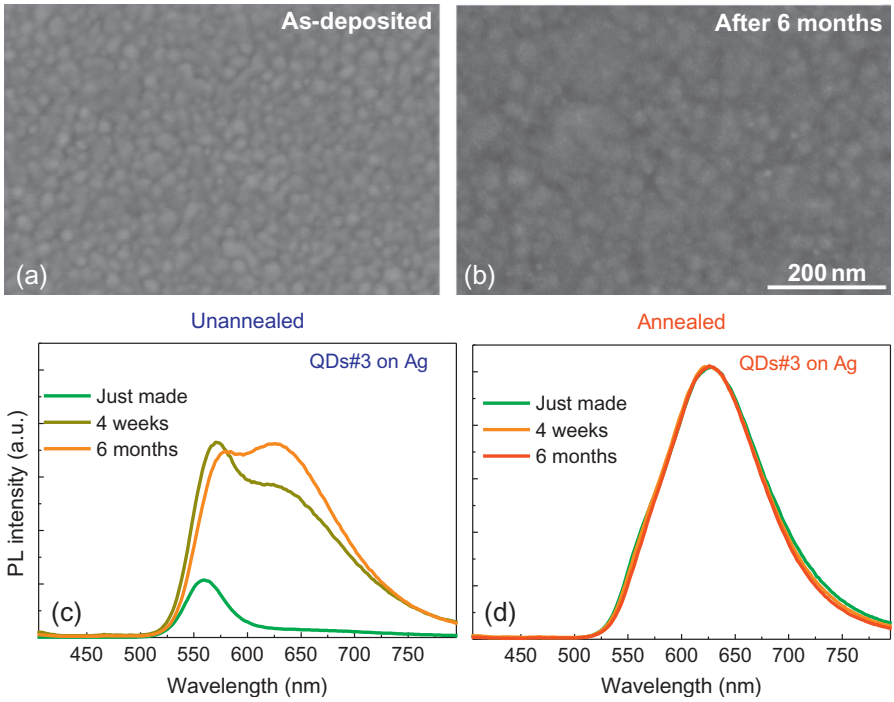

Figure 11.11 The SEM images of the Ag films covered with a #3 QDs layer: as-deposited (a); after 6 months (b); PL spectra measured at different storage periods for an unannealed #3 QDs/Ag/Si sample (c); and an annealed #3 QDs/Ag/Si sample (d).
Adapted from Hu et al. (2012a).

modifies the Ag films mainly through selectively etching the Ag surface and forming irregular Ag nanostructures with clear corners. It is known that the local electric field, which influences plasmonic coupling, is much greater around corners than at other places (Zhou et al., 2008; Mulvihill et al., 2010). Therefore, the interaction between the QDs emitters and LPs is greatly modulated through these intensive local fields in the Ag nanostructures. XRD characterization shows that the Ag films annealed in OA have better crystallinity favorable for the #3 QDs SSE enhancement. Figure 11.12a depicts the resonance between the emissions of QDs and those of LPs in the Ag nanostructures. SSs on CdSe CQDs are usually thought to be an essential path for nonradiative relaxation (Hines and Guyot-Sionnest, 1996). As illustrated in Figure 11.12a, large quantities of conduction-band electrons relax to valence band via nonradiative decay routes related to the SSs, thus we can only observe weak SSEs (through radiative decay routes) from the as-synthesized QDs as shown in Figure 11.1b. LPs coupling greatly intensifies the radiative decay rate related to SSs: By fast extracting the occupied SSs to the valence band, LPs coupling induces fast conduction-band electron transfer to the SSs, which leads to the evident enhancement of SSEs. The intensely

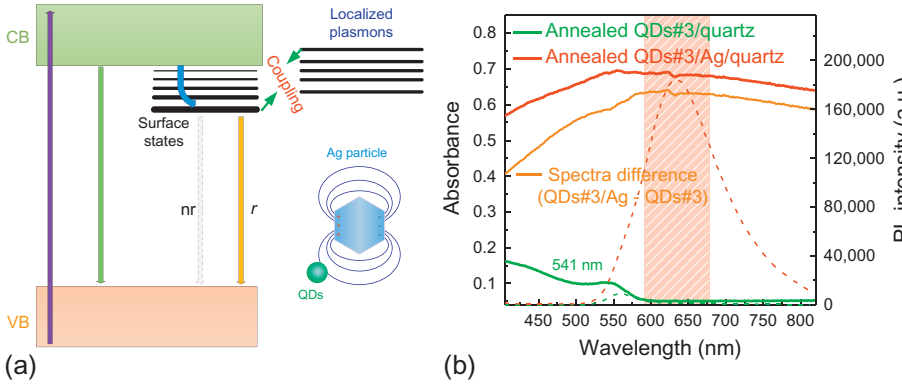

Figure 11.12 (a) Jablonsky diagram of the CdSe QDs with SSs and the energy levels of LPs in Ag nanostructures. (b) The absorption spectra (bold real lines) and PL intensity spectra (dotted lines) of the annealed samples. The difference spectrum (#3 QD/Ag minus QDs spectra) is also plotted out.
Adapted from Hu et al. (2012a).

enhanced SSEs observed in the QDs/Ag/Si hybrid structures are similar to those of the acceptors in resonance energy transfer systems (Sadhu et al., 2010).

Measurement of absorption spectra for the #3 QDs/Ag hybrid structures reveals the resonance (or correlation) of the plasmon frequencies with the light frequencies corresponding to the enhanced SSEs. To measure the extinction spectra of the QDs/Ag/Si samples, we deposited thin Ag films (15 nm) on transparent quartz substrates. Figure 11.12b shows the absorption spectra (bold solid lines) and PL spectra (dotted lines) of the annealed #3 QDs/Ag/quartz and #3 QDs/quartz samples. A difference spectrum (the intensity of absorption spectrum for #3 QDs/Ag/quartz minus that for QDs/quartz) is also plotted in a thin solid line. The difference spectrum reflects, to some extent, the extinction coefficient of the Ag film by revealing the interaction between QDs and Ag. The annealing process changes the extinction spectrum obviously: A broad peak appears at ~620 nm, close to the enhanced SSE peak (630 nm), in the annealed sample, whereas extinction coefficient monotonically increases as wavelength rises for the samples without annealing. The close correlation of LPs frequencies measured by absorption with the light frequencies of SSEs measured by PL also agrees with the results obtained by other experimental and theoretical investigations (Pompa et al., 2006; Fedutik et al., 2007).

The phenomenon of intense enhancement of SSEs in the QDs/Ag hybrid structures observed in Figure 11.6 can then be explicitly explained: As-deposited Ag films composed of myriad tiny Ag particles are favorable for the SSE enhancement of smaller QDs (#1 and #2). OA in QDs layers modifies Ag films by anisotropic etching that is reinforced by annealing. Hence, the annealed Ag films consisting of larger Ag crystals are favorable for the SSE enhancement of larger QDs (#3), i.e., the dominant plasmon modes in the Ag film red-shifted to ~630 nm. The red-shifted plasmon modes and the intensive local electric field in Ag nanostructures make strong resonance of the SSs of #3

QDs with LPs in Ag such that the SSs are extracted significantly through radiative decay routes. The observed size-selective PL enhancements in Figure 11.6 also agree with the previous theoretical and experimental reports (Kumbhar et al., 2005; Zhang et al., 2010), i.e., the increase of Ag particle sizes leads to red shifts of resonant wavelength of PL.

11.4.5 The combination of plasmonic coupling, annealing, and photooxidation

To demonstrate the changes of the luminescent characters of the QDs emitters via coupling with LPs in metallic nanostructures, 60-nm Ag films were first deposited on a silicon wafer, then followed by spin-coating of CdSe CQDs/toluene solution or PMMA-CQDs blends with #1 QDs. The wafer was cleaved into three pieces along the direction perpendicular to the boundary between the area coated with Ag and without Ag film. One of the pieces was kept as a reference sample while other two were annealed in ambient air at 150 °C in an oven for 30 min. Afterward one of the two annealed samples was irradiated by UV light for 6 h. The experimental details are illustrated in Figure 11.13a. Here, annealing process is an essential step to realize the effective coupling of LPs on Ag films with QDs. As demonstrated in Hu et al. (2011), annealing treatment decreased PL intensities of both BEE and SSE, whereas photooxidation processing enhanced (or recovered) the PL intensities. Therefore, UV irradiation processing was carried out on one piece of the annealed samples.

The measured PL spectra for the reference and processed samples are shown in Figure 11.13b–d. By comparison of PL spectra of QDs samples without Ag shown in Figure 11.13b and c, we find a BEE red shift (from 562 to 564 nm) after the annealing. When a sample was annealed, the OA ligand on CQDs desorbed from the CQDs surface. The loss of ligand made coalescence of the adjacent QDs, i.e., two or more QDs coming into approaching or contacting with each other. Consequently, the electron coupling between these QDs became possible, which is equivalent to the effective increase of the QDs sizes. This quantum size weakening effect leads to the red shifts and quenching of the BEEs.

As shown in Figure 11.13b, the PMMA-QDs on Ag film displays higher PL intensity than the one without Ag film, and the inset photo also shows that the area with Ag is brighter than the area without Ag. The QY for the CdSe QDs on Ag film is about 3.5%, whereas QY for the area without Ag is only 1.25%. Shown in Figure 11.13c, the annealing treatment of the area without Ag causes PL intensity decay accompanying with a BEE peak red-shift, and QY is lowered to 0.73%. A theatrical result is that the annealing treatment leads to the great enhancement of the SSE of the PMMA-QDs/Ag area in comparison with the reference area, and the QY increases to 14.9%. Consequently, the inset photo in Figure 11.13c demonstrates vivid brightness and hue contrast between the two areas. This phenomenon is assigned to the enhanced coupling effect of the fluorescent emission from QDs with LPs on the Ag nanostructures because annealing at a proper temperature induced the modification of Ag morphology that was catalyzed by the PMMA-QDs layer in the annealing process. The SSE at about 640 nm from the PMMA-QDs/Ag area is enhanced more intensely than BEE, indicating that SSE is more effectively coupled with LPs on Ag nanostructures than BEE.

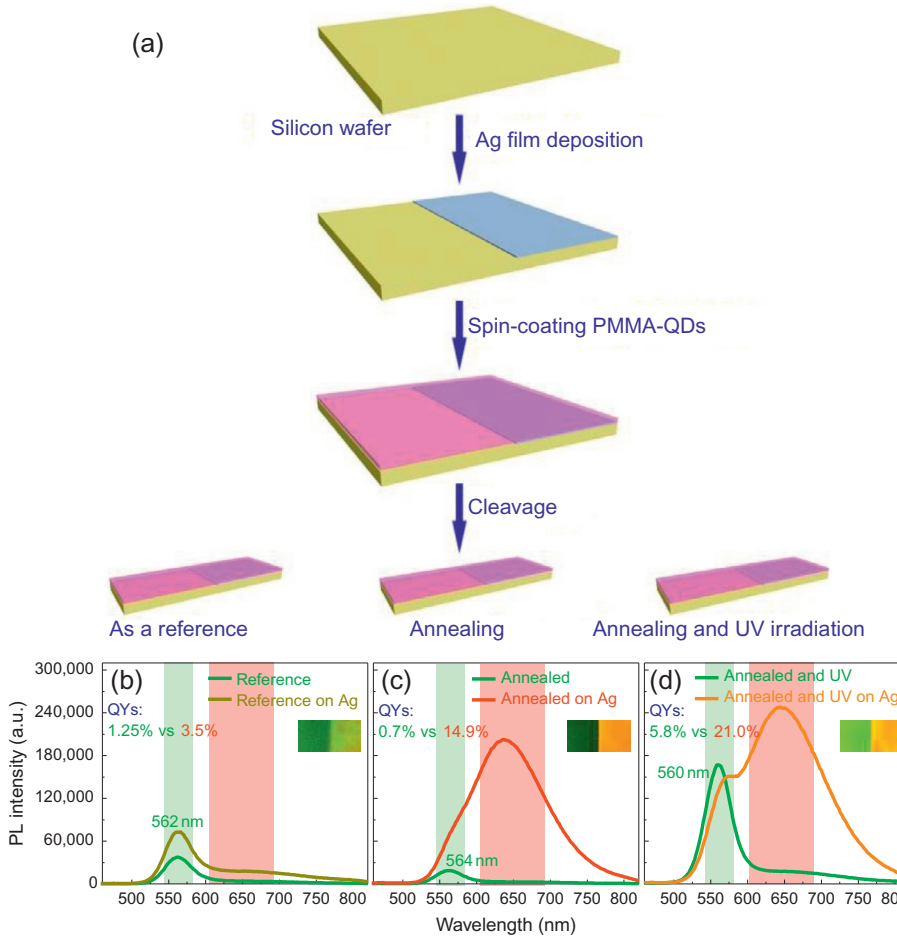

Figure 11.13 (a) Schematic diagrams for the fabrication of the PMMA-QDs on Ag nanostructures; (b) PL spectra for type #1 PMMA-QDs; (c) PL spectra for the annealed samples; and (d) PL spectra for the annealed and then UV-irradiated samples. The quantum yields of the PMMA-QDs reference and Ag coupled samples are labeled in (b)-(d).
Adapted from Hu et al. (2012b).

As shown in Figure 11.13d, after UV irradiation, the BEE intensities for both areas (with or without Ag) are distinctly enhanced in comparison with Figure 11.13c. The QYs for PMMA-QDs/Ag and without Ag are 21.0% and 5.8%, respectively. In the area without Ag, the color (green) was dominated by BEE, whereas the color (orange) of the area with Ag was dominated by the enhanced SSE. It is thus clear that the LPs enhancement and photooxidation effect can be combined for tuning the color of QDs.

11.5 Microscale fluorescent color patterns realized by plasmonic coupling

To demonstrate the tuning of the luminescence colors at designated areas via coupling CdSe CQDs emitters with LPs, we fabricated the luminescence patterns by deposition of Ag on the selective areas with hollow masks and followed by thermal annealing and UV irradiation. Figure 11.14 shows the colorful fluorescence patterns after subsequent processing steps: spin coating of PMMA-QDs blends on the patterned Ag film (left column: Figure 11.14a, d, and g), thermal annealing (middle column: Figure 11.14b, e, and h), and UV irradiation (right column: Figure 11.14c, f, and i). Color differences with high hue contrast between the areas with and without Ag nanostructures are seen. For example, in Figure 11.14a–c, the color letters of "ZJU" are the result of QDs sitting on Ag nanostructures, which are brighter than the background area without Ag coating. Notice that after annealing the color of the letters changes from yellow to red, whereas the background becomes dark (the ratio of PL intensity $\geq$20). After UV irradiation, the letters change to orange while the background area becomes bright. The diffusion (or leakage) of Ag vapor to the area beyond the hollow "ZJU" mask made a fuzzy red shadow-like special effect.

The CdSe CQDs with smaller sizes were used such that we could fabricate color patterns with shorter wavelength. Figure 11.14d shows vertical stripe patterns in which smaller QDs were coated on selectively evaporated Ag nanostructures. Distinct color changes occur after annealing as shown in Figure 11.14e. The PMMA-QDs/Ag films were then selectively irradiated under the hollow stripe mask that was aligned in the

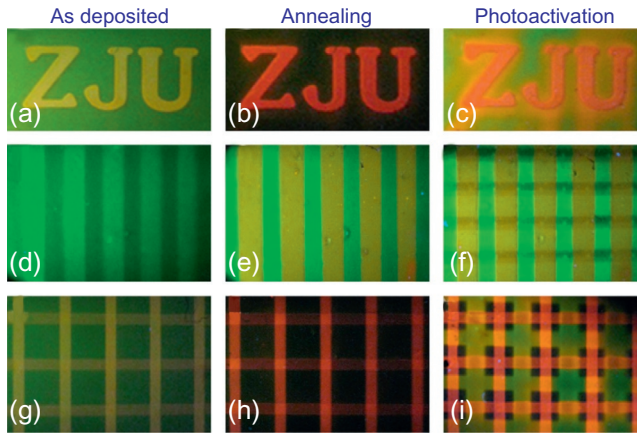

Figure 11.14 Fluorescent photos produced by patterned Ag deposition, annealing, and UV irradiation. Left column (a, d, g): spin-coated PMMA-QDs blends on patterned Ag nanostructures. Mid-column (b, e, h): after annealing. Right column (c, f, i): after UV irradiation. (g) The pattern was deposited twice with Ag strips that were cross each other; (h) after annealing; (i) the pattern was irradiated twice by UV light.
Adapted from Hu et al. (2012b).

horizontal direction perpendicular to Ag strips. Annealing and UV irradiation greatly highlight the brightness contrast and hue contrast of the color luminescence patterns.

More complex color patterns can be realized by multiple evaporations of Ag films and multiple UV irradiations. Figure 11.14g–i illustrates that the colors of luminescence patterns can also be tuned by the variation of Ag film thickness. In Figure 11.14g the vertical stripes correspond to 30 nm Ag while the horizontal ones correspond to 15 nm Ag. Clearly, the annealing process greatly highlights the brightness contrast and hue contrast of the multiple-color patterns shown in Figure 11.14h. Particularly, as demonstrated in Figure 11.14i, double UV irradiations made the patterns colorful. Even more colorful patterns can be produced by the magic combination of the coupling of QDs emitters with LPs on Ag nanostructures and UV irradiation.

Using the new approach of strongly coupled QDs-LPs nanostructures, microscale fluorescent color patterns are produced via altering the luminescence of CdSe QDs in designated microscale areas. Figure 11.15a illustrates the fabrication of microscale luminescence patterns in which PMMA-QDs composites were used as emitters. Similar to a bare QDs layer, PMMA-QDs composites can also modify the morphology of underneath Ag films in the annealing process. With the standard lithography technology, patterned photoresist on Ag can effectively separate the contact of the PMMA-QDs layer to the Ag film at designated areas. Thus, in the annealing process the Ag film is selectively modified in the areas where the QDs adhere. Figure 11.15b shows the realized microscale fluorescent color patterns by using standard photolithography.

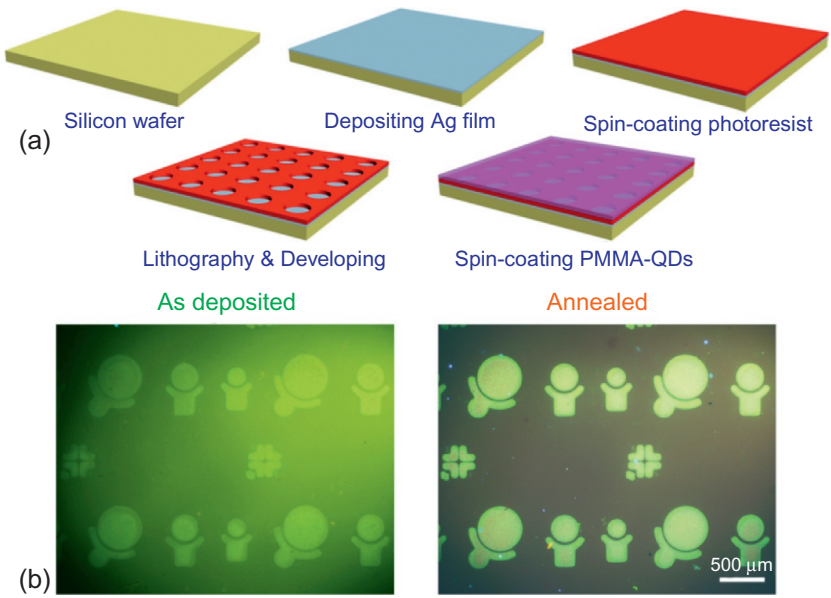

Figure 11.15 Microscale fluorescent color patterns of PMMA-QDs produced by LPs coupling. The fabrication procedure (a) and realized microscale fluorescent color patterns (b). Adapted from Hu et al. (2012b).

The luminescence of QDs is remarkably enhanced on the modified Ag areas, making the patterned areas different from background area. The bright microscale fluorescent patterns are the outcome of the coupling of QDs emitters with LPs on Ag nanostructures intensified by OA etching, whereas the interception of LPs coupling by insertion of an insulating layer leads to dark colors (background area). The realized colorful fluorescent patterns indicate clearly that the selective coupling of CdSe QDs-LPs makes it possible to tune fluorescence colors in microscale.

11.6 CQDs applications in white LEDs

CQDs have the advantage of high luminescent efficiency, facile bandgap tunability over the visible light region, and low fabrication cost. LEDs made of these CQDs have the potential to replace conventional inorganic- or organic-based LEDs and become a key part in high-performance next-generation LEDs. White LEDs using pure green-emitting CdSe(S) QDs with an Ag/ZnSnO/QDs/spiro-TPD/ITO structure have been fabricated in which ZnSnO and spiro-TPD serve as the electron and hole transport layer, respectively (Liu et al., 2013). The devices exhibit a wide electroluminescence (EL) spectrum consisting of three components: blue emission from spiro-TPD, green emission from QD band-band recombination, and red emission from QD surface-state recombination. The energy level diagram of the QD-LEDs is shown in Figure 11.16a. The work function of Ag cathode and ITO anode, the ZnSnO and QD conduction/valance band, and the TPD HOMO/HUMO are cited from published experimental data (Coe et al., 2002; Anikeeva et al., 2009). It illustrates that the conduction bands of ZnSnO and CdSeS QDs are located at −4.3 and −4.4 eV relative to the vacuum level, respectively, which facilitates the injection of electrons from ZnSnO to QDs. Holes can be injected into QDs because the step alignment between the HOMO level of TPD and the work function of ITO is small, even though a relatively high barrier exists between CdSeS QDs and TPD. The current density-voltage

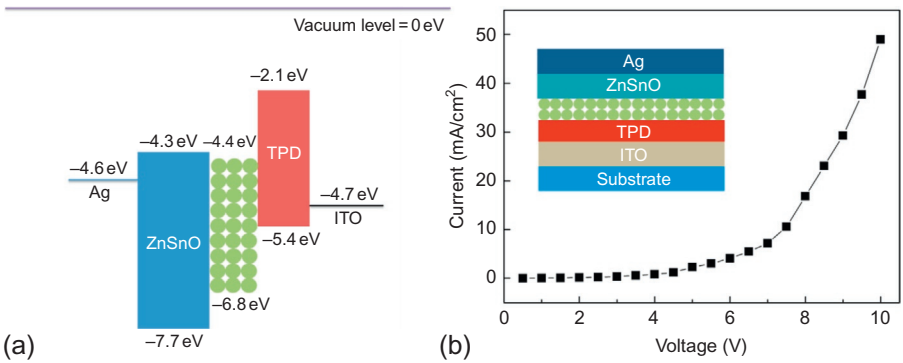

Figure 11.16 (a) Energy level diagram of the QD-LEDs; (b) current density-voltage curve of the device. Inset: the schematic diagram of the structure for the QD-LEDs.

curve of the device shown in Figure 11.16b demonstrates that QD-LEDs with the structure of Ag/ZnSnO/CdSeS-QDs/TPD/ITO exhibit a good rectification characteristic. The device turn-on voltage is at ~4 V.

Figure 11.17 displays a three-peak EL spectrum that consists of red color from SSE of the CdSeS QDs, green from BEE of the QDs, and blue from TPD. The EL spectrum of the CdSeS QDs device shows both BEE (the peak at 510 nm) and SSE (the peak at 665 nm) while PL spectrum in Figure 11.17a shows only a BEE peak. The SSE presence in EL is due to the excitation of SSs by injected electrons. Surface plasmon enhancement of EL can be excluded here because the thick Ag film (200 nm) is separated by a thick ZnSnO interlayer (60 nm). The red, green, and blue emission components in the device are in the same magnitude, and the resultant EL spectrum covers the whole visible light region, showing that the QD-LEDs exhibit a good white light-emitting characteristic with CIE coordinates of (0.281, 0.384).

11.7 Conclusions and future trends

In this chapter, we have described the synthesis technologies, optical properties, and the applications in LEDs of semiconductor CdSe CQDs. We have introduced the effects of three physical approaches to tuning luminescence processes of the semiconductor CQDs, including annealing, photooxidation, and surface plasmonic coupling, particularly with the modification of surface states. The QDs-PMMA composites demonstrated evident enhancement to the SSs-related emissions while annealing QDs-PMMA composites led to intensity quench of the BEE. The annealing process also caused the red shift of BEE. On the contrary, photooxidation of QDs-PMMA composites resulted in blue shifts accompanied with the remarkable enhancement of luminescence intensity. The coupling of CdSe CQDs with LPs in Ag nanostructures has been systematically studied. It is found that OA on surface of CdSe CQDs plays an important role in the formation of Ag nanostructures that show strong coupling of LPs with QDs emitters. The study of size effect of CQDs on coupling of SSEs with LPs showed that as-deposited small Ag particles favorably enhance the SSEs of small-size CdSe CQDs, whereas the annealed coupling structures are favorably enhance the SSEs of large-size CdSe CQDs because the annealing process promotes reshaping of small Ag particles into larger ones. The approach of OA-assisted modification of plasmonic properties of Ag nanostructures provides a new route to synthesizing bright luminescence materials and devices that use CQDs. The selective coupling of CQDs with LPs in Ag nanostructures allows feasible realization of microscale fluorescent multiple-color patterns using single-size CQDs. The combination of LPs coupling, thermal annealing, and photooxidation undoubtedly provide an effective way to precisely tune the colors of light-emitting CQDs in a postsynthesis stage. The LEDs based on CdSe CQDs were developed in which inorganic ZnSnO and organic TPD thin films were used as the ETL and HTL, respectively. Optical and electrical characterizations show that QD-LEDs have low turn-on voltages, good monochromaticity, and bright EL.

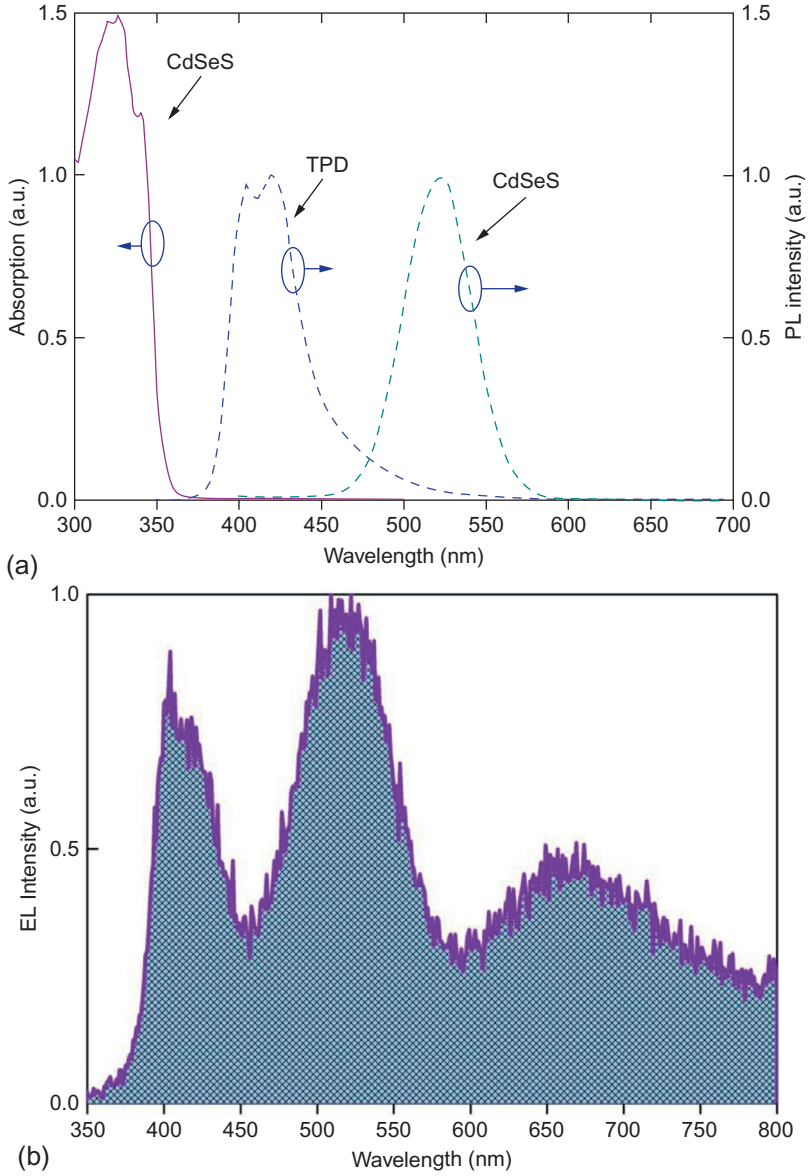

Figure 11.17 (a) Normalized PL spectra of TPD and CdSeS QDs (dashed line) and absorption spectrum of CdSeS QDs (solid line). (b) An EL spectrum measured from a CdSeS QDs LED device at a bias of 10 V.

During the last decade we have witnessed rapid progress in the development of CQDs. Over the next 5 years we will see important applications of CQDs in optoelectronic devices, such as new light-emitting sources, flat-panel displays, and solar cells. For these new devices applications the physical tuning approaches to the luminescence processes of CQDs and understanding their underlying mechanisms are key issues. Several challenges still remain to be solved. First, CQDs with well-defined surface states using surface state engineering in synthesis stages are needed for the precise tuning of the strong coupling between the QD emitters and plasmons in metallic nanostructures. Second, adjustability of SSs-LPs coupling via surface passivation of photooxidation of CQDs after synthesis stages is to be explored. Finally, the applications of the CQDs/Ag coupling structures in EL process of CQDs light-emitting devices will be investigated.

References

Anikeeva, P.O., Halpert, J.E., Bawendi, M.G., Bulović, V., 2009. Quantum dot light-emitting devices with electroluminescence tunable over the entire visible spectrum. Nano Lett. 9 (7), 2532–2536.

Baker, D.R., Kamat, P.V., 2010. Tuning the emission of CdSe quantum dots by controlled trap enhancement. Langmuir 26 (13), 11272–11276.

Beard, M.C., Knutsen, K.P., Yu, P., Luther, J.M., Song, Q., Metzger, W.K., Ellingson, R.J., Nozik, A.J., 2007. Multiple exciton generation in colloidal silicon nanocrystals. Nano Lett. 7 (8), 2506–2512.

Biteen, J.S., Lewis, N.S., Atwater, H.A., Mertens, H., Polman, A., 2006. Spectral tuning of plasmon-enhanced silicon quantum dot luminescence. Appl. Phys. Lett. 88 (13), 131109.

Bowers, M.J., McBride, J.R., Rosenthal, S.J., 2005. White-light emission from magic-sized cadmium selenide nanocrystals. J. Am. Chem. Soc. 127 (44), 15378–15379.

Brelle, M.C., Zhang, J.Z., Nguyen, L., Mehra, R.K., 1999. Synthesis and ultrafast study of cysteine-and glutathione-capped Ag_2S semiconductor colloidal nanoparticles. J. Phys. Chem. A 103 (49), 10194–10201.

Burda, C., Chen, X., Narayanan, R., El-Sayed, M.A., 2005. Chemistry and properties of nanocrystals of different shapes. Chem. Rev. 105 (4), 1025–1102.

Chatain, D., Chabert, F., Ghetta, V., Fouletier, J., 1994. New experimental setup for wettability characterization under monitored oxygen activity: II. Wettability of sapphire by silver-oxygen melts. J. Am. Ceram. Soc. 77 (1), 197–201.

Chen, H.-S., Lo, B., Hwang, J.-Y., Chang, G.-Y., Chen, C.-M., Tasi, S.-J., Wang, S.-J.J., 2004. Colloidal ZnSe, ZnSe/ZnS, and ZnSe/ZnSeS quantum dots synthesized from ZnO. J. Phys. Chem. B 108 (44), 17119–17123.

Coe, S., Woo, W.-K., Bawendi, M., Bulovic, V., 2002. Electroluminescence from single monolayers of nanocrystals in molecular organic devices. Nature 420 (6917), 800–803.

Cordero, S.R., Carson, P.J., Estabrook, R.A., Strouse, G.F., Buratto, S.K., 2000. Photo-activated luminescence of CdSe quantum dot monolayers. J. Phys. Chem. B 104 (51), 12137–12142.

Cozzoli, P.D., Pellegrino, T., Manna, L., 2006. Synthesis, properties and perspectives of hybrid nanocrystal structures. Chem. Soc. Rev. 35 (11), 1195–1208.

Efros, A.L., Rosen, M., 2000. The electronic structure of semiconductor nanocrystals. Annu. Rev. Mater. Sci. 30 (1), 475–521.

Eijt, S.W.H., Mijnarends, P.E., van Schaarenburg, L.C., Houtepen, A.J., Vanmaekelbergh, D., Barbiellini, B., Bansil, A., 2009. Electronic coupling of colloidal CdSe nanocrystals monitored by thin-film positron-electron momentum density methods. Appl. Phys. Lett. 94 (9), 091908.

Farva, U., Park, C., 2010. Influence of thermal annealing on the structural and optical properties of CdSe nanoparticles. Sol. Energy Mater. Sol. Cells 94 (2), 303–309.

Fedutik, Y., Temnov, V.V., Schöps, O., Woggon, U., Artemyev, M.V., 2007. Exciton-plasmon-photon conversion in plasmonic nanostructures. Phys. Rev. Lett. 99 (13), 136802.

Gaponik, N., Talapin, D.V., Rogach, A.L., Hoppe, K., Shevchenko, E.V., Kornowski, A., Eychmüller, A., Weller, H., 2002. Thiol-capping of CdTe nanocrystals: an alternative to organometallic synthetic routes. J. Phys. Chem. B 106 (29), 7177–7185.

Gaponik, N., Hickey, S.G., Dorfs, D., Rogach, A.L., Eychmüller, A., 2010. Progress in the light emission of colloidal semiconductor nanocrystals. Small 6 (13), 1364–1378.

Giermann, A.L., Thompson, C.V., 2005. Solid-state dewetting for ordered arrays of crystallographically oriented metal particles. Appl. Phys. Lett. 86 (12), 121903.

Han, X.-G., Jiang, Y.-Q., Xie, S.-F., Kuang, Q., Zhou, X., Cai, D.-P., Xie, Z.-X., Zheng, L.-S., 2010. Control of the surface of ZnO nanostructures by selective wet-chemical etching. J. Phys. Chem. C 114 (22), 10114–10118.

Heath, J.R., Shiang, J., Alivisatos, A., 1994. Germanium quantum dots: optical properties and synthesis. J. Chem. Phys. 101 (2), 1607–1615.

Hines, M.A., Guyot-Sionnest, P., 1996. Synthesis and characterization of strongly luminescing ZnS-capped CdSe nanocrystals. J. Phys. Chem. 100 (2), 468–471.

Hines, M.A., Scholes, G.D., 2003. Colloidal PbS nanocrystals with size-tunable near-infrared emission: observation of post-synthesis self-narrowing of the particle size distribution. Adv. Mater. 15 (21), 1844–1849.

Hu, L., Wu, H., 2013. Annealing-induced bimodal size distribution of small CdSe quantum dots with white-light emission. Phys. Status Solidi A 210 (9), 1726–1733.

Hu, L., Wu, H., Du, L., Ge, H., Chen, X., Dai, N., 2011. The effect of annealing and photoactivation on the optical transitions of band-band and surface trap states of colloidal quantum dots in PMMA. Nanotechnology 22, 125202.

Hu, L., Wu, H., Cai, C., Xu, T., Zhang, B., Jin, S., Wan, Z., Wei, X., 2012a. Plasmon-enhanced surface-state emission of CdSe quantum dots and its application to microscale luminescence patterns. J. Phys. Chem. C 116 (20), 11283–11291.

Hu, L., Wu, H., Wan, Z., Cai, C., Xu, T., Lou, T., Zhang, B., 2012b. Physical approaches to tuning the luminescence color patterns of colloidal quantum dots. New J. Phys. 14 (1), 013059.

Jasieniak, J., Mulvaney, P., 2007. From Cd-rich to Se-rich—the manipulation of CdSe nanocrystal surface stoichiometry. J. Am. Chem. Soc. 129 (10), 2841–2848.

Jun, Y.-W., Choi, J.-S., Cheon, J., 2006. Shape control of semiconductor and metal oxide nanocrystals through nonhydrolytic colloidal routes. Angew. Chem. Int. Ed. 45 (21), 3414–3439.

Jung, D.-R., Kim, J., Park, B., 2010. Surface-passivation effects on the photoluminescence enhancement in ZnS:Mn nanoparticles by ultraviolet irradiation with oxygen bubbling. Appl. Phys. Lett. 96 (21), 211908.

Khare, A., Wills, A.W., Ammerman, L.M., Norris, D.J., Aydil, E.S., 2011. Size control and quantum confinement in Cu_2ZnSnS_4 nanocrystals. Chem. Commun. 47 (42), 11721–11723.

Kruszynska, M., Borchert, H., Parisi, J., Kolny-Olesiak, J., 2010. Synthesis and shape control of $CuInS_2$ nanoparticles. J. Am. Chem. Soc. 132 (45), 15976–15986.

Kumbhar, A.S., Kinnan, M.K., Chumanov, G., 2005. Multipole plasmon resonances of submicron silver particles. J. Am. Chem. Soc. 127 (36), 12444–12445.

Lee, H.S., Lee, K.H., Park, H.L., Kim, T.W., Kim, Y.-H., 2005. Effect of thermal annealing on the interband transitions and activation energies of CdTe/ZnTe quantum dots. J. Appl. Phys. 98 (2), 023702.

Li, J.J., Wang, Y.A., Guo, W., Keay, J.C., Mishima, T.D., Johnson, M.B., Peng, X., 2003. Large-scale synthesis of nearly monodisperse CdSe/CdS core/shell nanocrystals using air-stable reagents via successive ion layer adsorption and reaction. J. Am. Chem. Soc. 125 (41), 12567–12575.

Liu, B., Li, R., Song, L., Hu, L., Zhang, B., Chen, Y., Wu, J., Bi, G., Wu, H., 2013. QD-LED devices using ZnSnO as an electron-transporting layer. Acta Phys. Sin. 62 (15), 158504.

Mangolini, L., Kortshagen, U., 2007. Plasma-assisted synthesis of silicon nanocrystal inks. Adv. Mater. 19 (18), 2513–2519.

Mattoussi, H., Mauro, J.M., Goldman, E.R., Anderson, G.P., Sundar, V.C., Mikulec, F.V., Bawendi, M.G., 2000. Self-assembly of CdSe-ZnS quantum dot bioconjugates using an engineered recombinant protein. J. Am. Chem. Soc. 122 (49), 12142–12150.

Micic, O.I., Curtis, C.J., Jones, K.M., Sprague, J.R., Nozik, A.J., 1994. Synthesis and characterization of InP quantum dots. J. Phys. Chem. 98 (19), 4966–4969.

Mohamed, M.B., AbouZeid, K.M., Abdelsayed, V., Aljarash, A.A., El-Shall, M.S., 2010. Growth mechanism of anisotropic gold nanocrystals via microwave synthesis: formation of dioleamide by gold nanocatalysis. ACS Nano 4 (5), 2766–2772.

Mulvihill, M.J., Ling, X.Y., Henzie, J., Yang, P., 2010. Anisotropic etching of silver nanoparticles for plasmonic structures capable of single-particle SERS. J. Am. Chem. Soc. 132 (1), 268–274.

Murphy, J.E., Beard, M.C., Norman, A.G., Ahrenkiel, S.P., Johnson, J.C., Yu, P., Mićić, O.I., Ellingson, R.J., Nozik, A.J., 2006. PbTe colloidal nanocrystals: synthesis, characterization, and multiple exciton generation. J. Am. Chem. Soc. 128 (10), 3241–3247.

Murray, C., Norris, D.J., Bawendi, M.G., 1993. Synthesis and characterization of nearly monodisperse CdE (E = sulfur, selenium, tellurium) semiconductor nanocrystallites. J. Am. Chem. Soc. 115 (19), 8706–8715.

Murray, C., Kagan, C., Bawendi, M., 1995. Self-organization of CdSe nanocrystallites into three-dimensional quantum dot superlattices. Science 270 (5240), 1335–1338.

Murray, C.B., Kagan, C., Bawendi, M., 2000. Synthesis and characterization of monodisperse nanocrystals and close-packed nanocrystal assemblies. Annu. Rev. Mater. Sci. 30 (1), 545–610.

Nizamoglu, S., Mutlugun, E., Akyuz, O., Perkgoz, N.K., Demir, H.V., Liebscher, L., Sapra, S., Gaponik, N., Eychmüller, A., 2008. White emitting CdS quantum dot nanoluminophores hybridized on near-ultraviolet LEDs for high-quality white light generation and tuning. New J. Phys. 10 (2), 023026.

Nozik, A.J., Beard, M.C., Luther, J.M., Law, M., Ellingson, R.J., Johnson, J.C., 2010. Semiconductor quantum dots and quantum dot arrays and applications of multiple exciton generation to third-generation photovoltaic solar cells. Chem. Rev. 110 (11), 6873–6890.

Pang, L., Shen, Y., Tetz, K., Fainman, Y., 2005. PMMA quantum dots composites fabricated via use of pre-polymerization. Opt. Express 13 (1), 44–49.

Parak, W.J., Gerion, D., Pellegrino, T., Zanchet, D., Micheel, C., Williams, S.C., Boudreau, R., Le Gros, M.A., Larabell, C.A., Alivisatos, A.P., 2003. Biological applications of colloidal nanocrystals. Nanotechnology 14 (7), R15.

Pellegrino, T., Kudera, S., Liedl, T., Muñoz Javier, A., Manna, L., Parak, W.J., 2005. On the development of colloidal nanoparticles towards multifunctional structures and their possible use for biological applications. Small 1 (1), 48–63.

Peng, Z.A., Peng, X., 2001. Formation of high-quality CdTe, CdSe, and CdS nanocrystals using CdO as precursor. J. Am. Chem. Soc. 123 (1), 183–184.
Peng, Z.A., Peng, X., 2002. Nearly monodisperse and shape-controlled CdSe nanocrystals via alternative routes: nucleation and growth. J. Am. Chem. Soc. 124 (13), 3343–3353.
Penn, S.G., He, L., Natan, M.J., 2003. Nanoparticles for bioanalysis. Curr. Opin. Chem. Biol. 7 (5), 609–615.
Pompa, P.P., Martiradonna, L., Torre, A.D., Sala, F.D., Manna, L., De Vittorio, M., Calabi, F., Cingolani, R., Rinaldi, R., 2006. Metal-enhanced fluorescence of colloidal nanocrystals with nanoscale control. Nat. Nanotechnol. 1 (2), 126–130.
Qian, X.M., Nie, S.M., 2008. Single-molecule and single-nanoparticle SERS: from fundamental mechanisms to biomedical applications. Chem. Soc. Rev. 37 (5), 912–920.
Qian, L., Zheng, Y., Xue, J., Holloway, P.H., 2011. Stable and efficient quantum-dot light-emitting diodes based on solution-processed multilayer structures. Nat. Photonics 5 (9), 543–548.
Qu, L., Peng, Z.A., Peng, X., 2001. Alternative routes toward high quality CdSe nanocrystals. Nano Lett. 1 (6), 333–337.
Radovanovic, P.V., Norberg, N.S., McNally, K.E., Gamelin, D.R., 2002. Colloidal transition-metal-doped ZnO quantum dots. J. Am. Chem. Soc. 124 (51), 15192–15193.
Reiss, P., Protière, M., Li, L., 2009. Core/shell semiconductor nanocrystals. Small 5 (2), 154–168.
Rogach, A., Kershaw, S.V., Burt, M., Harrison, M.T., Kornowski, A., Eychmüller, A., Weller, H., 1999. Colloidally prepared HgTe nanocrystals with strong room-temperature infrared luminescence. Adv. Mater. 11 (7), 552–555.
Rogach, A.L., Eychmüller, A., Hickey, S.G., Kershaw, S.V., 2007. Infrared-emitting colloidal nanocrystals: synthesis, assembly, spectroscopy, and applications. Small 3 (4), 536–557.
Sadhu, S., Haldar, K.K., Patra, A., 2010. Size dependent resonance energy transfer between semiconductor quantum dots and dye using FRET and kinetic model. J. Phys. Chem. C 114 (9), 3891–3897.
Sargent, E.H., 2009. Infrared photovoltaics made by solution processing. Nat. Photonics 3 (6), 325–331.
Schaller, R.D., Pietryga, J.M., Klimov, V.I., 2007. Carrier multiplication in InAs nanocrystal quantum dots with an onset defined by the energy conservation limit. Nano Lett. 7 (11), 3469–3476.
Schreuder, M.A., Xiao, K., Ivanov, I.N., Weiss, S.M., Rosenthal, S.J., 2010. White light-emitting diodes based on ultrasmall CdSe nanocrystal electroluminescence. Nano Lett. 10 (2), 573–576.
Shirasaki, Y., Supran, G.J., Bawendi, M.G., Bulovic, V., 2013. Emergence of colloidal quantum-dot light-emitting technologies. Nat. Photonics 7 (1), 13–23.
Smith, A.M., Nie, S., 2009. Semiconductor nanocrystals: structure, properties, and band gap engineering. Acc. Chem. Res. 43 (2), 190–200.
Spanhel, L., Haase, M., Weller, H., Henglein, A., 1987. Photochemistry of colloidal semiconductors. 20. Surface modification and stability of strong luminescing CdS particles. J. Am. Chem. Soc. 109 (19), 5649–5655.
Steinhagen, C., Panthani, M.G., Akhavan, V., Goodfellow, B., Koo, B., Korgel, B.A., 2009. Synthesis of Cu2ZnSnS$_4$ nanocrystals for use in low-cost photovoltaics. J. Am. Chem. Soc. 131 (35), 12554–12555.
Tamborra, M., Striccoli, M., Comparelli, R., Curri, M.L., Petrella, A., Agostiano, A., 2004. Optical properties of hybrid composites based on highly luminescent CdS nanocrystals in polymer. Nanotechnology 15 (4), 240–244.

Tan, Z., Zhang, Y., Xie, C., Su, H., Liu, J., Zhang, C., Dellas, N., Mohney, S.E., Wang, Y., Wang, J., Xu, J., 2011. Near-band-edge electroluminescence from heavy-metal-free colloidal quantum dots. Adv. Mater. 23 (31), 3553–3558.

Tang, J., Sargent, E.H., 2011. Infrared colloidal quantum dots for photovoltaics: fundamentals and recent progress. Adv. Mater. 23 (1), 12–29.

Tang, J., Hinds, S., Kelley, S.O., Sargent, E.H., 2008. Synthesis of colloidal $CuGaSe_2$, $CuInSe_2$, and $Cu(InGa)Se_2$ nanoparticles. Chem. Mater. 20 (22), 6906–6910.

Underwood, D.F., Kippeny, T., Rosenthal, S.J., 2001. Ultrafast carrier dynamics in CdSe nanocrystals determined by femtosecond fluorescence upconversion spectroscopy. J. Phys. Chem. B 105 (2), 436–443.

Wang, X., Koleilat, G.I., Tang, J., Liu, H., Kramer, I.J., Debnath, R., Brzozowski, L., Barkhouse, D.A.R., Levina, L., Hoogland, S., Sargent, E.H., 2011. Tandem colloidal quantum dot solar cells employing a graded recombination layer. Nat. Photonics 5 (8), 480–484.

Wehrenberg, B.L., Wang, C., Guyot-Sionnest, P., 2002. Interband and intraband optical studies of PbSe colloidal quantum dots. J. Phys. Chem. B 106 (41), 10634–10640.

Wong, E.M., Searson, P.C., 1999. ZnO quantum particle thin films fabricated by electrophoretic deposition. Appl. Phys. Lett. 74 (20), 2939–2941.

Wu, D., Kordesch, M.E., Van Patten, P.G., 2005. A new class of capping ligands for CdSe nanocrystal synthesis. Chem. Mater. 17 (25), 6436–6441.

Xie, R., Kolb, U., Li, J., Basché, T., Mews, A., 2005. Synthesis and characterization of highly luminescent CdSe-core $CdS/Zn_{0.5}Cd_{0.5}S/ZnS$ multishell nanocrystals. J. Am. Chem. Soc. 127 (20), 7480–7488.

Yang, J., Ling, T., Wu, W.-T., Liu, H., Gao, M.-R., Ling, C., Li, L., Du, X.-W., 2013. A top-down strategy towards monodisperse colloidal lead sulphide quantum dots. Nat. Commun. 4, 1695.

Ye, J., Thompson, C.V., 2011. Templated solid-state dewetting to controllably produce complex patterns. Adv. Mater. 23 (13), 1567–1571.

Yu, W.W., Peng, X., 2002. Formation of high-quality CdS and other II-VI semiconductor nanocrystals in noncoordinating solvents: tunable reactivity of monomers. Angew. Chem. Int. Ed. 41 (13), 2368–2371.

Zhang, Q., Li, W., Moran, C., Zeng, J., Chen, J., Wen, L.-P., Xia, Y., 2010. Seed-mediated synthesis of Ag nanocubes with controllable edge lengths in the range of 30-200 nm and comparison of their optical properties. J. Am. Chem. Soc. 132 (32), 11372–11378.

Zhang, Y., Xie, C., Su, H., Liu, J., Pickering, S., Wang, Y., Yu, W.W., Wang, J., Wang, Y., Hahm, J.-I., Dellas, N., Mohney, S.E., Xu, J., 2011. Employing heavy metal-free colloidal quantum dots in solution-processed white light-emitting diodes. Nano Lett. 11 (2), 329–332.

Zhong, H., Zhou, Y., Ye, M., He, Y., Ye, J., He, C., Yang, C., Li, Y., 2008. Controlled synthesis and optical properties of colloidal ternary chalcogenide $CuInS_2$ nanocrystals. Chem. Mater. 20 (20), 6434–6443.

Zhou, F., Li, Z.-Y., Liu, Y., Xia, Y., 2008. Quantitative analysis of dipole and quadrupole excitation in the surface plasmon resonance of metal nanoparticles. J. Phys. Chem. C 112 (51), 20233–20240.

Growth of GaN-based nanorod heterostructures (core-shell) for optoelectronics and their nanocharacterization

12

J. Eymery[1,2,4], *D. Le Si Dang*[1,3,4]
[1]Univ. Grenoble Alpes, Grenoble, France; [2]CEA, INAC-SP2M, Grenoble, France; [3]CNRS, Institut Néel, Grenoble, France; [4]CEA-CNRS-UJF group "Nanophysics and Semiconductors", Grenoble, France

12.1 Introduction

InGaN nitride materials have been extensively investigated during the last decade for their use as functional elements in micro- and optoelectronics (Li et al., 2006; Pauzauskie and Yang, 2006; Thelander et al., 2006). They were historically used in UV-blue and white light (with yellow phosphor) emitting diodes (LEDs). The extension to other wavelengths by changing the In-composition is presently the focus of several studies to take advantage of the theoretical bandgap of the alloy from 3.4 for GaN to 0.7 eV for InN. From the practical point of view, a phase separation and a reduced crystalline quality is observed due to the large lattice mismatch ~11% and to the chemical affinity of the binary compounds. Evidence that biaxial strain could suppress phase separation in InGaN alloys has been reported in several studies (e.g., Tabata et al., 2002), and successful attempts to alleviate the phase separation issue using multiple quantum wells (MQWs) solutions have been proposed (Dahal et al., 2010). With respect to alloy layers, main benefits relate to the strain-balance inside the active heterostructure, obtained by adjusting the relative well and barrier thicknesses and to the general material improvement in terms of dislocations, V-defects, and pits. Large lattice mismatch in heterostructures can also be conveniently accommodated in the wire geometry. Indeed, the wire one-dimensional nature may be used to integrate radial or longitudinal heterostructures that may benefit from strain relaxation at the free surface for small diameters or at the wire edge (Li and Wang, 2010; Lu et al., 2014), hence allowing higher indium incorporation with lower defect density. This would allow a better control of longer emission and absorption wavelengths than in planar heterostructures. Furthermore the one-dimensional shape can also favor light guiding effect, which could be used to enhance the light extraction efficiency (Yan et al., 2009).

Several epitaxial growth methods have been employed to get GaN wire heterostructures, mainly molecular beam epitaxy (MBE), metal-organic hydride vapor phase epitaxy (MO-HVPE), and metal-organic vapor phase epitaxy (MOVPE). In the last

Modeling, Characterization and Production of Nanomaterials. http://dx.doi.org/10.1016/B978-1-78242-228-0.00012-0
Copyright © 2015 Elsevier Ltd. All rights reserved.

10 years, this last technique, which features high volume and high throughput production, has promoted the development of a large number of commercially available planar GaN-based products such as blue, green, white LEDs, blue lasers, and high power devices, placing the nitride industry in the second rank behind silicon. Research on the wires/rods have also benefited from the dissemination of MOVPE commercial reactors using standard precursors.

Top-down and bottom-up-approaches have been both developed to grow longitudinal or radial InGaN/GaN MQWs with the objective to address the device market with these 3D heterostructures. Top-down methods took advantage of holographic lithography (Fichtenbaum et al., 2007), silica nanoparticles (Hsieh et al., 2008) and standard photolithography (Albert et al., 2014; Krylyuk et al., 2014) to get patterns of regular arrays of templates with smooth facets for growth, whereas bottom-up techniques were based on catalyst-assisted, catalyst-free/self-organized, and selected-area solutions to get templates for later growths.

Degradation of the optical and structural properties induced by metallic contamination and difficulties in getting well-aligned wires in epitaxy with the substrate lead to the development of epitaxial catalyst-free III-nitride wires. The insertion of axial (longitudinal) InGaN/GaN heterostructures for light emission has been demonstrated first by MBE growth of catalyst-free GaN nanowires (Calleja et al., 2000). Their interesting optical properties (Kikuchi et al., 2004) for light emitting devices (Guo et al., 2010; Kehagias, 2013) are related to the reduction of the piezoelectric field along the c-axis through an efficient strain relaxation of the longitudinal superlattices (Wang et al., 2008) that leads to a mitigation of the quantum-confined Stark effect (QCSE). The fabrication of such longitudinal c-axis InGaN/GaN MQWs has been also demonstrated without catalyst by MO-HVPE with GaCl, trimethyl-indium (TMIn), and NH_3 respectively used as Ga, In, and N precursors to obtain wire-based LED devices (Kim et al., 2004). More recently, high-quality homogeneous c-axis GaN wires and heterostructures have been obtained by MOVPE using NH_3, trimethylgallium, and indium precursors (Koester et al., 2010; Bergbauer et al., 2010). Many variations of the growth process have been proposed in the literature to obtain GaN wires (Eymery, 2014), they will not be detailed here, but some important ingredients for the realization of core-shell heterostructures on non-catalyzed GaN wires can be highlighted (Mandl et al., 2013).

12.2 MOVPE growth of InGaN/GaN core-shell heterostructures

The choice of the substrate and its chemical surface preparation are fundamental to control the epitaxial relationships and orientations between the wire and the substrate (Jung et al., 2014a). Up to now, c-sapphire, c-GaN, and (111)-silicon substrates have been mostly employed.

An annealing of the surface under controlled atmosphere and a thin layer deposition are usually performed to determine the initial surface termination. These steps allow selecting the polarity for the wire nucleation and those of the GaN rod/wires. By convention, the polarity in the GaN non-centrosymmetric wurtzite crystal is defined by the

bond pointing from the Ga cation to the N anion, which describes the polar +c axis labeled [0001] (also called Ga-polar orientation in the surface science community).

The polarity control is very important to master the growth shape, aspect ratio, and facet development and has a direct influence on the emission properties of MQWs as it will be discussed later. The one-dimensional growth is driven by an appropriate choice of the growth conditions: the facet surface diffusion and tip incorporation can be modified in MOCVD by many process parameters such as temperature, pressure, carrier gas, precursor flow rates, reactor pre-reactions, etc. Depending on the application and design of the device, a low or high aspect ratio (length/diameter) may be preferred (Auf der Maur et al., 2012; Römer et al., 2012; Li et al., 2013b). For example, the length of a wire-based LED is controlled by management of internal electrical resistance for an optimum current injection (Blanchard et al., 2014). Thus various one-dimensional geometries can be found in the literature and named, from rods, pillars to wires, with the nano prefix when it applies (generally for diameters smaller than 100 nm).

In practice, continuous and pulsed MOVPE processes have been adapted for different reactor geometries to get GaN templates for MQW depositions. A regular tendency for MOVPE continuous flow techniques (Eymery et al., 2013; Li et al., 2013a) is to reduce the ammonia flux with respect to planar growth (i.e., decrease the V/III molar ratio), to mix the H_2/N_2 carrier gas (etching and passivation effect) and/or to add silane gas during the GaN wire growth (sidewall passivation effects). The regularity of the wire template assembly is preferred to grow the core-shell structures in order to limit the fluctuations of dimensions and element incorporation that may impact the device features. Size-calibrated wire templates localized on arrays allow controlling the mass flows of the different incorporation paths (gas phase and surface diffusion) in order to limit possible heterogeneities in local thickness and composition. The selected area growth method is mostly applied to position wires with a given diameter (Hersee et al., 2006; Yeh et al., 2012). It uses silicon nitride or silicon oxide mask to prohibit the MOVPE growth of nitride compounds except in openings of well-chosen sizes and orientations. Within the pulsed-growth mode, growth interruption time of precursors allow defining the morphology of the tip of the wires, i.e., the template for the growth (Jung et al., 2014a). Generally, it allows also getting uniform wire length that simplifies the planarization process involved in many post-growth technological processes. Another solution to obtain wire heterostructures with highly regular length is to use a growth scaffold etched from a planar template. As said before, this method has been demonstrated for the realization of both longitudinal MQWs directly etched from planar growth, and core-shell MQWs overgrown on initially etched and passivated wires (Chang et al., 2012; Kim et al., 2014). One main challenge is to have vertical sidewalls with well-defined facets and very regular height distributions. Of course, in the last method, material deposition on the substrate surface between wires is more difficult to prevent during the growth of core-shell heterostructures (Le Boulbar et al., 2013).

The sidewall emission of InGaN/GaN core-shell has been first demonstrated in LED and optically pumped laser with Ni-catalyst wires of triangular cross-section. They were grown along the $[11\bar{2}0]$-axis (a-axis) with sidewalls corresponding to two equivalent semi-polar $\{1\bar{1}01\}$ planes and one polar $\{0001\}$ plane (Qian et al., 2004, 2005, 2008). But most of the recent MOVPE developments have optimized the $\pm c$-growth axis and $\{1\bar{1}00\}$-sidewall facets (m-plane) to take advantage of the epitaxial relationship with

usual substrates and to have equivalent planes (Frajtag et al., 2011; Li and Waag, 2012). As shown by several studies (Chen et al., 2010; Alloing et al., 2011; Li et al., 2011), the wire polarity defined by the $+c$ or $-c$-axis growth determines directly the morphology of the tip of the wire. For the growth along the $-c$-axis, the top surface of the wire is usually flat with the $\left[000\bar{1}\right]$ plane, whereas a pyramidal shape is obtained in $+c$-axis crystals with semipolar $\left\{10\bar{1}1\right\}$ and $\left\{10\bar{1}2\right\}$ (r-plane) side facets (Ra et al., 2014a). The MQW growth depends on the sidewall orientation as it has been observed for planar growth (Farrell et al., 2012). Moreover, in wires, the finite size of the facets and the presence of edges may add kinetic effects that complicate the modeling of relative growth rates and In-incorporation. As for planar growth, emission of wire-based MQWs is modified (as detailed later) by the presence of the spontaneous and piezoelectric fields also dependent on the plane orientation and strain state (Waltereit et al., 2000; Romanov et al., 2006; Park et al., 2007). As an example, the demonstration of purely nonpolar sidewall emission, which improves the optical quantum efficiency for planar epitaxy, has been reported for m-plane MQWs (Koester et al., 2011; Kim et al., 2014). In a very general way (see below), high spatial resolution techniques are therefore necessary to separate the contributions coming from different parts of the sample and to relate the structure/composition to the optical properties.

The MOVPE process parameters to obtain core-shell MQWs are very similar to those of planar growth and correspond to significant changes of flow and temperature values with respect to wire growth, that is, larger V/III ratio and use of trimethyl- or triethyl-indium precursors and N_2 carrier gas (see examples of experimental conditions in Koester et al., 2011 and Ra et al., 2014b). The MQW positioning at the top of the GaN template can be controlled by using a large addition of silane at the wire bottom. This produces deposition of a thin SiN_x passivation layer that can avoid MQW growth at the wire bottom part (Eymery et al., 2012). To improve the emission efficiency, the MQW electronic band profile's shape (square, trapezoidal, or triangular) can be tuned from growth parameter management to take into account In-diffusion and drift during deposition (Zhao et al., 2011), and an AlGaN electron blocking layer can also be grown between the MQW and the external p-doped GaN layer. Due to the size of the GaN templates, the difficulty of incorporating large In-content in MQWs with conventional MOVPE precursors is still present in these core-shell materials (Cho et al., 2001). The fine adjustment of the process parameters is related to the reactor geometry, as is usually the case in planar growth, but also to particular aspects of growth mechanisms related to the wire aspect ratio. Until now, this point has not been studied extensively in the literature as with MBE, but we can suspect a change of the incorporation and diffusion of the atoms on the wire sidewall and edges as a function of growth parameters and wire density (Borg et al., 2013).

12.3 Nanocharacterization: structure and optics

A combination of characterization techniques at different spatial resolutions is mandatory to quantify the structural, chemical, and optical properties of core-shell InGaN/GaN MQWs wires, to understand their physical properties, and to optimize their performances.

Average information of wire assemblies is first needed to optimize the general growth parameters and to evaluate their fluctuations. X-ray diffraction under grazing incidence gives access to the average strain tensor for planes parallel or perpendicular to the surface. The very high sensitivity of this technique to the surface has been demonstrated for the growth of GaN wires on sapphire and silicon (Koester et al., 2010; Kaganer et al., 2012), but also for homoepitaxially grown wires (Eymery et al., 2007). The measurements of the Bragg peak positions for 8-20 keV X-ray energies allows determining the epitaxial relationships and the misorientations of the wires with respect to the substrate. These tilt-and-twist disorientations that can be measured independently from in-plane and out-of-plane scans in reciprocal space are due to substrate surface miscut, interfacial dislocations, and patterning. The measurement of the crystal truncation rods perpendicular to the surface, also performed at grazing incidence to be surface sensitive, checks the atomic plane stacking along the wire's growth-axis and can determine the absence (or an upper value) of stacking faults parallel to the surface, that is, "cubic" stacking default domains inside the hexagonal wurtzite GaN lattice. In general, MOVPE-grown wires have a very low density of stacking faults as confirmed by many electron transmission microscopy observations. X-ray diffraction measurement of core-shell MQWs is very demanding, but necessary task for better growth control, by providing period and relative thickness fluctuations of the barriers and wells. A maximum of intensity for the multilayers is obtained for a "simultaneous scattering" of the MQW. It can be expressed as the square of the sum of the object's amplitudes over the coherence length of the experiments in the kinematical theory (Kaganer et al., 2012). This ideal condition, which requires small fluctuations of the MQWs size, strain, and position in the wire assembly, is much more easily fulfilled in planar growths. Indeed, for similar MQWs in terms of geometry and composition, for example, $5\times$ (2 nm $In_{0.15}Ga_{0.85}N$/8 nm GaN) heterostructures, much more intense superlattice peaks are measured on planar growths than on core-shell wires. This low intensity generally requires the use of synchrotron radiation, but regular arrays of core-shell wires should in principle be measured with laboratory setups. The detailed analysis of the peak position providing the strain relaxation inside the core-shell MQWs and the appearance of dislocations at the critical thickness, as well as the use of anomalous measurement (i.e., change of atomic scattering with energy) to extract the average indium composition, are presently under investigation and should be reported soon. Raman spectroscopy has been also applied to measure the strain in wires (Foltynski et al., 2014). The measured frequency shift can be related to the strain distributions taking into account resonant absorption and scattering for selection rules depending on the crystal structure and phonon confinement. This method has been already demonstrated for axial nanowires superlattices grown by MBE (Wölz et al., 2013) and to MOCVD core-shell MQWs using tip enhanced Raman spectroscopy (Poliani et al., 2013).

Single-object studies have been developed to quantify local strain and composition and their small-scale fluctuations. A large number of electron microscopy techniques have been successfully applied to the MOVPE nitride wires and provided first rank information (Wang and Wang, 2014). Transmission electron microscopy (TEM) has demonstrated many successes using diffraction contrast imaging (DC), high-angle annular dark-field imaging (HAADF), and high-resolution (HR-TEM). These techniques take advantage of the disponibility of new aberration-corrected microscopes,

of the possibility for having very small diameter electron probes, and of the development of tomography. The quantum well geometry and strains are quantified locally from mappings of the deformation states and the nature of extended defects (dislocation, stacking faults, antiphase boundaries) can be analyzed in details. The main drawback of this technique, that is, the substrate thinning that may relieve the strain in heterostructures, can be removed in small diameter heterostructures. This condition is generally fulfilled in axial MBE insertions and catalyst core-shell MOVPE growth (Qian et al., 2004), but not in general for noncatalyst MOVPE wires that need to be prepared, for example, by focused ion beams (Koester et al., 2011). Electron spectroscopy techniques such as energy loss (EELS) or energy dispersive X-ray spectroscopy (EDS) are also really useful to estimate the In-composition inside the MQWs when corrected from projection and resolution artifacts. More recently, atom probe techniques have proved very efficient for studying the chemistry of wire heterostructures using high-resolution secondary ion mass spectroscopy and correlated atom probe tomography (APT), see for example, Rigutti et al. (2014) and Mancini et al. (2014). Mapping and tomographic analysis of the In-distribution, interface morphology, and dopant clustering revealed the quality of core-shell InGaN/GaN MQWs (for limited In-content < 20 % and large diameter > 500 nm) comparable to that of planar growth (Riley et al., 2013). The heterogeneity with higher In-content or smaller diameter has not been studied yet in core-shell wires, but only in alloyed and longitudinal heterostructures. It may provide an interesting approach to understand clustering, phase separation, and segregation in these systems.

Of course, combined global and local structural and chemical characterizations are combined with emission spectroscopy to understand the emission properties. In principle, the same individual nanorods should be probed using various experimental techniques to help establishing some cross-correlation between growth conditions and structural and electronic properties. In the following, we discuss recent reports illustrating such correlation studies of single nitride nanorod heterostructures. As previously mentioned, it is important to ascertain the nanorod polarity, since it strongly impacts nanorod shape, optical and electrical properties (see for example Gogneau et al., 2014). Previous structural characterization of GaN layers grown by MOCVD on sapphire substrates showed that their polarity can be controlled by annealing at $\sim$1000°C the GaN buffer layer grown at lower temperature ($\sim$600°C), with the Ga polarity favored by short annealing times ($<$20 min) while both Ga and N polarities would coexist for longer annealing times (Sumiya et al., 1999). This dual-polarity has been also observed in wires. It induces Interface Domain Boundaries (IDB) that have been measured by electron microscopy in wires guided growth, close to the holes of patterned masks (Chen et al., 2010) and in the core of wires (Tessarek et al., 2014). More recently the dual polarity has been evidenced in GaN micropillars grown by MOVPE at $\sim$1000°C in a study combining KOH etching, TEM-Convergent Beam Electron Diffraction (CBED) and cathodoluminescence (CL) measurements at room temperature (Coulon et al., 2014). Precise structural analysis of core-shell wires is crucial for full understanding of one-dimensional growth mechanisms and physical properties. This can be achieved with HAADF imaging based on STEM (Scanning

Tunneling Electron Microscope), a nano-characterization tool highly sensitive to the atomic number Z of atoms. It could be complemented with APT to provide a complete three-dimensional picture of the heterostructure (Riley et al., 2013; Rigutti et al., 2014). As for TEM, HAADF, and APT necessitate heavy (destructive) sample preparation, by contrast to optical measurements. Cross-sectional HAADF-STEM image and the associated APT reconstruction of an InGaN/GaN MQW core-shell nanowire fabricated by a top-down approach and subsequent MOCVD growth have been performed by Riley et al. (2013). HAADF image showed that InGaN QWs are wider on non-polar $(1\bar{1}00)$ side-facets than on semi-polar $(10\bar{1}1)$ apex-facets. From APT analysis, the authors deduced an In distribution with random alloy fluctuations (bimodal-like distribution), but strongly anisotropic, i.e., 13.5% In mole fraction in non-polar QWs versus 8% in semi-polar QWs.

In another study of core-shell micro-wires, structural characterization by HAADF-STEM and Time of Flight-Secondary Ion Mass Spectroscopy (ToF-SIMS) was correlated with optical characterization by CL and micro-photoluminescence (μPL) measurements (Koester et al., 2011). Strongly n-doped GaN micro-wires were first grown catalyst-free by MOVPE on sapphire substrates, and an InGaN/GaN MQW was subsequently deposited on their sidefacets (non-polar m-planes) in the top parts of GaN wires. CL measurements at 5 K were employed to probe optical properties of single microwires along their length: the CL spectrum in the micro-wire top part is dominated by the InGaN/GaN MQW emission at ~396 nm, well distinct from the emission at ~350 nm in the micro-wire bottom part related to n-doped GaN. The core-shell nature of the MQW emission was confirmed by imaging the intensity distribution of CL at 396 nm in the wire cross-section plane. An important physical property of MQWs deposited on non-polar side-facets is the absence of QCSE, of great interest for wire emitting devices. The authors demonstrated it convincingly with μPL measurements of single micro-wires at 5 K. They showed that the MQW emission wavelength increases with increasing QW growth time, i.e. increasing QW width, but would eventually saturate beyond some critical well thickness, a behavior fully consistent with negligible QCSE. As a result, the radiative recombination rate should be higher in these core-shell MQW wires, which is one of the main motivations for emitting device applications.

Very recently, electrical properties of core-shell p-n junction GaN microwires were investigated by EBIC (Electron Beam Induced Current) measurements (Tchoulfian et al., 2014). EBIC measurements are particularly powerful in providing information on internal electric field, doping level, as well as minority carrier diffusion length. Buried p-n junctions were exposed by manually cleaving micro-wires in half along their axis. In core-shell p-n junction micro-wires, there are two types of junctions: radial junction along the wire radius and axial junction along the wire axis. Interestingly, the authors showed that the depletion widths and doping concentrations could also be deduced by analyzing the contrast of secondary electron voltage across the p-n junction. In these micro-wires, there was no difference in electrical characteristics observed between radial and axial junctions, both presenting similar doping levels. Further discussions on EBIC in core-shell nitride wires can be found in Lavenus et al. (2014).

In a more prospective way, synchrotron nanobeam hard X-ray techniques are now emerging for the characterization of nitride wires. The focused beams (generally smaller than 100 nm and already in the 20 nm range) can be used as a local probe to excite the current and the photoluminescence (Martinez-Criado et al., 2014). This information can be correlated to X-ray fluorescence and diffraction (Segura-Ruiz et al., 2014) to link the structural, chemical, and optical properties, for example to reveal the nature of quantum confinement in core-shell heterostructures using time-resolved and polarization experiments (Martinez-Criado et al., 2014). These techniques can be combined to spectroscopy mapping at lower energy to have surface information and to coherent X-ray diffraction imaging that exploits the ultra-high sensitivity of the diffraction pattern to the distortions of crystalline lattice.

12.4 Conclusions for nitride wire-LEDs practical issues

As illustrated by the latter discussions, the use of core-shell InGaN/GaN MQWs for the realization of efficient single-color wire-based devices must consider several important points to be competitive with more mature planar devices in terms of performance and costs:

(i) To solve the so-called "green-gap" in the internal quantum efficiency. The "green-gap" of InGaN MQWs refers to the drop of their internal quantum efficiency with increasing wavelengths. The physical origin of this effect is generally thought to be a combination of QCSE and Auger Effect (Iveland et al., 2013). In addition, strain/defect management is still a growth challenge with high In-content (>20%) on m-plane sidewalls and the control of the homogeneity along the height of the wire appears to be very problematic, especially for Ga polar wires with non-polar top facets.

(ii) To inject the current homogeneously in the active m-plane MQWs and not in other parts of the device. The use of patterned substrates for selective area growth seems at this moment mandatory to control the geometry and size fluctuations of heterostructures. Some growth solutions are already proposed in the literature, such as the growth of pyramidal undoped GaN structures on tops of the r-plane facets of Ga-polar structures. This layer minimizes the current flow through this portion and the current can be effectively guided to the sidewall m-plane InGaN/GaN MQWs (Tu et al., 2014). Growth or etching solutions must be combined with more usual optoelectronic deposition techniques to solve the question of top/bottom contacts and to integrate these 3D structures with convenient doping in full devices.

(iii) To generate multi-color devices. The implementation of multicolor sources (Qian et al., 2005) is still under development and has to solve, in parallel, the point (ii) for each color in order to manage color mixing.

(iv) To take advantage of light extraction coming from the wire geometry. Due to technological requirements in terms of planarization, contacting and choice of substrate, the light extraction has to be carefully optimized (Köelper et al., 2012). It can be performed by finite-difference time-domain calculations to estimate the ideal configuration in terms of diameter/length and distance between wires (Li & Li, 2013), but also the influence of complex 3D stacking with many materials.

References

Albert, S., Bengoechea-Encabo, A., Sabido-Siller, M., Müller, M., Schmidt, G., Metzner, S., Veit, P., Bertram, F., Sanchez-Garcia, M.A., Christen, J., Calleja, E., 2014. Growth of InGaN/GaN core-shell structures on selectively etched GaN rods by molecular beam epitaxy. J. Cryst. Growth 392, 5–10.

Alloing, B., Vezian, S., Tottereau, O., Vennegues, P., Beraudo, E., Zuniga-Perez, J., 2011. On the polarity of GaN micro- and nanowires epitaxially grown on sapphire 0001 and Si 111 substrates by metal organic vapor phase epitaxy and ammonia-molecular beam epitaxy. Appl. Phys. Lett. 98, 011914.

Auf Der Maur, M., Sacconi, F., Di Carlo, A., 2012. A parametric study of InGaN/GaN nanorod core-shell LEDs. IEEE Trans. Electron Devices 60 (1), 171–177.

Bergbauer, W., Strassburg, M., Kölper, C., Linder, N., Roder, C., Lähnemann, J., Trampert, A., Fündling, S., Li, S.F., Wehmann, H.-H., Waag, A., 2010. Continuous-flux MOVPE growth of position-controlled N-face GaN nanorods and embedded InGaN quantum wells. Nanotechnology 21 (30), 305201.

Blanchard, P., Bertness, K.A., Harvey, T., Sanford, N., 2014. Establishing an upper bound on contact resistivity of ohmic contacts to n-GaN nanowires. Semicond. Sci. Technol. 29, 054005.

Borg, M.B., Johansson, J., Storm, K., Deppert, K., 2013. Geometric model for metalorganic vapour phase epitaxy of dense nanowire arrays. J. Cryst. Growth 366, 15–19.

Calleja, E., Sanchez-Garcia, M.A., Sanchez, F.J., Calle, F., Naranjo, F.B., Munoz, E., 2000. Luminescence properties and defects in GaN nanocolumns grown by molecular beam epitaxy. Phys. Rev. B 62 (24), 16826–16834.

Chang, J.-R., Chang, S.-P., Li, Y.-J., Cheng, Y.-J., Sou, K.-P., Huang, J.-K., Kuo, H.-C., Chang, C.-Y., 2012. Fabrication and luminescent properties of core-shell InGaN/GaN multiple quantum wells on GaN nanopillars. Appl. Phys. Lett. 100 (26), 261103.

Chen, X.J., Perillat-Merceroz, G., Sam-Giao, D., Durand, C., Eymery, J., 2010. Homoepitaxial growth of catalyst-free GaN wires on N-polar substrate. Appl. Phys. Lett. 97 (15), 151909.

Cho, H.K., Lee, J.Y., Kim, C.S., Yang, G.M., 2001. Structural and optical investigation of InGaN/GaN multiple quantum well structures with various indium compositions. J. Electron. Mater. 30 (10), 1348–1352.

Coulon, P.M., Mexis, M., Teisseire, M., Jublot, M., Vennéguès, P., Leroux, M., Zuniga-Perez, J., 2014. Dual-polarity GaN micropillars grown by metalorganic vapour phase epitaxy: cross-correlation between structural and optical properties. J. Appl. Phys. 115, 153504.

Dahal, R., Li, J., Aryal, K., Lin, J.Y., Jiang, H.X., 2010. InGaN/GaN multiple quantum well concentrator solar cells. Appl. Phys. Lett. 97 (7), 073115.

Eymery, J., 2014. Metal organic vapour phase epitaxy. In: Consonni, V., Feuillet, G. (Eds.), Wide Band Gap Semiconductor Nanowires for Optical Devices: The Particular Case of GaN and ZnO. ISTE-Wiley, Hermes Science Publishing, London.

Eymery, J., Rieutord, F., Favre-Nicolin, V., Robach, O., Niquet, Y., Froberg, L., Martensson, T., Samuelson, L., 2007. Strain and shape of epitaxial InAs/InP nanowire superlattice measured by grazing incidence X-ray techniques. Nano Lett. 7, 2596–2601.

Eymery, J., Salomon, D., Chen, X.J., Durand, C., 2012. Process for catalyst-free selective growth on a semiconductor structure. Patent number WO2012136665.

Eymery, J., Chen, X.J., Durand, C., Kolb, M., Richter, G., 2013. Self-organized and self-catalyst growth of semiconductor and metal wires by vapour phase epitaxy: GaN rods versus Cu whiskers. C. R. Phys. 14, 221–227.

Farrell, R.M., Young, E.C., Wu, F., Denbaars, S.P., Speck, J.S., 2012. Materials and growth issues for high-performance nonpolar and semipolar light-emitting devices. Semicond. Sci. Technol. 27, 024001.

Fichtenbaum, N.A., Neufeld, C.J., Schaake, C., Wu, Y., Wong, M.H., Grundmann, M., Keller, S., Denbaars, S.P., Speck, J.S., Mishra, U.K., 2007. Metalorganic chemical vapor deposition regrowth of InGaN and GaN on N-polar pillar and stripe nanostructures. Jap. J. Appl. Phys. 46 (10), L230–L233.

Foltynski, B., Garro, N., Vallo, M., Finken, M., Giesen, C., Kalisch, H., Vescan, A., Cantarero, A., Heuken, M., 2014. The controlled growth of GaN microrods on Si (111) substrates by MOCVD. J. Crystal Growth. In press. http://dx.doi.org/10.1016/j.jcrysgro.2014.10.047.

Frajtag, P., Hosalli, A.M., Bradshaw, G.K., Nepal, N., El-Masry, N.A., Bedair, S.M., 2011. Improved light-emitting diode performance by conformal overgrowth of multiple quantum wells and fully coalesced p-type GaN on GaN nanowires. Appl. Phys. Lett. 98 (14), 143104.

Gogneau, N., Chretien, P., Galopin, E., Guillet, S., Travers, L., Harmand, J.-C., Houze, F., 2014. Impact of the GaN nanowire polarity on energy harvesting. Appl. Phys. Lett. 104, 213105.

Guo, W., Zhang, M., Banerjee, A., Bhattacharya, P., 2010. Catalyst-free InGaN/GaN nanowire light emitting diodes grown on (001) silicon by molecular beam epitaxy. Nano Lett. 10 (9), 3355–3359.

Hersee, S.D., Sun, X.Y., Wang, X., 2006. The controlled growth of GaN nanowires. Nano Lett. 6, 1808–1811.

Hsieh, M.-Y., Wang, C.-Y., Chen, L.-Y., Ke, M.-Y., Huang, J., 2008. InGaN-GaN nanorod light emitting arrays fabricated by silica nanomasks. IEEE J. Quant. Electron. 44 (5), 468–472.

Iveland, J., Martinelli, L., Peretti, J., Speck, J.S., Weisbuch, C., 2013. Direct measurement of Auger electrons emitted from a semiconductor light-emitting diode under electrical injection: identification of the dominant mechanism for efficiency droop. Phys. Rev. Lett. 110 (17), 177406.

Jung, B.O., Bae, S.-Y., Kato, Y., Imura, M., Lee, D.-S., Honda, Y., Amano, H., 2014a. Morphology development of GaN nanowires using a pulsed-mode MOCVD growth technique. CrystEngComm. 16, 2273–2282.

Jung, O.J., Bae, S-.Y., Kim, S.Y., Lee, S., Lee, J.Y., Lee, D.-S., Kato, Y., Honda, Y., Amano, H., 2014b. Highly ordered catalyst-free InGaN/GaN core-shell architecture arrays with expanded active area region. Nano Energy 11, 294–303.

Kaganer, V.M., Jenichen, B., Brandt, O., Fernández-Garrido, S., Dogan, P., Geelhaar, L., Riechert, H., 2012. Inhomogeneous strain in GaN nanowires determined from X-ray diffraction peak profiles. Phys. Rev. B 86, 115325.

Kehagias, T., Dimitrakopulos, G.P., Becker, P., Kioseoglou, J., Furtmayr, F., Koukoula, T., Häusler, I., Chernikov, A., Chatterjee, S., Karakostas, T., Solowan, H.-M., Schwarz, U. T., Eickhoff, M., Komninou, P., 2013. Nanostructure and strain in InGaN/GaN superlattices grown in GaN nanowires. Nanotechnology 24 (43), 435702.

Kikuchi, A., Kawai, M., Tada, M., Kishino, K., 2004. InGaN/GaN multiple quantum disk nanocolumn light-emitting diodes grown on (111) Si substrate. Jpn. J. Appl. Phys. 43, L1524–L1526.

Kim, H.-M., Cho, Y.-H., Lee, H., Kim, S., Ryu, S.R., Kim, D.Y., Kang, T.W., Chyng, K.S., 2004. High-brightness light emitting diodes using dislocation-free indium gallium nitride/gallium nitride multiquantum-well nanorod arrays. Nano Lett. 4 (6), 1059–1062.

Kim, J.-H., Ko, Y.-H., Cho, J.-H., Gong, S.-H., Ko, S.-M., Cho, Y.-H., 2014. Toward highly radiative white light emitting nanostructures: a new approach to dislocation eliminated

GaN/InGaN core-shell nanostructures with a negligible polarization field. Nanoscale 6, 14213–14220.

Koester, R., Hwang, J.S., Durand, C., Dang, D.L.S., Eymery, J., 2010. Self-assembled growth of catalyst-free GaN wires by metal-organic vapour phase epitaxy. Nanotechnology 21 (1), 015602.

Koester, R., Hwang, J.-S., Salomon, D., Chen, X., Bougerol, C., Barnes, J.-P., Dang, D.L.S., Rigutti, L., De Luna Bugallo, A., Jacopin, G., Tchernycheva, M., Durand, C., Eymery, J., 2011. M-plane core-shell InGaN/gan multiple-quantum-wells on GaN wires for electroluminescent devices. Nano Lett. 11, 4839–4845.

Kölper, C., Sabathil, M., Romer, F., Mandl, M., Strassburg, M., Witzigmann, B., 2012. Core-shell InGaN nanorod light emitting diodes: electrical and optical device properties. Phys. Stat. Sol. A. 209 (11), 2304–2312.

Krylyuk, S., Debnath, R., Yoon, H.P., King, M.R., Ha, J.-Y., Wen, B., Motayed, A., Davydov, A.V., 2014. Faceting control in core-shell GaN micropillars using selective epitaxy. Appl. Phys. Lett. Mat. 2, 106104.

Lavenus, P., Messanvi, A., Rigutti, L., De Luna Bugallo, A., Zhang, H., Bayle, F., Julien, F.H., Eymery, J., Durand, C., Tchernycheva, M., 2014. Experimental and theoretical analysis of transport properties of core-shell wire light emitting diodes probed by electron induced current microscopy. Nanotechnology 25, 255201.

Le Boulbar, E.D., Gîrgel, I., Lewins, C.J., Edwards, P.R., Martin, R.W., Satka, A., Allsopp, D. W.E., Shields, P.A., 2013. Facet recovery and light emission from GaN/InGaN/GaN core-shell structures grown by metal organic vapour phase epitaxy on etched GaN nanorod arrays. J. Appl. Phys. 114 (9), 094302.

Li, Q., Li, K., 2013. Analysis on the light extraction efficiency of GaN-based nanowires light-emitting diodes. IEEE J. Quant. Electron. 49, 697–704.

Li, S., Waag, A., 2012. GaN based nanorods for solid state lighting. J. Appl. Phys. 111 (7), 071101.

Li, Q., Wang, G.T., 2010. Strain influenced indium composition distribution in GaN/InGaN core-shell nanowires. Appl. Phys. Lett. 97 (18), 181107.

Li, Y., Qian, F., Xiang, J., Lieber, C.M., 2006. Nanowire electronic and optoelectronic devices. Mater. Today 9, 18–27.

Li, S.F., Fundling, S., Wang, X., Merzsch, S., Al-Suleiman, M.A.M., Wei, J.D., Wehmann, H.-H., Waag, A., Bergbauer, W., Strassburg, M., 2011. Polarity and its influence on growth mechanism during MOVPE growth of GaN sub-micrometer rods. Cryst. Growth Des. 11, 1573–1577.

Li, S., Wang, X., Mohajerani, M.S., Fündling, S., Erenburg, M., Wei, J., Wehmann, H.-H., Waag, A., Mandl, M., Bergbauer, W., Strassburg, M., 2013a. Dependence of N-polar GaN rod morphology on growth parameters during selective area growth by MOVPE. J. Cryst. Growth 364, 149–154.

Li, C.-K., Yang, H.-C., Hsu, T.-C., Shen, Y.-J., Liu, A.-S., Wu, Y.-R., 2013b. Three dimensional numerical study on the efficiency of a core-shell InGaN/GaN multiple quantum well nanowire light-emitting diodes. J. Appl. Phys. 113 (18), 183104.

Lu, P.F., Sun, C., Cao, H.W., Ye, H., Zhonh, X.X., Yu, Z.Y., Han, L.H., Wang, S.M., 2014. Strain induced composition profile in InGaN/GaN core-shell nanowires. Solid State Commun. 178, 1–6.

Mancini, L., Amirifar, N., Shinde, D., Blum, I., Gilbert, M., Velle, A., Vurpillot, F., Lefebre, W., Larde, R., Talbot, E., Pareige, P., Portier, X., Ziani, A., Davesne, C., Durand, C., Eymery, J., Butte, R., Carlin, J.-F., Grandjean, N., Rigutti, L., 2014. Composition of wide

bandgap semiconductor materials and nanostructures measured by atom probe tomography and its dependence on the surface electric field. J. Phys. Chem. C 118 (41), 24136–24151.

Mandl, M., Wang, X., Schimpke, T., Kölper, C., Binder, M., Ledig, J., Waag, A., Kong, X., Trampert, A., Bertram, F., Christen, J., Barbagini, F., Calleja, E., Strassburg, M., 2013. Group III nitride core-shell nano- and microrods for optoelectronic applications. Phys. Status Solidi RRL 7 (10), 800–814.

Martinez-Criado, G., Segura-Ruiz, J., Alen, B., Eymery, J., Rogalev, A., Homs, A., 2014. Exploring single semiconductor nanowires with a multimodal hard X-ray nanoprobe. Adv. Mat. 26, 7873–7879.

Park, S.H., Ahn, D., Chuang, S.L., 2007. Electronic and optical properties of a- and m-plane Wurtzite InGaN-GaN quantum wells. IEEE J. Quantum Electron. 43 (12), 1175–1182.

Pauzauskie, P.J., Yang, P., 2006. Nanowire photonics. Mater. Today 9, 36–45.

Poliani, E., Wagner, M.R., Reparaz, J.S., Mandl, M., Strassburg, M., Kong, X., Trampert, A., Sotomayor Torres, C.M., Hoffmann, A., Maultzsch, J., 2013. Nanoscale imaging of InN segregation and polymorphism in single vertically aligned InGaN/GaN multi quantum well nanorods by tip-enhanced Raman scattering. Nano Lett. 13 (7), 3205–3212.

Qian, F., Li, Y., Gradecak, S., Wang, D., Barrelet, C.J., Lieber, C.M., 2004. Gallium nitride-based nanowire radial heterostructures for nanophotonics. Nano Lett. 4 (10), 1975–1979.

Qian, F., Gradecak, S., Li, Y., Wen, C.Y., Lieber, C.M., 2005. Core/multishell nanowire heterostructures as multicolor, high-efficiency light-emitting diodes. Nano Lett. 5 (11), 2287–2291.

Qian, F., Li, Y., Gradecak, S., Park, H.-G., Dong, Y., Ding, Y., Wang, Z.L., Lieber, C., 2008. Multi-quantum-well nanowire heterostructures for wavelength-controlled lasers. Nat. Mater. 7, 701–706.

Ra, Y.-H., Navamathavan, R., Kang, S., Lee, C.-R., 2014a. Different characteristics of InGaN/GaN multiple quantum well heterostructures grown on m- and r-planes of a single n-GaN nanowire using metalorganic chemical vapor deposition. J. Mater. Chem. C 2, 2692–2701.

Ra, Y.-H., Navamathavan, R., Yoo, H.-I., Lee, C.-R., 2014b. Single nanowire light-emitting diodes using uniaxial and coaxial InGaN/GaN multiple quantum wells synthesized by metalorganic chemical vapor deposition. Nano Lett. 14 (3), 1537–1545.

Rigutti, L., Blum, I., Shinde, D., Hernandez-Maldonado, D., Lefebvre, W., Houard, J., Vurpillot, F., Vella, A., Tchernycheva, M., Durand, C., Eymery, J., Deconihout, B., 2014. Correlation of microphotoluminescence spectroscopy, scanning transmission electron microscopy, and atom probe tomography on a single nano-object containing an InGaN/GaN multiquantum well system. Nano Lett. 14, 107–114.

Riley, J.R., Padalkar, S., Li, Q., Lu, P., Koleske, D.D., Wierer, J.J., Wang, G.T., Lauhon, L.J., 2013. Three-dimensional mapping of quantum wells in a GaN/InGaN core-shell nanowire light-emitting diode array. Nano Lett. 13, 4317–4325.

Romanov, A.E., Baker, T.J., Nakamura, S., Speck, J.S., 2006. Strain-induced polarization in wurtzite III-nitride semipolar layers. J. Appl. Phys. 100, 023522.

Römer, F., Deppner, M., Andreev, Z., Kölper, C., Sabathil, M., Strassburg, M., Ledig, J., Li, S., Waag, A., Witzigmann, B., 2012. Luminescence and efficiency optimization of InGaN/GaN core-shell nanowire LEDs by numerical modelling. Proc. SPIE 8255 (1), 82550H–82550H–9.

Segura-Ruiz, J., Martinez-Criado, G., Denker, C., Malindretos, J., Rizzi, A., 2014. Phase separation in single InxGa1-xN nanowires revealed through hard X-ray synchrotron nanoprobe. Nano Lett. 14, 1300–1305.

Sumiya, M., Tanaka, M., Ohtsuka, K., Fuke, S., Ohnsihi, T., Ohkubo, I., Yoshimoto, M., Koinuma, H., Kawasaki, M., 1999. Analysis of the polar direction of GaN film growth by coaxial impact collision ion scattering spectroscopy. Appl. Phys. Lett. 75, 674.

Tabata, A., Teles, L.K., Scolfaro, L.M.R., Leite, J.R., Kharchenko, A., Frey, T., As, D.J., Schikora, D., Lischka, K., Furthmüller, J., Bechstedt, F., 2002. Phase separation suppression in InGaN epitaxial layers due to biaxial strain. Appl. Phys. Lett. 80, 769–771.

Tchoulfian, P., Donatini, F., Levy, F., Dussaigne, A., Ferret, P., Pernot, J., 2014. Direct imaging of p-n junction in core-shell GaN wires. Nano Lett. 14, 3491.

Thelander, C., Agarwal, P., Brongersma, S., Eymery, J., Feiner, L., Forchel, A., Scheffler, M., Riess, W., Ohlsson, B., Gosele, U., Samuelson, L., 2006. Nanowire-based one-dimensional electronics. Mater. Today 9, 28–35.

Tu, C.-G., Liao, C.-H., Yao, Y.-F., Chen, H.-S., Lin, C.-H., Su, C.-Y., Shih, P.-Y., Chen, W.-H., Zhu, E., Kiang, Y.-W., Yang, C.C., 2014. Regularly patterned nonpolar InGaN/GaN quantum-well nanorod light-emitting diode array. Opt. Express 22, A1799–A1809.

Waltereit, P., Brandt, O., Trampert, A., Grahn, H.T., Menniger, J., Ramsteiner, M., Reiche, M., Ploog, K.H., 2000. Nitride semiconductors free of electrostatic fields for efficient white light-emitting diodes. Nature 406, 865–868.

Wang, Y., Wang, C., 2014. TEM for characterization of core-shell nanomaterials. In: Kumar, C. S.S.R. (Ed.), Transmission Electron Microscopy Characterization of Nanomaterials. Springer, Berlin, Heidelberg, pp. 243–285.

Wang, C., Chen, L., Chen, C., Cheng, Y., Ke, M., Hsieh, M., Wu, H., Peng, L., Huang, J., 2008. GaN nanorod light emitting diode arrays with a nearly constant electroluminescent peak wavelength. Opt. Express 16 (14), 10549–10556.

Wölz, M., Ramsteiner, M., Kaganer, V.M., Brandt, O., Geelhaar, L., Riechert, H., 2013. Strain engineering of nanowire multi-quantum well demonstrated by Raman spectroscopy. Nano Lett. 13, 4053–4059.

Yan, R.X., Gargas, D., Yang, P.D., 2009. Nanowire photonics. Nat. Photonics 3 (10), 569–576.

Yeh, T.-W., Lin, Y.T., Stewart, L.S., Dapkus, P.D., Sarkissian, R., O'Brien, J.D., Ahn, B., Nutt, S.R., 2012. InGaN/GaN multiple quantum wells grown on nonpolar facets of vertical GaN nanorod arrays. Nano Lett. 12, 3257–3262.

Zhao, H., Liu, G., Zhang, J., Poplawsky, J.D., Dierolf, V., Tansu, N., 2011. Approaches for high internal quantum efficiency green InGaN light-emitting diodes with large overlap quantum wells. Opt. Express 19 (S4), A991–A1007.

Graphene photonic structures

13

N. Yue, Y. Zhang
The University of North Carolina at Charlotte, Charlotte, NC, USA

13.1 Introduction

Since the initial experimental investigation of monolayer graphene by Novoselov and Geim (Novoselov et al., 2004) in 2004, graphene research has evolved from the exploration and development of synthesis techniques of large-size graphene (Novoselov et al., 2005; Zhang et al., 2005; Hass et al., 2008; Kim et al., 2009; Li et al., 2009) to the patterning of graphene nanostructures (GNSs) (Jiao et al., 2009; Kosynkin et al., 2009). Typically, GNSs are patterned on a large-size graphene film either by photolithography or electron beam lithography and plasma etching or obtained by unzipping a carbon nanotube (Jiao et al., 2009; Kosynkin et al., 2009). For both patterning methods, prepatterned graphene has to undergo wet lithography and dry etching processes, which incurs some defects or contaminations to the surface-sensitive graphene. Furthermore, the subsequent transfer process could cause additional perturbation to the morphology or introduce defects to the fragile two-dimensional (2D) graphene during transportation or handling. In contrast, laser-induced local graphene formation (LLG) is a quick and clean approach to synthesizing and patterning graphene. Various LLG techniques have been explored in recent years (Ohkawara et al., 2003; Perrone et al., 2009; Lee et al., 2010; Yue et al., 2012, 2013; Yannopoulos et al., 2012). Among these laser-based approaches for making graphene from SiC, most of these efforts focused on the surface conversion of bulk single-crystalline SiC into graphene. In contrast, our effort (Yue et al., 2012, 2013) focuses on the conversion from polycrystalline SiC thin film or prepatterned SiC micro- and nanostructures grown on Si wafer substrates using molecular beam epitaxy (MBE), and the development of techniques for generating patterned micro- and even nanoscale graphene structures. With the formation of the graphene structures directly on the Si wafer, the integration of graphene-based photonic and electronic devices with existing silicon-based microelectronics becomes more feasible. Furthermore, SiC micro- and nanostructures themselves are of great interest for a number of photonics-related applications.

13.2 Growth of 3C-SiC thin film on Si (111) using MBE

An ultrahigh-vacuum MBE system (with 10^{-10} Torr base pressure) was used to grow SiC thin films on Si substrates. Fullerene (C_{60}) powders were used as carbon sources, and the Si source was directly from the Si (111) wafer substrate. C_{60} is found to

Modeling, Characterization and Production of Nanomaterials. http://dx.doi.org/10.1016/B978-1-78242-228-0.00013-2
Copyright © 2015 Elsevier Ltd. All rights reserved.

decompose when incident on the Si substrate then to react with Si from the substrate to form SiC, under an appropriate combination of substrate temperature (T_S) and C_{60} temperature (T_C) (Yue et al., 2013). In our MBE growth, the typical temperature ranges were $T_S = 700\text{-}800°C$ and $T_C = 500\text{-}600°C$; T_S and T_C are silicon substrate and carbon source temperatures, respectively. The optimal combination was found to be $T_S = 800°C$ and $T_C = 550°C$ in terms of crystallinity and uniformity. During growth, the gas or vapor in the chamber was monitored with a mass spectrometer, and the film surface quality was inspected with reflection high-energy electron diffraction (RHEED). After 10 min of growth, the samples were held at the growth temperature for 5-10 min to homogenize the epitaxial film. Then, the film was allowed to cool down slowly (10°C/min) to room temperature. Figure 13.1 shows the XRD patterns of 3C-SiC grown on Si (111) and bare Si (111). It can be clearly seen that 3C-SiC (111), corresponding to $2\theta = 35.6°$, was grown on Si (111). The surface morphology and cross-section images of a 3C-SiC (111) sample are shown in Figure 13.2, with polycrystalline grains of nearly uniform size and an average thickness of 188 nm.

Although the SiC grain size increases with increasing substrate temperature, the surface roughness also increases, which is undesirable for forming homogeneous graphene on top of the SiC thin film. However, the larger grain 3C-SiC requires higher laser power to induce Si sublimation, making the graphene structure susceptible to more defects and damage. Figure 13.3 shows the surface morphology evolution with increasing substrate temperature. It can be seen that 3C-SiC (111) grown at $T_S = 800°C$ is the most uniform among the different growth conditions.

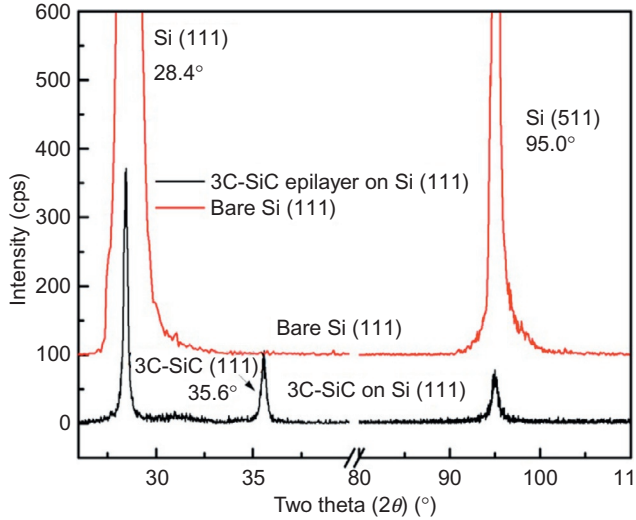

Figure 13.1 XRD patterns of 3C-SiC grown on Si (111) and bare Si (111).

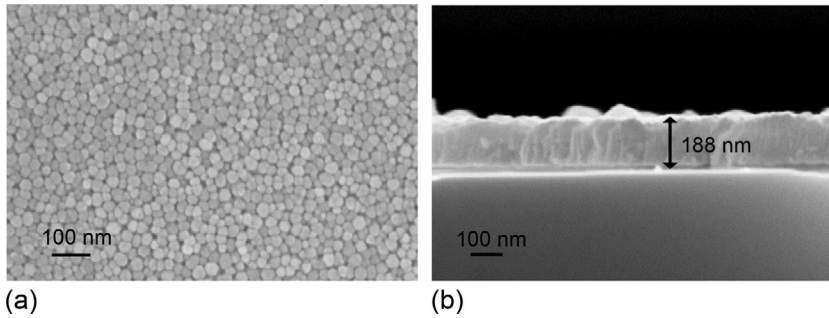

Figure 13.2 SEM images of 3C-SiC (111) on Si (111). (a) Surface morphology, (b) cross-section.

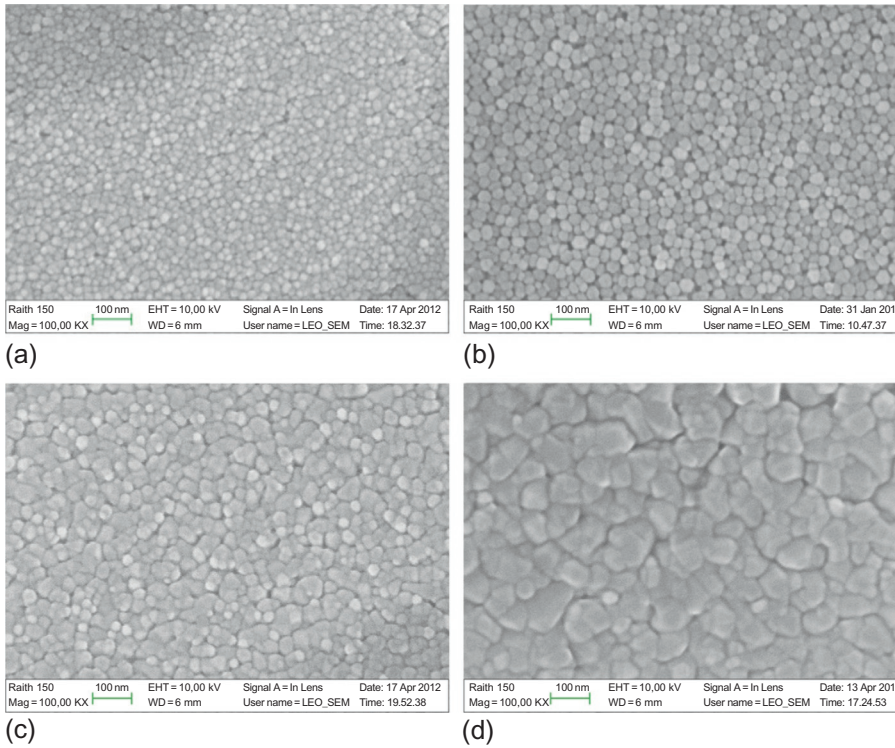

Figure 13.3 SEM surface morphology of 3C-SiC (111) grown on Si (111) at $T_C = 550$ °C and four different T_S temperatures. (a) 700 °C, (b) 800 °C, (c) 900 °C, (d) 1000 °C.

13.3 Laser-induced conversion from 3C-SiC thin film to graphene

The basic principle of this approach is that a tightly focused laser beam of sufficiently high power density can induce local heating, which may sublimate Si atoms of SiC and leave behind C atoms to recrystallize into graphene layers. Therefore, the general idea is similar to the approach of annealing SiC in high vacuum and high temperature (typically 1200-1600°C) (Shivaraman et al., 2009) to obtain graphene film. This annealing technique has been shown to yield high-quality graphene (e.g., with high electron mobility), in particular on the Si face of SiC where monolayer graphene can be obtained (de Heer et al., 2011). In contrast, our procedure has been carried out under ambient conditions (at room temperature in air), although it can also be performed in vacuum or appropriate gas environment and even under an elevated temperature. A 532 nm continuous wave (CW) Nd-YAG laser with maximum incident power of ~30 mW was used to illuminate and then decompose 3C-SiC (111) grown on Si (111) by MBE into graphene layers. The 532 nm CW laser is an integrated part of a confocal μ-Raman system (LabRAM HR800, Horiba Jobin Yvon). The beam size of 1-2 mm can be focused down to a diffraction limit spot with the size of ~0.7 μm on the sample surface when a 100 × objective lens with NA = 0.9 is used. The structural change can be monitored in-situ using μ-Raman. The Raman signal is collected in backscattering geometry. The Raman mapping is carried out by moving the translational stage where the sample sits, controlled with programmable software. With the addition of an external shutter synchronized with the motion control of the translation stage, the illumination site and shape can be controlled to generate different patterns, for instance, dots, lines, or areas. The Raman signal can be obtained simultaneously while the material is being illuminated or probed afterward using lower power. Micron-scale patterns can be obtained by directly using the focused laser beam with a diffraction limit spot size. Even smaller feature sizes (e.g., 100 nm) are possible, if illumination masks are used to define the illumination area or 3C-SiC thin film is selectively deposited in desired patterns. The external and internal shutters are used to control illumination and signal acquisition times, respectively. The laser illumination setup is shown in Figure 13.4, and the phase transformation mechanism is illustrated schematically in Figure 13.5. In the setup described above, the conversion typically requires a laser power of 20-30 mW, depending on the grain structure of the SiC thin film (to be discussed later in detail). In the afterward Raman characterization, the laser power was reduced to 1-2 mW to avoid the laser-heating effect. The Raman spectra of 3C-SiC thin film before and after laser illumination were displayed in Figure 13.6a. It can be clearly seen that three strong peaks of 1348, 1583, and 2691 cm^{-1}, which correspond to D, G, and G' (2D) bands of graphene, emerge after laser illumination. However, the spectrum of the as-grown 3C-SiC on Si (111) does not show these three peaks. A complementary observation is that the intensity of transverse optical phonon mode (TO) of 3C-SiC thin film drops significantly after laser illumination, which implies that the thickness of 3C-SiC decreases due to decomposition or phase change. Because fullerene (C_{60}) was used as a carbon source to grow 3C-SiC on Si (111) and the Raman spectrum of C_{60} was also found to show the D and

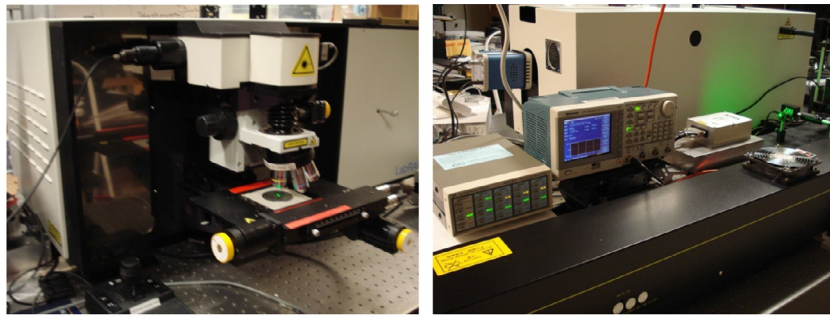

Figure 13.4 Laser illumination setup for SiC-to-graphene conversion, (a) showing that a laser beam is focused by a microscope objective lens on an SiC thin-film grown on an Si wafer, and (b) showing a CW 532-nm laser with a mechanical shutter for controlling the illumination time.

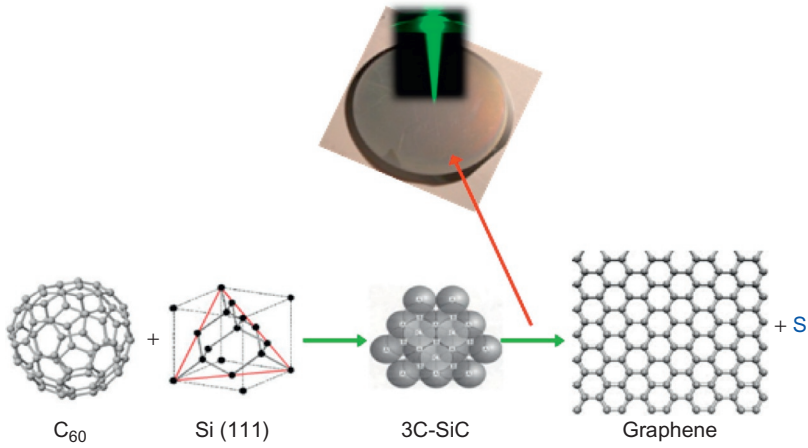

Figure 13.5 Schematic illustration of phase transformation of laser-induced SiC to graphene conversion.

G bands, there was a possibility that D and G peaks could be from C_{60} after laser illumination. However, the comparison of spectra of laser-illuminated 3C-SiC and C_{60}, as shown in Figure 13.6b, indicates that C_{60} possess only two broad bands D and G, and the double resonant 2D mode only appears in the spectrum of laser-illuminated 3C-SiC. Therefore, the 2D Raman mode is a more reliable confirmation of the graphene layers, and the Raman spectrum confirms the formation of graphene layers on the laser-illuminated 3C-SiC on Si (111).

In addition to Raman spectroscopy, transmission electron microscopy (TEM) (JEOL2100) and atomic force microscopy (AFM) (Nanoscope SPM V5r30, Veeco) were also used to further confirm the graphene sheets. The *d*-spacing between graphene layers was measured to be about 3.70 Å from TEM image shown in Figure 13.7. The measured spacing is larger than the interlayer spacing of the crystalline graphite with A-B or Bernal stacking ($c/2 = 3.35$ Å), but close to the theoretically

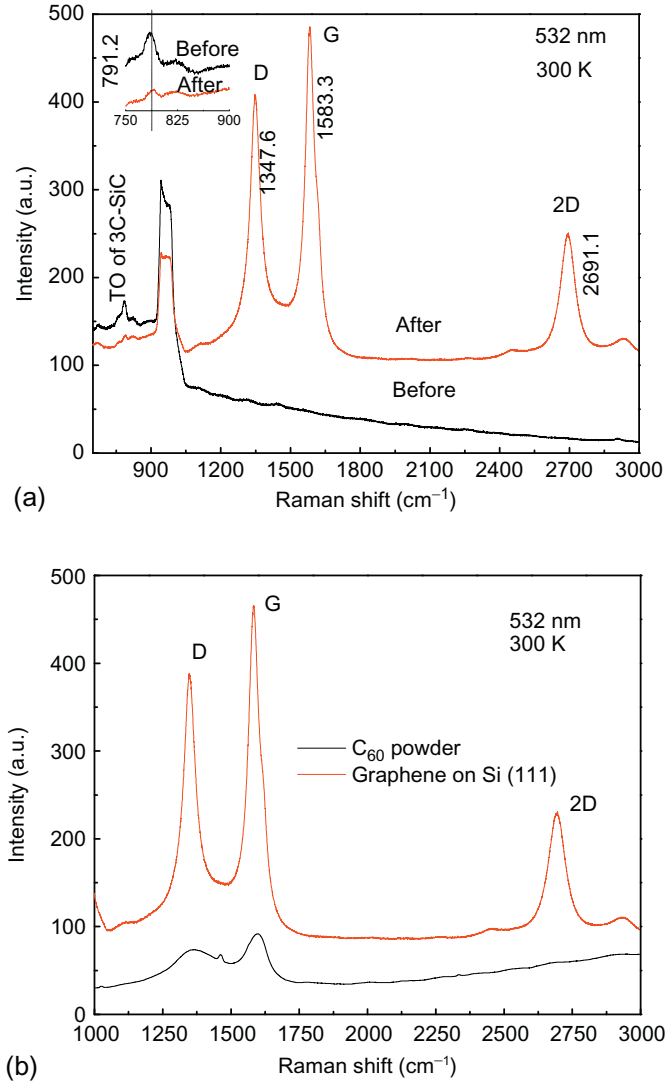

Figure 13.6 The Raman spectra of 3C-SiC on Si (111) before and after laser illumination and of C_{60}. (a) 3C-SiC before and after laser illumination, (b) graphene versus C_{60}.

predicted graphene layers separation of 3.61 Å (0 K) for the A-A stacking (turbostratic stacking) (Zhang and Tsu, 2010), implying that the stacking order of the multilayer graphene is different from that in the crystalline graphite such as HOPG (Ferrari, 2007) and expected to have weaker interlayer coupling. The turbostratic stacking might result from the fast heating and cooling rates of the laser, which may not give graphene layers enough time to equilibrate into the energetically more favorable stacking order. The number of graphene layers was found to be about eight to nine layers, falling in the range of few-layer-graphene (FLG). As corroborating evidence,

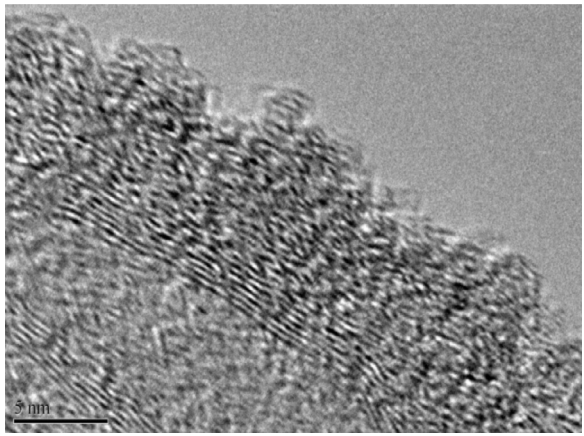

Figure 13.7 TEM micrograph of graphene layers on laser-illuminated 3C-SiC on Si (111).

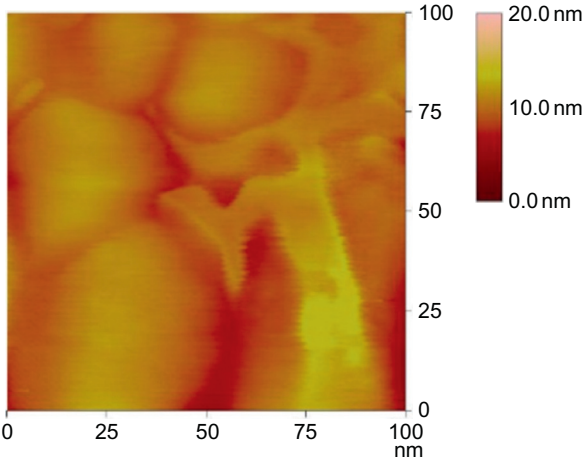

Figure 13.8 AFM topography image of graphene sheet on laser-induced 3C-SiC on Si (111).

the tapping mode AFM image shown in Figure 13.8 reveals a flake with thickness of 3.517 nm, which is approximately the thickness of 3.517/3.7 = 9-10 layers in agreement with the result from the TEM image.

To test the feasibility of patterning graphene structures on the SiC film with a laser, we did a 20 μm long line scan under the illumination of ~20 mW of the 532 nm laser. The illuminated line appears darker than the rest area, as revealed in the optical image in Figure 13.9a. The corresponding Raman mapping at the graphene 2D peak was performed with results shown in Figure 13.9b and c. The optical image shown in Figure 13.9a indicates that the line width of about 2 μm results from the laser spot size of about 0.7 μm. The comparison of Raman image shown in Figure 13.9b with optical image shown in Figure 13.9a indicates that the graphene signal distributes uniformly within the ribbon. The comparison between the two Raman spectra from illuminated and nonilluminated areas, as shown in Figure 13.9c, offers an unambiguous confirmation of the SiC-to-graphene conversion. These promising results

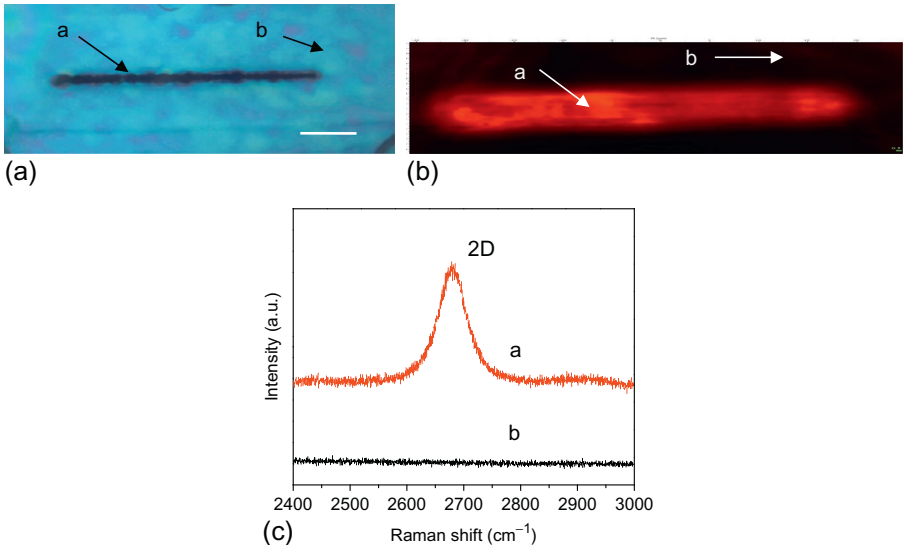

Figure 13.9 Raman mapping results of laser-illuminated 3C-SiC on Si (111). (a) Optical image (scale bar: 5 μm), (b) Raman mapping image (image size: 50×10 μm^2; spectral range: 2650-2750 cm^{-1}), (c) Raman spectra selected from different points.

provide inspiring possibility for patterning electronic devices and electron-photon superstructures.

13.4 Patterning of periodic graphene micro- or nanostructure for photonic application

In principle, three approaches can be applied to patterning graphene micro- or nanostructures based on the laser illumination technique: (a) direct writing (DW), (b) prepatterning (PP), and (c) illumination mask (IM), as schematically illustrated in Figure 13.10. Here we concentrate on evaluation of the first two methods. For the direct writing method, as shown in Figure 13.10a, the smallest feature size of the graphene microstructure depends on the laser spot size, which depends on the numerical aperture

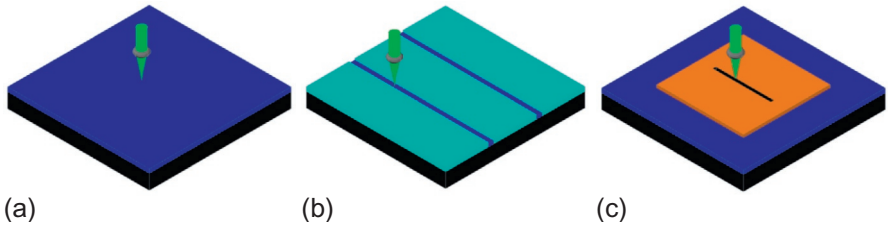

Figure 13.10 Three approaches to pattern graphene micro- or nanostructures using laser annealing technique. (a) Direct writing, (b) prepatterning, (c) illumination mask (black-Si, blue-SiC, light blue-SiO_2, brown-illumination mask, and green-laser).

(NA) of microscope lens, laser wavelength, laser power, and microstructure of 3C-SiC thin film. Figure 13.11 shows graphene microdiscs formed on three different (111) 3C-SiC on Si (111) samples. The three samples have different surface morphologies and crystalline quality, which requires different threshold laser power values to convert

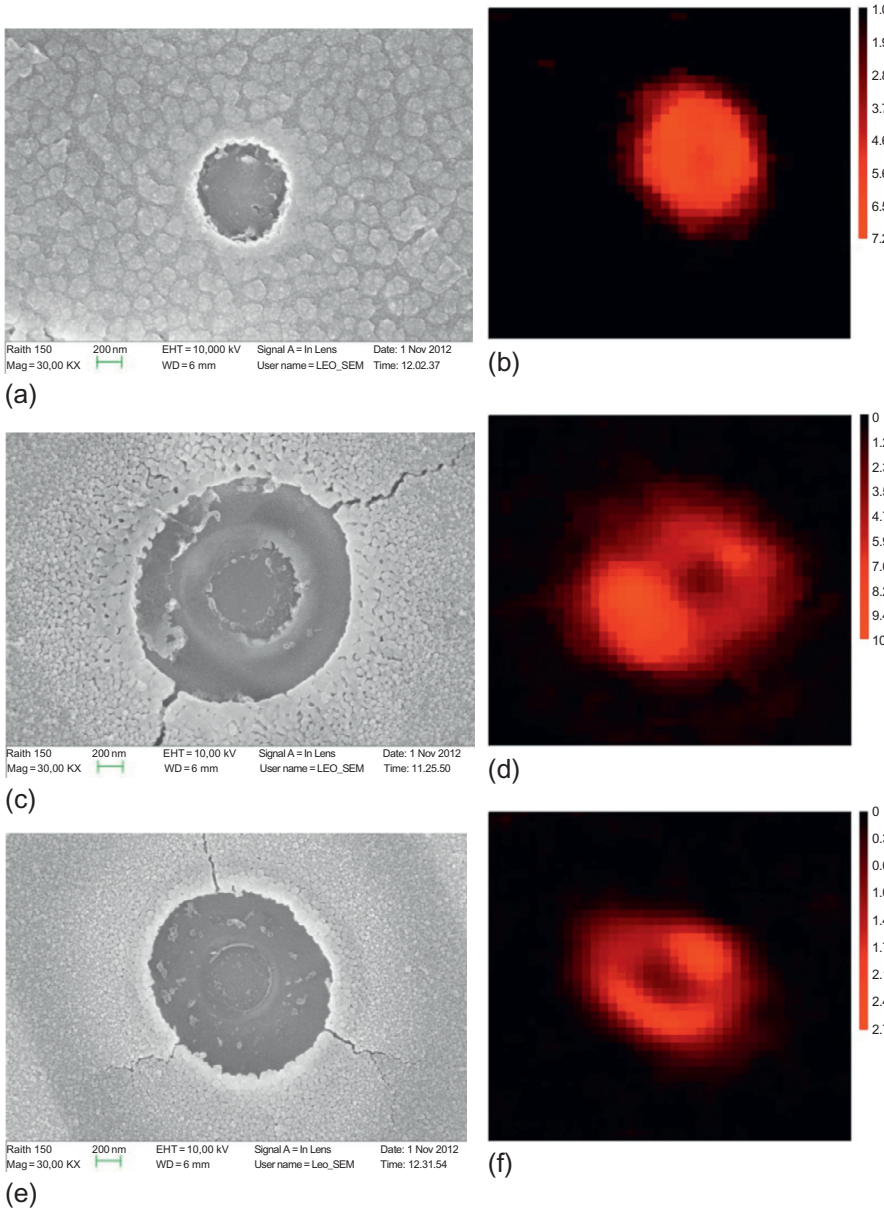

Figure 13.11 SEM and corresponding Raman images (4×4 μm^2) of three graphene dots illuminated with laser on three samples A, B, and C. (a) and (b) Sample A, (c) and (d) sample B, (e) and (f) sample C (Raman spectral range: 2650-2750 cm^{-1} of graphene 2D peak).

3C-SiC into graphene layers. Sample A has a rough surface or highly defective film due to a native SiO_2 layer remaining on the Si substrate, and thus requires the least laser power to induce graphene. Sample B is as thick as sample A, but with fewer defects; therefore, it requires a higher laser power. Sample C is also defective but thinner than sample B; therefore, it requires more laser power than sample B because light absorption is less due to the thinner SiC. Figure 13.11a-f shows scanning electron microscopy (SEM) micrographs of the laser-induced graphene microdiscs and the corresponding Raman images.

Similar to the laser patterning process used for generating individual graphene microdiscs, two, four, and nine graphene dots in arrays of 1×2, 2×2, and 3×3 as well as a 10 μm long graphene ribbon were also patterned by programmed laser illumination. Following the patterning of graphene dots, Raman mapping was performed on the patterned areas, with the Raman images shown in Figure 13.12a-d. In comparison with the direct writing method, the prepatterning method via selectively depositing 3C-SiC can enable smaller graphene feature sizes without the limitation of the laser spot size. This approach is based on the finding that C_{60} only reacts with exposed Si but not SiO_2 (Yue et al., 2013). The achievable feature size depends on the

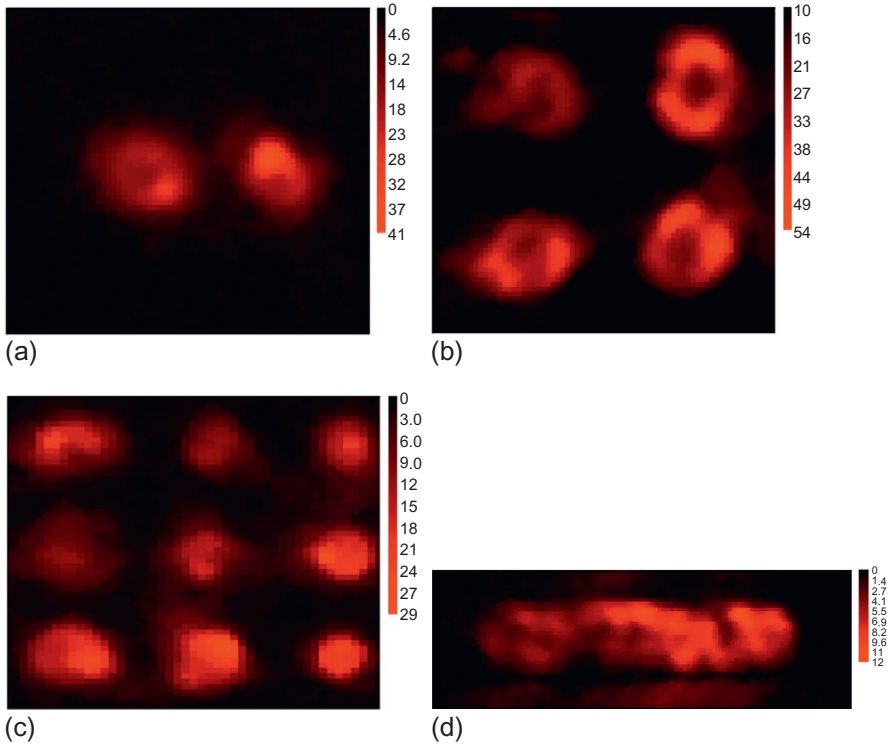

Figure 13.12 Raman mapping images (2650-2750 cm^{-1}) of different graphene microdisc arrays and a μ-ribbon. (a) Two dots in (1×2) array (image size: 6×6 μm^2), (b) four dots in (2×2) array (image size: 6×6 μm^2), (c) nine dots in (3×3) array (image size: 9×9 μm^2), (d) a μ-ribbon (image size: 14×4 μm^2).

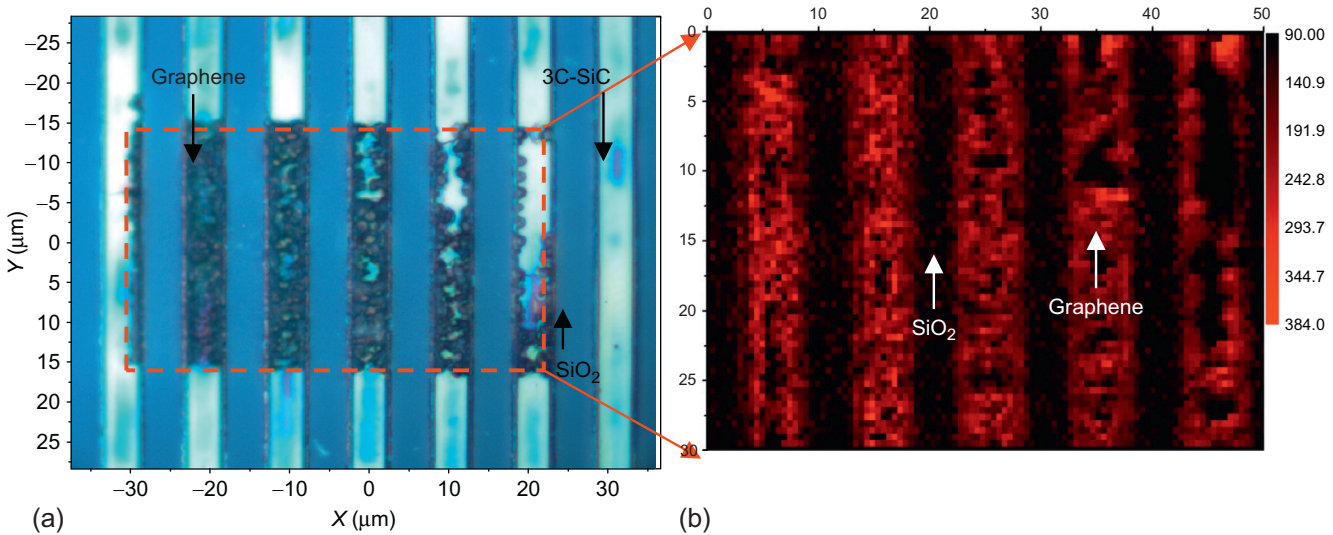

Figure 13.13 Optical and Raman images of selective deposited 3C-SiC/Si (111) (5 μm SiC/5 μm SiO_2). (a) Optical image, (b) Raman map image (2650-2750 cm^{-1}).

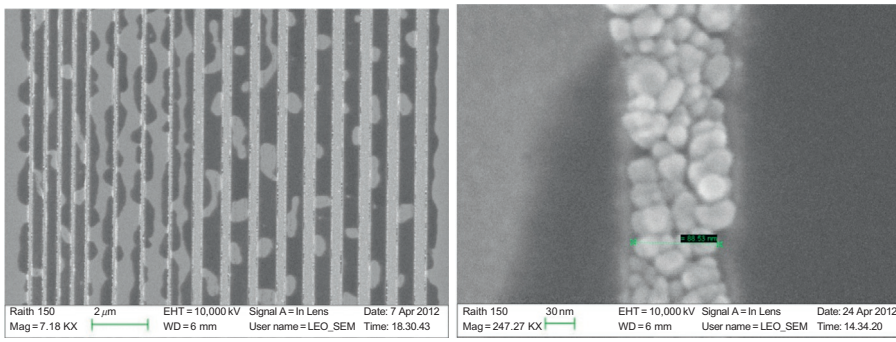

Figure 13.14 SEM micrograph of SiC nanowires grown on an Si substrate. (a) Overview, and (b) zoomed-in view for one thin nanowire with ~89 nm width.

capability of photo- or e-beam lithography, dry etching, and selective deposition. We used a photolithographic method to pattern a Si (111) substrate capped with ~100 nm thick SiO_2 and demonstrated the feasibility of this prepattern approach. Figure 13.13a shows an optical image of a laser-illuminated area with selectively deposited 3C-SiC over 5 μm wide silicon strips separated by 5 μm SiO_2 spacers. Figure 13.13b shows the corresponding Raman image of the laser-induced graphene bands. SiC ribbons in nanoscale were also selectively deposited on Si wafers successfully intended to be induced into graphene nanoribbons. The minimum width of SiC nanowire achieved is about 89 nm as shown in Figure 13.14. However, the conversion from SiC nanowire to graphene in the nanoscale presents a new challenge, namely a higher laser power is required, because the heat generated within the ~700 nm focused laser spot is dissipated mostly by the Si wafer, instead of being absorbed by the SiC nanostructure. Therefore, the optimal illumination conditions should be evaluated and identified in the future.

13.5 Conclusions

Conventionally, the fabrication of graphene-based devices involves a series of steps including deposition, transfer, and photolithography, which is typically a top-down process. The combination of the selective growth of 3C-SiC on an Si wafer and laser illumination can selectively pattern graphene micro- and nanostructures with required shapes and sizes at any desired location directly on a Si wafer for making graphene-based photonic and electronic devices. This laser-illumination technique may potentially open a route to integrate graphene with existing silicon-based devices. The advantages of laser techniques over other conventional approaches are speed, lower cost, and more flexibility. With the formation of a periodic array, laser-induced graphene can be applied to electronic-photonic superstructure devices. Electron beam lithography can enable the selective deposition of 3C-SiC on Si wafers in nanometer scale and thus produce GNSs for device fabrication.

Acknowledgments

The authors acknowledge supports of Army Research Office (ARO), Charlotte Research Institute, and Bissell Distinguished Professorship from UNCC.

References

De Heer, W.A., Berger, C., Ruan, M., Sprinkle, M., Li, X., Hu, Y., Zhang, B., Hankinson, J., Conrad, E., 2011. Large area and structured epitaxial graphene produced by confinement controlled sublimation of silicon carbide. Proc. Natl. Acad. Sci. U. S. A. 108, 16900–16905.

Ferrari, A.C., 2007. Raman spectroscopy of graphene and graphite: disorder, electron-phonon coupling, doping and nonadiabatic effects. Solid State Commun. 143, 47–57.

Hass, J., de Heer, W.A., Conrad, E.H., 2008. The growth and morphology of epitaxial multilayer. J. Phys. Condens. Matter 20, 323202.

Jiao, L., Zhang, L., Wang, X., Diankov, G., Dai, H., 2009. Narrow graphene nanoribbons from carbon nanotubes. Science 458, 877–880.

Kim, K.S., Zhao, Y., Jang, H., Lee, S.Y., Kim, J.M., Ahn, J.H., Kim, P., Ahn, J.H., Kim, P., Choi, J.Y., Hong, B.H., 2009. Large-scale pattern growth of graphene films for stretchable transparent electrodes. Nature (London) 457, 706.

Kosynkin, D.V., Higginbotham, A.L., Sinitskii, A., Lomeda, J.R., Dimiev, A., Price, B.K., Tour, J.M., 2009. Longitudinal unzipping of carbon nanotubes to form graphene nanoribbons. Nature 458 (16), 872–876.

Lee, S., Toney, M.F., Ko, W., Randel, J.C., Jung, H.J., Munakata, K., Lu, J., Geballe, T.H., Beasley, M.R., Sinclair, R., Manoharan, H.C., Salleo, A., 2010. Laser-synthesized epitaxial graphene. ACS Nano 4, 7524–7530.

Li, Y.S., Cai, W.W., An, J.H., Kim, S.Y., Nah, J.H., Yang, D.G., Piner, R., Velamakanni, A., Jung, I. H., Tutuc, E., Banerjee, S.K., Colombo, L., Ruoff, R.S., 2009. Large-area synthesis pf high-quality and uniform graphene films on copper foils. Science 324, 1312–1314, k.

Novoselov, K.S., Geim, A.K., Morozov, S.V., Jiang, D., Zhang, Y., Dubonos, S.V., Grigorieva, I.V., Firsov, A.A., 2004. Electric field effect in atomically thin carbon films. Science 306, 666.

Novoselov, K.S., Geim, A.K., Morozov, S.V., Jiang, D., Katsnelson, M.I., Grigorieva, I.V., Dubonos, S.V., Firsov, A.A., 2005. Two-dimensional gas of massless Dirac fermions in graphene. Nature (London) 438, 197.

Ohkawara, Y., Shinada, T., Fukada, Y., Ohshio, S., Saitoh, H., Hiraga, H., 2003. Synthesis of graphite using laser decomposition of SiC. J. Mater. Sci. 30, 2447–2453.

Perrone, D., Maccioni, G., Chiolerio, A., Martinez de Marigorta, C., Naretto, M., Pandolfi, P., Martino, P., Ricciardi, C., Chiodoni, A., Celasco, E., Scaltrito, L., Ferrero, S., 2009. Study on the possibility of graphene growth on 4H-silicon carbide surfaces via laser processing. In: Proceedings of the Fifth International WLT-Conference on Laser Manufacturing, Munich, June 2009.

Shivaraman, S., Barton, R.A., Yu, X., Alden, J., Herman, L., Chandrashekhar, M.V.S., Park, J., McEuen, P.L., Parpia, J.M., Craighead, H.F., Spencer, M.G., 2009. Free-standing epitaxial graphene. Nano Lett. 9 (9), 3100–3105.

Yannopoulos, S.N., Siokou, A., Nasikas, N.K., Dracopoulos, V., Ravani, F., Papatheodorou, G. N., 2012. CO_2-laser-induced growth of epitaxial graphene on 6H-SiC (0001). Adv. Funct. Mater. 22, 113–120.

Yue, N., Zhang, Y., Tsu, R., 2012. Selective formation of graphene on a Si wafer. Mater. Res. Soc. Symp. Proc. 1407.

Yue, N., Zhang, Y., Tsu, R., 2013. Ambient condition laser writing of graphene structures on polycrystalline SiC thin film deposited on Si wafer. Appl. Phys. Lett. 102, 071912.

Zhang, Y., Tsu, R., 2010. Binding graphene sheets together using silicon: graphene/silicon superlattice. Nanoscale Res. Lett. 5, 805–808.

Zhang, Y.B., Small, J.P., Pontius, W.V., Kim, P., 2005. Fabrication and electric-field-dependent transport. Appl. Phys. Lett. 86, 073104.

Nanophotonics: from quantum confinement to collective interactions in metamaterial heterostructures

14

L. Rast, V.K. Tewary
National Institute of Standards and Technology, Boulder, CO, USA

14.1 Introduction

14.1.1 Overview

Nanophotonic materials allow exceptional control over light-matter interactions on the nanoscale. Such materials circumvent the traditional diffraction limit by exploiting near-field optics, making feats such as single-molecule detection possible (Nie and Emory, 1997), and spurring new applications including near-field spectroscopy (Cuche et al., 2009) and data storage (an important innovation for the future of so-called "big data") (Nishida et al., 2007). The engineering of more advanced nanophotonic devices, particularly those that rely on metamaterial components with emergent physical properties (novel properties that derive from complex interactions within the material), will require close interplay between the new field of rational design and experimental model validation. Rational design of nanophotonic materials requires reliable and comprehensive data on material properties, efficient methods for multiscale calculation of composite properties and quasiparticle interaction, and advanced software frameworks for optimal design and model inversion. Then, multiscale models are needed that utilize accurate and efficient *ab initio* calculations and also efficiently bridge the gap from the atomic scale to the continuum in order to take into account behavior that occurs on all physically relevant scales in the nanomaterials hierarchy. In this chapter, we will discuss the theoretical background and modeling techniques necessary for creating such models.

At the heart of many nanophotonics applications is the nanoscale confinement of light by light-matter interactions. Spatial confinement of plasmons (quantized units of collective plasma oscillation) on length scales much smaller than the free-space wavelength of light greatly enhances the local electromagnetic field. The field enhancement induced by surface plasmon resonances (SPRs) in silver nanoclusters can provide up to a 10^{15} intrinsic Raman enhancement factor for molecules placed at the locations of greatest field enhancement (so-called "hot spots"), allowing for single molecule detection via surface enhanced Raman spectroscopy (SERS) (Nie and Emory, 1997).

Modeling, Characterization and Production of Nanomaterials. http://dx.doi.org/10.1016/B978-1-78242-228-0.00014-4

In bulk optoelectronic devices, when the dimensions of an optical component are near the wavelength of light, light propagation is limited by optical diffraction. In plasmonic-photonic circuits, however, the size of components such as lenses and fibers are not subject to this classical Abbe diffraction limit. This is a consequence of the small wavelength of the coupled photon-plasmon modes (surface plasmon polaritons or SPPs) relative to the free-space wavelength of light of the same frequency (Ozbay, 2006; Liu et al., 2013). Many nanophotonic devices support plasmon resonances—this provides the important advantage of strong plasmonic coupling with light near the resonant frequency. Optical signals in plasmonic-photonic circuits may be controlled at length scales similar to the feature size of current and future electronic devices (tens of nm), and plasmonic-photonic circuit components may be much smaller in size than "traditional" optoelectronic components (Dionne and Atwater, 2012).

In addition to confinement, particle and quasiparticle interactions also determine the behavior of these materials. Plasmon oscillations are able to couple strongly with a variety of particles and quasiparticles to form other quasiparticles and collective modes. These interactions can be particularly important in determining the behavior of nanophotonic devices based on 2D materials. These effects have been studied significantly in graphene-based devices. For example, coupled plasmon-phonon oscillations have been shown to dominate the mid-IR interfacial optical response of graphene on silicon (Fei et al., 2011). Additionally, intrinsic optical phonons have been shown to be a damping pathway for plasmon resonances in graphene, and plasmon-phonon hybridization at a graphene-SiO_2 interface has been shown to induce significant damping and modification of the plasmon dispersion in graphene (Yan et al., 2013). Finally, it has been shown in angle-resolved photoemission spectroscopy measurements that higher-order quasiparticle interactions lead to novel quasiparticles in graphene, such as plasmarons (plasmon-electron hybrid modes), and that these modes are important in determining the electronic structure of graphene at the Dirac point (Bostwick et al., 2006). Predicting the optoelectronic properties of nanophotonic devices, particularly those based on 2D materials with properties that have not been thoroughly studied, requires one to use computational methods with the ability to model various particle and quasiparticle interactions. Modern density functional theory (DFT) methods can be excellent tools for this type of modeling. One of the primary aims of this chapter is to give the reader guidance on the use of DFT for achieving this goal.

14.1.2 Low-dimensional materials for stratified metamaterial heterostructures: Fundamental interest and applications

Much progress has been made in the production of 2D materials, and the fabrication of heterostructures with tailored electronic and optical properties is on the horizon. 2D crystal-based nanophotonic metamaterials could, for example, combine the sizable bandgaps of the transition metal dichalcogenides, which can change from indirect to direct in single layers (Wang et al., 2012), with the incredible mechanical strength of graphene and the ultra-flat morphology of hexagonal boron nitride (hBN) (Dean et al., 2010).

Atomically thin materials also provide the advantage of unparalleled plasmonic and optical confinement.

Hybrid materials are also excellent candidates for low-loss plasmonic materials. As an example, devices that contain a plasmonic metal, as well as a combination of low and high refractive index dielectric materials, exhibit longer propagation distances without reduced confinement (Hosseini and Massoud, 2006). Metamaterial heterostructures have material properties that arise from the properties of their constituent materials, as well as "meta" properties that arise due to the collective interaction between component materials and various physical processes in each material layer. Interfacial phenomena are particularly important in metamaterial heterostructures. Rational design of 2D-based nanophotonic devices therefore requires well-validated data on material properties for the individual layers, efficient methods for multiscale calculation of composite properties, and advanced software frameworks for model optimization and inversion. Further reading on computational frameworks for materials by design may be found in Designer Nanophotonic Materials: Multiscale Modeling, Model Optimization, and Model Inversion Section.

14.2 Atomistic modeling of low-dimensional materials: modeling collective modes with DFT

14.2.1 Overview

DFT is among the most widely used tools for the calculation of excitations and collective modes in many-body systems. DFT is founded upon the Hohenburg-Kohn theorem that states that the ground-state Schrodinger equation is a unique functional of the electron density (Hohenberg and Kohn, 1964). For N interacting electrons subject to an external potential V_{ext}

$$E[n] = F[n] + \int n\left(\vec{r}\right) V_{\text{ext}}\left(\vec{r}\right) \mathrm{d}\,\vec{r} \tag{14.1}$$

where F is a universal functional of the electron density $n\left(\vec{r}\right)$ and F_{min} is the exact ground-state electronic energy.

The basic equations used in the modern DFT formalism were developed by Kohn and Sham (1965), who added exchange and correlation terms to the chemical potential. These are included in the DFT formulation as an additive potential term E_{xc} (Kohn and Sham, 1965):

$$\begin{aligned} E[n(r)] = K_{\text{s}}\left[n\left(\vec{r}\right)\right] + \frac{1}{2}\int\int \frac{n\left(\vec{r}\right) n\left(\vec{r}'\right)}{\left|\vec{r} - \vec{r}'\right|} \mathrm{d}\,\vec{r}\,\mathrm{d}\vec{r}' \\ + E_{xc}\left[n\left(\vec{r}\right)\right] + \int n\left(\vec{r}\right) V_{\text{ext}}\left(\vec{r}\right) \mathrm{d}\,\vec{r} \end{aligned} \tag{14.2}$$

where $K_s\left[n\left(\vec{r}\right)\right]$ is the kinetic energy of a noninteracting electron gas of density $n\left(\vec{r}\right)$. There are a wide variety of available exchange correlation energy functionals in the various DFT implementations. One of the most popular classes of functionals is based on the local density approximation (LDA).

$$\underset{xc}{\overset{\text{LDA}}{E}}\left[n\left(\vec{r}\right)\right] = \int\left[n\left(\vec{r}\right)\right]\varepsilon_{xc}\left[n\left(\vec{r}\right)\right]\mathrm{d}\,\vec{r} \tag{14.3}$$

where $\varepsilon_{xc}\left[n\left(\vec{r}\right)\right]$ is the exchange-correlation energy density.

Used properly, DFT can yield highly accurate results for band structure, plasmon resonances, phonon modes, excitonic resonances, electron transport properties, and a host of other properties of interest for nanophotonics. However, DFT calculations are by no means a "black box." The user must carefully consider the physics of the system of interest when selecting the DFT solution method and parameters, including the exchange correlation functional, planewave cutoff energy, number of bands for convergence, grid spacing, and so on. For example, the basic LDA formulation, while reasonably accurate for some systems, may not be the most accurate approach for certain materials or effects. Examples include materials with strong electron-electron correlation or the calculation of bandgaps in atomically thin wide bandgap materials. In such cases, a correction factor that accounts for the self-energy of the system is needed.

14.2.2 Sensible selection of an exchange-correlation functional

Simple LDA and generalized gradient approximation (GGA) methods for electronic structure calculations may underestimate bandgaps by over 50% for some materials (Janotti and Van de Walle, 2011). These errors often occur in the location of both conduction and valence bands, and this leads to errors in transition energies that are on the order of the bandgap error (Janotti and Van de Walle, 2011). Methods available for corrections that bring the electronic structure in closer agreement with experimental values include the LDA + U method, LDA + GW method, as well as a variety of hybrid functionals. A detailed analysis of all of these methods is beyond the scope of this chapter, but it is suggested that the reader consult the references in the DFT Methods section of the Suggested Reading list. Hybrid functionals are often a convenient and computationally efficient way of obtaining band structures with improved accuracy. This is true to varying degrees, and the reader is advised to do a careful search of the relevant literature for the material of interest in order to select an appropriate functional for creating an accurate representation of the behavior of the material. For example, some functionals may produce accurate electronic band structures for good conductors (such as metals), but give inaccurate results for wide bandgap semiconductors. DFT is among the most popular methods of predicting properties of hypothetical low-dimensional materials as well as not yet measured properties of recently discovered low-dimensional materials. Because of this, there has been much work done recently on improving both the accuracy and efficiency of these methods, including

the development of new functionals. One such hybrid functional, the GLLBSC functional (Kuisma et al., 2010), reproduces bandgaps for a wide variety of materials that agree very closely with experimental values. This functional incorporates the derivative discontinuity of the exchange correlation functional explicitly at integral particle numbers, a critical feature for obtaining an accurate band structure in a DFT calculation. The GLLBSC method has also been shown to have computational cost similar to the LDA, with the advantage of accuracy comparable to methods such as the LDA-GW method (Kuisma et al., 2010).

14.2.3 Optical limit and electron energy loss function calculations

Special consideration is also required in selecting the method for calculation of the optical limit (also known as the long wavelength limit) and EELS calculations. Methods available for the accurate prediction of absorption spectra and EELS, excitonic features in particular, include time-dependent density functional theory (TDDFT) or the Bethe-Salpeter equation (BSE) (Yan et al., 2012). The most accurate methods for calculations of spectroscopic properties of nanophotonic materials include the electronic self-energy and electron-hole exchange interactions via many-body perturbations (using, for example, the GW approximation for electron self-energy and the BSE for electron-hole interactions). The standard GW-BSE approach is as follows: Single-particle energies are calculated via a self-energy through the GW approximation, then diagonalizing the two-particle Hamiltonian yields the optical excitation energies. The GW self-energy computation can be costly. Alternatively, single-particle energies may be obtained using an efficient and accurate hybrid functional, such as the GLLBSC, and optical properties may subsequently be calculated using the BSE.

14.2.4 Available software packages

Although there are numerous DFT codes available, both open source and commercial, not all DFT packages have the capabilities for calculations of optical spectra. This section is intended to give an overview of a few of the available software packages that have integrated modules, or that may be used in combination with other packages, in order to perform optical limit or EELS calculations. Although this is by no means an exhaustive list, it should give the reader an idea of the wide variety of capabilities related to nanophotonics calculations of modern DFT software.

1. SIESTA (Soler et al., 2002): This Fortran 95 code (available for serial or parallel calculations under MPI) is capable of band structure calculations as well as *ab initio* molecular dynamics modeling of molecules and solids. This code is available through academic license, computer center license, or a commercial license for all other users. The Kohn-Sham self-consistent density functional method (using the numerical atomic orbitals basis) in the LDA-(LSD) or generalized gradient (GGA) approximations is used for the band structure calculations. Optical calculations (stored as the imaginary component of the dielectric function) are performed using dipolar transition matrix elements between divergent eigenfunctions of the Hamiltonian. The molecular computation uses the position operator matrix elements, and for solids, the calculation is performed in momentum space.

2. VASP (Vienna Ab-initio Simulation Package) (Kresse and Hafner, 1994; Kresse and Furthmüller, 1996a,b): VASP is a Fortran 90 code (available for serial or parallel calculations under MPI). This code is available for use through both academic and commercial licenses. The software calculates an approximate solution to the many-body Schrödinger equation, either within DFT using the Kohn-Sham equations, or within the Hartree-Fock (HF) approximation. Hybrid functionals that mix the HF approach with DFT are included in the implementation as well. A plane wave basis is utilized in VASP, and both many-body perturbation theory and GW corrections are possible with this code. A variety of optical calculations are possible with VASP, including dielectric tensor calculations that may be used to obtain absorption spectra in postprocessing. Optical calculations using the BSE are possible using this software. Available functionals include LDA, GGA and metaGGA-based functionals, HF, and HF/DFT hybrids.
3. Quantum ESPRESSO (Giannozzi et al., 2009): This open-source Fortran code (available for serial or parallel calculations under MPI or OpenMP) uses a plane wave basis set and pseudopotentials to perform DFT electronic structure calculations. Capabilities for TDDFT also exist as a specialized Quantum Espresso package. Optical spectra may be calculated from TDDFT perturbation theory within Quantum ESPRESSO. Output from Quantum Espresso may also be used as input to the Yambo program (Marini et al., 2009) in order to perform calculations involving electronic excitations with the GW correction and optical properties including absorption spectra via the BSE.
4. GPAW (Mortensen et al., 2005; Enkovaara et al., 2010; Walter et al., 2008; Yan et al., 2011): GPAW is an open-source Python/C DFT code that uses the projector-augmented wave method. It uses real-space uniform grids or multigrid approaches as well as atom-centered basis functions. The code has TDDFT and GW approximation capabilities, as well as a wide variety of functionals, including the GLLBSC functional. A variety of capabilities for absorption spectra and EELS calculations exist within GPAW, including calculations via the Bethe-Salpeter formalism.
5. Abinit (Gonze et al., 2005, 2009): Abinit is an open-source Fortran DFT code that can perform electronic structure calculations using pseudopotentials and a plane wave basis set. Excited states can be computed within the many-body perturbation theory via the GW approximation and the macroscopic dielectric function can be obtained in the Bethe-Salpeter formalism. Functionals implemented in Abinit include LDA and the GGA and capabilities for corrections for delocalization in strongly correlated materials exist, including the full localized limit and around mean field methods. Output from Abinit may also be used with the code Yambo for spectroscopic calculations, in a similar manner as previously described for Quantum ESPRESSO.

14.3 Spectral properties of multilayer structures

14.3.1 Continuum models for collective modes

Nanophotonics heterostrucutre materials are of interest for a variety of applications, including low-loss plasmonics. Engineering novel materials for nanophotonics requires efficient methods for predicting emergent material properties. Both individual material properties and interactions between various materials must be incorporated realistically into the calculation. Using *ab initio* methods such as DFT for modeling an entire

continuum structure can be prohibitively expensive, especially if one is interested in considering or comparing a variety of system components and geometries. However, there are hybrid techniques such as semiclassical or Green's function approaches that allow for efficient bridging of the gap between the atomistic and continuum scales. Used judiciously, these methods can be very powerful and useful as a step toward materials by design. As an example, this section describes one such semiclassical technique for modeling plasmon and phonon excitations in multilayer structures. This method has been shown to apply to phonons (Lambin et al., 1985) as well as plasmon polaritons (Dereux et al., 1988) in layered materials with step function-like complex dielectric functions (although the dielectric functions are required to be continuous throughout each layer) and interacting interfaces. In addition, although the Lambin paper, in which Eqs. (14.7) and (14.10) were derived, focused on modeling semiconductors, the expression and the formalism from which it originates are also applicable to plasmonic resonances in alternating metal-insulator layers. This method is extremely computationally efficient, as we will show in the next section, and because the method applies to both phonon and plasmon excitation in stratified structures with interacting interfaces and sharp changes in dielectric function across layer boundaries, it is convenient for modeling a variety of multilayer heterostructures for nanophotonics.

14.3.2 Details of the continued fraction model

Lambin's model (Lambin et al., 1985) for multilayer structures is derived from a specular reflection model. It has been previously demonstrated that for small values of the wave vector, the specular reflection model is in close agreement with the more well-known Bloch hydrodynamic model (Ritchie and Marusak, 1966). In the Lambin model, the z coordinate is normal to the surface of the material, extending from $z=0$ to $-\infty$ (as in Figure 14.1). ω is excitation frequency and k is the wave vector of the plasmon or phonon resonance. Let $\epsilon(\omega,z)$ be the (frequency-dependent) dielectric function in the long wavelength optical limit ($k \to 0$), which is a tensor of the material along the spatial coordinate z. **D** and **E** are the electric displacement and electric field, respectively. We have the following boundary conditions for the fields: $D \perp E_7$ must be continuous. The general relation between **D**, **E**, and the frequency-dependent dielectric function is given by:

$$\boldsymbol{D}(\boldsymbol{k},\omega,z) = \epsilon(\omega,z)\boldsymbol{E}(\boldsymbol{k},\omega,z) \tag{14.4}$$

Equation (14.4) ensures continuity of the effective dielectric function even in instances of sharp interfaces parallel to the x-y interfaces below the $z=0$ surface. The effective dielectric function $\xi(\boldsymbol{k},\omega,z)$ of the layered structure is given by:

$$\xi(\boldsymbol{k},\omega,z) = \frac{i\boldsymbol{D}(\boldsymbol{k},\omega,z)\,.\,\boldsymbol{n}}{\boldsymbol{E}(\boldsymbol{k},\omega,z)\,.\,\dfrac{\boldsymbol{k}}{k}} \tag{14.5}$$

where $\boldsymbol{n}$ is the surface normal vector. The effective dielectric function is a solution to the following Riccati differential equation, in the long-wavelength limit ($k \to 0$), at $z = 0$, as follows:

$$\frac{1}{k}\frac{\mathrm{d}\xi(z)}{\mathrm{d}z} + \frac{\xi^2(z)}{\epsilon(z)} = \epsilon(z) \tag{14.6}$$

At $z = 0$ we have for the effective dielectric function:

$$\xi_0 = a_1 - \cfrac{{b_1}^2}{a_1 + a_2 - \cfrac{{b_2}^2}{a_2 + a_3 - \cfrac{{b_3}^2}{a_3 + a_4 - \ldots}}} \tag{14.7}$$

where

$$a_i = \varepsilon_i \coth(kd_i) \tag{14.8}$$

and

$$b_i = \frac{\varepsilon_i}{\sinh(kd_i)} \tag{14.9}$$

ε_i are the frequency-dependent dielectric functions within each layer of the stratified material. We then have for the electron energy loss function (EELF):

$$\mathrm{EELF} = \mathrm{Im}\left[\frac{-1}{\xi(\omega, k) + 1}\right] \tag{14.10}$$

14.3.3 Applications

The following section is intended as an example of how a semiclassical method for predicting properties of advanced nanophotonic materials may be developed based on a classical expression for a hybrid material property, such as that of Lambin. The general concept is that individual material properties are calculated on the quantum or nanoscale using an *ab initio* method such as DFT, then composite properties are calculated using a computational bridge such as Eq. (14.7). Such methods can be very efficient and powerful, provided they are used thoughtfully, with all of the relevant limitations of the model in mind. Such considerations should include, for example, whether the dominant physical processes in the regime of interest are accurately represented by the model. In metamaterials heterostructures such as those described in this section, interfacial interactions are important and must be included in the model. Equation (14.7) represents

interfacial interactions classically, which is acceptable in this context because we are interested in modeling classical resonances (plasmons and phonons).

14.3.3.1 Graphene/noble metal multilayer composites

Lambin's continued fraction expression, given in Eq. (14.7), was utilized in our work on electron energy loss properties of graphene/noble metal/insulating substrate layered structures (Rast et al., 2013). Details of the semiclassical method are as follows: Dielectric functions for the individual material layers were initially obtained. For the 2D materials of interest (graphene and h-BN), *ab initio* calculations were performed according to the following procedure: Time-dependent DFT was employed (using the DFT code GPAW) in the LDA. These optical calculations were performed with atomically thin materials with armchair geometry and a momentum transfer value of 0.005 $Å^{-1}$ along Brillouin zone Γ-M direction.

Optical properties of other materials in the layered structure as depicted in Figure 14.1 were experimentally measured values obtained from the literature. With

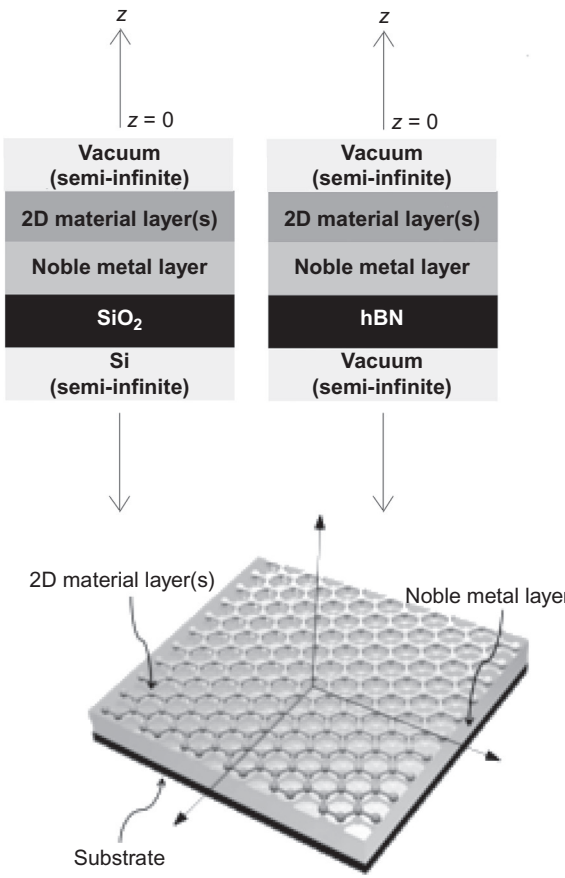

Figure 14.1 Multilayer structure made up of a graphene top layer (s), a noble metal intermediate layer, and semiconducting substrate. EELF functions were calculated for structures of this type by the methods discussed in the text.

the dielectric functions of the individual layers as input, Eq. (14.7) is used to obtain the composite dielectric function for the layered system, and then Eq. (14.10) is used to obtain the EELF. The use of this procedure allows for computationally efficient multiscale EELS calculations for layered structures based on many different materials. Layer thickness and material may easily be substituted as desired. EELS calculations may be performed in less than a second, nearly independent of the range of wavelengths. The graphene dielectric function was obtained in the optical limit, and the LDA calculation was executed with a Monkhorst-Pack grid of $20 \times 20 \times 1$ k-points. Johnson and Christy's empirical data (Johnson and Christy, 1972) were used for the silver dielectric function. The Si and SiO_2 dielectric constants used in the calculation were 11.68 and 3.9, respectively. These are broadly accepted values obtained from the literature (Murarka et al., 2003; Yi, 2012).

Figure 14.2a-c demonstrates the effect of graphene films with varying numbers of atomic layers on a noble metal/SiO_2/Si layered structure. In Figure 14.2a, where a silver metallic layer is used, for mono- to trilayer graphene, the lower energy surface peak near 2.6 eV remains virtually unchanged, while the bulk peak near 3.7 eV is reduced by 50% at three layers of graphene. Similar enhancement of the surface peak is also seen for gold and copper, as displayed in Figure 14.2b and c, although the effect is subtler than in the case of the silver film. The imposition of a boundary layer on the noble metal surface leads to strengthened surface coupling at the expense of bulk resonance modes. The physical interpretation of this effect is similar to that of the *begrenzung* effect, which has been well studied for increasingly thin metallic thin films (Ritchie, 1957). (In the case of metallic films, the *begrenzung* effect occurs on the imposition of a boundary to an infinite plasmonic metal slab, leading to a surface plasmon peak, which occurs at the expense—in terms of energy loss—to the bulk plasmon peak.) At 20 graphene layers, we begin to see behavior more like that of a bulk top layer. The surface peak broadens, which indicates increased losses, as one would expect for a bulk graphite top layer.

14.3.3.2 Comparison of hexagonal boron nitride and traditional silicon substrates for plasmonics

Figure 14.3 displays data for the combined effects of a graphene top coating (of varying numbers of graphene layers), silver middle layer, and highly insulating hBN substrate, also presented in our work in (Rast et al., 2013). The structure is displayed in Figure 14.1b. It can be seen that the substitution of the silicon substrate with hBN produces a drastic shift toward the surface resonance. In the context of our mesoscopic model, the diminished plasmonic losses for plasmonic metals with a graphene top coating on hBN substrates is due to two basic physical processes: (i) Adding a graphene boundary coating to the metal surface diminishes coupling to bulk plasmon oscillations via a process akin to the *begrenzung* effect. The *begrenzung* effect arises due to reduction in the number of degrees of freedom for resonances—additional surface confinement occurs at the expense of the bulk plasmon resonance intensity, leading to a reduction in bulk energy losses. (ii) hBN is highly insulating, so

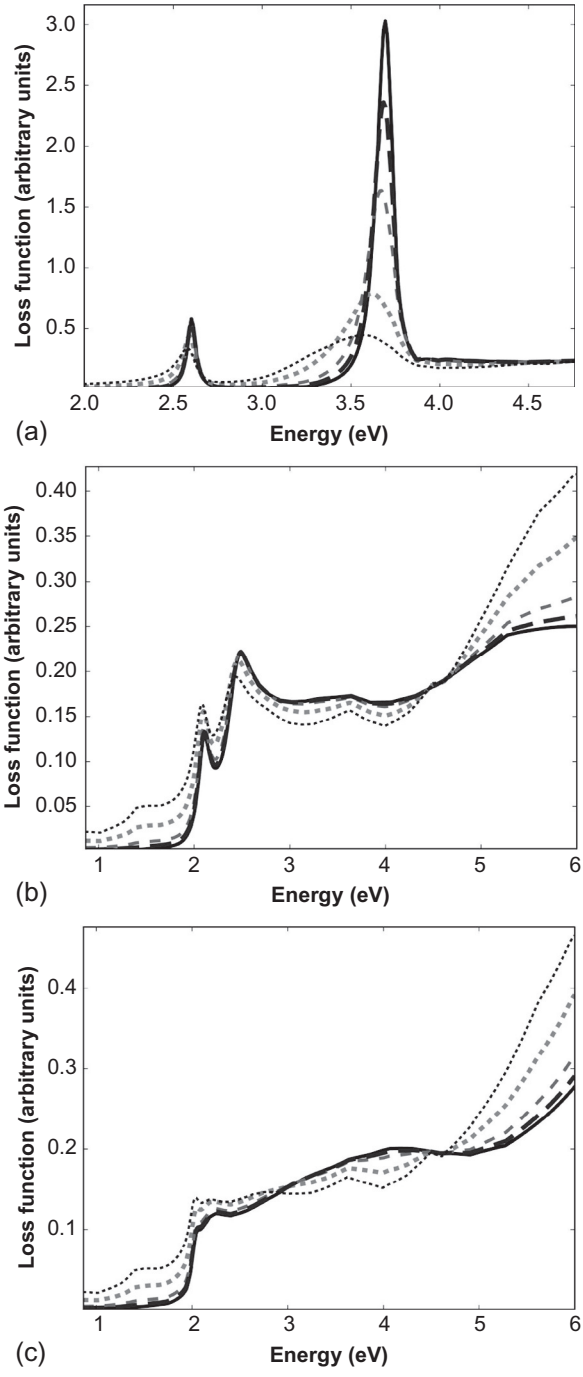

Figure 14.2 EELF for graphene films with different numbers of atomic layers three substrate structures: (a) 34 nm Ag layer and SiO_2/Si substrate. (b) 34 nm Au layer and SiO_2/Si substrate. (c) 34 nm Cu layer and SiO_2/Si substrate. For each substrate, the graphene layer numbers are 0 (solid line), single layer (long dashes), trilayer (intermediate-length dashes), 10 layers (short dashes), and 20 layers (dotted line). For few-layer graphene, the lower energy surface peak near 2.6 eV remains virtually unchanged, while the bulk peak near 3.7 eV is reduced by 50% at three layers of graphene. The physical interpretation of this effect is similar to that of the *begrenzung* effect—the imposition of a boundary layer enhances coupling to surface plasmon modes and reduces coupling to bulk modes.

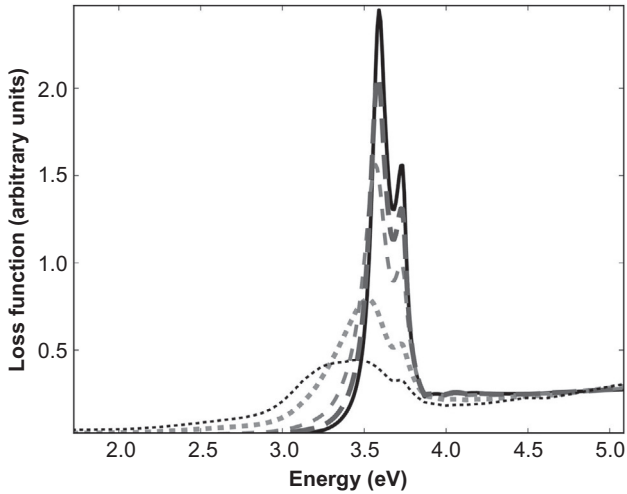

Figure 14.3 EELF for graphene films with varying numbers of layers on a 34 nm Ag film and single-layer hBN substrate. Without graphene (solid line), monolayer graphene (long dashes), trilayer graphene (intermediate-length dashes), 10 layer graphene (short dashes), and 20 layer graphene coating (dotted line). Because hBN is highly insulating, this substrate material reduces bulk losses and strengthens surface confinement due to reduced scattering losses.

this substrate material reduces bulk losses and strengthens surface confinement due to reduced scattering losses.

Figure 14.4 displays EELF data for (a) free-standing Ag films of varying thickness and (b) trilayer graphene coatings on Ag layers (of various thicknesses) with a single layer hBN substrate. Comparison of (a) and (b) reveals that the spectral profile of the system with an hBN substrate (b) is strikingly similar to the case of a "suspended sample" (a).

14.3.3.3 Silicene and germanene systems

Silicene and germanene are predicted to have electron transport properties similar to graphene, with the added advantage of increased compatibility with silicon-based technology. In addition, these materials have a buckled lattice structure that leads to inversion symmetry breaking. This may be taken advantage of through the application of an external electrical field perpendicular to the plane for highly controllable band-gap tunability. These materials are therefore also of recent interest for nanophotonics applications. Figure 14.5 displays the system considered in this section, a multilayer structure consisting of silicene or germanene top layers on a semi-infinite silver substrate. Further results and calculation details for the system described in this section may be found in our recent paper (Rast and Tewary, 2013). The method for EELF calculations are, in general, the same as those described for the graphene-based systems in Section 14.3.3. Equations (14.7) and (14.10) are used for the composite dielectric function, and the silver optical data are again those of Johnson and Christy. Both

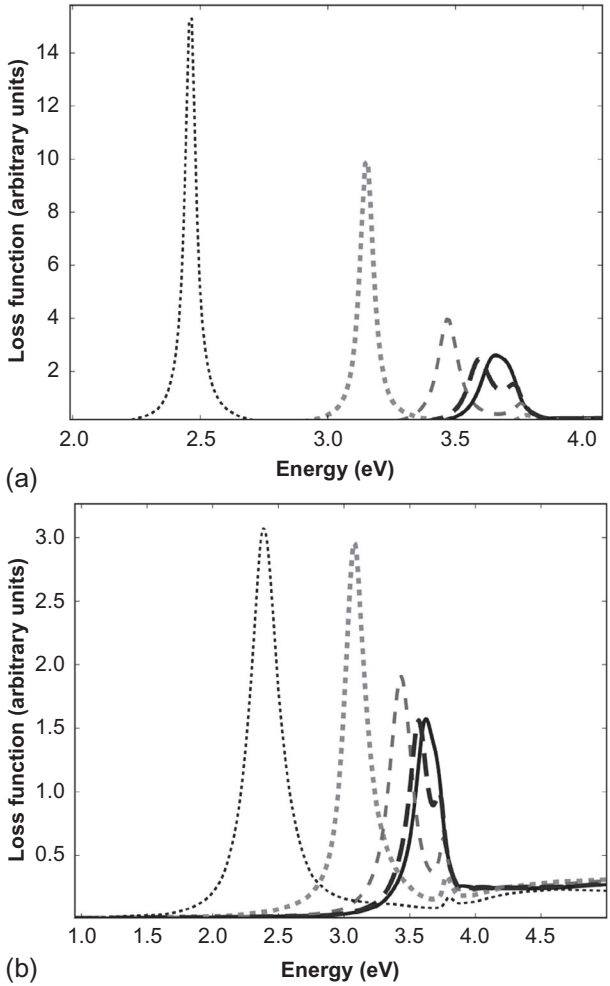

Figure 14.4 EELF for (a) free-standing Ag films of various thickness and (b) trilayer graphene on Ag films (of varying thickness) with a monolayer hBN substrate. In both cases (a) and (b), Ag films with thicknesses of 50 nm (solid line), 34 nm (long dashes), 20 nm (intermediate-length dashes), 10 nm (short dashes), and 4 nm (dotted line). The spectral profile of the system with an hBN substrate is remarkably similar to the case of a "suspended sample."

silicene and germanene dielectric functions are computed in the long wavelength optical limit with a momentum transfer of 0.005 $Å^{-1}$, along the Γ-M direction of the Brillouin zone. The k-point sampling with $20 \times 20 \times 1$ Monkhorst-Pack grid was selected for the band-structure computation.

Values of the silicene and germanene dielectric functions are obtained through *ab initio* DFT methods (this time using the GLLBSC functional), and the optical spectra are obtained using the BSE to include excitonic effects. This is the highly accurate and broadly applicable method described in (Kuisma et al., 2010), and our optical spectra compare well with previous results in the literature (Bechstedt et al., 2012). A two-dimensional Coulomb cutoff method is employed in order to model the monolayer structure, which is only periodic in 2D (Rozzi et al., 2006). The buckling amplitude, obtained from DFT structural calculations available in the literature, is 0.44 Å

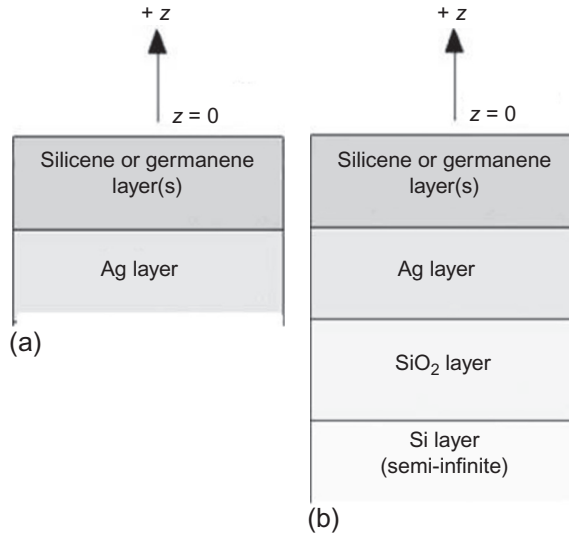

Figure 14.5 Multilayer structure consisting of silicene and germanene multilayers (a) on semi-infinite Ag substrate, and (b) on substrate layers consisting of Ag, SiO_2, and semi-infinite Si. EELS functions were calculated for structures of this type by the methods discussed in the text.

for silicene and 0.6 Å for germanene (Scalise et al., 2013). The results for the EELF for varying numbers of silicene and germanene layers on silver are displayed in Figure 14.6a and b, respectively. For up to three layers of silicene on silver, the bulk plasmon peak is diminished without significant broadening, as our calculations also showed for graphene. This indicates an overall reduction in bulk losses. The effect is most notable when the silver slab is coated with only one layer of silicene. The origin of the reduced bulk losses is similar to that of graphene, reduced coupling to bulk resonances and simultaneous enhancement of surface coupling. This effect could be useful for determining successful fabrication of monolayer silicene on silver through spectroscopic characterization. At 10 layers and above, the system approaches the expected behavior for a bulk Si/Ag system—a broad interfacial peak appears at about 2.5 eV. In the case of germanene, there is no well-defined interfacial plasmon for the germanene/silver system—in contrast to silicene, the real part of germanene's dielectric function is only momentarily slightly non-negative in the 2-4 eV regime. So, the sharp change in dielectric function needed for an enhanced surface plasmon does not occur. However, the bulk plasmon is damped in a manner similar to that of silicene with a few layers of germanene and broadens for layer thicknesses approaching the bulk. So, this effect may also be of use for determining if germanene has been deposited experimentally.

14.3.4 Limits of applicability of electromagnetic continuum models

While extremely convenient, and capable of revealing a range of phenomena of interest for nanophotonics, the semiclassical method used in the work described in this chapter has a variety of limitations. The continuum model described in Section 14.2

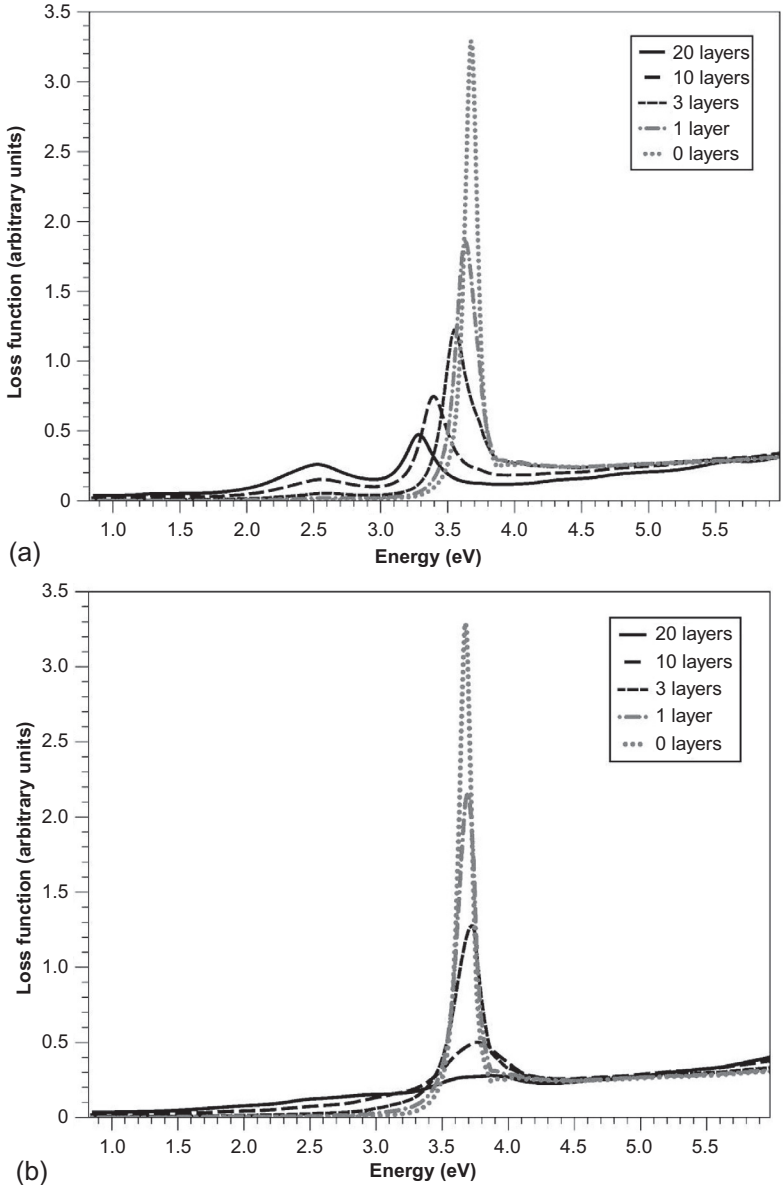

Figure 14.6 EELF for (a) multilayer film of silicene on a semi-infinite Ag substrate; (b) multilayer film of germanene on a semi-infinite Ag substrate. The effect of differing numbers of silicene/germanene layers is demonstrated. The silicene/germanene layer numbers are 20 (solid line), 10 (long dashes), 3 (short dashes), 1 (dash-dot), and 0 (dotted line). For both materials, in a manner similar to the graphene multilayer systems, the bulk plasmon is damped for a few layers and broadens for layer thicknesses approaching the bulk. This effect may be of use for confirming if few-layer silicene or germanene has been deposited experimentally.

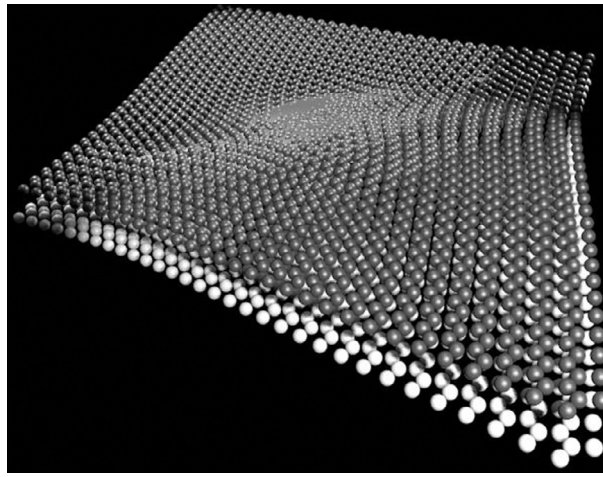

Figure 14.7 Conceptual configuration of a 2D heterostructure with strain-induced charge distortions. These structures typically have a lattice mismatch between layers in addition to inherent rippling and buckling of individual layers. These morphological features lead to strain-induced charge distortions, to which spectroscopic features such as plasmon resonances are very sensitive.

does not include effects due to interfacial strain and doping. Superlattice heterostructures typically have lattice mismatch between adjacent layers, as well as inherent rippling and buckling in individual layers. These morphological features introduce interfacial strain as indicated by the bright spot on the top layer in Figure 14.7. The strain induces charge distortions (leading to charge pooling, for example) to which material optical and electronic properties (such as plasmon resonances) are very sensitive (Sciammarella et al., 2010). DFT methods or a Green's function approach should be used in order to take these effects into account.

Another limitation of the continuum model is that as boundary interactions are considered classically, it does not incorporate interlayer-hopping effects. Angle-resolved photoemission spectroscopy on graphene has shown this tunneling effect to be important for graphene's electronic structure, because it causes π band splitting (Ohta et al., 2007). This effect is more important with increasing with layer numbers. For example, at four layers, the energy shift is approximately 0.7 eV. Ohta et al. calculated the graphene excitation spectrum, including interlayer hopping effects, in the Hamiltonian (Ohta et al., 2007). The authors found tunneling to be significant mainly in predicting the low energy behaviors ($\omega \sim v_F k$) with reasonable accuracy, where v_F is the Fermi velocity). Thus, predicting material properties for low-energy photonics necessitates the inclusion of tunneling effects.

Finally, an important limitation of the model, and many of the other current methods for modeling nanophotonics devices, is that it does not consider complex morphologies. As will be discussed in the next section, many of the new systems on the horizon for nanophotonics have quite complex geometries. There is a current need for the development of methods for accurate calculations of electronic and

optical properties of systems where the behavior on the quantum scale is important, but the scaling to the continuum is less ordered than simple multilayer structures. Examples of complex morphologies include quasiperiodic, aperiodic, and strongly scattering disordered media for nanophotonics. For example, quasiperiodic multilayers have been shown to have properties that lead to a more complex spectrum structure than periodic multilayers, and aperiodic optical media can produce photonic systems with improved optical properties (including narrow peaks and light emission enhancement) as well as more broad "materials by design" capabilities than periodic nanophotonic systems (Macia, 2011). Coupling of semiclassical methods such as we describe in this chapter or other multiscale methods with frameworks for uncertainty quantification (to include geometric uncertainties) is one possible solution to the problems introduced by complex morphologies. Resources for further reading in this area are listed in Designer Nanophotonic Materials: Multiscale Modeling, Model Optimization, and Model Inversion Section.

14.4 Sources of further information

This section includes suggested reading material related to current topics in low-loss nanophotonics applications and modeling of nanophotonic materials.

Many-body effects in atomically thin materials

Bostwick, A., Ohta, T., Seyller, T., Horn, K., Rotenberg, E., 2007. Quasiparticle dynamics in graphene. Nat. Phys. 3, 36–40.

Hwang, E.H., Sensarma, R., Das Sarma, S., 2010. Plasmon-phonon coupling in graphene. Phys. Rev. B 82 (19), 195406.

Wei, W., Dai, Y., Huang, B., Jacob, B., 2013. Many-body effects in silicene, silicane, germanene and germanane. Phys. Chem. Chem. Phys. 15, 8789–8794.

DFT methods

Janotti, A., Van de Walle, C.G., 2007. Native point defects in ZnO. Phys. Rev. B 76, 165202.

Janotti, A., Varley, J.B., Rinke, P., Umezawa, N., Kresse, G., Van de Walle, C.G., 2010. Hybrid functional studies of the oxygen vacancy in TiO2. Phys. Rev. B 81, 085212.

Oba, F., Togo, A., Tanaka, I., Paier, J., Kresse, G., 2008. Defect energetics in ZnO: a hybrid Hartree-Fock density functional study. Phys. Rev. B 77, 245202.

Rinke, P., Janotti, A., Scheffler, M., Van de Walle, C.G., 2009. Defect formation energies without the band-gap problem: combining density-functional theory and the GW approach for the silicon self-interstitial. Phys. Rev. Lett. 102, 026402.

Sholl, D., Steckel, J.A., 2011. Density functional theory: A practical introduction. Wiley, NJ.

Metal nanomaterial-functionalized two-dimensional materials

Shi, Y., Huang, J.K., Jin, L., Hsu, Y.T., Yu, S.F., Li, L.J., Yang, H.Y., 2013. Selective decoration of au nanoparticles on monolayer mos2 single crystals. Sci. Rep. 3, 1839.

Zaniewski, A.M., Schriver, M., Lee, J.G., Crommie, M.F., Zettl, A., 2013. Electronic and optical properties of metal-nanoparticle filled graphene sandwiches. Appl. Phys. Lett. 102, 023108.

Zedan, A.F., Moussa, S., Terner, J., Atkinson, G., El-Shall, M.S., 2012. Ultrasmall gold nanoparticles anchored to graphene and enhanced photothermal effects by laser irradiation of gold nanostructures in graphene oxide solution. ACS Nano 71, 627–636.

Plasmon-assisted gain media

Liu, N., Wei, H., Li, J., Wang, Z., Tian, X., Pan, A., Xu, H., 2013b. Plasmonic amplification with ultra-high optical gain at room temperature. Sci. Rep. 3, 1967.
Stockman, M.I., 2011. Loss compensation by gain and spacing. Philos. Trans. R. Soc. A 369, 3510–3524.
Wuestner, S., Pusch, A., Tsakmakidis, K.L., Hamm, J.M., Hess, O., 2011. Gain and plasmon dynamics in active negative-index metamaterials. Philos. Trans. R. Soc. A 369, 3525–3550.

Designer nanophotonic materials: multiscale modeling, model optimization, and model inversion

Dienstsfrey, A., Boisvert, R.F., 2011. Uncertainty quantification in scientific computing. Springer, New York.
Liu, V., Miller, D.A.B., Fan, S., 2013c. Highly tailored computational electromagnetics methods for nanophotonic design and discovery. Proc. IEEE 101 (2), 484–493.
Owhadi, H., Scovel, C., Sullivan, T.J., McKerns, M., Ortiz, M., 2013. Optimal uncertainty quantification. SIAM Rev. 55 (2), 271–345.
Yip, S., Short, M.P., 2013. Multiscale materials modelling at the mesoscale. Nat. Mater. 12, 774–777.

Disclaimer

Certain commercial equipment, instruments, or materials are identified in this paper in order to specify the experimental procedure adequately. Such identification is not intended to imply recommendation or endorsement by the National Institute of Standards and Technology, nor is it intended to imply that the materials or equipment identified are necessarily the best available for the purpose.

Acknowledgments

The authors thank Christina Richey, Timothy J. Sullivan, Katie Rice, Alex Smolyanitsky, and Ann Chiaramonti Debay for enlightening and helpful discussions. This research was performed while one of the authors held a National Research Council Research Associateship Award at the National Institute of Standards and Technology. This work represents an official contribution of the National Institute of Standards and Technology and is not subject to copyright in the USA.

References

Bechstedt, F., Matthes, L., Gori, P., Pulci, O., 2012. Infrared absorbance of silicene and germanene. Appl. Phys. Lett. 100 (26), 261906.
Bostwick, A., Ohta, T., Horn, K., Rotenberg, E., 2006. Quasiparticle dynamics in graphene. Nat. Phys. 3, 36–40.

Cuche, A., Drezet, A., Sonnefraud, Y., Faklaris, O., Treussart, F., Roch, J.F., Huant, S., 2009. Near-field optical microscopy with a nanodiamond-based single-photon tip. Opt. Express 17, 19969–19980.

Dean, C.R., et al., 2010. Boron nitride substrates for high-quality graphene electronics. Nat. Nanotech. 5, 722–726.

Dereux, A., Vigneron, J.P., Lambin, Ph., Lucas, A.A., 1988. Polaritons in semiconductor multilayered materials. Phys. Rev. B 38, 5438–5452.

Dionne, J.A., Atwater, H.A., 2012. Plasmonics: metal-worthy methods and materials in nanophotonics. MRS Bull. 37 (8), 717–724.

Enkovaara, J., et al., 2010. Electronic structure calculations with GPAW: a real-space implementation of the projector augmented-wave method. J. Phys. Condens. Matter 22, 253202.

Fei, Z., et al., 2011. Infrared nanoscopy of Dirac plasmons at the graphene-SiO_2 interface. Nano Lett. 11 (11), 4701–4705.

Giannozzi, P., et al., 2009. QUANTUM ESPRESSO: a modular and open-source software project for quantum simulations of materials. J. Phys. Condens. Matter 21, 395502.

Gonze, X., et al., 2005. A brief introduction to the ABINIT software package. Z. Krist. 220, 558–562.

Gonze, X., et al., 2009. ABINIT: first-principles approach of materials and nanosystem properties. Comput. Phys. Commun. 180, 2582–2615.

Hohenberg, P., Kohn, W., 1964. Inhomogeneous electron gas. Phys. Rev. 136, B864–B871.

Hosseini, A., Massoud, Y., 2006. A low-loss metal-insulator-metal plasmonic bragg reflector. Opt. Express 14 (23), 11318–11323.

Janotti, A., Van de Walle, C.G., 2011. LDA + U and hybrid functional calculations for defects in ZnO, SnO_2, and TiO_2. Phys. Status Solidi 248 (4), 799–804.

Johnson, P.B., Christy, R.W., 1972. Optical constants of the noble metals. Phys. Rev. B 6, 4370–4379.

Kohn, W., Sham, L.J., 1965. Self-consistent equations including exchange and correlation effects. Phys. Rev. 140, A1133–A1138.

Kresse, G., Furthmüller, J., 1996a. Efficiency of ab-initio total energy calculations for metals and semiconductors using a plane-wave basis set. Comput. Mater. Sci. 6, 15.

Kresse, G., Furthmüller, J., 1996b. Efficient iterative schemes for ab initio total-energy calculations using a plane-wave basis set. Phys. Rev. B 54 (11), 169.

Kresse, G., Hafner, J., 1994. Ab initio molecular-dynamics simulation of the liquid-metal-amorphous-semiconductor transition in germanium. Phys. Rev. B 49, 14251.

Kuisma, M., Ojanen, J., Enkovaara, J., Rantala, T.T., 2010. Kohn-Sham potential with discontinuity for band gap materials. Phys. Rev. B 82, 115106.

Lambin, Ph., Vigneron, J.P., Lucas, A.A., 1985. Electron-energy-loss spectroscopy of multilayered materials: theoretical aspects and study of interface optical phonons in semiconductor superlattices. Phys. Rev. B 32, 8203–8215.

Liu, N., Wei, H., Li, J., Wang, Z., Tian, X., Pan, A., Xu, H., 2013a. Plasmonic amplification with ultra-high optical gain at room temperature. Sci. Rep. 3, 1967.

Macia, E., 2011. Exploiting aperiodic designs in nanophotonic devices. Rep. Prog. Phys. 75, 036502.

Marini, A., Hogan, C., Grüning, M., Varsano, D., 2009. Yambo: an ab initio tool for excited state calculations. Comput. Phys. Commun. 180, 1392.

Mortensen, J.J., Hansen, L.B., Jacobsen, K.W., 2005. Real-space grid implementation of the projector augmented wave method. Phys. Rev. B 71, 035109.

Murarka, S.P., Eizenberg, M., Sinha, A.K., 2003. Interlayer Dielectrics for Semiconductor Technologies. Elsevier, Amsterdam.

Nie, S., Emory, S.R., 1997. Probing single molecules and single nanoparticles by surface-enhanced Raman scattering. Science 275 (5303), 1102–1106.

Nishida, T., Matsumoto, T., Akagi, F., Hieda, H., Kikitsu, A., Naito, K., 2007. Hybrid recording on bit-patterned media using a near-field optical head. J. Nanophoton. 10, 11597.

Ohta, T., Bostwick, A., McChesney, J.L., Seyller, T., Horn, K., Rotenberg, E., 2007. Interlayer interaction and electronic screening in multilayer graphene investigated with angle-resolved photoemission spectroscopy. Phys. Rev. Lett. 98, 206802.

Ozbay, E., 2006. Plasmonics: merging photonics and electronics at nanoscale dimensions. Science 311, 5758,189–5758,193.

Rast, L., Tewary, V.K., 2013. Electron energy loss function of silicene and germanene multilayers on silver. arXiv preprint, arXiv:1311.0838 [cond-mat.mtrl-sci].

Rast, L., Sullivan, T.J., Tewary, V.K., 2013. Stratified graphene/noble metal systems for low-loss plasmonics applications. Phys. Rev. B 87 (4), 045428.

Ritchie, R.H., 1957. Plasma losses by fast electrons in thin films. Phys. Rev. 106, 874–881.

Ritchie, R.H., Marusak, A.L., 1966. The surface plasmon dispersion relation for an electron gas. Surf. Sci. 4 (3), 234–240.

Rozzi, C.A., Varsano, D., Marini, A., Gross, E.K.U., Rubio, A., 2006. An exact Coulomb cutoff technique for supercell calculations. Phys. Rev. B 73, 205119.

Scalise, E., Houssa, M., Pourtois, G., Broek, B., Afanasev, V., Stesmans, A., 2013. Vibrational properties of silicene and germanene. Nano Res. 6, 19.

Sciammarella, C.A., Lamberti, L., Sciammarella, F.M., Demelio, G.P., Dicuonzo, A., Boccaccio, A., 2010. Application of plasmons to the determination of surface profile and contact strain distribution. Strain 46, 307.

Soler, J.M., Artacho, E., Gale, J.D., García, A., Junquera, J., Ordejón, P., Sánchez-Portal, D., 2002. The Siesta method for ab initio order-N materials simulation. J. Phys. Condens. Matter 14, 2745–2779.

Walter, M., Hakkinen, H., Lehtovaara, L., Puska, M., Enkovaara, J., Rostgaard, C., Mortensen, J.J., 2008. Time-dependent density-functional theory in the projector augmented-wave method. J. Chem. Phys. 128, 244101.

Wang, Q. Hua, Kalantar-Zadeh, K., Kis, A., Coleman, J.N., Strano, M.S., 2012. Electronics and optoelectronics of two-dimensional transition metal dichalcogenides. Nat. Nanotechnol. 7, 699–712.

Yan, J., Mortensen, J.J., Jacobsen, K.W., Thygesen, K.S., 2011. Linear density response function in the projector augmented wave method: applications to solids, surfaces, and interfaces. Phys. Rev. B 83, 245122.

Yan, J., Jacobsen, K.W., Thygesen, K.S., 2012. Optical properties of bulk semiconductors and graphene/boron nitride: the Bethe-Salpeter equation with derivative discontinuity-corrected density functional energies. Phys. Rev. B 86, 045208.

Yan, H., Low, T., Zhu, W., Wu, Y., Freitag, M., Li, X., Guinea, F., Avouris, P., Xia, F., 2013. Damping pathways of mid-infrared plasmons in graphene. Nat. Photonics 7, 394–399.

Yi, G.C., 2012. Semiconductor Nanostructures for Optoelectronic Devices: Processing, Characterization, and Applications. Springer, New York.

Plasma deposition and characterization technologies for structural and coverage optimization of materials for nanopatterned devices

15

B. Gittleman[1], *M. Stowell*[2]
[1]Applied Science and Technology Consulting LLC, Centennial, CO, USA;
[2]Advanced Technologies Group, Applied Materials, Santa Clara, CA, USA

15.1 Introduction

This chapter will discuss the need to optimize films deposited on devices with nanofeatures. Proper structural engineering of films enhance the yield and reliability of devices as well as reduce production costs. The discussion will focus on two applications: semiconductor interconnects and plasma displays. In semiconductor interconnect technology, line resistance must be minimized to minimize RC delay of the chip, minimize Joule heating, and increase the interconnect lifetime of the line. The discussion related to this topic will focus on the need to control the phase of the Ta barrier as the key to achieving low interconnect resistance. For plasma displays, planarization of oxide layers over topography with both 2 μm Ag pillars and 0.15 μm TCO pads must be achieved. The discussion related to this topic involves engineering low-stress layers while still achieving the required degree of topography coverage and planarization at a minimum oxide thickness to increase yield and device reliability and decrease production costs.

15.2 Need for structural engineering of patterned structures

This section of the chapter will begin with examples that show why the microstructure of materials in semiconductor interconnects need to be tailored for device reliability and how the deposition technology used impacts the ability to control that microstructure. That is followed by examples showing the need to engineer the properties of SiO_2 used in plasma displays to enable reliability and acceptable optical behavior of the device. Deposition of semiconductor interconnects is a complex combination of the interconnect topology (wall angle, aspect ratio), deposition technology, the barrier/adhesion layer, and conducting metal layers. The interconnect feature size and aspect ratio define what type

Modeling, Characterization and Production of Nanomaterials. http://dx.doi.org/10.1016/B978-1-78242-228-0.00015-6
Copyright © 2015 Elsevier Ltd. All rights reserved.

of deposition technology is required (standard sputtering, collimation, long throw, or ionized PVD), as discussed by Powell and Rossnagel (1999), and the barrier layer determines the crystalline texture and grain size of the subsequently deposited conducting metal.

The type of texture and grain size and structure of the conducting metal are important parameters in interconnect reliability as they have a strong impact on line electromigration lifetime (Cao et al., 2013, Vanasupa et al., 1999, Ryu et al., 1998).

Electromigration, a net mass transport of metal from one area to another during current flow, is caused by the current-carrying electrons transferring momentum to and dislodging lattice atoms, resulting in a void formation at the migration source and a whisker/hillock formation at the migration sink (Huntington and Grone, 1961). This often occurs when three grains meet and their grain boundaries intersect, allowing for a net influx or outflux of atoms. This section will focus on Cu interconnects for the 180-65 nm technology nodes that used a combination of ionized physical vapor deposition (iPVD) and electroplating. We begin with a discussion of how the engineering of the barrier layers is critical to achieve the lowest possible line resistance.

The sputtering process sequence for Cu interconnect metallization is TaN_x/Ta/Cu-seed performed in a single cluster tool followed by Cu electroplating and a subsequent recrystallization anneal. Copper film recrystallization at room temperature and during subsequent annealing is driven by the combined effect of system free energy and mechanical strain minimization. Free energy reduction is achieved by reducing the surface area through elimination of grain boundaries (grain growth). Strain and interface energy reduction is achieved through Cu texture reorientation (Mirpuri and Szpunar, 2005). The ability of Cu to recrystallize is partially driven by the phase of the Ta layer underneath the Cu. Recrystallization occurs slowly on the high resistivity β phase while proceeding significantly faster on the low resistivity α phase (Kozaczek et al., 2003). Formation of the more energetically stable α phase in refractory metals typically requires a deposition temperature of several hundred degrees centigrade. Feinstein and Huttemann (1973) showed that if certain impurities are present during the initial growth of refractory metals and the impurity concentration exceeds a critical threshold, the more energetically stable α phase will form at (low) fabrication temperatures that typically result in the refractory metal being in the β phase. The same phenomenon occurs for Ta depositions; α-Ta is achieved by having sufficient nitrogen content in the underlying TaN_x layer (Gittleman, 2013). While it may seem trivial to increase the nitrogen flow during the TaN_x deposition until the N concentration is well above the threshold required for α phase formation, actual production processing requires a delicate balance between the need for pure α phase and the increased particle generation and TaN_x resistivity that occurs with increasing nitrogen flow.

The importance of engineering the Ta phase across the entire area of a semiconductor substrate will now be discussed. Chains of vias are often used as test vehicles for evaluating metallization process flows. For the purpose of this discussion a via is a hole in a dielectric layer and a via chain is a series of holes connected by a metal line that lies at the bottom of the dielectric. The resistance is measured between the starting and ending vias to determine if the resistance of the chain is within the range specified for that device. If a via chain is measured as an open circuit or has very high resistance, the implication is that a void or voids in the via chain exist that reduce the metal cross-section or result in a complete interruption of the metal continuity.

Figure 15.1 shows a crescent-shaped pattern of open chain via yield on a 200 mm test wafer fabricated using best known production processes. The percentages in the legend represent the portion of via chains with resistance above the specified limit. Stress migration failures exhibited a similar pattern. Such patterns indicate there are systematic nonuniformity issues in one or more of the unit processes. Figure 15.2 shows X-ray diffraction (XRD) contour maps of 200 mm blanket test wafers exhibiting similar crescent shaped regions of TaN_x N concentration, α-Ta concentration, and Cu (111) volume fraction that spatially coincide with the crescent-shaped region where open via chains were occurring. Variation of light to dark in the contours represents high to low values of the quantity being mapped. As the sum of the α-Ta and β-Ta concentrations must equal one, the volume fraction of β-Ta grains increases as the α-Ta concentration decreases. The N concentration, Ta phase, and Cu volume fraction maps were produced by a fully automated XRD wafer mapping tool (Kozaczek et al., 2001, 2003). The volume fraction of a crystalline orientation is defined as the fraction of grains in the volume of the film with that orientation that have their axes statistically correlated with the direction of the surface normal. N concentration was determined from TaN_x peak position; lower 2θ values in nitrides and other solid solutions

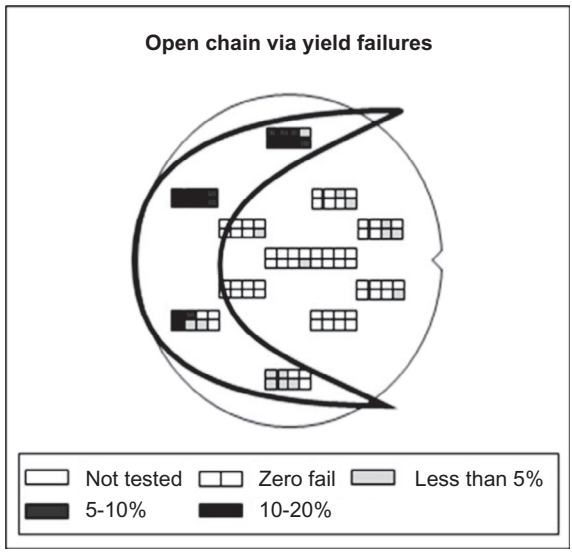

Figure 15.1 Open chain via yield as function of position on a 200 mm test wafer. Stress migration exhibited a similar pattern.

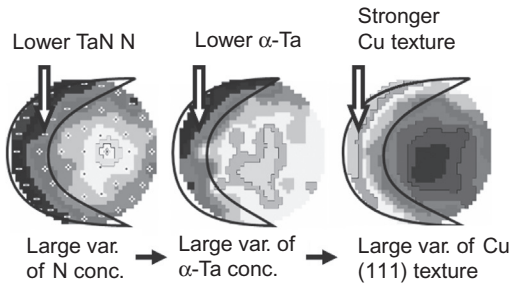

Figure 15.2 Crescent-shaped patterns of TaN_x peak position, α-Ta concentration, and Cu (111) volume fraction on 200 mm contour maps produced using XRD. The pattern correlates to the region with high occurrence of open via chain and stress migration failures in Figure 15.1.

correspond to larger lattices due to increased incorporation of N (Taxak et al., 2012). As described earlier, insufficient N concentration in TaN_x results in beta Ta growth, which in turn inhibits recrystallization of electroplated Cu. When electroplated Cu recrystallizes, the (111) volume fraction reduces (the texture becomes more random) and grain growth occurs (Kozaczek et al., 2003; Mirpuri and Szpunar, 2005). When recrystallization is inhibited, the result is a smaller-grained film with stronger texture. It was not determined why Cu voiding increased in the regions where recrystallization was inhibited; however, retarding of Cu recrystallization along the walls of a nanopatterned interconnects has also been shown to occur when the Ta phase is not engineered correctly, leading to incomplete consumption of the Cu seed layer (Gittleman, 2013), which in turn results in different grain structures in the trench possibly causing stress gradients in the interconnect. Alers et al. (2005) demonstrated that stress migration is driven by the tensile stress of the Cu and its elastic versus plastic energy dissipation and that stress gradients in Cu dominate stress migration performance. It is therefore plausible that nearby regions of Cu that have undergone different levels of recrystallization could have enough of a stress gradient to drive stress-induced voiding. The lesson from this analysis is that an issue with a single unit process can propagate downstream to subsequent layers, resulting in device failure. The issue was addressed by adjusting the N flow during the TaN_x process. The previous paragraph showed how reliability issues arise from nonoptimized process flows, but they often originate from the inherent limitations of process equipment as shown in the following example. In sputtering systems that operate at low pressure, and the deposition is primarily line of sight, the distance of the target from the wafer (substrate) and the location and orientation of a trench on the wafer determine the symmetry of deposition onto opposing faces of the trench sidewalls. The wafer edge-facing and wafer center-facing sidewalls of trenches perpendicular to the radial direction receive different amounts of flux from the target, resulting in asymmetric coverage, except at the wafer center. The edge-facing wall receives less deposition as shown in Figure 15.3. This issue increases

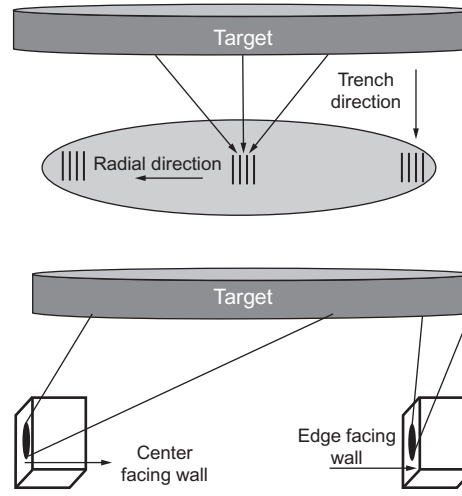

Figure 15.3 Top: trench orientation on a wafer and symmetric deposition received by trenches at the center of the wafer. Bottom: for trenches at the wafer edge, center-facing sidewalls receive deposition from a greater portion of the sputtering target than edge-facing sidewalls and therefore have a thicker deposition. The trenches in the figure are not drawn to scale to better illustrate the asymmetric deposition.

in severity with radial distance from the wafer center and with decreasing line width. Figure 15.4 shows transmission electron micrographs (TEMs) of 100 nm trenches from the center and edge of a 200 mm wafer with the barrier and Cu depositions being done by an applied materials (AMAT) self-ionized plasma (SIP) module. At the wafer center the trench wall coverage is observed to be nearly symmetric, while at the edge a significant asymmetry exists.

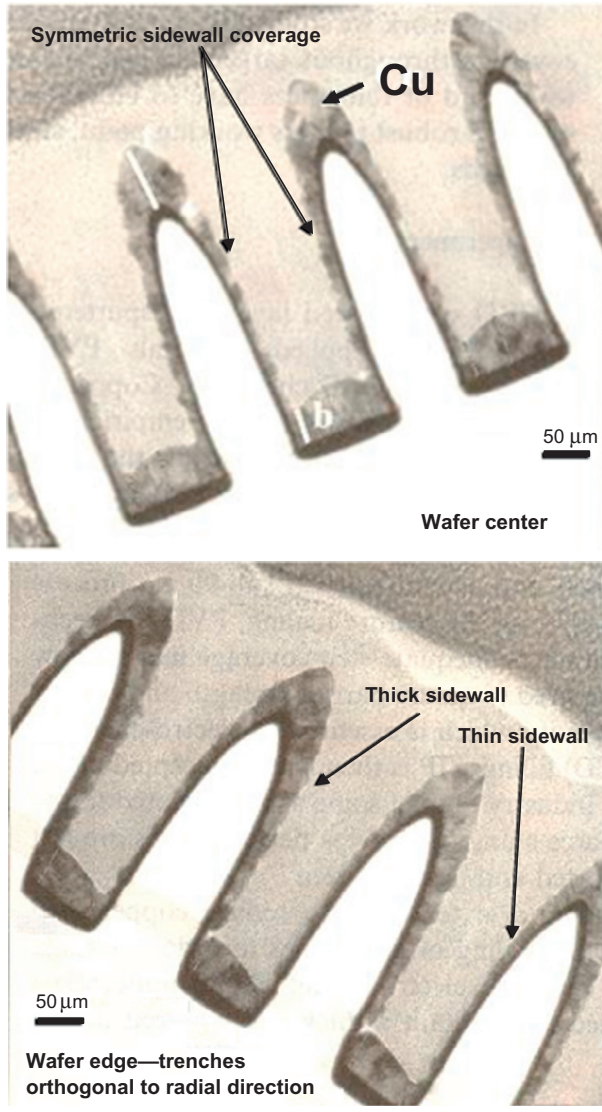

Figure 15.4 TEMs of AMAT SIP deposition of barrier/Cu-seed into 100 nm trenches. Top: wafer center, showing symmetric wall coverage. Bottom: wafer edge showing significant asymmetry.

The impact of thinner deposition on the edge-facing sidewalls is the inability to form α-Ta; the TaN_x layer can become too thin to provide sufficient N to produce the α phase (Brunoldi et al., 2006) and thickness has also been shown to play a role in the phase of refractory metals (Chen et al., 2002; Rossnagel et al., 2002). To verify that β-Ta exists on trench walls, patterned wafers were measured to determine the Ta phase. Figure 15.5 shows the α-Ta and β-Ta concentrations across a blanket wafer and wafers with 100 and 70 nm trenches as measured by XRD. Black indicates an α-Ta concentration of one (pure α phase) with lighter regions being a mix of α- and β-Ta. The α-Ta concentration decreases with trench width as wall coverage decreases.

If Cu recrystallization in trenches proceeds to completion, the Cu texture is oriented with respect to the trench floor normal and referred to as (111)[110] where the (111) planes are parallel to the surface normal and the [110] direction is parallel to the trench direction (Brunoldi et al., 2006). If β-Ta is present on a sidewall, however, the texture of the Cu seed layer on the sidewall is expected to exhibit stronger (111) texture than if the sidewall was α-Ta. Wong et al. (1998) showed that strong (111) Cu seed texture adversely effects the final texture of electroplated Cu. As discussed previously, there will be incomplete consumption of the Cu seed layer, which will be evident in (111) sidewall texture after the electroplating recrystallization anneal (Brunoldi et al., 2006). Per the discussion in the preceding paragraph, trenches perpendicular to the radial direction near the edge of the wafer are most likely to exhibit Cu sidewall texture. To verify that sidewall texture does not exist at the wafer center and does exist at the wafer edge, pole figures were collected on a patterned wafer with 70 nm line width. In the XRD tool used in this study a pole figure is accomplished by rotating the wafer in fixed increments and collecting data after each incremental rotation.

Figure 15.6 shows the results of the pole figure data collection from 70 nm trenches perpendicular to the radial direction. The top image is the (200) pole figure collected at the wafer center, while the lower left and right images are the (111) and (200) pole figures. Intensity from (111) planes for grains with floor texture will appear at 70.5° in a (111) pole and at 54.6° in a (200) pole figure. 70.5° is the angle between (111) planes in a (111) grain, and 54.6° is the angle between (200) and (111) planes in a (200) grain. The distance from the center of the pole figure to the edge of the grayscale portion represents 90°. Intensity form sidewall texture will show up near the edge of a (111) pole figure because the sidewall grains are oriented nearly 90° from the floor texture grains. The pole figure from the wafer center shows a similar intensity from all poles and that the position of the poles corresponds to that expected of (111)[110] texture. At the wafer edge, the higher pole densities on the upper hemisphere of the (111) pole figure indicate that the (111) sidewall texture originates from the inside (edge-facing) wall

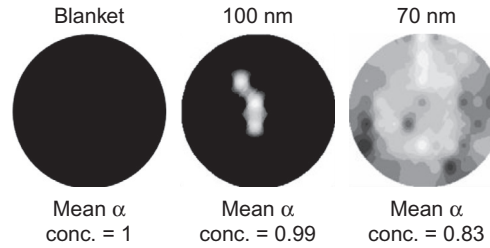

Figure 15.5 Contour maps of α and β-Ta concentration with mean α-Ta concentration for a blanket wafer and wafers with 100 and 70 nm trenches.

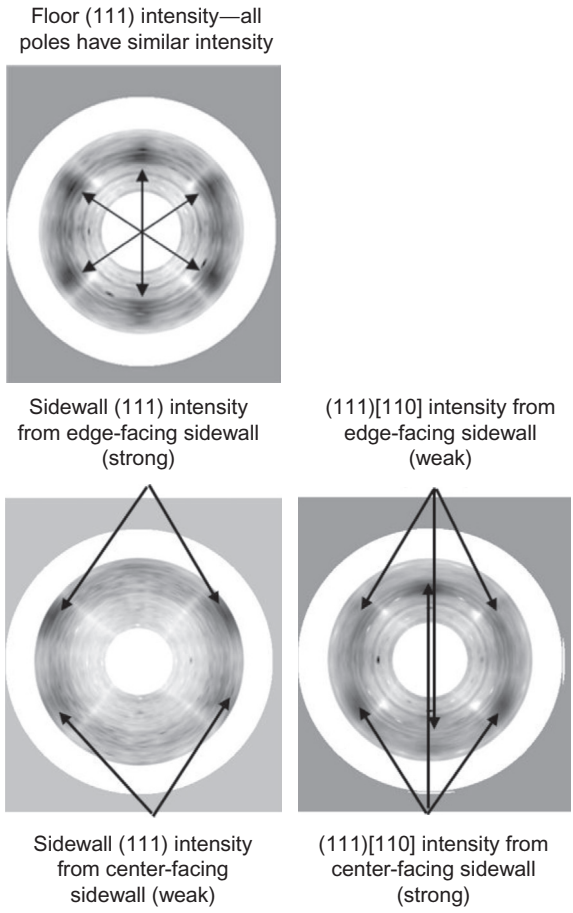

Figure 15.6 Experimental pole figures collected on 70 nm lines perpendicular to the radial direction. Top: (200) pole figure from the wafer center (top) showing uniform trench floor pole density. Bottom: wafer edge (111) pole figure (lower left) and wafer edge (200) pole figure (lower right) showing the existence of strong (111) sidewall texture for the edge-facing sidewall.

with the thinner, β-Ta rich barrier and the (111)[110] texture is concentrated on the outside (center-facing) wall covered with proper TaN/α-Ta bi-layer. While pole figures can take several hours to collect, mapping the intensity of floor texture across a wafer provides a means for rapid measurement that is compatible with production requirements. When that measurement is performed, trenches perpendicular to the radial direction are seen to exhibit much weaker floor texture than trenches near the wafer center or trenches parallel to the radial direction (Brunoldi et al., 2006).

Why is it important to be able to detect residual sidewall texture as line widths are decreased? Residual sidewall texture prevents formation of the bamboo structure (Figure 15.7 where grains extend across the entire trench width), which is known to give the longest electromigration lifetime (Jung et al., 2002). The above example illustrates how deposition module design can impact the ability to properly engineer the structure of films in nanopatterned features.

The discussion will now shift to the upper insulating layer for plasma display technology, which is SIO_2 in this example. The upper insulating layer plays the role of accumulating charge from the plasma and limiting the plasma discharge current.

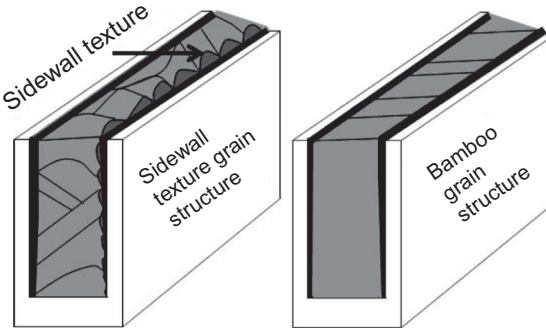

Figure 15.7 Depictions of trenches filled with electroplated Cu with (left) remnant Cu seed layer sidewall texture and (right) desired bamboo structure.

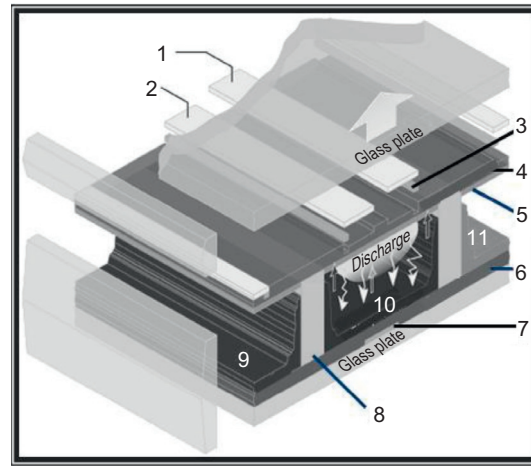

1. *X* electrode (sputtered ITO)
2. *Y* electrode (sputtered ITO)
3. Bus bars (silk screened silver paste)
4. Upper dielectric layer (SiO_2, CVD deposition)
5. Protection layer (MgO, electron beam deposition)
6. Lower dielectric layer (silk screened or leaded glass)
7. Addressing/data electrode (silk screened silver paste)
8. Barrier rib (silk screened paste, sandblast patterned)
9, 10, 11. red, blue, and red phosphors

Figure 15.8 Depiction of one phosphor cell of a plasma display with the material and deposition method for each layer identified.

Figure 15.8 is a depiction of one phosphor of a cell plasma display with the deposition method for each layer identified. As the fabrication process starts from the upper glass plate, it is evident that the SiO_2 layer needs to cover and planarize the nanopatterned topography created by fabrication of the electrodes and bus bars.

Depositing oxide films on nanopatterned structures pose a different challenge compared to interconnect metallization as the oxides often must cover metal lines with retrograde (inward sloping) topography even though the features are significantly larger than those for Cu interconnects.

The full range of requirements that the upper SiO_2 layer must fulfill are coverage of nonuniform and retrograde topography, creation of a planar surface, low stress, and excellent optical transmission. The low-stress requirement arises from concerns of film cracking and delamination, a common problem in plasma displays. Manufacturer evaluation of SiO_2 adhesion and integrity involve thermal cycling of test structures to temperatures at or above 500 °C. Given that the SiO_2 must meet topographical, mechanical, and optical properties, it is clear that success will be achieved without properly engineering the structure of the oxide.

The standard fabrication method for SiO_2 involves a silk screen deposition followed by a densification anneal at >500 °C. The high power requirements for the anneal necessitated locating plasma display fabrication facilities near power plants, limiting manufacturers' ability to locate plants based on economics, both of which result in a high cost for that layer. The following discussion involves a much lower cost SiO_2 deposition process using PECVD at microwave frequencies (MW-PECVD) with a HMDSO (hexamethyldisiloxane, $O[Si(CH_3)_3]_2$) precursor and O_2. The following results were obtained from a continuous wave (CW) microwave source. Figure 15.9 shows

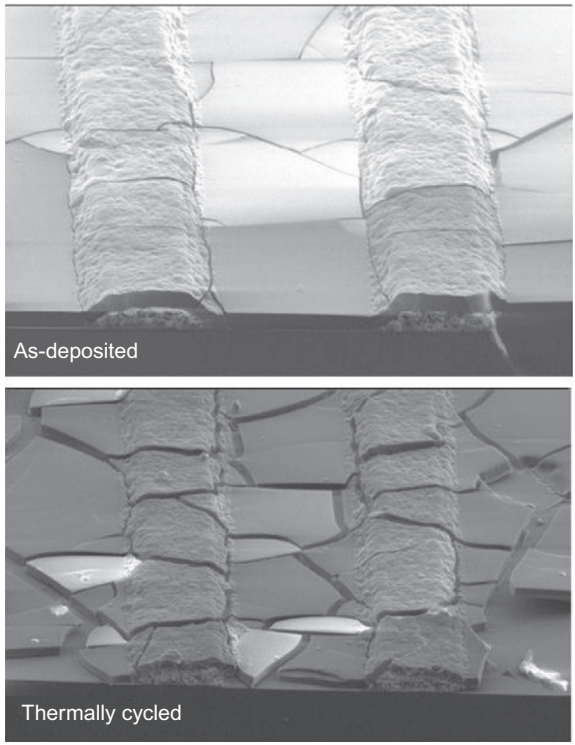

Figure 15.9 SEM images of MW-PECVD SiO_2 deposited on Ag lines. Top: As-deposited. Bottom: after thermal cycling at 580 °C.

13 μm thick SiO_2 on 70 μm wide, 13 μm tall Ag lines as deposited (top) and after thermal cycling to 580 °C (bottom). The figures show how nonoptimized depositions result in device failure. While the coverage of the lines is quite good, cracks are clearly evident in the as-deposited SiO_2 showing that the deposited film has high stress, resulting in catastrophic delamination during the thermal cycling adhesion test. Figure 15.10 shows that the transmission of the SiO_2 layer is not flat in the visible spectrum, exhibiting a significant decrease in the orange to red wavelengths that will distort the color experienced by a viewer. The expected transmission is ~92% due to reflection of light at the top and bottom surfaces of the SiO_2. The cause of the suboptimal stress and transmission of the SiO_2 may be related to the deposition conditions not being optimized to remove all unwanted components of the precursor. The FTIR spectrum of the SiO_2 in Figure 15.11 shows strong absorption by Si-OH and Si-CH_3 groups and the incorporation of water in the film. Water incorporation in SiO_2 has been reported to increase with increasing Si-OH content and lower film density (Ceiler et al., 1995), at least partially explaining the loss of optical transmission observed in Figure 15.10. Figure 15.12, a SEM cross-section of the SiO_2 film shows boundaries inside the film, indicating that the film is not fully dense, which concurs with the transmission and FTIR data. Water incorporation in SiO_2 is known to lead to corrosion cracking (Mahadevan and Garofalini, 2008) possibly explaining the stress cracking observed during thermal cycling. Obviously, the properties of the MW-PECVD SiO_2 are not yet acceptable and that process and possibly source modifications need to occur before a properly engineered film that is production worthy can be deposited.

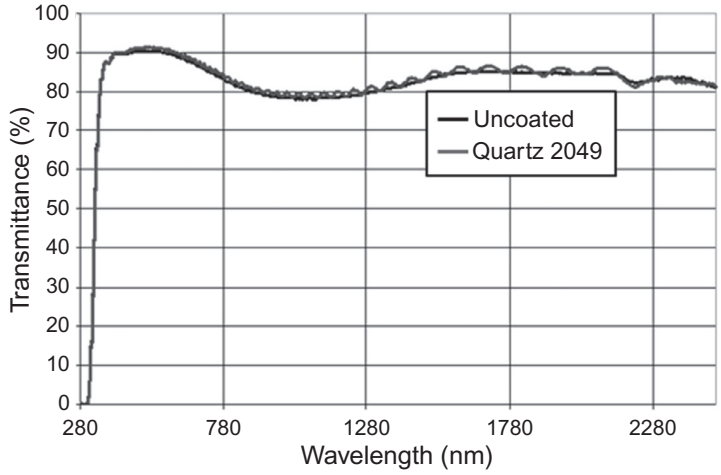

Figure 15.10 Optical transmission of MW-PECVD SiO_2 from the near UV to near IR. Note that the transmission in the visible spectrum drops in the orange and red wavelengths.

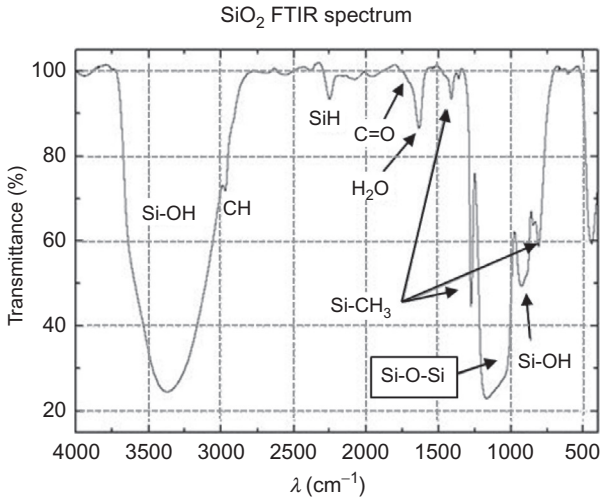

Figure 15.11 FTIR spectrum of MW-PECVD SiO_2 showing Si-OH, Si-CH_3, and Si-H contaminants as well as the incorporation of H_2O.

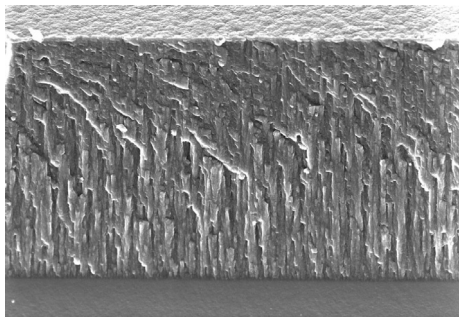

Figure 15.12 SEM cross-section of MW-PECVD SiO_2. The boundaries in the film support the conclusion from the FTIR and transmission results that the film is not fully dense.

15.3 Deposition technology and source design for nanopatterned devices

This section will elaborate on the pros and cons of various PVD and CVD deposition technologies with regard to feature coverage, film structure control, uniformity, and manufacturing cost. It will also discuss how enhancements to existing source technologies and modeling of the source chamber allow for proper engineering of film structure and the ability to meet coverage and planarization requirements of nanopatterned devices.

Table 15.1 compares the various vacuum deposition technologies used to deposit films in nanopatterned features with regard to the ability to structurally engineer films and provide feature coverage, uniformity, and production cost. It is clear that microwave PECVD performs well in all the categories listed and thus makes it the obvious choice for many nanotechnology device applications. iPVD is also an good choice when coverage requirements are not too extreme (e.g., no retrograde features) given its excellent structure tailoring attribute.

Table 15.1 Capability, uniformity, and cost comparison of deposition technologies used for fabrication of nanopatterned devices

Technique	Coverage	Structure control	Potential for film damage	Uniformity	Throughput	Cost
Enhanced PVD (collimation, long throw)	Fair	Poor	Low	Very good	Low	High
Ionized PVD (iPVD)	Good	Excellent	Low-moderate	Very good	Medium	High
CVD	Very good	Good	Low	Good	Low-medium	High
PECVD	Very good	Very good	Moderate-high	Good	Low-medium	Very high
LPCVD	Very good	Good	Low	Very good	High	High
Microwave PECVD	Very good	Very good	Low	Very good	Very high	Medium
ALD	Excellent	Good	Low	Good	Low	High
PEALD	Excellent	Good	Moderate	Good	Medium	Very high

15.3.1 Physics and modeling of highly ionized physical vapor deposition sources for Cu interconnect technology for optimization of deposition in nanopatterned features

In Section 15.2, it was shown how source design can limit the ability to achieve properly engineered film structure across a device wafer. Basic physics calculations and modeling can greatly enhance the design of deposition sources and provide important insights into the proper process space for using a source so that deposition into the features of patterned structures can be optimized across the substrate. With the continued drive to follow Moore's law and increase PC performance, semiconductor feature size has undergone continual reduction. At the 0.18 μm node, Cu interconnect technology started replacing aluminum interconnects for advanced logic chips. Cu interconnect technology is based on a dual damascene structure where trenches and the underlying vias were formed in a single fabrication process. Cu fill, as stated previously, was done by electroplating Cu into features with a previously deposited Cu seed layer that lined the interconnect walls to carry the plating current to the bottoms of trenches and vias (Quirk and Serda, 2001). This current-carrying requirement of the seed layer put a premium on having sufficient Cu sidewall coverage, which in turn requires minimal overhang after barrier and seed layer deposition. Standard enhancements to PVD sources used for sub 0.5 μm Al interconnects that limited the maximum angle from normal incidence that depositing atoms could have to reduce via overhang, such as collimation, in which a plate with high aspect ratio holes is inserted between the target and substrate, and long throw, in which the target is moved away from the substrate, could not provide sufficient sidewall coverage for the damascene feature geometries used for Cu interconnects. To illustrate this point, Figure 15.13 shows a simulation of long throw deposition from a conical target into a 0.25 μm aspect ratio 4 via at the edge of a 200 mm wafer by the ballistic (no scattering) simulation program SIMBAD created by Smy et al. (1998). The situation is very similar to that depicted in Figure 15.3. The deposition asymmetry in the via is quite striking and illustrates clearly why a new deposition technology is required. iPVD, an enhancement to standard sputtering technology, was invented to address this issue (Powell and Rossnagel, 1999).

iPVD sources were used to deposit both the barrier and Cu seed layers for dual damascene interconnects from about the 180-nm to about the 45-nm technology nodes. The purpose of an iPVD source is to create a plasma in which the great majority of atoms sputtered from a target are ionized so that the angular distribution of the sputtered atoms arriving at the substrate can be controlled by application of a substrate bias. To accomplish a high degree of ionization, RF energy is fed into a DC magnetron sputtering chamber. Figure 15.14 is a depiction of such a source. The essence of the source is a conical target, with an external RF coil that transmits RF energy through a dielectric window that makes a vacuum seal with the chamber. The Faraday shield, which attenuates the tangential component of the RF electric field, also acts as a deposition baffle to significantly attenuate the rate at which sputtered metal coats the dielectric window, greatly increasing the time during which the RF energy is transmitted with negligible attenuation. The wafer table is connected to a DC or RF power supply to provide substrate bias for accelerating the plasma ions.

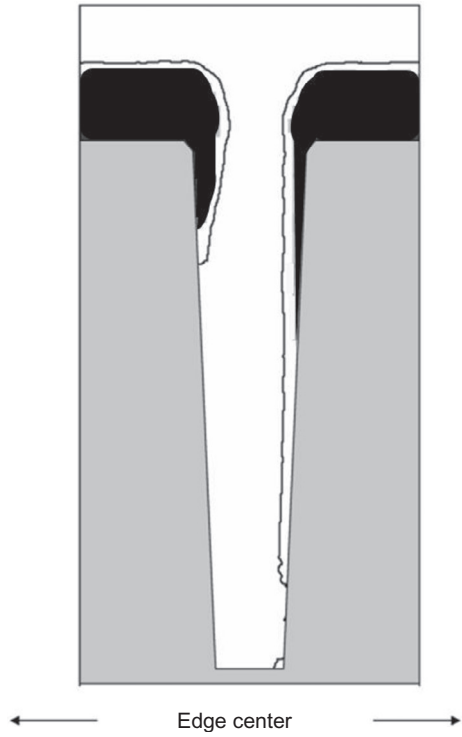

Figure 15.13 SIMBAD simulation of expected coverage in a 0.25 μm aspect ratio 4 via at the edge of a 200 mm wafer from a long throw deposition source.

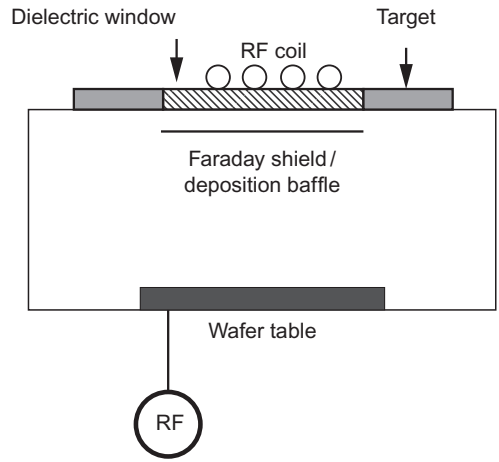

Figure 15.14 Depiction of the iPVD source used for all barrier and Cu seed layer depositions discussed in the chapter.

For such a source to create a high degree of ionization, there needs to be a large number of electrons available to ionize the sputtered atoms (electron impact is the dominant ionization mechanism in iPVD plasmas; Lu et al., 1999); the number of atom-electron collisions must be maximized, and the ion lifetime in the plasma must

be high. Neutralization of ions by electron impact is negligible (Tao et al., 2002) so the focus needs to be on what conditions are necessary to meet the first two requirements. Creation of a large number of electrons in the source requires an inductively coupled plasma (ICP) to create a high plasma density ($>10^{11}$ cm^{-3}), which in turn requires RF powers in the kW range for chambers that process 200- and 300-mm wafers. At the same time, maximizing the number of atom-electron collisions requires at least several inches between the target and wafer and sufficient pressure of the working gas to produce enough collisions between the working gas and sputtered atoms to slow down (thermalize) the sputtered atoms near the source so that their transit time to the wafer is increased. How to operate the source to achieve the best possible coverage of metal inside the feature also needs to be understood.

In plasmas, ion transport is driven by diffusion and by electric fields. At high plasma densities, ambipolar drift velocity becomes an important component of field-driven ion transport. Ambipolar drift occurs because electrons move to chamber walls more quickly than ions, due to the much smaller electron mass, creating a charge imbalance in the plasma that results in a radial electric field. The field accelerates ions toward the wall (toward the wafer edge), acting to equalize the radial flux of ions and electrons to the walls. The drift velocity toward the chamber walls breaks the lateral velocity symmetry for ions impacting the wafer, biasing the deposition in favor of the sidewall closer to the wafer edge (outboard sidewall). Mathematically, the ion velocity in a plasma with a nonnegligible ambipolar drift component can be described as a Maxwellian distribution with a drift term,

$$f(\mathbf{v}) = (m/2\mathrm{pkT})^{3/2}\exp\left(-m/2\mathrm{kT}\left[(v_x - v_{\mathrm{drift}})^2 + \left(v_y - v_{\mathrm{drift}}\right)^2 + v_z^2\right)\right] \tag{15.1}$$

where the z direction is along the target-to-substrate axis. The drift angle is equal to the ratio of the drift velocity to that of the velocity developed during acceleration by the sheath. The angular deflection of an ion by the radial drift field is given by

$$\tan\alpha = v_{\mathrm{drift}}/\,v_{\mathrm{sheath}} \propto (E/P)\left(kT_{\mathrm{gas}}/eV_{\mathrm{sheath}}\right)^{1/2} \tag{15.2}$$

where E is the magnitude of the radial electric field, P is the chamber pressure, T_{gas} is the gas temperature, V_{sheath} is the potential across the sheath, e is the elementary charge, and K is Boltzman's constant. Deposition conditions that can be used to control the deflection angle are pressure and sheath potential (through application of wafer power to bias the substrate). Increasing, Figure 15.15 depicts the angular deflection of an ion in the x direction caused by the radial electric field as the ion enters the mouth of a via.

Figure 15.16 shows the relative ion flux to the inboard and outboard walls of a 0.25-μm via for the case of $kT_{\mathrm{gas}}/eV_{\mathrm{sheath}} = 0.005$, which is equivalent to a sheath potential of 17 V for a gas temperature of 1000 K. With no ambipolar drift (0° deflection angle), coverage is symmetric about the via center, while the coverage increasingly favors the outboard or center-facing sidewall with increasing deflection angle and reaches a 5:1 ratio at $\alpha = 1.5°$. And this occurs for a situation where $kT_{\mathrm{gas}}/eV_{\mathrm{sheath}} \ll 1$, so it is not

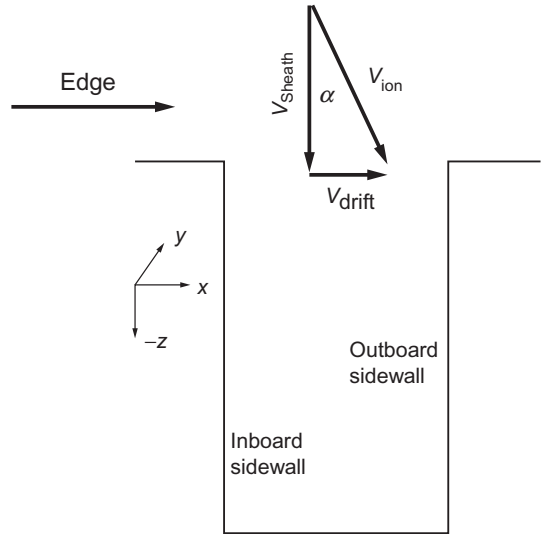

Figure 15.15 Depiction of ambipolar drift in the x direction for an ion entering the mouth of a via.

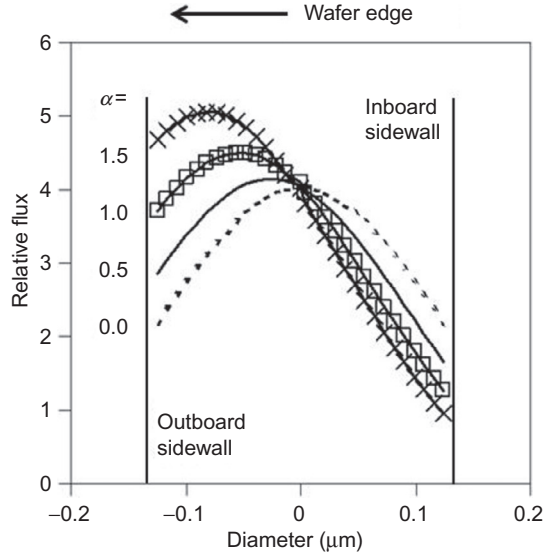

Figure 15.16 Calculated deposition flux to the outboard and inboard walls of a via for ambipolar drift angles ranging from 0° to 1.5°. The deposition is symmetrical when there is no ambipolar drift ($\alpha = 0$ degrees) and increasingly favors the outboard wall with increasing α.

possible to completely remedy this situation by only increasing the bias on the wafer! Examining the equation for the deflection angle, the only way to decrease its value is to either decrease the magnitude of the radial electric field, which is difficult because that is a function of the plasma and chamber design, or to increase the operating pressure. Increasing pressure acts to retard the effect of a radial field by decreasing the distance between collisions in the plasma, thus damping out any lateral acceleration produced by the radial electric field. Langmuir probe measurements in a test chamber

with the design elements of Figure 15.14 determined a radial electric field of between 0.1 and 0.4 V cm^{-1}. Calculations based on those values for the radial electric field, a gas temperature of 1000 K, and a sheath potential between 5 and 10 V, estimate that the deflection angle can be reduced from a range of 2.7° to 12° at 34 mTorr to a range of 2.3° to 8.3° by applying a wafer bias that raises the sheath potential to 10 to 15 V and a greater reduction to a range of 1.1° to 3.7° with a sheath potential ranging from 14 to 19 V at a pressure of 65 mTorr. The challenge then becomes how to design a system that can operate at high pressure and still provide good thickness uniformity.

To answer that question, the Hybrid Plasma Equipment Model (HPEM) developed by Mark Kushner's research group (Lu and Kushner, 2001) was used to model a 200 mm deposition chamber with the elements of Figure 15.14. Based on adjusting chamber parameters such as diameter and target to substrate distance (TS) and deposition parameters such as ICP power and pressure, a chamber design was finalized based on the metric of achieving ~3% relative standard deviation (%1σ), which is defined as

$$\%1\sigma = 100(\text{standard deviation})/\text{average}. \tag{15.3}$$

Table 15.2 compares modeled and measured %1σ for a 200 mm wafer, while Figure 15.17 compares the modeled and measured (XRF) radial thickness profile for the condition 50 mTorr, 8.5″ throw distance, and 4 kW ICP power. While the measured uniformity is worse than the modeled values, the uniformity follows the same trend, and, more importantly, the model is in agreement with the measurements in showing a fall off of deposition rate at the edge of the chamber. Modeling therefore played the critical role in the ability to design a beta phase chamber of correct diameter and throw distance that achieved reasonable uniformity at high pressures.

After the 200 mm beta platform was built, experiments were run to determine via coverage as a function of pressure and test the model predictions. Figure 15.18 is a TEM cross-section at the edge of a 200 mm wafer of a via of height 1.1 μm, bottom width 0.18 μm, and 0.25 μm mouth with a 1300 Å Cu seed layer deposited on 250 Å Ta. The Cu deposition pressure was 30 mTorr, the DC target power was 5.7 kW, the ICP power was 5.4 kW, and no substrate power was applied. The Ta deposition conditions were 85 mTorr pressure, 12.5 kW DC power, and 5 kW ICP power. It is clear the outboard wall has far greater coverage of Cu than the inboard wall. Because Cu is a soft metal that smears easily even during TEM preparation, wafers were deposited under identical conditions, except with the Cu seed layer thickness increased to 1800 Å were sent for Cu electroplating to verify the coverage asymmetry observed

Table 15.2 Comparison of modeled and measured deposition uniformity for two different sources to substrate distances for the 200 mm iPVD module

Condition	HPEM % 1σ	%1σ as determined by XRF measurements
50 mT, 8.5″ TS, 4 kW ICP	3.14	5.09
50 mT, 6.5″ TS, 4 kW ICP	3.85	6.08

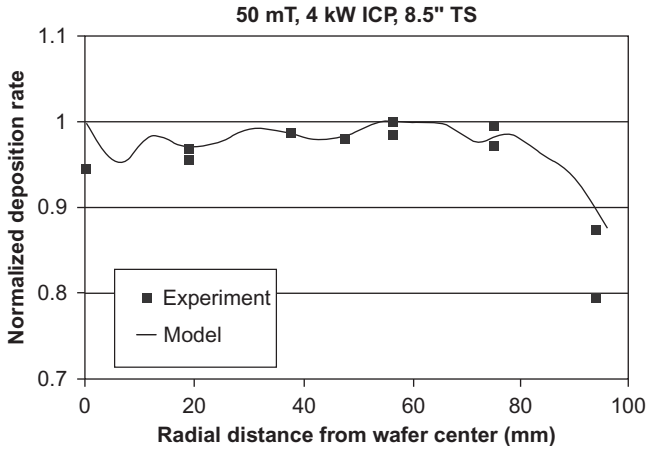

Figure 15.17 Modeled and measured radial thickness profiles for the 200 mm iPVD module depicted in Figure 15.14 for the deposition condition 50 mT, 4 kW ICP power, and 8.5″ throw distance.

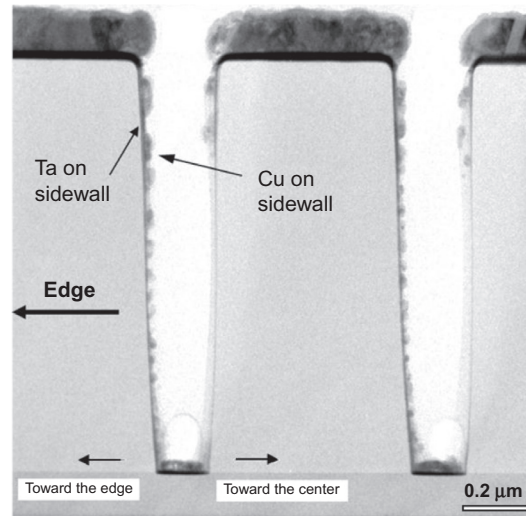

Figure 15.18 TEM cross-section of a via at the wafer edge after deposition of Ta(250 Å)/Cu (1300 Å) showing significant asymmetry of coverage between the inboard and outboard walls. The Cu was deposited at a pressure of 30 mT with 5.7 kW DC power and 5.4 kW ICP power.

in the TEM. Figure 15.19 shows FIB/SEM cross-sections taken at the edge (top picture) and center (bottom picture) of a plated wafer. Voiding is evident only on the inboard sidewalls at the wafer edge, where ambipolar drift is expected to deprive that sidewall of Cu, while complete filling is achieved on the via outboard walls at the wafer edge, which is expected to have greater Cu thickness due to ambipolar drift. Complete fill also occurs on both via walls at the wafer center where ambipolar drift will not be a factor. Equation (15.2) predicts that application of wafer power to

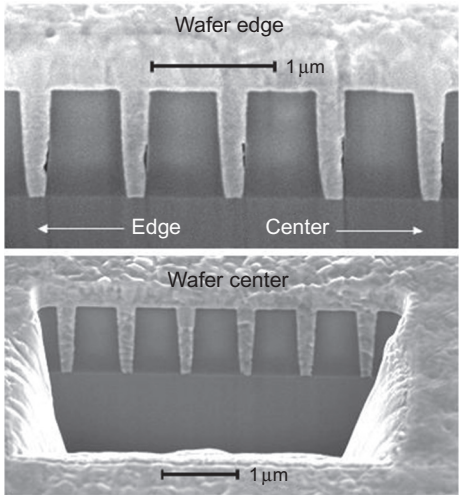

Figure 15.19 FIB/SEM cross-sections of Cu electroplating on vias with the same Ta barrier and Cu seed layers as in Figure 15.18. The top cross-section is from the wafer edge and the bottom cross-section is from the wafer center. At the wafer edge, voids are clearly evident on the inboard wall where the coverage in Figure 15.18 was observed to be less.

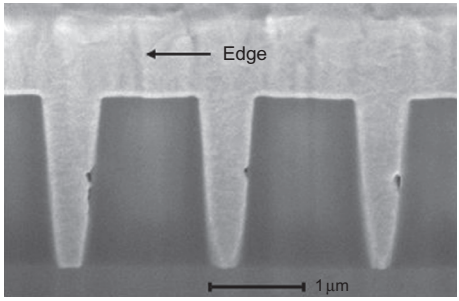

Figure 15.20 TEM cross-section at the edge of a 200-mm wafer for the same process as in Figures 15.18 and 15.19 except with the application of 100 W of wafer power to reduce the ambipolar drift angle. Note the reduced voiding on the inboard wall compared to Figure 15.19.

increase the sheath potential will reduce the deflection angle of the metal arriving at the substrate. A test to verify that prediction was performed by adding 100 W substrate power to the same Ta and Cu seed layer processes used for the sample in Figure 15.19. Figure 15.20, a FIB/SEM cross-section of the 100 W table power process at the edge of a 200 mm wafer shows a marked decrease of voiding on the inboard wall, verifying the prediction. Increasing pressure is the other deposition parameter predicted to reduce the ambipolar drift angle. Figure 15.21 shows the measured outboard to inboard ratio of Cu thickness for the same via geometry as Figures 15.18–15.20 at pressures from 60 to 100 mTorr for ICP powers of 3.5 and 5 kW. The ratio decreases with pressure, consistent with the prediction of Eq. (15.2). Based on the data generated by the 200 mm chamber, which enabled refinements to the model, a 300 mm chamber was designed that achieved deposition uniformity $<3\%$ 1σ at pressures above 30 mTorr. The important points to be taken from the preceding discussion are that an understanding of basic source physics allows definition of the useful operating space and that modeling provides a pathway to understanding what the critical elements for designing a source are. Both are critical for achieving good sidewall

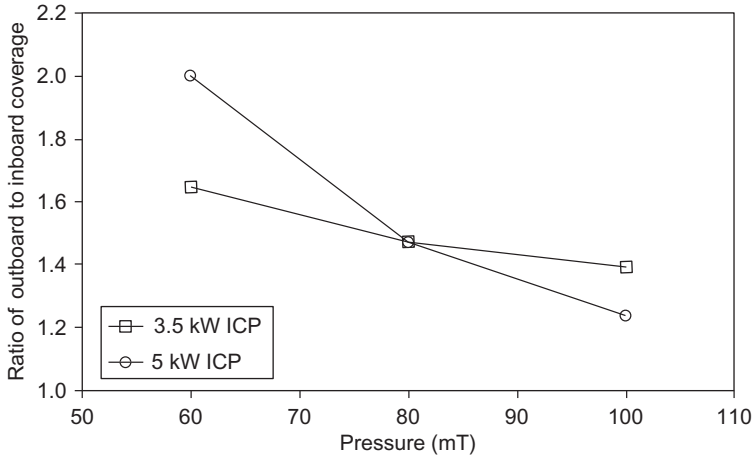

Figure 15.21 Ratio of inboard to outboard sidewall coverage as a function of ICP power and deposition pressure. The ratio decreases with increasing pressure as predicted by Eq. (15.2).

coverage in nanopatterned features, which results in the ability to properly engineer the structure of deposition inside those features.

15.3.2 Physics and modeling of microwave PECVD technology

For MW-PECVD SiO_2 films discussed in Section 15.2, the primary issue appeared to be inability to fully remove all precursor components in the film leading to loss of optical transmission and water retention, which in turn resulted in film cracking during subsequent thermal stress testing. Both source optimization and modeling played critical roles in the achieving MW-PECVD SiO_2 with the desired structural properties, that is, no precursor components or water in the film. Deposition of SiO_2 using an HMDSO precursor requires O_2 to enhance reduction of the precursor, decrease C content in the film, and obtain high deposition rates (Reuter et al., 2012). The mechanism for the rate increase and carbon reduction is reaction with atomic oxygen that is created by the plasma. Therefore, the distribution of both O_2 and HMDSO must be uniform and there cannot be local depletion of O_2. Figure 15.22 is a CAD rendering of the MW-PECVD deposition chamber showing the precursor gas distribution elements, MW source, pump port, and substrate. To prevent surface recombination of atomic O near the microwave source and ensure a sufficient quantity of it for HMDSO reduction, quartz tubes were used for the gas and source feeds. Figure 15.23, a normalized 3D rendering of the thickness uniformity across the chamber for a 2.45 GHz, 1500 W deposition done at 0.3 Torr, shows the asymmetry that occurs when there is localized depletion of O_2. The minimum deposition thickness occurs by the corner of the substrate closest to the pump port and the maximum thickness occurs on the portion of the substrate that is vertically farthest from the pump port. The thickness uniformity is 6% across the substrate, which is unacceptably high. The incorporation of silanol groups

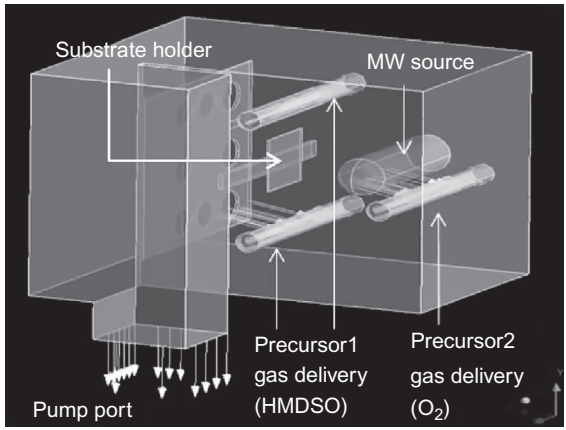

Figure 15.22 CAD rendering of the MW-PECVD deposition chamber showing the precursor gas distribution elements, MW source, pump port, and substrate.

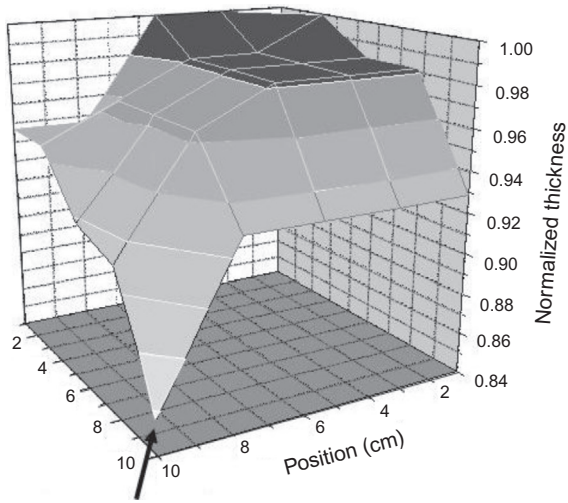

Figure 15.23 Thickness mapping of MW-PECVD SiO_2 deposition. The thickness profile is clearly asymmetric, with a minimum occurring at the point on the substrate closest to the pump port. Uniformity is $\pm 6\%$ across the substrate.

and water was also greatest where the deposition rate was lowest. Given the strong correlation between deposition rate and gas species distribution, modeling was used to simulate gas flow in the chamber, including the effect of the pump. Figure 15.24, the simulated O_2 velocity distribution (top) and HMDSO mass fraction or partial pressure distribution (bottom) both show asymmetries in gas distribution in the chamber with the O_2 flow velocity and precursor partial pressure both higher by the pump port. The darkest lines in the O_2 velocity simulation represent the lowest flow velocity. The lower O_2 flow velocity at the substrate edge that is vertically furthest from the pump port leads to a longer residence time, which will increase the SiO_2 deposition rate through longer times to react with the precursor. Modeling of source configurations

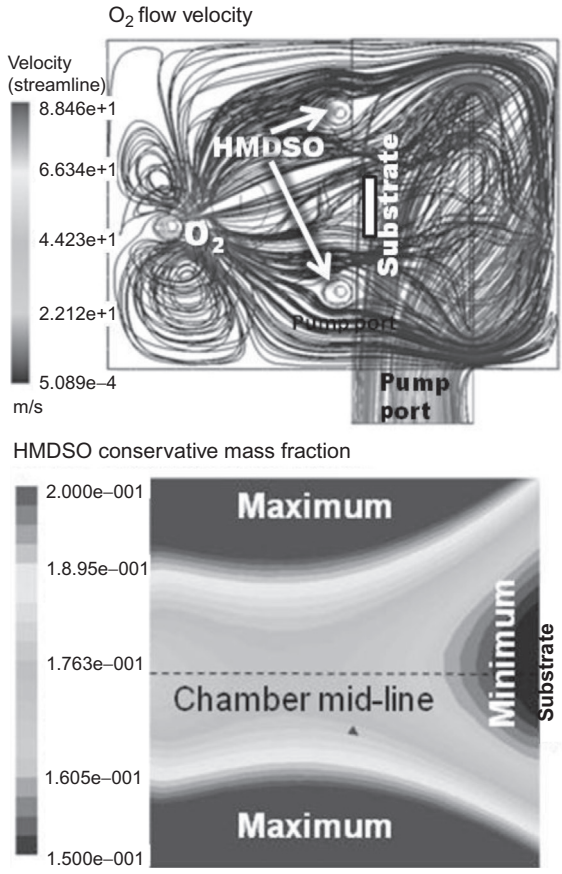

Figure 15.24 Simulation of O_2 velocity distribution (top) and HMDSO mass fraction distribution (bottom) for the MW-PECVD chamber. The darkest lines in the O_2 velocity simulation represent the lowest flow velocity.

was used to correct the flow asymmetries, resulting in the pump port being moved to the wall of the chamber furthest from the carrier gas delivery element and a baffle being placed in front of the pump port to reduce pumping speed. In that configuration, the thickness variation was reduced to $\pm 1.5\%$.

Once the nonuniform gas flow distribution was corrected, the issues of residual precursor and water in the SiO_2 needed to be addressed to maximize optical transmission and prevent film cracking. While it is well known that increasing substrate temperature can remove SiOH precursor products from SiO_2 films (Ceiler et al., 1995), and it is obvious that reducing the deposition rate allows for more time to decompose unwanted precursor products in the film, the objective of this process was a high rate, low temperature production deposition process. The film property issues resulted from the use of a continuous wave source. Electromagnetic radiation is strongly attenuated from RF frequencies through at least the lower GHz portion of the microwave spectrum by the free electrons in the plasma, a range that includes the operating frequency of the source under discussion. Therefore, a CW plasma will be strongly attenuated and result in a discharge that is confined to within 2-3 cm (two to three skin depths at the measured plasma density of $1\text{-}2 \times 10^{11}$ cm^{-3}) from the source and therefore not extend to the substrate, with

the subsequent loss of substrate bombardment by plasma ions that typically results in densification of the deposited film or removal of unwanted precursor products. Again, understanding the physics at operation in the source allows modifications that enable structural engineering of the deposited film.

How is the fundamental limitation of attenuation overcome so that the plasma can extend to the substrate and allow for control of film properties? Pulsing the source using high energy bursts takes advantage of the fact that the equilibrium state of the plasma needs a finite time to be established. During the turn-on period, the plasma density is lower, reducing attenuation such that the plasma extends to the substrate and produces a high density of atomic oxygen. As time progresses after the pulse turn-on, the plasma shrinks, eventually becoming confined to the vicinity of the source. Pandey and Bhattacharjee (2012) measured a 20% drop in electron temperature and up to a factor of three drop in electron energy analyzer current by the end of a pulse, depending on pulse duration. The higher density of atomic O (compared to the CW source) not only enhances the decomposition of HMDSO, but also results in more O-O to O_2 recombination events, which results in UV emission in the wavelength range that promotes dissociation of water and hydroxyls.

Deposition rate with pulsing is similar to CW operation over a wide range of pulse frequencies and pressure as shown in Figure 15.25. The CW deposition rate at each pressure is given by the solid horizontal lines. The loss of deposition rate during the off time is compensated for by the high rate immediately after pulse turn-on due to the extension of the plasma to the substrate that is accompanied by an increased reduction rate of HMDSO at the substrate. It can also be high during the pulse afterglow if the atomic O lifetime is long enough.

Figure 15.26 shows the FTIR spectrum of SiO_2 deposited with a 1:3 on:off duty cycle at a 440 Hz pulse frequency. The FTIR spectrum shows pulsing the source results in significant reductions in SiOH, Si-CH_3, and H_2O absorption compared to

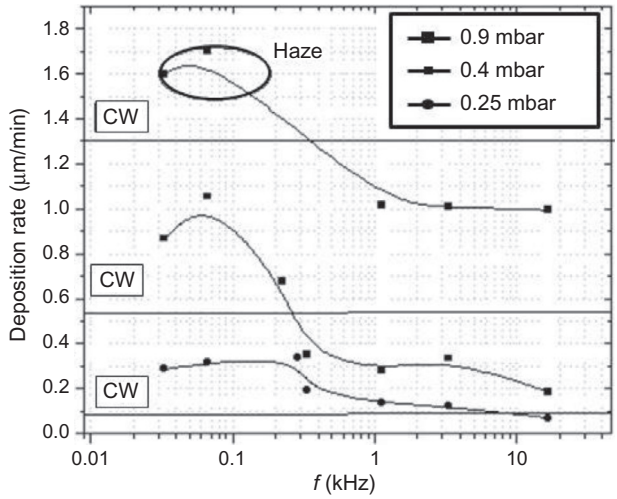

Figure 15.25 Pulsed microwave deposition rate as a function of pressure and pulse frequency. The CW rate is depicted as solid horizontal lines for comparison.

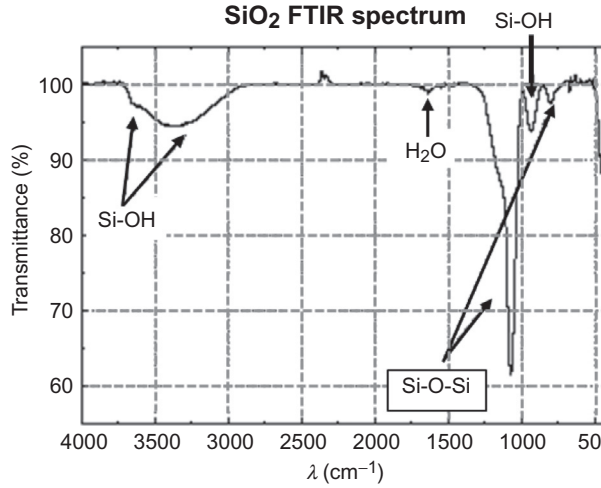

Figure 15.26 FTIR spectrum of SiO_2 deposited using a pulsed MW-PECVD process. Pulsing significantly reduces the presence of all contaminants seen in the CW SiO_2 FTIR spectrum in Figure 15.11

the CW FTIR spectrum of Figure 15.11, indicating an increase in film density with pulsing. Clearly, engineering of the film structure was achieved through understanding of the relevant plasma physics.

15.4 Use of advanced metrology on patterned features to optimize deposition technologies and enhance performance of nanopatterned devices

As seen in Section 15.2, metrology that can quantify the properties of materials deposited in nanopatterned features is an invaluable tool for gauging the performance of the deposition sources and for evaluating whether those materials have the required degree of structural engineering. The metrology techniques covered in this section are XRD and TEM cross-section analysis. The merits of XRD for metrology of materials in patterned structures arise from its ability to measure sidewall texture and phase of materials in patterned structures. TEM can be used to quantify feature coverage, overhang, and wetting angle as well as gauge the degree of agglomeration of mobile materials such as Cu on via sidewalls. A portion of this section will entail how metrology and source modeling can be incorporated into a feedback loop to provide inputs for modifying source technology or process conditions to achieve the best possible device performance across the deposition area.

In Section 15.2, the application of advanced XRD to determine the crystalline structure of materials deposited into interconnects was discussed in addition to how improper engineering of one layer has consequences for subsequently deposited layers and yield. We will now extend this discussion to include correlation between XRD metrics and expected device reliability. When evaluating correlations between measured parameters and device performance, it is important to include all parameters

known to have an impact on reliability. As discussed previously, the Ta phase dictates the recrystallization kinetics of electroplated Cu during annealing, and remnant small grains that occur with Cu sidewall texture can degrade interconnect electromigration performance. Grain size, determined by the full width at half maximum (FWHM) of XRD peaks, also impacts interconnect lifetime, which is expected to increase with increasing grain size (fewer potential triple boundaries). Another parameter that can be derived from XRD that can effect interconnect lifetime is the degree of grain tilt from the trench floor normal, which has been linked to electromigration performance of Al interconnects (Tracy et al., 1994 and references therein). The smaller the degree of grain tilt, the longer the electromigration lifetime. All polycrystalline materials have grains that are tilted with respect to the sample normal direction. For this study, a parameter called texture tightness was defined and is equal to the number of grains tilted from 0°to 10° from the sample normal divided by the number of grains tilted from 0°to 5° degrees from the sample normal. As this parameter approaches one, the number of grains with tilts greater than 5° goes to zero, and the texture becomes tighter. For interconnects, it is important to determine the relative importance of texture tightness and degree of recrystallization on interconnect electromigration performance so that structural engineering can focus on optimizing of the most important metric.

Barrier/Cu seed/electroplated Cu depositions were performed on two-level electromigration test structures with 90 nm lines of aspect ratio 4.9 and length 250 μm connected by 150 nm vias. The same deposition was performed on 90 nm comb structures for XRD analysis. All wafers underwent the same electroplating anneal. Figure 15.27 shows a SEM cross-section of the electromigration test structure used to evaluate the barrier process flow. Two different barrier types were employed for the study, a standard iPVD TaN/Ta stack that was subjected to a brief etch back after deposition and an iPVD-Ta/ALD-TaN stack, the acronym ALD standing for atomic layer deposition. Electromigration testing was performed at 300 °C with a current density of 1.5 mA/cm^2. Table 15.3 shows the Cu XRD data from 90 nm comb structures for both barrier types, while Figure 15.28 shows the electromigration data with mean time to failure (MTTF) and standard deviation for each barrier. The XRD values are averages of 88 pairs of two perpendicular comb structures on a 300 mm wafer. Electromigration testing was performed on 60 lines for each barrier type.

The XRD data show a higher degree of Cu recrystallization for the all iPVD barrier compared to the iPVD-ALD barrier (stronger texture), which is consistent with the

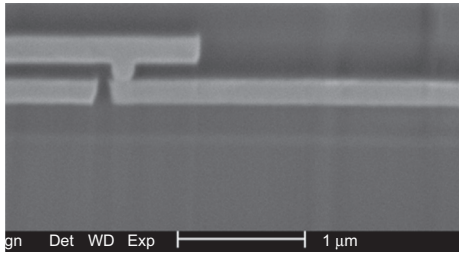

Figure 15.27 Electromigration test structure used for evaluation of barrier process flow.

Table 15.3 A 90 nm comb structure Cu texture, texture tightness, Cu FWHM, and Ta phase composition for iPVD-TaN/iPVD-Ta and IpVD-Ta/ALD-TaN barriers

Barrier type	Cu <111> volume fraction	Texture tightness	Cu <111> FWHM (°2θ)	Fraction of α-Ta grains
iPVD-TaN/iPVD-Ta	0.37	2.0	0.52	0.87
iPVD-Ta/ALD-TaN	0.55	1.1	0.55	No Ta peak detected

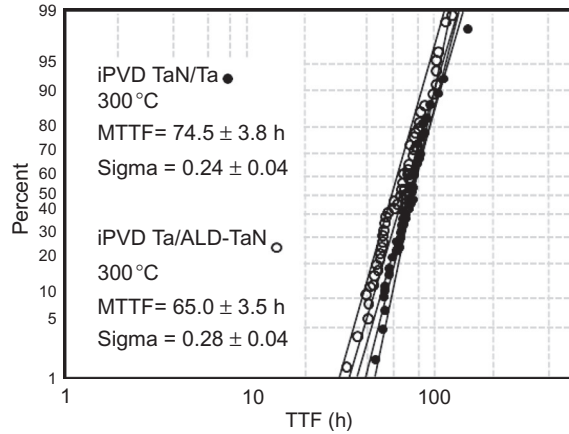

Figure 15.28 Electromigration data for the all-iPVD TaN/Ta and iPVD-Ta/ALD-TaN barriers. The all-iPVD barrier is seen to have a longer MTTF.

high degree of α-Ta present in the all-iPVD barrier and no detectable α-Ta peak for the iPVD-ALD barrier. The iPVD-ALD barrier produced a tighter angular distribution of Cu grains than the all-iPVD barrier. The FWHM data show a slightly larger grain size (smaller FWHM) for the all-iPVD barrier, but the difference is likely small enough not to impact the electromigration results. Therefore, the Cu properties that determine electromigration lifetime can be reduced to grain tilt and remnant sidewall texture.

The electromigration data show a 15% increase in MTTF for the all iPVD barrier relative to the iPVD-ALD barrier with almost identical statistical distributions, indicating that remnant Cu sidewall texture is the most important structure parameter, and the barrier stack must be engineered to provide consumption of as much of the Cu seed layer as possible during the electroplating anneal. It is reasonable to hypothesize that the electromigration lifetime of Cu with an all-iPVD barrier would become longer if the phase composition of α-Ta was increased from 0.87 to 1. It is evident that advanced XRD metrology can be a crucial tool in determining how to engineer the structure of interconnect materials for increased electromigration lifetime, determine the impact of alternative barriers or barrier deposition methods on Cu line reliability, and possibly be used to predict reliability of interconnects after node shrinks.

The previous sections made use of cross-section TEM analysis to gauge sidewall coverage of high aspect ratio vias. TEM analysis can also be used to determine fundamental physics of film growth that can be fed back into the chamber engineering to drive process improvements. Figure 15.29 shows a high magnification TEM image of a via sidewall with coated with a Cu seed layer deposited on β-Ta. It is clear that the Cu is agglomerated (a series of separate islands instead of one continuous layer) on at least a portion of the sidewall. From the individual grains, an average wetting angle of 40° for Cu on β-Ta was measured. The Cu thickness on the sidewall is only ~130 Å, and given that the wetting angle is not close to 0°, that Cu is a highly mobile species on surfaces, and that it is more mobile on α-Ta than on β-Ta, it will not be possible to have a (nearly) continuous Cu layer on via sidewalls without low substrate temperature to significantly reduced Cu mobility. As a reminder, electroplating current needs to be reach the bottom of the via for electroplating to occur everywhere in the via. Also, the electroplating bath is acidic and can dissolve isolated islands of Cu, leaving large sections of via sidewalls without Cu, resulting in voids. The wetting angle measurement and observation of agglomeration on via sidewalls were key factors that drove a realization that sparked a change from standard chillers that achieved a minimum substrate temperature of −6 °C and allowed a temperature rise to about 35 °C during deposition to Galden fluid chillers that achieved a minimum substrate temperature of −40 °C and limited the maximum temperature during deposition to about 0 °C.

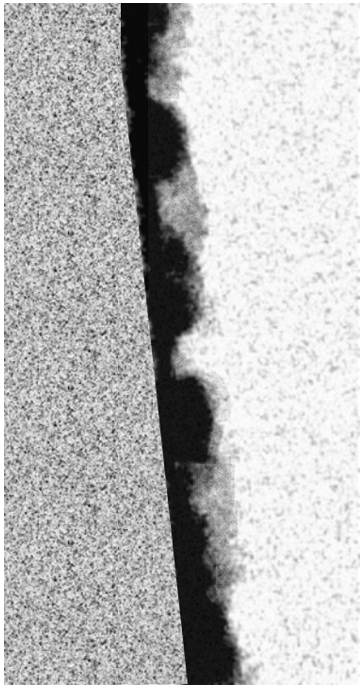

Figure 15.29 TEM of Cu grains on a via sidewall showing Cu agglomeration (islanding).

15.5 Examples of optimized nanopatterned devices

This section will present examples of semiconductor interconnects and plasma displays with structurally engineered films that were created using the lessons learned in Section 15.3.

15.5.1 Optimized iPVD technology and process for deposition of Cu interconnects

In Section 15.3.1, the elimination of feature coverage asymmetry in a high density ICP plasma using basic physics calculations and the use of modeling to improve deposition uniformity was discussed, while in Section 15.4 high resolution TEM cross-section analysis was used to understand the basic nature of film growth and help drive deposition chamber changes to enable continuous coverage of very thin films of Cu on sidewalls. In this section, the culmination of this work is shown.

Figure 15.30 shows TEMs of iPVD TaN/Ta/Cu deposited in 0.2 μm vias of aspect ratio 5. The Cu was deposited at a pressure of 65 mT, with the substrate power set at 150 W and an initial wafer temperature of −40 °C. The left via was from the wafer center and the right via is from the wafer edge. The direction of the wafer center is indicated at the top of each figure. The coverage of Cu is very symmetrical at both the center and edge of the wafer with a high degree of continuity, showing the mitigation of the ambipolar drift effect and the impact of reducing the deposition temperature. Figure 15.31 is a wafer-edge FIB/SEM cross-section showing the results of

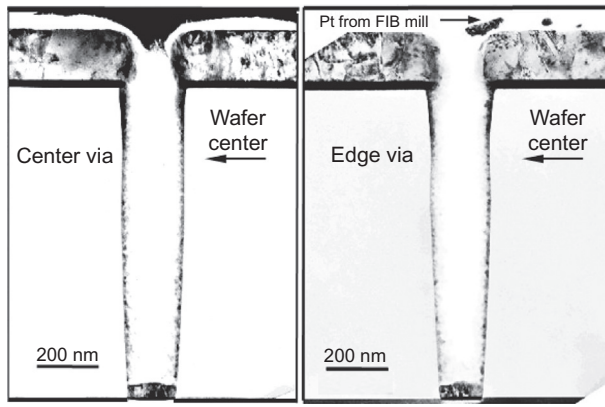

Figure 15.30 TEM cross-sections of aspect ratio 5, 0.2 μm vias at the center and edge of a 200 mm wafer using an optimized iPVD deposition process. Note the excellent symmetry of coverage at the wafer edge.

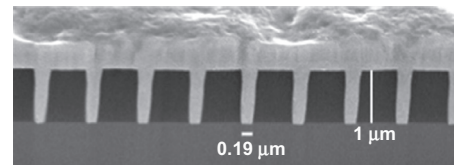

Figure 15.31 FIB/SEM cross-section showing void-free Cu electroplating of aspect ratio 5, 0.2 μm vias at the edge of a 200 mm wafer using the optimized iPVD process of in this figure.

electroplating of a via array with the same geometry as Figure 15.30 and the same process conditions. The void-free electroplating confirms the symmetrical deposition seen in the TEM and shows that the iPVD source technology and process conditions have been optimized.

15.5.2 Optimized MW-PECVD technology and process for SiO_2 deposition for plasma displays

This section presents data from a properly engineered SiO_2 layer for plasma display. The optimized deposition conditions used 4500 W of pulse power to create a sufficient concentration of atomic O to achieve reduction of nearly all the precursor gas near the wafer and enough O-O recombination events to produce SiO_2 with no visible traces of SiOH, Si-CH_3, and water in the FTIR spectrum shown in Figure 15.32. The peak positions of the unwanted species in the FTIR spectrum are 3000-3500 cm^{-1} for SiOH, ~1300 cm^{-1} for CH_3, and ~1600 cm^{-1} for H_2O. SEM cross-section images in Figure 15.33 of pulsed MW-PECVD SiO_2 deposited on Ag lines and subjected to the standard vendor 580 °C thermal cycling test show that the SiO_2 is dense, crack free, and exhibiting no delamination. The bottom cross-section shows the excellent coverage of a retrograde feature provided by pulsed MW-PECVD. The transmittance spectrum is now nearly flat from the near UV to the near IR as shown in Figure 15.34 with a near theoretical transmission of ~92% over the visible wavelengths.

15.6 Commentary on future trends

A future application involves iPVD deposition electroplating of through silicon vias (TSVs). TSVs are emerging as a way to perform three-dimensional chip stacking to vertically integrate multiple devices such as a logic chip coupled with stacked dynamic ram (DRAM) cells as depicted in Figure 15.35. TSVs range from several microns wide with depths of more than 20 μm to more than 20 μm wide with depths

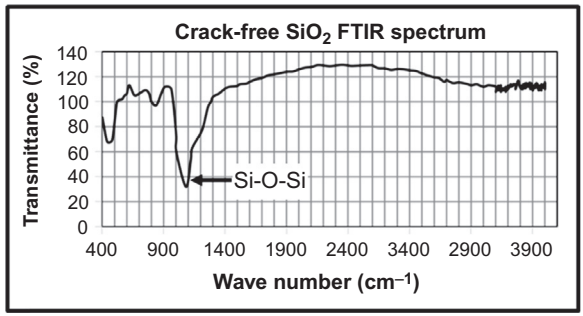

Figure 15.32 FTIR spectrum of the optimized MW-PECVD SiO_2 process. No evidence of contaminants is observed in the spectrum.

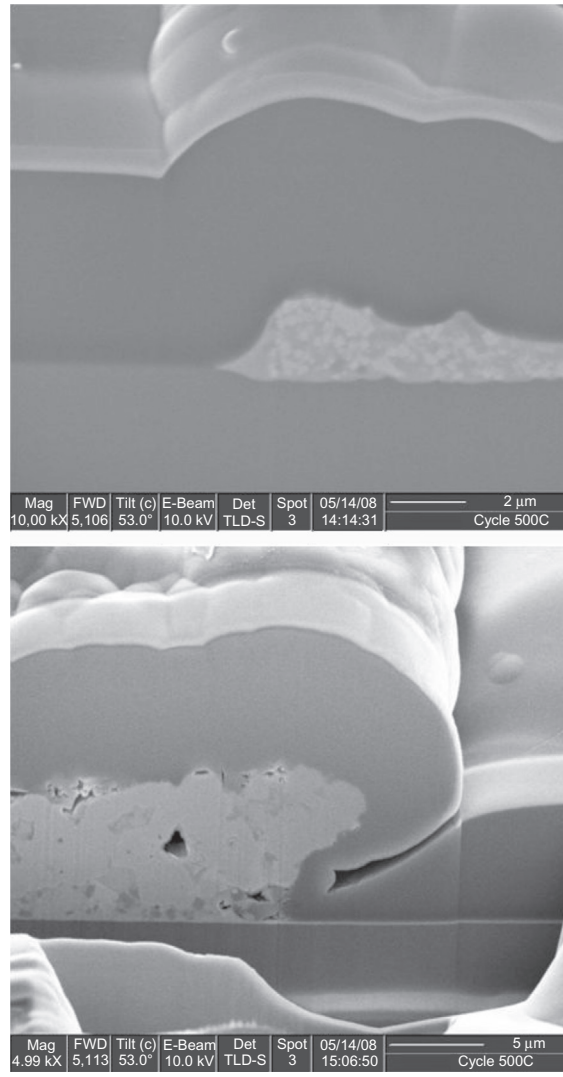

Figure 15.33 SEM cross-sections showing excellent coverage of optimized MW-PECVD SiO_2 deposited on Ag lines with nonuniform and retrograde topographies. Both samples were annealed at 580 °C and show no cracking or delamination.

up to 100 µm. Vias are etched into the Si, metallized, and the wafer thinned to expose the bottom of the via. Metallization of the via can be accomplished using the same process flows as for interconnects, iPVD barrier, and Cu seed layer followed by Cu electroplating. The most common approach to fabricate the via is after front-end-of-line processing (transistor formation), field-oxide deposition, and W via formation but before back-of-the-line (BEOL) steps that comprise multiple levels of interlayer dielectrics and Cu interconnects. This is referred to as the via middle process. A more complete description of the process flow is provided by Tsai et al. (2010). Depictions of three points in this process flow are shown in Figure 15.36. The top

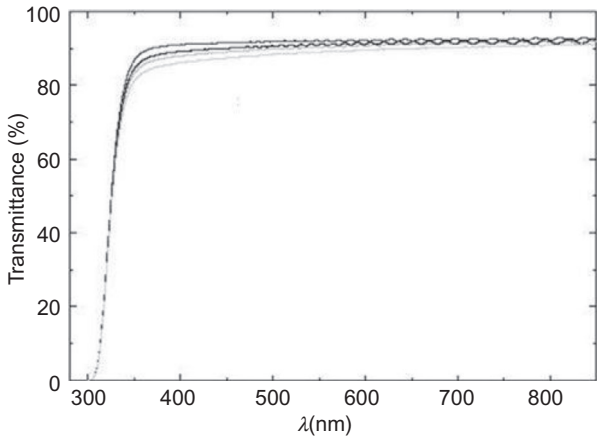

Figure 15.34 Transmittance spectrum of optimized MW-PECVD SiO_2 from the near UV to the near IR showing a near flat profile over the visible wavelengths with transmission near the theoretical value of 92%.

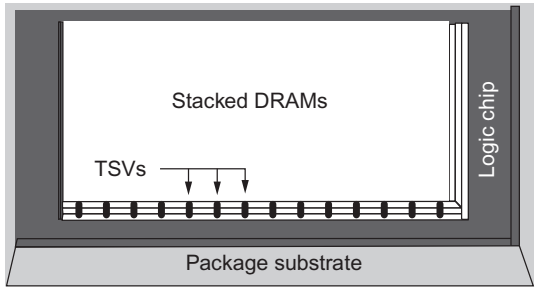

Figure 15.35 Depiction of through silicon vias vertically connecting a logic chip and stacked DRAM cells.

picture is just after the TSV via etch, the middle picture is after insulator (to protect the Si from Cu diffusion), iPVD barrier, and iPVD seed layer deposition, and the bottom picture is after wafer thinning to expose the TSV metal.

Although the TSV aspect ratios are similar to those of conventional interconnects, the extreme depth of TSVs create stringent requirements for iPVD deposition. Challenges include the ability to achieve sufficient sidewall coverage on the lowest portions of the via sidewalls and to understand if iPVD is capable of covering imperfections in the sidewall profile of deep vias. Integration challenges for metallization of TSVs have been discussed by Van Olmen et al. (2011).

Measurement and modeling of the ion angular and energy distributions in deep vias may be crucial for optimizing sidewall coverage. For example, whether the plasma actually penetrates through the via, potentially causing significant changes to the angular and energy distribution of ions inside the via and potentially causing resputtering of the deposited material, is a determined by the relative sizes of the plasma sheath and the via diameter (Kim and Shin, 2005). For most TSV schemes, this likely will not be an issue, but some plasma penetration into the via may impact deposited topography over the upper portion of the TSV.

For plasma displays, as consumer demand drives higher and higher resolution displays and larger televisions, MW-PECVD will be required to extend its current

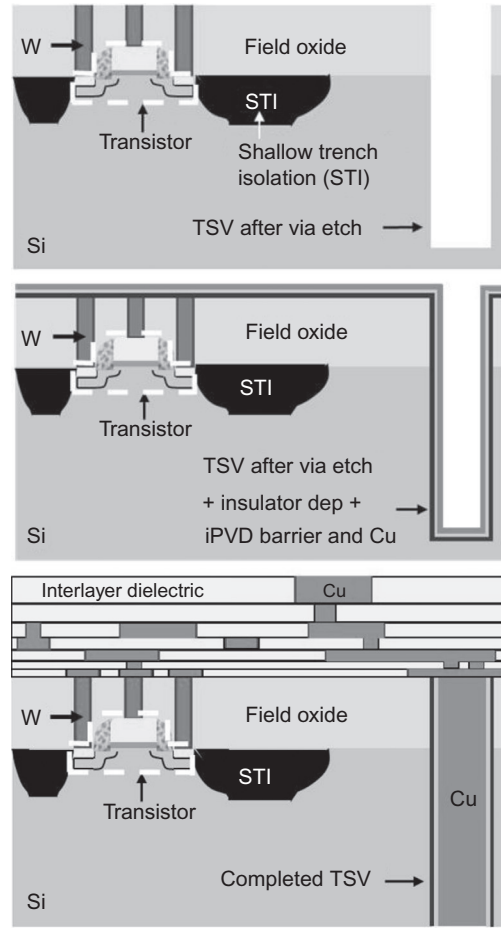

Figure 15.36 Depictions of three points in the via middle TSV fabrication process. The top picture is just after the TSV via etch, the middle picture is after insulator, iPVD barrier, and iPVD seed layer deposition, and the bottom picture is after wafer thinning to expose the TSV metal.

capabilities. The higher display density requires Ag lines of greater height to compensate for their shrinking width and preserve line cross-section. Ag is deposited by silk screening and doped with Bi to maintain line integrity during the subsequent 200 °C anneal required to lower the resistivity of the low-quality silk-screened Ag. The need for cross-section compensation results in a second silk-screened Ag layer (a single silk screening of the required Ag height will result in too much lateral spread of the line to meet packing density requirements). The resulting profile is shown in Figure 15.37 where it is apparent that the second deposition of silk screened Ag clearly creates a severe retrograde profile and higher aspect ratio that has to be conformally covered by MW-PECVD SiO_2. To avoid the need for ever-increasing Ag line heights and increased coverage requirements, it will be advisable to deposit low-resistivity Ag that allows for lower aspect ratio and most importantly, no retrograde profile. Microwave deposition will be the ideal method to accomplish this uniformly over a large area. Microwave deposition of metals can be accomplished by using a

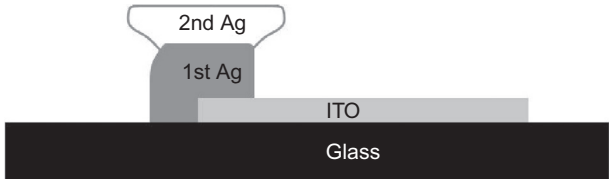

Figure 15.37 Depiction of a cross-section of a high density plasma display built up through Ag metallization. The second deposition of silk-screened Ag clearly creates a severe retrograde profile and higher aspect ratio that has to be covered by MW-PECVD SiO_2.

deposition baffle to protect the dielectric used to transmit microwave energy from the linear source into the deposition chamber. Larger displays will require understanding how to scale MW-PECVD to larger substrates and will require extensive modeling and improved understanding of the microwave power delivery.

15.7 Instructive sources related to deposition technology and structural engineering of films

The following literature is recommended for readers wishing to gain a deeper understanding of plasma physics and engineering of thin films.

Plasma physics

Lieberman, M.A., Lichtenberg, A.J., 1994. Principles of Plasma Discharges and Materials Processing, second ed. Wiley, New York.

Liehr, M., Dieguez-Campo, M., 2005. Microwave PECVD for large area coating. Surf. Coat. Technol. 200, 21–25.

Moisan, M., Pelletier, J., 1992. Microwave Excited Plasmas. Elsevier Science, Amsterdam.

Structural engineering

Machlin, E.S., 2005. Materials Science in Microelectronics. I: The Relationships Between Thin Film Processing and Structure. Elsevier Science, Amsterdam.

Ohring, M., 2001. Materials science of thin films deposition and structure. second ed. Academic Press (now Elsevier Science), San Diego, CA.

Schlom, D.G., Chen, L.-Q., Pan, X., Schmehl, A., Zurbuchen, J.M.A., 2008. A thin film approach to engineering functionality into oxides. J. Am. Ceram. Soc. 91, 2429–2454.

References

Alers, G.B., Sukamto, J., Woytowitz, P., Lu, X., Kailasam, S., Reid, J., 2005. Stress migration and the mechanical properties of copper. In: Proc. IEEE Int'l Rel. Phys. Symp, pp. 36–40.

Brunoldi, G., Kozaczek, K.J., Gittleman, B., Marangon, T., Young, M., 2006. Impact of narrow trench geometries on copper film crystallography. J. Microelectron. Eng. 83, 2208–2212.

Cao, L., Ganesh, K.J., Zhang, L., Aubel, O., Hennesthal, C., Hauschildt, Ferreira, P.J., Ho, P.S., 2013. Grain structure analysis and effect on electromigration reliability in nanoscale Cu interconnects. Appl. Phys. Lett. 102, 131907.

Ceiler Jr., M.F., Kohl, P.A., Bidstrup, S.A., 1995. Plasma-enhanced chemical vapor deposition of silicon dioxide deposited at low temperatures. J. Electrochem. Soc. 142, 2067–2071.

Chen, J., Parikh, S., Vo, T., Rengarajan, S., Mandrekar, T., Ding, P., Chen, L., Mosely, R., 2002. Barrier crystallographic texture control and its impact on copper interconnect reliability. In: Proc. IEEE International Interconnect Technology Conference, pp. 185–187.

Feinstein, L.G., Huttemann, R.D., 1973. Factors controlling the structure of sputtered Ta films. Thin Solid Films 16, 129–145.

Gittleman, B., 2013. Advanced X-ray diffraction metrology as a means of improving semiconductor device reliability. http://ieeexplore.ieee.org/xpl/articleDetails.jsp?arnumber=6647895.

Huntington, H.B., Grone, X.R., 1961. Current induced marker motion in gold wires. J. Phys. Chem. Solids 20, 76–87.

Jung, J.-K., Hwang, N.-M., Joo, Y.-C., 2002. Microstructure evolution in damascene interconnects. J. Korean Phys. Soc. 40, 90–93.

Kim, C.-K., Shin, C.B., 2005. Plasma molding over surface topography: measurement of energy and angular distributions of ions extracted through a large hole. Thin Solid Films 475, 24–31.

Kozaczek, K.J., Martin, R.I., Huang, L.-Y., Moran, P.R., 2003. Room temperature electroplated copper recrystallization: in-situ mapping on 200/300 mm patterned wafers. AIP Conf. Proc. 683, 485–489.

Kozczek, k.J., Martin, R.I., Kurtz, D.S., Moran, P.R., O'Leary, S.P., Martin, R.L., 2001. An instrument for rapid texture mapping on 200 mm wafers. Adv. X-ray Anal. 44, 266–271.

Lu, J., Kushner, M.J., 2001. Inflight electron impact excitation in ionized metal physical vapor deposition. J. Appl. Phys. 89, 878–882.

Lu, Z.C., Foster, J.E., Snodgrass, T.G., Booske, J.H., Wendt, A.E., 1999. Measurement of electron energy distribution function in an argon/copper plasma for ionized physical vapor deposition. J. Vac. Sci. Technol. A 17, 840–844.

Mahadevan, T.S., Garofalini, S.H., 2008. Dissociative chemisorption of water onto silica surfaces and formation of hydronium ions. J. Phys. Chem. C 112, 1507–1515.

Mirpuri, K., Szpunar, J., 2005. Impact of annealing, surface/strain energy and linewidth to line spacing ratio on texture evolution in damascene Cu interconnects. Mater. Charact. 54, 107–122.

Pandey, S., Bhattacharjee, S., 2012. Transition from interpulse plasmas to afterglows in pulsed microwave discharge. In: Proc. XX1 Europhysics Conf. Atom. and Molec. Phys. Ioniz. Gases, http://escampig2012.ist.utl.pt/Proceedings/files/Topic%209/escampig2012_submission_302.pdf.

Powell, R.A., Rossnagel, S.M., 1999. PVD for Microelectronics: Sputter Deposition Applied to Semiconductor Manufacturing. Academic Press, London.

Quirk, M., Serda, J., 2001. Semiconductor Manufacturing Technology. Prentice Hall, New Jersey.

Reuter, R., Rugner, K., Ellerweg, D., de los Arcos, T., von Keudell, A., Benedikt, J., 2012. The role of oxygen and surface reactions in the deposition of silicon oxide like films from HMDSO at atmospheric pressure. Plasma Processes Polym. 9, 1116–1124.

Rossnagel, S.M., Noyan, I.C., Cabral Jr., C., 2002. Phase transformations of thin sputter deposited tungsten films at room temperature. J. Vac. Sci. Technol. B 20, 2047–2051.

Ryu, C., Kwon, K.-W., Loke, A.L.S., Dubin, V.M., Kavari, R.A., Ray, G.W., Wong, S., 1998. Electromigration of submicron damascene copper interconnects. In: Proc. Symp. VLSI Tech, pp. 156–157.

Smy, T., Tan, L., Chan, K., Tait, R.N., Broughton, J.N., Dew, S.K., Brett, M.J., 1998. A simulation study of long throw sputtering for diffusion barrier deposition into high aspect vias and contacts. IEEE Trans Elec. Dev. 45, 1414–1425.

Tao, K., Mao, D., Hopwood, J., 2002. Ionized physical vapor deposition of titanium nitride: a global plasma model. J. Appl. Phys. 91, 4040–4048.

Taxak, M., Kumar, S., Krishnamurthy, N., Suri, A.K., Tiwari, G.P., 2012. Change in lattice parameter of tantalum due to dissolved hydrogen. Proc. Appl. Ceramics 6, 73–76.

Tracy, D.P., Knorr, D.B., Rodbell, K.P., 1994. Texture in multilayer metallization structures. J. Appl. Phys. 79, 2671–2680.

Tsai, T.C., Tsao, W.C., Lin, W., Hsu, C.L., Lin, C.L., Hsu, C.M., Lin, J.F., Huang, C.C., Wu, J.Y., 2010. CMP process development for the via-middle TSV applications at 28 nm technology mode. http://www.internationalsematech.org/meetings/archives/3d/8964/pres/Hsien_2.pdf.

Vanasupa, L., Joo, Y.-C., Besser, P.R., Pramanick, S., 1999. Texture analysis of damascene-fabricated Cu lines by X-ray diffraction and electron backscatter diffraction and its impact on electromigration performance. J. Appl. Phys. 85, 2583–2590.

Van Olmen, J.V., Huyghebaert, C., Coenen, J., Van Aelst, J., Sleecks, E., Van Ammel, A., Armini, S., Vaes, J., Dehaene, W., Beyne, E., Travaly, Y., 2011. Integration challenges of copper through silicon via (TSV) metallization for 3D-stacked IC integration. Microelectron. Eng. 88, 745–748.

Wong, S.S., Lee, H., Ryu, C., Loke, A.L.S., Kwon, K.-W., 1998. Effects of barrier/seed layer on copper microstructure. In: Proc. Adv. Metal. Conf, pp. 53–54.

Calculation of bandgaps in nanomaterials using Harbola-Sahni and van Leeuwen-Baerends potentials

16

P. Singh[1], *M.K. Harbola*[2], *A. Mookerjee*[3]
[1]Ames Laboratory, Ames, IA, USA; [2]Indian Institute of Technology Kanpur (IITK), Kanpur, India; [3]S N Bose National Centre for Basic Sciences, Kolkata, India

16.1 Introduction

Solving the Schrödinger equation for the many-body system of interacting valence electrons in a solid is one of the more difficult problems in condensed matter physics. To perform such calculations, several methods, such as Hartree-Fock theory, based on approximating the wavefunctions, have been proposed. However, the most successful first-principles approach to the electronic structure of solids is density functional theory (DFT) (Jones and Gunnarsson, 1989; Kümmel and Kronik, 2008; Sahni, 2004), which uses the ground-state density as the basic variable. The ideas behind DFT are quite simple and remarkably easy to implement for numerical calculations. As a result, DFT has proven to be a very powerful method for obtaining the ground-state density, total energy, and other properties associated with the ground-state of a many-electron system. Furthermore, it can handle systems ranging from a single atom to molecules, clusters, and solids with equal ease. On the other hand, one problem that has not been amenable to DFT methods is predicting the bandgap of semiconductors and insulators. Thus, interest in obtaining accurate bandgaps using DFT methods continues unabated (Godby et al., 1986; Knorr and Godby, 1992; Gonze et al., 1995). This chapter describes our efforts to solve the problem by looking at it afresh. In the following we first describe the Kohn-Sham (KS) approach to bandgap calculations and discuss (Perdew and Levy, 1983; Sham and Schlüter, 1983) why it cannot be expected to give accurate fundamental gap, defined (Mott and Friedman, 1974; Mott, 1974) as $(I-A)$, where I is the ionization potential and A is the electron affinity of a system, in solids. We then motivate the reader to regard the bandgap calculation as an excited-state problem and demonstrate that good estimates of bandgaps can be obtained by treating the exchange-correlation potential accurately.

Modeling, Characterization and Production of Nanomaterials. http://dx.doi.org/10.1016/B978-1-78242-228-0.00016-8
Copyright © 2015 Elsevier Ltd. All rights reserved.

16.2 Band-gap calculations in density-functional theory and derivative discontinuity of Kohn-Sham potential

The KS scheme of obtaining the bandgaps relies on the fact that the eigenvalue $\epsilon_{\max}$ of the highest occupied molecular orbital (HOMO) of the exact KS Hamiltonian for an electronic system with N electrons is equal to the negative of its ionization energy I (Levy et al., 1984; Perdew et al., 1982). Consequently, $\epsilon_{\max}$ for $N+1$ electron system equals negative of the electron affinity A of the system. Furthermore, in an insulator or a semiconductor, it is expected that adding an extra electron at the bottom of the conduction band would hardly change the density of the bulk system and therefore all the eigenvalues of the KS spectrum will remain essentially unchanged. It is therefore anticipated that the difference in the KS eigenenergies corresponding to the lowest orbital of the unoccupied band (negative of the electron affinity $-A$) and the highest orbital of the occupied band (negative of the ionization energy $-I$) should give the correct fundamental gap $(I-A)$ of semiconductors and insulators (Mott and Friedman, 1974; Mott, 1974). However, the results obtained by applying the traditional exchange-correlation functionals such as the local density approximation (LDA) (Von Barth and Hedin, 1972) are contrary to this expectation and grossly underestimate the bandgap with respect to experiments. This does not change even with more accurate functionals, for example, generalized gradient approximation (GGA) (Perdew et al., 1996; Perdew, 1986). The understanding of why it happens is based on the generalization (Perdew et al., 1982) of density-functional theory to fractional number of electrons. Accordingly, when the electron number changes across an integer, the chemical potential of the system changes discontinuously by $(I-A)$. This indicates that the exchange-correlation potential should also change by a constant ($\triangle > 0$) (Sham and Schlüter, 1983; Perdew et al., 1982) when a small fraction of an electron is added to a system with an integer number of electrons. For example, in the helium ion He^+, as the electron number is increased fractionally by δ from 1 to $1+\delta$, the exchange-correlation potential jumps by 1.1 atomic units (Sen and Harbola, 1991). This is known as the derivative (with respect to the electron number) discontinuity of the exchange-correlation potential. As a result of this discontinuity, the Kohn-Sham eigenenergy $\epsilon_{(N+1)}(N+1)$ for the highest occupied orbital, indicated by the subscript $(N+1)$, of the $(N+1)$ electron insulator will be higher than the eigenenergy $\epsilon_{(N+1)}(N)$ of this orbital for the N electron g system by energy $\triangle$. Therefore, the Kohn-Sham gap $E_g^{KS} = \epsilon_{(N+1)}(N) - \epsilon_N(N)$ will always underestimate the fundamental gap by the same amount.

Let us now look at the LDA or other approximations, such as the GGA, to the exchange-correlation functional in light of our discussion above. Because all these approximations depend directly on the density or its gradient, they cannot and do not have any derivative discontinuity in the corresponding potential. It is therefore argued that the Kohn-Sham gap calculated using these approximations cannot give the correct fundamental gap of a semiconductor or an insulator. For example, in silicon the E_g^{KS} calculated with the LDA is 0.49 eV, whereas the experimental gap is 1.17 eV. Does this mean that accurate bandgaps cannot be predicted by a

Kohn-Sham calculation? In this chapter we argue that this need not be the case if we look at the bandgap as transition energy between the top of the valence band and the bottom of the conduction band. This is based on the observation that the optimized potential method does give reasonably accurate bandgaps for a large number of systems (Talman and Shadwick, 1976; Kotani, 1995; Kotani, 1994). Furthermore, it has been shown (Savin et al., 1998) in atomic systems that if the exchange-correlation potential has correct behavior in the outer regions of an atom, the difference between the eiegenenergies of the highest occupied orbital and higher unoccupied orbitals is close to experimentally observed excitation energies of these systems. Note that this is in spite of the fact that the unoccupied orbitals of a Kohn-Sham system have no particular significance. On similar grounds, we may expect that when exchange-correlation potential is treated exactly, the Kohn-Sham bandgap will be close to the experimental gap. In this chapter, we show this to be the case. Although the exact exchange (EXX) correlation potential is not known, the exchange potential alone can be calculated exactly or highly accurately. We therefore present our study employing one such exchange potential, namely, the Harbola-Sahni (HS) potential for exchange; the correlation effects are still treated approximately within the LDA.

16.3 Kohn-Sham potential in terms of the orbitals: exact exchange and HS potential

As is well known, the Kohn-Sham potential of density-functional theory is a local potential that gives orbitals leading to the exact density of a system. The potential is made up of its external, classical Coulomb and the exchange-correlation potentials; in performing Kohn-Sham calculations it is the exchange-correlation potential that is approximated. The exchange-only (XO) Kohn-Sham potential is the potential whose orbitals reproduce the Hartree-Fock density of a system. Equivalently, the ground-state orbitals of the exchange-only Kohn-Sham potential minimize the Hartree-Fock expression for the energy of a given system. However, in contrast to Hartree-Fock theory, the exchange-potential in the XO Kohn-Sham theory is a local potential and is identified as the EXX potential. The question arises how such a potential can be constructed.

Sharp and Horton (1953) built upon Slater's (1951) idea to develop the optimized effective potential (OEP) method in 1957, but it was first applied in 1976 by Talman and Shadwick (1976) to numerically generate the required local potential for atoms. We now briefly describe how this is done. In the OEP method, one solves for a local potential $v_s(\mathbf{r})$ so that the corresponding orbitals ϕ_is minimize the Hartree-Fock expression for the energy. The potential $v_s(\mathbf{r})$ comprises the external potential, the Hartree potential, and the exchange potential. Because in general the expression for the EXX energy E_x is not known in terms of the density, the exchange potential $v_x(\mathbf{r})$ in the EXX is written in terms of the orbitals as

$$v_x([p];\mathbf{r}) = \frac{\delta E_x}{\delta \rho(\mathbf{r})} = \sum_i^{\text{occ}} \int d\mathbf{r}' \int d\mathbf{r}'' \left[\frac{\delta E_x}{\delta \phi_i(\mathbf{r}'')} \frac{\delta \phi_i(\mathbf{r}'')}{\delta v_s(\mathbf{r}')} + c.c. \right] \frac{\delta v_s(\mathbf{r}')}{\delta \rho(\mathbf{r})} \tag{16.1}$$

In the expression above, $\delta E_x/\delta\phi_i$ are the nonlocal potentials of Hartree-Fock theory, $\delta\phi_i/\delta v_s(\mathbf{r})$ is calculated using the first-order perturbation theory, and $\delta v_s(\mathbf{r})/\delta\rho(\mathbf{r})$ is the inverse of the noninteracting linear response function $\chi(\mathbf{r}, \mathbf{r}')$ defined via

$$\delta\rho(\mathbf{r}) = \int d\mathbf{r}' \chi(\mathbf{r}, \mathbf{r}') \delta v_s(\mathbf{r}') \tag{16.2}$$

and given as

$$\chi(\mathbf{r}, \mathbf{r}') = \sum_i^{\text{occ}} \sum_j^{\text{unocc}} \frac{\phi_i^*(\mathbf{r})\phi_j(\mathbf{r}')\phi_j^*(\mathbf{r}')\phi_i(\mathbf{r}')}{\epsilon_i - \epsilon_j} + c.c \tag{16.3}$$

where ϵ_i and ϵ_j are the orbital eigenenergies of the noninteracting system.

The first systematic study using EXX potential for a range of semiconducting materials was performed by Kotani (1994, 1995). These studies showed that EXX leads to bandgaps that are close to their experimental values. This led to many more studies (Städele et al., 1999; Sharma et al., 2005) of semiconductors, in particular their bandgaps, using the EXX theory. These studies showed that EXX leads to bandgaps that are close to their experimental values for a large number of systems. The explanation put forth (Städele et al., 1999) for this agreement is that the derivative discontinuity of the exchange and the correlation components of the exchange-correlation potential may be in opposite directions and hence cancel each other. However, as stated above, a possible reason for this is that the accuracy of the potential leads to differences in eigenenergies of occupied and unoccupied orbitals that are close (Savin et al., 1998) to the corresponding excitation energies of a system. With this in mind, we wish to use an easy and physically motivated potential, that is, the HS exchange potential, to calculate the bandgaps of semiconductors.

The HS exchange-correlation potential (Harbola and Sahni, 1989) is derived from the exchange-correlation (XC) hole because the work is done in moving a unit charge (atomic units) in the electric field produced by the XC hole; to calculate the exchange potential, it is the exchange hole, also known as the Fermi hole, $\rho_x(\mathbf{r}, \mathbf{r}')$, that is employed to calculate the field $\varepsilon_x(\mathbf{r})$. Thus the exchange potential is given as a line integral

$$W_{\text{HS}}(\mathbf{r}) = -\int_\infty^{\mathbf{r}} \boldsymbol{\varepsilon}_x(\mathbf{r}') \cdot d\ell' \tag{16.4}$$

where

$$\boldsymbol{\varepsilon}_x(\mathbf{r}) = \int \frac{\rho_x(\mathbf{r}, \mathbf{r}')}{|\mathbf{r} - \mathbf{r}'|^3} (\mathbf{r} - \mathbf{r}') d\mathbf{r}' \tag{16.5}$$

For a set of single particle orbitals $\{\phi_{i\sigma}\}$ with occupation $f_{i\sigma}$ for the ith orbital with spin σ, the Fermi hole is given (Krieger et al., 1992) as

$$\rho_x(\mathbf{r},\mathbf{r}') = \frac{1}{\rho(\mathbf{r})}\sum_{\sigma}\sum_{i,j} f_{i\sigma}f_{j\sigma}\phi^*_{i\sigma}(\mathbf{r})\phi^*_{j\sigma}(\mathbf{r}')\phi_{i\sigma}(\mathbf{r}')\phi_{j\sigma}(\mathbf{r}) \tag{16.6}$$

For an electron, the potential will have the opposite sign to that given in Eq. (16.6).

The HS approach provides (Sahni, 1997, 2004) a fundamental understanding of Kohn-Sham theory. The HS potential can be derived (Holas and March, 1997) directly from the Schrödinger equation via the differential virial theorem. From this derivation, it also becomes clear that the HS potential differs from the exact KS potential by the difference in the true kinetic energy and the Kohn-Sham kinetic energy of an interacting system. However, this difference is numerically very small. From the implementation point of view, a comparison of Eqs. (16.4)–(16.6) with Eqs. (16.1)–(16.3) makes it clear that the HS approach is much easier to employ numerically than the EXX. We note that the computational complexity of EXX is somewhat simplified in the KLI approximation (Krieger et al., 1992) of the EXX.

A question that can be raised is whether the HS potential is path independent (Rasolt and Geldart, 1990; Levy and Perdew, 1985) and the field $\varepsilon(\mathbf{r})$ is curl free. It is not so in general. However, for particular cases, for example, spherically symmetric densities such as those used in the atomic sphere approximations (ASA) of tight binding linearized muffin-tin orbital (TB-LMTO) method (Jepsen and Andersen, 2000; Andersen and Jepsen, 1984; Skriver, 1984), the field is indeed curl free (Sahni, 2004; Harbola and Sahni, 1990; Wang et al., 1990). On the other hand, for nonspherical charge densities, the solenoidal part of the electric field is numerically rather small (Slamet et al., 1994) and is related to the difference in kinetic energies between the Hartree-Fock and the HS approaches (Sahni, 1997).

The EXX calculations give the KS BGs (Kotani, 1994; Städele et al., 1999) in reasonable agreement with experiments. As mentioned above, it is believed that the agreement is due to a fortuitous cancellation of errors in these systems and does not hold in general (Sharma et al., 2005). However, if we think of the BG as transition energy, the agreement can be understood as arising from the accurate treatment of the exchange potential. It is with this understanding that we perform our calculations of bandgaps employing the HS potential.

16.4 Calculation of bandgaps for bulk materials using the HS potential

We have performed our calculations for the bandgaps using the HS potential within the LMTO as follows: We calculate the potential inside the atomic sphere using Eq. (16.4) and in the empty sphere as the LDA exchange-correlation potential. We do so because in the empty sphere the density of electrons is rather small and close to being homogeneous. Thus, the LDA can be expected to be a good approximation

in the ES. Furthermore, because the density is small, correlation effects would be relatively large and must be included in the potential. The HS potential inside the AS is calculated by fixing its value at the AS/ES boundary to be $-1/r$ atomic units. We present the results of our calculations in Table 16.1.

Also presented there are results obtained by employing other potentials along with the experimental values for the bandgaps of these materials.

It is clear from Table 16.1 that our predictions for BGs calculated using the HS-EX are far superior to the results of the LDA calculations and are in excellent agreement with experimental values for a majority of the systems studied. This, along with the results of the OEP/EXX, demonstrates that treating the potential accurately indeed may give accurate values of bandgaps and also that the bandgap problem may also be looked at as an excited-state problem.

We sum up this section by noting that improvement in the accuracy of the potential, calculated either via the OEP or via the HS method, gives accurate results for bandgaps. However, both these methods are based on obtaining the potential using orbitals. The question is whether the conclusion drawn will still remain valid if the potential were calculated using density alone. We now show that this is indeed the case by performing our calculations employing the van Leeuwen-Baerends (vLB) potential that is written entirely in terms of the density and its derivative.

16.5 Density-based calculations using the vLB potential

Because the LDA potential for finite systems does not have the correct asymptotic behavior, that is, it does not go as $-1/r$ far away from the system, vLB proposed (van Leeuwen and Baerends, 1994) that a correction term be added to it that makes it go as $-1/r$ in regions far from a system and improves (van Leeuwen and Baerends, 1994; Banerjee and Harbola, 1999) the eigenvalues for the highest occupied orbitals of atoms significantly. We therefore anticipate that with this correction, the resulting potential—referred to as the vLB potential—should also lead to accurate bandgaps in all systems.

The vLB potential is given as

$$v_{xc,\sigma}^{\mathrm{vLB}}(\mathbf{r}) = \left[v_{x,\sigma}^{\mathrm{LDA}}(\mathbf{r}) + v_{x,\sigma}^{\mathrm{LB}}(\mathbf{r})\right] + v_{c,\sigma}^{\mathrm{LDA}}(\mathbf{r}) \tag{16.7}$$

where $v_{x}^{\mathrm{LDA}}(\mathbf{r})$ is the standard LDA exchange potential while $v_{c,\sigma}^{\mathrm{LDA}}(\mathbf{r})$ is the usual LDA correlation. Here $v_{x,\sigma}^{\mathrm{LB}}(\mathbf{r})$ is

$$v_{x,\sigma}^{\mathrm{LB}}(\mathbf{r}) = -\beta\rho_{\sigma}^{1/3}\frac{x_{\sigma}^{2}}{1+3\beta x_{\sigma}\sinh^{-1}(x_{\sigma})} \tag{16.8}$$

with $\beta = 0.05$ and $x = |\nabla\rho(\mathbf{r})|/\rho^{4/3}(\mathbf{r})$.

The correction vLB in Eq. (16.8) is motivated by the Becke formula (Becke, 1988a) for exchange energy and therefore leads to correct $-1/r$ behavior of the vLB

Table 16.1 Band-gaps of several materials obtained using different theories and their comparison with experimental numbers

BGs								
	BG (eV)							
System	LDA	HS-EX	vLB	GW	QPC	MBJLDA	EXX	Expt.
Ne (A1)	11.39	22.07	23.64	22.1	16.55	22.72	–	20.75
Ar (A1)	8.09	11.29	12.76	14.9	11.95	13.91	–	14.32
Kr (A1)	6.76	9.10	10.91	–	9.98	10.83	–	11.40
Xe (A1)	5.56	6.63	8.61	–	8.23	8.52	–	9.15
C (A4)	2.70	5.47	5.18	6.18	–	4.93	5.12	5.48
Si (A4)	0.49	1.24	1.21	1.41	–	1.17	1.93	1.17
MgO (B1)	4.94	6.23	6.94	9.16	–	7.17	–	7.78
CaO (B1)	3.36	7.29	7.15	–	–	–	–	7.09
LiF (B1)	8.94	9.52	12.61	15.9	–	12.94	–	13.60
LiCl(B1)	6.06	6.50	7.84	–	–	8.64	–	9.40
AlN (B3)	2.44	5.05	5.13	4.90	–	–	5.03	5.11
AlP (B3)	1.16	2.53	2.75	2.86	–	2.32	–	2.51
BP (B3)	1.51	2.22	2.09	1.90	–	2.28	–	2.00
3C-SiC(B3)	1.38	2.88	2.58	2.76	–	2.52	–	2.42

The comparison of LMTO-LB (vLB) BGs of rare-gas solids with fcc (A1), diamond (A4), rock-salt (B1), and zinc-blende (B3) crystal structure has been made with LMTO-HS-EX (Singh et al., 2013), LMTO-LDA, GW (Fuchs et al., 2007; Shang-Peng and Tong, 2012), quasi-particle corrections (QPC) (Bacalis et al., 1988), MBJLDA (Tran and Blaha, 2009), EXX (Kotani, 1994; Städele et al., 1999), and experimental (Heyd et al., 2005; Magyar et al., 2004; Paier et al., 2006; Faleev et al., 2004; Shishkin et al., 2007; Rohlfing and Louie, 2000; Hufner et al., 1984; Sawatzky and Allen, 1984; Marsman et al., 2008; Rossler, 1970; Rössler, 1975; Madelung and Poerschke, 1992; Cohen and Chelikowsky, 1998; Hybersten and Louie, 1986; Levinshtein et al., 2001; Ambacher, n.d.; Berger, 1990; Stukel, 1970; Hellwege et al., 1982).

potential in the outer regions of a finite systems. The potential has been employed in the past to study (Banerjee and Harbola, 1999) the effect of the correct asymptotic behavior of the potential on response properties of atoms. In the present work, we employ it to obtain the exchange-correlation potential in the AS and use only the LDA potential in the ES to perform self-consistent calculation within TB-LMTO-ASA. The results of the BGs obtained from these calculations are given in Table 16.1. As is evident from the results, the vLB potential of Eq. (16.7) gives BGs that show vast improvement over the LDA results and are in good agreement with experimental values. This shows that an improved exchange-correlation potential, even if it is given entirely in terms of the density, which is particularly accurate in the outer regions of the AS, gives significantly improved results over the LDA. In this connection we further note that modifying the LDA potential by the Becke-Johnson potential (Becke, 1988b) also leads to substantially improved BGs for a variety of solids (Becke and Johnson, 2006). For completeness, these results are also shown in Table 16.1. Having established in the above that calculating the potential accurately gives good bandgaps for bulk systems, we are now ready to employ these potentials for nanomaterials. We choose to use the vLB potential for this purpose because it is easier to implement and gives results similar to the orbital-based methods of OEP/EXX or the HS.

16.6 Application to clusters of graphene and hexagonal boron nitride

In this section, we apply TB-LMTO-LB with the vLB potential to the two-dimensional finite clusters of hexagonal boron nitride (h-BN) and graphene to study variation in bandgaps with increasing cluster size. As is well known, pure graphene has no band gap (Jiang, 2013), while h-BN shows bandgap that varies from 3.6 to 7.1 eV (CastroNeto et al., 2009; Fomichev, 1971; Khusidman, 1972; Baronian, 1972). To model our system, we considered cells of orthorhombic symmetry with physical parameters $a = 40$ Å, $b = 25$ °ÅÅ, and $c = 40$ Å. We have modeled h-BN (Carpenter and Kirby, 1982) and graphene (Solozhenko et al., 1995) clusters of different sizes using experimental structure. In our calculations, we considered h-BN and graphene clusters with one, three, and seven ring sizes. The graphene cluster with one, three, and seven ring sizes has 6, 13, and 24 carbon atoms in the basis set arranged on a regular hexagonal lattice. The h-BN with 1 ring has 3 boron and 3 nitrogen atoms; with 3 rings, it has 6 boron and seven nitrogen atoms; and with 7 rings, it has 12 boron and 12 nitrogen atoms in the basis set. In the h-BN, the boron and the nitrogen are arranged on a regular hexagonal lattice. Here, we are dealing with finite-size systems, so BG is calculated as the difference of lowest unoccupied orbital (LUMO) and highest occupied orbital (HOMO). The BG in all three cases increases with increasing system size. However, we have shown here that the HOMO-LUMO gap changes substantially with

an increase in the size of the clusters with the vLB-potential in compared with the LDA. The results have been quoted in Table 16.2. In Figure 16.1, we also show the density of states, which indicate the position of the occupied and virtual levels, for the three different sizes of h-BN and graphene clusters considered. The zero in the DOS is defined to be the Fermi energy.

Table 16.2 The BGs of quantum dots of hexagonal-boron nitride and graphene with one, three, and seven rings within TB-LMTO-LB and TB-LMTO-LDA

System size	BG (eV)			
	BN (vLB)	BN (LDA)	C (vLB)	C (LDA)
1	2.00	0.50	2.90	1.50
3	3.00	1.90	3.46	1.85
7	5.70	2.40	5.20	2.50

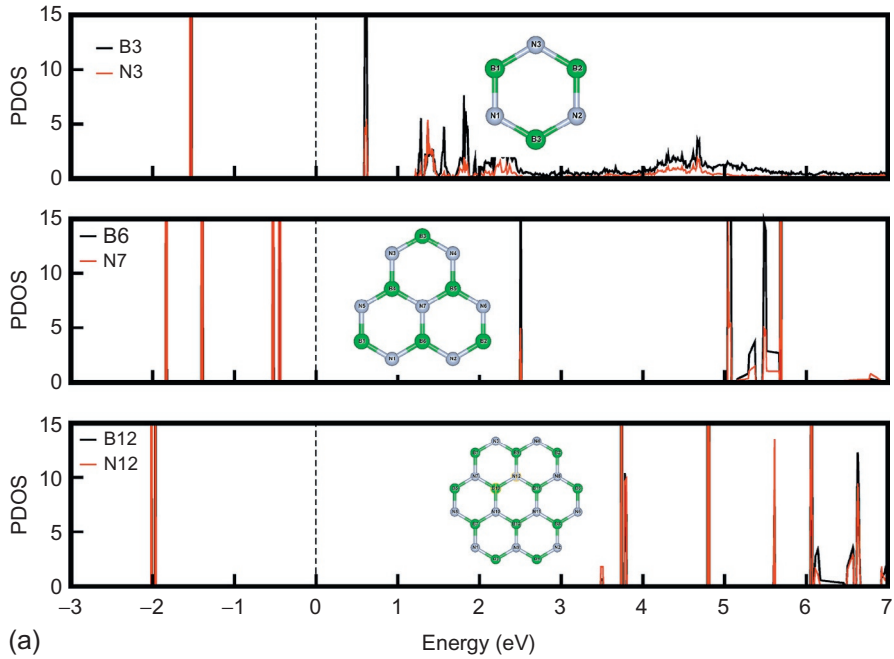

Figure 16.1 (a) and (b) Density of states of boron nitride and graphene rings of varying sizes. *(Continued)*

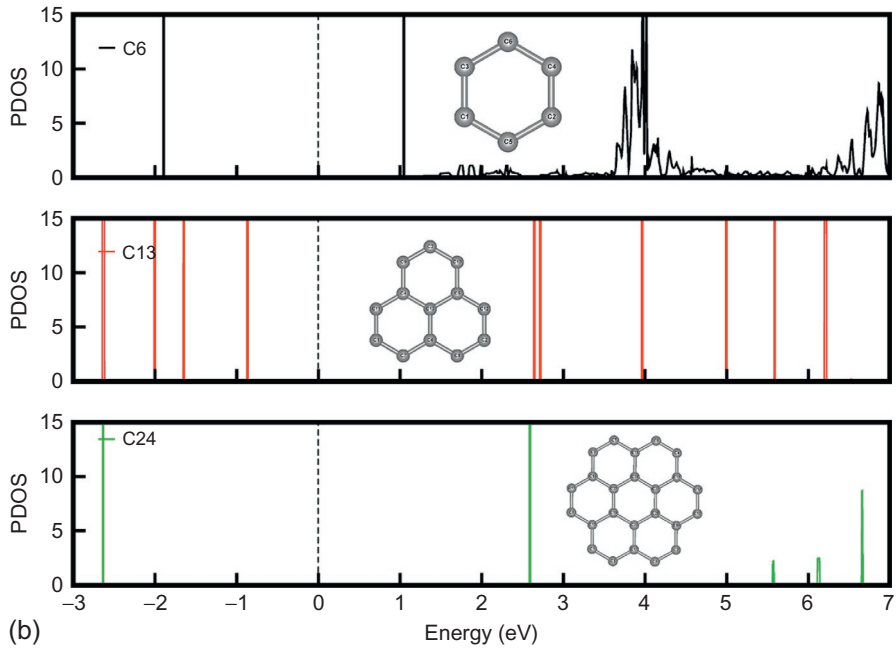

Figure 16.1 Continued.

16.7 Discussion and concluding remarks

In this chapter, we have put forth a different perspective on the bandgap problem and emphasized that it be studied as a problem of calculating excitation energies. Then the accuracy of bandgap determination depends crucially on the correct treatment of exchange-correlation potential in the asymptotic region (outer regions of the atomic sphere). Keeping this in mind, we have used the HS and the vLB potentials and developed them within the TB-LMTO-ASA. We have tested this method for calculating the bandgap behavior of a range of semiconducting materials with different crystal structures. Not only are the calculated bandgaps of several bulk semiconductors in very good agreement with experiments, but the methods employed are computationally less expensive with the possibility of easy implementation in more accurate full potential methods. Finally, we have applied the vLB-based method to calculate bandgap in finite-sized clusters of graphene and hexagonal-boron nitride. We have shown that an easy-to-implement density based potential, which is also asymptotically correct, gives good HOMO-LUMO gaps for small clusters that are larger than the LDA.

References

Ambacher, O., (private communication).
Andersen, O.K., Jepsen, O., 1984. Phys. Rev. Lett. 53, 2571.
Bacalis, N.C., Papaconstantopoulos, D.A., Pickett, W.E., 1988. Phys. Rev. B 38, 6218.
Banerjee, A., Harbola, M.K., 1999. Phys. Rev. A 60, 3599.
Baronian, W., 1972. Mater. Res. Bull. 7, 119.
Becke, A.D., 1988. Phys. Rev. A 38, 3098.
Becke, A., Johnson, E.R., 2006. J. Chem. Phys. 124, 221101.
Berger, L.I., 1990. Semiconductor Materials. CRC Press, New York.
Carpenter, L.G., Kirby, P.Y., 1982. J. Phys. D 15, 1143.
CastroNeto, A.H., Guinea, F., Peres, N.M.R., Novoselov, K.S., Geim, A.K., 2009. Rev. Mod. Phys. 81, 109.
Cohen, M.L., Chelikowsky, J.R., 1998. Electric Structure and Optical Properties of Semiconductors. Springer, New York.
Faleev, S.V., van Schilfgaarde, M., Kotani, T., 2004. Phys. Rev. Lett. 93, 126406.
Fomichev, V.A., 1971. Fizika Tverdogo Tela (Sov. J. Solid State Phys.) 13, 907.
Fuchs, F., Furthmüller, J., Bechstedt, F., Shishkin, M., Kresse, G., 2007. Phys. Rev. B 76, 115109.
Godby, R.W., Schlüter, M., Sham, L.J., 1986. Phys. Rev. Lett. 56, 2415.
Gonze, X., Ghosez, P., Godby, R.W., 1995. Phys. Rev. Lett. 74, 4035.
Harbola, M.K., Sahni, V., 1989. Phys. Rev. Lett. 62, 489.
Harbola, M.K., Sahni, V., 1990. Phys. Rev. Lett. 65, 277.
Hellwege, K.H., et al., 1982. Numerical Data and Functional Relationships in Science and Technology. In: New Series, GroupIII, vol. 17. Springer-Verlag, New York.
Heyd, J., Peralta, J.E., Scuseria, G.E., Martin, R.L., 2005. J. Chem. Phys. 123, 174101.
Holas, A., March, N.H., 1997. Phys. Rev. A 56, 3597.
Hufner, S., Osterwalder, J., Riesterer, T., Hulliger, F., 1984. Solid State Commun. 52, 793.
Hybersten, M.S., Louie, S.G., 1986. Phys. Rev. B 34, 5390.
Jepsen, O., Andersen, O.K., 2000. The Stuttgart TB-LMTO-ASA Program, version 4.7. Max-Planck-Institut für Festkörperforschung, Stuttgart, Germany.
Jiang, H., 2013. J. Chem. Phys. 138, 134115.
Jones, R.O., Gunnarsson, O., 1989. Rev. Mod. Phys. 61, 689.
Khusidman, M.B., 1972. Fizika Tverdogo Tela (Sov. J. Solid State Phys.) 14, 3287.
Knorr, W., Godby, R.W., 1992. Phys. Rev. Lett. 68, 639.
Kotani, T., 1994. Phys. Rev. B 50, 14816.
Kotani, T., 1995. Phys. Rev. Lett. 74, 2989.
Krieger, J.B., Li, Y., Iafrate, G.J., 1992. Phys. Rev. A 46, 5453.
Kümmel, S., Kronik, L., 2008. Rev. Mod. Phys. 80, 3.
Levinshtein, M.E., Rumyantsev, S.L., Shur, M.S., 2001. Properties of Advanced Semiconductor Materials. Wiley, New York.
Levy, M., Perdew, J.P., 1985. Phys. Rev. A 32, 2010.
Levy, M., Perdew, J.P., Sahni, V., 1984. Phys. Rev. A 30, 2745.
Madelung, O., Poerschke, R. (Eds.), 1992. Semiconductor: Other than Group IV Elements and III-V Compounds. Springer, Berlin.
Magyar, R.J., Fleszar, A., Gross, E.K.U., 2004. Phys. Rev. B 69, 045111.
Marsman, M., Paier, J., Stroppa, A., Kresse, G., 2008. J. Phys. Condens. Matter 20, 064201.
Mott, N.F., 1974. Metal-Insulator Transitions. Taylor and Francis, London, p. 237.

Mott, N.F., Friedman, L., 1974. Philos. Mag. 30, 389.
Paier, J., Marsman, M., Hummer, K., Kresse, G., Gerber, I.C., Ańgyán, J.G., 2006. J. Chem. Phys. 124, 154709, **125**, 249901 (2006).
Perdew, J.P., 1986. Phys. Rev. B 34, 7406.
Perdew, J.P., Levy, M., 1983. Phys. Rev. Lett. 20, 1884.
Perdew, J.P., Parr, R.G., Levy, M., Balduz, J.L., 1982. Phys. Rev. Lett. 42, 1691.
Perdew, J.P., Burke, K., Ernzerhof, M., 1996. Phys. Rev. Lett. 77, 3865.
Rasolt, M., Geldart, D.J.W., 1990. Phys. Rev. Lett. 65, 276.
Rohlfing, M., Louie, S.G., 2000. Phys. Rev. B 62, 4927.
Rossler, U., 1970. Physica Status Solidi B 42, 345.
Rössler, U., 1975. In: Klein, M.L., Venables, J.A. (Eds.), Rare-Gas Solids. Academic Press, New York, p. 545.
Sahni, V., 1997. Phys. Rev. A 55, 1846.
Sahni, V., 2004. Quantal Density Functional Theory. Springer, Berlin.
Savin, A., Umrigar, C.J., Gonze, X., 1998. Chem. Phys. Lett. 288, 391.
Sawatzky, G.A., Allen, J.W., 1984. Phys. Rev. Lett. 53, 2339.
Sen, K.D., Harbola, M.K., 1991. Chem. Phys. Lett. 178, 347.
Sham, L.J., Schlüter, M., 1983. Phys. Rev. Lett. 51, 1888.
Shang-Peng, G., Tong, Z., 2012. Acta Phys. Sin. 61 (13), 137104.
Sharma, S., Dewhurst, J.K., Ambrosch-Draxl, C., 2005. Phys. Rev. Lett. 95, 136402.
Sharp, R.T., Horton, G.K., 1953. Phys. Rev. 90, 317.
Shishkin, M., Marsman, M., Kresse, G., 2007. Phys. Rev. Lett. 99, 246403.
Singh, P., Harbola, M.K., Sanyal, B., Mookerjee, A., 2013. Phys. Rev. B 87, 235110.
Skriver, H.L., 1984. The LMTO Method: Muffin-Tin Orbitals and Electronic Structure. Springer-Verlag, New York.
Slamet, M., Sahni, V., Harbola, M.K., 1994. Phys. Rev. A 49, 809.
Slater, J.C., 1951. Phys. Rev. 81, 385.
Solozhenko, V.L., Will, G., Elf, F., 1995. Solid State Commun. 96, 1.
Städele, M., Moukara, M., Majewski, J.A., Vogl, P., Görling, A., 1999. Phys. Rev. B 59, 10031.
Stukel, D.J., 1970. Phys. Rev. B 1, 12.
Talman, J.D., Shadwick, W.F., 1976. Phys. Rev. A 14, 36.
Tran, F., Blaha, P., 2009. Phys. Rev. Lett. 102, 226401.
van Leeuwen, R., Baerends, E.J., 1994. Phys. Rev. A 49, 2421.
Von Barth, U., Hedin, L., 1972. J. Phys. C 5, 1629.
Wang, Y., Perdew, J.P., Chevary, J.A., Macdonald, L.D., Vosko, S.H., 1990. Phys. Rev. A 41, 78.

Modeling and simulation of nanomaterials in fluids: nanoparticle self-assembly

17

D.M. Bortz
University of Colorado, Boulder, CO, USA

17.1 Introduction

A nanofluid consists of a colloidal suspension of nanometer-scale particles dispersed in a liquid. In their well-known report from 1997, Lee and Choi describe an impressive threefold improvement in heat transfer performance for a nanofluid over water (Lee and Choi, 1997). This anomalous property of thermal conductivity has the potential to lead to a commercial market of over $2 billion dollars per year (Saidur et al., 2011b). Accordingly, over the last 17 years, substantial research has been devoted to the study of nanoparticles in fluids, and as of January 1, 2014, Web of Science reports 5694 publications on the "nanofluids" topic.

Nanoparticle self-assembly arises when nanoscale subcomponents spontaneously assemble themselves to form larger units. This is intrinsically dependent on how the underlying forces drive population-level effects such as aggregation and fragmentation. In this chapter, we review population balance equation (PBE) modeling and simulation in fluids from a mathematical and computational perspective. Specific analytical results and discretization techniques are discussed. We also provide an introduction to statistical model selection that has recently proven useful to researchers in identifying appropriate nanofluid viscosity models (Nwosu et al., 2014). Section 17.2 provides a brief discussion of likely future trends, and Section 17.3 directs the interested reader to sources of further information and insight. Section 17.4 provides the mathematical reader with an overview of some of the available experimental techniques and protocols. Section 17.5 focuses on the mathematics for PBE-based models of nanoparticle self-assembly, while Section 17.6 presents several computational schemes for accurately simulating such equations. Section 17.7 discusses some recent statistical results and provides an introduction to model selection criteria (MSC) (to help promote its wider use in the nanofluids community). Last, Section 17.8 concludes with a brief summary of this chapter.

Modeling, Characterization and Production of Nanomaterials. http://dx.doi.org/10.1016/B978-1-78242-228-0.00017-X
Copyright © 2015 Elsevier Ltd. All rights reserved.

17.2 Experimental techniques

In this section, we present a brief survey of some experimental techniques used for studying nanofluids. The goal of this section is to communicate to the more theoretical reader what empirical methodologies are available from laboratory researchers.[1]

Bilati et al. (2005) provide a good overview of nanoprecipitation techniques (in addition to proposing an improved protocol). Sau and Murphy (2005) describe how to create gold nanocrystals of varying structures (rods, cubes, hexagons) and how using the cationic surfactant (and antiseptic) cetyltrimethylammonium bromide helps to stabilize the resulting particle sizes when used as a medium for self-assembly. Srinivasachari et al. (2006) present novel glycopolymers that inhibit aggregation and can be used to help stabilize colloidal nanoparticle systems and prevent serum aggregation. They used dynamic light scattering (DLS) to show that their polyplexes have a low degree of flocculation.

An important subfield of nanoparticles involves nanoclusters created via DNA encoding. We direct the interested reader to Maye et al. (2009), who discuss a method for high-yield self-assembly of particles using DNA encoding, and Prabhu and Hudson (2009), who place this work in the context of that subfield.

Murphy et al. (2010) developed an interesting experimental methodology for directly studying nanoparticle aggregation. DLS was used to measure the initial kinetics of aggregation of carboxylated polystyrene nanoparticles. Subsequent UV light exposure excited an aqueous photoacid generator, which altered the pH and in turn led to aggregation. This experimental apparatus allows the study of how specified jumps in pH impact diffusion- and reaction-limited nanoparticle aggregation.

Last, Mudanyali et al. (2013) developed a high-throughput, on-chip detection scheme that uses biocompatible wetting films to self-assemble aspheric liquid nanolenses around individual nanoparticles to enhance the contrast between the scattered and the background light. In essence, they created a lipid that binds to and covers the surface of a nanoparticle so as to make it visible using light microscopy.

The above techniques are, of course, not comprehensive but should give the mathematical reader an idea about the types of data to be expected when working with an experimental collaborator.

17.3 Modeling and analysis

As has become clear since Lee and Choi's original paper, aggregation phenomena play a central role in explaining the anomalous thermal properties. Eastman et al. (2001) reported improved thermal conductivity k for an ethylene glycol-based nanofluid with aggregated copper nanoparticles[2] while Shima et al. (2009) also reported an

[1]Naturally, readers with more knowledge of the science of nanoparticle self-assembly can safely skip this section.

[2]Note that aggregation is not explicitly discussed in this article, but electron micrographs of the fluid clearly depict aggregated particles.

improved k with larger aggregates.[3] Prasher et al. (2006) propose and partially validate a unified model to explain how the thermal conductivity k is influenced by nanoparticle Brownian motion-based aggregation, temperature, pH, and thermal transport. Further, Wu et al. (2010) provide strong (experimental and theoretical) evidence that (for an SiO_2-based nanofluid) nanocluster structure and size distribution have a huge impact on k. These articles and many others have influenced many nanofluid researchers to turn to the study of flocculation models.

17.3.1 Flocculation modeling overview

Flocculation phenomena occur in a wide range of fields including aerosols (Drake, 1972), meteorology (Pruppacher and Klett, 1980), surfactants (Stechemesser and Dobiáš, 2005), algal dynamics (Ackleh and Fitzpatrick, 1997; Riebesell and Wolf-Gladrow, 1992), immunology (Pawar et al., 2004), mud (Mietta et al., 2011), planetesimal evolution (Makino et al., 1998), and of course, nanoparticle self-assembly (Tohver et al., 2001; Bilati et al., 2005; Schwarzer and Peukert, 2005; Sefcik et al., 2006; Prasher et al., 2006; Grzelczak et al., 2010; Rao, 2010). The seminal ideas were originally developed in the early 1900s by van Smoluchowski (1916, 1917) to model the rapid aggregation of colloids.

By considering a static dispersing medium, and assuming that all interactions were binary and driven by Brownian motion, Smoluchowski proposed the equation

$$\frac{\mathrm{d}c_r}{\mathrm{d}t} = \frac{1}{2}\sum_{s=1}^{r-1} a_{s,r}c_s c_{r-s} - \sum_{s=1}^{\infty} a_{r,s}c_r c_s \tag{17.1}$$

where r is the number of particles, c_r is the number of clusters containing r particles, and $a_{r,s}$ is the rate of aggregation. Individual units irreversibly aggregate

$$C_r + C_s \rightarrow C_{r+s} \tag{17.2}$$

and the equation for $r = 1$ is understood to be

$$\frac{\mathrm{d}c_1}{\mathrm{d}t} = -\sum_{s=1}^{\infty} a_{1,s}c_1 c_s \tag{17.3}$$

Smoluchowski analytically solved this infinite cascade of ODEs. Later work by Müller (1928) (and others) extended the original discrete equation to the continuum partial differential equation (PDE)

$$\frac{\partial}{\partial t}p(t,x) = \frac{1}{2}\int_0^x K_{\mathrm{A}}(y, x-y)p(t,y)p(t,x-y)\mathrm{d}y - p(t,x)\int_0^{\infty} K_{\mathrm{A}}(x,y)p(t,y)\mathrm{d}y \tag{17.4}$$

[3] They also provide solid evidence that microconvection is not responsible for the observed changes in k.

where p is a continuous floc size density function and $K_A(x_1, x_2)$ is a kernel describing the rate with which particles of size x_1 aggregate with particles of size x_2.

In the case that particles do not bind irreversibly, the model can be adapted to include fragmentation

$$\frac{\partial}{\partial t}p = A_{\text{in}}(x,p) - A_{\text{out}}(x,p) + F_{\text{in}}(x,p) - F_{\text{out}}(x,p)$$

The functions A_{in} and A_{out} model aggregation and F_{in} and F_{out} model fragmentation and the terms are defined as

$$A_{\text{in}}(x,p) = \frac{1}{2}\int_{\underline{x}}^{x-\underline{x}} K_A(y, x-y)p(t,y)p(t,x-y)\mathrm{d}y; \quad F_{\text{in}}(x,p) = \int_{x}^{\overline{x}} \Gamma(x;y)K_F(y)(t,y)\mathrm{d}y$$

$$A_{\text{out}}(x,p) = p(t,x)\int_{\underline{x}}^{\overline{x}-x} K_A(x,y)p(t,y)\mathrm{d}y; \qquad F_{\text{out}}(x,p) = \frac{1}{2}K_F(x)p(t,x) \tag{17.5}$$

The function K_A is the aggregation kernel defined above. Analogously, K_F is the fragmentation kernel, describing the rate with which a floc of size x fragments. We also denote $\Gamma(x; y)$ as a conditional probability density depicting the postfragmentation floc sizes.[4]

The mathematical forms of K_A and K_F are clearly dictated by the fluid flow regime and the forms corresponding to laminar and turbulent flow have been well studied for many years (Drake, 1972; Pruppacher and Klett, 1980; Saffman and Turner, 1956; Somasundaran et al., 2005). For example, the aggregation kernel for Hagen-Poiseuille flow is commonly written as $K_A(x, y) = \kappa_A(x^{1/3} + y^{1/3})^3$ for $\kappa_A = \gamma_A\gamma_G$ where γ_G is the shear rate and γ_A is the adhesive efficiency (a parameter to be fit) (Saffman and Turner, 1956; Somasundaran et al., 2005). In a turbulently mixing flow, κ_A depends on the energy dissipation per unit mass and the kinematic viscosity (see Flesch et al., 1999; Spicer and Pratsinis, 1996). More recently, several researchers have even rigorously derived fragmentation kernels accounting for both the floc fractal dimension as well as the multifractal spectrum of the dissipation length scale in turbulent mixing (Bäbler, 2008; Bäbler et al., 2010; Meneveau and Sreenivasan, 2006).

For a system where aggregation dominates and is irreversible, there is no (nonzero) equilibrium solution. Accordingly, much work has been devoted to understanding classes of transient solutions such as the so-called "self-similar" solutions in which scaling the independent variables yields a scaled version of the solution.[5] For example, a common scaling of (2) is reviewed in Wattis (2006)

[4]We note that (as mentioned elsewhere), the engineering literature designates this type of modeling a PBE.

[5]In many cases, cleverly chosen scaling can transform a PDE to an ODE, which are typically easier to analyze (numerically and analytically). See Barenblatt (1996, 2003) for more insight into scaling and self-similarity.

$$c_r(t) = k(t)g(\eta); \quad \text{where} \quad \eta = \eta(r,t) = \frac{r}{h(t)}$$

for some h. In particular, a very active area of mathematics research involves assuming that the aggregation kernel is self-similar, for example, $a_{r,s} = r^{\lambda} a(r/s)$ for some function $a(\cdot)$, and then proving that this kernel yields a solution that itself is self-similar. We draw attention to the review by Menon and Pego (2006) that thoroughly summarizes several known kernels yielding self-similar solutions. Dubovskii (1994) provides a more mathematical survey of equation properties while Ramkrishna (2000) presents a broader engineering-focused perspective.

Another important property of the solutions to Eq. (17.4) is called "gelation." For example, multiplicative kernels, for example, $K(x, y) \propto xy$, yield solutions that "gel" after a finite time. This means that the solution to the governing PDE does not conserve mass. One could interpret this analysis to suggest that a particle of "infinite" size has been created. A more pragmatic interpretation would suggest that the particle has grown so large that different physical phenomena dominate (e.g., settling via gravity) and thus the governing PDE is no longer valid. We direct the interested reader to Wattis (2006), who provides a nice overview of the gelation properties for the class of kernels $K(x, y) \propto (x^{\mu} y^{\eta} + x^{\eta} y^{\mu})$ for $\mu, \eta > 0$.

17.3.2 Modeling nanofluids with PBEs and particle size distributions

With the above introduction, we can now survey several influential nanofluid research efforts for which PBEs and particle size distributions (PSDs) form the crucial tool for providing insight.

Schwarzer and Peukert (2005) were some of the first to fully incorporate PSD-models into their study of nanoparticles. They used a PBE-based PSD model to control the stability ratio W for the barium sulfate flocs. The article by Sefcik et al. (2006) from Morbidelli's group was among the first to use both mathematical modeling and control theory to address the stability question in nanoparticle aggregation and gelation. It is important to note, however, that this publication is primarily theoretical and includes only qualitative comparisons and theoretical predictions. Also, as mentioned above, Prasher et al. (2006) proposed a unified model to explain how the thermal conductivity k is influenced by nanoparticle Brownian motion-based aggregation, temperature, pH, and thermal transport. They also partially validate their model via a combination of quantitative comparisons with alumina nanofluids and qualitative predictions when parameters are unknown.

17.3.3 Mathematical analysis

As PBE/PSD mathematical modeling has become more widespread, so has theoretical analysis of the equations. In this section, we survey a few important articles, some of which have mathematical results that could be applied to areas far outside self-assembly in nanofluids.

Building on the work mentioned above, Hawa and Zachariah (2006) extended PBE nanoparticle modeling by considering the coalescence of unequal size nanoparticles. By analyzing the equations, they discovered that the Koch-Friedlander predictions for coalescence time (Koch and Friedlander, 1990) match with molecular dynamics simulations for silicon nanoparticles.

Some of the most mathematical analyses were presented in Fournier and Laurençot (2006) and Fernández-Díaz and Gómez-García (2007). In particular, Fournier and Laurençot (2006) present one of the most thorough recent mathematical investigations of the coagulation-fragmentation PBE. They prove the existence and uniqueness of solutions for wide classes of aggregation and fragmentation kernels as well as initial conditions. While not as theoretical, Fernández-Díaz and Gómez-García (2007) do provide the analytical solution to the aggregation PBE with an additive kernel for multispecies systems.

More recently, Darabi Sahneh et al. (2013) consider a discrete PBE to study the dynamics of nanoparticle corona complex formation from PBEs. They extend a basic ODE model given in Dell'Orco et al. (2010) and derive an approximate formula for metastable and stable compositions of corona complex.

17.4 Simulation methods

There has been substantial work in the numerical simulations of flocculation, because no analytical solutions have been discovered for many realistic aggregation and fragmentation kernels. In this section, we will discuss several popular numerical discretization schemes. We also note that these discretization schemes are for models describing monospecies phenomena. Below we focus on the core numerical ideas and thus only present methods for monospecies distributions, although methods for multispecies do exist.

17.4.1 Finite element method

The core of a finite element method (FEM) approach lies in constructing an approximate numerical solution p^N via a sum of the projections of the analytical solution onto prespecified basis functions. The general idea is that there is a function space for the solutions to the PDE, for example, H, and then the basis functions span the approximate solutions space H^N with N basis functions. As N increases, the approximation p^N should converge to the solution p. The simplest set of basis functions would be the step function

$$\beta_i(x) = \left\{ \begin{array}{ll} 1; & x_{i-1}^N \le x < x_i^N \\ 0; & \text{otherwise} \end{array} \right\}; \quad i = 1, \ldots, N$$

for positive integer N and $\{x_i^N\}_{i=0}^N$ a partition of $\left[\underline{x}, \overline{x}\right]$ with largest mesh size $\triangle x$ and $\triangle x_j = x_j - x_j$. The functions form an orthogonal basis for

$$H^N = \left\{ h \in H : h = \sum_{i=1}^{N} \alpha_i \beta_i^N, \alpha_i \in R \right\}$$

and accordingly, we can define the projections π^N: $H \to H^N$

$$\pi^N h = \sum_{j=1}^{N} \alpha_j \beta_j^N; \text{ where } \alpha_j = \frac{1}{\Delta x_j} \int_{x_{j-1}^N}^{x_j^N} h(x) \mathrm{d}x$$

which is an orthogonal projection of H onto H^N. When considering both aggregation and fragmentation, this yields the following system of N ODEs

$$\frac{\mathrm{d}}{\mathrm{d}t} p^N = \pi^N (A_{\text{in}}(p^N) - A_{\text{out}}(p^N) + F_{\text{in}}(p^N) - F_{\text{out}}(p^N))$$

$$p^N(0, x) = \pi^N p_0(x)$$

Regarding the actual implementation, the application of π^N to $A_{\text{in}}(p^N) - A_{\text{out}}(p^N)$ yields

$$\left[\pi^N \left(A_{\text{in}}\left(p^N\right) - A_{\text{out}}\left(p^N\right)\right)\right] = \begin{bmatrix} -\alpha_1 \sum_{j=1}^{N-1} K_A\left(x_1; x_j\right) \alpha_j \Delta x_j \\ \frac{1}{2} K_{\text{A}}(x_1, x_1) \alpha_1 \alpha_1 \Delta x_1 - \alpha_2 \sum_{j=1}^{N-2} K_{\text{A}}\left(x_2, x_j\right) \alpha_j \Delta x_j \\ \vdots \\ \frac{1}{2} \sum_{j=1}^{N-2} K_{\text{A}}\left(x_j, x_{N-1-j}\right) \alpha_j \alpha_{N-1-j} \Delta x_j - \alpha_{N-1} K_{\text{A}}(x_{N-1}, x_1) \alpha_1 \Delta x_1 \\ \frac{1}{2} \sum_{j=1}^{N-1} K_{\text{A}}\left(x_j, x_{N-j}\right) \alpha_j \alpha_{N-j} \Delta x_j \end{bmatrix}$$

and to $(F\text{in}(pN) - F\text{out}(pN))$ is

$$\left[\pi^N \left(F_{\text{in}}\left(p^N\right) - F_{\text{out}}\left(p^N\right)\right)\right] = \begin{bmatrix} \sum_{j=2}^{N} \Gamma\left(x_1; x_j\right) K_{\text{F}}\left(x_j\right) \alpha_j \Delta x_j \\ \sum_{j=3}^{N} \Gamma\left(x_2; x_j\right) K_{\text{F}}\left(x_j\right) \alpha_j \Delta x_j - \frac{1}{2} K_{\text{F}}(x_2) \alpha_2 \Delta x_2 \\ \vdots \\ \Gamma(x_{N-1}; x_N) K_{\text{F}}(x_N) \alpha_N \Delta x_N - \frac{1}{2} K_{\text{F}}(x_{N-1}) \alpha_{N-1} \Delta x_{N-1} \\ -\frac{1}{2} K_{\text{F}}(x_N) \alpha_N \Delta x_N \end{bmatrix}$$

This N-dimensional system can then be solved using standard ODE-solvers in Matlab, R, numpy, or other software.

In general, the FEM is the simplest discretization strategy and illustrations using this approach are presented in Ackleh and Fitzpatrick (1997), Bortz et al. (2008), and Keck (2014). Conventionally, the spatial order of accuracy of these methods is understood to be $k+1$, where k is the order of the basis functions. For example, the zeroth order functions used above were understood to yield a first-order method. However, the superconvergence results in the discontinuous Galerkin literature (Cheng and Shu, 2008, 2010) suggest that the convergence is of order $k+2$ for $k>0$, and recent numerical results suggest that this $k+2$ convergence is true for $k=0$ as well (Keck, 2014).

Last, we also note that the *h-p* Galerkin methods (related to FEMs) are also popular (Schwarzer and Peukert, 2005), partially due to their use in the commercially available flocculation software Parseval (Wulkow et al., 2001).

17.4.2 Flux method

An alternative method is one based on a "finite volume" approach (Eymard et al., 2000), which creates an approximate solution by estimating the flux in and out of subdomains of the size axis. A good illustration of this flux method applied to the pure aggregation case in Eq. (17.4) is described in Filbet and Laurençot (2004).[6] It does offer a higher order of convergence (in size), but typically at the cost of more floating point operations.

By defining the flux $J(t, x)$ as the mass flux passing by position x at time t, Eq. (17.4) can be recast as

$$x\partial_t p = -\partial_x J[p], \quad (t,x) \in \mathrm{R}^2_+ \tag{17.6}$$

where

$$J[p](t,x) = \int_0^x \int_{x-u}^{\infty} uK_{\mathrm{A}}(u,v)p(t,u)p(t,v)\mathrm{d}v\mathrm{d}u \tag{17.7}$$

Naturally, the improper integral must be approximated and Filbet and Laurençot (2004) describe several options (both conservative and nonconservative) and recommend a nonconservative truncation of the limit because of the improved accuracy for gelating solutions (Bak and Heilmann, 1991; da Costa, 1998; Filbet and Laurençot, 2004).

The mean value of the volume density[7] in subdomain $[x_i, x_{i+1})$ is denoted as q_i with approximation q_i^N and discretized mass flux, which we denote as $J_i^N(t_j)$. At the midpoint of each subdomain (denoted $x_{\mathrm{mid}(i)}$), there is an ODE.

$$\frac{\mathrm{d}}{\mathrm{d}t}q_i^N = \frac{J_{i+1}^N(t) - J_i^N(t)}{\Delta x}$$

[6]One can easily add fragmentation by adjusting Eq.(17.7) to include fragmentation.

[7]Note how this contrasts with p, which was defined as the number density.

where

$$J_i^N(t) = \sum_{s=1}^{i-1} \Delta x q_s^N(t) \left\{ \int_{x_{\text{mid}(i-s)}}^{x_{i-s+1}} \frac{K_A\left(x_{\text{mid}(s)}, y\right)}{y} q_{i-s}^N(t) \mathrm{d}y + \sum_{j=1-s+1}^{N-1} \int_{x_j}^{x_{j+1}} \frac{K_A\left(x_{\text{mid}(s)}, y\right)}{y} q_j^N(t) \mathrm{d}y \right\}$$

For simplicity, we assume a uniform discretization of N subdomains. Once in this structure, any standard ODE solver can again be used to obtain second order spatial accuracy in the $L^!$ norm.

17.4.3 Alternative approaches

While the two above approaches are still being actively researched, there are two other classes of methods that have gained popularity in recent years: the method of moments (MOM) and sectional methods (SM).

For the MOM, the original coagulation equation (Eq. 17.4) is multiplied by x^m and then integrated over the whole size domain, resulting in

$$\frac{\mathrm{d}}{\mathrm{d}t} p_m(t) = \frac{1}{2} \int_0^\infty \int_0^\infty \left((x_1 + x_2)^m - x_2^m - x_1^m \right) K_A(x_1, x_2) p(t, x_1) p(t, x_2) \mathrm{d}x_1 \mathrm{d}x_2 \tag{17.8}$$

where

$$p_m(t) = \int_0^\infty x^m p(t, x) \mathrm{d}x \tag{17.9}$$

is the mth moment (see Friedlander (2000) for a more thorough derivation). With this as a foundation, McGraw (1997) proposed the quadrature method of moments (QMOM), which employs Gaussian quadrature to approximate the integrals. The algorithm then alternates between updating p_m at each timestep using Eq. (17.8), followed by solving for p using Eq. (17.9). Frenklach (Frenklach and Harris, 1987; Frenklach, 2002) proposed a different approach, the MOM with interpretive closure (MoMIC), by interpolating among the known whole-order moments to close the fractional-order moments arising due to coagulation and surface growth processes. Both QMOM and MoMIC are popular realization of the MOM idea because they are well suited to connecting with existing computational fluid codes.

For example, Akroyd et al. (2011) developed a model of nanoparticle formation in turbulent reacting flows. They used a projected fields method to approximate the joint composition probability density function (pdf) transport equation that describes the evolution of the nanoparticles. They combined detailed chemistry and a MoMIC-based PDE model in a commercial computational fluid dynamics (CFD) code.

The SM originally proposed by Gelbard and Seinfeld (1980) partitions the size domain, then provide a structured scheme to compute the rates of physical and chemical processes on each subdomain. They do solve for the full distribution, but tend to be more computationally expensive than FEM, flux, and moment methods.

17.5 Statistical inference and model selection

As mentioned in Section 17.2, within the nanofluids literature there has been a recent interest in the development of more sophisticated mathematical and statistical techniques to better assist experimentalists in interpreting data. In this section, we provide a brief survey of nanoparticle velocity estimation and number concentrations. We also provide a review of "model selection," which has proven useful in a recent nanofluids article (Nwosu et al., 2014).

17.5.1 Useful statistical methods

Nanoparticle velocity profiles can be constructed using evanescent wave illumination techniques (Sadr et al., 2004). However, the technique itself is restricted by a limited ability to move the depth of field. By accounting for Brownian motion and the hydrodynamic interaction between the fluid and the wall, Hohenegger and Mucha (2007) were able to correct for the reduced mobility and adapt a maximum likelihood estimator (MLE) to robustly reconstruct the nanoparticle velocity profile.

More recently, Röding et al. (2013) proposed a method for estimating absolute number concentrations of nanoparticles based on a fluctuating time series of particle counts (known as a Smoluchowski process). The method is able to estimate the concentrations without explicit tracking of individual particles and find good estimations with 0.2- and 0.5-μm polymer nanospheres in water.

17.5.2 Nanofluid viscosity and model selection

The viscosity of a nanofluid is intrinsically connected to the overall performance of thermal conductivity as well as the system hydraulics. Accordingly, an accurate viscosity model is essential for the design of robust nanofluidic systems. Nwosu et al. (2014) thoroughly studied the variability between empirical data and model predictions. To address this discrepancy, they developed a selection algorithm as an aid in identifying the viscosity model appropriate for certain nanofluidic compositions and use conditions. They identified seven properties that a nanofluid model should accurately predict: (1) volume fraction/concentration, (2) temperature, (3) packing fraction, (4) thickness of the nanolayer, (5) particle shape/aspect ratio, (6) aggregate radius, (7) interparticle spacing, and (8) the capping layer. They then proposed a selection/sort routine that automatically chooses a viscosity model based on user-defined criteria. This approach is exciting because it offers theoreticians and experimentalists a structured mechanism for selecting accurate (and predictive) viscosity models.

As Nwosu et al. (2014) mention, there is an entire subfield of statistics devoted to model selection. MSC are statistical tools designed to rank a set of candidate models with regard to their ability to parsimoniously describe data. Contemporary criteria are formed from a sum of metrics for goodness-of-fit and statistical complexity, thus while additional model terms/parameters may generate a better fit to data, unnecessarily sophisticated models will be penalized for their complexity.

To further advance this nascent subfield of applying model selection theory to nanofluid models, here we review some of the basic concepts of statistically rigorous model selection. The major distinction between the approach proposed by Nwosu et al. (2014) and conventional MSC is that the device measurement error is fully specified and incorporated into the MSC. Typically, the goodness-of-fit term takes the form of a MLE, while the complexity term can include parameter dimension, variance, or sensitivity (adjoint) information.

The core of several of the criteria rests on a measure of distance between two probability distributions. If p^* is a pdf representing the reality of some phenomenon and p represents the pdf of a given candidate model, one way to quantify the "discrepancy" between p and p^* is by using the Kullback-Leibler (KL) divergence (Kullback and Leibler, 1951)

$$\mathcal{I}(p^*, p) = \varepsilon_{p*}[\ln(p^*/p)] = \int_{\Omega} \ln\left(\frac{p^*(x)}{p(x)}\right) p^*(x)\mathrm{d}x$$

where Ω is the set of all realizable values for x (one or more of the eight properties above). Given a Q-dimensional parametrization $\Theta \in R^Q$ and by assuming that a minimum for $I(p^*, p(\cdot|\Theta))$ exists and then asymptotically expanding I around it, Akaike (1973) computed an expected estimate of $I(p^*, p)$ up to a data-dependent, additive constant. The nonconstant part of this estimate is the Akaike Information Criterion (AIC)

$$-2^{\ell}\left(\widehat{\Theta}|\mathbf{V}\right) + 2Q \tag{17.10}$$

where $\widehat{\Theta}$ is the best-fit MLE and R is the log-likelihood function, conditioned on the given data $\mathbf{V}$. Because the criterion estimates the KL distance up to an additive constant, this allows relative ranking of a set of candidate models, when all are fit to the same set of data. Over the last 40 years, a large number of researchers have extended and expanded Akaike's original work. Later developments and refinements of MSCs include the small sample size AIC (Hurvich and Tsai, 1989)

$$\mathrm{AIC}_C = -2^{\ell}\left(\widehat{\Theta}|\mathbf{V}\right) + 2Q\left(\frac{N}{N-Q-1}\right)$$

and Takeuchi Information Criteria (TIC) (Takeuchi, 1976)

$$\mathrm{TIC} = -2^{\ell}\left(\widehat{\Theta}|\mathbf{V}\right) + 2\mathrm{tr}\left(J\left(\widehat{\Theta}\right)I\left(\widehat{\Theta}\right)^{-1}\right) \tag{17.11}$$

where

$$I\left(\widehat{\Theta}\right) = \varepsilon_{p*}\left[-\frac{\partial^2 \ell\left(\widehat{\Theta}|\cdot\right)}{\partial\Theta\partial\Theta^{\mathrm{T}}}\right],\quad J\left(\widehat{\Theta}\right) = \varepsilon_{p*}\left[\left[\frac{\partial}{\partial\Theta}\ell\left(\widehat{\Theta},\cdot\right)\right]\left[\frac{\partial}{\partial\Theta}\ell\left(\widehat{\Theta},\cdot\right)\right]^{\mathrm{T}}\right]$$

which are the Hessian and outer product forms of the inverse Fisher information matrix, respectively. The TIC is simply one of many ways to incorporate more sophisticated parametric sensitivities into the criteria.

Anderson (2010), Burnham and Anderson (2002), and McQuarrie and Tsai (1998) provide good overviews from the statistical perspective, while the books by Vapnik (2000), Hastie et al. (2001), and Grünwald (2007) are more oriented toward the machine learning and information theory communities. Last, for a full illustration of how to apply MSCs to rank differential equation-based models, we direct the interested reader to Bortz and Nelson (2006).

We note that the above criteria are all frequentist methods, but there are parallel subfields including Bayesian model selection (Dukic et al., 2012; Hoeting et al., 1999; Kass and Raftery, 1995; Schwarz, 1978; Toni et al., 2009), minimum description length-based stochastic complexity (Grünwald et al., 2005; Grünwald, 2007; Rissanen, 1978, 1989, 1996), and others.

17.6 Direct study of nanofluids

The above methods focus on accurate modeling, analysis, simulation, and estimation of PBEs. However, it is important to realize that many other researchers simply treat a nanofluid as a non-Newtonian fluid and employ traditional analytical and CFD approaches. In this section, we provide a brief survey of several fluid-focused approaches, including those that do and do not explicitly include aggregates.

Among those performing direct simulations of nanofluids, Moraveji et al. (2012) illustrate use of a finite volume method, and Rana and Bhargava (2011) describe using a FEM. There are also hybrid analytical/numerical strategies for simulation that include deriving a similarity transform that reduces the fluid PDE to a nonlinear ODE (Hamad and Ferdows, 2012b; Makinde, 2012) as well approaches based on renormalization of Lie groups (Hamad and Ferdows, 2012a).

The magneto-hydrodynamic (MHD) nanofluid literature draws heavily on the traditional MHD community in which both homotopy analysis methods (HAMs) and renormalization groups are very popular. The HAM methods can be employed to provide asymptotic analytical solutions (Ellahi et al., 2012; Ellahi, 2013) as well as facilitate numerical simulations (Hamad et al., 2011). The renormalization group, that is, Lie group, methods can also provide efficient strategies for fluid simulations (Rosmila et al., 2012; Turkyilmazoglu, 2012).

Last, we note that these methods can be used to phenomenologically investigate nanoparticle/nanofluid viscosity and thermal coefficients, but they do not explicitly

include aggregation mechanisms. The Monte Carlo methods (Gharagozloo and Goodson, 2011) and lattice Boltzmann methods (Sheikholeslami et al., 2013) do include aggregates, but we still recommend the strategies in Section 17.6 as the best balance between computational cost and accuracy.

17.7 Conclusion and future trends

To deeply understand nanoparticle self-assembly, one must understand not only the relevant forces but also how population-level effects arise from these forces. Underlying such an investigation are the mathematical models for flocculation of nanoparticle aggregates. In this chapter, we have presented an introduction to the important sources of information about the field as well as a survey of available experimental protocols. We have discussed the mathematical modeling and computational methods currently used to investigate nanoparticles in fluids and provided an introduction to statistical model selection, which we hope will see wider adoption by the field. Last, we have also provided a brief description of alternative nanofluid simulation and analysis strategies.

It is always challenging to precisely predict future trends, more so in an active field such as nanofluids. As mentioned before, the focus of this work has been on the mathematical modeling, computational simulation, and statistical inference and thus the description of trends is biased accordingly (other chapters undoubtedly cover the application-focused trends in great detail). Overall, it is encouraging that more mathematical, computational, and statistical researchers are beginning to engage with nanofluids as a research topic. We will focus on these three areas and draw the reader's attention to significant and notable recent works. We will also comment on how recent "big data" initiatives have impacted these areas.

As discussed in Section 17.5, the aggregation (and fragmentation) equations derived by Smoluchowski have been studied for almost a century (van Smoluchowski, 1916, 1917). A substantial part of the subsequent theoretical work involves establishing the conditions (e.g., initial PSD, mathematical forms of the aggregation rate), which yield a so-called "self-similar solution" (see Section 17.5). In the recent nanofluid physics and engineering literature, there is substantial evidence that aggregation plays a central role in nanoparticle self-assembly and nanofluid thermal properties. Therefore, we envision that the interface between the study of the mathematics of self-similarity and the thermal conductivity experiments will be incredibly fruitful. We note that some of the most cited publications in this area are those by Xuan et al. (2003), Shima et al. (2009), and Wu et al. (2010), all of which draw from results in the aggregation literature.

Across the sciences, computational software is becoming more of a commodity and less a customized code designed to solve only one problem or a limited class of problems. Multiphysics simulation software such as COMSOL is now standard in the design of fluidic devices. As long as the continuum-limit assumption for fluids is satisfied, even micro- and nanofluidic simulations are highly accurate. This trend

will clearly not disappear, and the need for customized numerical and computational schemes in this regime will continue to be substantially reduced.

We note that for simulations below the continuum limit, the best numerical discretization strategy is not yet clear. This is, however, due more to the lack of consensus for the correct model rather than a fault of numerical and computational schemes.

While excellent statistical questions are also widespread in nanofluids research, only recently have advanced statistical techniques appeared in the literature. The work by Hohenegger and Mucha (2007) was an early effort in this direction, and they performed a thorough investigation of how to infer velocity profiles of nanoparticles. Last year, a publication by Röding et al. (2013) considered the challenging statistical question of estimating absolute number concentrations in single-nanoparticle microscopy. And, just recently, Nwosu et al. (2014) advocated for using a more structured model selection methodology for identifying accurate viscosity models among several candidates.

We also note that the field of nanofluids is relatively new, and our understanding of the environmental impact of discarded nanofluids is incomplete. Ju-Nam and Lead (2008) provide an overview of issues related to the environmental impact of TiO_2 nanoparticles used with ZnO in sunscreen. Zhang et al. (2008) provide evidence that that some commercially available nanoparticles are stable in water for up to 8 hours, but that DLS measurements suggest that nonsilica nanoparticles flocculate in tap water. These are just two examples, but as more commercial applications of nanofluids are discovered, there will undoubtedly be more interest in studying the long-term environmental impact.

Last, with the funding of "big data" initiatives by the NSF, there has been a substantial expansion of research into the relevant statistics, mathematics, and algorithms for these data sets. Accordingly, medicine and pharmacology are poised to take advantage of any relevant results. It is only a matter of time before a major drug discovery is initiated via correlating a database of nanomaterials (including nanofluids) such as the NIH-funded Nanomaterials Registry[8] (Ostraat et al., 2013) and a database of drug targets.

17.8 Sources of further information

Over the years, there have been a large number of review articles. While not directly reviewing mathematical models, the reviews do reflect the highly active nature of the field. Specifically, in the mid to late 2000s, as the field expanded, so did the number of reviews (Das et al., 2006; Daungthongsuk and Wongwises, 2007; Trisaksri and Wongwises, 2007; Murshed et al., 2008; Hwang et al., 2008; Yu et al., 2008; Li et al., 2009; Chandrasekar and Suresh, 2009; Kakaç and Pramuanjaroenkij, 2009; Chen et al., 2009; Taylor and Phelan, 2009; Wen et al., 2009; Pradeep and Anshup, 2009). For exhaustive year-by-year descriptions of the field, we direct the interested reader to the extensive reviews in *Renewable and Sustainable Energy*

[8] http://www.nanomaterialregistry.org/.

Reviews (Trisaksri and Wongwises, 2007; Godson et al., 2010; Paul et al., 2010; Mohammed et al., 2011a,b; Murshed et al., 2011; Saidur et al., 2011a,b; Sarkar, 2011; Haddad et al., 2012; Huminic and Huminic, 2012; Chandrasekar et al., 2012; Nkurikiyimfura et al., 2013; Sundar et al., 2013; Syam Sundar and Singh, 2013; Salman et al., 2013; Hussein et al., 2014), *International Journal of Heat and Mass Transfer* (Kakaç and Pramuanjaroenkij, 2009; Taylor and Phelan, 2009; Ghadimi et al., 2011; Yu et al., 2012; Liu and Li, 2012; Mahian et al., 2013a,b), and several others (Das et al., 2006; Daungthongsuk and Wongwises, 2007; Hwang et al., 2008; Murshed et al., 2008; Yu et al., 2008; Chandrasekar and Suresh, 2009; Chen et al., 2009; Li et al., 2009; Pradeep and Anshup, 2009; Wen et al., 2009; Rao, 2010; Liu and Li, 2012; Philip and Shima, 2012; Puliti et al., 2012; Witharana et al., 2013; Wu and Zhao, 2013; Ashrafmansouri and Nasr Esfahany, 2014; Haddad et al., 2014; Narrein and Mohammed, 2014; Sidik et al., 2014).

Because the field is moving so fast, even the sheer number of reviews can be overwhelming. Here we recommend several specific reviews and describe their individual themes. Rao (2010) provides a good overview of the scientific disciplines that are important to nanofluids. The review article by Wang and Mujumdar (2007) presents an excellent early review of the known thermal properties of nanofluids and in particular thoroughly summarizes much of the early work by Lee and Choi and their collaborators. Heurtault et al. (2003) review the flocculating and deflocculating abilities of nanoparticles on lipid systems. They describe several strategies for optimizing the floc stability via chemical (antioxidant, elimination of H_2O) and physical (steric and electrostatic stabilization, lipid composition, hydrogel incorporation, and storage parameter optimization) means. Zhou et al. (2009) review the known properties of gold nanoparticles and in particular how aggregation properties are determined by the self-assembled monolayers on their surface. They also do an excellent job of reviewing where Derjaguin, Landau, Verwey, and Overbeek (DLVO) theory works well and where it underestimates floc stability. Özerinç et al. (2009) provide a more recent overview of understanding of nanofluid thermal properties, highlighting the existing discrepancies between theory and experiment as well as the importance of flocculation. There are a huge number of experimental protocols available to study nanofluids. Wang and Fan (2010) review the experimental methodologies available through liquid-phase chemical reactions in continuous-flow microfluidic microreactors. Lim et al. (2013) review the use of DLS to study the size distribution and colloidal stability of magnetic nanoparticles (MNPs). Note that the self-assembly process of MNP with anisotropic structure can also be monitored effectively by DLS.

Concerning modeling and mathematical analysis, Yu and Lin (2010) review recent advances in multidimensional, multispecies PBE modeling in nanoparticle-laden multiphase flow. They explain connections with moment closure techniques and the interactions between particle dynamics and flow coherent structures. Concerning modeling and computational schemes, Puliti et al. (2012) review current the models and numerical methods in the context of known thermophysical properties of nanofluids.

There are also several good books to recommend. Das et al. (2007) and Pradeep (2008) are devoted specifically to nanofluids, while Volume 3 of the *Handbook of Nanophysics* series published in 2010 (Sattler, 2010) includes several contributed

articles on nanofluids and nanoparticles. For the interested mathematical reader, there have been a few nanofluid articles in journals run by the *Society for Industrial and Applied Mathematics* (SIAM), such as in *SIAM J. Applied Math* (Hohenegger and Mucha, 2007), *Multiscale Modeling and Simulation* (Ollila et al., 2013), and *SIAM Review* (Wei et al., 2012).

However, the majority of the nanofluid work has been published in more scientific- and engineering-oriented journals such as *ACS Nano*, *J. Colloid and Interface Science*, *International Journal of Heat and Mass Transfer*, and *Heat Transfer Engineering*.

Acknowledgments

This work was supported in part by the National Science Foundation grant DMS-1225878. The author would also like to thank D. D. Keck for comments on a previous draft of this work.

References

Ackleh, A.S., Fitzpatrick, B.G., 1997. Modeling aggregation and growth processes in an algal population model: analysis and computations. J. Math. Biol. 35 (4), 480–502.

Akaike, H., 1973. Information theory and an extension of the maximum likelihood principle. In: Petrov, B.N., Csaki, F. (Eds.), Second International Symposium on Information Theory. Akadémiai Kiadó, Budapest Hungary, pp. 267–281.

Akroyd, J., Smith, A.J., Shirley, R., McGlashan, L.R., Kraft, M., 2011. A coupled CFD-population balance approach for nanoparticle synthesis in turbulent reacting flows. Chem. Eng. Sci. 66 (17), 3792–3805.

Anderson, D.R., 2010. Model Based Inference in the Life Sciences: A Primer on Evidence. Springer, New York, NY.

Ashrafmansouri, S.-S., Nasr Esfahany, M., 2014. Mass transfer in nanofluids: a review. Int. J. Thermal Sci. 82, 84–99.

Bäbler, M.U., 2008. A collision efficiency model for flow-induced coagulation of fractal aggregates. AIChE J. 54 (7), 1748–1760.

Bäbler, M.U., Moussa, A.S., Soos, M., Morbidelli, M., 2010. Structure and kinetics of shear aggregation in turbulent flows. I. Early stage of aggregation. Langmuir 26 (16), 13142–13152.

Bak, T.A., Heilmann, O., 1991. A finite version of Smoluchowski's coagulation equation. J. Phys. A 24 (20), 4889–4893.

Barenblatt, G.I., 1996. Scaling, self-similarity, and intermediate asymptotics: dimensional analysis and intermediate asymptotics. Cambridge Texts in Applied Mathematics. Cambridge University Press, Cambridge, UK.

Barenblatt, G.I., 2003. Scaling. Cambridge Texts in Applied Mathematics. Cambridge University Press, Cambridge, UK.

Bilati, U., Allémann, E., Doelker, E., 2005. Development of a nanoprecipitation method intended for the entrapment of hydrophilic drugs into nanoparticles. Eur. J. Pharm. Sci. 24 (1), 67–75.

Bortz, D.M., Nelson, P.W., 2006. Model selection and mixed-effects modeling of HIV infection dynamics. Bull. Math. Biol. 68 (8), 2005–2025.

Bortz, D.M., Jackson, T.L., Taylor, K.A., Thompson, A.P., Younger, J.G., 2008. *Klebsiella pneumoniae* flocculation dynamics. Bull. Math. Biol. 70 (3), 745–768.

Burnham, K.P., Anderson, D.R., 2002. Model Selection and Multimodel Inference: A Practical Information-Theoretic Approach, second ed. Springer-Verlag, New York, NY.

Chandrasekar, M., Suresh, S., 2009. A review on the mechanisms of heat transport in nanofluids. Heat Transfer Eng. 30 (14), 1136–1150.

Chandrasekar, M., Suresh, S., Senthilkumar, T., 2012. Mechanisms proposed through experimental investigations on thermophysical properties and forced convective heat transfer characteristics of various nanofluids—a review. Renew. Sustain. Energy Rev. 16 (6), 3917–3938.

Chen, H., Witharana, S., Jin, Y., Kim, C., Ding, Y., 2009. Predicting thermal conductivity of liquid suspensions of nanoparticles (nanofluids) based on rheology. Particuology 7 (2), 151–157.

Cheng, Y., Shu, C.-W., 2008. Superconvergence and time evolution of discontinuous Galerkin finite element solutions. J. Comput. Phys. 227 (22), 9612–9627.

Cheng, Y., Shu, C.-w, 2010. Superconvergence of discontinuous Galerkin and local discontinuous Galerkin schemes for linear hyperbolic and convection-diffusion equations in one space dimension. SIAM J. Numer. Anal. 47 (6), 4044–4072.

Da Costa, F.P., 1998. A finite-dimensional dynamical model for gelation in coagulation processes. J. Nonlinear Sci. 8 (6), 619–653.

Darabi Sahneh, F., Scoglio, C., Riviere, J., 2013. Dynamics of nanoparticle-protein corona complex formation: analytical results from population balance equations. PLoS One 8 (5), e64690.

Das, S.K., Choi, S.U.S., Patel, H.E., 2006. Heat transfer in nanofluids—a review. Heat Transfer Eng. 27 (10), 3–19.

Das, S.K., Choi, S.U.S., Yu, W., Pradeep, T., 2007. Nanofluids: Science and Technology. Wiley-Interscience, USA.

Daungthongsuk, W., Wongwises, S., 2007. A critical review of convective heat transfer of nanofluids. Renew. Sustain. Energy Rev. 11 (5), 797–817.

Dell'Orco, D., Lundqvist, M., Oslakovic, C., Cedervall, T., Linse, S., 2010. Modeling the time evolution of the nanoparticle-protein corona in a body fluid. PLoS One 5 (6), 1–8.

Drake, R.L., 1972. A general mathematical survey of the coagulation equation. In: Hidy, G.M., Brock, J.R., Hidy, G.M., Brock, J.R. (Eds.), Topics in Current Aerosol Research (Part 2). In: International Reviews in Aerosol Physics and Chemistry, vol. 3. Pergamon Press, New York, NY, pp. 201–376.

Dubovskii, P.B., 1994. Mathematical Theory of Coagulation. Number 23 in Lecture Notes Series. Seoul National University, Research Institute of Mathematics, Global Analysis Research Center, Seoul National University, Seoul, Korea.

Dukic, V., Lopes, H.F., Polson, N.G., 2012. Tracking epidemics with Google Flu Trends data and a state-space SEIR model. J. Am. Stat. Assoc. 107 (500), 1410–1426.

Eastman, J.A., Choi, S.U.S., Li, S., Yu, W., Thompson, L.J., 2001. Anomalously increased effective thermal conductivities of ethylene glycol-based nanofluids containing copper nanoparticles. Appl. Phys. Lett. 78 (6), 718.

Ellahi, R., 2013. The effects of MHD and temperature dependent viscosity on the flow of non-Newtonian nanofluid in a pipe: analytical solutions. Appl. Math. Model. 37 (3), 1451–1467.

Ellahi, R., Raza, M., Vafai, K., 2012. Series solutions of non-Newtonian nanofluids with Reynolds' model and Vogel's model by means of the homotopy analysis method. Math. Comput. Model. 55 (7–8), 1876–1891.

Eymard, R., Gallouët, T., Herbin, R., 2000. The finite volume method. In: Ciarlet, P.G., Jions, J.L. (Eds.), In: Handbook of Numerical Analysis, vol. VII. North Holland Publishing Company, Amsterdam, pp. 713–1020.

Fernández-Díaz, J.M., Gómez-García, G.J., 2007. Exact solution of Smoluchowski's continuous multi-component equation with an additive kernel. Europhys. Lett. 78 (5), 56002.

Filbet, F., Laurençot, P., 2004. Numerical simulation of the Smoluchowski coagulation equation. SIAM J. Sci. Comput. 25 (6), 2004.

Flesch, J.C., Spicer, P.T., Pratsinis, S.E., 1999. Laminar and turbulent shear-induced flocculation of fractal aggregates. AIChE J. 45 (5), 1114–1124.

Fournier, N., Laurençot, P., 2006. Well-posedness of Smoluchowski's coagulation equation for a class of homogeneous kernels. J. Funct. Anal. 233 (2), 351–379.

Frenklach, M., 2002. Method of moments with interpolative closure. Chem. Eng. Sci. 57, 2229–2239.

Frenklach, M., Harris, S.J., 1987. Aerosol dynamics modeling using the method of moments. J. Colloid Interface Sci. 118 (1), 252–261.

Friedlander, S.K., 2000. Smoke, Dust, and Haze: Fundamentals of Aerosol Dynamics, second ed. Oxford University Press, USA.

Gelbard, F., Seinfeld, J.H., 1980. Simulation of multicomponent aerosol dynamics. J. Colloid Interface Sci. 78 (2), 485–501.

Ghadimi, A., Saidur, R., Metselaar, H.S.C., 2011. A review of nanofluid stability properties and characterization in stationary conditions. Int. J. Heat Mass Transfer 54 (17–18), 4051–4068.

Gharagozloo, P.E., Goodson, K.E., 2011. Temperature-dependent aggregation and diffusion in nanofluids. Int. J. Heat Mass Transfer 54 (4), 797–806.

Godson, L., Raja, B., Mohan Lal, D., Wongwises, S., 2010. Enhancement of heat transfer using nanofluids—an overview. Renew. Sustain. Energy Rev. 14 (2), 629–641.

Grünwald, P.D., 2007. The minimum description length principle. Adaptive Computation & Machine Learning. MIT Press, Cambridge, MA.

Grünwald, P.D., Myung, I.J., Pitt, M.A. (Eds.), 2005. Advances in Minimum Description Length: Theory and Applications. Neural Information Processing. MIT Press, Boston, MA.

Grzelczak, M., Vermant, J., Furst, E.M., Liz-Marzán, L.M., 2010. Directed self-assembly of nanoparticles. ACS Nano 4 (7), 3591–3605.

Haddad, Z., Oztop, H.F., Abu-Nada, E., Mataoui, A., 2012. A review on natural convective heat transfer of nanofluids. Renew. Sustain. Energy Rev. 16 (7), 5363–5378.

Haddad, Z., Abid, C., Oztop, H.F., Mataoui, A., 2014. A review on how the researchers prepare their nanofluids. Int. J. Thermal Sci. 76, 168–189.

Hamad, M., Ferdows, M., 2012a. Similarity solution of boundary layer stagnation-point flow towards a heated porous stretching sheet saturated with a nanofluid with heat absorption/generation and suction/blowing: a Lie group analysis. Commun. Nonlinear Sci. Numer. Simulat. 17 (1), 132–140.

Hamad, M.A.A., Ferdows, M., 2012b. Similarity solutions to viscous flow and heat transfer of nanofluid over nonlinearly stretching sheet. Appl. Math. Mech. 33 (7), 923–930.

Hamad, M., Pop, I., Md Ismail, A., 2011. Magnetic field effects on free convection flow of a nanofluid past a vertical semi-infinite flat plate. Nonlinear Anal.: Real World Appl. 12 (3), 1338–1346.

Hastie, T., Tibshirani, R., Friedman, J., 2001. The Elements of Statistical Learning: Data Mining, Inference, and Prediction. Springer Series in Statistics. Springer, New York, NY.

Hawa, T., Zachariah, M., 2006. Coalescence kinetics of unequal sized nanoparticles. J. Aerosol Sci. 37 (1), 1–15.
Heurtault, B., Saulnier, P., Pech, B., Proust, J.-E., Benoit, J.-P., 2003. Physico-chemical stability of colloidal lipid particles. Biomaterials 24 (23), 4283–4300.
Hoeting, J.A., Madigan, D., Raftery, A.E., Volinsky, C.T., Raferty, A.E., Volinshy, C.T., 1999. Bayesian model averaging: a tutorial (with discussion). Statist. Sci. 14 (4), 382–417.
Hohenegger, C., Mucha, P.J., 2007. Statistical reconstruction of velocity profiles for nanoparticle image velocimetry. SIAM J. Appl. Math. 68 (1), 239–252.
Huminic, G., Huminic, A., 2012. Application of nanofluids in heat exchangers: a review. Renew. Sustain. Energy Rev. 16 (8), 5625–5638.
Hurvich, C.M., Tsai, C.-L.L., 1989. Regression and time series model selection in small samples. Biometrika 76 (2), 297–307.
Hussein, A.M., Sharma, K.V., Bakar, R.A., Kadirgama, K., 2014. A review of forced convection heat transfer enhancement and hydrodynamic characteristics of a nanofluid. Renew. Sustain. Energy Rev. 29, 734–743.
Hwang, Y., Lee, J.-K., Lee, J.-K., Jeong, Y.-M., Cheong, S.-i, Ahn, Y.-C., Kim, S.H., 2008. Production and dispersion stability of nanoparticles in nanofluids. Powder Technol. 186 (2), 145–153.
Ju-Nam, Y., Lead, J.R., 2008. Manufactured nanoparticles: an overview of their chemistry, interactions and potential environmental implications. Sci. Total Environ. 400 (1–3), 396–414.
Kakaç, S., Pramuanjaroenkij, A., 2009. Review of convective heat transfer enhancement with nanofluids. Int. J. Heat Mass Transfer 52 (13–14), 3187–3196.
Kass, R.E., Raftery, A.E., 1995. Bayes factors. J. Am. Stat. Assoc. 90 (430), 773–795.
Keck, D.D., 2014. Aggregation Dynamics: Numerical Approximations, Inverse Problems, and Generalized Sensitivity. PhD, University of Colorado, Boulder.
Koch, W., Friedlander, S., 1990. The effect of particle coalescence on the surface area of a coagulating aerosol. J. Colloid Interface Sci. 140 (2), 419–427.
Kullback, S., Leibler, R.A., 1951. On information and sufficiency. Am. Statist. 22, 79–86.
Lee, S., Choi, S.U.S., 1997. Application of metallic nanoparticle suspensions in advanced cooling systems. Argonne National Laboratory Technical Report, ANL/ET/CP.
Li, Y., Zhou, J., Tung, S., Schneider, E., Xi, S., 2009. A review on development of nanofluid preparation and characterization. Powder Technol. 196 (2), 89–101.
Lim, J., Yeap, S.P., Che, H.X., Low, S.C., 2013. Characterization of magnetic nanoparticle by dynamic light scattering. Nanoscale Res. Lett. 8 (1), 381.
Liu, Z.-H., Li, Y.-Y., 2012. A new frontier of nanofluid research—application of nanofluids in heat pipes. Int. J. Heat Mass Transfer 55 (23–24), 6786–6797.
Mahian, O., Kianifar, A., Kalogirou, S.A., Pop, I., Wongwises, S., Mahian, O., Kianifar, A., Kalogirou, S.A., Pop, I., Wongwises, S., 2013a. A review of the applications of nanofluids in solar energy. Int. J. Heat Mass Transfer 57 (2), 582–594.
Mahian, O., Kianifar, A., Kleinstreuer, C., Al-Nimr, M.A., Pop, I., Sahin, A.Z., Wongwises, S., 2013b. A review of entropy generation in nanofluid flow. Int. J. Heat Mass Transfer 65, 514–532.
Makinde, O.D., 2012. Analysis of Sakiadis flow of nanofluids with viscous dissipation and Newtonian heating. Appl. Math. Mech. 33 (12), 1545–1554.
Makino, J., Fukushige, T., Funato, Y., Kokubo, E., 1998. On the mass distribution of planetesimals in the early runaway stage. New Astron. 3 (7), 411–417.
Maye, M.M., Nykypanchuk, D., Cuisinier, M., van der Lelie, D., Gang, O., 2009. Stepwise surface encoding for high-throughput assembly of nanoclusters. Nat. Mater. 8 (5), 388–391.

McGraw, R., 1997. Description of aerosol dynamics by the quadrature method of moments. Aerosol Sci. Tech. 27 (2), 255–265.
McQuarrie, A.D.R., Tsai, C.L., 1998. Regression and Time Series Model Selection. World Scientific Press, Hackensack, NJ.
Meneveau, C., Sreenivasan, K.R., 2006. The multifractal nature of turbulent energy dissipation. J. Fluid Mech. 224, 429.
Menon, G., Pego, R.L., 2006. Dynamical scaling in Smoluchowski's coagulation equations: uniform convergence. SIAM Rev. 48 (4), 745.
Mietta, F., Chassagne, C., Verney, R., Winterwerp, J., 2011. On the behavior of mud floc size distribution: model calibration and model behavior. Ocean Dyn. 61 (2), 257–271.
Mohammed, H.A., Al-aswadi, A.A., Shuaib, N.H., Saidur, R., 2011a. Convective heat transfer and fluid flow study over a step using nanofluids: a review. Renew. Sustain. Energy Rev. 15 (6), 2921–2939.
Mohammed, H.A., Bhaskaran, G., Shuaib, N.H., Saidur, R., 2011b. Heat transfer and fluid flow characteristics in microchannels heat exchanger using nanofluids: a review. Renew. Sustain. Energy Rev. 15 (3), 1502–1512.
Moraveji, M.K., Haddad, S.M.H., Darabi, M., 2012. Modeling of forced convective heat transfer of a non-Newtonian nanofluid in the horizontal tube under constant heat flux with computational fluid dynamics. Int. Commun. Heat Mass Transfer 39 (7), 995–999.
Mudanyali, O., McLeod, E., Luo, W., Greenbaum, A., Coskun, A.F., Hennequin, Y., Allier, C. P., Ozcan, A., 2013. Wide-field optical detection of nanoparticles using on-chip microscopy and self-assembled nanolenses. Nat. Photonics 7 (3), 247–254.
Müller, H., 1928. Zur allgemeinen Theorie der raschen Koagulation. Kolloidchem. Beih. 27, 257–311.
Murphy, R.J., Pristinski, D., Migler, K., Douglas, J.F., Prabhu, V.M., 2010. Dynamic light scattering investigations of nanoparticle aggregation following a light-induced pH jump. J. Chem. Phys. 132 (19), 194903.
Murshed, S.M.S., Leong, K.C., Yang, C., 2008. Thermophysical and electrokinetic properties of nanofluids—a critical review. Appl. Therm. Eng. 28 (17–18), 2109–2125.
Murshed, S.M.S., Nieto de Castro, C.A., Lourenço, M.J.V., Lopes, M.L.M., Santos, F.J.V., 2011. A review of boiling and convective heat transfer with nanofluids. Renew. Sustain. Energy Rev. 15 (5), 2342–2354.
Narrein, K., Mohammed, H.A., 2014. Heat transfer and fluid flow characteristics in helically coiled tube heat exchanger (HCTHE) using nanofluids: a review. J. Comput. Theor. Nanosci. 11 (4), 911–927.
Nkurikiyimfura, I., Wang, Y., Pan, Z., 2013. Heat transfer enhancement by magnetic nanofluids—a review. Renew. Sustain. Energy Rev. 21, 548–561.
Nwosu, P.N., Meyer, J., Sharifpur, M., 2014. Nanofluid viscosity: a simple model selection algorithm and parametric evaluation. Comput. Fluids. To appear.
Ollila, S.T.T., Smith, C.J., Ala-Nissila, T., Denniston, C., 2013. The hydrodynamic radius of particles in the hybrid lattice Boltzmann–molecular dynamics method. Multiscale Model. Simul. 11 (1), 213–243.
Ostraat, M.L., Mills, K.C., Guzan, K.A., Murry, D., 2013. The Nanomaterial Registry: facilitating the sharing and analysis of data in the diverse nanomaterial community. Int. J. Nanomed. 8 (Suppl. 1), 7–13.
Özerinç, S., Kakaç, S., Yazicioˇglu, A.G., 2009. Enhanced thermal conductivity of nanofluids: a state-of- the-art review. Microfluid. Nanofluid. 8 (2), s145–s170.
Paul, G., Chopkar, M., Manna, I., Das, P.K., 2010. Techniques for measuring the thermal conductivity of nanofluids: a review. Renew. Sustain. Energy Rev. 14 (7), 1913–1924.

Pawar, P., Shin, P.K., Mousa, S.A., Ross, J.M., Konstantopoulos, K., 2004. Fluid shear regulates the kinetics and receptor specificity of *Staphylococcus aureus* binding to activated platelets. J. Immunol. 173, 1258–1265.
Philip, J., Shima, P.D., 2012. Thermal properties of nanofluids. Adv. Colloid Interface Sci. 183–184, 30–45.
Prabhu, V.M., Hudson, S.D., 2009. Nanoparticle assembly: DNA provides control. Nat. Mater. 8 (5), 365–366.
Pradeep, T., 2008. Nano: The Essentials. McGraw Hill, New Delhi.
Pradeep, T., Anshup, 2009. Noble metal nanoparticles for water purification: a critical review. Thin Solid Films 517 (24), 6441–6478.
Prasher, R., Phelan, P.E., Bhattacharya, P., 2006. Effect of aggregation kinetics on the thermal conductivity of nanoscale colloidal solutions (nanofluid). Nano Lett. 6 (7), 1529–1534.
Pruppacher, H.R., Klett, J.D., 1980. Microphysics of Clouds and Precipitation. Riedel, Boston, MA.
Puliti, G., Paolucci, S., Sen, M., 2012. Nanofluids and their properties. Appl. Mech. Rev. 64 (3), 030803.
Ramkrishna, D., 2000. Population Balances: Theory and Applications to Particulate Systems in Engineering. Academic Press, San Diego, CA.
Rana, P., Bhargava, R., 2011. Numerical study of heat transfer enhancement in mixed convection flow along a vertical plate with heat source/sink utilizing nanofluids. Commun. Nonlinear Sci. Numer. Simulat. 16 (11), 4318–4334.
Rao, Y., 2010. Nanofluids: stability, phase diagram, rheology and applications. Particuology 8 (6), 549–555.
Riebesell, U., Wolf-Gladrow, D.A., 1992. The relationship between physical aggregation of phytoplankton and particle flux: a numerical model. Deep-Sea Res. 39 (7/8), 1085–1102.
Rissanen, J., 1978. Modeling by shortest data description. Automatica 14 (5), 465–471.
Rissanen, J., 1989. In: Stochastic Complexity and Statistical Inquiry, vol. 15. World Scientific Press, Singapore.
Rissanen, J., 1996. Fisher information and stochastic complexity. IEEE Trans. Informat. Theory 42 (1), 40–47.
Röding, M., Deschout, H., Braeckmans, K., Rudemo, M., 2013. Measuring absolute nanoparticle number concentrations from particle count time series. J. Microsc. 251 (1), 19–26.
Rosmila, A.B., Kandasamy, R., Muhaimin, I., 2012. Lie symmetry group transformation for MHD natural convection flow of nanofluid over linearly porous stretching sheet in presence of thermal stratification. Appl. Math. Mech. 33 (5), 593–604.
Sadr, R., Yoda, M., Zheng, Z., Conlisk, A.T., 2004. An experimental study of electro-osmotic flow in rectangular microchannels. J. Fluid Mech. 506, 357–367.
Saffman, P.G., Turner, J.S., 1956. On the collision of drops in turbulent clouds. J. Fluid Mech. 1, 16–30.
Saidur, R., Kazi, S.N., Hossain, M.S., Rahman, M.M., Mohammed, H.A., 2011a. A review on the performance of nanoparticles suspended with refrigerants and lubricating oils in refrigeration systems. Renew. Sustain. Energy Rev. 15 (1), 310–323.
Saidur, R., Leong, K.Y., Mohammad, H.A., 2011b. A review on applications and challenges of nanofluids. Renew. Sustain. Energy Rev. 15 (3), 1646–1668.
Salman, B.H., Mohammed, H.A., Munisamy, K.M., Kherbeet, A.S., 2013. Characteristics of heat transfer and fluid flow in microtube and microchannel using conventional fluids and nanofluids: a review. Renew. Sustain. Energy Rev. 28, 848–880.

Sarkar, J., 2011. A critical review on convective heat transfer correlations of nanofluids. Renew. Sustain. Energy Rev. 15 (6), 3271–3277.
Sattler, K.D. (Ed.), 2010. Handbook of Nanophysics: Nanoparticles and Quantum Dots, 3. CRC Press, Boca Raton, FL.
Sau, T.K., Murphy, C.J., 2005. Self-assembly patterns formed upon solvent evaporation of aqueous cetyltrimethylammonium bromide-coated gold nanoparticles of various shapes. Langmuir 21 (7), 2923–2929.
Schwarz, G., 1978. Estimating the dimension of a model. Ann. Statist. 6, 461–464.
Schwarzer, H.-C., Peukert, W., 2005. Prediction of aggregation kinetics based on surface properties of nanoparticles. Chem. Eng. Sci. 60 (1), 11–25.
Sefcik, J., Soos, M., Vaccaro, A., Morbidelli, M., 2006. Effects of mixing on aggregation and gelation of nanoparticles. Chem. Eng. Process.: Process Intesif. 45 (10), 936–943.
Sheikholeslami, M., Gorji-Bandpy, M., Domairry, G., 2013. Free convection of nanofluid filled enclosure using lattice Boltzmann method (LBM). Appl. Math. Mech. (English Edition) 34 (7), 833–846.
Shima, P.D., Philip, J., Raj, B., 2009. Role of microconvection induced by Brownian motion of nanoparticles in the enhanced thermal conductivity of stable nanofluids. Appl. Phys. Lett. 94 (22), 223101.
Sidik, N.A.C., Mohammed, H., Alawi, O.A., Samion, S., 2014. A review on preparation methods and challenges of nanofluids. Int. Commun. Heat Mass Transfer 54, 115–125.
Somasundaran, P., Runkanan, V., Kapur, P., Stechemesser, H., Dobiáš, B., 2005. Flocculation and dispersion of collodial suspensions by polymers and surfactants: experimental and modeling studies. second ed. In: Coagulation and Flocculation, vol. 126. Taylor and Francis, pp. 767–803 (Chapter 11).
Spicer, P.T., Pratsinis, S.E., 1996. Coagulation and fragmentation: universal steady-state particle-size distribution. AIChE J. 42 (6), 1612–1620.
Srinivasachari, S., Liu, Y., Zhang, G., Prevette, L., Reineke, T.M., 2006. Trehalose click polymers inhibit nanoparticle aggregation and promote pDNA delivery in serum. J. Am. Chem. Soc. 128 (25), 8176–8184.
Stechemesser, H., Dobiáš, B., Stechemesser, H., Dobiáš, B., 2005. Coagulation and Flocculation, second ed. Surfactant Science Series, 126. Taylor and Francis, Boca Raton, FL.
Sundar, L.S., Sharma, K.V., Naik, M.T., Singh, M.K., 2013. Empirical and theoretical correlations on viscosity of nanofluids: a review. Renew. Sustain. Energy Rev. 25, 670–686.
Syam Sundar, L., Singh, M.K., 2013. Convective heat transfer and friction factor correlations of nanofluid in a tube and with inserts: a review. Renew. Sustain. Energy Rev. 20, 23–35.
Takeuchi, K., 1976. Distribution of informational statistics and criterion of model fitting. Suri-Kagaku (Mathematic Sciences) 153, 12–18.
Taylor, R.A., Phelan, P.E., 2009. Pool boiling of nanofluids: comprehensive review of existing data and limited new data. Int. J. Heat Mass Transfer 52 (23–24), 5339–5347.
Tohver, V., Smay, J.E., Braem, A., Braun, P.V., Lewis, J.A., 2001. Nanoparticle halos: a new colloid stabilization mechanism. Proc. Natl. Acad. Sci. U. S. A. 98 (16), 8950–8954.
Toni, T., Welch, D., Strelkowa, N., Ipsen, A., Stumpf, M.P., 2009. Approximate Bayesian computation scheme for parameter inference and model selection in dynamical systems. J. R. Soc. Interface 6 (31), 187–202.
Trisaksri, V., Wongwises, S., 2007. Critical review of heat transfer characteristics of nanofluids. Renew. Sustain. Energy Rev. 11 (3), 512–523.
Turkyilmazoglu, M., 2012. Exact analytical solutions for heat and mass transfer of MHD slip flow in nanofluids. Chem. Eng. Sci. 84, 182–187.

van Smoluchowski, M., 1916. Drei Vorträge über Diffusion, Brownsche Bewegung und Koagulation von Kolloidteilchen. Z. Phys. 17, 557–571.
van Smoluchowski, M., 1917. Versuch einer mathematischen theorie der koagulation kinetic kolloider losungen. Z. Phys. Chem. 92, 129–168.
Vapnik, V.N., 2000. The nature of statistical learning theory. Statistics for Engineering & Information Science, second ed. Springer-Verlag, New York, NY.
Wang, L., Fan, J., 2010. Nanofluids research: key issues. Nanoscale Res. Lett. 5, 1241–1252.
Wang, X.-Q., Mujumdar, A.S., 2007. Heat transfer characteristics of nanofluids: a review. Int. J. Thermal Sci. 46 (1), 1–19.
Wattis, J.A.D., 2006. An introduction to mathematical models of coagulation-fragmentation processes: a discrete deterministic mean-field approach. Phys. D 222 (1–2), 1–20.
Wei, G.-W., Zheng, Q., Chen, Z., Xia, K., 2012. Variational multiscale models for charge transport. SIAM Rev. 54 (4), 699–754.
Wen, D., Lin, G., Vafaei, S., Zhang, K., 2009. Review of nanofluids for heat transfer applications. Particuology 7 (2), 141–150.
Witharana, S., Weliwita, J.A., Chen, H., Wang, L., 2013. Recent advances in thermal conductivity of nanofluids. Recent Pat. Nanotechnol. 7 (3), 198–207.
Wu, J., Zhao, J., 2013. A review of nanofluid heat transfer and critical heat flux enhancement—research gap to engineering application. Prog. Nucl. Energy 66, 13–24.
Wu, C., Cho, T.J., Xu, J., Lee, D., Yang, B., Zachariah, M.R., 2010. Effect of nanoparticle clustering on the effective thermal conductivity of concentrated silica colloids. Phys. Rev. E 81 (1), 011406.
Wulkow, M., Gerstlauer, A., Nieken, U., 2001. Modeling and simulation of crystallization processes using parsival. Chem. Eng. Sci. 56 (7), 2575–2588.
Xuan, Y., Li, Q., Hu, W., 2003. Aggregation structure and thermal conductivity of nanofluids. AIChE J. 49 (4), 1038–1043.
Yu, M., Lin, J., 2010. Nanoparticle-laden flows via moment method: a review. Int. J. Multiphase Flow 36 (2), 144–151.
Yu, W., France, D.M., Routbort, J.L., Choi, S.U.S., 2008. Review and comparison of nanofluid thermal conductivity and heat transfer enhancements. Heat Transfer Eng. 29 (5), 432–460.
Yu, W., France, D.M., Timofeeva, E.V., Singh, D., Routbort, J.L., 2012. Comparative review of turbulent heat transfer of nanofluids. Int. J. Heat Mass Transfer 55 (21–22), 5380–5396.
Zhang, Y., Chen, Y., Westerhoff, P., Hristovski, K., Crittenden, J.C., 2008. Stability of commercial metal oxide nanoparticles in water. Water Res. 42 (8–9), 2204–2212.
Zhou, J., Ralston, J., Sedev, R., Beattie, D.A., 2009. Functionalized gold nanoparticles: synthesis, structure and colloid stability. J. Colloid Interface Sci. 331 (2), 251–262.

Atomistic modeling of nanostructured materials for novel energy application

18

M. Hu
RWTH Aachen University, Aachen, Germany

18.1 Introduction

Nanostructured materials or nanomaterials are materials with a characteristic size of structural elements on the order of several hundreds of nanometers or less at least in one dimension. Examples of nanostructured materials include, but are not limited to, nanocrystalline materials, nanofibers, nanotubes, and nanoparticle-reinforced nanocomposites, multilayered systems with layers of submicron thickness. Recent advances in nanotechnology have provided a variety of nanostructured materials with highly controlled and interesting properties—from exceptionally high strength in terms of enhanced mechanical ability to target drugs in biophysics, from high-performance heat dissipation in thermal science to unique optical properties. By controlling structure at the nanoscale dimensions, one can control and tailor the properties of nanostructures, such as semiconductor nanocrystals and metal nanoshells, in a very predictable manner to meet the needs of a specific application. These materials can bring new and unique capabilities to a variety of engineering and technological applications ranging from diagnosis of diseases to novel energy nanotechnologies. In fact, the past decades have witnessed rapid advances in the synthesis of nanostructured materials combined with reports of their enhanced or unique properties that have created a new active area of materials research. Due to the nature of the nanoscopic size of the structural elements in nanomaterials, the interfacial regions, which represent an insignificant volume fraction in traditional materials with coarse microstructures, start to play the dominant role in defining the physical and chemical properties of nanostructured materials. This implies that the behavior of nanomaterials cannot be understood and predicted by simply applying scaling arguments from the structure-property relationships developed for conventional polycrystalline, multiphase, and composite materials. New models and fundamentally new structure-property relationships, therefore, are needed for an adequate description of the behavior and properties of nanomaterials.

Computer modeling is playing a prominent role in the development of the theoretical understanding of the connections between the atomic-level structure and the effective (macroscopic) properties of nanomaterials. Atomistic modeling has been

Modeling, Characterization and Production of Nanomaterials. http://dx.doi.org/10.1016/B978-1-78242-228-0.00018-1
Copyright © 2015 Elsevier Ltd. All rights reserved.

at the forefront of computational investigation of nanomaterials and has revealed a wealth of information on structure and properties of individual structural elements (various nanolayers, nanoparticles, nanofibers, nanowires, and nanotubes) as well as the characteristics of the interfacial regions and modification of the material properties at the nanoscale. Generally speaking, atomistic modeling is based on atoms as elementary units in the models, thus providing the atomic-level resolution in the computational studies of materials structure and properties. The main atomistic methods in material research are (1) molecular dynamics (MD) technique that yields "atomic movies" of the dynamic material behavior through the integration of the equations of motion of atoms and molecules, (2) the Metropolis Monte Carlo (MC) method that enables evaluation of the equilibrium properties through the ensemble averaging over a sequence of random atomic configurations generated according to the desired statistical-mechanics distribution, and (3) the kinetic MC method that provides a computationally efficient way to study systems where the structural evolution is defined by a finite number of thermally activated elementary processes.

Rapid progress in the synthesis and processing of materials with structures on nanometer length scales has created an urgent demand for greater scientific understanding of thermal transport in nanoscale devices, individual nanostructures, and nanostructured materials. On one hand, as transistor power density has been exponentially increasing in recent years, efficient heat dissipation across interfaces is one of the crucial challenges that limits the development of innovative microelectronic device technologies. Because of the unique architecture of nanoelectronic devices, interfacial thermal transport has become the dominant factor in the performance of electronic cooling systems. On the other hand, thermoelectric materials find important applications in the direct conversion of thermal energy to electric power and in solid-state cooling. Although thermoelectric devices possess unique advantages such as high reliability, lack of moving parts, and the ability to be scaled down to small sizes, the energy conversion efficiencies of these devices remain a generally poor factor that severely limits their competitiveness and range of employment. To materialize widespread use of thermoelectrics at levels that would impact global energy issues, the material and device efficiencies existing currently will need to be improved significantly. The energy conversion efficiency of thermoelectric devices is characterized by the figure-of-merit: $ZT = S^2\sigma T/\kappa$, where S, σ, and κ are the Seebeck coefficient, electrical conductivity, and thermal conductivity of the material, respectively, and T is the absolute temperature. In general, development schemes to improve thermoelectric conversion efficiency are driven by the need to maximize the Seebeck coefficient and to balance the competing requirements of high electrical conductivity and low thermal conductivity. To this end, considerably large amounts of scientific effort have been dedicated to reducing the thermal conductivity. Nanostructuring of existing thermoelectrics (e.g., nanowires, superlattices, composites) has emerged as a promising pathway to improve thermoelectric performance by manipulating phononic transport. The development of advanced thermoelectric materials calls for understanding emergent phonon behavior in various structures, especially in nanostructured materials.

However, the physics of heat transfer at the nanoscale can differ distinctly from that predicted by classical laws, primarily due to the significance of surface, boundary, and size effects. When characteristic length scales of the device or structure are comparable to the mean-free path of heat carriers (mainly phonons for semiconductors and insulators), conventional heat transfer theory is no longer valid. Tremendous progress has been made in the past two decades to understand and characterize heat transfer in nanostructures. From a numerical modeling point of view, computational methods including lattice dynamics (LD) based on force constants from empirical force fields or first-principles calculations and in combination with Boltzmann transport equation (BTE), nonequilibrium Green's function (NEGF), classical MD simulations, and MC simulations have been used to study nanoscale thermal transport. These will be introduced in sequence below.

18.2 Overview of computational methods

18.2.1 Lattice dynamics

LD, combined with the BTE (Majumdar, 1993), has been able to predict phonon properties and thermal conductivity with unprecedented accuracy and without the need for any empirical input, when using first-principles calculations (Broido et al., 2007; Esfarjani et al., 2011). Evaluating force constants from first-principles calculations has been made possible thanks to aggressive improvements in computational hardware and software. However, it becomes more challenging if inhomogeneity has to be taken into account, which involves significantly large supercells that require unbearable computational demands. In addition, the method has difficulty studying the effect of free surface and boundary.

18.2.2 Atomistic Green's function

A Green's function is a mathematical method for solving differential equations such as the Schrodinger equation. In an atomistic Green's function approach, the system is represented at the molecular level by atomistic potential models. Heat current in the system subject to a small temperature difference is related to the interatomic force constants. This heat current is expressed in terms of Green's function, and the phonon transmission is calculated as a function of phonon frequency (Mingo and Yang, 2003; Mingo, 2006; Yamamoto and Watanabe, 2006; Wang et al., 2008). The Green's function method can provide frequency-dependent transmission, but its disadvantage is that to this point it can only deal with ballistic transport.

18.2.3 Classical MD simulations

Classical MD simulations trace the time-dependent trajectories of all atoms in the simulation domain based on Newton's second law of motion and interatomic potentials (Schelling et al., 2002a; He et al., 2012). Nonequilibrium molecular dynamics

(NEMD) and equilibrium molecular dynamics (EMD) simulations are the two major methods to calculate thermal transport properties such as thermal conductivity and interfacial thermal conductance with their respective advantages and disadvantages. MD has also been developed to study detailed phonon properties such as density of state, dispersion relation, relaxation time (Thomas et al., 2010), and transmission across interfaces (Chalopin and Volz, 2013). The serious disadvantage of MD simulation is that it relies on accurate interatomic potential.

18.2.4 Boltzmann transport equation

As an alternative method to classical MD, a phonon BTE, a first-order partial differential equation for a phonon distribution function, has been used for small time and space scales. The distribution function is a scalar quantity in the six-dimensional phase space, namely three space coordinates and three wave-vector coordinates. Generally, the BTE is very difficult to solve thus practical relaxation time approximation is used. MC simulations are often used to solve the Boltzmann equation for arbitrary structures (Tian and Yang, 2007; Jeng et al., 2008; Hao et al., 2009; Peraud and Hadjiconstantinou, 2011; Minnich, 2012). However, when frequency-dependent phonon mean-free paths need to be considered, the computational time of MC simulation becomes very large. Although recently researchers have developed some methods of sampling the free path of phonon-phonon scattering with a Poisson distribution and added boundary scattering by launching phonons in a random position in the structure (McGaughey and Jain, 2012), the widely used Matthiessen rule was found to be large especially when the structure sizes have a large variation and such a treatment can significantly overestimate thermal conductivity when applied to more complex structures.

18.2.5 Multiscale simulation

Although atomistic simulations can handle systems with heterogeneity on the order of nanometer up to micrometer scale, this size is not large enough to consider the heterogeneous effects occurring in realistic systems. To this end, multiscale simulation tools are needed to bridge the length-scale and time-scale gaps between atomistic simulations and real materials and devices, because the traditional Fourier heat conduction model is inapplicable at length scales below the mean-free path, and the atomistic simulation methods are inadequate for simulating large systems. The phonon Boltzmann equation has been an important multiscale tool for thermal transport studies. The information that is required as input for BTE can be obtained from phonon relaxation time calculation for bulk materials and interfacial phonon transmission for interfaces using the technique such as wave packet MD simulation.

The comparison of the main advantage and disadvantage between the above approaches is summarized in Table 18.1. Generally speaking, among the above methods MD simulation is the most popular approach in simulating nanoscale heat transfer, primarily because of its ease for coding (e.g., less effort to implement in a code, high parallel computing efficiency) and also its strong ability to deal with

Table 18.1 Advantages and disadvantages of typical computational approaches for nanoscale heat transfer

Method	Advantages	Disadvantages
LD/BTE	Very accurate when combining with first-principle calculations; no need for any input parameters; can obtain phonon mode-specific conductivity	High computation demand for large supercells; cannot simulate free surface and boundary
NEGF	Accurate (can combine with first-principle calculations as well); can obtain frequency-dependent transmission coefficient; can simulate free surface, boundary, and interface	Only calculates ballistic transport so far; lack of accurate interfacial interaction model; cannot obtain phonon mode-specific transmittance
Classical MD	Fast; ease for coding; high computing efficiency; can tackle various systems including free surface and boundary, especially when inhomogeneity occurs at large length scale	Empirical approach; relies on accurate interatomic potential; lack of quantum effect
MC/BTE	Fast; can simulate length scale beyond microns	Needs input parameters for inhomogeneous system

relatively large length scale and long time scale problems, as compared with first-principles calculations (He et al., 2012). However, because MD simulation is principally based on empirical interatomic potential and classical Newton's second law, the interatomic potential used directly determines the quality of a MD simulation. Even worse, MD simulation may have severe problems when the interatomic potential for a specific material is not available, for example, the novel nanostructures and their chemical modifications. Another significant drawback of classical MD simulation is the lack of quantum effect that should be taken into account when the system temperature is well below the Debye temperature. In these cases, first-principles-based LD/BTE and NEGF methods are more suitable, because they do not need any fitting parameters.

18.3 Selected topics of modeling nanomaterials for energy nanotechnology

18.3.1 Low thermal conductivity of nanostructures for efficient thermoelectrics

18.3.1.1 Research motivation

Meeting the constantly increasing global demand for energy is one of the most important challenges facing humanity in the twenty-first century. One way to improve the sustainability of our energy base, and especially our electricity supply, is through

the direct conversion of heat to electricity and by the scavenging of waste heat with thermoelectric generators. Home heating, automotive exhaust, and industrial processes all generate an enormous amount of unused waste heat that could be converted to electricity by using thermoelectrics. The thermoelectric effect is the direct conversion of temperature differences to electric voltage, and vice versa, by taking advantage of the Seebeck effect. Because thermoelectric generators are solid-state devices with no moving parts, they are small, lightweight, silent, reliable, scalable, and environmentally friendly, making them ideal for small, distributed power generation and even for tasks in harsh environments such as automobiles, incinerators, and spacecraft. Actually, efforts are already underway to replace the alternators in cars with thermoelectric generators mounted on the exhaust stream, thereby improving fuel efficiency.

The energy conversion efficiency of a thermoelectric material is given by figure of merit, ZT, $ZT = S^2\sigma T/(\kappa_p + \kappa_e)$, where S is the Seebeck coefficient, σ is the electrical conductivity, T is the absolute temperature, and κ_p and κ_e are the lattice (phonon) and electronic contributions to thermal conductivity, respectively. An ideal thermoelectric with high ZT should be an electrical conductor and also a thermal insulator. This conflicting requirement poses a material challenge. In general, development schemes to improve thermoelectric conversion efficiency in the past decades were guided by the concept of "phonon glass-electron crystal" (Figure 18.1) (i.e., reducing the lattice contribution to the thermal conductivity as closely as possible to an amorphous state, while keeping relatively high electrical conductivity and Seebeck coefficient (high thermopower)). Along this line, a considerably large amount of scientific effort has been dedicated to reducing the lattice thermal conductivity. Initially, a "phonon glass-electron crystal" material featured cages or tunnels in its crystal structure inside which reside massive atoms that are small enough relative to the cage to "rattle." This situation produced a phonon-damping effect that could result in the dramatic reduction of the lattice thermal conductivity. In the "phonon glass-electron crystal" picture, a glass-like thermal conductivity can, in principle, coexist with charge carriers of high mobility. The "phonon glass-electron crystal" approach has stimulated a significant amount of new research and has led to significant increases in ZT for several compounds such as clathrates, skutterudites, and half-heusler intermetallic compounds (see "Single Phases" in Figure 18.1). Later on, due to the gained ability to create nanostructured materials, the nanostructuring of existing thermoelectric materials of interest has emerged as a promising pathway to greatly reduce the lattice thermal conductivity to values lower than were previously thought possible and, as a result, improve thermoelectric performance. Typical examples in this route include low-dimensional nanostructures such as superlattices, quantum dots, and nanowires along with subsequent structure modulation, nanocomposites, and bulk nanostructured materials. By exploiting nanoscale effects, such as strong boundary or interfacial phonon scattering, and by taking advantage of the nanoconfinement effect, the nanostructured materials are able to achieve decent ZT values at room-temperature and record-high ZT values in the range of 1.5-2.0 at medium and high temperatures (see "Nanostructured Materials" in Figure 18.1), which cannot be achieved in traditional bulk materials. The above nanostructuring routes will be explained in detail in sequence.

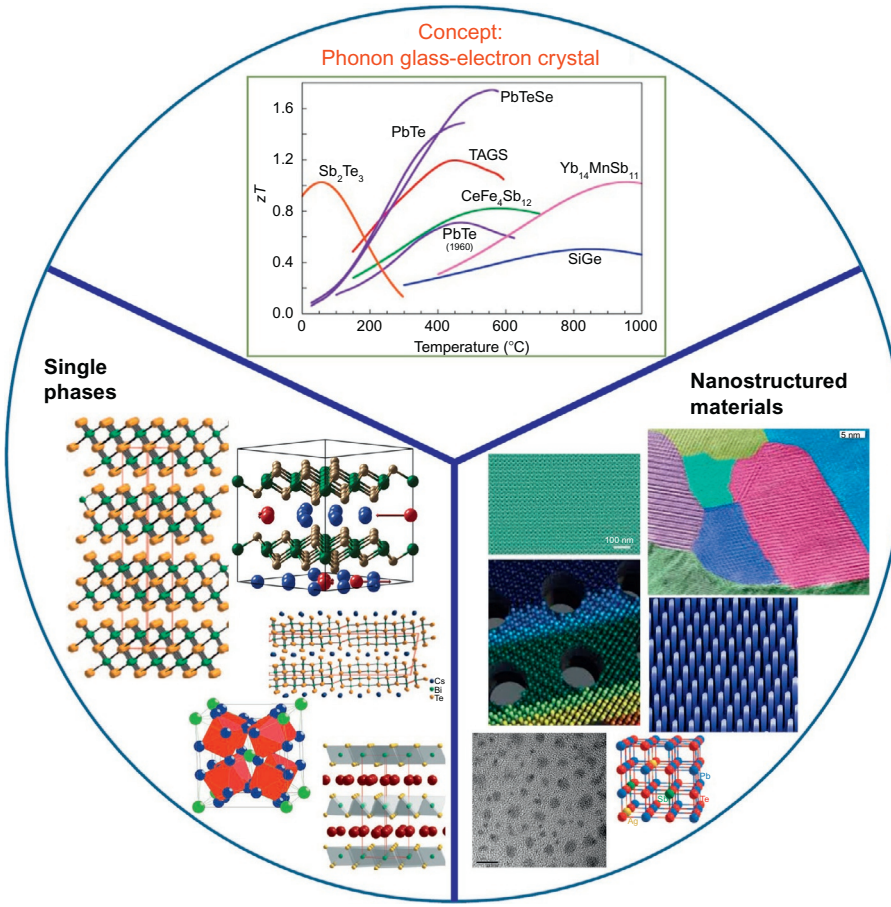

Figure 18.1 Schematic of representative important progress (single phases and nanostructured materials) in the previous and current thermoelectrics study.

18.3.1.2 Bulk (three-dimensional) materials

Among various types of nanostructured materials, bulk nanostructured materials have shown the most promise for commercial use because, unlike many other nanostructured materials (in particular low-dimensional materials), they can be fabricated in large quantities and in a form that is compatible with existing thermoelectric device configurations. The generation of these bulk nanostructured materials is currently being developed for commercialization, but it still requires a fundamental understanding of carrier transport in these complex materials, which is presently lacking for next-generation high-performance thermoelectrics.

In the past decade, significantly large amounts of bulk nanostructured materials have experimentally demonstrated a higher ZT than that of their bulk counterparts by reducing the thermal conductivity to values lower than were previously thought possible, such as n-type $Si_{80}Ge_{20}$, p-type $Si_{80}Ge_{20}$, and p-type $Bi_xSb_{2-x}Te_3$. Despite tremendous successes in experiments, fundamental understanding of transport in these complex materials and how their nanoscale structure affects bulk properties are still lacking. In particular, the precise way in which interfaces affect phonon transport to reduce thermal conductivity in nanocomposites remains poorly understood. Obviously, pure atomistic simulation such as MD is not enough to capture the real physics of phonon transport in bulk-like nanostructured materials, such as nanocrystallines. This is because the heterogeneity, for example, grains and grain boundaries that are essentially the dominant scattering process in nanocomposites and nanocrystallines, usually occurs at large length scale and the size of the grains can vary from a few nanometers up to several microns. This situation makes it almost impossible for the explicit atomistic simulations to obtain a reliable thermal conductivity result. To this end, solving the BTE at large length scales with input information obtained from atomistic simulations might be an efficient and promising method to tackle the phonon transport problem in bulk nanostructured materials. Numerical modeling that helps reveal the fundamental physics of phonon transport is key to further reducing the thermal conductivity. It is expected that, with a better understanding of phonon transport, further lattice thermal conductivity reductions should be possible.

18.3.1.3 Two-dimensional materials

Graphene and graphene-based heterostructures

Two-dimensional (2D) materials have historically been one of the most intensely studied materials, due to the tremendously large amount of unusual physical phenomena that occur when charge and heat transport is confined to a plane. The discovery of graphene in 2004 by Novoselov and Geim (Novoselov et al., 2004; Geim and Novoselov, 2007) has shown that it is not only possible to isolate stable, single-atom-thick 2D layers from van der Waals solids, but that these materials can exhibit unique and fascinating physical properties, which have led to novel routes for many applications. Graphene is an only one-atom-thick layer of sp^2-bonded carbon in a honeycomb crystal structure and was probably the most investigated system in materials science during the last decade. The recent developments in the "science of graphene" prompted an unprecedented surge of activity and demonstrations of new physical phenomena. These developments also triggered a renewed emphasis on the interdisciplinary nature of nanoscience and created new opportunities in materials science, physics, chemistry, and electrical engineering. Two most striking physical properties of graphene that have already been explored extensively are the following: (1) In single-layer graphene's band structure, the conduction π band and the valence π band of graphene meet exactly at the corners of the hexagonal first Brillouin zone called the Dirac points. Around the Dirac points, the dispersion relation of the π bands is linear with the separation distance, opposite to the other semiconductors, which chiefly exhibit a parabolic dispersion at the Fermi energy. Originating from this, electrons

in graphene mimic the behavior of photons or other ultrarelativistic particles, with an energy-independent Fermi velocity that is only 300 times smaller than the speed of light. The linear dispersion at the K point gives rise to novel phenomena, such as the anomalous room-temperature quantum Hall effect (Novoselov et al., 2007), and has opened up a new category of "Fermi-Dirac" physics. (2) Even at a single-atom-thick, high-quality graphene is very strong, light, nearly transparent, and an excellent conductor of heat. The experimentally measured thermal conductivity of suspended single-layer graphene at room temperature is reported to be as high as $\sim(4.84 \pm 0.44) \times 10^3$ to $(5.30 \pm 0.48) \times 10^3$ W/mK (Balandin et al., 2008), which is almost the highest thermal conductivity among the existing materials.

Qiu and Ruan (2012) addressed the problem of relative contributions of ZA phonons to thermal transport in the framework of the EMD simulations. Their conclusion was that in suspended single-layer graphene, out-of-plane ZA phonons are coupled with in-plane phonons because of the third-order and higher-order anharmonic interactions, which results in about 25% to 30% contribution of ZA phonons to the thermal conductivity of graphene. In supported single-layer graphene, the contribution of all acoustic and ZO phonon branches are reduced owing to the SLG-substrate interface scattering and breakdown of the symmetries for both in-plane and out-of-plane phonons. The contributions of ZA phonons to thermal conductivity are suppressed more strongly than the contributions of TA and LA phonons. However, Ong and Pop (2011) examined thermal transport in graphene supported on SiO_2 using MD simulations with reactive empirical bond order potential. They found from their calculations that increasing the strength of the graphene-substrate interactions further can enhance the heat flow and effective thermal conductivity along the supported graphene. The authors attributed this result to the coupling of graphene ZA modes to the substrate Rayleigh waves, which linearizes the phonon dispersion, increases the group velocity of the hybridized modes, and thus enhances the thermal flux.

In addition to pristine single-layer graphene, the chemical modifications of graphene and graphene-based heterostructures have been proposed for a host of applications ranging from transparent conductors to thermal interface materials (Balandin, 2011) to field effect transistors (Jia et al., 2011). Furthermore, because single-layer graphene is entirely surface area, its properties and reactivity profoundly depend on the chemical modifications, for example, surface functionalization (Hu et al., 2010a) and mechanical deformations.

Graphene analogs (silicene)

Graphene's success created a new era in materials science, especially in 2D materials, showing the promise that it is possible to create stable, single- or few-atom-thick layers out of other materials and also that these materials can exhibit fascinating and technologically useful properties. It was not until the recent surge of intense research on graphene that the general potential of 2D materials became apparent. In fact, two of the strongest motivations for exploring other graphene-like 2D materials stem from the facts that first, intrinsic graphene is a semimetal or zero bandgap semiconductor. However, the presence of a sizable gap in the electronic band is an

essential requirement for the realization of common electronic devices such as field effect transistors, and finding the best way to induce such a gap in graphene has been a very active research topic in the past few years. Second, notwithstanding its phenomenal properties, the integration of graphene with the actual silicon-based technologies has proven a quite challenging task whose solution would probably require the complete redesign of all electronic devices. Because our present technology is primarily based on silicon (Si) semiconductors, a natural question is raised: Could Si, which is another element of the same IV-group of the periodic table as carbon, also form graphene-like structures? Fortunately, the answer is affirmative.

Structurally, the Si counterpart of graphene is called silicene, that is, the Si atoms can also form a one-atom-thick honeycomb crystal structure. Silicene was first mentioned in a theoretical study by Takeda and Shiraishi (1994) and then reinvestigated by Guzman-Verri and Lew Yan Voon (2007), who named it silicene. Experimentally, in recent years silicene and silicene nanoribbons have been successfully grown on various metal substrates, such as Ag (Vogt et al., 2012; Feng et al., 2012), Ir, and ZrB_2. Free-standing silicene has been difficult to synthesize until now. The experimental synthesis stimulated tremendous theoretical investigation of its physical properties. Among these, significant effort has been invested on its electronic property. For instance, it has been shown theoretically that the band structure of silicene resembles that of graphene, featuring Dirac-type electron dispersion in the vicinity of the corners of its hexagonal Brillouin zone (Cahangirov et al., 2009; Liu et al., 2011). As a result, the Fermi velocity of silicene is predicted to be approximately half that of graphene. A very recent study demonstrated that silicene decorated with certain 3D transition metals (vanadium) can sustain a stable quantum anomalous Hall effect. Moreover, silicene has been shown theoretically to be metastable as a free-standing 2D crystal (Cahangirov et al., 2009), implying that it is possible to transfer silicene onto an insulating substrate and gate it electrically. Despite the significant progress that has been made in the theoretical investigation of the electrical transport property of silicene, however, thermal transport (mainly phonons, according to our preliminary calculation) property has not yet been cultivated. For almost all nanoelectronics applications, thermal conductivity is one of the most important physical parameters in electronics design and operation. Thermal transport can play crucial role in many applications such as heat dissipation, thermal management, and electronic packaging. Therefore, there is an emerging need for characterizing thermal transport properties of silicene-based nanostructures for the development of relevant micro-/nanoelectronics.

We have optimized Stillinger-Weber (SW) parameters for silicene, and the new parameters successfully reproduce the low buckling structure of silicene and the phonon dispersion curves from *ab initio* calculations (Zhang et al., 2014). We then calculated the thermal conductivity of silicene by both EMD and NEMD simulations, as well as the anharmonic lattice dynamics (ALD) method. The mode-specific contribution to lattice thermal conductivity is analyzed using the ALD method, and we found that the thermal conductivity of silicene is mainly contributed by phonons with MFP smaller than 10 nm, which is quite different from bulk Si. Moreover, by qualifying the relative contributions of lattice vibrations in different directions, we found that the longitudinal phonon modes dominate the thermal transport in silicene, which is

fundamentally different from graphene, despite the similarity of their 2D honeycomb lattices. We then calculated thermal conductivity of monolayer silicene from first-principles method (Xie et al., 2014). At 300 K, the thermal conductivity of monolayer silicene is found to be 9.4 W/mK and much smaller than bulk Si. The contributions from in-plane and out-of-plane vibrations to thermal conductivity are quantified, and the out-of-plane vibration contributes less than 10% of the overall thermal conductivity, which is different from the results of the similar studies on graphene. The difference is explained by the presence of small buckling, which breaks the reflectional symmetry of the structure. The flexural modes are thus not purely out-of-plane vibration and have strong scattering with other modes. We also conducted investigation of thermal transport in a single-layer silicene sheet under uniaxial stretching (Hu et al., 2013) and hybrid graphene/silicene structures (Jing et al., 2013) with NEMD simulations.

18.3.1.4 One-dimensional materials

Single-component nanowires

Experiments have demonstrated that rough Si nanowires that are 20-300 nm in diameter have Seebeck coefficient and electrical resistivity values that are the same as doped bulk Si, but those with diameters of about 50 nm exhibit 100-fold reduction in thermal conductivity, yielding $ZT \sim 0.6$ at room temperature. For such nanowires, the lattice contribution to thermal conductivity approaches the amorphous limit for Si, which cannot be explained by current theories. Motivated by experiments, Wang et al. (2009) calculated the thermal conductivity of Si nanowires using the NEMD method with the SW potential model and the Nose-Hoover thermostat. The dependence of the thermal conductivity on the wire length, cross-sectional area, and temperature was investigated. The surface along the longitudinal direction was set as a free boundary with potential boundaries in the other directions. The cross-sectional areas of the nanowires ranged from about 5 to 19 nm^2 with lengths ranging from 6 to 54 nm. The thermal conductivity dependence on temperature agrees well with the experimental results. The reciprocal of the thermal conductivity was found to be linearly related to the nanowire length. These results quantitatively show that decreasing the cross-sectional area reduces the phonon mean-free path in nanowires. Martin et al. (2010) modeled thermal properties of artificially rough Si, germanium (Ge), and GaAs NWs based on a perturbative treatment of the interaction between lattice vibrations and surface asperities. This approach, based on a full phonon dispersion in each material, accurately accounts for the frequency dependence of phonon scattering processes resulting from surface roughness, isotope, boundary, and anharmonic decays. The model predicts that for the same diameter and roughness, GaAs and Ge NWs are expected to have approximately 5 times and 10 times lower thermal conductivity than Si NWs, respectively, at room temperature. Later on, we performed NEMD simulations to investigate schemes for enhancing the energy conversion efficiency of Si nanowires (Zhang et al., 2012), including (1) roughening of the nanowire surface, (2) creating nanoparticle inclusions in the nanowires, and (3) coating the nanowire surface with other materials. The enhancement in energy conversion efficiency was inferred from the reduction in thermal conductivity of the nanowire, which was calculated by imposing

a temperature gradient in the longitudinal direction. Compared to pristine nanowires, our simulation results show that the schemes proposed above led to nanocomposite structures with considerably lower thermal conductivity (up to 82% reduction), implying ~5X enhancement in the ZT coefficient. This significant effect appears to have two origins: (1) the increase in phonon-boundary scattering and (2) the onset of interfacial interference. The results suggest new fundamental yet realizable ways to improve markedly the energy conversion efficiency of nanostructured thermoelectrics.

Nanowire-based heterostructures

Recently, we proposed two new concepts to significantly reduce the thermal conductivity of Si-based nanowires in terms of enhancing thermoelectric properties: (1) Si-core Ge-shell nanowire (Hu et al., 2011a,b) and (2) Si/Ge superlattice nanowire (Hu and Poulikakos, 2013a). First, we investigated the effect of Ge coatings on the thermal transport properties of Si nanowires using NEMD simulations. Our results showed that a simple deposition of a Ge shell of cells of only 1 to 2 units in thickness on a single-crystalline Si nanowire can lead to a dramatic 75% decrease in thermal conductivity at room temperature compared to an uncoated Si nanowire. By analyzing the vibrational density states of phonons and the participation ratio of each specific mode, we demonstrated that the reduction in the thermal conductivity of Si/Ge core-shell nanowire stems from the depression and localization of long-wavelength phonon modes at the Si/Ge interface and of high-frequency nonpropagating diffusive modes. After that, we presented main results of an investigation with NEMD simulations on thermal transport in Si/Ge superlattice nanowires, aiming at taking advantage of the inherent one-dimensionality and the combined presence of surface and interfacial phonon scattering to yield ultralow values for their thermal conductivity. Our calculations revealed that the thermal conductivity of a Si/Ge superlattice nanowire varies nonmonotonically with both the Si/Ge lattice periodic length and the nanowire cross-sectional width. The optimal periodic length corresponds to an order of magnitude (92%) decrease in thermal conductivity at room temperature, compared to pristine single-crystalline Si nanowires. We also identified two competing mechanisms governing the thermal transport in superlattice nanowires, responsible for this nonmonotonic behavior: interface modulation in the longitudinal direction significantly depressing the phonon group velocities and hindering heat conduction and coherent phonons occurring at extremely short periodic lengths counteracting the interface effect and facilitating thermal transport. Our results showed trends for superlattice nanowire design for efficient thermoelectrics.

18.3.2 Low interfacial thermal resistance for high-performance electronic cooling

18.3.2.1 Research motivation

Large heat generation and insufficient heat removal mechanisms due to inherent limitations in manufacturing methods and materials employed in electronics comprise one of the crucial challenges hindering the development of disruptive high-power

microelectronic device technologies. In most modern electronics systems (e.g., supercomputers, thermal tower, high-power amplifiers), the electronic device is the warmest element in the system, and waste heat is removed by conduction, spreading, and convection to an appropriate working fluid (e.g., air, water, or a refrigerant) with gradual reductions in the temperature as heat travels through a series of thermal resistances from the source to the ambient. Although large air fans and/or liquid-based cooling solutions have been applied and can dissipate more than 100 W of total power, thermal resistances at multiple interfaces from the die through the heat spreader to the outside heat sink remain a bottleneck. Therefore, fundamental understanding of thermal transport across interfaces (including solid-solid and solid-liquid) is crucial to design and generate high-efficiency thermal management systems.

18.3.2.2 Thermal transport across single interface

The majority of previous research is focused on studying how phonons transport from one material to the other, that is, a single interface. To facilitate heat transfer across interfaces, interfacial nanoengineering seems to hold promise for both experiments and numerical simulations (Hu et al., 2008a, 2009a,b). For solid-solid interfaces, molecular simulations were used to evaluate thermal resistance between crystalline Si and a vertically oriented carbon nanotube (CNT) (Hu et al., 2008b). Without chemical bonds between CNT and Si, the thermal resistance is high and its values are consistent with those measured in experiments on vertical CNT arrays. With chemical bonds, the thermal resistance is reduced by two orders of magnitude, demonstrating significant potential of CNT arrays for thermal management applications. The underlying mechanism for the very large effect of chemical bonding is revealed by simulations of individual phonon scattering across the interface and understood within an analytical solution of a simple spring-mass chain model. For solid-liquid interfaces, later on we proposed two mechanisms that enhance heat dissipation at solid-liquid interfaces investigated from the atomistic point of view using NEMD simulation (Goicochea et al., 2011). The mechanisms include surface functionalization, where –OH terminated headgroups and self-assembled monolayers (SAMs) with different chain lengths are used to recondition and modify the hydrophilicity of silica surface, and vibrational matching between crystalline silica and liquid water, where three-dimensional nanopillars are grown at the interface in the direction of the heat flux with different lengths to rectify the vibrational frequencies of surface atoms. The heat dissipation is measured in terms of the thermal conductance of the solid-liquid interface and is obtained by imposing a one-dimensional heat flux along the simulation domain. A comparison with reported numerical and experimental thermal conductance measurements for similar interfaces indicates that the thermal conductance is enhanced by 1.8 to 3.2 times when the silica surface is reconditioned with hydrophilic groups. The enhancement is further promoted by SAMs, which results in a 20% higher thermal conductance compared with that of the fully hydroxylated silica surface. Likewise, the presence of nanopillars enhances the interface thermal conductance by 2.6 times compared with a bare surface (without nanopillars). Moreover, for different nanopillar densities, the conductance increases linearly with the length of the pillar and saturates at around 4.26 nm. Changes

in the vibrational spectrum of surface atoms and water confinement effects are found to be responsible for the increase in conductance. The modification of surface vibrational states provides a tunable path to enhance heat dissipation, which can also be easily applied to other fluids and interfaces.

18.3.2.3 Thermal transport across multi-interfaces

At nanoscale, sometimes it is possible to incorporate a third material between two different materials to reduce overall thermal resistance. This is realized by taking advantage of phonon confinement and the phonon bridge effect. We first introduced this idea in solid-liquid interfaces. We studied the effect of water nanoconfinement on the thermal transport properties of two neighbor hydrophilic quartz interfaces (Hu et al., 2010b). A significant increase and a nonintuitive, nonmonotonic dependence of the overall interfacial thermal conductance between the quartz surfaces on the water layer thickness were found. By probing the interfacial structure and vibrational properties of the connected components, we demonstrated that the mechanism of the peak occurring at submonolayer water originates from the freezing of water molecules at extremely confined conditions and the excellent match of vibrational states between trapped water and hydrophilic headgroups on the two contact surfaces. Our results showed that incorporation of polar molecules into hydrophilic interfaces is very promising for enhancing the thermal transport through thermally smooth connection of these interfaces.

Later on, for solid-solid interfaces, we studied a model system of SiC/GaN interface (Hu et al., 2011c; Hu and Poulikakos, 2013b). A thin AlN layer was introduced in the GaN-SiC gap to serve as a phonon bridge. The vibrational density of states (VDOS) of Al and N atoms in the low-frequency region (<8 THz) falls between that of Ga and Si atoms. This feature enables the N. . .Al ensemble to serve as a vibrational bridge between the GaN and SiC surfaces. The matched VDOS between N. . .Al and Ga/Si facilitates the thermal transport across the GaN/N. . .Al/SiC interface. Our simulation results indicated that for both epitaxial and nonepitaxial crystal AlN with thickness up to 12.5 nm the overall thermal conductance across the interface is at least 45% to 55% higher than that for a bare surface. $Al_xGa_{1-x}N$ ($0 < x < 1$) heterostructures were also considered to thermally bridge the GaN-SiC interface. It was found that for both epitaxial and nonepitaxial growths, the overall thermal conductance increases monotonically with Al content from the value for pure GaN to that for pure AlN. Furthermore, the conductance for 1 nm thick $Al_xGa_{1-x}N$ only depends on the Al content and is independent of the Al distribution in the heterostructure. However, it is important to stress that the interfacial thermal conductance in possible future experiments is expected to be much lower than that in all theoretical cases studied herein, due to the presence of, for example, impurities and dislocations.

We also proposed a junction structure where the CNT is bonded with a monolayer graphene, which could potentially enhance the interface thermal conductance (Bao et al., 2014). NEMD simulations showed that the interface thermal conductance can be enhanced by at least 40% compared to direct CNTs and Si interfaces with strong covalent bonding, while for weak van der Waals bonding, the conductance

can be enhanced by almost one order of magnitude. The enhancement of thermal conductance is attributed to the efficient thermal transport between the CNT and graphene, as well as the good contact between graphene and Si surface.

18.4 Summary and perspective

The continuous decrease in the size of devices and structures, the increase in their operating speeds and frequencies, and the ever more aggressive thermal conditions imposed upon them requires sophisticated understanding and control of thermal transport at the nanoscale. Today thermal performance itself is a key metric for applications such as thermal barrier coatings, nuclear fuels, and materials for thermoelectric energy conversion. Fundamental understanding of nanoscale thermal transport has resulted from significant advances in experiment, theory, and simulation over the past decades. Modeling and simulation of thermal transport in nanostructures or nanostructured materials and interfacial heat transport has been the focus of numerous computational efforts in the past decade. The most prominent atomistic approach is to use MD simulations where atoms and molecules follow classical dynamics based on the numerical solution of the Newton's second law of motion. The forces between atoms and molecules are derived from interatomic potentials. EMD and NEMD thermal conductivity techniques have shown the power in characterizing either macroscopic or interfacial behavior "integrated" over all vibrations. More information is explicitly needed on the underlying mechanism of heat flow in terms of individual vibrations. Although recently developed phonon dynamics MD (Schelling et al., 2002b) based techniques have proved to be useful, the method has some significant drawbacks: (a) It is restricted to zero temperature, that is, the anharmonic effect where phonon-phonon scattering occurs is lost, and (b) the non-normal incident, which is the general case for realistic interfaces, is very time consuming. In this line, we anticipate that more robust, fast, and efficient methods will be developed in the near future in terms of revealing the contribution of each individual phonon mode and the detailed phonon-phonon scattering in complex structures.

References

Balandin, A.A., 2011. Thermal properties of graphene and nanostructured carbon materials. Nat. Mater. 10, 569–581.

Balandin, A.A., Ghosh, S., Bao, W.Z., Calizo, I., Teweldebrhan, D., Miao, F., Lau, C.N., 2008. Superior thermal conductivity of single-layer graphene. Nano Lett. 8, 902–907.

Bao, H., Shao, C., Luo, S., Hu, M., 2014. Enhancement of interfacial thermal transport by carbon nanotube-graphene junction. J. Appl. Phys. 115, 053524–053527.

Broido, D., Malorny, M., Birner, G., Mingo, N., Stewart, D., 2007. Intrinsic lattice thermal conductivity of semiconductors from first principles. Appl. Phys. Lett. 91, 231922–231923.

Cahangirov, S., Topsakal, M., Akturk, E., Sahin, H., Ciraci, S., 2009. Two- and one-dimensional honeycomb structures of silicon and germanium. Phys. Rev. Lett. 102, 236804.

Chalopin, Y., Volz, S., 2013. A microscopic formulation of the phonon transmission at the nanoscale. Appl. Phys. Lett. 103, 051602–051605.
Esfarjani, K., Chen, G., Stokes, H.T., 2011. Heat transport in silicon from first-principles calculations. Phys. Rev. B 84, 085204–085211.
Feng, B., Ding, Z., Meng, S., Yao, Y., He, X., Cheng, P., Chen, L., Wu, K., 2012. Evidence of silicene in honeycomb structures of silicon on Ag(111). Nano Lett. 12, 3507–3511.
Geim, A.K., Novoselov, K.S., 2007. The rise of graphene. Nat. Mater. 6, 183–191.
Goicochea, J.V., Hu, M., Michel, B., Poulikakos, D., 2011. Surface functionalization mechanisms of enhancing heat transfer at solid-liquid interfaces. J. Heat Transfer 133, 082401–082406.
Guzman-Verri, G.G., Lew Yan Voon, L.C., 2007. Electronic structure of silicon-based nanostructures. Phys. Rev. B 76, 075131.
Hao, Q., Chen, G., Jeng, M.-S., 2009. Frequency-dependent Monte Carlo simulations of phonon transport in two-dimensional porous silicon with aligned pores. J. Appl. Phys. 106, 114321.
He, Y., Savic, I., Donadio, D., Galli, G., 2012. Lattice thermal conductivity of semiconducting bulk materials: atomistic simulations. Phys. Chem. Chem. Phys. 14, 16209–16222.
Hu, M., Poulikakos, D., 2013a. Si/Ge superlattice nanowires with ultralow thermal conductivity. Nano Lett. 13, 5487–5494.
Hu, M., Poulikakos, D., 2013b. Graphene mediated thermal resistance reduction at strongly coupled interfaces. Int. J. Heat Mass Transfer 62, 205–213.
Hu, M., Keblinski, P., Li, B.W., 2008a. Thermal rectification at silicon-amorphous polyethylene interface. Appl. Phys. Lett. 92, 211908.
Hu, M., Keblinski, P., Wang, J.-S., Raravikar, N., 2008b. Interfacial thermal conductance between silicon and a vertical carbon nanotube. J. Appl. Phys. 104, 083503–083504.
Hu, M., Goicochea, J.V., Michel, B., Poulikakos, D., 2009a. Thermal rectification at water/functionalized silica interfaces. Appl. Phys. Lett. 95, 151903.
Hu, M., Keblinski, P., Schelling, P.K., 2009b. Kapitza conductance of silicon-amorphous polyethylene interfaces by molecular dynamics simulations. Phys. Rev. B 79, 104305–104307.
Hu, J., Schiffli, S., Vallabhaneni, A., Ruan, X., Chen, Y.P., 2010a. Tuning the thermal conductivity of graphene nanoribbons by edge passivation and isotope engineering: a molecular dynamics study. Appl. Phys. Lett. 97, 133107.
Hu, M., Goicochea, J.V., Michel, B., Poulikakos, D., 2010b. Water nanoconfinement induced thermal enhancement at hydrophilic quartz interfaces. Nano Lett. 10, 279–285.
Hu, M., Giapis, K.P., Goicochea, J.V., Zhang, X., Poulikakos, D., 2011a. Significant reduction of thermal conductivity in Si/Ge core-shell nanowires. Nano Lett. 11, 618–623.
Hu, M., Zhang, X., Giapis, K.P., Poulikakos, D., 2011b. Thermal conductivity reduction in core-shell nanowires. Phys. Rev. B 84, 085442–085449.
Hu, M., Zhang, X., Poulikakos, D., Grigoropoulos, C.P., 2011c. Large "near junction" thermal resistance reduction in electronics by interface nanoengineering. Int. J. Heat Mass Transfer 54, 5183–5191.
Hu, M., Zhang, X., Poulikakos, D., 2013. Anomalous thermal response of silicene to uniaxial stretching. Phys. Rev. B 87, 195417.
Jeng, M.-S., Yang, R., Song, D., Chen, G., 2008. Modeling the thermal conductivity and phonon transport in nanoparticle composites using Monte Carlo simulation. J. Heat Transfer 130, 042410–042411.
Jia, X., Campos-Delgado, J., Terrones, M., Meuniere, V., Dresselhaus, M.S., 2011. Graphene edges: a review of their fabrication and characterization. Nanoscale 3, 86–95.
Jing, Y., Hu, M., Guo, L., 2013. Thermal conductivity of hybrid graphene/silicon heterostructures. J. Appl. Phys. 114, 153518.

Liu, C.C., Feng, W., Yao, Y., 2011. Quantum spin hall effect in silicene and two-dimensional germanium. Phys. Rev. Lett. 107, 076802–076804.
Majumdar, A., 1993. Microscale heat conduction in dielectric thin films. J. Heat Transfer 115, 7–16.
Martin, P.N., Aksamija, Z., Pop, E., Ravaioli, U., 2010. Reduced thermal conductivity in nanoengineered rough Ge and GaAs nanowires. Nano Lett. 10, 1120–1124.
McGaughey, A.J.H., Jain, A., 2012. Nanostructure thermal conductivity prediction by Monte Carlo sampling of phonon free paths. Appl. Phys. Lett. 100, 061911–061913.
Mingo, N., 2006. Anharmonic phonon flow through molecular-sized junctions. Phys. Rev. B 74, 125402–125413.
Mingo, N., Yang, L., 2003. Phonon transport in nanowires coated with an amorphous material: An atomistic Green's function approach. Phys. Rev. B 68, 245406–245412.
Minnich, A.J., 2012. Determining phonon mean free paths from observations of quasiballistic thermal transport. Phys. Rev. Lett. 109, 205901–205905.
Novoselov, K.S., Geim, A.K., Morozov, S.V., Jiang, D., Zhang, Y., Dubonos, S.V., Grigorieva, I.V., Firsov, A.A., 2004. Electric field effect in atomically thin carbon films. Science 306, 666–669.
Novoselov, K.S., Jiang, Z., Zhang, Y., Morozov, S.V., Stormer, H.L., Zeitler, U., Maan, J.C., Boebinger, G.S., Kim, P., Geim, A.K., 2007. Room-temperature quantum hall effect in graphene. Science 315, 1379.
Ong, Z.-Y., Pop, E., 2011. Effect of substrate modes on thermal transport in supported graphene. Phys. Rev. B 84, 075471–075477.
Peraud, J.-P.M., Hadjiconstantinou, N.G., 2011. Efficient simulation of multidimensional phonon transport using energy-based variance-reduced Monte Carlo formulations. Phys. Rev. B 84, 205331.
Qiu, B., Ruan, X.L., 2012. Reduction of spectral phonon relaxation times from suspended to supported graphene. Appl. Phys. Lett. 100, 193101–193104.
Schelling, P.K., Phillpot, S.R., Keblinski, P., 2002a. Comparison of atomic-level simulation methods for computing thermal conductivity. Phys. Rev. B 65, 144306–144312.
Schelling, P.K., Phillpot, S.R., Keblinski, P., 2002b. Phonon wave-packet dynamics at semiconductor interfaces by molecular-dynamics simulation. Appl. Phys. Lett. 80, 2484–2486.
Takeda, K., Shiraishi, K., 1994. Theoretical possibility of stage corrugation in Si and Ge analogs of graphite. Phys. Rev. B 50, 14916–14922.
Thomas, J.A., Turney, J.E., Iutzi, R.M., Amon, C.H., McGaughey, A.J.H., 2010. Predicting phonon dispersion relations and lifetimes from the spectral energy density. Phys. Rev. B 81, 081411(R).
Tian, W., Yang, R., 2007. Thermal conductivity modeling of compacted nanowire composites. J. Appl. Phys. 101, 054320–054325.
Vogt, P., De Padova, P., Quaresima, C., Avila, J., Frantzeskakis, E., Asensio, M.C., Resta, A., Ealet, B., Le Lay, G., 2012. Silicene: compelling experimental evidence for graphenelike two-dimensional silicon. Phys. Rev. Lett. 108, 155501–155505.
Wang, J.S., Wang, J., Lü, J.T., 2008. Quantum thermal transport in nanostructures. Eur. Phys. J. B 62, 381–404.
Wang, S.-C., Liang, X., Xu, X.-H., Ohara, T., 2009. Thermal conductivity of silicon nanowire by nonequilibrium molecular dynamics simulations. J. Appl. Phys. 105, 014316.
Xie, H., Hu, M., Bao, H., 2014. Thermal conductivity of silicene from first-principles. Appl. Phys. Lett. 104, 131906.
Yamamoto, T., Watanabe, K., 2006. Nonequilibrium Green's function approach to phonon transport in defective carbon nanotubes. Phys. Rev. Lett. 96, 255503–255504.

Zhang, X., Hu, M., Giapis, K.P., Poulikakos, D., 2012. Schemes for and mechanisms of reduction in thermal conductivity in nanostructured thermoelectrics. J. Heat Transfer 134, 102402–102407.

Zhang, X., Xie, H., Hu, M., Bao, H., Yue, S., Qin, G., Su, G., 2014. Thermal conductivity of silicene calculated using an optimized Stillinger-Weber potential. Phys. Rev. B 89, 054310–054317.

The mechanical and electronic properties of two-dimensional superlattices

19

C.V. Ciobanu
Colorado School of Mines, Golden, CO, USA

19.1 Introduction

With the recent advances in controllable growth of large-area, high-quality, two-dimensional (2D) layered materials (e.g., graphene (Bae et al., 2010; Li et al., 2009; Reina et al., 2009; Sun et al., 2010) and hexagonal boron nitride (hBN) (Lee et al., 2012; Song et al., 2010)) on metallic substrates, the field has naturally progressed toward the design and/or investigation of heterostructures based on out-of-plane (Liu et al., 2011; Ramasubramaniam et al., 2011; Wang et al., 2013; Xue et al., 2011; Yang et al., 2013) or in-plane (Ci et al., 2010; Jun et al., 2011; Sutter et al., 2012) stacking of these nanomaterials. Layered heterostructures of graphene on boron nitride offer the best avenue of preserving the exotic properties of graphene and using them in nanoscale devices because of the near-perfect epitaxial lattice match, small van der Waals interactions between graphene and hBN, and most importantly because of the insulating nature of the underlying hBN layer(s).

On the other hand, if a bandgap is necessary for certain applications and if close control of that bandgap over a wide range is desired (so as to fit the different purposes/applications), then in-plane heterostructures or arrangements of domains whose atomic type alternates in the plane may offer a good avenue for creating and controlling the bandgap. New and stable 2D materials, likely based on hybrid domains, offer a way to make available a finer range of key electronic properties such as the bandgap. That range is rather sparse at the moment, with graphene being a semimetallic, hBN insulator with a bandgap of $\sim$5 eV and MoS_2 semiconducting having a gap of $\sim$1.8 eV. The ideas of bandgap control by exploiting the domain width as a control parameter come from the studies of nanoribbons of graphene (Han et al., 2007), in which a bandgap appears due to the presence of edges. This bandgap varies with the width of the nanoribbon; moreover, it can be induced in one spin component and not in the other—a phenomenon commonly referred to half-metallicity (Son et al., 2006). Like graphene nanoribbons (GNRs), the hybrid domains include edges that separate the domains of each type; these edges are multiple and periodic in space, are not reactive (hence more stable), and are expected to produce similar novel electronic properties as well. Indeed, recent density functional theory (DFT) computations on graphene-hBN hybrid heterostructures have revealed half-metallicity in these 2D

Modeling, Characterization and Production of Nanomaterials. http://dx.doi.org/10.1016/B978-1-78242-228-0.00019-3
Copyright © 2015 Elsevier Ltd. All rights reserved.

materials (Pruneda, 2010). This is an important advance, because creating a bandgap in one spin component and not the other is the key to selective electronic transport based on spin (spintronics), which may lead to novel fundamental science and applications in terms of magnetic memories/storage, spin-based logic devices, and possibly others.

In this chapter, we present a brief review of the current state of the hybrid domains in terms of their synthesis and mechanical and electronic properties, which are presented in separate sections below. With excellent mechanical stability and exotic electronic properties, the bottleneck in the large-scale usage of these 2D nanomaterials is probably the current lack of availability of large-scale synthesis techniques with reliable and controllable hybrid-domain dimensions. Nevertheless, given the pace at which the field is moving, it is expected that this desire for reliable, controllable, large-scale synthesis will be fulfilled, as can be inferred from very recent works on interface formation between graphene and hBN (Sutter et al., 2012) and on using graphene edges as templates for the one-dimensional epitaxial growth of hBN domains (Liu et al., 2014).

19.2 Synthesis of 2D hybrid-domain superlattices

The discovery of coherent and sharp in-plane boundaries between graphene and BN domains (Ci et al., 2010) sparked numerous investigations into the synthesis of interfaces between 2D materials and domain structures, along with the detailed characterization of the synthesis process and electronic properties. The reason for these new investigations is the implied potential/promise that new 2D materials and combinations thereof could lead to new physical phenomena, to new ways of synthesizing such nanomaterials, and also to new ways of controlling some of their properties to facilitate the observation of new phenomena and their applications. Indeed, at least as far as the hybrid-domain monolayer is concerned, there are interesting electronic properties associated with the interfaces between graphene and boron nitride, such as the opening of a variable bandgap (He et al., 2010; Jun et al., 2011; Pruneda, 2010), magnetism (Ramasubramaniam and Naveh, 2011), unique thermal transport properties (Jiang et al., 2011), robust half-metallic behavior without applied electric fields (Jun et al., 2011; Pruneda, 2010), and interfacial electronic reconstructions analogous to those observed in oxide heterostructures (Ohtomo and Hwang, 2006). Access to these properties depends on methods for controlling the formation of graphene-boron nitride interfaces within a single atomic layer.

The synthesis approach of Ci et al. was in essence chemical vapor deposition (CVD) performed on copper and using methane and ammonia borane as simultaneous carbon and BN sources, respectively (Ci et al., 2010). The atomic percentage of C was controlled in a desired range, while the B:N ratio was always unity. Subsequent lithographic patterning was performed, along with a suite of characterization experiments (the data from some of which are shown in Figure 19.1). By combining in-plane domains of carbon and BN, a whole range of electronic transport properties could

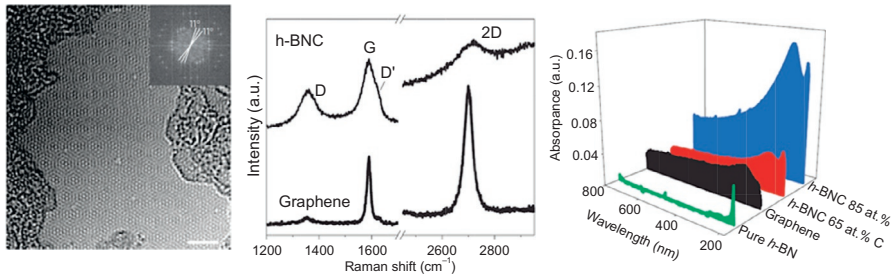

Figure 19.1 Evidence of graphene-BN domain boundaries from Ci et al. (2010). Left: High resolution transmission electron images of moire pattern of hybridizer graphene-BN structure. Middle: Raman spectrum of a hybridized domain structure in comparison to that of graphene. Right: Adsorption spectra of pure hBN, pure graphene, and hybridized domain is varying levels of carbon.
Adapted from Ci et al. (2010), with permission from Nature Publishing Group.

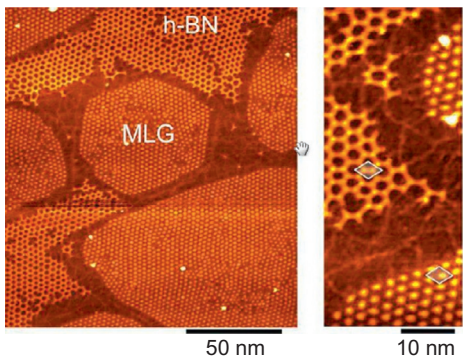

Figure 19.2 Graphene and h-BN domains on Ru(0001), identified by the distinct moiré patterns in scanning tunneling microscopy experiments. In the region between the clearly identified graphene and hBN, any moiré patterns are absent but the substrate is not barren: in that region, the substrate is covered with a C-B-N alloy. From Sutter et al. (2012), with permission from American Chemical Society.

be engineered. It is therefore not surprising that subsequent work has focused on closer control of the interfaces and domains widths. It is not the intent here to review all the subsequent work on the formation and characterization of domains and interfaces between graphene and boron nitride; mentioning several key examples of engineering graphene-BN interfaces will suffice for the purpose of illustrating the degree of control that is currently achievable in experiments.

In recent experiments, Sutter et al. (2012) (see scanning tunneling microscopy images in Figure 19.2), as well as Han et al. (2013) have shown that in-plane monolayer domains of graphene and hBN can form both diffuse interfaces and sharp ones, depending on how one controls the amount of carbon adatoms remaining on the surface during the CVD growth of hBN. In both experiments, the formations of the interfaces were carefully controlled and characterized. This seems to indicate that large-scale production of in-plane superlattices with alternate domains of different atomic/molecular types should not be too far away.

19.3 Mechanical properties of heterostructures

The discovery of graphene (Novoselov et al., 2004) has been followed by observations of a variety of other 2D monolayer crystals (Jin et al., 2009; Novoselov et al., 2005), in particular, hBN. The near-match of the lattice parameters of graphene and BN has triggered theoretical studies of combined graphene-BN ribbons (Ding et al., 2009; Dutta et al., 2009; Pruneda, 2010). More recently, domain-hybridized graphene-BN monolayers have been fabricated (Ci et al., 2010). Meanwhile, still-hypothetical silicon carbide nanoribbons have also been attracting growing interest (Lou and Lee, 2009; Sun et al., 2008; Xu et al., 2010), motivated by the synthesis of silicon carbide nanotubes (Sun et al., 2002). While these studies have been focused on the electronic and magnetic properties, rigorous study on their structural and mechanical properties have only appeared later (Jun, 2008; Jun et al., 2011; Shenoy et al., 2008). We draw our review of mechanical properties from these studies, in particular from that by Jun et al. (2011). In order to tailor their physical and chemical properties for future nanoscale device applications, we need to understand their structural and mechanical properties, in particular their elastic stability.

In this section, we review the fundamental elastic properties and deformation behaviors of the pristine edges in boron nitride and silicon carbide monolayer nanoribbons (BNNR and SiCNR, respectively) and of the domain boundaries in freestanding domain-hybridized graphene-BN monolayer superlattices (CBNSL). Edge and boundary energies have been reported for certain cases (Ci et al., 2010), but these can only provide us with knowledge of chemical stability. To understand their mechanical stability and deformation behavior, we start by determining the edge (or boundary in the case of heterophase domains) stresses for nanoribbons. We present below our first-principles DFT calculations of edge (boundary) energy and stress for nanoribbons (domain superlattices), and we analyze the results in comparison with previous reports on GNRs (Bets and Yakobson, 2009; Huang et al., 2009; Jun, 2008; Shenoy et al., 2008).

Similar to the interface energy and stress in 3D crystals (Cahn and Larche, 1982; Cammarata, 1994), the boundary energy quantifies the cost to form a new boundary separating different domains (i.e., graphene and BN domains), while boundary stress characterizes the work necessary to stretch a pre-existing boundary along the boundary direction. As a brief definition, the boundary energy is the total excess energy (with respect to individual bulk 2D crystals) possessed by all atoms in the vicinity of the boundary, per unit boundary length. On the other hand, the boundary stress characterizes the work per unit boundary length needed to deform a boundary by elastically straining both monolayer domains by the same amount of strain along the boundary direction (Cammarata, 1994). The relationship between boundary energy σ and boundary stress h is similar to the Shuttleworth relation (Shuttleworth, 1950) and is written as

$$h = \sigma + \frac{\mathrm{d}\sigma}{\mathrm{d}e}$$

where h and the strain e are scalar quantities because we only consider one-dimensional deformation along the straight line of boundary. We note that e is the elastic strain applied to the boundary across which the lattices of both 2D crystal phases are already matched. We do not include in the boundary energy the strain that is required to match one lattice with another. We have confirmed that this mismatch strain makes less than 2% difference in the boundary energy values because the difference between the lattice parameters of perfect graphene and BN phases is sufficiently small. The above equation also applies to the relation between edge energy and edge stress.

Boundary energies are calculated from the total-energy difference between model systems with and without a boundary, and boundary stresses are obtained by numerical differentiation of the boundary energy calculated at a series of strain values within the elastic range. The total-energy calculation is thus the main numerical procedure in this work. Total-energy DFT calculations were performed using the program SIESTA (Soler et al., 2002) based on local density approximation, with pseudopotentials and basis set functions similar to those used in earlier work by Jun (2008). An energy cutoff of 250 Ry was set for the real-space integrations. The atomic positions were relaxed via the conjugate gradient procedure with force tolerances set to 0.02 eV/Å. We have first obtained the lattice constants of perfect graphene (2.468 Å), hBN (2.492 Å), and SiC (3.081 Å) monolayers; these values agree well with previous reports, for example, 2.465 Å for graphene (Reich et al., 2002a,b), 2.49 Å for BN (Jin et al., 2009), and 3.094 Å for 2D SiC (Bekaroglu et al., 2010).

We considered two types of boundary models, armchair and zigzag, depending on the way in which the two phases face each other at the C-BN boundary. Experimental fabrication of domain-hybridized graphene-BN monolayers revealed that the local atomic structure of heterophase boundaries is either armchair or zigzag, although at large-length scales the boundary has an arbitrary shape (Ci et al., 2010). Two examples of supercells with domain boundaries for armchair and zigzag graphene-BN superlattices (aCBNSL22 and zCBNSL12, respectively) are shown in Figure 19.3. We have used various supercell widths of up to ~80 Å for armchair and up to ~86 Å for zigzag models. The numbers in our naming scheme follow the convention for nanoribbons and thus give the supercell width as the number of dimers in armchair models or as the number of zigzag lines in zigzag supercells. In the out-of-plane direction of all supercells, we insert a vacuum spacing of 15 Å to the interactions between periodic images; a 15 Å vacuum spacing is also introduced along one in-plane direction for nanoribbon models. We kept the same number of dimer (or zigzag) lines for the graphene and BN domains in a supercell; however, it is expected that varying independently the widths of the two domains will provide a valuable additional degree of control.

For the C-BN superlattice models, we computed the boundary energy as

$$\sigma = \frac{E_T - N_C E_C - N_{BN} E_{BN}}{2L}$$

where E_T is the total energy of a model supercell that has N_C number of carbon atoms and N_{BN} number of boron-nitrogen pairs. L is the length of the boundary, E_C is the energy per atom in perfect graphene, and E_{BN} is the energy per B-N pair in a perfect

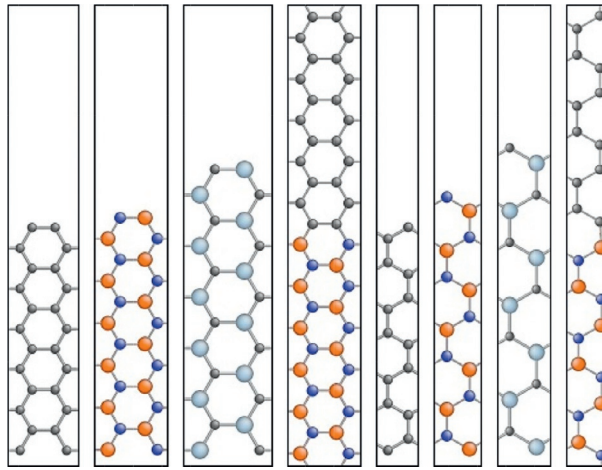

Figure 19.3 Typical supercell models for nanoribbons and domain supperlattices before relaxation. (From left to right) Armchair graphene nanoribbon (aGNR12), armchair BN nanoribbon (aBNNR12), armchair SiC nanoribbon (aSiCNR12), armchair graphene-BN superlattice (aCBNSL22), zigzag graphene nanoribbon (zGNR07), zigzag BN nanoribbon (zBNNR07), zigzag SiC nanoribbon (zSiCNR07), and zigzag graphene-BN superlattice (zCBNSL12).
Reproduced from Jun et al. (2011) with permission of American Physical Society.

BN monolayer. Without the term of E_{BN} (E_C), the excess energy σ becomes the edge energy of a graphene (boron nitride) nanoribbon. To calculate the energy of one carbon atom in perfect graphene, or one BN or SiC pair in perfect hBN or perfect SiC, respectively, we employed their fully periodic four-atom unit cells and chose $16 \times 16 \times 1$ ($24 \times 24 \times 1$ for SiC) k-point mesh by the Monkhorst-Pack scheme. This k-point sampling was scaled according to the size of supercells. Typical nanoribbon models having pristine armchair and zigzag edges are also shown in Figure 19.3. Elastic properties of graphene edges have also been reported in other works (Bets and Yakobson, 2009; Huang et al., 2009; Jun, 2008; Shenoy et al., 2008).

In Figure 19.4, we present our numerical results of edge (boundary) energy and stress for all models with respect to the width of ribbon (stripe). As the first observation, the boundary and edge energies show little dependence on the widths. The width-averaged edge (and boundary) energy and stress values are summarized in Table 19.1. From plane-wave-based DFT calculations, Huang et al. (2009) have reported graphene edge energies of $\sim$1.00 and $\sim$1.40 eV/Å for armchair and zigzag edges, respectively, which are somewhat smaller than our values (1.190 and 1.490 eV/Å, respectively). Plane-wave-based DFT calculations have also lead to a value of 0.29 eV/Å zigzag boundary energy in graphene-BN domain superlattices (Ci et al., 2010), which agrees well with our average value of 0.293 eV/Å.

For both armchair and zigzag cases, boundary energies are substantially lower than edge energies of pristine graphene, BN, and SiC nanoribbons due to the absence of

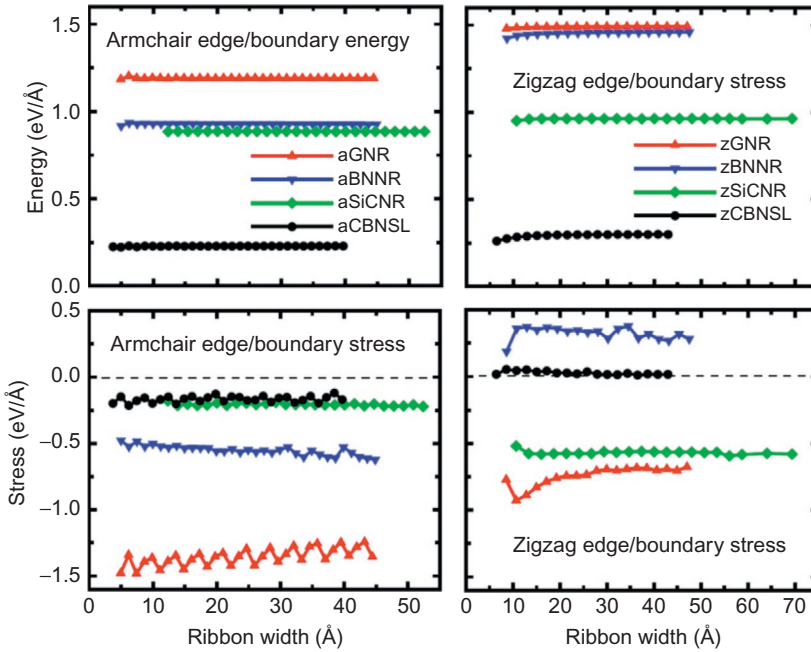

Figure 19.4 Edge/domain-boundary energy and stress as functions of the nanoribbon/stripe width.
Reproduced from Jun et al. (2011) with permission from American Physical Society.

Table 19.1 Average edge/boundary energy and stress (eV/Å)

	Edge/boundary energy		Edge/boundary stress	
	Armchair	**Zigzag**	**Armchair**	**Zigzag**
GNR	1.190	1.490	−1.355	−0.743
BNR	0.927	1.453	−0.552	+0.323
SiCNR	0.885	0.962	−0.207	−0.507
CBNSL	0.228	0.293	−0.167	+0.027

dangling bonds at the boundary. It is known that the armchair edge energy of GNR is lower than its zigzag counterpart. We note the same trend in other ribbon edges and graphene-BN boundaries. However, the physical origins of these lower armchair energies are somewhat different. The difference of edge energy between armchair and zigzag GNRs is approximately 0.300 eV/Å. This relatively large difference comes from the fact that along armchair edge the edge-parallel C–C bond is relaxed to a shorter length than that of interior C–C bond, due to the strong pair of the *sp* hybridization, which results in the healing of the dangling-bond nature of the armchair edge carbon

dimers (Okada, 2008). In contrast, the zigzag edge does not significantly change its atomic structure after relaxation, and thus it does not substantially reduce the high edge energy caused by dangling bonds.

The edge energy difference between armchair and zigzag becomes even larger for BNNRs. After relaxation, the armchair edge in graphene still maintains the hexagonal lattice structure fairly well in spite of the shortened C–C bond. However, in the armchair BNNR (SiCNR as well), the edge hexagons are distorted so significantly that the original hexagonal symmetry is broken (we show such distorted hexagons of armchair BN and SiC ribbons in a subsequent figure, when we discuss edge stresses). Such distortion provides the armchair BN edge with the opportunity to reduce energy by further relaxing its edge structure while such relaxation is not present for zigzag BN edges. On the other hand, the difference of edge energies between armchair and zigzag SiCNRs is not as large as GNRs and BNNRs. The originally edge-parallel Si–C bond was shortened by 4.93% while those of GNR and BNNR were 12.20% and 9.91% shortened. We therefore believe that the dangling-bond healing effect is less significant in armchair SiCNR edges and that the distortion of edge hexagons is the main source of lowering the armchair edge energy of SiCNR. The boundary energy difference between armchair and zigzag boundaries is remarkably smaller, 0.065 eV/Å, than the above two cases of graphene and BN edges. In our superlattice models of both armchair and zigzag boundaries, we could not observe any obvious change in lattice structure and atomic positions after relaxation, even in the vicinity of boundary. Therefore, the absence of dangling bonds is the key physical reason for which the armchair and zigzag boundaries have similar energies in CBNSL.

The lower two panels of Figure 19.4 show our results of edge (boundary) stress calculations for armchair and zigzag edges (boundaries). Determinations of BNNR and SiCNR edge stresses and CBNSL boundary stresses have not been previously reported, because only reports of GNR edge stresses are present in the literature so far (Bets and Yakobson, 2009; Huang et al., 2009; Jun, 2008; Shenoy et al., 2008). Edge (boundary) stresses are seen to depend more sensitively on the width of the ribbon (stripe) than the edge (boundary) energies. The average stress values are given in Table 19.1. Our edge stress values for GNR are comparable with those (-1.45 eV/Å for armchair and -0.7 eV/Å for zigzag) obtained using plane-wave basis (Huang et al., 2009). We note that the edge stress of pristine zBNNR is positive. However, all other edges have negative stress values. This means that they are in compression and that their edges tend to ripple whenever they are free to deform at a finite temperature (Shenoy et al., 2008). In contrast, the bare zigzag edge of BNNR is in tension and tends to shorten relative to the interior domain. Therefore, rippling is likely to take place at the interior domain of BN ribbon, away from the zigzag edge, while the edge itself will stay straight.

There are two different types of pristine zigzag edges of BNNR, B-terminated, and N-terminated edges. If one edge side is B-ended, then the other side is N-ended. Because the charge densities of N- and B-terminated edges are substantially different, their edge energies and edge stresses are quite different as well, and consequently these two pristine zigzag edges may deform in distinct ways. The edge energy and stress presented for zBNNR in Table 19.1 are the average values between these

two zigzag edge types. This argument also applies to the zigzag edge of SiCNR and to the zigzag boundary of CBN superlattice.

To verify the distinct behaviors of zigzag edges with different terminations, we calculate edge stresses of both sides separately. Because DFT approaches are unable to yield separate edge energies, we performed energy minimizations and classical molecular dynamics simulations using the Tersoff potential (Tersoff, 1989) for Si–C systems. Because the Tersoff potential energy is a sum over (environment-dependent) contributions of individual atoms, summing the individual atomic contributions over sufficient distance from the edge leads to edge-specific energies upon subtraction of the contributions of same atoms in bulk-like (edge-free) configurations. The edge energies and stresses calculated using the Tersoff potential are virtually independent of the ribbon width. The edge energy of C-side (Si-side) zigzag edge is 0.559 (0.596) eV/Å, and their average value is 0.577 eV/Å. The edge stress of C-side (Si-side) zigzag edge is −0.587 (−0.222) eV/Å while the average value of zigzag edge stress is −0.406 eV/Å. Although this average edge stress value is somewhat lower than that obtained by DFT calculations (−0.570 eV/Å), our empirical potential calculations clearly evidence that the C-side zigzag edge has a higher compressive edge stress value than Si-side edge. This implies that the C edge has a higher rippling tendency than the Si edge, which we have also confirmed by constant-temperature molecular dynamics simulations at 300 K. A snapshot of a large SiC monolayer with 18,718 atoms (dimensions of 320.22 Å × 240.34 Å) is shown in the bottom inset of Figure 19.5, which verifies the more frequent rippling (higher compressive stress) of the C-ended zigzag edge.

One of our findings is that the boundary stresses in graphene-BN superlattices are significantly lower than the edge stresses of the GNR and BNNR. Our results of −0.167 eV/Å for armchair and +0.027 eV/Å for zigzag boundaries are even lower than the edge stresses of hydrogen-passivated graphene edges, −0.35 eV/Å (armchair) and +0.13 eV/Å (zigzag) reported earlier (Huang et al., 2009). This strongly suggests that C-BN superlattice boundaries experience very low stress, and therefore they do not have a tendency to ripple within a hybrid-domain heterostructure. We predict that

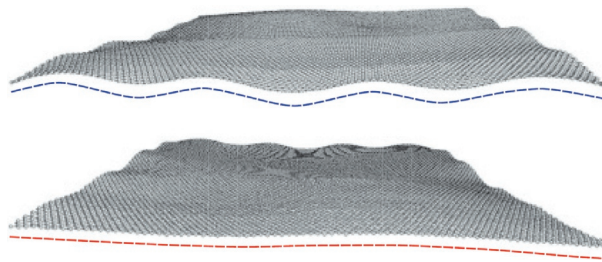

Figure 19.5 Deformation behaviors of (top) C-terminated and (bottom) Si-terminated zigzag edges in a SiC monolayer, simulated via constant-temperature molecular dynamics using the Tersoff interatomic potentials. Rippling patterns correctly reflect the edge stress values of C-terminated (−0.587 eV/Å) and Si-terminated (−0.222 eV/Å) edges. Dash lines are a guide to the eye.
Reproduced from Jun et al. (2011) with permission from American Physical Society.

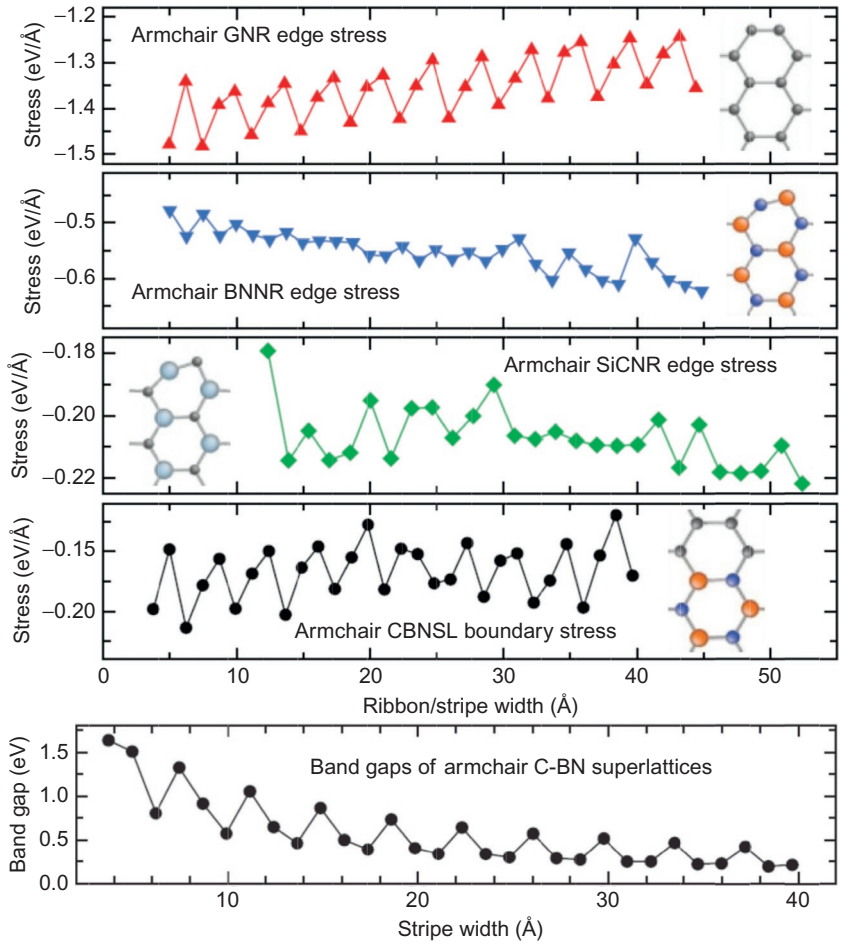

Figure 19.6 Top four panels correspond to armchair edge/boundary stresses as functions of ribbon/stripe width. Insets show the relaxed structures at the corresponding edges or domain boundaries. The lowest panel shows results of the oscillating bandgaps of C-hBN superlattices with respect to the domain (stripe) width.
Reproduced from Jun et al. (2011) with permission from American Physical Society.

the existence of domain boundaries in graphene-BN monolayer structures will cause neither structural change nor severe deformation.

Another interesting result is the oscillating behavior of boundary energy and stress in armchair CBN superlattices as functions of stripe width. It has been known that the values of armchair graphene edge energy and stress oscillate as the ribbon width is increased (Huang et al., 2009; Wassmann et al., 2010), and that the oscillating period is every three ribbon widths (three-family pattern) (Huang et al., 2009). This oscillating behavior is closely related to the energy bandgap of the three-family pattern that has been found in H-passivated semiconducting armchair GNRs and understood in the framework of topological analysis of armchair edges (Son et al., 2006). In Figure 19.6,

we present magnified plots for the stresses of four armchair models. Boundary stresses follow a similar three-family pattern. As shown in the bottom panel of Figure 19.6, we confirm that armchair graphene-hBN superlattices are semiconducting and their bandgaps depend on the stripe width following a three-fold pattern.

In contrast to armchair CBNSL and GNR, the edge energies and stresses of armchair BNNR and SiCNR do not exhibit a clear three-family pattern in their oscillations because the shapes of edge hexagons are distorted after relaxation, as shown in the insets of Figure 19.6. Park and Louie (2008) reported the oscillating energy bandgap of BNNRs with armchair edges, but in their work the edges were passivated and thus the original shape of the edge hexagons was preserved. However, the pristine armchair BN (SiC) edge changes its configuration significantly, and the edge B–N (Si–C) bond is no longer parallel with the edge direction. Consequently, the topological analysis does not apply anymore. This broken hexagonal symmetry eliminates the three-family pattern and results in irregular fluctuation of edge stress values of armchair BN and SiC nanoribbons.

19.4 Electronic properties of hybrid-domain superlattices

The key property of these superlattices appears for those with zigzag edges and consists in different bandstructures for the two spin components. Figure 19.7, from a recent report of Pruneda (2010) shows the variation of the bandgap for the two spin components.

If the graphene domains are large, then the (expected) semimetallic behavior is recovered. In the other limit, in which the graphene domains are narrow, the antiferromagnetic state becomes unstable, and with it the system becomes nonmagnetic and insulating. As seen in Figure 19.7, there is a range of domain widths in which the system is metallic in the spin-down component and semiconducting in the spin-up component. Based on DFT calculations, Pruneda has provided an

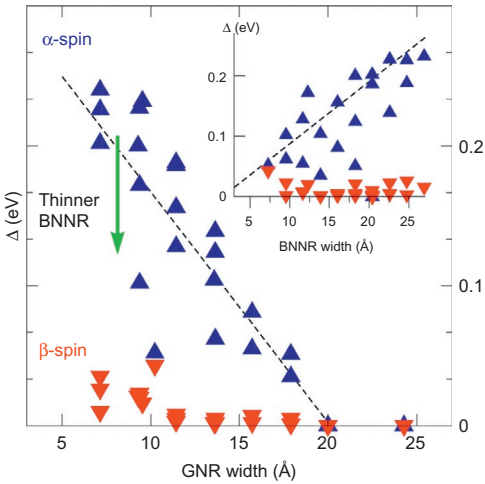

Figure 19.7 Bandgaps for the spin-up component (▲) and spin-down component (▼) as functions of the stripe width in the antiferromagnetic ground state for the graphene-hBN superlattices. The green arrow shows the dependence of the spin-up bandgap on the width of the BN strip.
From Pruneda (2010), with permission of American Physical Society.

explanation for the half-metallicity of the hybrid-domain superlattices (Pruneda, 2010): The magnetic properties of the stripe edges of graphene, coupled with the polarity of the BN stripes, lead to asymmetries in the spin screening, thereby inducing an electronic rearrangement ("reconstruction") at the domain edges. As seen in Figure 19.7, the bandgap in the spin-up component can be as high as 0.3 eV, while the other spin component can be metallic. This finding is anticipated to lead to very interesting phenomena at the 1D domain interfaces, phenomena that may include even superconductivity (by analogy with 2D interfaces in perovskites). Furthermore, electronic conduction is expected to be highly anisotropic, especially within the hBN domains.

Another interesting property of this very system, that is, the graphene-BN domain superlattice, is the very large Seebeck coefficient that can be achieved (Yokomizo and Nakamura, 2013). This coefficient is crucial in characterizing the efficiency of thermoelectric conversion and is the primary indicator of a large thermoelectric figure of merit. While the physical origins of this increase in the Seebeck coefficient are not fully understood, the coefficient has been computed for a wide range of graphene-BN superlattices, and its dependence on the stripe width is known. The key to achieve it is a low width for the hBN, which seems to be the factor that has most effect regarding the deviation of the Seebeck coefficient from the value corresponding to pure graphene.

Structurally, the domain boundaries (while not very reactive in a chemical sense) have shown promise as templates for 1D nanostructures (essentially wires or very small atomic clusters) grown on top of the graphene-BN superlattices. In a recent work, Haldar and coworkers (2013) have calculated the diffusion barriers of Fe atoms on such superlattices. They have shown that iron atoms diffuse much more easily on BN than on graphene and that during only a few picoseconds at room temperature they diffuse across the C-N domain boundary to get trapped at the C-B boundaries. Furthermore, Haldar et al. showed that the magnetic exchange coupling between Fe clusters at C-B domain boundaries varies nonmonotonically as a function of the hBN stripe width. These superlattices can therefore act as templates for the spontaneous formation of magnetic nanostructures at specific interfaces.

Last, we mention that Bristowe et al. (2013) have predicted half-metallic 1D interfaces between two insulating domains, made, for example, from several II-VI, III-V, and IV-IV compounds, whose stable bulk phase is wurtzite but that may assume highly planar phases in atomically thin films. These authors show, expectedly, that 1D domain boundaries in these insulator-insulator superlattices are polar, having a net excess charge determined from using the formal valence charges of the atomic species involved, irrespective of the predominant covalent character of the bonding in these materials. Furthermore, they rationalize such findings by analyzing the topology of the formal polarization lattice in the parent bulk materials. DFT calculations similar to those in Pruneda (2010) show an electronic compensation mechanism due to a Zener-like charge transfer between interfaces of opposite polarity. The emergence of one-dimensional electron and hole gases, which in some cases are ferromagnetic half-metallic, is predicted (Bristowe et al., 2013).

19.5 Perspectives and concluding remarks

In conclusion, we have reviewed recent reports on the mechanical and electronic properties of hybrid-domain superlattices. In terms of mechanical properties, we have shown that a key quantity characterizing the stability and "flatness" of a domain boundary is the domain boundary stress. Calculating the stresses is rather straightforward, with rapid meaningful conclusions for the stability of the domain edges. We have found that the C-BN boundaries experience very little stress and thus the existence of such domain boundaries will cause neither structural change nor severe deformation in C-BN superlattices. The oscillating values of armchair boundary stress indicate that armchair CBNSL may be semiconducting. Furthermore, it is shown that the broken hexagonal symmetry of armchair BN and SiC ribbons results in their irregularly oscillating stress values as functions of ribbon width. Last, we have shown that two types of zigzag edges in SiC nanoribbons undergo distinctly different deformations; we have also shown that the two types of zigzag edges in SiC nanoribbons undergo distinctly different deformations.

In terms of electronic properties, three major ones stand out, all of which dependent on the size of the domain widths: (a) half-metallicity, (b) edge magnetism, and (c) giant Seebeck coefficient. These properties pertain to graphene-hBN superlattices, although it is expected that conditions favorable to their occurrence can be met in superlattices made of other materials as well (Bristowe et al., 2013). These exotic properties, along with their immediate "control knobs" (domain widths), are evolving into a new niche in the field of 2D materials. Fundamental and technological advances based on these properties are expected to rapidly take off in the near future, and we expect that an enhanced understanding of the transport at the interface will lead to game-changing paradigms as far as the miniaturization of the nanoelectronic devices is concerned.

Acknowledgments

I would like to thank Dr. Tewary for his kind invitation to write this chapter and to the staff at Woodhead Publishing for their unmatched patience and professionalism. I am indebted to my coauthors of Jun et al. (2011), the late Prof. S. Jun, X. Li, and F. Meng, most of which has been included in Section 19.3 of this chapter. Various parts of this work have benefited from the financial support of the National Science Foundation through Grants Nos CMMI-0856250, -0825592, -0846858.

References

Bae, S., Kim, H., Lee, Y., Xu, X., Park, J.-S., Zheng, Y., Balakrishnan, J., Lei, T., Kim, H.R., Song, Y.I., Kim, Y.-J., Kim, K.S., Ozyilmaz, B., Ahn, J.-H., Hong, B.H., Iijima, S., 2010. Roll-to-roll production of 30-inch graphene films for transparent electrodes. Nat. Nanotechnol. 5, 574–578.

Bekaroglu, E., Topsakal, M., Cahangirov, S., Ciraci, S., 2010. First-principles study of defects and adatoms in silicon carbide honeycomb structures. Phys. Rev. B 81, 075433.

Bets, K.V., Yakobson, B.I., 2009. Spontaneous twist and intrinsic instabilities of pristine graphene nanoribbons. Nano Res. 2, 161–166.

Bristowe, N.C., Stengel, M., Littlewood, P.B., Artacho, E., Pruneda, J.M., 2013. One-dimensional half-metallic interfaces of two-dimensional honeycomb insulators. Phys. Rev. B 88, 161411.

Cahn, J.W., Larche, F., 1982. Surface stress and the chemical-equilibrium of small crystals. 2. Solid particles embedded in a solid matrix. Acta Metall. 30, 51–56.

Cammarata, R.C., 1994. Surface and interface stress effects in thin-films. Prog. Surf. Sci. 46, 1–38.

Ci, L., Song, L., Jin, C., Jariwala, D., Wu, D., Li, Y., Srivastava, A., Wang, Z.F., Storr, K., Balicas, L., Liu, F., Ajayan, P.M., 2010. Atomic layers of hybridized boron nitride and graphene domains. Nat. Mater. 9, 430–435.

Ding, Y., Wang, Y., Ni, J., 2009. Electronic properties of graphene nanoribbons embedded in boron nitride sheets. Appl. Phys. Lett. 95, 123105.

Dutta, S., Manna, A.K., Pati, S.K., 2009. Intrinsic half-metallicity in modified graphene nanoribbons. Phys. Rev. Lett. 102, 096601.

Haldar, S., Srivastava, P., Eriksson, O., Sen, P., Sanyal, B., 2013. Designing Fe nanostructures at graphene/h-BN interfaces. J. Phys. Chem. C 117, 21763–21771.

Han, M.Y., Ozyilmaz, B., Zhang, Y.B., Kim, P., 2007. Energy band-gap engineering of graphene nanoribbons. Phys. Rev. Lett. 98, 206805.

Han, G.H., Rodriguez-Manzo, J.A., Lee, C.W., Kybert, N.J., Lerner, M.B., Qi, Z.J., Dattoli, E. N., Rappe, A.M., Drndic, M., Johnson, A.T.C., 2013. Continuous growth of hexagonal graphene and boron nitride in-plane heterostructures by atmospheric pressure chemical vapor deposition. ACS Nano 7, 10129–10138.

He, J., Chen, K.-Q., Fan, Z.-Q., Tang, L.-M., Hu, W.P., 2010. Transition from insulator to metal induced by hybridized connection of graphene and boron nitride nanoribbons. Appl. Phys. Lett. 97, 193305.

Huang, B., Liu, M., Su, N., Wu, J., Duan, W., Gu, B.-l., Liu, F., 2009. Quantum manifestations of graphene edge stress and edge instability: a first-principles study. Phys. Rev. Lett. 102, 166404.

Jiang, J.-W., Wang, J.-S., Wang, B.-S., 2011. Minimum thermal conductance in graphene and boron nitride superlattice. Appl. Phys. Lett. 99, 043109.

Jin, C., Lin, F., Suenaga, K., Iijima, S., 2009. Fabrication of a freestanding boron nitride single layer and its defect assignments. Phys. Rev. Lett. 102, 195505.

Jun, S., 2008. Density-functional study of edge stress in graphene. Phys. Rev. B 78, 073405.

Jun, S., Li, X., Meng, F., Ciobanu, C.V., 2011. Elastic properties of edges in BN and SiC nanoribbons and of boundaries in C-BN superlattices: a density functional theory study. Phys. Rev. B 83, 153407.

Lee, K.H., Shin, H.-J., Lee, J., Lee, I.-Y., Kim, G.-H., Choi, J.-Y., Kim, S.-W., 2012. Large-scale synthesis of high-quality hexagonal boron nitride nanosheets for large-area graphene electronics. Nano Lett. 12, 714–718.

Li, X., Cai, W., An, J., Kim, S., Nah, J., Yang, D., Piner, R., Velamakanni, A., Jung, I., Tutuc, E., Banerjee, S.K., Colombo, L., Ruoff, R.S., 2009. Large-area synthesis of high-quality and uniform graphene films on copper foils. Science 324, 1312–1314.

Liu, Z., Song, L., Zhao, S., Huang, J., Ma, L., Zhang, J., Lou, J., Ajayan, P.M., 2011. Direct growth of graphene/hexagonal boron nitride stacked layers. Nano Lett. 11, 2032–2037.

Liu, L., Park, J., Siegel, D.A., McCarty, K.F., Clark, K.W., Deng, W., Basile, L., Idrobo, J.C., Li, A.P., Gu, G., 2014. Heteroepitaxial growth of two-dimensional hexagonal boron nitride templated by graphene edges. Science 343, 163–167.

Lou, P., Lee, J.Y., 2009. Band structures of narrow zigzag silicon carbon nanoribbons. J. Phys. Chem. C 113, 12637–12640.

Novoselov, K.S., Geim, A.K., Morozov, S.V., Jiang, D., Zhang, Y., Dubonos, S.V., Grigorieva, I.V., Firsov, A.A., 2004. Electric field effect in atomically thin carbon films. Science 306, 666–669.

Novoselov, K.S., Jiang, D., Schedin, F., Booth, T.J., Khotkevich, V.V., Morozov, S.V., Geim, A.K., 2005. Two-dimensional atomic crystals. Proc. Natl. Acad. Sci. U. S. A. 102, 10451–10453.

Ohtomo, A., Hwang, H.Y., 2006. A high-mobility electron gas at the $LaAlO_3/SrTiO_3$ heterointerface (vol. 427, p. 423, 2004). Nature 441, 120.

Okada, S., 2008. Energetics of nanoscale graphene ribbons: edge geometries and electronic structures. Phys. Rev. B 77, 041408.

Park, C.-H., Louie, S.G., 2008. Energy gaps and Stark effect in boron nitride nanoribbons. Nano Lett. 8, 2200–2203.

Pruneda, J.M., 2010. Origin of half-semimetallicity induced at interfaces of C-BN heterostructures. Phys. Rev. B 81, 161409.

Ramasubramaniam, A., Naveh, D., 2011. Carrier-induced antiferromagnet of graphene islands embedded in hexagonal boron nitride. Phys. Rev. B 84, 075405.

Ramasubramaniam, A., Naveh, D., Towe, E., 2011. Tunable band gaps in bilayer graphene-BN heterostructures. Nano Lett. 11, 1070–1075.

Reich, S., Maultzsch, J., Thomsen, C., Ordejon, P., 2002a. Tight-binding description of graphene. Phys. Rev. B 66, 035412.

Reich, S., Thomsen, C., Ordejon, P., 2002b. Elastic properties of carbon nanotubes under hydrostatic pressure. Phys. Rev. B 65, 153407.

Reina, A., Jia, X., Ho, J., Nezich, D., Son, H., Bulovic, V., Dresselhaus, M.S., Kong, J., 2009. Large area, few-layer graphene films on arbitrary substrates by chemical vapor deposition. Nano Lett. 9, 30–35.

Shenoy, V.B., Reddy, C.D., Ramasubramaniam, A., Zhang, Y.W., 2008. Edge-stress-induced warping of graphene sheets and nanoribbons. Phys. Rev. Lett. 101, 245501.

Shuttleworth, R., 1950. The surface tension of solids. Proc. Phys. Soc. A 63, 444.

Soler, J.M., Artacho, E., Gale, J.D., Garcia, A., Junquera, J., Ordejon, P., Sanchez-Portal, D., 2002. The SIESTA method for ab initio order-N materials simulation. J. Phys. Condens. Matt. 14, 2745–2779.

Son, Y.-W., Cohen, M.L., Louie, S.G., 2006. Energy gaps in graphene nanoribbons. Phys. Rev. Lett. 97, 216803.

Song, L., Ci, L., Lu, H., Sorokin, P.B., Jin, C., Ni, J., Kvashnin, A.G., Kvashnin, D.G., Lou, J., Yakobson, B.I., Ajayan, P.M., 2010. Large scale growth and characterization of atomic hexagonal boron nitride layers. Nano Lett. 10, 3209–3215.

Sun, X.H., Li, C.P., Wong, W.K., Wong, N.B., Lee, C.S., Lee, S.T., Teo, B.K., 2002. Formation of silicon carbide nanotubes and nanowires via reaction of silicon (from disproportionation of silicon monoxide) with carbon nanotubes. J. Am. Chem. Soc. 124, 14464–14471.

Sun, L., Li, Y., Li, Z., Li, Q., Zhou, Z., Chen, Z., Yang, J., Hou, J.G., 2008. Electronic structures of SiC nanoribbons. J. Chem. Phys. 129, 174114.

Sun, Z., Yan, Z., Yao, J., Beitler, E., Zhu, Y., Tour, J.M., 2010. Growth of graphene from solid carbon sources. Nature 468, 549–552.

Sutter, P., Cortes, R., Lahiri, J., Sutter, E., 2012. Interface formation in monolayer graphene-boron nitride heterostructures. Nano Lett. 12, 4869–4874.

Tersoff, J., 1989. Modeling solid-state chemistry—interatomic potentials for multicomponent systems. Phys. Rev. B 39, 5566–5568.

Wang, M., Jang, S.K., Jang, W.-J., Kim, M., Park, S.-Y., Kim, S.-W., Kahng, S.-J., Choi, J.-Y., Ruoff, R.S., Song, Y.J., Lee, S., 2013. A platform for large-scale graphene electronics—CVD growth of single-layer graphene on CVD-grown hexagonal boron nitride. Adv. Mater. 25, 2746–2752.

Wassmann, T., Seitsonen, A.P., Saitta, A.M., Lazzeri, M., Mauri, F., 2010. Clar's theory, pi-electron distribution, and geometry of graphene nanoribbons. J. Am. Chem. Soc. 132, 3440–3451.

Xu, B., Yin, J., Xia, Y.D., Wan, X.G., Liu, Z.G., 2010. Ferromagnetic and antiferromagnetic properties of the semihydrogenated SiC sheet. Appl. Phys. Lett. 96, 143111.

Xue, J., Sanchez-Yamagishi, J., Bulmash, D., Jacquod, P., Deshpande, A., Watanabe, K., Taniguchi, T., Jarillo-Herrero, P., Leroy, B.J., 2011. Scanning tunnelling microscopy and spectroscopy of ultra-flat graphene on hexagonal boron nitride. Nat. Mater. 10, 282–285.

Yang, W., Chen, G., Shi, Z., Liu, C.-C., Zhang, L., Xie, G., Cheng, M., Wang, D., Yang, R., Shi, D., Watanabe, K., Taniguchi, T., Yao, Y., Zhang, Y., Zhang, G., 2013. Epitaxial growth of single-domain graphene on hexagonal boron nitride. Nat. Mater. 12, 792–797.

Yokomizo, Y., Nakamura, J., 2013. Giant Seebeck coefficient of the graphene/h-BN superlattices. Appl. Phys. Lett. 103, 113901.

Nanostructured two-dimensional materials

20

S. Zhuiykov
CSIRO, Materials Science and Engineering Division, Highett, VIC, Australia

20.1 Layered two-dimensional semiconductors as competitive rivals of graphene

20.1.1 Properties of two-dimensional semiconductor nanocrystals

Development of new ultrathin nanostructured materials that retain a high level of processability and possess high charge carrier mobility is imperative for the next generation of advanced functional devices. Both graphene and two-dimensional (2D) semiconductors can address the challenge of miniaturization and thus offer exciting new possibilities (Zhuiykov, 2014). The real technology-push strategy was definitely provided after the 2010 Noble Prize in Physics for graphene. However, apart from graphene, other 2D nanomaterials have steadily attracted significant interest in the research community (Butler et al., 2013). So far, they have exhibited intriguing physical properties, quantum confinement effects at the few-layer limit, and exciting prospects for a variety of applications (Nikoobakht and Li, 2012; Tang and Zhou, 2013; Yang et al., 2013; Zhuiykov and Kats, 2013; Zhuiykov, 2014). Similar to graphene, they are found in layered forms that can be mechanically and/or chemically exfoliated down to monolayers (Bohr et al., 2007; Radisavljevic et al., 2011; Balendhran et al., 2012; Lee et al., 2012a; Nikoobakht and Li, 2012). In the single-layer form, some of these materials, such as molybdenum disulfide (MoS_2), are direct bandgap semiconductors (Radisavljevic et al., 2011), which could have important implications for their use in the next generation of modern electronic devices. The direct bandgap means that 2D MoS_2 or WS_2 can be used in light-emitting diodes, photodetectors, and solar cells (Mak et al., 2010). Due to their ultrathin nature, the devices may be made transparent, light, and flexible, and could provide a variable alternative to devices based on organic semiconductors, which degrade relatively quickly in ambient conditions. The interest in this type of materials, in particular MoS_2, has been exponentially increasing during last decade owing to their potential remarkable semiconducting and optical properties, as presented by the worldwide citations summarized in Figure 20.1.

Although this figure represents citations at the time of writing this chapter, there is no doubt that the milestone of ~30,000 citations per annum within the next years will be reached. Most of the semiconductor nanocrystals have so far been studied for their various physical, chemical, and electrochemical applications at microstructural

Modeling, Characterization and Production of Nanomaterials. http://dx.doi.org/10.1016/B978-1-78242-228-0.00020-X
Copyright © 2015 Elsevier Ltd. All rights reserved.

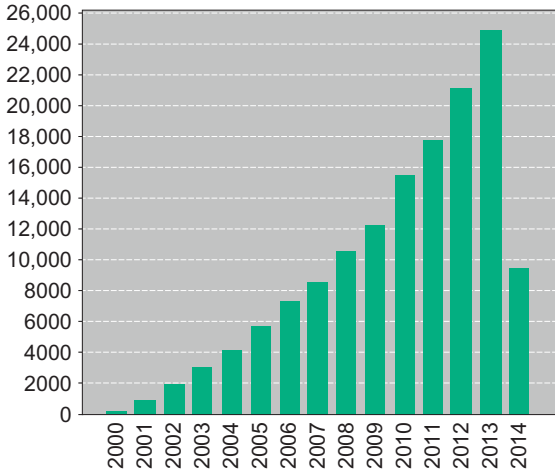

Figure 20.1 Changes in citation for "2D semiconductors" based on Web of Knowledge™.

dimensions; however, their 2D capabilities are yet to be fully investigated and explored.

The first reported class of the atomically thin 2D materials is layered dichalcogenides (XY_2, where X = Mo, Ti, W and Y = S, Se, and Te), which have been extensively investigated from 2011 to 2015 (Myron and Freeman, 1974; Zhang et al., 2006, 2014; Bohr et al., 2007; Park et al., 2008; Mak et al., 2010; Jeong et al., 2011; Radisavljevic et al., 2011; Teich et al., 2011; Balendhran et al., 2012; Lee et al., 2012a, 2013; Nikoobakht and Li, 2012; Plashnitsa et al., 2012; Chhowalla et al., 2013; Heyderman, 2013; Jones et al., 2013; Koski and Cui, 2013; Late et al., 2013; Li et al., 2013, 2014a,b; Lopez-Sanchez et al., 2013; Najmaei et al., 2013; Roy et al., 2013; Sundaram et al., 2013; Tang and Zhou, 2013; Tserkovnyak, 2013; Yu et al., 2013; Baugher et al., 2014; Pospischil et al., 2014; Ross et al., 2014; Wang et al., 2014; Zhuiykov, 2014). The results obtained at this stage have confirmed that the dichalcogenide semiconductors have sizable differences in 2D and bulk conductivities ($\sigma_1/\sigma_2 \sim 10^2$-$10^3$) (Lee et al., 2012a). These findings and other anisotropies arise from the presence of strong, interlayer X–Y bonding, which is in contrast to the weak van der Waals interactions between layers (Balendhran et al., 2012). For example, TiS_2 crystallizes in a hexagonal layered structure, where one hexagonally packed sheet of Ti atoms is sandwiched between two hexagonal sheets of sulfur for each monolayer (Plashnitsa et al., 2012).

Similarly to graphene, most of the abovementioned dichalcogenides are naturally layered materials. Thus they can be dispersed as thin nanosheets by using a liquid exfoliation method employing appropriate solvents or other developed state-of-the-art techniques. Eventually, these dichalcogenides can be manufactured as thin-film nanocomposites with turned-up electronic, thermal, and/or mechanical properties. In order to overcome these challenges and generate appropriate nanostructures for various applications, it is vital to control the number of stacked layers on the substrate or the graphene surface. This can be achieved by manipulation of nanosheets or the

two-step thermal evaporation approach (Balendhran et al., 2012) before exfoliation takes place. The reported combination of two-step thermal evaporation and exfoliation methods may offer a new opportunity, because it has already been demonstrated that the layered hexagonal MoS_2 can be successfully sintered at temperatures less than 830 °C, which is significantly lower than the sintering temperature required for the direct evaporation of MoS_2 (Radisavljevic et al., 2011). Layered dichalcogenides are relatively abundant in nature, their deposition is compatible with standard nanofabrication techniques, and layered 2D semiconductors are generally considered stable and nonhazardous.

There are plenty of techniques for the synthesis of these nanostructured 2D semiconductors; a number of them have been adopted from their bulk and micro counterparts, and many other layer specific synthesis methods have been recently developed (Kalantar-zadeh et al., 2010a,b; Coleman et al., 2011; Liu et al., 2012). The summary of the most important fabrication techniques used for the development of 2D nanostructures is presented in Table 20.1.

However, diversification of the manufacturing techniques and methods, and controlling the single-crystalline structure of formed 2D crystals are among the biggest existing challenges.

Similarly to 2D dichalcogenides, 2D oxide semiconductors (MO_x, where M = Mo, W, Ti) have also attracted substantial interest due to tunability of their physical and electrochemical properties. For example, α-MoO_3 is an indirect wide bandgap semiconductor (~3.0 eV). However, in its 2D form, bandgap can be decreased to ~2.6 eV by H^+ intercalation (Hu et al., 2008; Al-Khawaja and Kassem, 2012; Balendhran et al., 2013a). Moreover, other alkali metals such as Li, Na, and K, as well as organic compounds have also been adopted as intercalants for the stoichiometry and bandgap changes (Ye et al., 2013).

Another example is the *n*-type semiconductor WO_3. It has a bandgap of 2.6 to 2.9 eV (Ou et al., 2012) with excellent electrochromic and gasochromic properties (Deb, 2008). In the bulk form, it has electron Hall mobility of ~12 $cm^2\ V^{-1}\ s^{-1}$ at room temperature and is responsive to the blue end of the visible spectrum ($\lambda < 470$ nm) (Berak and Sienko, 1970). Extrinsic *n*-doping is therefore not required for WO_3 to exhibit significant conductivity. Similar to graphene, WO_3 can be mechanically or chemically exfoliated to produce and implement fundamental layers. However, unlike graphene, which does not possess bandgap, 2D WO_3 has a significantly large bandgap, making 2D WO_3 nanoflakes more versatile as candidates for thin, flexible devices and potential applications in catalysis (Ham et al., 2010), optical switches (Granquist, 2000), displays and smart windows (Lee et al., 2006), solar cells (Ou et al., 2013), and optical recording devices (Labidi et al., 2005). However, despite the great interest of research and industrial communities to the micro- and nanostructured WO_3, the nanoscaled 2D WO_3 with a thickness of less than ~10 nm so far has received relatively little attention compared to its microstructured counterparts. Approaches to change the thickness, bandgap, and properties of 2D WO_3 will discussed later in this chapter.

While the development of fabrication techniques and appropriate procedures for specific 2D nanostructures is an ongoing process, an alternative exciting strategy is

Table 20.1 Properties of various methods for the thin-film deposition

Property	Deposition technique					
	Chemical vapor deposition (CVD)	**Molecular beam epitaxy (MBE)**	**Atomic layer deposition (ALD)**	**Pulsed layer deposition (PLD)**	**Evaporate**	**Sputtering**
Deposition rate	Good	Fair	Poor	Good	Good	Good
Film density	Good	Good	Good	Good	Fair	Good
Lack of pinholes	Good	Good	Good	Fair	Fair	Fair
Thickness uniformity	Good	Fair	Good	Fair	Fair	Good
Sharp dopant profiles	Fair	Good	Good	Varies	Good	Poor
Industrial applicability	Good	Varies	Varies	Poor	Good	Good
Automated multilayers	Fair	Good	Good	Fair	Fair	Good
Step coverage	Varies	Poor	Good	Poor	Poor	Poor
Sharp interfaces	Fair	Good	Good	Varies	Good	Poor
Low substrate temperature	Varies	Good	Good	Good	Good	Good
Smooth interfaces	Varies	Good	Good	Varies	Good	Varies
No plasma damage	Varies	Good	Good	Fair	Good	Poor

rapidly emerging. This approach is based on the combination of different 2D nanosheets into artificially produced layered mixed nanomaterials. It was recently shown that this procedure generates structures with clean atomic interfaces (Lu et al., 2006), and tunneling transistors have been fabricated using this method (Avari et al., 2007; Mora-Sero and Bisquert, 2010; Orentas et al., 2012). Consequently, the entire new range of devices could be potentially created by accurately combining highly conductive graphene, insulating boron nitride, and semiconducting 2D nanocrystals (Geim and Grigorieva, 2013).

20.1.2 Properties of 2D MoS_2 nanocrystals

MoS_2 is a typical example of a layered transitional-metal dichalcogenide. So far it has been considered as one of the most favorable nanomaterials among all the abovementioned 2D dichalcogenides, because it has a relatively small band gap of 1.29 and 1.90 eV for the bulk material and single layers, respectively (Lee et al., 2010, 2012a,b; Splendiani et al., 2010; Ghatak et al., 2011; Radisavljevic et al., 2011; Castellanos-Gomez et al., 2012; Bratschitsch, 2014). Figure 20.2 shows a three-dimensional representation of the structure of MoS_2 and the corresponding atomic force microscopy (AFM) imaging of monolayer MoS_2 (Radisavljevic et al., 2011). It was exhibited that single layers 6.5 Å thick can be extracted using scotch tape or lithium-based intercalation (Wang et al., 2013). It has recently been shown that the bandgap of relatively large flakes of 2D MoS_2 increases with decreasing thickness of nanocrystal less than 100 nm and eventually reaches ~1.9 eV for a monolayer (Ghatak et al., 2011). At the same time, the bandgap has also changed from indirect to direct owing to the hybridization between p_z orbitals of S atoms and d orbitals of Mo atoms (Bratschitsch, 2014). Such an indirect-to-direct bandgap transition leads to a strong photoluminescence (PL) effect in monolayer MoS_2, which can be controlled electrochemically (Bratschitsch, 2014).

Because it is a direct-gap semiconductor, single layers of MoS_2 offer the intriguing possibility for the realization of an interband tunnel field-effect transistor (FET), which is characterized by a turn-on sharper than the theoretical limit of 60 mV dec^{-1} for classical transistors and consequently smaller power dissipation. This feature has remained difficult to achieve in the case of silicon, an indirect gap semiconductor, because interband transitions there require phonons and recombination centers (Castellanos-Gomez et al., 2012). One of the interesting recent applications of 2D MoS_2 nanocrystals is the transistor (Radisavljevic et al., 2011) and phototransistor (Lee et al., 2012a) based on a single-layer MoS_2 nanosheet. Structurally, these functional devices are shown in Figures 20.3 and 20.4, respectively.

A MoS_2 nanosheet-based transistor is displayed in Figure 20.3. A very interesting technical solution was found in compiling the transistor's layers (Figure 20.3c), because an atomic layer deposition (ALD) of 30 nm HfO_2 was achieved as a high-κ gate dielectric for the local top gate and mobility booster to realize the full potential of the single-layer MoS_2 (Li et al., 2013). HfO_2 was selected due to its high dielectric constant of 25, large bandgap of 5.7 eV, and the fact that it is commonly used as a gate dielectric both by the research community and the major

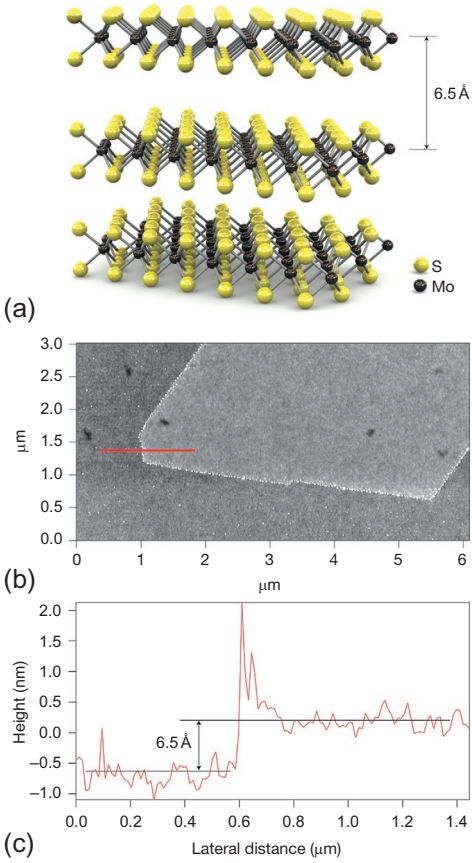

Figure 20.2 Structure and AFM imaging of monolayer MoS_2. (a) Three-dimensional representation of the structure of MoS_2. Single layers, 6.5 Å thick, can be extracted using scotch tape-based micromechanical cleavage. (b) Atomic force microscope image of a single layer of MoS_2 deposited on a silicon substrate with a 270 nm thick oxide layer. (c) Cross-sectional plot along the red line in (b). (Reprinted from Radisavljevic et al. (2011) with permission from Nature Publishing Group.)

microprocessor manufacturers (Bohr et al., 2007). MoS_2 monolayers were deposited on doped silicon substrates covered with 270 nm thick SiO_2 (Figure 20.3a). Because the correlation between contrast and thickness for optical detection of single-layer MoS_2 has been established (Mak et al., 2010), electrical contacts were prepared using electron-beam lithography followed by the deposition of 50 nm thick Au electrodes. The device was then annealed at 200 °C to remove excess residue (Ishigami et al., 2007) and decrease the contact resistance. At this point, the single MoS_2-layer devices exhibited a typical mobility in the range 0.1 to 10 $cm^2\ V^{-1}\ s^{-1}$, similar to reported values for single layers (Novoselov et al., 2005) and thin crystals containing more than 10 layers of MoS_2 (Avari et al., 2007). This is lower than the previously reported phonon-scattering-limited room temperature mobility in the 200 to 500 $cm^2\ V^{-1}\ s^{-1}$ range for bulk MoS_2 (Fivaz and Mooser, 1967). The final structure, composed of two FETs connected in series, is shown in Figure 20.3b: It has the width of the top gate of 4 µm and the top-gate length, source-gate, and gate-drain spacing of approximately 500 nm.

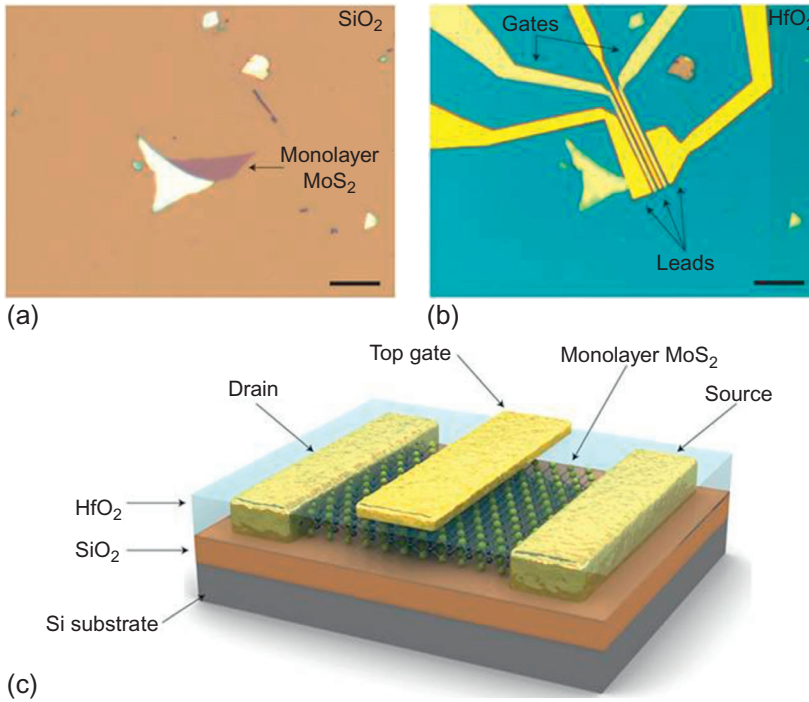

Figure 20.3 Fabrication of MoS_2 monolayer transistors. (a) Optical image of a single layer of MoS_2 (thickness, 6.5 Å) deposited on top of a silicon substrate with a 270 nm thick SiO_2 layer. (b) Optical image of a device based on the flake shown in (a). The device consists of two field-effect transistors connected in series and defined by three gold leads that serve as source and drain electrodes for the two transistors. Monolayer MoS_2 is covered by 30 nm of ALD-deposited HfO_2 that acts both as a gate dielectric and a mobility booster. Scale bars (a,b), 10 μm. (c) Three-dimensional schematic view of one of the transistors shown in (b).
(Reprinted from Radisavljevic et al. (2011) with permission from Nature Publishing Group.)

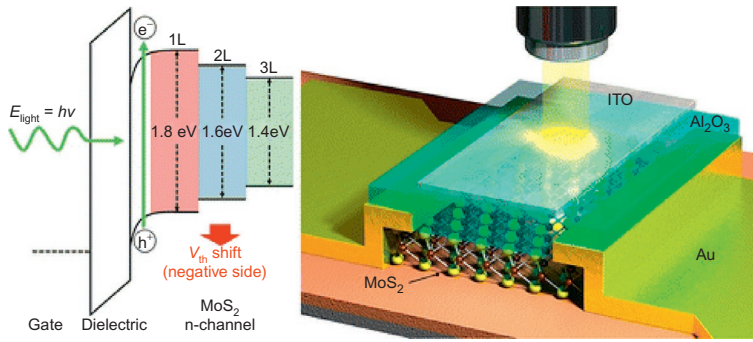

Figure 20.4 Thickness-modulated phototransistor based on layered MoS_2 nanosheets.
(Reprinted from Lee et al. (2012a) with permission from The American Chemical Society.)

It is well-known that the ability to control charge density in a local manner independently of a global backgate is one of the crucial requirements for building integrated circuits based on single MoS_2 layers. This has been accomplished by applying a voltage V_{tg} to the top gate, separated from the monolayer MoS_2 by 30 nm of HfO_2, while keeping the substrate grounded (Radisavljevic et al., 2011). The corresponding transfer characteristic is illustrated in Figure 20.5a.

For a bias of 10 mV, an on-current of 150 nA (37 nA μm^{-1}) has been recorded, current on/off ratio $I_{on}/I_{off} > 1 \times 10^6$ for the ± 4 V range of V_{tg}, an off-state current that was smaller than 100 fA (25 fA μm^{-1}), and gate leakage lower than 2 pA μm^{-2}. The observed current variation for different values of V_{tg} indicated that the field-effect behavior of the transistor based on single-layer MoS_2 is dominated by the MoS_2 channel and not the contacts. At the bias voltage $V_{ds} = 500$ mV, the maximal measured on-current was 10 μA (2.5 μA μm^{-1}), with I_{on}/I_{off} higher than 1×10^8 for the ± 4 V range of V_{tg} (Radisavljevic et al., 2011). The device transconductance, defined as $g_m = dI_{ds}/dV_{tg}$ at $V_{ds} = 500$ mV, is ~4 μS (1 μS μm^{-1}), similar to values obtained for high-performance CdS nanoribbon array transistors (2.5 μS μm^{-1} at $V_{ds} = 1$ V) (Duan et al., 2003a). For comparison, high-performance top-gated graphene transistors can have normalized transconductance values as high as 1.27 mS μm^{-1} (Liao et al., 2010a). Figure 20.5b clearly illustrates the large degree of current control in the single-layer MoS_2-based transistor, where the drain-source current versus drain-source bias is plotted for different values of voltage applied to the local gate. The subthreshold slope for the transition between the on- and off-states was deduced from the channel-current dependence on top-gate voltage, which was 74 mV dec^{-1} for a bias $V_{ds} = 500$ mV.

A phototransistor based on a mechanically exfoliated single-layer MoS_2 nanosheet is presented in Figure 20.4, and its light-induced electric properties were recently investigated in detail. It was shown that the photocurrent generated from the phototransistor is solely determined by the illuminated optical power at a constant drain or gate voltage. It should be stressed that the single-layer MoS_2-based phototransistor exhibited better photo-responsivity compared to the graphene-based device (Lee et al., 2012a). The switching behavior of photocurrent generation and annihilation could be completely finished within approximately 50 ms, and the device exhibited acceptable stability.

Another recent approach for development of 2D MoS_2 nanosheets is a liquid-phase exfoliation followed by the electrochemical intercalation of Li^+, Na^+, and K^+ ions into the MoS_2 crystal structure (Wang et al., 2013). This approach enabled active control of the PL by electrochemical manipulation of amount of metal cations in the structure of 2D MoS_2. It has been exhibited that the intercalated ions modify the crystal phase and electronic band structures of 2D MoS_2, as schematically presented in Figure 20.6 (Wang et al., 2013).

The detailed optical properties of the 2D MoS_2 nanoflakes are studied by measuring their UV-vis-NIR absorption spectra. The weak absorption peaks at 609 and 668 nm were ascribed to B and A excitonic peaks, respectively, arising from the K point of the Brillouin zone in 2D MoS_2 with large lateral dimensions (Mak et al., 2010). The weak features of these peaks are due to the small concentration of the relatively

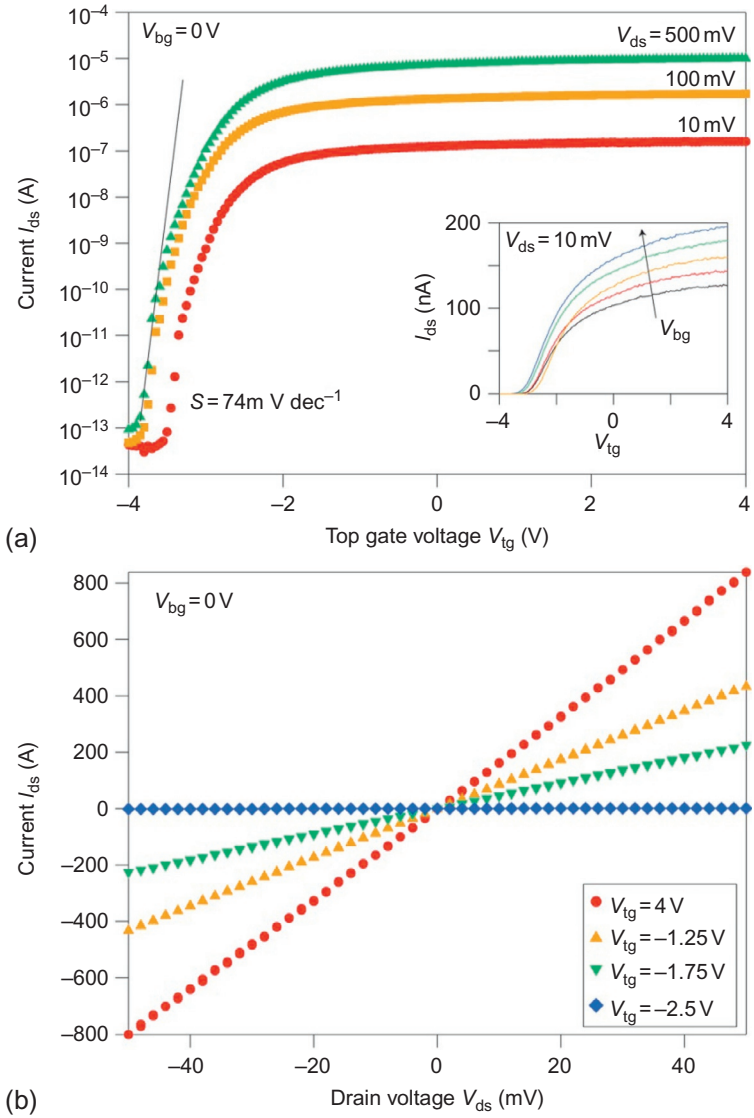

Figure 20.5 Local gate control of the MoS_2 monolayer transistor. (a) I_{ds}–V_{tg} curve recorded for a bias voltage ranging from 10 to 500 mV. Measurements are performed at room temperature with the backgate grounded. Top-gate width, 4 μm; top-gate length, 500 nm. The device can be completely turned off by changing the top-gate bias from −2 to −4 V. For $V_{ds} = 10$ mV, the I_{on}/I_{off} ratio is $>1 \times 10^6$. For $V_{ds} = 500$ mV, the I_{on}/I_{off} ratio is $>1 \times 10^8$ in the measured range while the subthreshold swing $S = 74$ mV dec^{-1}. Top and bottom gate leakage is negligible. Inset: I_{ds}–V_{tg} for values of $V_{bg} = -10, -5, 0, 5$ and 10 V. (b) I_{ds}-V_{ds} curves recorded for different values of V_{tg}. The linear dependence of the current on bias voltage for small voltages indicates that the gold contacts are ohmic.
(Reprinted from Radisavljevic et al. (2011) with permission from Nature Publishing Group.)

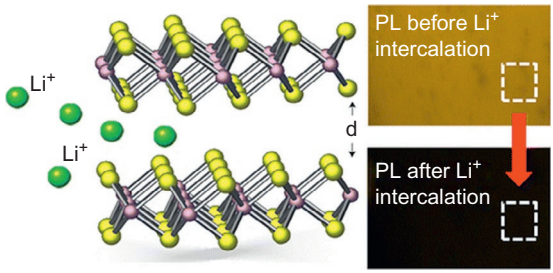

Figure 20.6 Schematical representation of 2H 1T phase transition in the 2D MoS_2 nanoflakes upon Li^+ ion intercalation and deintercalation. (Reprinted from Wang et al. (2013) with permission from The American Chemical Society.)

larger 2D flakes in the suspension (Wang et al., 2013). In addition to these two weak peaks, a well-known broad peak centered at ~400 nm is observed. There is also a less prominent shoulder seen at 500 nm. It has been suggested that the optical absorption of low-dimensional or quantum dot MoS_2 exhibits a strong blue shift when the lateral dimensions of the MoS_2 nanostructures are reduced to <50 nm, ascribed to the quantum size effect (Wilcoxon and Samara, 1995; Wilcoxon et al., 1997; Chikan and Kelley, 2002; Zhu et al., 2013). Considering that the majority of 2D MoS_2 nanoflake sizes are within the 10 to 40 nm range, their optical absorption peaks should be also blue-shifted. In addition, the broad absorption peak below 350 nm can be assigned to blue-shifted convoluted Z, C, and D excitonic peaks as suggested by several research groups (Wilcoxon and Samara, 1995; Wilcoxon et al., 1997; Chikan and Kelley, 2002).

The PL spectra using fluorescence spectroscopy at four different excitation wavelengths of 600, 500, 400, and 300 nm are measured to provide a comprehensive view of the PL properties of the 2D nanoflakes (Wang et al., 2013). While no obvious emission peak is observed at the excitation wavelength of 600 nm (inset in Figure 20.7a), two weak peaks at ~610 and ~661 nm were detected (inset in Figure 20.7b) when the excitation wavelength is 500 nm. It is well-known that the observed peaks are mainly from the direct bandgap hot PL from the K point of the 2D MoS_2 flakes with the large lateral dimensions (Mak et al., 2010). However, when the excitation energies are larger (at lower wavelengths of 400 and 300 nm), a strong broad peak centered at ~420 nm and a weaker shoulder at 530 nm appear. In this case, the characteristics of these PL peaks are similar to those of MoS_2 quantum dots or liquid-exfoliated 2D MoS_2 with small lateral dimensions, which are ascribed to the strongly blue-shifted hot PL from the K point (Stengl and Henych, 2013). Interestingly, similar phenomena were also observed in nanostructured MoS_2 film consisting of 2D nanoflakes under the excitation of the light sources with various wavelengths (Zhou et al., 2012).

It was demonstrated that upon the intercalation/deintercalation of Li^+, Na^+, and K^+ ions, the PL intensities can be effectively tuned. In order to establish the system for investigating the interaction with ions, the 2D MoS_2 supernatant was drop-casted onto conductive fluorine-doped tin oxide (FTO) substrates to obtain nanostructured thin films with the thicknesses of ~1 μm. The Li^+ ion intercalation is discussed in details. During the intercalation process, an external voltage is applied across the working cathode (FTO coated with the 2D MoS_2 nanoflake film) and the counter electrode (Pt). It is known that in bulk MoS_2 this leads to the intercalation of the x quantity ($0 \leq x \leq 1$) of Li^+ ions and injection of an equal quantity of electrons (e^-) into

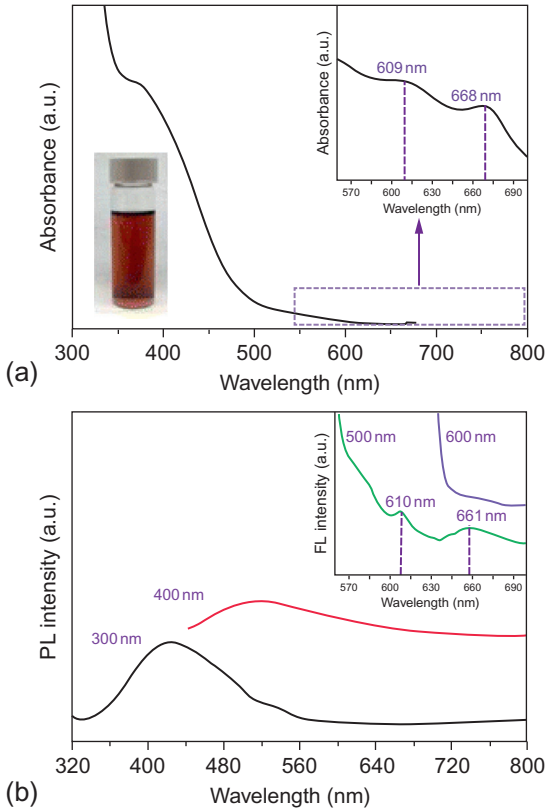

Figure 20.7 Optical and PL properties of 2D MoS_2 nanoflakes. (a) Absorbance spectrum of 2D MoS_2 nanoflakes (insets are the optical image of a liquid-exfoliated MoS_2 suspension in NMP solvent and its zoomed-in region of the same spectrum showing two absorption peaks at 609 and 668 nm). (b) PL spectra of 2D MoS_2 nanoflakes at different excitation wavelengths (300, 400, 500, and 600 nm). (Reprinted from Wang et al. (2013) with permission from The American Chemical Society.)

MoS_2 (Julien et al., 1991). This double intercalation/injection of charges results in the formation of Li_xMoS_2, hence leading to the modification of their original crystal phase (from trigonal prismatic 2H to octahedral 1T phase) and electronic band structures (Julien et al., 1991; Enyashin and Seifert, 2012). Conversely, when the polarity of the applied voltages is reversed, Li^+ ions are deintercalated, which leads to the restoration of the initial crystal phase and electronic band structures.

Therefore, the PL modulations of the 2D MoS_2 nanoflakes can be directly attributed to the ion intercalation into the MoS_2 crystal structure. For the case of Li^+ ions, it is suggested that the intercalated Li^+ ions are weakly bonded to the S atoms of the MoS_2 layers and placed in the van der Waal's gap between the MoS_2 planes when more than one monolayer exists (Sekine et al., 1989; Julien et al., 1991). It has been also suggested that a high concentration of these intercalating Li^+ ions eventually forces the transition of the MoS_2 crystal from stable hexagonal semiconducting phase (2H phase) to a metastable metallic phase (1T phase) (Chrissafis et al., 1989; Alexiev et al., 2000; Enyashin et al., 2011). This type of a phase transition can be evidenced by X-ray photoelectron spectroscopy (XPS) measurements shown in Figure 20.8 (Wang et al., 2013).

As presented in Figure 20.8, $Mo3d_{3/2}$, $Mo3d_{5/2}$, S2s, $S2p_{1/2}$, and $S2p_{3/2}$ peaks can be observed at 232.5, 229.3, 226.5, 163.7, and 162.2 eV, respectively, indicating the

dominant 2H MoS_2 phase in the crystal structure of pristine 2D MoS_2 nanoflakes (Lukowski et al., 2013). After Li^+ ion intercalation at −10 V, new peaks at 230.9 and 227.7 eV for Mo and 162.8 and 161.3 eV for S can be found at lower binding energies in comparison with those of 2H phase peaks (Figure 20.8e and f). These new peaks can be identified as 1T phase peaks, which suggests that a large portion of the 2D MoS_2 flakes undergoes a phase transition to a metastable phase, where the coordination of Mo atoms becomes octahedral (1T phase) upon Li^+ ion intercalation (Lukowski et al., 2013). However, the peaks representing the 2H phase can still be observed after the intercalation process, indicating the coexistence of 1T and 2H phases in the crystal structure of intercalated material. This 2H → 1T phase transition can be one of the main reasons that contribute to the PL quenching of 2D MoS_2 nanoflakes, because the 1T phase appears to be metallic (Sekine et al., 1989). Notice also that a small peak emerges at 236.0 eV (Figure 20.8e), corresponding to Mo^{6+} $3d_{5/2}$,

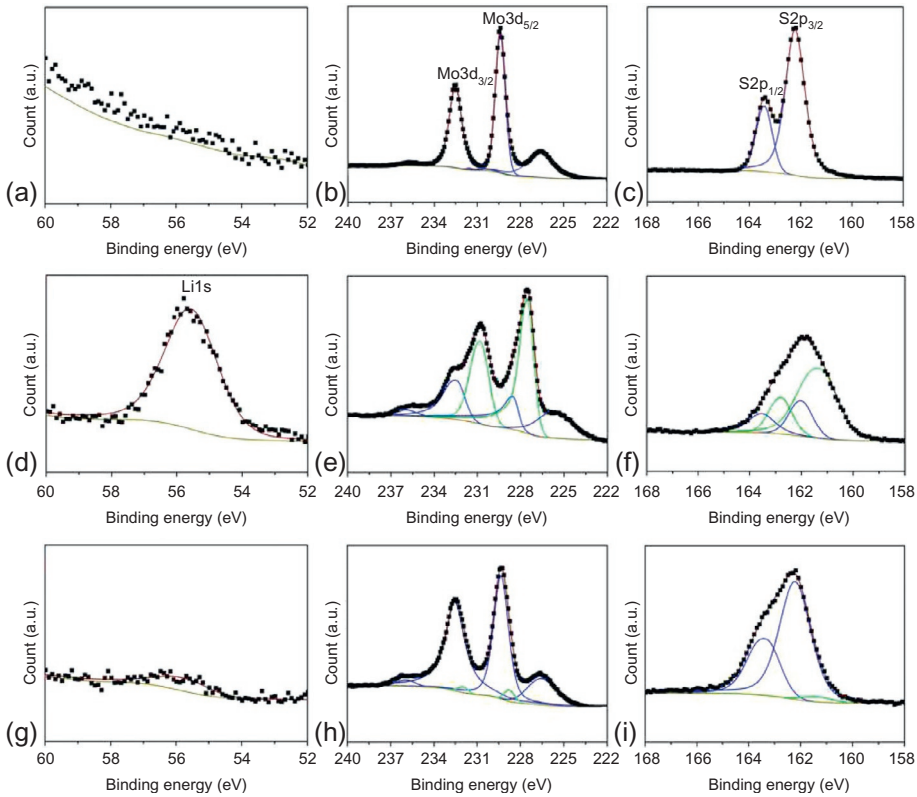

Figure 20.8 Characterization of 2D MoS_2 nanoflakes after Li^+ ion intercalation and deintercalation. XPS spectra of the elements of (a) Li, (b) Mo, and (c) S in 2D MoS_2 nanoflakes before Li^+ ion intercalation. (d–f) Aforementioned elements in 2D MoS_2 nanoflakes after Li^+ ion intercalation, where the blue and green lines represent the 2H and 1T phase, respectively. (g–i) Three elements in 2D MoS_2 nanoflakes after Li^+ ion deintercalation.
(Reprinted from Wang et al. (2013) with permission from The American Chemical Society.)

which is a common characteristic for Li^+-intercalated MoS_2 possibly due to the oxidation of a very small portion of MoS_2 (Papageorgopoulos and Jaegermann, 1995). The deintercalation process of Li^+ ions results in the near full restoration of the 2H phase crystal structure in 2D MoS_2 nanoflakes, with less than 15% of the 1T phase and a very small portion of residual Li^+ ions remaining within the overall crystal structure (Figure 20.8g–i).

Consequently, the reversible controlling approach described above will provide a viable solution to develop a high-performance and practical-nanostructured PL system based on 2D MoS_2 with active controllability. The demonstrated phenomenon can also play an important role in developing highly sensitive photoelectrochemical sensors, as well as high-performance optical modulators and solar cells. In addition, this controlled PL will offer great opportunities for the development of optical displays and switches at relevant wavelengths.

Recently, an ultradoping approach for tunability of 2D MoS_2 semiconductor toward plasmon resonance was also reported (Alsaif et al., 2014). This approach allows development of practical nanophotonic biosensors at low dimensions. Li^+ ion intercalation/deintercalation into 2D MoS_2 nanoflakes demonstrated tunable plasmon resonances in the visible and NIR regimes.

20.1.3 Properties of 2D WSe_2 nanocrystals

Although MoS_2 was the most studied transitional-metal dichalcogenide until 2014, it had proven difficult to obtain hole conduction in this monolayer material (Bratschitsch, 2014), hindering fabrication of an atomically thin *p-n* junction. Alternative interesting developments were recently achieved for 2D WSe_2. These 2D nanocrystals were used to create *p-n* diodes (Baugher et al., 2014; Pospischil et al., 2014; Ross et al., 2014; Zhang et al., 2014). The design concept of a lateral diode, in which the *p-n* junction is created electrostatically within a WSe_2 monolayer by means of two independent gate voltages applied to adjacent regions of the layer, is presented in Figure 20.9 (Bratschitsch, 2014). The diodes show ambipolar transport: Both electrons and holes are injected from different sides into the channel area. In contrast to the chemical doping, electrostatic doping allowed these 2D WSe_2 diodes to be operated either as *p-n* or *n-p* diodes, depending on the applied gate voltages (Jariwala et al., 2014). In this way, the devices are able to rectify current flowing in either direction. When applying gate voltages of the same polarity to both regions of the monolayer (in *p-p* or *n-n* configurations), the devices act as simple resistors.

Besides a display of rectifying current-voltage characteristics, the monolayer *p-n* diodes fabricated by the three teams can also be used as different types of optoelectronic device. In particular, they can operate as a photovoltaic solar cell, a photoconductor, a photodiode, or a light-emitting diode. The solar cells have power-conversion efficiency, which measures the percentage of incident energy of light converted into electrical energy, less than 1% (Pospischil et al., 2014). This value is relatively high, keeping in mind that the atomically thin WSe_2 layer is almost entirely transparent, so that only a few percent of the incident photons are absorbed. When operated as a resistor, the device behaves as a photoconductor; however, its slow response time and large

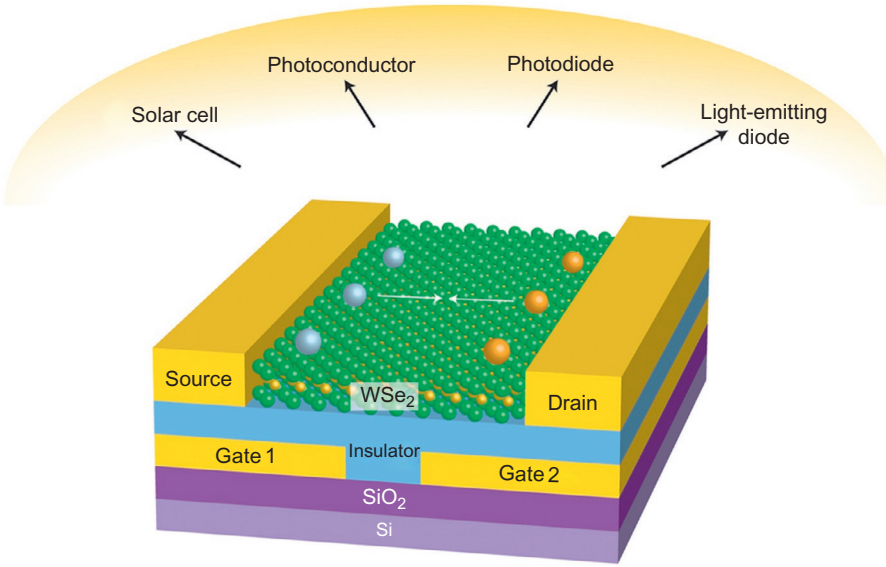

Figure 20.9 Schematic drawing of a lateral monolayer WSe_2 *p-n* diode with split-gate electrodes. The metal backgates separated from the WSe_2 monolayer by an insulator, which can be SiN, HfO_2, or BN. Blue and orange spheres represent electrons and holes, respectively. (Reprinted from Bratschitsch (2014) with permission from Nature Publishing Group.)

power consumption render it impractical for real-world applications. The WSe_2 monolayer diodes, however, perform better when operated as photodiodes, showing a responsivity to light detection of hundreds of mA W^{-1} (Baugher et al., 2014; Pospischil et al., 2014). Moreover, the versatility of the monolayer *p-n* diodes allows them to be operated as electrically driven light emitters, with bright electroluminescence observed at room temperature (Baugher et al., 2014; Pospischil et al., 2014; Ross et al., 2014). In this setup, electrons and holes are electrically injected on either side of the WSe_2 monolayer, and the devices emit light when the electrons and holes recombine in the center (Figure 20.9 (Bratschitsch, 2014)). Spatial mapping of the electroluminescence (electrically driven light emission) shows that the light originates from the entire length of the monolayer junction between the two gates (Ross et al., 2014). The electroluminescence and the PL (optically driven light emission) spectra are almost identical, suggesting that the same physical mechanism is at work for both excitations. No electroluminescence is detected in *n-n* or *p-p* configurations, confirming that light emission is generated exclusively by the *p-n* junction. The driving current of monolayer WSe_2 *p-n* diodes is of the order of a few nanoamperes, which compares favorably with the much higher current levels in light-emitting MoS_2 FETs. However, the electroluminescence efficiency—the optical output power divided by electrical input power—is still low, and less than 1%. Resistive losses at the contacts and nonradiative recombination in the atomically thin WSe_2 sheet are likely to be the factors limiting this value (Pospischil et al., 2014).

It was shown that monolayer WSe_2 *p-n* diodes were capable of photovoltaic power generation. With the device in the NP configuration, current is measured as a function of V_{ds} for various laser powers from white-light source bandpass filtered at 700 nm. Figure 20.10a presents a zoomed-in view of the I_{ds}-V_{ds} curve, focusing on the quadrant of photovoltaic power generation. The short-circuit current I_{sc}, which is the zero-bias current through the illuminated device, increases linearly with power up to at least 10 μW (Figure 20.10a, inset). The power generated by the photovoltaic device, $P = I_{ds}V_{ds}$, is shown for laser powers of 0-10 μW in Figure 20.10b. The photovoltaic power generation also has a linear dependence on laser power. Varying V_J, the asymmetric gate voltage that defines the junction at different laser powers, we observe a saturation in short-circuit current when $V_J \approx \pm 5$ V is observed (Figure 20.10c). The current is higher for NP than for PN due to a difference in contact resistances between the two contacts. We also note that the photocurrent due to the photovoltaic effect in these WSe_2 diodes is approximately an order of magnitude larger than photothermoelectric currents observed at the contacts of a monolayer MoS_2 FET (Buscema et al., 2013).

To obtain spectrally resolved photocurrent in the NP configuration, I_{sc} as a function of excitation wavelength was measured. To quantify the efficiency of light conversion into current, the external quantum efficiency, $EQE = (I_{sc}/P_{laser})(hc/e\lambda)$, as a function of wavelength λ, can be extracted at constant laser power P_{laser}, where h, c, and e are Planck's constant, the speed of light, and electron charge, respectively. One can observe three peaks in the spectrally resolved photocurrent at 755, 591, and 522 nm (Figure 20.10d), corresponding to energies of 1.64, 2.10, and 2.38 eV, respectively. These energies match well with the values obtained via PL, differential reflectance, and optical absorption spectroscopy (Huang et al., 2014) for the A, B, and A′ transitions of monolayer WSe_2, as depicted in the band diagram in the inset to Figure 20.10d. The maximum EQE of 0.2% was measured at 522 nm. This value does not take into account the low absorption of monolayer WSe_2 or the narrow cross-section of the *p-n* junction relative to the size of the laser spot, which together suggest internal quantum efficiency at least an order of magnitude larger than the EQE reported here.

Finally, measurement of the electroluminescence spectrum of a second monolayer WSe_2 *p-n* diode is presented in Figure 20.10d. To improve the hole injection, this device was fabricated with palladium instead of gold to contact the *p*-type WSe_2. In the PN configuration ($V_{ds} = 2$ V, $I_{ds} = 100$ nA), the device behaves as a light-emitting diode. The emitted light spectrum peaks at 752 nm, corresponding to the direct-gap exciton transition seen in the photocurrent spectrum (Figure 20.10d). Using a blackbody source for calibration, we estimate the electroluminescence efficiency, defined as optical output power divided by electrical input power, to be ~1%. Light emission and a peak at ~750 nm are also seen in the NP configuration ($V_{ds} = -2$ V, $I_{ds} = 4$ nA), with a peak height smaller in proportion to I_{ds}. No emission is seen in either NN (with $V_{ds} = 2$ V and $I_{ds} = 300$ nA) or PP (with $V_{ds} = 2$ V and $I_{ds} = 500$ nA) configurations, confirming that the gate-defined *p-n* junction generates the electroluminescence. Based on the device performance presented (Baugher et al., 2014), a prominent role for diodes and optoelectronic devices based on monolayer dichalcogenide *p-n* junctions is anticipated. Taking into account the three-atom thickness and low optical absorption of

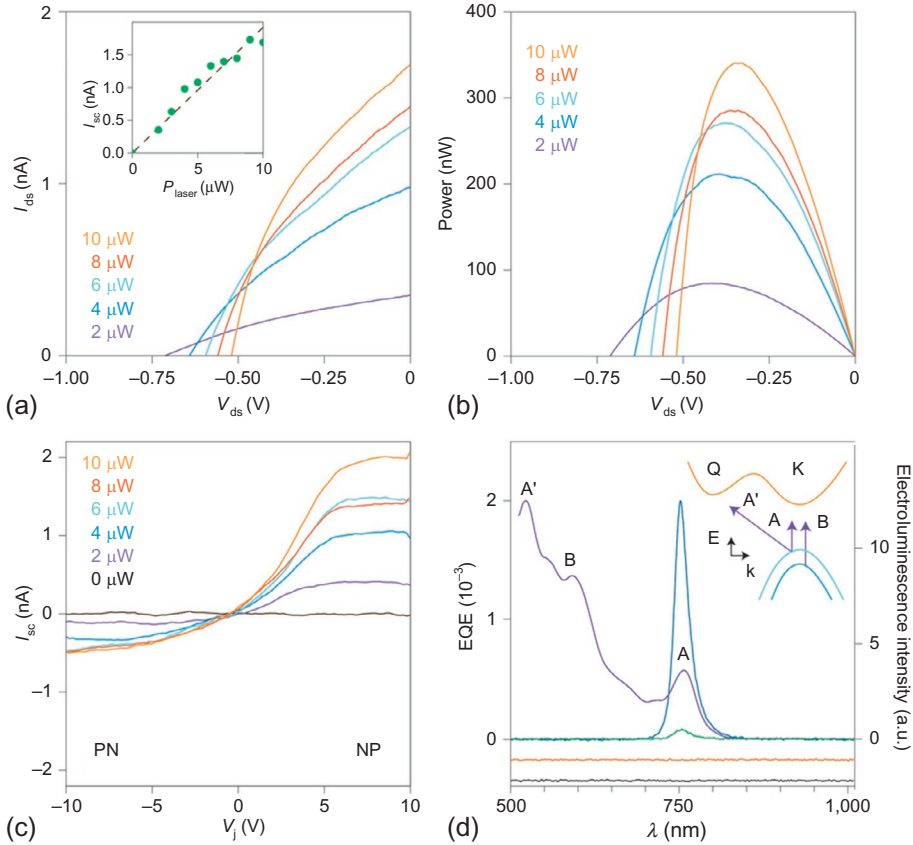

Figure 20.10 (a) I_{ds} as a function of V_{ds} in the NP configuration for laser powers 2-10 μW (wavelength 700 nm). Positive I_{ds} and negative V_{ds} in this regime reflects photovoltaic power generation. Inset: Short-circuit current I_{sc} (green dots) versus laser power with a linear fit (black dashed line). (b) Power $P = I_{ds}V_{ds}$ produced by the device as a function of V_{ds} for different incident laser powers, calculated from the data in (a). (c) I_{sc} as a function of asymmetric gate voltage, V_J, for different laser powers. I_{sc} is nearly linear with power up to 10 μW in the NP configuration, although it saturates in the PN configuration beyond 6 μW. As a function of gate voltage, the current saturates in both configurations for $V_J = \pm 5$ V. (d) Left axis: EQE as a function of wavelength at a constant laser power of 2 μW in the NP configuration (purple line). Peaks in the EQE correspond to exciton transitions A, B, and A′, as labeled. Right axis: electroluminescence intensity from a second monolayer WSe_2 device with one gold and one palladium contact. $V_{ds} = 2$ V in the PN (blue trace), NN (yellow trace), and PP (black trace) configurations, and $V_{ds} = -2$ V in the NP (green trace) configuration. NN and PP traces are offset vertically for clarity. Inset: Diagram of the band structure around the K and Q points, with arrows indicating the lowest-energy exciton transitions for monolayer WSe_2.
(Reprinted from Baugher et al. (2014) with permission from Nature Publishing Group.)

monolayer WSe_2 (Huang et al., 2014), the responsivity and EQE reported here are quite substantial. Furthermore, the device geometry could be optimized to significantly enhance the photoresponse. It is expected that vertical junctions based on transfer-aligned exfoliated flakes (Lee et al., 2012a) or large-area dichalcogenides grown by chemical vapor deposition (CVD) (Huang et al., 2014) could increase responsivity and EQE by more than an order of magnitude. Additionally, improved contact resistance, particularly for holes, should dramatically improve device performance.

Thus, there is a scope for improving the performance of these monolayer WSe_2 diodes by optimizing the fabrication methods. The WSe_2 monolayers were prepared by mechanical exfoliation (Baugher et al., 2014; Pospischil et al., 2014; Ross et al., 2014) and transfer techniques involving polymers. Mechanically exfoliated flakes have sizes of only a few micrometers, and the usefulness of these monolayer diodes for lighting and transparent display technologies will depend on the ability to produce these materials with large areas. The growth of transition-metal dichalcogenide monolayers under controlled conditions, together with more sophisticated fabrication techniques, will significantly improve the electrical and optical properties of the *p-n* diodes. Better performance would also be expected by shifting from a lateral to a vertical diode design, where the monolayer materials are stacked on top of each other (Geim and Grigorieva, 2013). In this way, the area of the junction is significantly increased. The possibility of optically accessing the valley degree of freedom of carriers, instead of using their charge or spin, by circularly polarized light could lead to the design of devices with novel functionalities (Jariwala et al., 2014). Finally, it is expected that further development of 2D atom-thin semiconductors will help to utilize incredibly thin electronic devices that can be flexible and even wrap around the arm.

20.1.4 Properties of 2D WO_3 nanocrystals

Tungsten oxide (WO_3) is a transition-metal oxide that consists of perovskite units that are well-known for their nonstoichiometric properties (Polaczek et al., 1994). Its phase classification is based on the tilting angles and rotation direction of WO_6 octahedra with reference to the "ideal" structure (ReO_3 type). Crystals are generally formed by corner and edge sharing of WO_6 octahedra. In parallel to other metal oxides, WO_3 crystal-phase transitions can occur during annealing and cooling. It has been previously reported that for WO_3, in bulk form, phase transformation takes place in the following sequence: monoclinic II (ϵ-WO_3, $<-43\,^{\circ}C$) $\rightarrow$ triclinic (δ-WO_3, -43 to $17\,^{\circ}C$) $\rightarrow$ monoclinic I (γ-WO_3, 17 to $330\,^{\circ}C$) $\rightarrow$ orthorhombic (β-WO_3, 330 to $740\,^{\circ}C$) $\rightarrow$ tetragonal (α-WO_3, $>740\,^{\circ}C$) (Vogt et al., 1999). The main physical-chemical properties and applications of WO_3 have been comprehensively described in a recent review (Zheng et al., 2011).

The great interest in WO_3 from researchers and various industries has been based on the versatile and exceptional chromic properties of nanocrystalline WO_3. In comparison to many other semiconductor metal oxides, such as TiO_2, ZnO, NiO, and their substoichiometric forms, the investigation of WO_3 chromic properties is much more advanced (Mukherjee et al., 2003). Consequently, nanostructured WO_3 has also been studied for photocatalysis and sensing (Galatsis et al., 2001). Despite these facts, the

importance of developing the WO_3-based nanostructures for electrochromic devices (smart windows and EC displays) (Rauh, 1999), dye-sensitized solar cells (Zheng et al., 2010), optical recording devices (Takeda et al., 2004), and sensing applications cannot be overestimated. Consequently, new approaches to the synthesis of the advanced WO_3-based nanocrystals have emerged during the last few years (Livage and Ganguli, 2001a; Balazsi and Pfeifer, 2002; Takeda et al., 2004; Breedon et al., 2010a; Kalantar-zadeh et al., 2010a; Zheng et al., 2010). Among those approaches, synthesis of the atomically thin nanosheets from hydrated tungsten oxide has proved to be a very effective and efficient method in the development of quasi-2D WO_3 (Kalantar-zadeh et al., 2010a).

More importantly, new exceptional thickness-dependent electrical properties of nonstoichiometric 2D β-WO_{3-x} nanoflakes with thickness below ~10 nm have been reported. (Zhuiykov et al., 2014) Ultrathin 2D WO_{3-x} nanoflakes were obtained via a two-step sol-gel exfoliation process. Advantageously, the electrical properties, including bandgap, of ultrathin Q2D WO_{3-x} nanoflakes can be largely tuned using well-known chemical and physical approaches (Osada and Sasaki, 2012; Wang et al., 2013). Such manipulations, which impose their effects on the 2D environment, categorize these 2D semiconductor oxides as excellent templates for achieving the optimum quantum parameters required for target applications. Using various techniques, it was verified that the exfoliated 2D WO_3 nanoflakes are chemically pure and do not contain measurable impurities (Zhuiykov et al., 2014). 2D β-WO_3 nanoflakes as thin as ~2.5 nm were obtained, which represented the triple-layered structure depicted in Figure 20.11a. Their impedance was ~1.6 Ω and negligible compared to the electronic circuit impedance. Analysis of AFM images (Figure 20.11b,c,d) revealed that the most 2D β-WO_3 nanoflakes have widths in the 50 to 700 nm range with the measured thickness from ~2.5 to 10.0 nm. Bearing analysis obtained for the thinnest 2D WO_3 nanoflake delineated the relative roughness of a surface in terms of high and low areas and displayed that ~90% of the thickness of exfoliated WO_3 nanoflakes does not exceed 2.0 nm (Figure 20.11e and Table 20.2). The structure of exfoliated 2D WO_3 nanoflakes was studied in detail, and it was confirmed that it has high crystallinity. All reflections were indexed to an orthorhombic β-WO_3 phase with space group P and the following lattice parameters: $a = 7.384$ Å, $b = 7.512$ Å, $c = 3.864$ Å. The results obtained were similar to the previously published data for orthorhombic β-WO_3 (Chen et al., 2012). Generally, the orthorhombic phase of WO_3 is stable in the temperature range of 320 to 700 °C (Zheng et al., 2011).

Previous reports on the charge carrier mobility in metal dichalcogenides have shown that their mobility is in 200 to 500 $cm^2\ V^{-1}\ s^{-1}$ range and is limited by phonon scattering (Radisavljevic et al., 2011; Radisavljevic and Kis, 2013). This is partially due to the small dielectric constant for many transitional-metal dichalcogenides (e.g., ~5 for MoS_2) (Yoon et al., 2011). In contrast, 2D semiconductor oxides with high-k advantageously exhibited mobility of up to 1100 $cm^2\ V^{-1}\ s^{-1}$ (α-MoO_3 with thickness of 11 nm) (Balendhran et al., 2013a; Zhuiykov and Kats, 2013), which indicated that the charge carrier mobility in their structures is limited by the acoustic scattering rather than Coulomb scattering at room temperature (Balendhran et al., 2013b). Considering that WO_3 has a similar layered structure comprising the perfect planar crystals held together by van der Waals forces (Figure 20.11a) and has also a large

dielectric constant (from 42 (Gupta, 2009) to 105 (Hirose and Furukawa, 2003)), it is possible to lower its bandgap. H^+ intercalation makes 2D WO_{3-x} substoichiometric, where the increasing x can lower the bandgap (Hu, 2008). In low-k semiconductors, this process increases the number of embedded Coulomb charges and has a possible detrimental effect on electron scattering. On the contrary, in high-k layered semiconductors, the Coulomb scattering effect is minimal and acoustic phonon scattering has the most impact at room temperature (Balendhran et al., 2013a).

H^+ intercalation of 2D WO_3 results in the partial transition of W^{6+} to W^{5+} with development of oxygen vacancies in substoichiometric WO_{3-x}, as well as causes the transformation of the original crystal structure into hydrogen tungsten bronze: $WO_3 + x6H^+ + xe^- \rightarrow H_xWO_{3-x}$, leading to a colored state. In this structure oxygen, atoms are doubly and triply bonded with development of oxygen vacancies with variable composition parameter x in WO_{3-x} (Kanan and Tripp, 2007). The additional electron from the

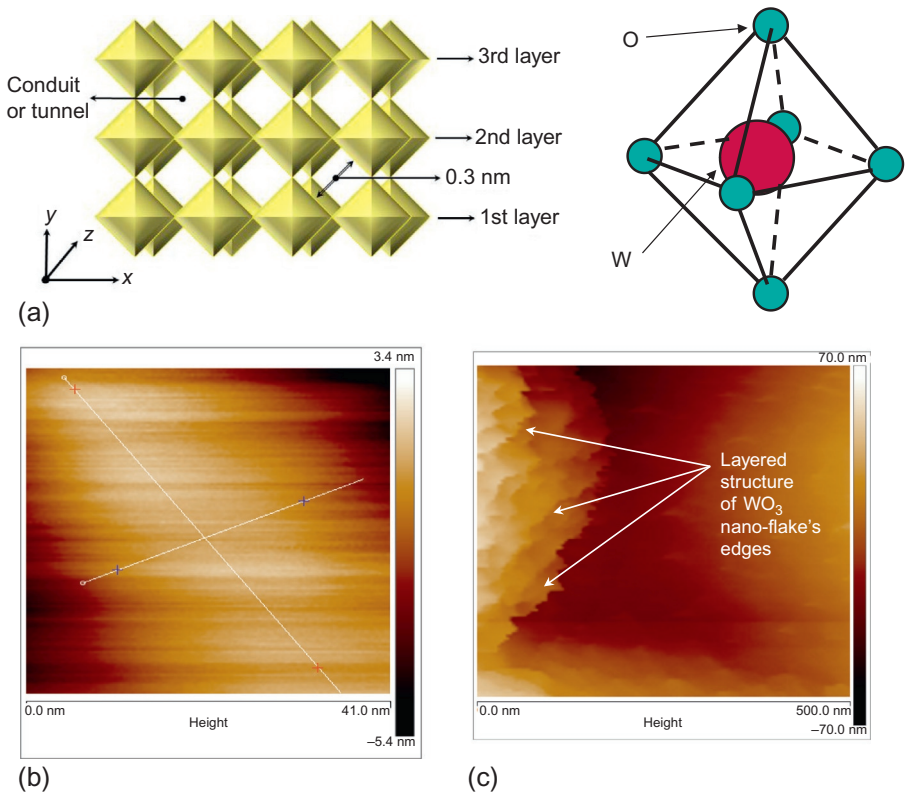

Figure 20.11 Developed 2D WO_3 nanoflake. (a) Structural model of layered WO_3 nanoflake. W atom is coordinated with six oxygen atoms and resulting WO_6 octahedra are joined via edge sharing to produce the 2D lattice. (b) AFM image of WO_3 nanoflake with thickness of ~2.0 nm, which represents approximately three fundamental layers of WO_3. Roughness of the nanoflake comes from the roughness of the substrate. (c) AFM image of the edges of layered structure of WO_3 nanoflakes.

(*Continued*)

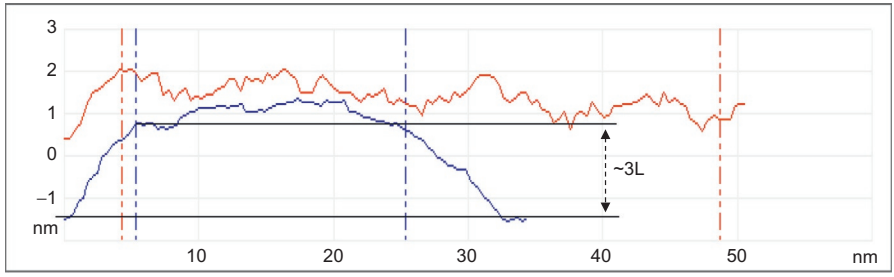

(d)

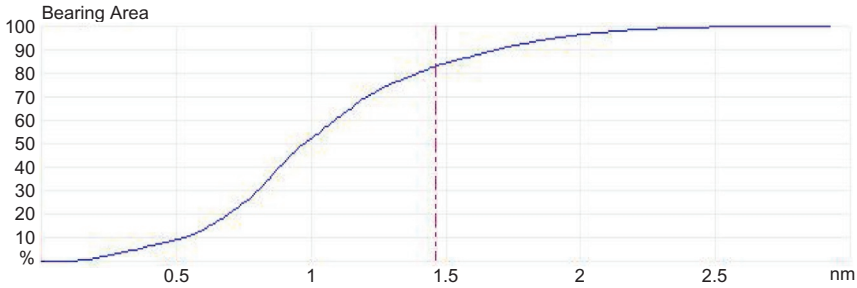

(e)

Figure 20.11 Continued. (d) Measured cross-sectional thickness of WO_3 nano-flake deposited on a SiO_2/Si/Au substrate. (e) Bearing analysis of WO_3 nanoflake with thickness of ~2.0 nm.

Table 20.2 Results of bearing analysis of exfoliated 2D WO_3 nanoflakes with measured thickness of 4.0 and 2.5 nm

N/N	Results	WO_3 nano-flake with thickness 4.0 nm	WO_3 nanoflake with thickness 2.5 nm
1	Bearing area	1464.40 nm^2	291,298 nm^2
2	Bearing area percent	87.05%	83.20%
3	Bearing depth	4.13351 nm	1.46694 nm
4	Bearing volume	9514.03 nm^3	596,813 nm^3
5	Box area	1682.28 nm^2	350.133 nm^2
6	Center line average	1.74382 nm	0.974142 nm
7	Histogram area	10.6785 nm^2	0.718748 nm^2

developed W^{5+} is delocalized within the layers, because it is not tightly bound to any W^{6+} core cation. This will give rise to a gap state between the valence and conduction bands of WO_3, hence narrowing its bandgap. On the other hand, W^{5+} ($5d^1$) ions form the complexes of $W^{5+}O_3{}^-$, acting as modifiers and inducing structural disorder in the top layers of Q2D material. Changes in the bandgap of 2D WO_3 nanoflakes upon H^+ intercalation are presented in Figure 20.12a. The measured bandgap of an exfoliated 2D WO_3

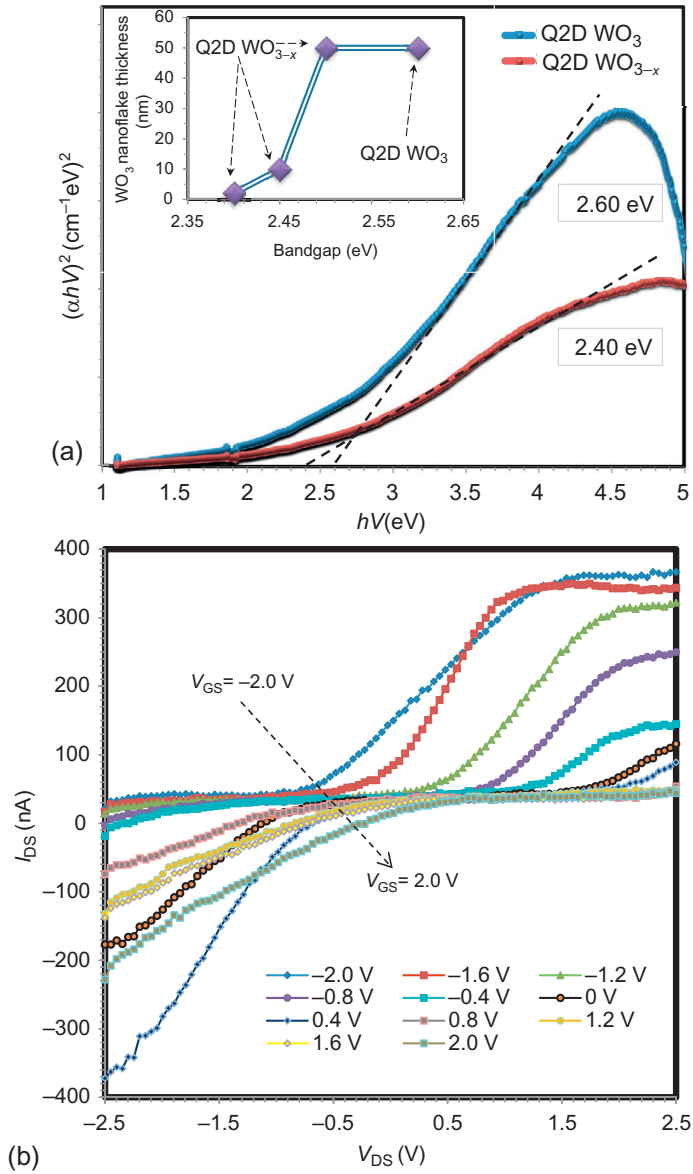

Figure 20.12 Experimental characteristics on 2D WO_3 and WO_{3-x} nanoflakes. (a) Photon energy versus $(\alpha hV)^2$ curves derived from the absorbance spectrum of 2D WO_3 nanoflakes (thickness 50 nm) and 2D H^+-intercalated substoichiometric WO_{3-x} (thickness 2 nm). Intersection of the linear fit with the x-axis indicates the bandgap energy, used to depict the change in estimated optical bangap. Inset is the bandgap changes recorded for 2D WO_3 and WO_{3-x} nanoflakes of different thickness. (b) The experimental drain current (I_{DS}) versus drain voltage (V_{DS}) characteristics of the FET with varying backgate voltages (V_{GS}) in steps 0.4 V from −2.0 to +2.0 V for 2D WO_3.

(*Continued*)

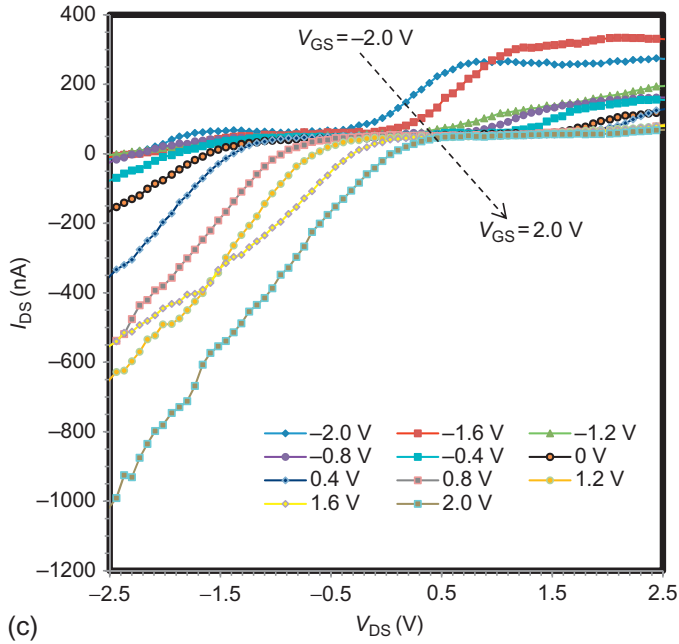

Figure 20.12 Continued. (c) The experimental I_{DS} vs. V_{DS} characteristics of the FET with varying V_{GS} in steps 0.4 V from −2.0 to +2.0 V for H^+-intercalated 2D substoichiometric WO_{3-x}.

nanoflake with a thickness of 50 nm was 2.60 eV, which was consistent with the reported data for bulk polycrystalline orthorhombic β-WO_3 (from 2.62 (Zheng et al., 2011) to 2.90 eV (Chang et al., 2007)) at the room temperature. After H^+ intercalation, the bandgap in this nanoflake was reduced from 2.60 to 2.50 eV. Further reduction was obtained for the thinner nanoflakes, as displayed in the inset of Figure 20.12a. The thinnest layered 2D WO_{3-x} nanoflake with a thickness of ∼2.5 nm has exhibited the reduction in bandgap to 2.40 eV. Collectively, these results confirm the presence of nonstoichiometric 2D WO_{3-x} and the reduction of bandgap as a function of x.

The performances of exfoliated and H^+-intercalated 2D WO_{3-x} nanoflakes were measured in air at room temperature. Typical source-to-drain I_{DS}-V_{DS} characteristics were obtained for a range of backgate voltages as presented in Figure 20.12b and c. The gate modulation seems significant under the small range of gate bias (from −2.0 to 2.0 V) (Liu et al., 2011) considering that the FET has a very thick gate dielectric layer (300 nm of SiO_2). Double sweeps of I_{DS}-V_{DS} characteristics show nonlinear behavior with negligible hysteresis. The current I_{DS} markedly increases as V_{DS} increases at positive gate bias (V_{GS}), indicating that the channel is n-type. The I_{DS} -V_{DS} characteristics exhibited a clear pinch-off and current saturation, confirming that the 2D WO_3-based transistor follows the standard FET theory. The transistor function for the FET device based on exfoliated 2D WO_3 at various V_{GS} at room temperature is presented in Figure 20.13a. It is important to acknowledge that the FETs

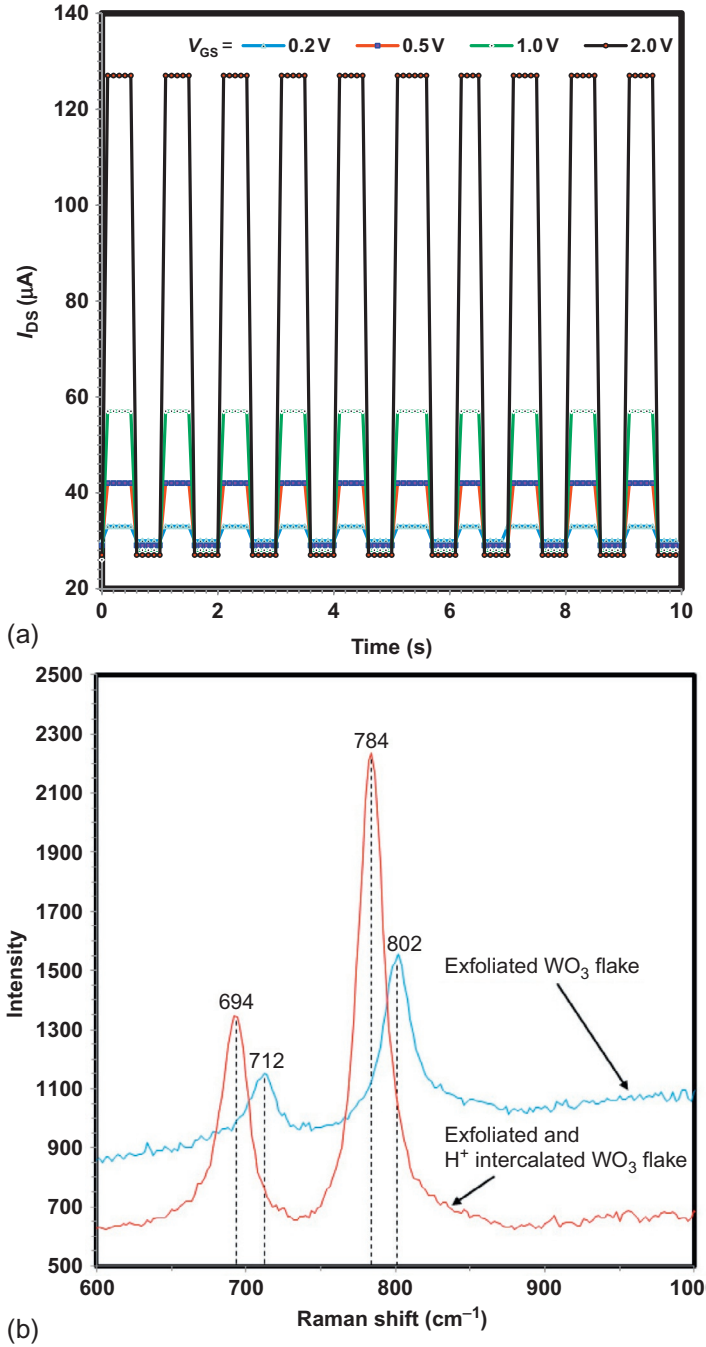

Figure 20.13 Experimental characteristics of FET device based on 2D WO_3 and WO_{3-x} nanoflakes. (a) Transistor function of FET based on exfoliated 2D WO_3 nanoflake at various V_{GS} at room temperature. (b) Raman spectra (shift in perturbation region 600–1000 cm^{-1}) for both 2D WO_3 and WO_{3-x} nanoflakes.

could not be completely switched off. The H^+ intercalation process caused the top oxide layer to become nearly metallic (discussed later) effectively reducing the on/off ratio to $<10^3$. Owing to H^+ intercalation, the near metallic top layer of the 2D WO_{3-x} nanoflake has been confirmed as very effective for injection of excess electrons, similar to high-mobility transistor structures (Ando et al., 1982a).

The charge carrier mobility was calculated from the obtained *I-V* curves (Figure 20.12b and c). The carrier mobility increased from 275 $cm^2\ V^{-1}\ s^{-1}$ for 2D WO_3 nanoflake to 319 $cm^2\ V^{-1}\ s^{-1}$ for a substoichiometric 2D WO_{3-x} nanoflake with thickness of 10 nm. Such high-mobility values are compatible with reported charge carrier mobility in Q2D MoO_3 (1100 $cm^2\ V^{-1}\ s^{-1}$) (Balendhran et al., 2013a; Zhuiykov and Kats, 2013; Zhuiykov, 2014), 2D MoS_2 (200-500 $cm^2\ V^{-1}\ s^{-1}$) (Radisavljevic et al., 2011; Radisavljevic and Kis, 2013), 2D black phosphorus FETs (Li et al., 2014b) (984 $cm^2\ V^{-1}\ s^{-1}$), and compared favorably with typical silicon-based devices that are commercially available ($\sim$500 $cm^2\ V^{-1}\ s^{-1}$) (Schwierz, 2010). The gate modulation was determined to be significant under a small range of gate bias (from -2.0 to 2.0 V), considering that we have a thick gate dielectric layer of SiO_2 ($\sim$300 nm). As top-gate bias is increased above $V_{GS} = 1.0$ V, the stable characteristics were impossible to obtain, the system was driven into a metallic phase, and weak localization seemed to be the dominant effect. At various gate biases, small electron leakage was also observed (Figure 20.12b and c). The enhanced performance of FETs based on 2D WO_3 and WO_{3-x} can be explained by the physics of a high-*k* layer of material. Although the calculated theoretical mobility based on the Born approximation (Ando et al., 1982b) was higher than the measured one, this was possibly due to the roughness of the SiO_2 surface, which increased the roughness scattering effect. Owing to near Ohmic contacts between 2D WO_{3-x} nanoflakes and established Au electrodes, electrons can be easily transferred from Au to the near metallic top layer of 2D WO_{3-x} during the FET operation. They then can be further injected into the underneath layers of WO_{3-x} through van der Waals gaps. The Coulomb charges introduced by H^+ intercalation and the reduction of WO_3 to the substoichiometric WO_{3-x} produced gap states, resulting in the lowering of the material's bandgap. In low-*k* materials, the incorporation of Coulomb charges decreases the carrier mobilities due to the Coulomb scattering effect, whereas in high-*k* substoichiometric WO_{3-x}, the Coulomb scattering effect is minimized and the carrier mobility increased. The reduction of Coulomb scattering effect resulted in the enhanced carrier mobility values (319 $cm^2\ V^{-1}\ s^{-1}$), which are substantially higher than those reported for the bulk WO_3 (Berak and Sienko, 1970). The increase in the carrier mobility confirmed the fact that substoichiometric 2D WO_{3-x} is genuinely an attractive 2D system with strong acoustic scattering.

Raman spectroscopy was employed to study the impact of H^+ intercalation on 2D WO_3 and results are presented in Figure 20.13b. For exfoliated 2D WO_3, two major relatively sharp bending modes at 712 and 802 cm^{-1} were observed, suggesting that 2D WO_3 has high crystallinity and order. The prominent band situated at 802 cm^{-1} has been assigned to the symmetric stretching mode of terminal ($W^{6+}=O$) groups, which may also be vibrationally coupled (Ou et al., 2013). This peak represents lattice discontinuities leading to short-range (lattice) order. The presence of an O–W–O bond is typically associated with β-WO_3. There were no other substantial peaks noted, indicating that no impurities and other phases were present in the samples. Bridging

(O–W–O) vibrations, which occur around 700 cm^{-1}, are influenced significantly by hydration, and as a result, the recorded 712 cm^{-1} bond can be used as a spectral marker for the hydration level of WO_3 (Breedon et al., 2010a). However, care should be exercised using this approach, because the crystalline hexagonal phase (h-WO_3) also exhibits bonds at these frequencies, but is absent in the sample that was confirmed by XRD results. Strong new Raman peaks are observed at 784 and 694 cm^{-1} for the H^+-intercalated substoichiometric 2D WO_{3-x}, representing the deformation W_3–O and W_2–O stretching bonds of H_xWO_{3-x}, respectively (Sze and Kwok, 2007). The large shift ($\sim$18 cm^{-1}) for both W_3–O and W_2–O stretching bonds suggested that the H^+ ions interact preferably with sites in the sequence of doubly coordinated oxygen → terminated oxygen → triply coordinated oxygen. The increased intensity of 784 and 694 cm^{-1} bonds for intercalated substoichiometric WO_{3-x} also signified that the first fundamental layer of WO_3 became more metallic. The absorbed H^+ ions mainly interacted with the lattice corner-sharing oxygen atoms of the WO_3 first monolayer, developing H_xWO_{3-x} structures. The remaining H^+ ions then transferred deeper into the second layer of WO_3 and repeated the same interaction, leaving lone oxygen vacancies and resulting in formation of substoichiometric WO_{3-x}. All these findings and compilations indicate the transformation from the original β-WO_3 into H_xWO_{3-x} upon H^+ intercalation. Collectively, these results confirmed the development of substoichiometric WO_{3-x} and the ability of the bandgap reduction as function of x.

The electronic structure and surface chemical composition of both exfoliated and H^+-intercalated 2D WO_{3-x} was analyzed by the XPS method. The decomposition of W4f and O1s spectra was carried out by the Gauss-Newton method. The area of peaks was determined after subtraction of background by the Shirley method (Briggs and Search, 1983). Figure 20.14a depicts the XPS survey scan spectra of exfoliated and H^+-intercalated 2D WO_{3-x}. The C1s peak at 284.6 eV, which originates from the surface-adsorbed carbon species, is used for calibration purpose. The detailed core-level spectra of W4f and O1s peaks for both exfoliated 2D WO_3 and H^+-intercalated WO_{3-x} are shown in Figure 20.14b and c. The high resolution spectra of W4f presents doublet peaks and fitted results after Shirley background subtraction, the maxima of peak couples corresponded to $W4f_{7/2} = 35.76$ eV (line 2, Figure 20.14b), and $W4f_{5/2} = 37.85$ eV (line 4, Figure 20.14b). The energy position of the main peaks corresponded to the W^{6+} state. The $W4f_{7/2}$ peak at 35.76 eV in this work is in good agreement with the literature value of 35.70 eV characterizing the W^{6+} state in WO_3 (Breedon et al., 2010b). The measured maxima of peak couples corresponded to $W4f_{7/2}$- and $W4f_{5/2}$-levels of sol-gel, and prepared nanostructures for W^{6+}-states of tungsten oxide differ from the maxima of the same peaks recorded for the RF sputtered WO_3 nanostructures ($W4f_{7/2} = 34.35$ eV; $W4f_{5/2} = 36.57$ eV) (Charton et al., 2002), WO_3 nanoparticles sintered at 280 °C ($W4f_{7/2} = 35.83$ eV; $W4f_{5/2} = 37.93$ eV) (Dupin et al., 2000), and for WO_3 microspheres ($W4f_{7/2} = 34.50$ eV; $W4f_{5/2} = 36.80$ eV) (Shpak et al., 2007). Of note, the maxima of peak couples corresponded to $W4f_{7/2}$- ($W4f_{7/2} = 35.19$ eV) and $W4f_{5/2}$- ($W4f_{5/2} = 37.35$ eV) levels have repositioned when the WO_3 was exfoliated and H^+-intercalated: lines 1 and 3 of Figure 20.14b, respectively. This shift indicates the contribution of W^{5+}-states from the substoichiometric oxide phase of WO_{3-x} in comparison with stoichiometric WO_3 owing to the increased number of oxygen vacancies created during the intercalation (Leftheriotis et al., 2003).

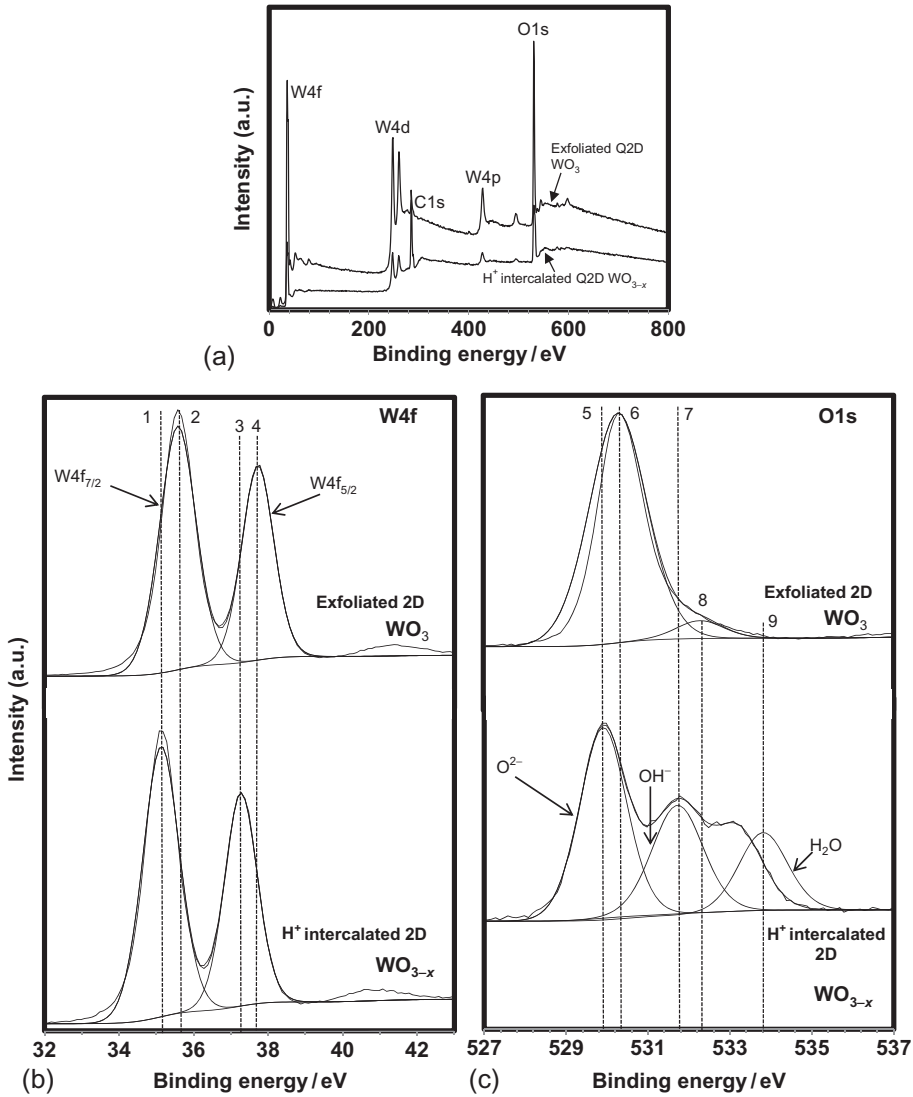

Figure 20.14 XPS measurements and analysis of core-level photoelectron peaks for 2D WO_3 nanoflakes. (a) XPS survey scan spectra for exfoliated 2D WO_3 and H^+-intercalated WO_{3-x}. (b) The high resolution spectra changes for W4f. (c) The high resolution spectra changes for O1s. All measurements are performed at $T = 20\ ^\circ C$.

Figure 20.14c displays O1s peaks for exfoliated 2D WO_3 and H^+-intercalated WO_{3-x}, respectively. The peak with maximum O1s = 530.5 eV corresponds to O1s-levels of oxygen atoms O^{2-} in the lattice (line 6, Figure 20.14c) (Leftheriotis et al., 2003). A small contribution from OH-groups (line 8, Figure 20.14c) must also be noted, confirming that the structure of all the components (lines 6 and 8) is quite complex. This is due to the fact that free oxide surfaces contacting the atmosphere are always

hydrated, that is, contain water molecules and hydroxyl groups. However, because WO_3 nanocrystals were exfoliated and further H^+-intercalated, their O1s spectra exhibited stimulating and engaging features as the influence of other components on the spectra was enhanced. First of all, the peak's maximum, assigned to the presence of O^{2-} ions forming the strong W=O bonds in the crystalline network, has been shifted to 529.9 eV (line 5, Figure 20.14c). This value correlates well with the previously published data for substoichiometric WO_{3-x} (Wagner et al., 1979). Although the contribution from O^{2-} lattice oxygen atoms dominates in the O1s-line, the second peak at 531.8 eV (line 7, Figure 20.14c) can be described as the existence of weakly adsorbed species, and O^- oxygen states agreed with OH^- groups (Shpak et al., 2007). There are two types of OH-groups on the surface: single M–OH and double OH=M=OH. They are present only in substoichiometric oxides (Wagner et al., 1979). Nevertheless, this peak has also been attributed to O atoms in substoichiometric WO_{3-x}. The third peak at 533.9 eV (line 9, Figure 20.14c), corresponds to the oxygen bound in H_2O adsorbed on the surface (Vemuri et al., 2011). In the exfoliated and H^+-intercalated 2D WO_3 samples, the contributions of OH^- and H_2O components into O1s-line are more considerable and comparable to the input from O^{2-}-states. The growth of OH-groups in the substoichiometric WO_{3-x} can be explained by the possibility of oxygen vacancy infill by OH-group, where the W^{5+}-cation should be in the center of the octahedron of five O^{2-}-ions and one OH^--anion. Consequently, the formula of such a substoichiometric compound can be presented as ${W_x}^{5+}{W_{1-x}}^{6+}O_{3-x}(OH)_x$, where x are the hydroxyl groups that filled oxygen vacancies in the lattice (Shpak et al., 2007).

XPS measurements of exfoliated and H^+-intercalated 2D WO_3 samples confirmed the development of substoichiometric WO_{3-x}. Considering that the content of OH-groups and H_2O in substoichiometric WO_{3-x} oxides is proportional to the substoichiometry value x, it can be concluded that there is a direct link between the catalytic and electrochemical activity of oxide-hydroxide compounds and ion component of conductivity formed by hydroxyl groups. Therefore, in nonstoichiometric Q2D tungsten oxides, the following transition ${W_x}^{5+}{W_{1-x}}^{6+}O_{3-0.5x} \rightarrow {W_x}^{5+}{W_{1-x}}^{6+}O_{3-x}(OH)_x \rightarrow WO_3 \cdot (OH_2)_n$ is observed as a result of H^+ intercalation.

Consequently, the developed FET architecture based on 2D β-WO_3 and WO_{3-x} nanoflakes with tunable flake bandgap exhibited the enhanced charge carrier mobility of 319 $cm^2\ V^{-1}\ s^{-1}$ at room temperature. By controlling and decreasing the thickness of WO_{3-x} from 50 to ~2.0 nm and by H^+ intercalation, we engineered the bandgap of this Q2D material from 2.6 to 2.4 eV and preferentially developed substoichiometric WO_{3-x}, enabling the significant improvement in charge carrier mobility. In the context of electronic applications, the layered Q2D materials with enhanced charge carrier mobility, proven transistor function, and adjustable bandgap enable the development of devices built entirely from ultrathin, flexible, and transparent 2D materials. The tunability of bandgap combined with the enhanced charge carrier mobility for substoichiometric WO_{3-x} is a necessary benefit for optoelectronic, electrochromic, and nanoelectronic applications. Moreover, both the fabrication process and its framework have great compatibility with other emerging 2D semiconductors and conductors such as graphene. Research efforts in these directions could potentially ensure that the 2D WO_{3-x} is able to compete with the best 2D semiconductor materials available today.

20.1.5 Properties of 2D black phosphorus FETs

Although the most stable and least reactive form of phosphorus was discovered in bulk form about 100 years ago, its realization in 2D form has brought black phosphorus back to the spotlight in 2014 (Vemuri et al., 2011; Li et al., 2014b). Black phosphorus layers have an anisotropic structure, unique among layered materials. Inside of a single layer, each phosphorus atom is covalently bonded with three adjacent phosphorus atoms to form a puckered honeycomb structure (Churchill and Jarillo-Herrero, 2014) (Figure 20.15a). Two atoms in-plane, in mutually perpendicular directions, have armchair and zigzag edges. The structural anisotropy strongly influences the electronic properties in these two directions. For example, the electron effective mass is several times lighter in the armchair direction than in the zigzag direction (Vemuri et al., 2011), and recent studies have indeed shown a strong angular dependence of the conductivity of few-layer black phosphorus. 2D black phosphorus is a semiconductor with direct bandgap of ~0.3-1.0 eV (Li et al., 2014b) (Figure 20.15b). This band structure provides a bandgap suitable for FET applications in 2D form for optoelectronics, particularly for the infrared region. One intriguing prospect is that in heterostructures created from black phosphorus and other layered materials, the anisotropy of black phosphorus could "leak" into neighboring layers and induce new characteristics and capabilities. For example, graphene, which is isotropic, may inherit anisotropic electrical, optical, or mechanical properties when draped over black phosphorus. It also worth noting that similar buckling also occurs for the layered semiconductors silicene (Butler et al., 2013) and germanane (Koski and Cui, 2013), but electronic devices have not yet been fabricated with these materials because they have so far had to remain bound to metal growth substrates.

The configuration of the FET-based device on 2D phosphorus is presented in Figure 20.16a (Li et al., 2014b). The backgate voltage V_g, applied to the degenerated doped silicon, with the source-drain bias V_{ds} across the black phosphorus conductive channel, held at fixed values. The results obtained from a device with a 5 nm thick channel on top of a 90 nm SiO_2 gate dielectric are shown in Figure 20.16b. When the gate voltage was varied from −30 to 0 V, the channel switched from the on-state to the off-state, and a drop in drain current by a factor of $\sim 10^5$ was observed. The measured drain current modulation is four orders of magnitude larger than that in graphene (due to its lack of a bandgap) and approaches the value recently reported in MoS_2 devices (Lee et al., 2012a). Similar switching behavior (with varying drain current modulation) was observed on all black phosphorous thin-film transistors with thicknesses up to 50 nm. It has to be noted that on-state current of devices has not yet reached saturation due to the fact that the doping level is limited by the breakdown electric field of the SiO_2 backgate dielectric. It is therefore possible to achieve even higher drain current modulation by using high-k materials as gate dielectrics for higher doping. Meanwhile, a subthreshold swing of ~5 V per decade is observed, which is much larger than the subthreshold swing in commercial silicon-based devices (~70 mV per decade). The subthreshold swing in the devices varies from sample to sample (from ~3.7 V per decade to ~13.3 V per decade) and is of the same order of magnitude as reported in multilayer MoS_2 devices with a similar backgate configuration (Cartz et al., 1979). The relatively big subthreshold swing is mainly attributed

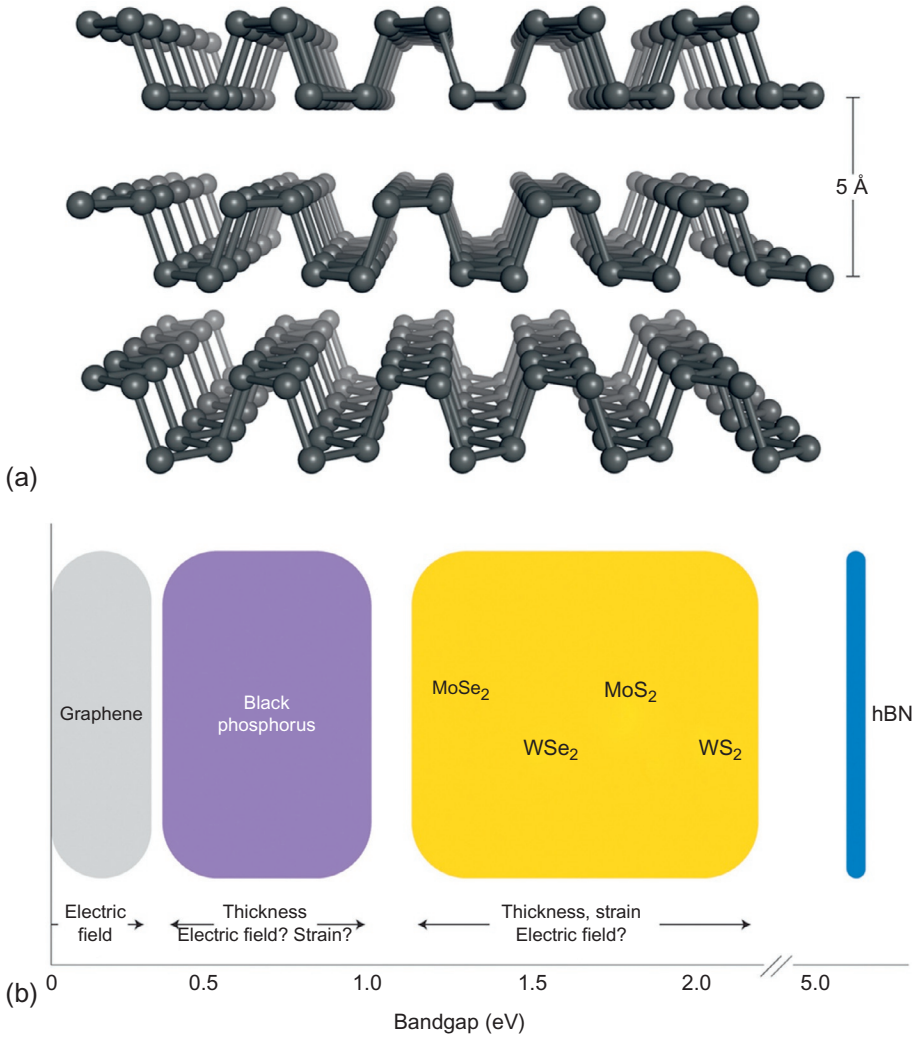

Figure 20.15 Black phosphorus structure of layered materials. (a) The layered and anisotropic crystal structure of elemental black phosphorus. (b) Bandgap energies of several layered materials used for nanoelectronics. The range of values for each material can be achieved through a variety of means. For example, it is expected that variations in an applied perpendicular electric field, film thickness, or strain could modify the bandgap value. hBN, hexagonal boron nitride.
(Reprinted from Vemuri et al. (2011) with permission from Nature Publishing Group.)

to the large thickness of the SiO_2 backgate dielectric and multiple factors such as insulator layer thickness (Das et al., 2013) and the Schottky barrier at the subthreshold region (Cartz et al., 1979). The sample-substrate interface state may also have an influence.

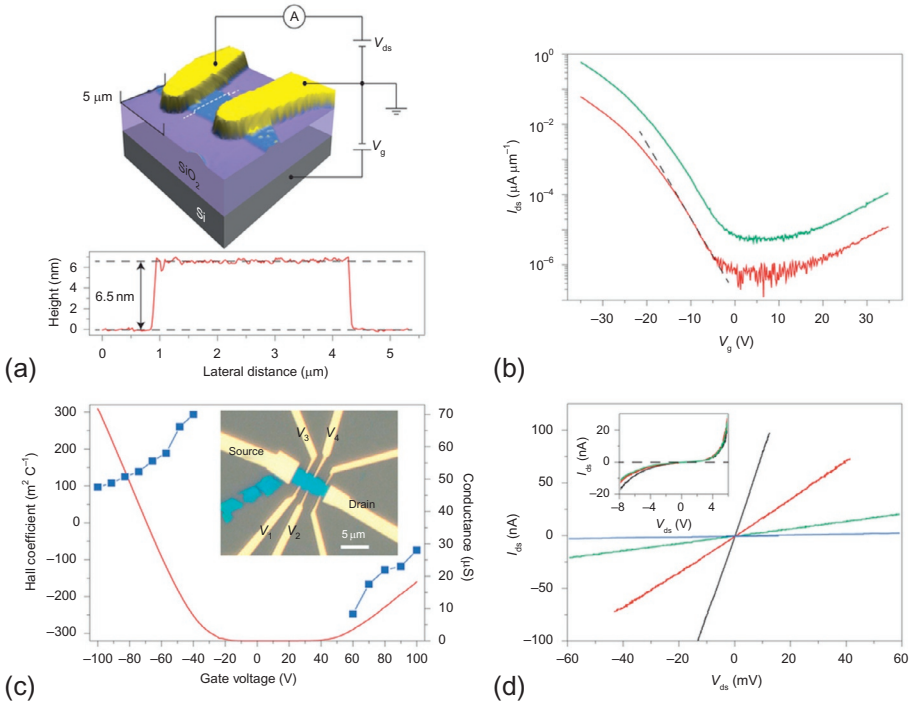

Figure 20.16 (a) Top: Schematic of device structure of a few-layer phosphorene FET. The device profile shown here is the three-dimensional rendering of the AFM data. Bottom: Cross-section of device along the white dashed line in the schematic. (b) Source-drain current (on a logarithmic scale) as a function of gate voltage obtained from a 5 nm thick device on a Si substrate with 90 nm SiO_2 at room temperature, with drain-source voltages of 10 mV (red curve) and 100 mV (green curve). Channel length and width of the device are 1.6 and 4.8 μm, respectively. (c) Hall coefficient (blue curve) and conductance (red curve) as a function of gate voltage from a 8 nm thick sample. Inset: Optical image of a typical multiterminal few-layer phosphorene device. (d) *I-V* characteristics of the device in (b). Linear behavior is seen at $V_g = -30$, -25, -20, and -15 V (black, red, green, and blue curves, respectively), indicating ohmic contact on the hole side of the gate doping. Inset: Nonlinear behavior on the electron side ($V_g = 30$, 25, and 20 V; black, red, and green curves, respectively) of the gate doping indicates the formation of a Schottky barrier at the contacts.
(Reprinted from Li et al. (2014b) with permission from Nature Publishing Group.)

The switching off at the negative side of the V_g sweep is accompanied by a slight turn-on at positive gate voltages, presented in Figure 20.16b. To further explore this ambipolar behavior, few-layer phosphorene devices were fabricated with multiple electrical contacts (inset in Figure 20.16c), and Hall measurements were performed using two opposing contacts (V_2 and V_4, for example) perpendicular to the drain-source current path to measure the transverse resistance R_{xy}. The Hall coefficient R_H, defined as the slope of R_{xy} as a function of external magnetic field B, reflects both the sign and density of the charge carriers in the sample. As shown in Figure 20.16c, a

carrier sign inversion is clearly observed in the on states, with positive and negative gate voltages corresponding to hole and electron conduction, respectively. This unambiguously shows that the ambipolar switching of the devices is caused by Fermi level shifting from the valence band into the conduction band.

The nature of the electrical conduction was probed further by performing *I-V* measurements in a two-terminal configuration (Figure 20.16a). Figure 20.16d exhibited that the source-drain current I_{ds} varies linearly with V_{ds} in the on state of the hole side, indicating an ohmic contact in this region. Meanwhile, I_{ds} versus V_{ds} is strongly nonlinear on the electron side (inset in Figure 20.16d), as is typical for semiconducting channels with Schottky barriers at the contacts. The observed *I-V* characteristics can be readily explained by work-function mismatch between the metal contacts and few-layer phosphorene; the high work-function of the metal electrodes causes hole accumulation at the metal-semiconductor interface, which forms a low-resistance Ω contact for the *p*-doped sample, while for the *n*-doped sample a depletion region is formed at the interface, leading to Schottky barriers and thus nonlinear conduction. This model also explains the observed disparity between conduction at the electron and hole sides in all our samples (Figure 20.16b) and is widely accepted to describe the contact behavior in MoS_2 devices (Knoch et al., 2007). For potential applications in digital and radiofrequency devices, saturation of the drain current is crucial in order to reach maximum possible operation speeds (Schwierz, 2010). By carefully choosing the ratio between channel length and SiO_2 layer thickness, a well-defined current saturation can be achieved in the high drain-source bias region. Meanwhile, the electrical contacts remained ohmic in the linear region at low drain-source biases. Coupled with the fact that the channel thickness is on the order of nanometers and thus robust against short-channel effects when the channel length is reduced to the nanometer scale, the results (Li et al., 2014b) suggest the high potential of black phosphorus in high-speed FET-based devices. It has to be also noted that the state conductance of the device is relatively low and the threshold source-drain bias is relatively high compared to typical silicon-based devices. Both factors are attributed to the long channel length in presented current device. Better device performance, that is, larger saturation current and lower threshold bias, is expected if the channel length and the gate oxide thickness are reduced.

Nevertheless, black phosphorus is an exciting rediscovery for the materials science community, and it has quickly become the subject of significant theoretical and experimental investigations. However, it is not yet clear how well thin black phosphorus performs compared to other layered materials such as graphene and MoS_2. It was established that the electronic mobility—a key indicator of device quality—reaches the promising value of 984 $cm^2\ V^{-1}\ s^{-1}$ in multilayer black phosphorus devices, but the mobility drops as the material is thinned down (Li et al., 2014b). As a result, an 8 nm thick film of black phosphorus (about 15 layers) is shown to possess a mobility comparable to the best devices made from monolayer MoS_2. Furthermore, although black phosphorus is the most stable allotrope of phosphorus, it may not be as robust in air as other layered materials (Vemuri et al., 2011). This may partially explain the mobility degradation of thinner films and could be overcome by exfoliating and encapsulating few-layer black phosphorus while in an inert atmosphere.

20.2 Improvement of fabrication methods for 2D semiconductors

20.2.1 Overview of strategies toward synthesis of 2D nanocrystals

The rapid rising of graphene research evidences not only its basic scientific interest but also its potential technological impact. Actually, graphene is just the tip of the iceberg in the research area of 2D nanomaterials. Other 2D nanocrystals beyond graphene, such as inorganic BN, transition-metal dichalcogenides, zirconium phosphates, perovskites, birnessite-type manganese oxide (MnO_2), and other metal oxide nanosheets, as well as organic self-assembled porphyrin, C60, and polymer nanosheets, have also triggered worldwide interest. Similar to graphene, these 2D nanocrystals also exhibit unique physical and chemical properties that are accompanied with many intriguing potentials. Most importantly, the unique features of 2D nanosheets imparted from dimensional-size effect differ significantly from their respective 3D bulk forms.

Therefore, the development of 2D semiconductors with controlled architectures plays a key role in various applications and will open up new possibilities to a level that is significantly higher than today's commercial semiconductor technologies. However, despite substantial efforts and unique scientific discoveries in the 2D semiconductors during last few years, most of them were obtained in the laboratories using quite simple technologies that cannot be used for industrial production.

In order to improve existing approaches toward the synthesis of 2D semiconductors and identify new possibilities for unification of their technologies, two basic strategies for fabrication 2D nanosheets schematically are presented in Figure 20.17. One scenario is the *top-down* method (Figure 20.17a), which typically involves the delamination/exfoliation of layered inorganic materials (such as graphene, BN, MoS_2, WSe_2, TiO_2, MoO_3, WO_3) and layered covalent organic frameworks (COFs). However, the bottleneck in this method is the extremely low yield of product and restacking of sheets during solidification. The other procedure is based on the *bottom-up* anisotropic assembly of inorganic, organic, or polymeric precursors in a 2D manner. Despite success in the fabrication of some 2D nanomaterials based on the above two approaches, the deep investigations of rationally designed 2D nanosheets with various functionalities in electrochemical energy storage and conversion remain primitive. Thereby, the full exploration of the uniqueness of 2D nanomaterials with tailored thickness, high surface area, good conductivity, and mechanical flexibility to accelerate ion diffusion and electron transport in various applications will be highly demanded. As to applications in supercapacitors and batteries, 2D nanosheets can be based on graphene, exfoliated inorganic nanosheets such as MoS_2, MnO_2, CoO_2, layered double hydroxide, and $Ni(OH)_2$, for example. For the purpose of catalysis in fuel cells, cobalt porphyrin nanosheets, nitrogen/boron-doped graphene, or carbon, Fe-N4, or Co-N4 chelated porous carbon and carbon nitride nanosheets can be promising candidates.

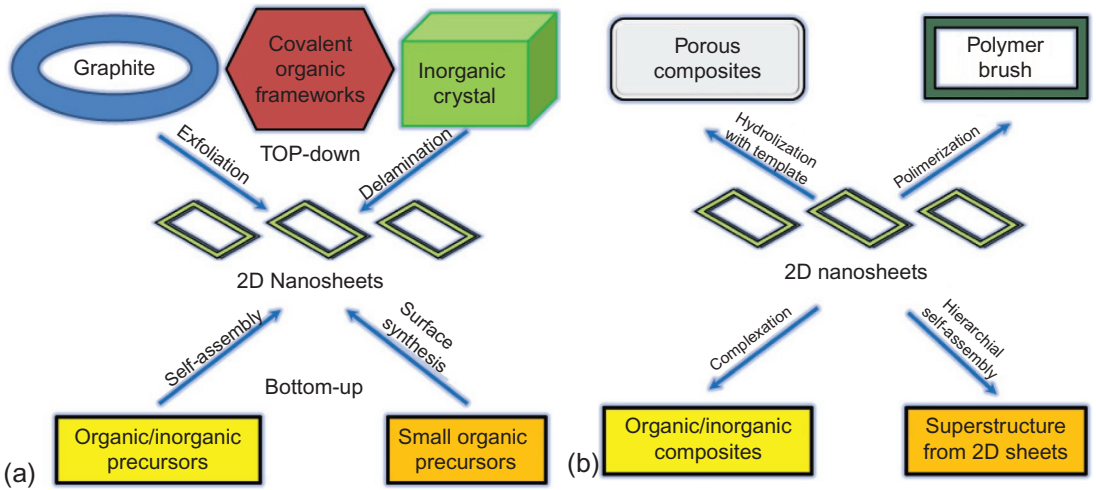

Figure 20.17 (a) Schematic illustration of different strategies toward the synthesis of 2D nanosheets. (b) Schematic presentation of various approaches toward fabrication of 2D and other dimensional nanocrystals based on the precursor 2D nanosheets.

In the near future the cost-effective fabrication of graphene, namely top-down chemical exfoliation of graphite into graphene oxide nanosheets, will be developed, followed by chemical, thermal, or photocatalytic reductions. The advantages of these approaches include high throughput synthesis, easy processability from solution, and tailor-made property via chemical modification. The promise of graphene thin films for replacing conventional metal oxide and metal electrodes in organic electronics, such as organic solar cells, organic FETs, and organic photodetectors, has already been demonstrated (Fontana et al., 2013). The rational incorporation of metal or metal oxide/hydroxide nanoparticles and porous polymers on graphene surface to build up hierarchical nanocomposites consisting of core-shell, 2D-sandwich, or 3D macro-porous framework architectures has also been demonstrated (Zhuiykov, 2014). These unique features lead to high-performance electrode materials in energy storage and conversion, such as batteries, supercapacitors, and fuel cells. Main properties and typical applications, where 2D semiconductors can be utilized, are presented in Figure 20.18.

The ambitious and adventurous goal of the existing research programs, dedicated to the development of new technologies of making 2D semiconductors, is to create chemical approaches toward the synthesis and applications of 2D nanosheets and their 2D composite materials for different applications. In this regard, more reliable and fundamental correlation between structures and physical properties of 2D nanomaterials must be established.

Based on the existing knowledge, the main focus of such programs initially will be on synthesizing and processing various 2D nanosheets across a broad range of inorganic, organic, and polymeric materials with atomic and thin thickness through both the top-down and bottom-up strategies. Second, various nanosheet-based 2D composite materials (Figure 20.17b) with ordered structures and thicknesses of less than 100 nm will be developed and synthesized. The thickness and composition of the

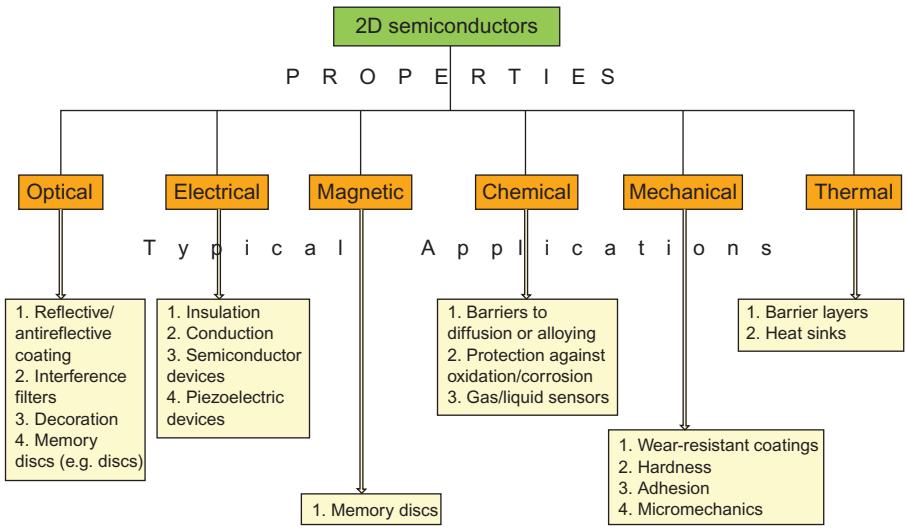

Figure 20.18 Properties and typical applications of 2D semiconductors.

2D nanosheets will be tailored by using layered precursors and processing methodologies. Control over the aspect ratio, morphology, and chemical nature of all isolated 2D nanosheets will be a key issue to differentiate our present approach from existing literature efforts; it will be also significantly different from the previous work on graphene itself. The assembly/processing of 2D nanosheets into different hierarchical superstructures such as 1D, 2D, and 3D (aerogels, multilayer films, spheres, porous particles, nanotubes) will be the third key direction in this research, which stands out in contrast to the current state-of-art research on 2D nanosheets. As a result of this approach, new 2D nanomaterials for specific applications will be created by applying the defined functional components and processing methods of chemical assembly. Further characteristics of the research work will involve the investigation of the surface chemistry, morphology, composition, conductivity, and electrochemical behavior. Although these research programs constitute a great chemical challenge in their own right, they also hold tremendous promise for condensed matter physics and materials science. The gain resulting from these programs will be novel 2D nanomaterials that can be effective and favorable not only for energy-related technologies, such as high-performance lithium ion batteries (anode and cathode), supercapacitors (symmetric, asymmetric, and all solid-state device), and fuel cells, but also for many other purposes, such as thermoelectrics, electronics, molecular adsorption, membrane and photocatalysis.

In addition to the method- and concept-oriented issues, there are many open questions that are presently uncertain regarding, for instance, the structure-property relationships. Which kind of 2D nanosheets can be obtained from the anisotropic assembly of inorganic components in a controlled 2D manner? How can we synthesize soft organic and polymer sheets, in particular for 2D polymers and 2D supramolecular polymers? How can we assemble inorganic/organic nanostructures (such as particles or rods) on 2D nanosheets with a strong interface coupling for producing 2D-ordered nanohybrids? How can we build up ordered mesoporous structures of inorganic species on the 2D nanosheet templates? What is the role of the 2D nanosheets in improving the electron transport and ion diffusion in the bulk electrode of energy-related systems? Which nanosheet and 2D nanomaterials can be assembled into 1D or 3D hierarchical superstructures? These questions pose obvious risks. However, the implementation of the new approaches into feasible research programs could provide answers to those questions. This will be associated with attempts at combining chemistry and processing of 2D nanomaterials with the needs of materials science and device fabrication.

The first target is the fabrication of new high-quality 2D nanosheets by top-down exfoliation of layered materials including graphite, COFs, BN, and other inorganic crystals as well as bottom-up assembly of organic and polymeric components (Figure 20.17). These pose enormous challenges in producing 2D nanosheets with molecular-level thickness, listed as follows:

(a) The exfoliation process of lamellar crystals occurs because of the strong interaction between the composing layers and intercalates solvent molecules such as alkali metal cations and large cationic ions, which will be utilized to expand the interlayer space of layered compounds. Taking graphite as an example, because graphite intercalation compounds

generally show much larger interlayer spacing than the natural graphite, solvent molecules can be expected to readily penetrate within the graphitic layers and consequently promote the exfoliation process. Many-layered inorganic crystals can also be exfoliated/delaminated into 2D nanosheets by this type of method. On the one hand, one can explore bulky guest organic salts, such as Gemini-type ammonium ions tethered with large aromatic rings (like pyrene), to expand the interlayer distance of inorganic crystals and COFs, therefore enhancing surfactant-layer interactions and improving the exfoliation yield of single 2D nanosheets. Alternatively, the electrochemical exfoliation of layered inorganic crystals (such as BN, MoS_2) or graphite in the suitable acidic or ionic electrolyte systems to produce 2D nanosheets will also be advantageous. Nevertheless, one important obstacle needs to be overcome—stabilization of the dispersion of 2D nanosheets with high concentration in water or polar organic solvents, which are essential for the processing and exploration of their intrinsic properties and related composite materials.

(b) The next goal will be the fabrication of the 2D nanosheet-based ordered porous composite materials (Figure 20.17b) by utilizing the above inorganic (including graphene) or organic 2D nanosheets as the template. The critical issue is to establish an effective bottom-up approach to the large-scale production of 2D inorganic or organic-based porous silica, metal oxide, or polypyrrole sheets, in which each nanosheet is fully separated by an ordered porous shell in a sandwich manner. For instance, a possible strategy can be considered on the basis of the well-established sol-gel methods (Liao et al., 2010b) employing block-copolymers as structure-directing surfactants for controlling the porous structure of silica or polypyrrole. Thus, the aggregation of the precursor nanosheets can be fully prevented by the silica layer. A high surface area with ordered porous structure will be achieved as the result of the nature of porous silica shell. Through the use of 2D silica-based nanosheets as templates, a series of ordered porous 2D nanocomposites with a sandwich-like structure can be envisioned for their suitable applications in batteries (such as carbon, Fe_3O_4, SnO_2, Co_3O_4, NiO, and $Ni(OH)_2$), supercapacitors (such as polypyrrole, polyaniline, V_2O_5, MnO_2), and catalysis (such as Pt, Pd, Au, nitrogen-doped carbon, carbon nitride, titanium nitride, ferric nitride).

(c) The third goal is to fabricate various 2D nanosheets decorated with metal or metal oxide nanoparticles (such as Pt, Pd, Au, Fe, Co, TiO_2, Fe_3O_4, SnO_2), for which the high surface area of 2D nanosheets can be well maintained (Figure 20.17b). The resulting 2D nanocomposites, especially graphene or porous-carbon-based 2D nanomaterials, may serve as efficient catalysts for oxygen reduction reaction in fuel cells due to the favorable features:

- Homogeneous dispersion of metals on graphene/carbon sheet will render a high surface area, which can provide more active site to catalyze the oxygen reduction.
- Existence of graphene/carbon in composites can establish sufficient electrical conductivity network.
- Close interaction between graphene/carbon and metal nanoparticles could improve the cycling stability. Moreover, we may also use nitrogen- and/or boron-rich graphene/carbon sheets for further incorporation of catalytically active metals, such as Fe or Co with controlled FeN_4 or CoN_4 chelate formation. It is expected that not only high electrocatalytic performance, but also good tolerance to methanol and CO oxidation during oxygen reduction will be achieved.

(d) The fourth goal is to develop the assembly strategies toward the synthesis of 3D hierarchical materials on the basis of 2D nanosheets (Figure 20.17b). Due to the flexible nature of 2D nanosheets with high mechanical stability, they can be used to build up other

low-dimensional nanomaterials with different complexity. For instance, 2D nanosheets can roll up to form 1D nanotubes or fibers, while the stacking and curling of nanosheets can lead to the synthesis of 3D materials with layered or particle/vesicle structures (Figure 20.17b). Therefore, in order to attain these unique 3D architectures made from 2D nanosheets, the thermodynamic control of these materials in the solution will be applied by taking advantage of their flexible nature. The templating method can also be used by coating the 2D nanosheets on the surface of other low-dimensional materials to build up 3D or 1D architectures. The process involves layer-by-layer assembly of organic or inorganic materials on the surface of colloid particles as a template and subsequent removal of the templates through chemical or thermal methods resulting in hollow shell structures. 2D-nanosheet-based thin films and flexible papers will also be fabricated for high-performance, solid-state, and flexible electrochemical energy storage devices. One simple and versatile method to assemble variously dispersed 2D nanosheets into thin films is by using LBL assembly, which consists of the repeated, sequential immersion of a substrate into aqueous solutions of the functionalized materials such as carbon, polymer, and metal oxide. The freestanding paper-based materials with inherent flexibility will be prepared by vacuum filtration or electrochemical deposition. The obtained thin and flexible paper-like materials will be directly used for flexible energy storage devices.

The unique features of 2D nanosheets and their 2D nanocomposites with controllable porosity, high surface area, high aspect ratio, and high conductivity will efficiently facilitate their use in various applications:

(1) 2D nanomaterials such as mesoporous graphene-based nanomaterials can maintain the high electrical conductivity of the overall electrode.
(2) Mesoporous structure with thin thickness will facilitate the rapid diffusion of ions (for a battery) or the electrolyte to the interior.
(3) 2D feature will also effectively accommodate the large volume change during the cycling process.
(4) The loading content of metal or metal oxide in the composite sheets will be higher than that of the traditional composite materials.

Therefore, it is envisioned that this research direction will allow us to achieve high capacity, excellent cycle and rate performance electrode materials for various applications, which are dramatically different from the conventional bulk material-based electrochemical devices. It is believed that the prospective 2D graphene, metal oxides, metal dichalcogenides, BN, organic and polymeric nanomaterials will possess great potential for many other purposes, such as thermoelectrics, electronics, optoelectronics, molecular adsorption, water splitting, photocatalysis, and magnetic materials.

20.2.2 ALD for nano- and interfacial engineering of 2D semiconductors

Implementation of the strategies toward fabrication of the thickness-controlled 2D semiconductors and various 2D sandwich nanostructures can be achieved by ALD technique. ALD was first developed in the 1970s by T. Suntola and co-workers for the deposition of ZnS for display devices (Livage and Ganguli, 2001b). Since then, it has been used for the deposition of many types of materials, including oxides,

sulfides, selenides, tellurides, nitrides, and metals (Suntola, 1989). A key requirement is that suitable molecular precursors must undergo self-limiting reactions, because the primary distinction between ALD and other vapor deposition methods is that a self-saturating surface monolayer is formed after every precursor exposure. A thorough description of recent developments in ALD chemistry can be found in many review articles (e.g., Kim, 2003; Puurunen, 2005). So far ALD has been implemented in a diverse number of fields including microelectronics (Leskelä and Ritala, 2003), catalysis (Bakke et al., 2011), photovoltaics (George et al., 1996), and sensors (Jiang et al., 2008). Presently, ALD implementation toward the synthesis of 2D semiconductors and 2D sandwich structures is limited.

ALD is a deposition technique consisting of a series of self-limiting, surface-saturated reactions to form thin conformal films at a controllable rate. In implementation, it is similar to CVD, except that the precursors are not introduced into the reactor simultaneously but are typically separated in time by inert gas purges. As distinct from the other CVD techniques, in ALD the source vapors are pulsed into the reactor alternately, one at a time, separated by purging, or evacuation periods. Each precursor exposure step saturates the surface with a monolayer of that precursor. A monolayer's thickness is dependent on the reactivity of the precursor with the surface. This results in unique self-limiting film growth mechanism with a number of advantageous features, such as excellent uniformity and simple and accurate film thickness control. Consequently, the reaction is limited to the monolayer of reactant that has been adsorbed to the substrate. Through this modification, uniform, conformal films may be produced with precise control over the thickness of the film.

A mechanism for one cycle of an idealized binary ALD reaction is presented in Figure 20.19 (Leskelä and Ritala, 2003). First, a reactant is dosed into the chamber (step 1). The reactant either chemi-sorbs or physi-sorbs to the substrate, but does not react with other molecules of the same reactant. Once a monolayer of the reactant has been formed, the excess reactant is purged from the chamber with an inert gas such as N_2 or Ar (step 2). The counter reactant is then pulsed into the chamber, where it reacts with the layer of original reactant on the substrate (step 3), and once the surface becomes saturated with the counter reactant, the excess counter reactant is pulsed from the chamber (step 4). The surface is now primed for a new layer of reactant. This

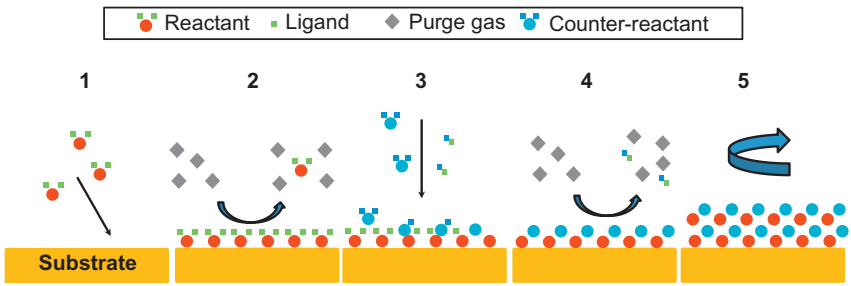

Figure 20.19 Schematic view of the one cycle for a binary material in an ALD reaction. (Reprinted from Leskelä and Ritala (2003) with permission from Royal Society of Chemistry.)

process is repeated until the desired thickness is achieved (step 5). In most cases, a complete monolayer is not deposited even when the surface is completely saturated with precursor due to various reasons such as hindrance from the precursor's ligands (Du and George, 2008). Regardless, conformal films are observed because of the self-limiting nature of the reactions.

ALD is usually performed at elevated temperatures to promote or initiate the reaction and to reduce the amount of condensed, unreacted precursor on the substrate; however, the temperature range is bounded by excess condensation or thermal activation at low temperatures and precursor degradation or desorption at high temperatures (Tanskanen et al., 2010). The temperature range where ALD can occur, the so-called "ALD window," varies between systems. Not all combinations of precursors have ALD windows, hence the precursors must be carefully chosen. In some cases, thermal energy alone is not enough to activate the reactions, and the ALD process may be assisted through the use of UV light or plasma. Plasma-enhanced ALD may expand the number of precursors that can be used, increase the growth rates, and improve the film's properties; however, it may also limit the ability to form conformal coatings over 2D nanostructures with high aspect ratios (George, 2010). One of the examples of the ALD-deposited 2D Al_2O_3 layer with thickness of ~2.6 nm achieved at CSIRO in 2014 is displayed in Figure 20.20. It is clearly shown that precise control of the deposition process enabled the structurally uniform 2D nanocrystal the relatively large scale with measured deviation in thickness of only ±0.5%.

The innate self-limiting nature of ALD endows it with the ability to produce conformal thin films, even on materials with high aspect ratios. The self-limiting nature of ALD also allows for excellent composition control, and nanolaminates, mixtures, and alloys have been formed by exploiting this characteristic (Tanskanen et al., 2010). ALD has also been used to create films that are denser and have more uniform grain sizes than available through other methods (Kim, 2011). These advantages place ALD in a unique position to address many challenges in further development of 2D semiconductors and 2D sandwich nanostructures.

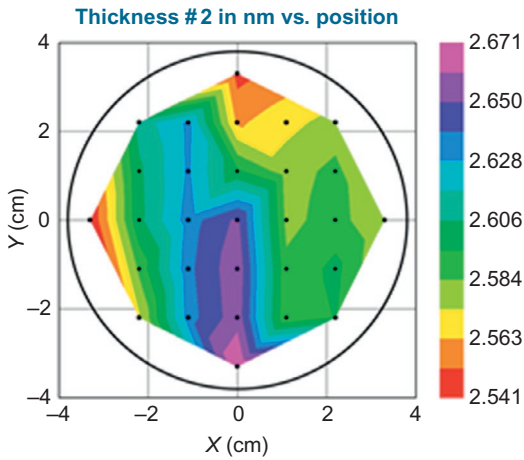

Figure 20.20 ALD-deposited 2D Al_2O_3 layer with thickness of ~2.6 nm.

Nevertheless, challenges still remain for incorporation of ALD into manufacturing. For ALD to succeed as a deposition technique, it must reach the goal of matching its existing capabilities with the current requirements of potential applications. Thus, understanding device performance and increasing efficiency are crucial considerations. Decreasing the cost of ALD in manufacturing is another important factor. ALD requires significant energy input for heating and vacuum. Consequently, the throughput is a necessary step for ALD as is its integration with existing manufacturing methods. Precursors can also be quite expensive. Therefore, reactors must be tuned to optimize use of the precursors at a larger scale. Moreover, research into new ALD precursors is another important aspect of its application, because each type of functional device has stringent manufacturing conditions that must be met. For example, many organic and hybrid solar cells require processing temperatures well below 200 °C. Temperature is also an issue for thin-film devices because it has been seen at elevated temperatures that thermal diffusion at the *p-n* junction can be detrimental to device performance. In addition, because the issues surrounding charge recombination are vital, ALD-deposited materials must be pure (i.e., without contaminants such as carbon) so that trap states are not created in the film. Finally, designs of functional devices should be environmentally friendly and minimize the use of toxic elements such as Cd, Pb, or Se and rare elements such as In, Ga, and Te (Leskelä and Ritala, 2003). Thus, studying earth-abundant and nontoxic materials will continue to be a major effort. These challenges present many opportunities, and we expect that researchers will continue to tackle these problems with the goal that 2D semiconductors will 1 day be the major supplier building blocks for global manufacturing of new generation of advanced functional devices.

20.3 Future trends

The present chapter has surveyed the recent advancements in the development of one of the fastest growing emerging fields in nanostructured semiconductors-2D nanocrystals. The thriving expansion of new capabilities of 2D semiconductors has been progressed rapidly during the last few years. While physical fundamentals for the thickness-dependent properties of this class of nanomaterials remain to be clarified, many exciting developments and groundbreaking results produced from 2011 until 2015 have already opened new and unexpected opportunities for the different practical applications.

It is not difficult to explain the increasing worldwide interest in the development of advanced functional 2D nanocrystals, because they have been considered as potential candidates for replacing the conventional microstructured materials in various applications. Today, the conventional applied and industrial sciences are approaching their limits and are inevitably seeking alternative breakthroughs. In this regard, graphene and 1D and/or 2D semiconductors represent the potential building blocks for the next generation of advanced functional electronics and devices with superior properties utilized in much smaller volumes (Zhuiykov, 2014). In this context, quazi-1D and 2D semiconductors represent an ideal channel for electrical carrier transport and are suitable for device integration (Costescu et al., 2004).

The most important lesson from the recent progress in the development of nanostructured 2D semiconductors is the fact that the results achieved so far are only a very small portion of what can be studied with respect to the universe of 2D nanocrystals. Each of them has its own unique features, complexity, architecture, and attractiveness. It is fair to say that the great field of 2D nanocrystals lies undiscovered before us.

Furthermore, the area of 2D semiconductors that can be modified and tuned to tailor the desired properties by careful chemical and molecular doping has not been explored at all. Great discoveries are expected in this area in the next few years, particularly in the field of flexible electronics. The continually evolving domain of flexible electronics promises to deliver products that are shaped, formed, and colored in ways bear little resemblance to today's rigid devices. Think roll-up TV screens, wearable devices, and paper-thin solar cells as part of our everyday lives. Given the exciting possibilities, one can expect intense consumer demand for flexible electronic products. The market will be colossal and pervasive, estimated to grow from \$16 billion in 2013 to ~\$77 billion in 2023.

Absolutely new functional opportunities can be initiated and launched if the next generation of advanced functional 3D devices can be designed. The outstanding performance of these devices can be achieved through combinatorial multistacking (in analogy with combinatorial chemistry). Considering that each of these 1D and 2D nanocrystals has a different functionality, multifunctional nanomaterials can be created with an enormous economy in terms of energy and volume. It can be envisaged that a library of 1D and 2D nanocrystals and nanosheets will be established (Orentas et al., 2012; Peng et al., 2013; Zhuiykov, 2014). From these 1D and 2D nanocrystals new 3D functional nanodevices could be designed. Using this library and advanced robotics, new 3D structures can be efficiently developed at low cost and high speed. With the help of the constructed library, the outcome would be a "nano-crystals-on-demand" strategy with attached portfolio of novel complex architectures and nanostructures possessing accurately tailored properties for different purposes and practices.

Acknowledgments

The work was supported by the Research and Development Program of both CSIRO Sensors and Sensor Networks Transformational Capability Platform (SSN TCP) and CSIRO Materials Science and Engineering Division. The author is grateful to Mr. Eugene Kats, CSIRO, for his help in preparation of materials for this chapter. The author also thanks Dr. Lachlan Hyde of the Melbourne Centre for Nanofabrication for his help, support, and invaluable information in regard to development of the ALD-produced 2D semiconductors.

References

Alexiev, V., Prins, R., Weber, T., 2000. Ab initio study of MoS_2 and Li adsorbed on the (1010) face of MoS_2. Phys. Chem. Chem. Phys. 2, 1815–1827.

Al-Khawaja, S., Kassem, M., 2012. Low-frequency dielectric response in two-dimensional layered MoO_3 system doped with Nb_2O_5 at low temperatures. Curr. Sci. India 102, 478–484.

Alsaif, M.M.Y.A., Latham, K., Field, M.R., Yao, D.D., Medehkar, N.V., Beane, G.A., Kaner, R. B., Russo, S.P., Ou, J.Z., Kalantar-zadeh, K., 2014. Tunable plasmon resonances in two-dimensional molybdenum oxide nanoflakes. Adv. Mater. 26, 3931–3937.

Ando, T., Fowler, A.B., Stern, F., 1982. Electronic properties of two-dimensional systems. Rev. Mod. Phys. 54, 437–672.

Avari, A., Cobas, E., Ogundadegbe, O., Fuhrer, M.S., 2007. Realisation and electrical characterisation of ultrathin crystals of layered transition-metal dichalcogenides. J. Appl. Phys. 101, 014507.

Bakke, J.R., Pickrahn, K.L., Brennan, T.P., Bent, S.F., 2011. Nanoengineering and interfacial engineering of photovoltaics by atomic layer deposition. Nanoscale 3, 3482–3508.

Balazsi, C., Pfeifer, J., 2002. Development of tungsten oxide hydrate phases during precipitation, room temperature ripening and hydrothermal treatment. Solid State Ion. 151, 353–358.

Balendhran, S., Ou, J.Z., Bhaskaran, M., Sriram, S., Ippolito, S., Vasic, Z., Kats, E., Bhargava, S., Zhuiykov, S., Kalantar-zadeh, K., 2012. Atomically thin layers of MoS_2 via a two step thermal evaporation–exfoliation method. Nanoscale 4, 461–466.

Balendhran, S., Deng, J., Ou, J.Z., Scott, J., Tang, J., Wang, K., Field, M.R., Russo, S., Zhuiykov, S., Strano, M., Medhekar, N., Sriram, S., Bhaskaran, M., Kalantar-zadeh, K., 2013a. Enhanced charge carrier mobility in two-dimensional high dielectric molybdenum oxide. Adv. Mater. 25, 109–114.

Balendhran, S., Walia, S., Nili, H., Ou, J.Z., Zhuiykov, S., Kaner, R.B., Sriram, S., Bhaskaran, M., Kalantar-zadeh, K., 2013b. Two-dimensional molybdenum trioxide and dichalcogenides. Adv. Func. Mater. 23, 3952–3970.

Baugher, B.W.H., Churchill, H.O.H., Yang, Y., Jarillo-Herrero, P., 2014. Optoelectronic devises based on electrically tunable *p-n* diodes in a monolayer dichalcogenide. Nat. Nanotechnol. 9, 262–267.

Berak, J.M., Sienko, M.J., 1970. Effect of oxygen-deficiency on electrical transport properties of tungsten trioxide crystals. J. Solid State Chem. 2, 109–133.

Bohr, M.T., Chau, R.S., Chani, T., Misty, K., 2007. The high-*k* solution. IEEE Spectr. 44, 29–35.

Bratschitsch, R., 2014. Monolayer diodes light up. Nat. Nanotechnol. 9 (247), 248.

Breedon, M., Spizzirri, P., Taylor, M., du Plessis, J., McCulloch, D., Zhu, J., Yu, L., Hu, Z., Rix, C., Wlodarski, W., Kalantar-zadeh, K., 2010. Synthesis of nanostructured tungsten oxide thin films: a simple, controllable, inexpensive, aqueous sol–gel method. Cryst. Growth Des. 10, 430–439.

Briggs, D., Search, M.P., 1983. Practical surface analysis by Auger and X-ray photoelectron spectroscopy. John Wiley & Sons, Chichester, New York.

Buscema, M., Barkelid, M., Zwiller, V., van der Zant, H.S.J., Steele, G.A., Castellanos-Gomez, A., 2013. Large and tunable photo-thermoelectric effect in single-layer MoS_2. Nano Lett. 13, 358–363.

Butler, S.Z., Hollen, S.M., Cao, L., Cui, Y., Gupta, J.A., Gutierrez, H.R., Heinz, T.F., Hong, S. S., Huang, J., Ismach, A.F., Johnston-Halperin, E., Kuno, M., Plashnitsa, V.V., Robinson, R.D., Ruoff, R.S., Salahuddin, S., Shan, J., Shi, L., Spencer, O.M.G., Terrones, M., Windl, W., Goldberger, J.E., 2013. Progress, challenges, and opportunities in two-dimensional materials beyond graphene. ACS Nano 7, 2898–2926.

Cartz, L., Srinivasa, S.R., Riedner, R.J., Jorgensen, J.D., Worlton, T.G., 1979. Effect of pressure on bonding in black phosphorus. J. Chem. Phys. 71, 1718–1721.

Castellanos-Gomez, A., Barkelid, M., Goossens, A.M., Calado, V.E., van der Zant, H.S.J., Steele, G.A., 2012. Laser-thinning of MoS_2: on demand generation of a single-layer semiconductor. Nano Lett. 12, 3187–3192.

Chang, M.T., Chou, L.-J., Chueh, Y.-L., Lee, Y.-C., Hsieh, C.-H., Chen, C.-D., Lan, Y.-W., Chen, L.-J., 2007. Nitrogen-doped tungsten oxide nanowires: low temperature synthesis on Si and the electrical, optical, and field-emission properties. Small 3, 658–664.

Charton, P., Gengembre, L., Armand, P., 2002. TeO_2-WO_3 glasses: infrared, XPS and XANES structural characterisations. J. Solid State Chem. 168, 175–183.

Chen, X., Zhou, Y., Liu, Q., Li, Z., Liu, J., 2012. Zhigang Zou, Ultrathin, single-crystal WO_3 nanosheets by two-dimensional oriented attachment toward enhanced photocatalystic reduction of CO_2 into hydrocarbon fuels under visible light. Appl. Mater. Interfaces 4, 3372–3377.

Chhowalla, M., Shin, H.S., Eda, G., Li, L.-J., Loh, K.P., Zhang, H., 2013. The chemistry of two-dimensional layered transition metal dichalcogenide nanosheets. Nat. Chem. 5, 263–275.

Chikan, V., Kelley, D.F., 2002. Size-dependent spectroscopy of MoS_2 nanoclusters. J. Phys. Chem. B 106, 3794–3804.

Chrissafis, K., Zamani, M., Kambas, K., Stoemenos, J., Economou, N.A., Samaras, I., Julien, C., 1989. Structural studies of MoS_2 intercalated by lithium. Mater. Sci. Eng. B 3, 145–151.

Churchill, H.O.H., Jarillo-Herrero, P., 2014. Two-dimensional crystals: phosphorus joins the family. Nat. Nanotechnol. 9, 330–331.

Coleman, J.N., Lotya, M., O'Neill, A., Bergin, S.D., King, P.J., Khan, U., Young, K., Gaucher, A., De, S., Smith, R.J., Shvets, I.V., Arora, S.K., Stanton, G., Kim, H., Lee, K., Kim, G.T., Duesberg, G.S., Hallam, T., Boland, J.J., Wang, J.J., Donegan, J.F., Grunlan, J.C., Moriarty, G., Shmeliov, A., Nicholls, R.J., Perkins, J.P., Grieveson, E. M., Theuwissen, K., McComb, D.W., Nellist, P.D., Nicolosi, V., 2011. Two-dimensional nano-sheets produced by liquid exfoliation of layered materials. Science 331, 568–571.

Costescu, R.M., Cahill, D.G., Fabreguette, F.H., Sechrist, Z.A., George, S.M., 2004. Ultra-low thermal conductivity in W/Al_2O_3 nanolaminates. Science 303, 989–990.

Das, S., Chen, H.-Y., Penumatcha, A.V., Appenzeller, J., 2013. High performance multilayer MoS_2 transistors with scandium contacts. Nano Lett. 13, 100–105.

Deb, S.K., 2008. Opportunities and challenges in science and technology of WO_3 for electrochromic and related applications. Solar Energy Mater. Solar Cells 92, 245–258.

Du, X., George, S.M., 2008. Thickness dependence of sensor response for CO gas sensing by tin oxide films grown using atomic layer deposition. Sens. Actuators B 135, 152–160.

Duan, X., Niu, C., Sahi, V., Chen, J., Parce, J.W., Empedocles, S., Goldman, J.L., 2003. High-performance thin-film transistors using semiconductor nanowires and nanoribbons. Nature 425, 274–278.

Dupin, J.C., Gonbeau, D., Vinatier, P., Levasseur, A., 2000. Systematic XPS studies of metal oxides, hydroxides and peroxides. Phys. Chem. Chem. Phys. 2, 1319–1324.

Enyashin, A.N., Seifert, G., 2012. Density-functional study of Li_xMoS_2 intercalates ($0 \leq x \leq 1$). Comput. Theor. Chem. 999, 13–20.

Enyashin, A.N., Yadgarov, L., Houben, L., Popov, I., Weidenbach, M., Tenne, R., Bar-Sadan, M., Seifert, G., 2011. New route for stabilization of 1T-WS_2 and MoS_2 phases. J. Phys. Chem. C 115, 24586–24591.

Fivaz, R., Mooser, E., 1967. Mobility of charge carriers in semiconducting layer structures. Phys. Rev. 163, 743–755.
Fontana, M., Deppe, T., Boyd, A.K., Rinzan, M., Liu, A.Y., Paranjape, M., Barbara, P., 2013. Electron–hole transport and photovoltaic effect in gated MoS_2 Schottky junctions. Sci. Rep. 3, 1634.
Galatsis, K., Li, Y.X., Wlodarski, W., Kalantar-zadeh, K., 2001. Sol–gel prepared MoO_3–WO_3 thin films for O_2 gas sensing. Sens. Actuators B: Chem. 77, 478–483.
Geim, A.K., Grigorieva, I.V., 2013. Van der Waals heterostructures. Nature 499, 419–425.
George, S.M., 2010. Atomic layer deposition: an overview. Chem. Rev. 110, 111–131.
George, S.M., Ott, A.W., Klaus, J.W., 1996. Surface chemistry for atomic layer growth. J. Phys. Chem. 100, 13121–13131.
Ghatak, S., Pal, A.N., Ghosh, A., 2011. Nature of electronic states in atomically thin MoS_2 field-effect transistors. ACS Nano 5, 7707–7712.
Granquist, C.G., 2000. Electrochromic tungsten oxide films: review of progress 1993–1998. Solar Energy Mater. Solar Cells 60, 201–262.
Gupta, T., 2009. Copper Interconnect Technology. Springer, New York, 418.
Ham, D.J., Phuruangrat, A., Thongtem, S., Lee, J.S., 2010. Hydrothermal synthesis of monoclinic WO_3 nanoplates and nanorods used as an electrocatalyst for hydrogen evolution reactions from water. Chem. Eng. J. 165, 365–369.
Heyderman, L.L., 2013. Crystal-clear order. Nat. Nanotechnol. 8, 705–706.
Hirose, T., Furukawa, K., 2003. Dielectric anomaly of tungsten trioxide WO_3 with giant dielectric constant. Phys. Status Solidi 203, 608–615.
Hu, X.K., 2008. Comparative study on MoO_3 and H_xMoO_3 nanobelts: structure and electric transport. Chem. Mater. 20, 1527–1535.
Huang, J.-K., Pu, J., Hsu, C.-L., Chiu, M.-H., Juang, Z.-Y., Chang, Y.-H., Chang, W.-H., Iwasa, Y., Takenobu, T., Li, L.-J., 2014. Large-area and highly crystalline WSe_2 monolayers: from synthesis to device applications. ACS Nano 8, 923–930.
Ishigami, M., Chen, J.H., Cullen, W.G., Fuhrer, M.S., Williams, E.D., 2007. Atomic structure of graphene on SiO_2. Nano Lett. 7, 1643–1648.
Jariwala, D., Sangwan, V.K., Lauhon, L.J., Marks, T.J., Hersam, M.C., 2014. Emerging device applications for semiconducting two-dimensional transition metal dichalcogenides. ACS Nano 8, 1102–1120.
Jeong, S., Han, J.H., Jang, J.-T., Seo, J.-W., Kim, J.G., Cheon, J., 2011. Transformative two-dimensional layered TiS_2 nanocrystals. J. Am. Chem. Soc. 133, 14500–14503.
Jiang, X., Huang, H., Prinz, F.B., Bent, S.F., 2008. Application of atomic layer deposition of platinum to solid oxide fuel cells. Chem. Mater. 20, 3897–3905.
Jones, A.M., Yu, H., Ghimire, N.J., Wu, S., Aivazian, G., Ross, J.S., Zhao, B., Yan, J., Mandrus, D.G., Xiao, D., Yao, W., Xu, X., 2013. Optical generation of excitonic valley coherence in monolayer WSe_2. Nat. Nanotechnol. 8, 634–638.
Julien, C., Sekine, T., Balkanski, M., 1991. Lattice dynamics of lithium intercalated MoS_2. Solid State Ion. 48, 225–229.
Kalantar-zadeh, K., Vijayaraghavan, A., Ham, M.H., Zheng, H.D., Breedon, M., Strano, M.S., 2010a. Synthesis of atomically thin WO_3 sheets from hydrated tungsten trioxide. Chem. Mater. 22, 5660–5666.
Kalantar-zadeh, K., Tang, J.S., Wang, M.S., Wang, K.L., Shailos, A., Galatsis, K., Kojima, R., Strong, V., Lech, A., Wlodarski, W., Kaner, R.B., 2010b. Synthesis of nanometre-thick MoO_3 sheets. Nanoscale 2, 429–433.
Kanan, S.M., Tripp, C.P., 2007. Synthesis, FTIR studies and sensor properties of WO_3 powders. Curr. Opin. Solid State Mater. Sci. 11, 19–27.

Kim, H., 2003. Atomic layer deposition of metal and nitride thin films: current research efforts and applications for semiconductor device processing. J. Vac. Sci. Technol. B 21, 2231–2261.

Kim, H., 2011. Characteristics and applications of plasma enhanced-atomic layer deposition. Thin Solid Films 519, 6639–6644.

Knoch, J., Zhang, M., Appenzeller, J., Mantl, S., 2007. Physics of ultrathin-body silicon-on-insulator Schottky-barrier field-effect transistors. Appl. Phys. A 87, 351–357.

Koski, K.J., Cui, Y., 2013. The new skinny two-dimensional nanomaterials. ACS Nano 7, 3739–3743.

Labidi, A., Jacolin, C., Bendahan, M., Abdelghani, A., Guérin, J., Aguir, K., Maaref, M., 2005. Impedance spectroscopy on WO_3 gas sensor. Sens. Actuators B: Chem. 106, 713–718.

Late, D.J., Huang, Y.-K., Liu, B., Acharya, J., Shirodkar, S.N., Luo, J., Yan, A., Charles, D., Waghmare, U.V., Dravid, V.P., Rao, C.N.R., 2013. Sensing behavior of atomically thin-layered MoS_2 transistors. ACS Nano 7, 4879–4891.

Lee, S.H., Deshpande, R., Parilla, P.A., Jones, K.M., To, B., Mahan, A.H., Dillon, A.C., 2006. Crystalline WO_3 nanoparticles for highly improved electrochromic applications. Adv. Mater. 18, 763–766.

Lee, C., Yan, H., Brus, L.E., Heinz, T.F., Hone, J., Ryu, S., 2010. Anomalous lattice vibrations of single- and few-layer MoS_2. ACS Nano 4, 2695–2700.

Lee, H.S., Min, S.W., Chang, Y.G., Park, M.K., Nam, T., Kim, J.H., Ryu, S., Im, S., 2012. MoS_2 nanosheet phototransistors with thickness-modulated optical energy gap. Nano Lett. 12, 3695–3700.

Lee, G.-H., Yu, Y.-J., Cui, X., Petrone, N., Lee, C.-H., Choi, M.S., Lee, D.-Y., Lee, C., Yoo, W. J., Watanabe, K., Taniguchi, T., Nuckolls, C., Kim, P., Hone, J., 2013. Flexible and transparent MoS_2 field-effect transistors on hexagonal boron nitride-graphene heterostructures. ACS Nano 7, 7931–7936.

Leftheriotis, G., Papaefthimiou, S., Yianoulis, P., Siokou, A., Kefalas, D., 2003. Structural and electrochemical properties of opaque sol-gel deposited WO_3 layers. Appl. Suf. Sci. 218, 276–281.

Leskelä, M., Ritala, M., 2003. Atomic layer deposition chemistry: recent developments and future challenges. Angew. Chem. Int. Ed. 42, 5548–5554.

Li, L., Wang, Y., Xie, S., Li, X.-B., Wang, Y.-Q., Wu, R., Sun, H., Zhang, S., Gao, H.-J., 2013. Two-dimensional transition metal honeycomb realized: Hf on Ir(111). Nano Lett. 13, 4671–4674.

Li, H., Duan, X., Wu, X., Zhuang, X., Zhou, H., Zhang, Q., Zhu, X., Hu, W., Ren, P., Guo, P., Ma, L., Fan, X., Wang, X., Xu, J., Pan, A., Duan, X., 2014a. Growth of alloy $MoS_{2x}Se_{2(1-x)}$ nanosheets with fully tunable chemical compositions and optical properties. J. Am. Chem. Soc. 136, 3756–3759.

Li, L., Yu, Y., Ye, G.J., Ge, Q., Ou, X., Wu, H., Feng, D., Chen, X.H., Zhang, Y., 2014b. Black phosphorus field-effect transistors. Nat. Nanotechnol. 9, 372–377.

Liao, L., Lin, Y.-C., Bao, M., Cheng, R., Bai, J., Liu, Y., Qu, Y., Wang, K.L., Huang, Y., Duan, X., 2010. High-speed graphene transistors with a self-aligned nanowire gate. Nature 467, 305–308.

Liu, L.T., Kumar, B., Ouyang, S.Y., Jing, G., 2011. Performance limits of monolayer transition metal dichalcogenide transistors. IEEE Trans. Electron Devices 58, 3042–3047.

Liu, Y.H., Porter, S.H., Goldberger, J.E., 2012. Dimensional reduction of a layered chalcogenide into a 1D near-IR direct band gap semiconductor. J. Am. Chem. Soc. 134, 5044–5047.

Livage, J., Ganguli, D., 2001. Sol–gel electrochromic coatings and devices: a review. Solar Energy Mater. Solar C 68, 365–381.

Lopez-Sanchez, O., Lembke, D., Kayci, M., Radenovic, A., Kis, A., 2013. Ultrasensitive photodetectors based on monolayer MoS_2. Nat. Nanotechnol. 8, 497–501.

Lu, J.G., Chang, P., Fan, Z., 2006. Quasi-one-dimensional metal oxide materials-synthesis, properties and applications. Mater. Sci. Eng. R 52, 49–91.

Lukowski, M.A., Daniel, A.S., Meng, F., Forticaux, A., Li, L., Jin, S., 2013. Enhanced hydrogen evolution catalysis from chemically exfoliated metallic MoS_2 nanosheets. J. Am. Chem. Soc. 135, 10274–10277.

Mak, K.F., Lee, C., Hone, J., Shan, J., Heinz, T.F., 2010. Atomically thin MoS_2: a new direct-gap semiconductor. Phys. Rev. Lett. 105, 136805.

Mora-Sero, I., Bisquert, J., 2010. Breakthroughs in the development of semiconductor-sensitized solar cells. J. Phys. Chem. Lett. 1, 3046–3052.

Mukherjee, N., Paulose, M., Varghese, O.K., Mor, G.K., Grimes, C.A., 2003. Fabrication of nanoporous tungsten oxide by galvanostatic anodization. J. Mater. Res. 18, 2296–2299.

Myron, H.W., Freeman, A.J., 1974. Electronic structure and optical properties of layered dichalcogenides TiS_2 and $TiSe_2$. Phys. Rev. B 9, 481–486.

Najmaei, S., Liu, Z., Zhou, W., Zou, X., Shi, G., Lei, S., Yakobson, B.I., Idrobo, J.-C., Ajayan, P.M., Lou, J., 2013. Vapour phase growth and grain boundary structure of molybdenum disulphide atomic layers. Nat. Mater. 12, 754–759.

Nikoobakht, B., Li, X., 2012. Two-dimensional nanomembranes: can they outperform lower dimensional nanocrystals? ACS Nano 6, 1883–1887.

Novoselov, K.S., Jiang, D., Schedin, F., Booth, T.J., Khotkevich, V.V., Morozov, S.V., Geim, A.K., 2005. Two-dimensional atomic crystals. Proc. Natl. Acad. Sci. U. S. A. 102, 10451–10453.

Orentas, E., Lista, M., Lin, N.T., Sakai, N., Matile, S., 2012. A quantitative model for the transcript of 2D pattern into functional 3D architectures. Nat. Chem. 4, 746–750.

Osada, M., Sasaki, T., 2012. Two-dimensional dielectric nanosheets: novel nanoelectronics from nanocrystal building blocks. Adv. Mater. 24, 210–223.

Ou, J.Z., Balendhran, S., Field, M.R., McCulloch, D.G., Zoolfakar, A.S., Rani, R.A., Zhuiykov, S., O'Mullane, A.P., Kalantar-zadeh, K., 2012. The anodized crystalline WO_3 nanoporous network with enhanced electrochromic properties. Nanoscale 4, 5980–5988.

Ou, J.Z., Rani, R.A., Balendhran, S., Zoolfakar, A.S., Field, M.R., Zhuiykov, S., O'Mullane, A. P., Kalantar-zadeh, K., 2013. Anodic formation of a thick three-dimensional nanoporous WO_3 film and its photocatalytic property. Electrochem. Commun. 27, 128–132.

Papageorgopoulos, C.A., Jaegermann, W., 1995. Li intercalation across and along the Van der Waals Surfaces of MoS_2 (0001). Surf. Sci. 338, 83–93.

Park, K.H., Choi, J., Kim, H.J., Oh, D.-H., Ahn, J.R., Son, S.U., 2008. Unstable single-layered colloidal TiS_2 nanodisks. Small 4, 945–950.

Peng, L., Peng, X., Liu, B., Wu, C., Xie, Y., Yu, G., 2013. Ultrathin two-dimensional MnO_2/graphene hybrid nanostructures for high-performance, flexible planar supercapacitors. Nano Lett. 13, 2151–2157.

Plashnitsa, V.V., Vietmeyer, F., Petchsang, N., Tonguing, P., Kosel, T.H., Kuno, M., 2012. Synthetic strategy and structural and optical characterisation of thin highly crystalline titanium disulfide nanosheets. J. Phys. Chem. Lett. 3, 1554–1558.

Polaczek, A., Pekala, M., Obuszko, Z., 1994. Re-entrant disordering of colloidal molecular crystals on two-dimensional periodic substrates. J. Phys. Condens. Mater. 6, 7909–7916.

Pospischil, A., Furchi, M.M., Mueller, T., 2014. Solar-energy conversion and light emission in an atomic monolayer *p-n* diode. Nat. Nanotechnol. 9, 257–261.

Puurunen, R.L., 2005. Surface chemistry of atomic layer deposition: a case study for the trimethylaluminum/water process. J. Appl. Phys. 97, 121301–121352.

Radisavljevic, B., Kis, A., 2013. Mobility engineering and a metal-insulator transition in monolayer MoS_2. Nat. Mater. 12, 815–820.
Radisavljevic, B., Radenovic, A., Brivio, J., Giacometti, V., Kis, A., 2011. Single-layer MoS_2 transistors. Nat. Nanotechnol. 6, 147–150.
Rauh, R.D., 1999. Electrochromic windows: an overview. Electrochim. Acta 44, 3165–3176.
Ross, J.S., Klement, P., Jones, A.M., Ghimire, N.J., Yan, J., Mandrus, D.G., Taniguchi, T., Watanabe, K., Kitamura, K., Yao, W., Cobden, D.H., Xu, X., 2014. Electrically tunable excitonic light-emitting diodes based on monolayer WSe_2 *p-n* junctions. Nat. Nanotechnol. 9, 268–272.
Roy, K., Padmanabhan, M., Goswami, S., Sai, T.P., Ramalingam, G., Raghavan, S., Ghosh, A., 2013. Graphene–MoS_2 hybrid structures for multifunctional photoresponsive memory devices. Nat. Nanotechnol. 8, 826–830.
Schwierz, F., 2010. Graphene transistors. Nat. Nanotechnol. 5, 487–496.
Sekine, T., Julien, C., Samaras, I., Jouanne, M., Balkanski, M., 1989. Vibrational modifications on lithium intercalation in MoS_2. Mater. Sci. Eng. B 3, 153–158.
Shpak, A.P., Korduban, A.M., Medvedskij, M.M., Kandyba, V.O., 2007. XPS studies of active elements surface of gas sensors based on WO_{3-x} nanoparticles. J. Electron Spect. Related Phenom. 156–158, 172–175.
Splendiani, A., Sun, L., Zhang, Y.B., Li, T.S., Kim, J., Chim, C.Y., Galli, G., Wang, F., 2010. Emerging photoluminescence inmonolayer MoS_2. Nano Lett. 10, 1271–1275.
Stengl, V., Henych, J., 2013. Strongly luminescent monolayered MoS_2 prepared by effective ultrasound exfoliation. Nanoscale 5, 3387–3394.
Sundaram, R.S., Engel, M., Lombardo, A., Krupke, R., Ferrari, A.C., Avouris, P., Steiner, M., 2013. Electroluminescence in single layer MoS_2. Nano Lett. 13, 1416–1421.
Suntola, T., 1989. Atomic layer epitaxy. Mater. Sci. Rep. 4, 261–312.
Sze, S.M., Kwok, K.N., 2007. Physics of Semiconductor Devices. Wiley, USA.
Takeda, Y., Kato, N., Fukano, T., Takeichi, A., Motohiro, T., Kawai, S., 2004. WO_3/metal thin-film bilayered structures as optical recording materials. J. Appl. Phys. 96, 2417–2422.
Tang, Q., Zhou, Z., 2013. Graphene-analogous low-dimensional materials. Prog. Mater. Sci. 58, 1244–1315.
Tanskanen, J.T., Bakke, J.R., Bent, S.F., Pakkanen, T.A., 2010. ALD growth characteristics of ZnS films deposited from organozinc and hydrogen sulphide precursors. Langmuir 26, 11899–11906.
Teich, D., Lorenz, T., Joswig, J.-O., Seifert, G., Zhang, D.-B., Dumitrica, T., 2011. Structural and electronic properties of helical TiS_2 nanotubes studied with objective molecular dynamics. J. Phys. Chem. C 115, 6392–6396.
Tserkovnyak, Y., 2013. An insulator-based transistor. Nat. Nanotechnol. 8, 706–707.
Vemuri, R.S., Noor-A-Alam, M., Gullapalli, S.K., Engelhard, M.H., Ramana, C.V., 2011. Nitrogen-incorporated induced changes in the microstructure of nanocrystalline WO_3 thin films. Thin Solid Films 520, 1446–1450.
Vogt, T., Woodward, P.M., Hunter, B.A., 1999. The high-temperature phases of WO_3. J. Solid State Chem. 144, 209–215.
Wagner, C.D., Moulder, J.F., Davis, L.E., Riggs, W.M., 1979. Handbook of X-ray Photoelectron Spectroscopy. Perking-Elmer Corp, New York.
Wang, Y., Ou, J.Z., Balendhran, S., Chrimes, A.F., Mortazavi, M., Yao, D.D., Field, M.R., Latham, K., Bansal, V., Friend, J.R., Zhuiykov, S., Medhekar, N.V., Strano, M.S., Kalantar-zadeh, K., 2013. Electrochemical control of photoluminescence in two-dimensional MoS_2 nanoflakes. ASC Nano 11, 10083–10093.

Wang, T., Li, J., Zhao, G., 2014. Synthesis of MoS_2 and MoO_3 hierarchical nanostructures using a single-source molecular precursor. Power Technol. 253, 347–351.

Wilcoxon, J.P., Samara, G.A., 1995. Strong quantum-size effects in a layered semiconductor: MoS_2 nanoclusters. Phys. Rev. B 51, 7299–7302.

Wilcoxon, J.P., Newcomer, P.P., Samara, G.A., 1997. Synthesis and optical properties of MoS_2 and isomorphous nanoclusters in the quantum confinement regime. J. Appl. Phys. 81, 7934–7944.

Yang, J., Voiry, D., Ahn, S.J., Kang, D., Kim, A.Y., Chhowalla, M., Shin, H.S., 2013. Two-dimensional hybrid nanosheets of tungsten disulfide and reduced graphene oxide as catalysts for enhanced hydrogen evolution. Angew. Chem. Int. Ed. Engl. 52, 13751–13754.

Ye, J.T., Zhang, Y.J., Kasahara, Y., Iwasa, Y., 2013. Interface transport properties in ion-gated nano-sheets. Eur. Phys. J.: Spec. Top. 222, 1185–1201.

Yoon, Y., Ganapathi, K., Salahuddin, S., 2011. How good can monolayer MoS_2 transistor be? Nano Lett. 11, 3768–3773.

Yu, W.J., Liu, Y., Zhou, H., Yin, A., Li, Z., Huang, Y., Duan, X., 2013. Highly efficient gate-tunable photocurrent generation in vertical heterostructures of layered materials. Nat. Nanotechnol. 8, 952–958.

Zhang, Y., Li, Z., Jia, H., Luo, X., Xu, J., Zhang, X., Yu, D., 2006. TiS_2 whisker growth by a simple vapour-deposition method. J. Cryst. Growth 293, 124–127.

Zhang, Y., Chang, T.-R., Zhou, B., Cui, Y.-T., Yan, H., Liu, Z., Schmitt, F., Lee, J., Moore, R., Chen, Y., Lin, H., Jeng, H.-T., Mo, S.-K., Hussain, Z., Bansil, A., Shen, Z.-X., 2014. Direct observation of the transition from indirect to direct bandgap in atomically thin epitaxial $MoSe_2$. Nat. Nanotechnol. 9, 111–115.

Zheng, H., Tachibana, Y., Kalantar-zadeh, K., 2010. Dye-sensitized solar cells based on WO_3. Langmuir 26, 19148.

Zheng, H., Ou, J.Z., Strano, M.S., Kaner, R.B., Mitchell, A., Kalantar-zadeh, K., 2011. Nanostructured tungsten oxide—properties, synthesis and applications. Adv. Func. Mater. 21, 2175–2196.

Zhou, K., Zhu, Y., Yang, X., Zhou, J., Li, C., 2012. Demonstration of photoluminescence and metal-enhanced fluorescence of exfoliated MoS_2. Chem. Phys. Phys. Chem. 13, 699–702.

Zhu, C., Zeng, Z., Li, H., Li, F., Fan, C., Zhang, H., 2013. Single-Layer MoS_2-based nanoprobes for homogeneous detection of biomolecules. J. Am. Chem. Soc. 135, 5998–6001.

Zhuiykov, S., 2014. Nanostructured Semiconductor Oxides for the Next Generation of Electronics and Functional Devices: Properties and Applications. Woodhead Publishing, Cambridge, UK, 484.

Zhuiykov, S., Kats, E., 2013. Atomically thin two-dimensional materials for functional electrodes of electrochemical devices. Ionics 19, 825–865.

Zhuiykov, S., Kats, E., 2014. Nanoscale investigation of electrical properties in sub-10-nm WO_3 nano-flakes via a two-step sol–gel exfoliation method. Nanoscale Res. Lett. 9, 401.